Polymer-derived carbides and carbons with and without nitrogen-doping for electrochemical energy applications

Dissertation
zur Erlangung des Grades
des Doktors der Naturwissenschaften
der Naturwissenschaftlich-Technischen Fakultät
der Universität des Saarlandes

von

Benjamin Krüner

Saarbrücken

2018

Tag des Kolloquiums: 28.11.2018

Dekan: Prof. Dr. Guido Kickelbick

Vorsitz: Prof. Dr. Wulff Possart

Berichterstatter: Prof. Dr. Volker Presser
Prof. Dr. Guido Kickelbick

Akad. Mitarbeiter: Dr. Frank Aubertin

Table of content

Acknowledgments

This PhD thesis was carried out at the INM – Leibniz Institute for New Materials in the Energy Materials Group of Prof. Volker Presser. I acknowledge funding by the German Federal Ministry for Research and Education (BMBF) in support of the nanoEES^{3D} project (award number 03EK3013) and the Minerva Foundation via the Award for Research Cooperation and High Excellence in Science (ARCHES).

I would like to express my acknowledgments to people who supported me during my time at the INM. First of all, I am very grateful for the supervision of Prof. Volker Presser who gave me the chance to work in his young, dynamic, and innovative group on highly relevant research topics. Prof. Presser was always open-minded for new ideas and help me to try new things. He especially supported me during manuscript preparation for publications and created a family-friendly atmosphere in his group.

I also thank Prof. Guido Kickelbick for being my scientific advisor and for reviewing my thesis. We had fruitful discussions, and the work with him and his group was always a pleasure.

I learned a lot during my time at the Energy Materials Group at the INM from many helpful people and I would like to thank all current and former members, namely Dr. Mesut Aslan, Mathias Baltes, Öznil Budak, Dr. Soumyadip Choudhury, Simon Fleischmann, Dr. Ingrid Grobelsek, Dr. Nicolas Jäckel, Dr. Choonsoo Kim, Juhan Lee, Valeria Lemkova, Dr. Eunho Lim, Rafael Linzmeyer Zornitta, Pau Massuti-Ballester, Jemma Rowlandson, Anna Schreiber, Hwirim Shim, Pattarachai Srimuk, Aura Tolosa, Dr. Daniel Weingarth, Mathias Widmaier, Dr. Marco Zeiger, and Yuan Zhang. We had a wonderful time together which I will always remember.

I also acknowledge the support from people from the INM and UdS namely, Tobias Dörr, Robert Drumm, Andrea Jung, Rudolf Karos, Dr. Marcus Koch, Christina Odenwald, Karl-Peter Schmitt, Jana Staudt, the INM workshop, and the administration department. I thank Ralph Schäfer from Allnex Germany GmbH for the supply of phenolic resins and fruitful discussions.

I always enjoyed working together with our collaboration partners. Only with your help, it was possible to answer certain questions we had. My work benefited from the joined work together with Prof. Jürgen Janek, Prof. Oskar Paris, Prof. Bernhard Roling, Prof. Bernd Smarsly, Prof. Matthew Suss, Dr. Lars Borchardt, Dr. Christian Prehal, Dr. Anjte Quade, Dr. Joachim Sann, Felix Badaczewski, Steffen Emge, and Torben Pfaff.

Last but not least, I want to thank my family for supporting me in the past years. You helped me to concentrate on my work with many small and big things.

Abstract

Porous carbon materials are widely used in electrochemical applications for intermediate energy storage or water desalination. This work aimed to synthesize nanoporous carbons with well-controlled properties (e.g., specific surface area, average pore size, chemical composition) to correlate them to the performance in electrochemical applications (e.g., supercapacitors, LiS batteries). Especially the surface chemistry of highly porous carbons with different oxygen and nitrogen groups influences the electrochemical behavior.

The carbon materials were obtained from polymeric precursors, including phenolic resins and polysilsesquioxanes. A physical activation with CO_2 or NH_3 that additionally introduced nitrogen groups was applied to adjust the porosity of the phenolic resin-derived carbons. Thereby, it was possible to obtain materials with different properties from the same precursor.

The polysilsesquioxanes were first pyrolyzed and then thermally treated with chlorine gas to produce carbide-derived carbons. The porosity was tuned by the composition of the precursor and the synthesis temperature. The intermediate product (silicon oxycarbide) is also an attractive electrode material for Li-ion batteries. It was shown that optimization of the carbon content resulted in extended cycling stability.

Zusammenfassung

Poröse Kohlenstoffe werden häufig in elektrochemischen Anwendungen zum Speichern von Energie oder zur Wasserentsalzung verwendet. Ziel dieser Arbeit war die Synthese von nanoporösen Kohlenstoffen mit definierten Eigenschaften (z.B. spezifische Oberfläche, Porengröße, chemische Zusammensetzung) um ihren Einfluss auf verschiedene elektrochemische Anwendungen (z.B. Superkondensatoren, LiS Batterien) zu untersuchen. Besonders die Oberflächenchemie von hochporösen Kohlenstoffen mit unterschiedlichen Sauerstoff- und Stickstoffgruppen beeinflussen das elektrochemische Verhalten.

Die Kohlenstoffmaterialien wurden aus verschiedenen makromolekularen Vorstufen (Phenolharze und Polysilsesquioxane) hergestellt. Die physikalische Aktivierung mittels CO_2 oder NH_3, welche ebenfalls Stickstoffgruppen erzeugt, erlaubten eine hohe Kontrolle über die Porosität der phenolharz-abgeleiteten Kohlenstoffe. Dies erlaubt die Synthese von Materialien mit unterschiedlichen Eigenschaften aus den gleichen Vorstufen.

Die Polysilsesquioxane wurden zunächst pyrolysiert und thermisch in Chlorgas behandelt um karbid-abgeleitete Kohlenstoffe herzustellen. Durch die Zusammensetzung der Vorstufe und die Synthesetemperatur wurde die Porosität eingestellt. Die Zwischenprodukte (Siliziumoxykarbid) sind ebenfalls attraktive Elektrodenmaterialien für Li-Ionen Batterien. Durch die Optimierung des Kohlenstoffanteils konnte dabei die Zyklenstabilität deutlich verbessert werden.

Abbreviations

A	surface area of the electrode
ACN	acetonitrile
C	capacitance
CDC	carbide-derived carbon
CDI	capacitive deionization
Ch.	chapter
CV	cyclic voltammogram
d	charge separation distance
DEM	1,2-dimethoxyethane
DMC	dimethyl carbonate
DOL	1,3-dioxolane
EC	ethylene carbonate
EDLC	electrical-double-layer-capacitor
E_{el}	stored electrical energy
EMIM-BF_4	1-ethyl-3-methyl imidazolium tetrafluoroborate
EMIM-TFSI	1-ethyl-3-methyl imidazolium bis(trifluoromethanesulfonyl)imidate
HL	distance of closest approach of charges
IH	inner Helmholtz layer
IUPAC	International Union of Pure and Applied Chemistry
LiTFSI	lithium bis(trifluoromethane-sulfonyl)imidate
MTMS	methyltrimethoxysilane
NaCMC	sodium carboxymethylcellulose
OH	outer Helmholtz layer
ORMOSIL	organically modified silica
PAPTMS	(3-(phenylamino)propyl)-trimethoxysilane
PDC	polymer-derived ceramic
PTMS	phenyltrimethoxysilane
Q	accumulated charge
RTIL	room temperature ionic liquid
SiOC	silicon oxycarbide
SSA	specific surface area
TEA-BF_4	tetraethylammonium fluoroborate
TPD	thermal programmed desorption
U	applied voltage
VTMS	vinyltrimethoxysilane
XPS	X-ray photoelectron spectroscopy
ε_0	dielectric constant of vacuum
ε_r	dielectric permittivity of the isolator
Φ	potential
*	Stern layer

1. Motivation

In 2008, the US National Academy of Engineering selected 14 grand challenges for engineering, including the improvement of urban infrastructure, secure cyberspace, and prevention of nuclear terror.[1] Two other problems concern the power supply to stop global warming, namely, make solar energy economically viable and provide energy from nuclear fusion.[1] **Fig. 1A** illustrates the power demand for a generalized household and the electrical power produced by a solar cell on a sunny day. There is an extended mismatch between the power demand and its supply that mandates intermediate energy storage or additional power sources like wind or fossil energy. A stationary electrochemical energy storage device could store excess power produced by photovoltaic systems during the day and release them usable when the demand exceeds its production. These electrochemical energy storage devices must be produced economically and ecologically for a large-scale application. Since present-day technology fails to reach desired performance metrics, further improvements are needed.

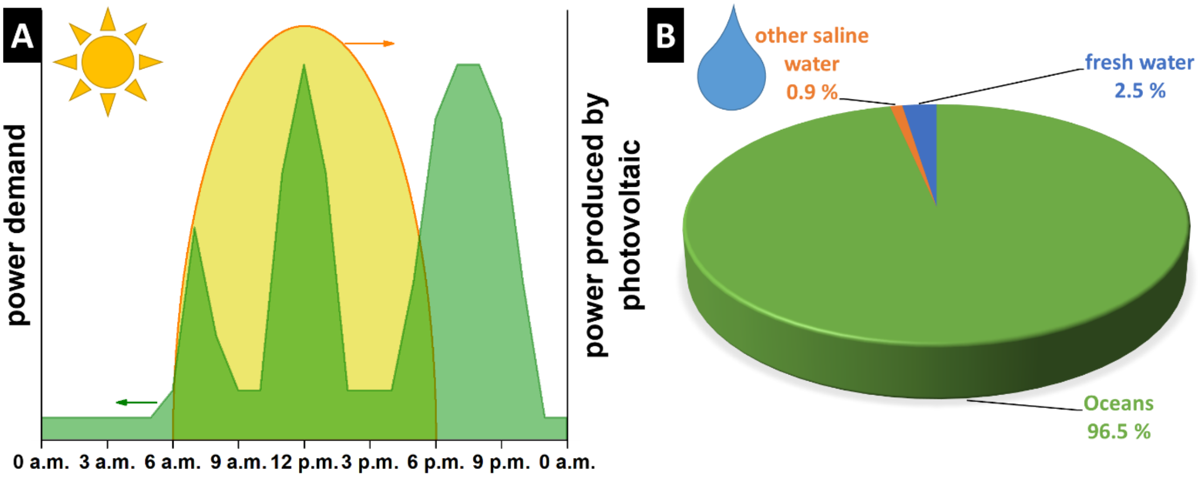

Figure 1: (A) The power demand of a generalized household and power produced by photovoltaic on a sunny day and (B) amount of fresh water on earth compared to saline water with data from Ref. [2].

Another challenge selected by the US National Academy of Engineering is the accessibility of clean water since one out of six people worldwide lacks access to clean drinking water.[1] It is also needed in large scales for the production of food and other goods. More than 97 % of the water on earth is saline water as visualized in **Fig. 1B**. Therefore, advanced desalination techniques are required to provide access to clean drinking water. One out of many desalination techniques is the capacitive deionization (CDI), where the adsorption of ions on the surface of porous materials is triggered after applying an electric potential difference.[3] Thereby the salt concentration of the solution is reduced, which could be used to provide drinking water. In summary, advanced porous carbon materials offer the potential to be used to stabilize the power supply, when they are used in an energy storage device, and to produce fresh water with filtration and desalination techniques.[3-6]

2. Introduction

Electrochemical energy storage devices are commonly used in applications like mobile phones, laptops, remote controls, (electric) vehicles, medical aids, and measuring instruments. Different applications exhibit different requirements on the energy storage device, like high energy, high power, or a long lifetime. Various batteries and supercapacitors fulfill the several requests and complement each other. Supercapacitors on the one side operate at high powers and at relatively low energy, while lithium-ion batteries have a much higher specific energy but a lower specific power, which is shown in **Fig. 2A**. Low specific energy leads to a large mass of the battery to store the required energy. Therefore, the selection of electrochemical energy storage technologies is based on the requirements of the particular applications. A stationary energy storage device, for example, can be quite heavy because it is not transported. An electric vehicle, on the other hand, requires a minimized battery mass because it contributes to the mass of the car and thus directly influences its range. The energy consumption for an electric vehicle like the BMW i3 is ~13.5 kWh per 100 km.[7] **Fig. 2B** shows the space and mass of electrochemical energy storage devices required for an electric vehicle to drive 100 km. Supercapacitors and lead-acid batteries have a very low specific energy, which results in a large device volume and mass. Therefore, the use of electric vehicles which only store the energy capacitive is limited to buses and metro trains, which can be recharged at each stop.[8-9] Supercapacitors are additionally used in combination with other techniques to provide high power for a short time to increase the acceleration in electric vehicles.[10] Nevertheless, the prevalent drive technology is based on lithium-ion batteries, owing to their low volume and mass requirement. A further spatial or gravimetric reduction can only be achieved with new high energy material types, for example, as presented by the lithium-sulfur battery.

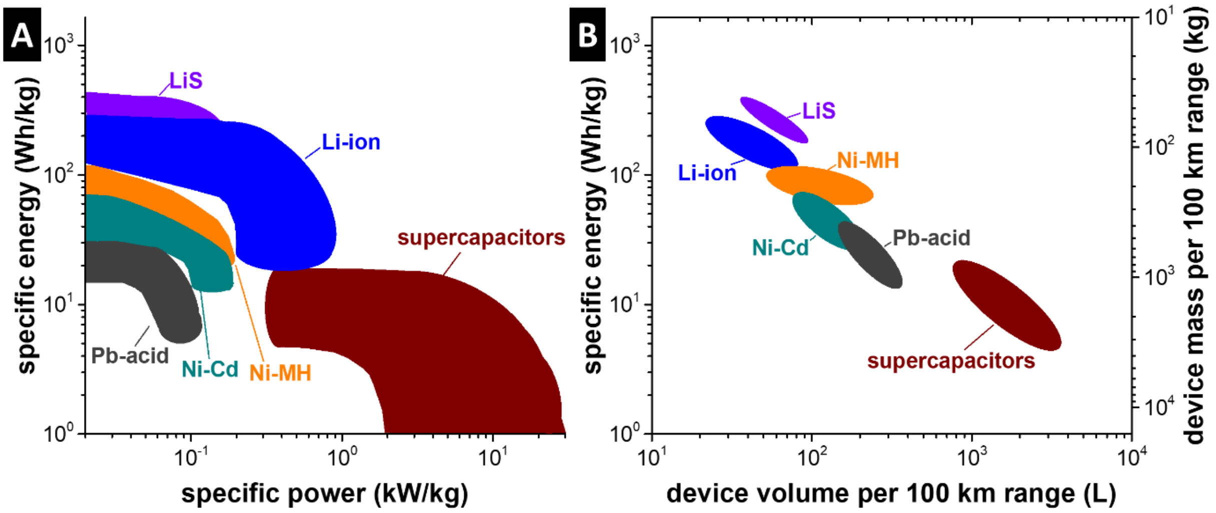

Figure 2: (A) Ragone chart of selected electrochemical energy storage devices and (B) device volume and mass per 100 km range of an electric vehicle (17.5 kWh) with data from Ref. [11-13].

Carbon materials are used in many electrodes for different electrochemical energy storage devices as a conductive additive, intercalation, or adsorption material, owing to their beneficial electrical conductivity, low density, abundance, and non-toxicity.[14-18] The carbon modification has a big influence on its materials properties. **Fig. 3** gives an overview on the density, hardness, transparency, electric resistance, and elastic modulus of diamond, graphite, and glassy carbon.[19-22]

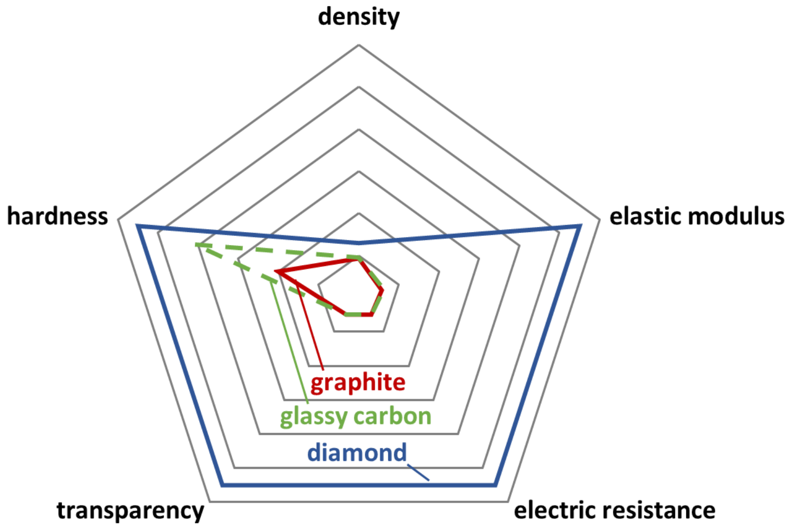

Figure 3: Radar graph of different properties of various carbon materials according to data from Ref. [19-22].

These carbon materials have a relatively low density ranging from ~1.9 g/cm^3 for graphite to 3.5 g/cm^3 for diamonds, due to their crystal structure.[22] Diamonds are sp^3-hybridized which leads to an extraordinary hardness combined with high electrical resistance and transparent appearance.[21-22] Graphite has many opposite properties compared to diamonds: it is sp^2-hybridized, electrically conductive, mechanically soft, and optically non-transparent.[21-22] Glassy carbon has similar materials properties than graphite, because consists of disordered sp^2-hybridized carbon atoms, but it is much harder than graphite.[19-20, 22]

Diamonds, graphite, and glassy carbon are in general non-porous materials with a low specific surface area (SSA). The SSA of carbon materials can be expanded by reducing the particle size and the formation of pores which leads to large SSA of up to 3000 m^2/g.[14] The high surface area materials combined with low electrical resistance and density are interesting for electrochemical energy applications like supercapacitors or CDI.[14, 23]

2.1. Porous carbon materials

Porous carbon materials can be classified by the kind of porosity, the precursor, or the synthesis method. The International Union of Pure and Applied Chemistry (IUPAC) distinguishes three different types of pores based on their size, namely, micropores, mesopores, and macropores.[24] Microporous materials have a pore size below 2 nm, while mesopores range from 2 nm to 50 nm, and macropores are larger than 50 nm.[24]

Carbon materials can also be differentiated based on the precursor. The three main groups of carbon precursors are ceramics (e.g., metal carbides), organic polymers, or biomass (which often contain polymers as well). Examples of biomass-derived carbon materials are carbonized coconut shells[25] or lignin[26]. These materials have usually a low porosity after pyrolysis which is increased with a physical or chemical activation step. Common polymers to produce carbons are phenolic resins,[27-28] polyacrylonitrile,[29] or pitch[30]. The porosity of polymer-derived carbon materials is also often increased by an additional activation step.[29-30] An alternative method to obtain a highly porous polymer-derived carbon material is the use of a template, which is initially filled and later removed during the pyrolysis or in a separate step.[31-32] Another carbon precursor is the family of metal carbides, like SiC or TiC, or carbonitrides/carboxides, like SiCN or SiOC.[4, 33-35] The crystal structure maintains carbon and non-carbon atoms. The removal of the latter usually directly introduces micropores, which makes an additional activation step unnecessary. The details of the synthesis of carbide-derived carbons will be explained in chapter 2.1.2.

The type of porous carbon can also be classified based on the synthesis method. The term "activated carbon" refers to porous carbon obtained by so-called activation of an otherwise poorly porous or non-porous material.[25-26, 28, 33, 36] One can be distinguished between a physical activation, where carbon is partially removed by a gaseous reactant or a chemical activation, where liquid or solid reactants produce the porosity.[30] The specifics of the physical and chemical activation are further discussed in chapter 2.1.1.

Another synthesis method to produce porous carbons uses templates, and we can differentiate between soft- and hard-templated-carbon materials.[31-32] Soft-templates are usually polymers or surfactants which co-assembly with the carbon precursor, and they often decompose in the following pyrolysis.[32, 35, 37] Hard-templates like zeolites or porous SiO_2 are usually infiltrated with small polymers or monomers which crosslink within the template.[31, 38] The carbonization of the polymers is carried out in the present of the hard-template. This method includes an additional step to remove the template with reactive chemicals (e.g., $HF_{(aq)}$).[31] However, some hard-templates can also be removed at high temperatures with gaseous reactants (e.g., $Cl_{2(g)}$) during the carbonization.[38] Thereby the number of synthesis steps is reduced, and additional washing to remove the HF or other acids from the carbon surface is not necessary. The salt-templating represents a combined approach of the chemical activation and the templating method.[39] Thereby, the salt crystals (e.g., LiCl, NaCl, or $ZnCl_2$) serve as a template, and some ions interact with the carbon during carbonization and produce a microporosity. The remaining salt can easily be removed by washing the porous carbon with water. Nevertheless, a combination of various synthesis methods with a carbon precursor is often applied to optimize the properties of the carbon material for certain applications.

2.1.1. Synthetic organic polymers as carbon precursor

Carbon materials can be derived from numerous synthetic and biomass related organic polymers. This work focuses on the use of synthetic polymers that are carbonized at high temperatures under an inert atmosphere. Thereby, small organic compounds, often containing heteroatoms such as oxygen or nitrogen, are released from the sample which leads to a precursor-dependent mass loss. **Table 1** summarizes the carbon yield of selected precursors treated at high temperatures. These values are approximate ones, and the carbon yield of a certain polymer can deviate due to a strong depends on the polymer chain length and the synthesis conditions. Biomass is also often used as a carbon source and consists of various low- and high-molecular organic compounds and have in general a relatively low carbon yield (12-40 mass%). The most synthetic polymers have a carbon yield of 35-55 mass%. In general, a high aromatic content is beneficial for an efficient synthesis, and phenolic resins (resol and novolac) have one of the highest carbon yields of up to 55 mass%, only surpassed by certain pith phases with up to 60 mass%.

Table 1: Carbon yield of different polymeric carbon (including biomass) precursors after pyrolysis at high temperatures.

carbon precursor	**carbon yield after pyrolysis (mass%)**	**carbonization temperature (°C)**	**Ref.**
poly(furfuryl alcohol)	35	800	[40]
polyacrylonitrile	45	600	[41]
polyaniline	33-45	800	[42-43]
resol	55	800	[44]
novolac	45-55	800-900	[45-46]
pitch	35-60	1000	[47]
cellulose	12	800	[48]
coconut shell	25	800	[49]
lignin	40	750	[50]
tobacco	22	750	[51]

Phenolic resins can be distinguished as resol or novolac, which are both produced by the co-polymerization of phenol and formaldehyde.[52-53] A scheme of the resol synthesis is shown in **Fig. 4**. The reactants can attach to various active sites, which leads to the formation of different oligomers. One possibility is exemplified in **Fig. 4**. In a first step, deprotonation of the phenol hydroxyl function produces a phenoxide anion ($C_6H_5O^-$), promoted via basic catalysis (**Fig. 4A**).[52-53] Electron delocalization statistically activates different reactive sites (2, 4, and 6) that enable the electrophile addition of formaldehyde (**Fig. 4B**). The formed hydroxymethyl phenols pre-condensates at around 60 °C to oligomers (**Fig. 4C**) that crosslink via condensation at around 95 °C and establish a polymeric network (**Fig. 4D**).[52-53] A change of the synthesis conditions led to various chain length and connections with different chemical and physical properties. A significant difference between resol and novolac is that the resol does not need a crosslinking agent to crosslink, due to the reactive hydroxymethyl groups.[52-53]

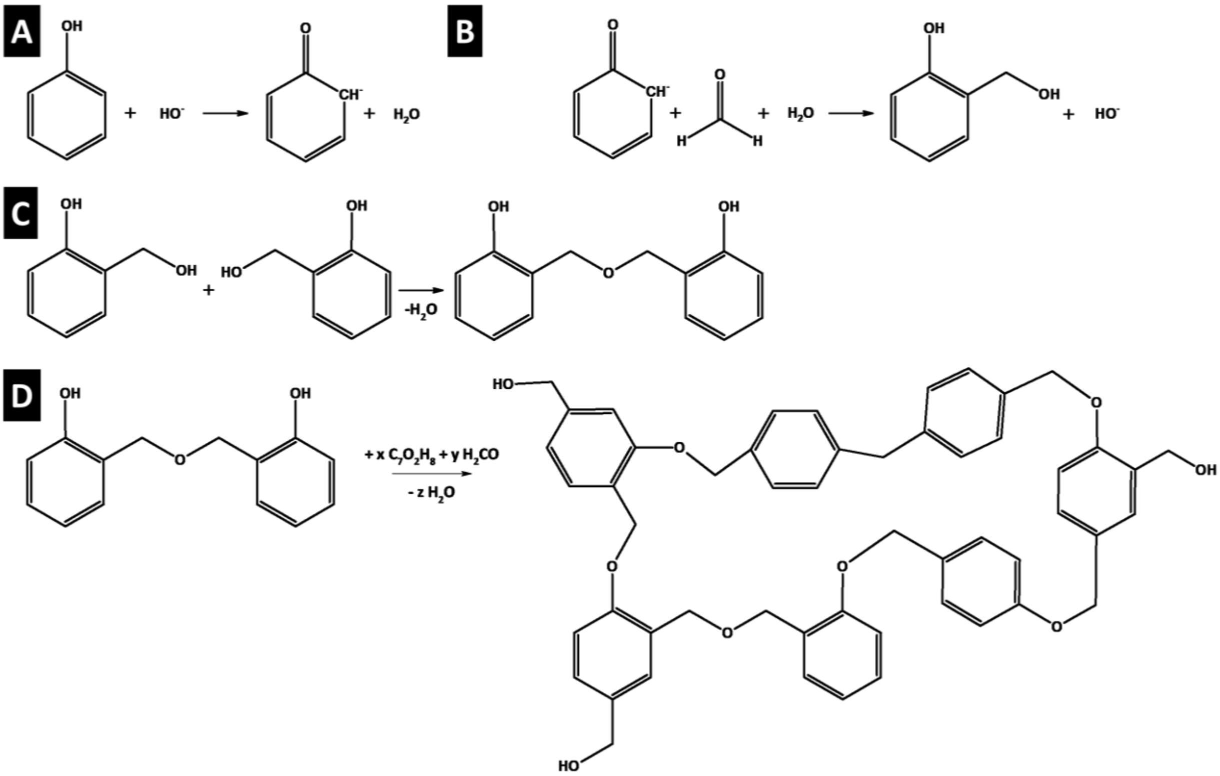

Figure 4: Synthesis pathway of a resol. (A) deprotonation of the phenol, (B) reaction with formaldehyde, (C) pre-condensation reaction at around 60 °C, and (D) formation of a polymeric network by condensation according to Ref. [52-53].

The synthesis of novolac includes an acidic catalyzed reaction (oxalic acid or hydrochloric acid) as shown in **Fig. 5**. In contrast to the resol synthesis, the acid protonates with the formaldehyde (**Fig. 5A**) to produce methylol cation ($^+CH_2OH$).[52-53] This cation undergoes a nucleophilic reaction with the phenol preferentially towards para- and ortho-methylolphenol (**Fig. 5B**).[52-53] Then, the acidic catalyst forms a methylene cation that condenses via dehydrogenation to novolac oligomers (**Fig. 5C**).[52] These oligomers require the addition of a crosslinking agent to enable network formation.[52-53] The most common crosslinking agent for the novolac synthesis is hexamethylenetetramine which decomposes to dimethylolamine. The dimethylolamine reacts with the aromatic groups of the novolac and forms a polymeric network (**Fig. 5D**).[52-53]

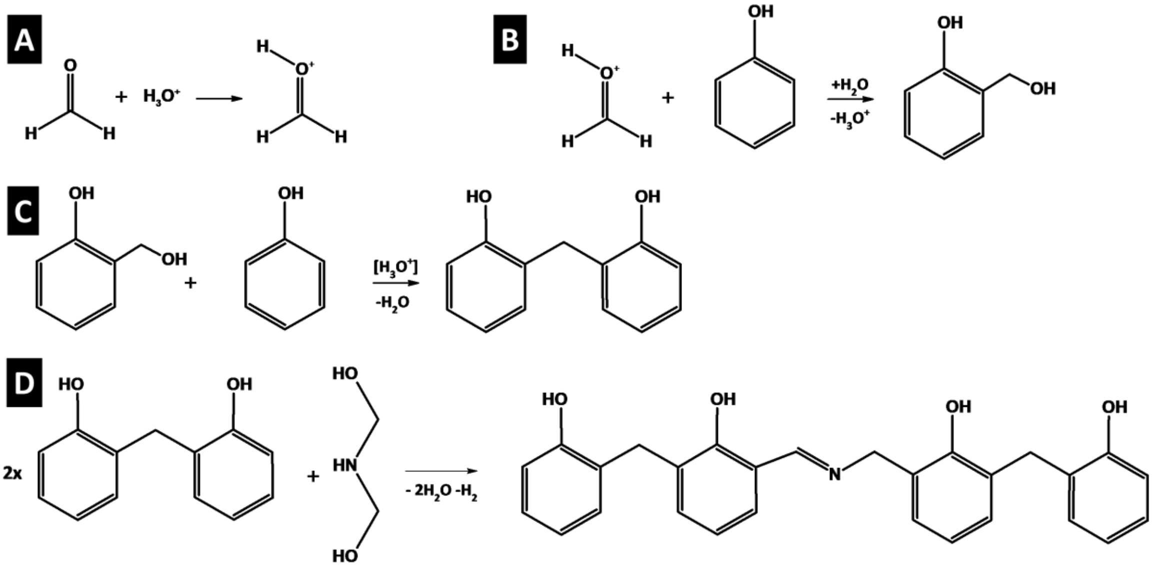

Figure 5: Synthesis pathway of a novolac. (A) formation of methylol cation, (B) reaction of the methylol cation with phenol, (C) formation of novolac oligomers via a condensation reaction, and (D) crosslinking reaction of the novolac with dimethylolamine according to Ref. [52-53].

The carbonization of a phenolic resin towards porous carbon materials is generally carried out by pyrolysis at high temperatures in an inert atmosphere. It has been shown that low temperatures lead to an incomplete graphitic carbon structure, mostly comprises amorphous carbon.[27] Higher temperatures increase the mobility of the carbon atoms, which favors the degree of carbon ordering.[54] The pyrolysis of phenolic resins can be classified in three (partially overlapping) phases: I. crosslinking via condensation at 200-500 °C, II. breaking of crosslinking bonds (i.e., amino, methylene, and oxygen groups) at 400-800 °C, and III. dehydrogenation of the benzene ring at 560-900 °C.[55]

The mass loss during those steps by the release of small groups can produce pores in the pyrolyzed carbon. These pores are in the sub-nanometer range, and the porosity is rather low, which makes an activation step necessary to enlarge the specific surface area and the total pore volume.[45] Both chemical and physical activation methods are suitable for phenolic resin-derived carbons. The chemical activation process requires the use of chemicals like KOH, K_2CO_3, $AlCl_3$, $ZnCl_2$, $CuCl_2$, $FeCl_3$, or H_3PO_4.[56-59] The activation mechanism is different for each reactant and the obtained pore structure also varies.[58] Therefore, an optimization of the carbon material with varying reactants for the chemical activation can be quite challenging, but the synthesis procedure for all reactants is quite similar.[58] The less porous or non-porous carbon material is first impregnated with a solution that contains the activation species (e.g., KOH). During evaporation of water, the activation reactant is statistically distributed on the carbon surface. The mixture is then heated up to high temperatures typically in the range of 700-

1000 °C. After cooling, washing is required to remove the remaining salt until a neutral pH is obtained. The synthesis of the chemically activated carbon samples is finished after water evaporation.

KOH and K_2CO_3 are the most common salts used for the chemical activation following mostly identical reaction pathways.[57, 59] The activation via KOH comprises three steps: formation of K_2CO_3 (**Eq. (1)**), carbon oxide formation by the decomposition of K_2CO_3 with carbon at around 480 °C (**Eq. (2)**), and evolution of CO by reactions of K_2CO_3 and K_2O above 650 °C (**Eq. (3-4)**).[59-62]

$$4\ KOH_{(s)} + {=}CH_{2(s)} \rightarrow K_2CO_{3(s)} + K_2O_{(s)} + 3\ H_{2(g)} \tag{1}$$

$$K_2CO_{3(s)} + C_{(s)} \rightarrow 2K_{(s)} + CO_{(g)} + CO_{2(g)} \tag{2}$$

$$K_2O_{(s)} + C_{(s)} \rightarrow 2K_{(s)} + CO_{(g)} \tag{3}$$

$$C_{(s)} + CO_{2(g)} \rightleftharpoons 2CO_{(g)} \tag{4}$$

Eq. (2-4) indicates that the Boudouard equilibrium plays a significant role for the chemical activation as well as for the physical activation with CO_2. The gaseous CO_2 reacts with the solid towards thermodynamically favored CO at elevated temperatures above 700 °C.[61] Next to the temperature also the activation time, the flow pattern of the gas in the furnace, and the flow rate of the gas influence the activation.[28] Longer activation and a lower flow rate usually increase the porosity due to the longer dwell time of the reactive gas.[28]

Physical activation requires fewer steps since a dry carbon powder is usually heated up in a furnace and treated with a gaseous atmosphere which increases the porosity.[45] Therefore, no additional washing or neutralization is needed which reduces the synthesis steps and costs. A synthesis involving only solid and gaseous reactants can also be implemented efficiently in a chemical plant.[63]

Gases like H_2O, O_2, H_2, and NH_3 can also be used for the physical activation of carbon.[45] All physical activation methods aim to transfer the solid carbon to gaseous compounds reducing the yield and enlarging the porosity. The chemical reactions for the activation with H_2O, O_2, and H_2 are shown below in **Eq. (5-7)**, where gaseous CO, CO_2, or CH_4 are produced.[45] The required temperature for each activation gas is different, based on their particular reactivity. CO_2 activation is usually carried out at 800-1000 °C,[28, 45] while the activation in more reactive air or oxygen (O_2) is performed at only 350-550 °C.[64]

$$C_{(s)} + H_2O_{(g)} \rightleftharpoons CO_{(g)} + H_{2(g)} \tag{5}$$

$$C_{(s)} + O_{2(g)} \rightleftharpoons CO_{2(g)} \tag{6}$$

$$C_{(s)} + 2\ H_{2(g)} \rightleftharpoons CH_{4(g)} \tag{7}$$

Another gas that can be used for physical activation is NH_3 which decomposes at high temperatures in the first step to NH_2 and NH (**Eq. (8)**).[65] These molecules have reactive free radicals and electron pairs which react with the carbon surface (**Eq. (9)**). The nitrogen functionalities decompose again at high temperatures (>700 °C) to different nitrogen-containing products like HCN (**Eq. (10)**).[66-67] Also hydrogen is evolved during the activation with NH_3 which can also react with the carbon producing CH_4 as mentioned before (**Eq. (7)**).[68]

$$3\ NH_{3(g)} \rightleftharpoons 2\ NH_{2(g)} + NH_{(g)} + 2\ H_{2(g)} \tag{8}$$

$$C_{(s)} + NH_{(g)} \rightleftharpoons CNH_{(s)} \tag{9}$$

$$CNH_{(s)} \rightleftharpoons HCN_{(g)} \tag{10}$$

In conclusion, polymers like phenolic resins are well suited as carbon precursor due to the high carbon yield and processability because they are fusible and soluble in many solvents. An activation step is usually necessary to produce a large porosity, which is favorable for applications like as electrode material in supercapacitors.

2.1.2. Carbide-derived carbon

Other well-suited inorganic carbon precursors are metal carbides,[69] carbonitrides,[70] or oxycarbides[71]. Carbide-derived carbon (CDC) is produced by the removal of the metal atom, which leaves a pore within the carbon.[4] The metal can be removed by gaseous halogens (F_2, Cl_2, Br_2, or I_2) or by a hydrogen halide (e.g., HF, HCl).[4] The most common method is the removal of metals with gaseous chlorine at high temperatures.[4, 72] Chlorine gas reacts with a binary carbide to metal chloride and carbon as mentioned in **Eq. (11)** for metals with a valence of four. The metal atoms and the carbon within a metal carbide are mixed on an atomic scale, and selective removal of the metal leads to small pores in the (sub)nanometer range.[4] The pore structure is mainly influenced by the structure of the metal carbide and the synthesis temperature.[4, 69]

$$M(IV)C_{(s)} + 2\ Cl_{2(g)} \rightarrow M(IV)Cl_{4(g)} + C_{(s)} \tag{11}$$

Various metal carbides have been investigated for the synthesis of CDCs like SiC,[33] Fe_3C,[73] ZrC,[74] TiC,[69, 75] VC,[76] or Ti_3SiC_2,[77] among others.[4] Also, silicon-based polymers like polysilsesquioxanes are suited to produce CDCs when they are transformed to a silicon oxycarbide (SiOC).[71] An advantage of these polymeric precursors is that they can be processed in various shapes as they are soluble or liquid before crosslinking.[78-79] Crosslinking connects the oligomers to form large high-molecular-weight polymeric networks.

The variety of organosilicon polymers like polyborosilanes, polysilazanes, or polysilsesquioxanes provides an array of chemical composition and structure of the polymer-derived ceramics (PDC).[78] These polymers are commonly synthesized by sol-gel processes, where silicon alkoxides form a network by an acidic or base catalyzed hydrolysis and condensation reaction.[78, 80-81] An example of the sol-gel process is shown in **Fig. 6** for trialkoxysilane that forms an organically modified silica (ORMOSIL) network. It is also possible to use several different silicon alkoxides, which can introduce multiple functional groups in the polymer. The sol-gel reaction often leads to a formation of oligomers, which have to be crosslinked by an additional crosslinking agent like, hexachloroplatinate(IV),[79] zirconium acetylacetonate,[82] or zinc acetylacetonate,[83] which leads to an additional synthesis step, often associated with introducing impurities to the synthesis products.

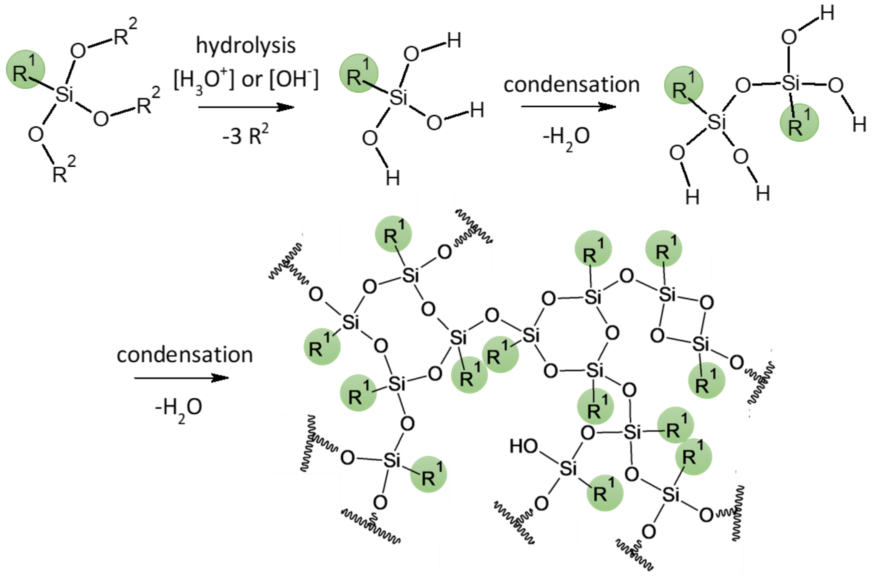

Figure 6: Synthesis of polysilsesquioxanes via sol-gel processing.

A highly crosslinked network is essential to prevent the softening of the particles and to maintain the morphology during the pyrolysis whereby SiOC ceramics are formed.[79, 83] Otherwise, the SiOC form large monoliths which have to be milled before they can be further processed.[71] The maintained morphology after CDC synthesis is one key advantage enabling the synthesis of complex structures, like free-standing fiber mats, aerogels, or spheres.[4, 79, 83-84]

The SiOC structure and properties strongly depend on the pyrolysis temperature.[85-86] The polymeric network is not entirely crosslinked after the sol-gel process or the reaction with a crosslinking agent. This leads to further condensation during the pyrolysis at temperatures below 500 °C, characterized by the evolution of H_2O.[87-88] A dehydrocarbonation with a larger mass loss takes place from 500 °C to ~800 °C.[87-88] Beyond 1000 °C, $SiO_{2(1-x)}C_x$ undergoes phase separation, forming domains of SiO_2, SiC, and C.[89] The SiOCs produced at these temperatures are characterized by small amorphous silicon oxide domains in the nanometer regime, which are surrounded by nanocrystalline graphite domains as shown in **Fig. 7**.[85] The arrangement of these materials on a nanometer scale creates unique properties. These SiOCs show a viscoelastic behavior, due to the graphitic domains and the electrical conductivity highly increases along with the carbon content.[86, 90] The carbon domains transition at high temperatures from turbostratic carbon towards graphene layers by growth and ordered stacking.[85] Pyrolysis temperatures above 1300 °C lead to a carbothermal reduction which results in the formation of crystalline silicon carbides.[91-92] Therefore, the pyrolysis temperature for SiOCs is often carried out in the range of 900-1300 °C. The optimum pyrolysis temperature for SiOCs as Li-ion anode material is around 1100 °C, where graphitic domains can be obtained that improve the conductivity while no crystalline SiC is formed.[91]

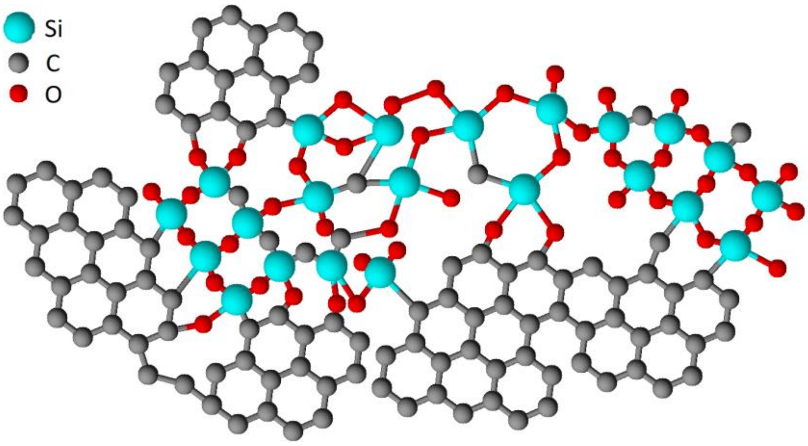

Figure 7: An exemplary structure of a SiOC ceramic with a large graphitic content.

The synthesis of SiC-CDC with gaseous chlorine (**Eq. (12)**) is well studied also because of the valuable silicon tetrachloride as product, which was first established in 1918.[4, 93-94] Thereby, the carbide is heated up to a synthesis temperature (>600 °C) before an excessive amount of chlorine is added.[4] Higher temperatures up to 1200 °C leads to higher yields, a higher graphitic ordering, and higher pore volume with larger average pore sizes.[4, 69] The synthesis mechanism of the production of SiOC-CDC is less studied, and further investigations have to verify the suggested reaction per **Eq. (13)**. It is likely that also silicon tetrachloride is one of the byproducts by the reaction of SiOC with Cl_2. The yield of the reaction is lower than the carbon content, which suggests that also carbon is removed.[88] It is possible that the oxygen could be released by the formation of CO and CO_2 depending on the synthesis temperature.

$$SiC_{(s)} + 2\ Cl_{2(g)} \rightarrow SiCl_{4(g)} + C_{(s)} \tag{12}$$

$$(SiO_{2-x}C_x + y\ C_{free})_{(s)} + 2\ Cl_{2(g)} \rightarrow SiCl_{4(g)} + z\ C_{(s)} + i\ CO_{(g)} + j\ CO_{2(g)} \tag{13}$$

Depending on the process parameters, various carbon structures, such as turbostratic carbon, amorphous carbon, onion-like carbon, polyhedral carbon, carbon-nanotubes, graphitic carbon, and nanodiamonds, have been identified in CDCs.[95] In addition to sp^2-hybridized carbon, also an sp^3-

hybridization can be found as minor carbon phase.[95] The high porosity hinders the formation of large graphitic domains. Therefore, nanocrystalline graphitic carbon is the most discovered carbon modification for CDCs synthesized at around 1000 °C.[35]

2.1.3. Nitrogen-doped carbon

Doping graphene with heteroatoms (e.g., nitrogen) can benefit the electrochemical properties, for instance via increasing the conductivity and the specific capacitance, by modifying the electronic structure.[96-98] Nitrogen-doped carbons also form strong N-S bonds with the polysulfides in a LiS battery, which reduces the detrimental polysulfide shuttling.[99-100]

Nitrogen-doped carbon materials may contain different types of nitrogen groups.[101-103] **Fig. 8A** illustrates the structural formula of nitrogen groups in a graphene layer. Nitrogen-doping in this context means that the nitrogen atom is replacing a carbon atom in the graphitic structure.[101] Graphitic nitrogen (or quaternary nitrogen) is surrounded by three carbon atoms within a graphene layer.[101] Pyridinic nitrogen, pyrrolic nitrogen, and pyridine oxide groups also replace carbon atoms in a graphitic structure, and at least one of their electrons contributes to the aromatic π system.[101] They are typically located on the edge of a graphene plane and have only two carbon neighbors.[101] Pyridinic nitrogen groups donate one p-electron to the aromatic π system and have an additional electron pair.[101] Pyridine oxide also contributes with one electron to the aromatic system, while the electron pair establishes a bond to oxygen.[101] Pyrrolic nitrogen bonds next to the carbon atoms to a hydrogen atom and contributes two electrons to the π system.[101]

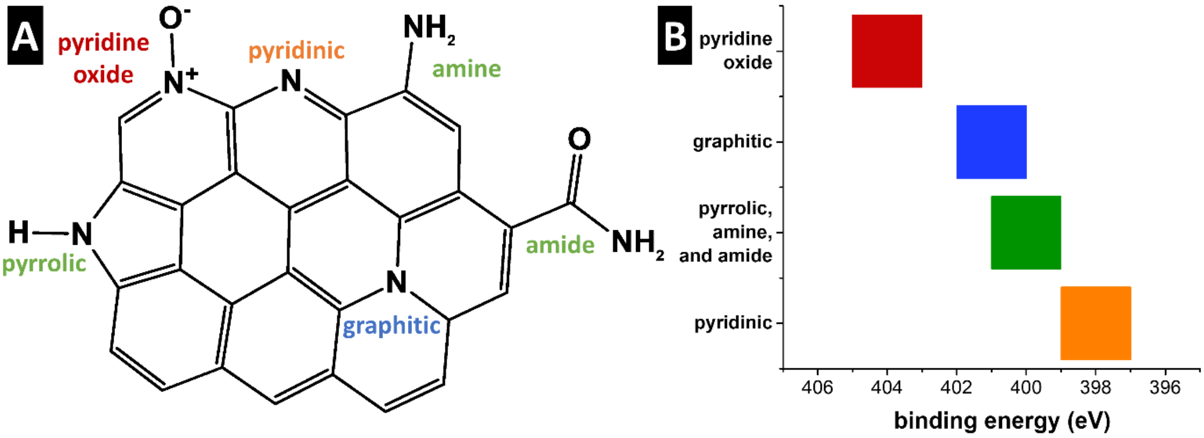

Figure 8: The structural formula of several nitrogen groups in a graphitic structure (A) and binding energy measured by XPS of each group according to the Ref. [102-103] (B).

The aforementioned nitrogen groups can be considered as nitrogen-doping groups; in addition, also the formation of nitrogen functional groups can be found in nitrogen-containing carbon materials. These functional groups (amine and amide) are located on the surface, and they do not contribute with one of their electrons to the aromatic π system. The identification of nitrogen groups in carbon materials is often carried out with X-ray photoelectron spectroscopy (XPS). The binding energies of the aforementioned nitrogen groups are shown in **Fig. 8B**. Pyrrolic, amine, and amide groups have similar binding energy that impedes clear identification.[102-103] The binding energy of graphitic and pyridinic nitrogen is also close to the value for the pyrrolic, amine, and amide groups.[102-103] The close binding energy combined with broad peaks make identification of nitrogen groups via XPS quite challenging also considering that this technique is highly surface-sensitive with an information depth of only a few nanometers. Therefore, other methods like thermal programmed desorption (TPD) may be needed to complement the XPS analysis.

There is a large number of synthesis methods to produce nitrogen-doped carbons, which can be classified as pyrolysis of nitrogen-containing carbon precursors,[104-106] post-synthesis treatment of a carbon material with a nitrogen source,[65-66, 107-108] or in-situ pyrolysis of carbon precursors in nitrogen-containing atmospheres[109]. Suited nitrogen-containing carbon precursors for the direct synthesis are melamine resin,[104-105, 110] polypyrrole,[111] glucosamine,[112] polyaniline,[43] or biomass[57, 113]. The nitrogen content is reduced after the pyrolysis at high temperatures, while the ratio of graphitic to other nitrogen groups increases.[111-114] Further activation steps to increase the porosity may reduce the amount of nitrogen.[114] Therefore, a templating method may be more attractive for nitrogen-containing precursors. A post-synthesis treatment of porous carbon materials is well suited for activated and templated carbon materials. Common liquid or gaseous reactants for this methods are NH_3,[66] HCN,[65] urea,[107] or HNO_3[108]. Post-synthesis treatments often additionally form nitrogen functionalities instead of pure nitrogen-doping, especially when they are carried out at low temperatures.[66, 114] In-situ pyrolysis in nitrogen containing atmospheres, like NH_3, combines the physical activation according to **Eq. (8-10)** with the incorporation of nitrogen in the carbon structure and reduces the number of individual synthesis steps.[109] A formation of nitrogen-functionalities and nitrogen-doping depending on the synthesis temperature can be obtained by the in-situ synthesis, which makes this method attractive for further studies.

2.2. Electrochemical applications

2.2.1. Supercapacitors

A supercapacitor is an electrochemical energy storage device, which provides high specific powers but low specific energies compared to state-of-the-art Li-ion batteries, as shown in **Fig. 2**.[11, 18] The most common kind of supercapacitors is the electrical-double-layer-capacitor (EDLC) that stores energy by the formation of an electrical double-layer.[115] This is accomplished by electrosorption of ions from an electrolyte at the fluid-solid interface on the surface of the electrode.[115] These non-Faradaic reactions on the interface are much faster than the intercalation of ions in a bulk material, which leads to a high specific power of supercapacitors compared to Li-ion batteries (further discussed in chapter 2.2.3.).[116] Another kind of supercapacitors are pseudocapacitors, where a surface or surface near faradaic reaction leads to an enhanced specific energy combined with a capacitor-like behavior.[18] Depending on the operational parameters, supercapacitors typically combine a long cycling performance stability and high Coulombic efficiency.[115-116]

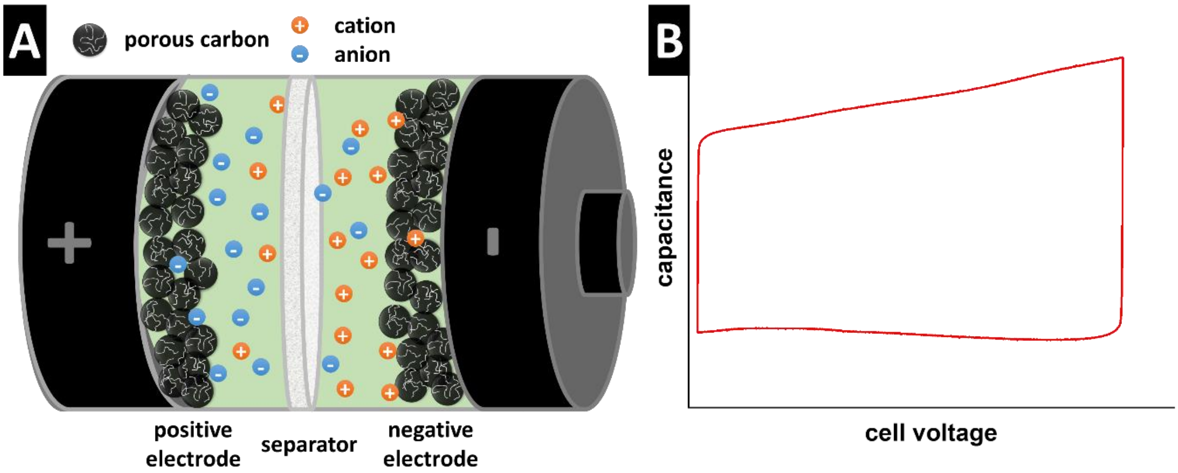

Figure 9: Schematic cell model (A) and typical cyclic voltammogram (B) of a symmetric supercapacitor with porous carbon particles as the electrode material.

A scheme of an EDLC cell is shown in **Fig. 9A**, where two porous carbon electrodes face each other with a non-conductive separator in-between. The residual space in the cell is filled with an ion-containing electrolyte. The ions move toward the electrodes when a cell voltage is applied and are electro-adsorbed on the electrode surface. **Fig. 9B** shows a typical rectangular cyclic voltammogram (CV) of a supercapacitor and the absence of redox peaks. The capacitance of a classical capacitor increases linearly to the surface area according to **Eq. (14)**.[117] Therefore, a high surface area is needed to achieve a large charge storage capacity in an EDLC. Highly porous carbon materials which can have specific surface areas of up to 3000 m^2/g and sufficient electrical conductivity are well suited as the electrode material for supercapacitors.[18]

$$C = \frac{Q}{U} = \frac{\varepsilon_0 \cdot \varepsilon_r \cdot A}{d} \tag{14}$$

with C: capacitance, Q: accumulated charge, U: applied voltage, ε_0: dielectric constant of vacuum, ε_r: dielectric permittivity of the isolator, d: charge separation distance, and A: surface area of the electrode.[117]

Generally, smaller pores yield a larger specific surface area. Yet, too small pores may become too small for certain ions to fit in.[118-119] For example, tetraethylammonium tetrafluoroborate (TEA-BF_4) is a common salt used in organic electrolytes with a cation diameter of 0.67 nm and an anion diameter of 0.45 nm.[120] The diameters of the solvated ions are even larger, for example, 1.30 nm and 1.16 nm for TEA^+ and BF_4^-, dissolved in acetonitrile (ACN), respectively.[121] Pores smaller than the ionic diameters do not contribute towards the storage of ions by electrosorption.[118]

Aqueous electrolytes have the advantage that the ionic diameters are typically smaller (e.g., 0.23 nm sodium cation[122]), but the disadvantage of a smaller electrochemical stability window of only 1.23 V.[18] It can be expanded up to 2.1 V by an asymmetrical cell design and pH variations on the positive and negative electrode.[123-125] A wide electrochemical stability window of an electrolyte is essential since the stored electrical energy (E_{el}) in **Eq. (15)** is proportional to the square of the applied voltage.[18, 117]

$$E_{el} = \int U\,dQ = \frac{1}{2} C \cdot U^2 \tag{15}$$

with E_{el}: stored electrical energy, U: applied voltage, Q: accumulated charge, C: capacitance.[117]

An alternative to aqueous and organic electrolytes with their limited stability window of ~1.2 V and ~2.7 V, respectively, are room temperature ionic liquids (RTILs).[18, 126] These latter are molten salts which have a higher ionic concentration than aqueous or organic electrolytes. Many of these RTILs, like 1-ethyl-3-methyl imidazolium tetrafluoroborate (EMIM-BF_4), are stable up to 3.5 V.[126] Nevertheless, there are still many open questions regarding the freezing, and the electrosorption mechanism of ionic liquids in carbon nanopores.[127]

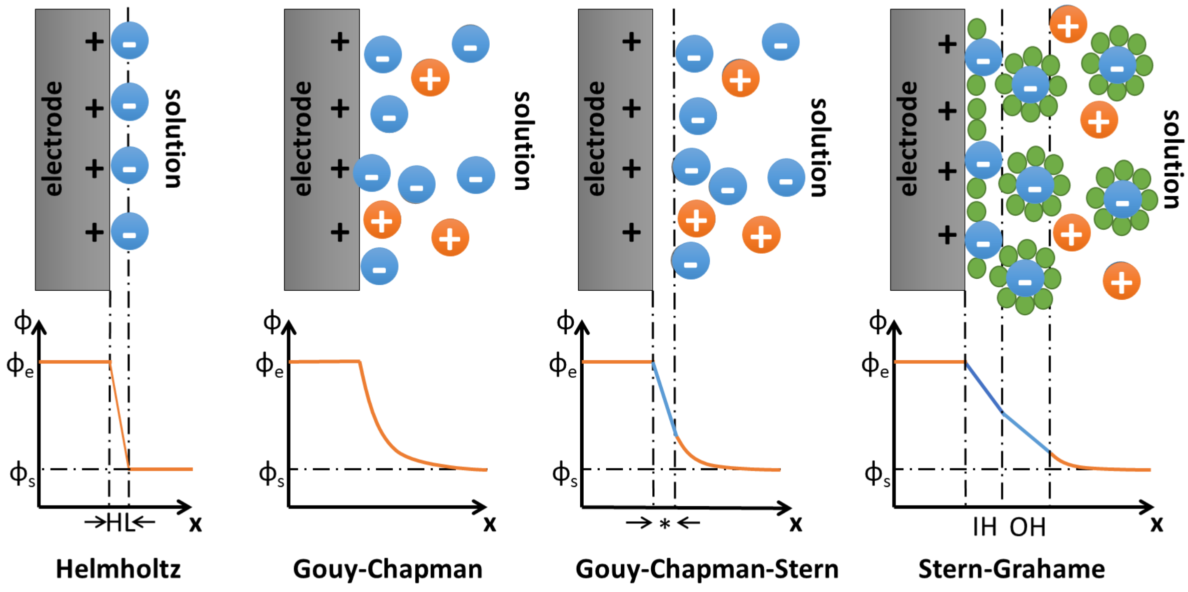

Figure 10: Models to describe the electrical double-layer formation at the electrode-electrolyte interface, with Φ: potential; Φ_e: potential at the electrode; Φ_s: potential in the solution; x: distance from electrode; HL: distance of closest approach of charges (ionic radius); *: Stern layer; IH: inner Helmholtz layer; OH: outer Helmholtz layer.

Several models have been developed over time to quantify the electrical double-layer, and some of these are shown in **Fig. 10**. Helmholtz described the electrical double-layer as two static layers of opposite charge.[128] He proposed that the distance between the electrode and the ions is similar to the ionic radius and that the voltage drops linearly across the interface. Gouy and Chapman revised the model of Helmholtz by considering the thermal fluctuation, the applied voltage, and the concentration of the ions, which leads to an exponential decrease of the potential.[129-130] Otto Stern combined the Helmholtz model with the Gouy-Chapman model by introducing the so-called Stern layer close to the electrode where ions are absent to overcome the issue in the model of Gouy and Chapman where ions are approximated as volume-free point-charges.[131] The solvation of ions leads to a charge screening which reduces the electron density, as considered in the Stern-Grahame model.[132] It introduces an inner Helmholtz layer where the ions are desolvated and adsorbed directly on the electrode and an outer Helmholtz layer where the solvated ions are adsorbed on top of the first layer. The electric potential across the inner and outer Helmholtz layer drops linearly with different slopes, while a diffuse layer on top of the outer layer shows an exponential potential drop like in the Gouy-Chapman model. These models consider a planar surface, but it is more accurate to describe a nanopore as cylinder or 3D pore structure.[133-135] Huang et al. proposed that the stored ions inside a cylindrical pore can be described as an electric double-cylinder capacitor for mesopores or electric wire-in-cylinder capacitor for micropores.[133] A modeling of these complex systems with the ions confined in pores is often carried out via molecular dynamic computer simulations.[134, 136]

2.2.2. Capacitive deionization

Ion electrosorption can also be applied to desalinate water.[3, 137] The process of capacitive deionization (CDI) removes ions from an electrolyte by immobilizing them via the formation of an electrical double-layer at the fluid/solid interface of the porous electrode material with the aqueous medium.[3, 137-138] The principles for CDI are similar to these of supercapacitors, which means that highly porous and conductive materials, like porous carbons, are well-suited electrodes.[3, 137] While the electrolyte of a supercapacitor is highly concentrated (~1 mol/L) to provide sufficient ion mobility and to prevent the emergence of ion depletion, the electrolyte used for CDI is low-concentration brackish water (~5 mmol/L).[3, 139] The desalination of brackish water with CDI is attractive because less energy is needed to remove a low number of ions compared to other desalination methods.[3] The lower salt concentration used for CDI changes the charge storage process, and we have to consider co-ion expulsion and counter-ion adsorption. Non-permselective ion swapping happens at low cell voltages, where cations (Na^+) and anions (Cl^-) replace each other inside the pores.[140-141] Thereby, no additional ions are removed out of the solution.[140] Higher cell voltages align with a larger total amount of transferred charge; at low molar concentration, this translates to a transition of non-permselective ion swapping to permselective counter-ion electro-adsorption.[140-141] Too high cell voltages may lead to parasitic Faradaic reactions which increases the leakage current and oxidizes the carbon electrode.[3, 140]

A schematic CDI setup is depicted in **Fig. 11**. It consists of one reservoir for brackish and one for remediated (fresh) water. Brackish water flows through the CDI cell were the ions are adsorbed when applying an electric potential. The produced fresh water is collected in the remediated water reservoir. The electrodes recover their desalination capacity after subsequent discharging or voltage reversal. That solution increases its salt concentration during the electrode recovery, and it has to be collected separately. The energy is also partly recovered by the release of the ions.[139] A new desalination cycle can begin with brackish water after electrode regeneration via discharging.

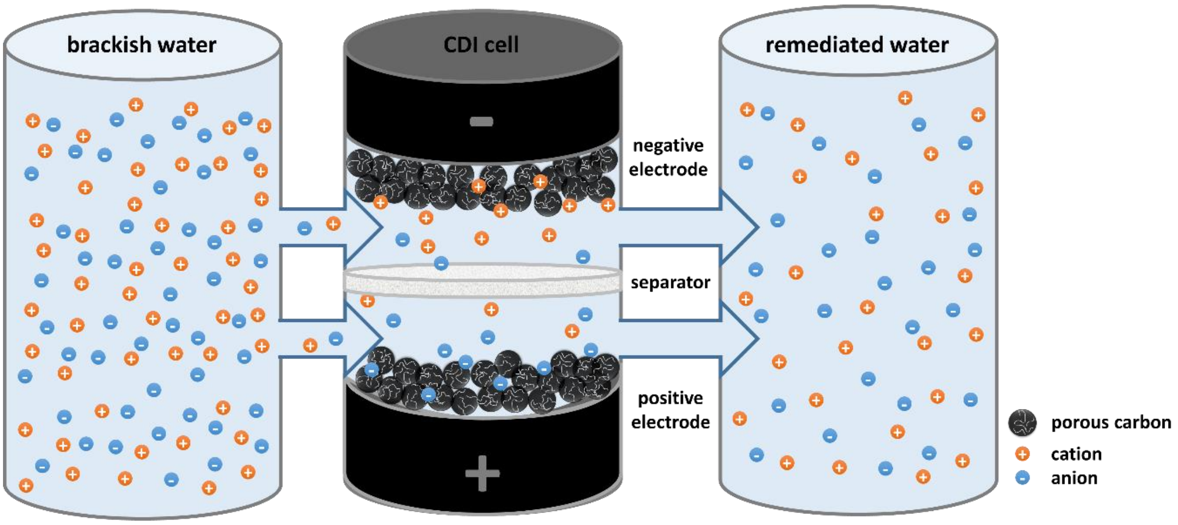

Figure 11: Schematic CDI set-up with the brackish water tank on the left, the CDI cell in the middle, and the remediate water tank on the right.

Anion and cation exchange membranes are often used to separate the electrodes from the electrolyte, which reduces the carbon oxidation which increases the lifetime of the carbon electrodes, and the added permselectivity enhances the desalination capacity.[3] The electrode material should have a high pore volume consisting of micropores because their contribution towards the salt removal capacity is larger compared to meso- and macropores.[138, 142] Next to a high porosity also the surface groups of the carbon material influences the performance of a CDI cell.[43, 139, 143] This regards the wetting behavior, the reaction mechanism, the open circuit potential, and the electrode balancing to optimize the CDI process.[43, 139, 143] Surface groups can also adsorb ions due to their chemical charge; these ions can be released by applying a cell voltage, which (depending on the sign and amount of the charge) leads to an inverse CDI peak reducing the salt adsorption capacity and efficiency in conventional symmetrical CDI experiments.[144] An asymmetrical CDI cell or inverted CDI system may benefit from inverse CDI peaks and enhance the performance.[143, 145]

Also other materials, like layered transition metal carbides (MXenes) or TiO_2/C hybrids, have been used in the past few years to improve the stability of the electrodes and the salt removal capacity.[137, 146] Such materials capitalize on the enhanced ion storage capacity inherent to some Faradaic processes and enhanced electrochemical stability. These materials are very promising for future desalination technologies and open the field for hybrid CDI and Faradaic deionization.[43, 137]

2.2.3. Lithium-ion batteries

Lithium-ion batteries are the most commonly used battery types due to their high specific energy, high efficiency, and long lifetime.[147] The set-up of a Li-ion battery is shown in **Fig. 12A**, where two electrodes face each other with a separator in between. The free space in the battery is filled with a lithium-containing electrolyte, like $LiPF_6$ dissolved in a mixture of ethylene carbonate and dimethyl carbonate.

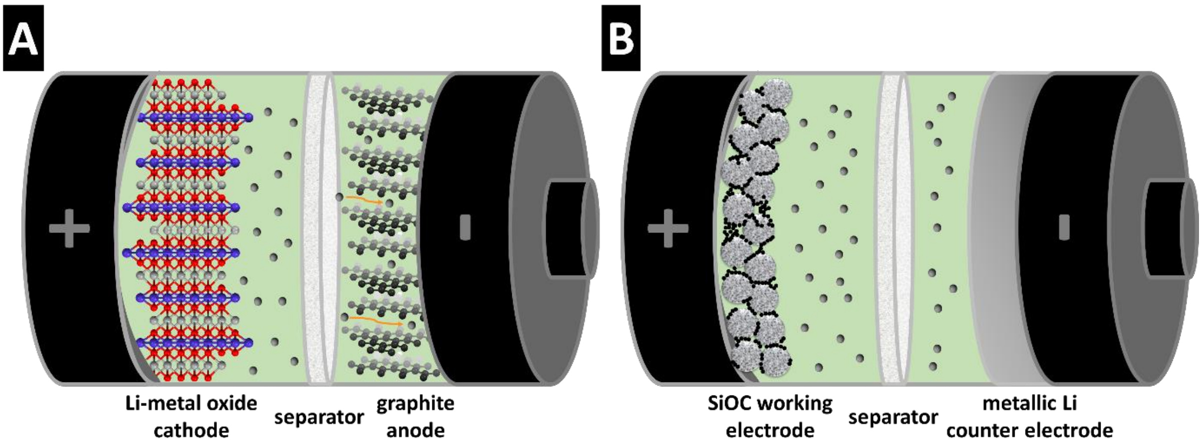

Figure 12: Schematic model of a conventional Li-ion battery with lithium metal oxide as the cathode and graphite as the anode (A) and a half-cell model with a SiOC working electrode and metallic lithium as the counter electrode (B).

The electrode materials in a Li-ion battery determine amongst other things the specific energy. $LiCoO_2$ as intercalation cathode material as for Li-ion batteries was investigated in the early 1980s by the group of John Goodenough.[148] Today, common cathode materials are lithium metal oxides, like $LiCoO_2$, $LiNiO_2$, $LiMn_2O_4$, $LiFePO_4$, or a mixture thereof.[147, 149-151] The electrochemical reactions of the Li-ion battery which has $LiCoO_2$ as the cathode and graphite as the anode are provided in **Eq. (16-18)**.[147, 152] The lithium ions are released from the metal oxide (cathode) during charging and intercalate in the graphitic carbon (anode). Thereby, the graphite is reduced, while the $LiCoO_2$ is oxidized to $Li_{(1-x)}CoO_2$ (with x ~0.5).[147, 152]

$$\text{Cathode: } LiCoO_2 \rightleftharpoons Li_{(1-x)}CoO_2 + x\,Li^+ + x\,e^- \tag{16}$$

$$\text{Anode: } C_6 + x\,Li^+ + e^- \rightleftharpoons Li_xC_6 \tag{17}$$

Cell reaction: $C_6 + LiCoO_2 \rightleftharpoons Li_xC_6 + Li_{(1-x)}CoO_2$ (18)

The theoretical capacities of some cathode and anode materials are listed in **Table 2**. These selected cathode materials have a theoretical capacity up to 272 mAh/g.[150] The actual specific capacity of a Li-ion battery is generally much lower because the lithium metal oxide cannot be completely delithiated and other components of the cell, like the separator, current collector, polymer binder, and conductive additive increase the weight of the whole device. Therefore, it is common to normalize the capacity to the active mass of the electrode to compare different electrode materials for one battery or electrode type. A comparison of various energy storage devices should be normalized to the mass of the whole device, for example, as illustrated in the Ragone plot depicted in **Fig. 2A**. The increase of the capacity of batteries can be obtained by optimization, for example by reducing the mass of the inactive material, or using electrode materials with higher capacities.

Table 2: The theoretical capacity of selected cathode and anode materials for Li-ion batteries.

	material	**theoretical specific capacity (mAh/g)**	**Ref.**
cathode	lithium cobalt oxide ($LiCoO_2$)	272	[150]
	lithium nickel oxide ($LiNiO_2$)	192	[151]
	lithium manganese oxide ($LiMn_2O_4$)	148	[149]
	lithium iron phosphate ($LiFePO_4$)	170	[147]
anode	lithium (Li)	3862	[153]
	graphite (C)	372	[154]
	lithium titanate (LTO, $Li_4Ti_5O_{12}$)	175	[153]
	silicon (Si)	4200	[154]
	silicon oxycarbide (SiOC)	372-1300	[155]

Graphite is the most popular anode material for Li-ion batteries, and it has a theoretical capacity of 372 mAh/g.[154] Metallic lithium anode has a theoretical specific capacity of 3862 mAh/g, but it is highly flammable and may present severe safety concerns.[5, 153] Another high-energy alternative for the anode is silicon, which has a theoretical capacity of 4200 mAh/g.[154] In contrast to graphite or the layered lithium metal oxides where Li^+ intercalates, silicon forms an alloy with Li^+ and results in $Li_{22}Si_5$ when it is fully lithiated (**Eq. (19)**). Consequently, silicon expands massively by 400 %, which leads to a pulverization of the electrode over time and drastically reduces the lifetime.[154, 156]

$5\ Si + 22\ Li^+ + 22\ e^- \rightleftharpoons Li_{22}Si_5$ (19)

Another promising anode material for Li-ion batteries is SiOC, which was investigated in the past years.[91, 155] The theoretical specific capacity of these materials strongly depend on the chemical composition ($SiO_{(2-2x)}C_x+C_{free}$) and structure.[155] It is in between the values of graphite and Si with a proposed maximum of 1300 mAh/g.[155] The graphitic domains of the SiOC increase the electrical conductivity and lead to a viscoelastic behavior, which mitigates electrode pulverization.[86, 90] Nevertheless, the reaction mechanism of SiOC with lithium in a Li-ion battery is still not fully understood, and the vast variety of SiOC materials and structures complicates the identification of individual processes.[91, 155]

2.2.4. Lithium-sulfur batteries

The cathode of a state-of-the-art Li-ion battery consists of lithium metal oxides, which are expensive, rare, and they have a low theoretical specific capacity (**Table 2**).[157] Beyond reversible Li^+ intercalation between two electrodes, other lithium battery concepts capitalize on conversion reactions. One of them is the lithium-sulfur (LiS) battery, in which the lithium reacts with molecular sulfur to lithium sulfide and lithium polysulfides (Li_2S, Li_2S_2, …, Li_2S_8) according to **Eq. (20)**.[5] Thereby, maximum 16 electrons are transferred per 1 sulfur molecule which leads to a high theoretical capacity of 1672 mAh/g.[5]

$$S_8 + 16\,Li^+ + 16\,e^- \rightleftharpoons 8\,Li_2S \qquad (20)$$

A typical CV of a LiS battery is shown in **Fig. 13B** where two peaks occur during discharge at ~2.4 V and ~2.1 V vs. Li/Li^+ and one peak during charge at ~2.5 V vs. Li/Li^+. Several intermediates species (lithium polysulfides) are formed at different potentials. The peak during discharge at ~2.4 V vs. Li/Li^+ indicates the oxidation of the sulfur molecule (S_8) by the lithium ions to longer polysulfides (Li_2S_{4-8}).[158-159] The formation of Li_2S and Li_2S_2 takes place at ~2.1 V vs. Li/Li^+.[160] These reactions overlap during the charging cycle, and only one peak at ~2.5 V vs. Li/Li^+ can be observed.[161]

Sulfur as a cathode material provides high capacity, is abundant, cost-attractive, and low-toxic.[5] Nevertheless, the low electrical conductivity of sulfur and the soluble intermediates (lithium polysulfides) are the main disadvantages.[5] A conventional approach to overcome these issues is the confinement of sulfur in a conductive matrix.[5] Porous carbon materials are well suited as sulfur host for LiS batteries due to their high conductivity, low weight, and high porosity. Various microporous,[162-163] mesoporous,[38] and hierarchical porous carbon composites[164-166] have been investigated as sulfur host. The confinement of sulfur and some polysulfides also reduces the polysulfide shuttling which is one of the main causes for the reduced lifetime of LiS batteries.[5] During polysulfide shuttling, dissolved lithium polysulfides diffuse to the anode due to potential and concentration gradients.[5] The lithium polysulfides oxidize at the anode leading to a rapid capacity fading, an increase of the internal resistance, poor Coulombic efficiency, and enhanced self-discharge.[5]

The schematic LiS battery cell is presented in **Fig. 13A**. The carbon/sulfur cathode is paired with a metallic Li anode and a separator. The use of metallic lithium as an anode is often used for research to focus on the performance of the cathode. However, it would be replaced by other anode materials for commercial LiS batteries, due to aforementioned safety concerns.[5] A lithium-containing electrolyte like lithium bis(trifluoromethanesulfonyl)imidate (LiTFSI) dissolved in a mixture of 1,2-dimethoxyethane (DEM) and 1,3-dioxolane (DOL) is often used in such LiS cells.[5] This work concentrates on the use of porous carbon materials as host for sulfur and its use in LiS batteries.

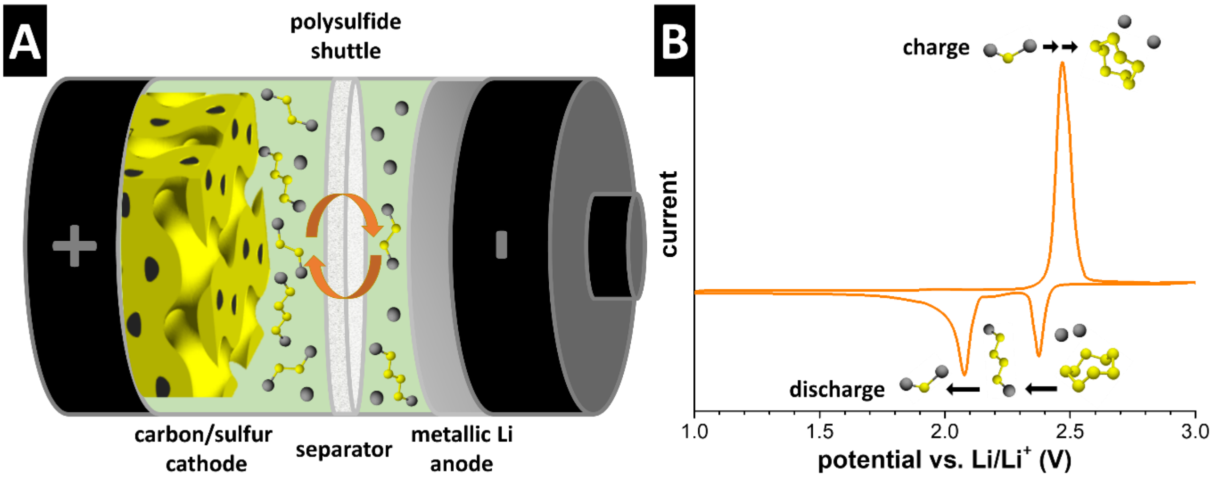

Figure 13: Schematic cell model (A) and typical cyclic voltammogram (B) of a LiS battery.

Many ways can be found in the literature to implement the sulfur in a porous carbon material, like melt infiltration, in-situ formation of sulfur inside the pores, or vapor phase infiltration.[5, 167] Melt infiltration is the most common method to infiltrate porous carbons with sulfur. Thereby, the carbon is mixed with the sulfur in optimized ratio and heated up in an inert atmosphere to around 155 °C, where the viscosity of sulfur is low.[5, 167] The capillary forces lead to an infiltration of the sulfur into carbon nanopores.[5] In addition to an optimized pore structure to confine the polysulfides inside the pores, also heteroatoms like nitrogen may further increase the performance stability of LiS batteries.[100, 168] The strong N-S bond increases the capacity and performance stability of LiS due to a reduced polysulfide shuttling.[100, 168] Thereby, it was possible to obtain a very high specific capacity of up to 1200 $\mathrm{mAh/g_{sulfur}}$ after 200 cycles.[100] It is common to normalize the specific capacity of a LiS battery to the mass of sulfur in the electrode, but these electrodes usually contain also the carbon matrix, an additional carbon black as a conductive additive, and a polymeric binder, which are doctor bladed on a metallic current collector. The electrode-normalized specific capacity in usually only 50-60 % of the sulfur-normalized capacity.[5, 100] Therefore, the ratio of the carbon matrix material and the sulfur should be at least 1:2 to provide a sufficient capacity of the LiS battery.[5]

3. Scope

Porous carbon materials with optimized properties are essential for high-performance electrochemical applications. This dissertation focuses on the synthesis of nanoporous carbon materials and the fundamental relationships between the materials properties and their electrochemical performance. An overview of the synthesized materials and the investigated application is provided in **Table 3**.

Table 3: Overview of the publications with the focus of this dissertation (Ch.: Chapter).

Ch.	**material**	**N**		**synthesis of the material**	**modification of the material**	**served as model material**	**application**			
		with	**without**				**supercaps**	**CDI**	**Li-ion**	**LiS**
4.1.	Novolac-derived carbon		X	X			X			
4.2.	Novolac-derived carbon		X		X		X	X		
4.3.	Novolac-derived carbon		X			X	X			
4.4.	Novolac-derived carbon	X			X		X			
4.5.	MicroJet SiOC-CDC		X	X			X			
4.6.	MicroJet SiOC-CDC	X	X		X		X			
4.7.	MicroJet SiOC		X	X					X	
4.8.	Novolac-derived carbon / S		X			X				X
4.9.	Gyroidal carbon / S	X	X	X	X					X

Chapter 4.1 explores phenolic resins as carbon precursors.[169-174] A commercial low-cost novolac was used to prepare novolac-derived carbon beads with a self-emulsifying process, followed by pyrolysis and physical activation with CO_2.[169] These materials were applied as an electrode for supercapacitors in an organic electrolyte, aqueous electrolyte, and redox-active aqueous electrolyte.

Chapter 4.2 investigates the salt removal performance of these CO_2 activated novolac-derived carbon beads in brackish water (5 mM NaCl), which was lower than predicted by the porosity.[170] Therefore, we analyzed the surface chemistry of the novolac-derived carbon beads. The functional groups on the surface of the CO_2 activated samples caused an inversion peak and fast performance decay. Removal of the functional groups by a hydrogen treatment at high temperatures was efficient to increase the performance stability and the salt removal capacity.

Another characteristic of the novolac-derived carbon materials is the narrow pore size, which increases with the activation time.[169] Therefore, we chose the novolac-derived carbon beads with an average pore size of 1.2 nm as a model material to investigate the electrosorption of ionic liquids (EMIM-BF_4 and EMIM-TFSI) in nanopores (**Chapter 4.3**).[171] Combining data obtained from electrochemical dilatometry and quartz crystal microbalance measurements yielded quantitative information about the electrosorption mechanism. We found that the charge storage mechanism of these electrolytes is different at low and high states of charges. Concurrent co-ion expulsion and counter-ion adsorption of small ions are predominant at a low state of charge, while permselective counter-ion adsorption occurs mainly at higher states of charge, increases the electrode volume, and causes macroscopically measurable expansion.

The introduction of nitrogen in the novolac-derived carbon beads was accomplished by a combination of the pyrolysis and activation in NH_3 containing atmosphere (**Chapter 4.4**).[172] The ammonia physically activated the carbon materials and simultaneously introduced nitrogen groups. The nitrogen content varied between 5-7 mass% depending on the synthesis temperature (750-950 °C). The SSA_{DFT} was increased from 865 m^2/g of the sample produced at 750 °C to 1827 m^2/g for the sample produced at 950 °C. The larger porosity of the material made it interesting for the use as the electrode in a supercapacitor. Half-cell and symmetrical full-cell supercapacitors were investigated with an organic electrolyte (1 M TEA-BF_4 in ACN), and we compared the performance of the NH_3 treated samples with the CO_2 activated novolac-derived carbon beads.

Polysilsesquioxanes pyrolyzed to SiOC can serve as an attractive precursor to carbon synthesis as outlined in **Chapter 4.5**.[71] We used the continuous MicroJet method to produce spherical polysilsesquioxane particles, pyrolyzed them, and carried out a thermal chlorine gas to produce nanoporous SiOC-CDCs.[88, 175] Vinyltrimethoxysilane (VTMS) was added to the phenyltrimethoxysilane (PTMS) solution to prevent the softening of the polymer particles at high temperatures. We varied different ratios of VTMS and PTMS monomers to adjust the total pore volume (1.3-2.1 cm^3/g), and the average pore size (1.4-2.9 nm) of the CDC materials.[88] The resulting CDC materials showed an SSA_{DFT} of 2000-2200 m^2/g and they were tested as electrodes for supercapacitors in an organic electrolyte

(1 M TEA-BF_4 in ACN) and an aqueous electrolyte (1 M Na_2SO_4). This study investigated the influence of the pore volume and average pore size for the performance at high specific powers.

As shown in **Chapter 4.6**, nitrogen-doping of the SiOC-CDCs can be achieved by using nitrogen-containing precursor (3-(phenylamino)propyl)trimethoxysilane (PAPTMS)) mixed with VTMS.[175] A similar alkoxysilane without nitrogen was also tested as a comparison. The polysilsesquioxanes were pyrolyzed at 1000 °C, and the chlorine gas treatment was carried out at 600 °C, 800 °C, and 1000 °C. The sample produced at 600 °C had a nitrogen content of 7 mass%, which was reduced to 4 mass% and 1 mass% for the samples synthesized at 800 °C and 1000 °C, respectively. The SSA_{DFT} was in the range of 1400-2300 m^2/g, and the samples produced at 600 °C showed the lowest porosity. The normalized pore size distribution of all materials was quite similar with an average pore size of 1.6-1.9 nm. Thereby, we were able to compare the supercapacitor performance of materials with and without nitrogen-doping, while the pore structure was highly comparable.

SiOC, which are obtained by the pyrolysis of polysilsesquioxanes, are also well-suited anode materials for Li-ion batteries (**Chapter 4.7**). Methyltrimethoxysilane (MTMS), VTMS, and a mixture of VTMS with PTMS were used to produce SiOC with different carbon contents (22-40 mass%).[176] Electrodes were prepared with 5 mass% of carbon black (C65) as a conductive additive, and 5 mass% of sodium carboxymethylcellulose (NaCMC) as a binder and 1 M $LiPF_6$ in ethylene carbonate/dimethyl carbonate (EC/DMC) was used as an electrolyte in a half-cell vs. metallic lithium. Thereby, we explored the impact of the carbon content of the SiOC on the specific capacity and cycling stability of the Li-ion batteries.

Chapter 4.8 explores the microporous activated and non-activated novolac-derived carbon materials as host for sulfur and applied two different synthesis methods (melt infiltration and in-situ formation of sulfur).[173] The pore volume of 0.3 cm^3/g of the non-activated samples was not sufficient to host a high sulfur content of ~66 mass% inside the micropores. The CO_2 activated samples had a higher total pore volume and produced with sulfur a homogeneous C/S mixture by melt infiltration and in-situ formation. The micropore structure and the infiltration method had a major influence on the performance of the C/S mixtures in the LiS battery.

A gyroidal mesoporous carbon may further reduce the polysulfide shuttling.[177-178] Therefore, **Chapter 4.9** explores gyroidal porous carbon using a commercial resol and a block copolymer.[174] We applied the CO_2 activation and NH_3 treatment during the pyrolysis to produce highly micro- and mesoporous carbons with and without nitrogen groups. Sulfur was introduced in the gyroidal carbons via melt infiltration. We investigated the influence of the activation method (CO_2/NH_3) and the nitrogen groups on the specific capacity and cycling stability of a LiS battery.

4. Results and Discussion

4.1. Sub-micrometer novolac-derived carbon beads for high performance supercapacitors and redox electrolyte energy storage

4.2. Hydrogen-treated, sub-micrometer carbon beads for fast capacitive deionization with high performance stability

4.3. Quantitative information about electrosorption of ionic liquids in carbon nanopores from electrochemical dilatometry and quartz crystal microbalance measurements

4.4. Nitrogen-containing novolac-derived carbon beads as electrode material for supercapacitors

4.5. Carbide-derived carbon beads with tunable nanopores from continuously produced polysilsesquioxanes for supercapacitor electrodes

4.6. Influence of nitrogen-doping for carbide-derived carbons on the supercapacitor performance in an organic electrolyte and an ionic liquid

4.7. Silicon oxycarbide beads from continuously produced polysilsesquioxane as stable anode material for Li-ion batteries

4.8. Microporous novolac-derived carbon beads/sulfur hybrid cathode for lithium-sulfur batteries

4.9. Gyroidal porous carbon activated with NH_3 or CO_2 as lithium−sulfur battery cathodes

4.1. Sub-micrometer novolac-derived carbon beads for high performance supercapacitors and redox electrolyte energy storage

Benjamin Krüner,[1,2] Juhan Lee,[1,2] Nicolas Jäckel,[1,2] Aura Tolosa,[1,2] Volker Presser[1,2]

[1] *INM - Leibniz Institute for New Materials, 66123 Saarbrücken, Germany*

[2] *Department of Materials Science and Engineering, Saarland University, 66123 Saarbrücken, Germany*

Krüner, Benjamin et al. (2016) *ACS applied materials & interfaces*, 8(14), 9104-9115.
https://doi.org/10.1021/acsami.6b00669

Own contribution: Design, planning, writing, synthesis of the activated and non-activated carbon beads, SEM, particle size analysis, TGA analysis, TGA coupled with MS analysis, CO_2 and N_2 sorption analysis, Raman analysis, XRD measurements, Helium pycnometry, EDX analysis, electrochemical analysis for double-layer capacitors.

Abstract:

Carbon beads with sub-micrometer diameter were produced with a self-emulsifying novolac–ethanol–water system. A physical activation with CO_2 was carried out to create a high microporosity with a specific surface area varying from 771 (DFT) to 2237 m^2/g (DFT) and a total pore volume from 0.28 to 1.71 cm^3/g. The carbon particles conserve their spherical shape after the thermal treatments. The controllable porosity of the carbon spheres is attractive for the application in electrochemical double layer capacitors. The electrochemical characterization was carried out in aqueous 1 M Na_2SO_4 (127 F/g) and organic 1 M tetraethylammonium tetrafluoroborate in propylene carbonate (123 F/g). Furthermore, an aqueous redox electrolyte (6 M KI) was tested with the highly porous carbon and a specific energy of 33 W·h/kg (equivalent to 493 F/g) was obtained. In addition to a high specific capacitance, the carbon beads also provide an excellent rate performance at high current and potential in all tested electrolytes, which leads to a high specific power (>11 kW/kg) with an electrode thickness of ca. 200 µm.

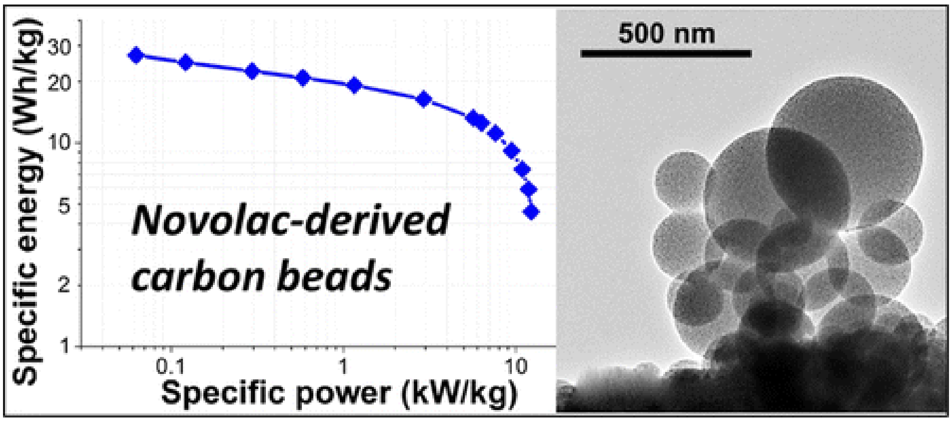

ACS APPLIED MATERIALS & INTERFACES

Research Article

www.acsami.org

Sub-micrometer Novolac-Derived Carbon Beads for High Performance Supercapacitors and Redox Electrolyte Energy Storage

Benjamin Krüner,[†,‡] Juhan Lee,[†,‡] Nicolas Jäckel,[†,‡] Aura Tolosa,[†,‡] and Volker Presser*,[†,‡]

[†]INM—Leibniz Institute for New Materials, 66123 Saarbrücken, Germany

[‡]Department of Materials Science and Engineering, Saarland University, 66123 Saarbrücken, Germany

Supporting Information

ABSTRACT: Carbon beads with sub-micrometer diameter were produced with a self-emulsifying novolac−ethanol−water system. A physical activation with CO_2 was carried out to create a high microporosity with a specific surface area varying from 771 (DFT) to 2237 m^2/g (DFT) and a total pore volume from 0.28 to 1.71 cm^3/g. The carbon particles conserve their spherical shape after the thermal treatments. The controllable porosity of the carbon spheres is attractive for the application in electrochemical double layer capacitors. The electrochemical characterization was carried out in aqueous 1 M Na_2SO_4 (127 F/g) and organic 1 M tetraethylammonium tetrafluoroborate in propylene carbonate (123 F/g). Furthermore, an aqueous redox electrolyte (6 M KI) was tested with the highly porous carbon and a specific energy of 33 W·h/kg (equivalent to 493 F/g) was obtained. In addition to a high specific capacitance, the carbon beads also provide an excellent rate performance at high current and potential in all tested electrolytes, which leads to a high specific power (>11 kW/kg) with an electrode thickness of ca. 200 μm.

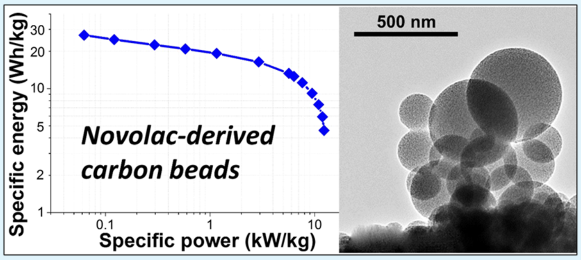

KEYWORDS: *supercapacitors, porous carbon, energy storage, redox electrolyte, self-emulsifying*

1. INTRODUCTION

Electrical double layer capacitors, also known as supercapacitors or ultracapacitors, store electrical energy via fast ion electrosorption processes at the fluid−solid interface between a charged electrode and electrolyte.[1] Due to the nonfaradaic and interfacial nature of this process, a supercapacitor typically shows a power handling ability superior to lithium ion batteries where the ions intercalate into a solid material with a suitable (often layered) structure.[2] In consequence, supercapacitors have higher specific power (800−2000 W/kg) than lithium ion batteries (typical specific power, 100 W/kg).[3] Another advantage of supercapacitors is their long cycling performance stability and high Coulombic efficiency. However, this comes at the price of a comparably low specific energy of 5−15 W·h/kg for supercapacitor cells (lithium ion batteries, ca. 100 W·h/kg).[3]

Commonly, electrodes for supercapacitor applications employ micrometer-sized particles of nanoporous carbon consolidated by the use of polymer binder.[4,5] To further enhance the power performance via fast ion transport, sub-micrometer particles are of high interest.[6−9] For example, using an emulsion synthesis process, we have recently shown the superior rate handling ability of sub-micrometer carbide-derived carbon (CDC) beads with diameters ranging from 20 to 200 nm.[10] This aligns with the enhanced performance of nanometer-sized TiC powders, which demonstrate an enhanced power rating compared to their micrometer-sized counterparts.[8] Yet, the necessity of chlorine gas to etch all noncarbon atoms makes the production of CDCs less attractive to large scale industrial processing. Also alternative synthesis methods for sub-micrometer-sized carbon particles (especially spherical ones) have been reported, such as camphoric carbon nanobeads (ca. 80 m^2/g specific surface area (SSA))[11] or spongy carbon nanobeads (16 m^2/g SSA),[12] but commonly high porosity values cannot be achieved without postsynthesis activation.

A well-established method to synthesize spherical particles (including sub-micrometer diameter) is emulsion polymerization.[13] The advantages of particle synthesis from emulsions are (i) the simplicity of the setup and scalability, (ii) the possibility to prepare a great variety of materials with a broad range in particle sizes, and (iii) a flexibility on adjusting the composition.[14] The diameters of the emulsion's liquid droplets may range from 10 nm to 100 μm, and phenolic resins can be used as carbon precursor for emulsion polymerization.[15−19] Phenolic resin systems are formed with a base or acid catalyst to obtain resoles or novolacs.[20] Resoles can cross-link without the help of cross-linking agents in contrast to novolacs which can only cross-link by adding a hardener (e.g., hexamethylenetetramine).[20] As reported in the literature so far, as-pyrolyzed beads from phenolic resin may exhibit a specific BET surface area (SSA_{BET}) up to 1131 m^2/g which can be further increased by physical or chemical activation.[17,21] Typical SSA_{BET}, which can be obtained with physical or chemical activations of carbon materials, are between 500 and 3100 m^2/g.[16,22,23] For example, the physical activation of carbon microspheres (200−1000 μm)

Received: January 18, 2016
Accepted: March 21, 2016
Published: March 21, 2016

DOI: 10.1021/acsami.6b00669
ACS Appl. Mater. Interfaces 2016, 8, 9104−9115

with CO_2 gas has been investigated by Singh and Lal, varying the CO_2 flow rate, the gasification temperature, and the activation time.[16] An increased flow rate decreased the porosity because of a shorter dwell time, while increasing the temperature from 850 to 1150 °C led to an enhanced SSA_{BET} of up to 1031 m^2/g while sacrificing the total yield of the final product.[16] A prolonged activation time from 5 to 15 h at 950 °C was the most effective step to increase the porosity: the burnoff increased from 32 to 88 mass% while the SSA_{BET} increased from 574 to 3101 m^2/g.[16]

To establish industrial production, Tennison (MAST Carbon) developed the synthesis of nonspherical phenolic-resin-derived carbon particles with a particle size of 1−50 μm.[24] By using physical activation with carbon dioxide, it was possible to achieve SSA_{BET} from 800 to 1500 m^2/g.[24] Later, Tennison et al. improved the synthesis procedure to obtain phenolic-resin-derived carbon with adjusted particle sizes between 5 and 2000 μm by using a water-in-oil emulsion.[25] Using this approach, they reached a SSA_{BET} of up to 750 m^2/g with total pore volume of ca. 1 cm^3/g. The unique feature of their synthesis is the use of pore formers, such as diols, diol-ethers, cyclic esters, cyclic and linear amides, or aminoalcohols. These pore formers do not react with the polymer but remain within the cross-linked resin and can be removed in a later stage. An initial study of the electrochemical properties of such novolac-derived carbon microbeads was provided by Fernández et al.[26] These beads were pyrolyzed at 800 °C and activated with carbon dioxide at 900 °C to obtain a SSA_{BET} up to 1773 m^2/g and up to 124 F/g capacitance in 1 M TEA-BF_4 in acetonitrile (ACN).

To overcome the inherently limited specific energy of electrical double layer capacitor, the use of redox-active electrolytes has emerged as a facile and powerful approach.[27−29] Unlike supercapacitors, redox electrolytes do not limit the energy storage capacity of the system to ion electrosorption at the fluid/solid interface at the electrode. Instead, the electrolyte volume actively participates in the energy storage mechanisms through soluble redox couples, for instance, quinone/hydroquinone, iodine/iodide/triodide, ferricyanide/ferrocyanide, or vanadium oxide.[30,31] Redox electrolyte systems provide not only a very high specific energy (10−50 W·h/kg) but also high specific power almost close to that of supercapacitors.[32] The latter can be explained by the enhanced diffusion kinetic of the redox ions in the carbon nanopores where the pore size is smaller than the equivalent diffusion layer thickness.[32] Thus, an electrode should exhibit a synergistic combination of larger transport pores for the transport of redox ions and a total high pore volume to provide a large reservoir of redox-active species. This requirement can be met with nanoporous carbon spheres with sub-micrometer size, where the large intraparticle pore volume serves as reservoir, short diffusion path lengths are provided via the small particle size, and an additional reservoir for ions is provided by large interparticle porosity.

Our work presents the synthesis of sub-micrometer novolac-derived carbon (abbreviated as NovoCarb or PNC) beads by a simple emulsion polymerization, followed by carbonization and physical activation. The self-emulsifying characteristic of the emulsion (novolac−ethanol−water) makes this synthesis method particularly practical because no high shear mixer or ultrasonic device is needed. This and the small particle size set our synthesis apart from established approaches, such as that developed by Tennison.[25] For the highly nanoporous NovoCarb spheres, we first establish the performance as a conventional supercapacitor electrode in aqueous (1 M Na_2SO_4) and organic media (1 M TEA-BF_4 in propylene carbonate, PC). Finally, the very high energy storage capacity of the material is demonstrated for aqueous 6 M KI (potassium iodide). Such a high molar concentration of potassium iodide has not been studied before, and we benchmark all data vs conventional activated carbon (AC, YP-80F from Kuraray).

2. EXPERIMENTAL DESCRIPTION

2.1. Synthesis of Ultrasmall Novolac-Derived Carbon Beads. A 25 g amount of novolac (ALNOVOL PN320, Allnex Germany GmbH) was dissolved in 100 mL of ethanol. The cross-linker, 2.5 g of hexamethylenetetramine (TCI Deutschland GmbH), was dissolved in 500 mL of Milli-Q water. The novolac−ethanol solution was added to the aqueous phase in a 1 L autoclave. The transparent solutions became milky directly after the addition of the second phase, and the self-emulsifying effect of the system eliminated the need for additional stirring of the emulsion. A pressure of approximately 3×10^6 Pa of nitrogen was applied to the autoclave before heating. The autoclave was heated to 150 °C (measured inside the autoclave) with a heating rate of 5 °C/min and held at this temperature for 8 h. The pressure increased from 3×10^6 Pa to approximately 4.3×10^6 Pa during the reaction. After synthesis, the suspension was freeze-dried using liquid nitrogen to minimize agglomeration so that a dry powder was obtained.

The novolac beads were pyrolyzed at 700 °C with a heating rate of 20 °C/min in argon (purity, 4.6) and held at this temperature for 2 h. Subsequently, physical activation via CO_2 treatment (purity of CO_2, 4.5) was carried out by heating to 1000 °C with a heating rate of 20 °C/min while CO_2 flow rate was controlled to 100 cm^3/min at 1000 °C. The process time (denoted as X; see Supporting Information Figure S1) was varied between 0 and 3 h to adjust the porosity of the carbon beads. In this work, the activation time is reflected by the subscript in the sample's name; for example, PNC_{2h} refers to phenol novolac carbon (PNC = NovoCarb) that has been exposed to 2 h of CO_2 activation.

2.2. Materials Characterization. The carbon beads were imaged by a field emission scanning electron microscope (SEM; JEOL-JSM-7500F from JEOL Ltd.) and a transmission electron microscope (TEM; JEOL JEM-2100F operating at 200 kV). The bead diameter was measured on the basis of the SEM images with ImageJ 1.47t for a number of 150 beads.[33] Chemical characterization via CHNS analysis was carried out with the Vario Micro Cube of Elementar GmbH with a temperature of the reduction tube of 850 and 1150 °C of the combustion tube. The device was calibrated with sulfanilamide.

Raman spectra were measured with a Renishaw inVia Raman Microscope, equipped with a grating of 2400 lines/mm and a 50× objective (numeric aperture, 0.9), reaching a spectral resolution of ~1.2 cm^{-1}. An Nd:YAG laser with an excitation wavelength of 532 nm was used. The acquisition time was 20−30 s, and 3−10 accumulations were used to enhance the signal-to-noise ratio. After the background noise was subtracted from the obtained Raman spectra, the D- and G-peaks were fitted with a Voigt function, as was the background contribution.

The nitrogen and carbon dioxide gas sorption analyses were carried out with a Quantachrome Autosorb iQ system. The pyrolyzed and activated samples were degassed at 150 °C for 1 h and subsequently heated to 300 °C and kept at this temperature for up to 20 h at a relative pressure of 0.1 Pa to remove volatile molecules from the surface. The nitrogen sorption analysis was performed in liquid nitrogen at −196 °C and the carbon dioxide sorption analysis at 0 °C using ethylene glycol as cooling agent. The relative pressure with nitrogen was 5×10^{-7} to 1.0 in 76 steps and 4.5×10^{-4} to 1×10^{-2} in 55 steps for the CO_2 measurements. The pore size distribution (PSD) was derived using the quenched-solid density functional theory (QSDFT), assuming slit-like pores, for the nitrogen measurements and the nonlocal density functional theory (NLDFT) for the carbon dioxide measurements.[34−36] The specific surface area (SSA) was also calculated using the Brunauer−Emmett−Teller equation (BET) in the linear regime of the measured isotherms, typically 3×10^{-2} to 2×10^{-1} (relative pressure), with a Quantachrome Autosorb 6B.[37] All calculations were performed with the ASiQwin-software 3.0, and the average pore size was calculated by volume weighing (i.e., d_{50} value = cumulative pore size corresponding with half of the total pore volume).[38]

The novolac beads were pyrolyzed in an Ar atmosphere (purity, 4.6) in a thermogravimetric analysis (TGA; TG209F1 Libra from Netzsch) with a heating rate of 10 °C/min to 1100 °C. A similar experiment was performed in a CO_2 atmosphere (purity, 4.5) with the pyrolyzed sample. The pyrolysis in Ar (purity, 5.0) was also investigated in a TGA with mass spectrometer (TGA-MS; STA449F3 Jupiter and QMS 403C Aëolos from Netzsch). The density of the NovoCarb particles was measured by helium pycnometry (AccuPyc 1330 pycnometer from Micromeritics; purity, 5.0).

2.3. Electrochemical Measurements. Freestanding carbon electrodes were prepared either with NovoCarb beads or commercially available activated carbon (AC, YP-80F from Kuraray) by applying polytetrafluoroethylene (PTFE; 60 mass % in H_2O) as binder. After dispersing the carbon material in ethanol, the PTFE solution was added. Then, the mixture was crushed in a mortar during the evaporation of the ethanol. The doughy carbon paste was then rolled out via a rolling machine (HR01 hot rolling machine from MTI Corp.). Finally, 120−220 μm thick freestanding electrodes were produced with 5−10 mass % PTFE for the AC based electrode and 9−12 mass % for the NovoCarb beads. Afterward, the electrodes were dried in a vacuum oven at 120 °C for 48 h at 2×10^3 Pa. For the cell assembly, an electrode disc was punched out of the rolled blank with a diameter of 12 mm. The active electrode mass varied between 2 and 15 mg depending on the activation time (Supporting Information Table S1) since the particle packing and electrode thickness were kept constant.

For the organic electrolyte (1 M TEA-BF_4 in PC; BASF, battery grade) and the aqueous system (1 M Na_2SO_4 in Milli-Q water; Sigma-Aldrich), custom-built cells were assembled employing a symmetrical two-electrode setup.[39] In order to minimize the contact resistance between the cell piston made of titanium and the electrode, a carbon-coated aluminum current collector (type Zflo 2653, Coveris Advanced Coatings, Matthews, NC, USA) was placed between the electrode and the cell piston made of titanium for measurements in organic media. In aqueous media, we used a platinum current collector instead. The electrodes were separated with a glass-fiber separator with a diameter of 13 mm (GF/A, Whatman, GE Healthcare Life Science). Before the cells were filled with the organic electrolyte in an argon-filled glovebox (MBraun Labmaster 130; O_2, H_2O < 1 ppm), they were dried at 120 °C and at 2×10^3 Pa for 24 h.

For the redox electrolyte system, a custom-made cell with graphite current collectors (10 mm thickness) was used with two-electrode configuration using two symmetric electrodes with a diameter of 12 mm. A schematic drawing is provided in Supporting Information Figure S2. To prevent the possible redox shuttling of the redox ions between anode and cathode,[40] a cation exchange membrane (FKS15, FuMA-Tech; thickness, ca. 15 μm) was used as a separator. In order to provide an effective seal for the membrane, polymer gasket layers were placed between graphite current collectors and the membrane. Through the circular inner cut (1.33 cm^2) of the gaskets, the electrodes were placed between the membrane and the current collector. Before the cell assembly, the electrodes were soaked in the redox electrolyte (1 or 6 M KI) with application of vacuum (10^4 Pa) for 5 min for degassing. During the cell assembly, the electrolyte was dropped on the electrode and the empty space in the gasket inner cut was completely filled with the electrolyte as the cell was sealed afterward.

All of the electrochemical measurements were conducted with a VMP300 potentiostat/galvanostat form BioLogic. From the obtained data, the specific capacitance was calculated with eq 1 from cyclic voltammograms (CVs) and with eq 2 for data from galvanostatic cycling with potential limitation (GCPL). The calculated capacitance values in this work are always the average of two measurements with a standard deviation below 10%. To compare the capacitance of different materials, it is common to normalize the capacitance to the active mass of the electrode material.[41]

$$C_S = \frac{I(t)}{(dU(t)/dt)m} \tag{1}$$

where C_S is the specific capacitance per electrode; $I(t)$, the discharge current; $dU(t)/dt$, the scan rate; and m, the mass of carbon in the electrode.

$$C_S = \frac{4Q_{dis}}{Um} \tag{2}$$

where C_S is the specific capacitance per electrode; Q_{dis}, the charge of the discharging cycle; U, the IR-drop corrected cell voltage; and m, the mass of carbon in the electrode.

For the calculation of the specific energy (W·h/kg) of the cells with the redox electrolyte, eq 3 was applied by integrating the cell voltage with respect to the discharging time measured in GCPL mode.

$$E = \frac{i}{m_{total}} \int U\, dt \tag{3}$$

where E is the specific energy of the cell; i, the constant current applied during the measurement; and m_{total}, the total mass of the two carbon electrodes of equal weight.

To determine the electrochemical stability window of KI aqueous solution with AC activated carbon and NovoCarb beads, a voltage opening test with cyclic voltammetry was initially applied to the cells at the scan rate of 1 mV/s from 0.6 to 1.4 V in intervals of 0.05 V. In order to characterize rate handling performance, CV, and GCPL were carried out in a full cell (symmetric two-electrode setup) with 1 M TEA-BF_4 in PC, 1 M Na_2SO_4, or 1 or 6 M KI.

For long-term stability testing, voltage floating was performed with a battery cycler (BAT-SMALL battery cycler from Astrol Electronic AG) with a symmetric two-electrode cell configuration. The voltage was kept at 1.2 V in aqueous and at 2.7 V in organic electrolyte for 100 h, and the specific capacity was measured every 10 h by galvanostatic cycling (aqueous, 1.2 V; organic, 2.5 V). In the case of the redox electrolyte system, a galvanostatic cycling test was carried out at 1 A/g from 0 to 1.4 V in a symmetric two-electrode configuration.

2.4. Electrochemical Dilatometry. The height change (strain) of the carbon electrodes during charging and discharging was measured with a ECD-nano dilatometer from EL-CELL. The dilatometer cell is based on a two-electrode design using an oversized PTFE-bound AC as counter and quasi-reference electrode. The investigated electrodes were compressed between the separator and a movable titanium plunger with a constant weight load of 10 N. Prior to the experiments, the cell was dried for 12 h at 120 °C under vacuum (2 kPa). A DP1S displacement transducer (Solartron Metrology), with an accuracy of 15 nm, was used. The experiments were performed at constant temperature of 25.0 ± 0.1 °C using a climate chamber (Binder). Prior to the electrochemical characterization, the cell was conditioned with a holding period at 0 V vs carbon for 10 h followed by five charge/discharge cycles between 0 and 2.5 V vs carbon, and only data of the fifth cycle are shown.

3. RESULTS AND DISCUSSION

3.1. Morphology and Porosity. Electron microscopy confirmed conservation of the spherical droplets structure generated in the emulsion after polymerization and pyrolysis (Figure 1A,B). Image analysis yielded an average number-dependent sphere diameter of 302 ± 142 nm for PNC_{0h}. Transmission electron microscopy (TEM) also showed the highly homogeneous character of the beads with no differentiation, for example, between core and shell. The overall nonordered character of the carbon is also evident from the absence of lattice fringes or visible crystalline domains (Figure 1B, inset). As seen from Figure 1C,D, the size of the particles

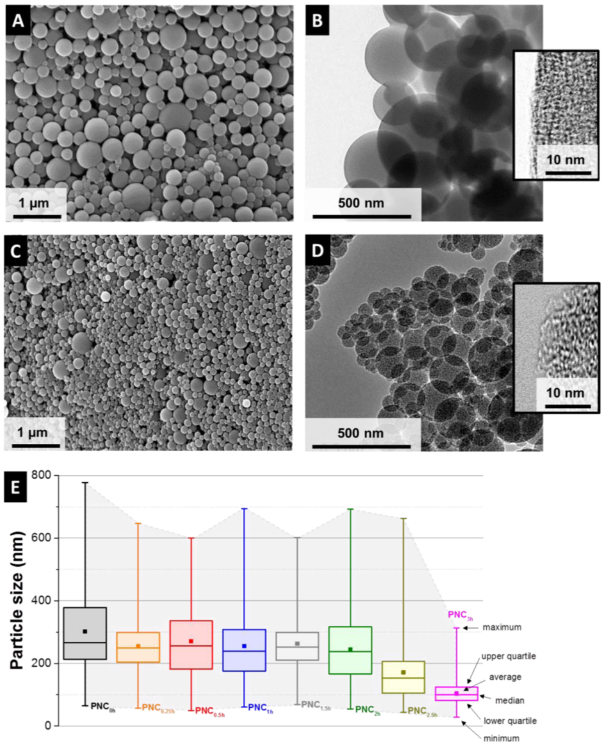

Figure 1. SEM images (A, C) and TEM images (B, D) of PNC_{0h} (A, B) and PNC_{3h} (C, D). Box–whisker plot (E) with maximum and minimum, upper and lower quartile, and number-dependent average and median of the carbon beads after the pyrolysis PNC_{0h} and after CO_2 activation ($PNC_{0.25h}$, $PNC_{0.5h}$, PNC_{1h}, $PNC_{1.5h}$, PNC_{2h}, $PNC_{2.5h}$, and PNC_{3h}).

after 3 h of CO_2 activation was significantly reduced to 104 ± 40 nm as was the spread of minimum and maximum diameters (Figure 1E and Supporting Information Figures S3 and S4). No significant change in bead diameter was encountered for CO_2 activation up to 2.5 h. The noncrystalline character of the carbon beads can be seen well from high resolution TEM micrographs (Figure 1D, inset) and the increased transparency of CO_2-treated beads indicates that the particles became less dense through removal of carbon by the physical activation (see also Supporting Information Figure S5).

To further investigate the pyrolysis process and CO_2 activation as a facile way to enhance the porosity of NovoCarb beads, we carried out thermogravimetric analysis. The TGA data presented in Figure 2A show the mass loss of the carbon beads during the pyrolysis and the CO_2 treatment. The pyrolysis of phenolic resins can be classified in three phases.[42] The small mass loss at approximately 100 °C was not part of the three stages of the pyrolysis and was caused by desorption of water and other light molecules (e.g., ethanol and ammonia; Supporting Information Figure S5). The first stage is identified by the formation of cross-links and the evolution of water and other condensates between 200 and 500 °C. The second stage is dominated by breaking cross-linking bonds between 400 and 800 °C (i.e., amino, methylene, and oxygen groups). This leads to the evolution of water, carbon monoxide, nitrogen, and amino groups among others (Supporting Information Figure S5). The oxygen signal is dropping at approximately 350 and 630 °C because of the evolution of carbon dioxide. The residual oxygen of the Ar flow is also reacting with the sample during the pyrolysis, and the final stage (560–900 °C) is dominated by the production of hydrogen by the splitting of hydrogen atoms directly bonded to benzene nuclei.[42] Pyrolyzed carbon is formed in this temperature range via the coalescence of aromatic rings, and the yield is 48 mass % at 700 °C and 43 mass % at 1100 °C of the initial sample mass. During the CO_2 treatment, we observed a massive oxidation-induced mass loss above 950 °C and adjusted the activation parameters to 1000 °C for this study.

As seen from electron micrographs, the beads became smaller and rougher with progressed activation (Figure 1C–E). With an additional decrease in contrast, TEM images indicate an increase in particle porosity, while the small nanopores themselves cannot be resolved by the imaging method directly. A more detailed characterization of the porosity of the beads prior to and after thermal activation with CO_2 for different durations can be gained by gas sorption analysis (GSA), as shown in Figure 2B–D.[38] Values for the mass loss, SSA_{BET} and SSA_{DFT}, total pore volume, and average pore size are provided in Table 1. The pyrolyzed carbon beads showed exclusively micropores with pores only smaller than 0.8 nm and a SSA_{DFT} of 771 m^2/g. The average pore size was 0.5 nm which is similar to the calculated molecular diameter of ethanol (0.52 nm),[43] indicating the role of ethanol as a pore former. The CO_2 activation and the increase in activation time led to a higher total mass loss. The SSA_{DFT} also increased to reach a maximum of 2237 m^2/g (SSA_{BET}, 3104 m^2/g) with a total pore volume of 1.71 cm^3/g at a mass loss of 90 mass %. These values are similar to the highest SSA_{BET} reported in literature for activated carbon materials.[16,22,23] Progressing activation caused a coalescence of the pores and a progressing increase of the average pore size. Finally, the enhanced pore coalescence at an activation of more than 2 h led to an ultimate decrease of the SSA and total pore volume while the average pore size constantly increased (Figure 2B). Additionally, the width of the pore size dispersity increased from 0.3 to 1.1 nm (PNC_{0h}) to 0.4–2.0 nm (PNC_{1h}) and to 0.5–3.4 nm (PNC_{3h}).

3.2. Structure, Density, and Chemical Composition.

TEM micrographs (Figure 1) evidenced the amorphous nature of NovoCarb beads and the lack of crystalline ordering after pyrolysis and CO_2 activation. Further insights into the carbon structure can be gained by means of Raman spectroscopy (Table 2). The Raman spectrum of PNC_{0h} is shown in Figure S6A (Supporting Information) with the fitted peaks for D-mode (at 1345 cm^{-1}) and G-mode (at 1602 cm^{-1}). The I_D/I_G ratio can be used to calculate the average in-plane domain size (L_a),[44] for example with the Tuinstra–Koenig[45] or the Ferrari–Robertson equation.[46] To understand the data, we need to consider that the two equations are only valid for different domain sizes: the Tuinstra–Koenig (TK) equation can be used for $L_a < 2$ nm and the Ferrari–Robertson (FR) equation for $L_a > 2$ nm.[47] We have to assume a transition in the values from the TK to the FR model, as shown in Figure S6C. Starting from an amorphous polymeric precursor, the pyrolyzed carbon showed a relatively small L_a of 1.4 nm. This value slightly increased after activation due to the longer holding time at higher temperatures and the removal of nongraphitic carbon for $PNC_{0.25h}$ (1.5 nm) and $PNC_{0.5h}$ (1.7 nm). For longer activation durations and L_a close to the critical domain size of 2 nm, we have to transition to the use of the FR model. Accordingly, the L_a values for PNC_{1h} to PNC_{3h} showed a small level of variation between 2.3 and 2.5 nm.

The two competing effects of graphitic domain size growth at high temperatures and the removal of carbon atoms by the

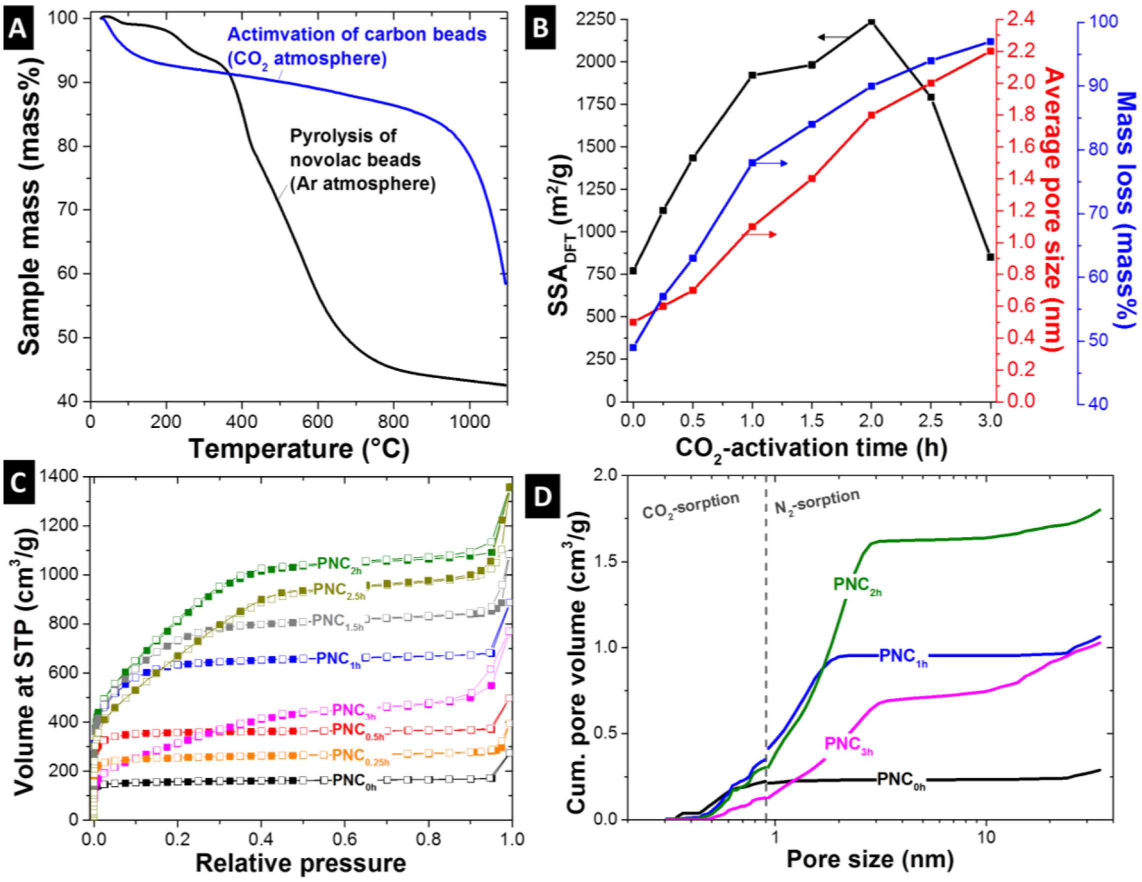

Figure 2. TGA of the pyrolysis of novolac beads in Ar atmosphere and of the CO_2 treatment of the pyrolyzed beads recorded with a heating rate of 10 °C/min (A). Correlation of SSA_{DFT}, average pore size, and mass loss on the CO_2-activation time (B). Nitrogen sorption isotherms at −196 °C on carbon beads (C). Cumulative pore size distributions of the CO_2 (at 0 °C) and N_2 (at −196 °C) gas adsorption measurement of the samples PNC_{0h}, PNC_{1h}, PNC_{2h}, and PNC_{3h} (D).

Table 1. Mass Loss of the Beads Introduced by the Pyrolysis and CO_2-Activation and Surface Characteristics of the Carbon Beads[a]

	mass loss (mass %)	SSA_{DFT} (m^2/g)	SSA_{BET} (m^2/g)	total pore vol (cm^3/g)	av pore size (nm)
PNC_{0h}	49	771	624	0.28	0.5
$PNC_{0.25h}$	57	1125	998	0.44	0.6
$PNC_{0.5h}$	63	1434	1433	0.57	0.7
PNC_{1h}	78	1921	2383	1.05	1.1
$PNC_{1.5h}$	84	1982	2633	1.32	1.4
PNC_{2h}	90	2237	3104	1.71	1.8
$PNC_{2.5h}$	94	1792	2571	1.58	2.0
PNC_{3h}	97	851	1189	0.88	2.2
AC		1756	2347	1.15	1.6

[a] For data on AC, see also ref 61.

physical activation influence the domain size of the carbon materials, as also seen from Raman spectroscopy (Supporting Information Figure S6c). The position of the D-mode shifted from 1345 to 1335 cm^{-1} when increasing the activation time. For comparison, the G-mode of all samples was located at approximately 1600 cm^{-1}, which indicates partially graphitic carbon, as also supported by a range of I_D/I_G ratio between 2.02 and 2.49.[48] For the physical activation, we have to consider the preferential etching of less-ordered carbon in addition to structural ordering caused by the thermal treatment.

Table 2. Peak Fitting Results of the Raman Spectra, with Position of the D- and G-Mode, the FWHM, I_D/I_G Ratio and L_a

	mode	position (cm^{-1})	FWHM (cm^{-1})	I_D/I_G	L_a (nm)
PNC_{0h}	D	1345.0	165.9	2.49	1.43
	G	1601.9	66.7		
$PNC_{0.25h}$	D	1346.2	173.5	2.32	1.55
	G	1600.8	74.7		
$PNC_{0.5h}$	D	1345.7	164.5	2.02	1.71
	G	1597.8	81.5		
PNC_{1h}	D	1339.6	132.9	2.17	2.49
	G	1601.2	61.2		
$PNC_{1.5h}$	D	1339.4	126.7	2.03	2.31
	G	1601.8	62.4		
PNC_{2h}	D	1336.2	122.9	2.07	2.39
	G	1600.9	59.4		
$PNC_{2.5h}$	D	1335.1	122.2	2.08	2.37
	G	1599.8	58.7		
PNC_{3h}	D	1335.1	122.0	2.11	2.41
	G	1599.7	57.9		

The analysis of the skeletal density supports the transition toward a higher degree of carbon ordering. Initially, the density of the pyrolyzed carbon beads was 1.99 ± 0.01 g/cm^3. For comparison, glassy carbon has a density of 1.48 g/cm^3 and graphite of 2.25 g/cm^3.[49] Activation led to an initial increase of the skeletal density after 1 h (2.33 ± 0.08 g/cm^3), as shown in

Table 3. Results of the CHNS Analysis[a]

	C (mass %)	H (mass %)	N (mass %)	S (mass %)	ΔO (mass %)
ALNOVOL PN 320	73.4 ± 1.7	5.83 ± 0.27	≤0.2	b.d.	20.8 ± 1.7
polymer beads	70.8 ± 1.3	6.32 ± 2.22	2.3 ± 0.1	b.d.	20.5 ± 2.6
PNC_{0h}	92.6 ± 1.5	1.34 ± 0.02	≤0.4	b.d.	5.7 ± 1.5
$PNC_{0.25h}$	90.7 ± 2.2	1.04 ± 0.03	≤0.5	b.d.	7.8 ± 2.3
$PNC_{0.5h}$	90.4 ± 1.6	1.13 ± 0.02	≤0.4	b.d.	8.1 ± 1.6
PNC_{1h}	90.1 ± 2.8	0.82 ± 0.05	≤0.5	b.d.	8.6 ± 2.8
$PNC_{1.5h}$	90.4 ± 8.7	0.77 ± 0.04	≤0.5	b.d.	8.3 ± 8.7
PNC_{2h}	89.3 ± 2.5	0.90 ± 0.13	≤0.8	b.d.	9.0 ± 2.6
$PNC_{2.5h}$	82.1 ± 4.5	0.66 ± 0.40	≤0.7	b.d.	16.6 ± 4.6

[a] The difference to 100% is attributed to oxygen and listed as ΔO; as no other elements were seen by elemental analysis with energy-dispersive X-ray analysis (EDX), the value for ΔO is an approximation for the actual oxygen content (b.d.: below limit of detection).

Figure S7 (Supporting Information). This value is relatively high compared to other CO_2-activated resol-derived carbons in the literature (2.2 g/cm^3; see ref 24), and this can be explained with the removal of less-dense material by the CO_2 activation and enhanced structural ordering of disordered carbon at high temperature. Continued CO_2 activation decreased the density to 1.95 ± 0.07 g/cm^3 after 1.5 h and to 1.51 ± 0.05 g/cm^3 after 2 h (the latter is the sample with the highest SSA and pore volume). The measured skeletal density after 2.5 h of CO_2 treatment was the lowest, namely, 1.44 ± 0.05 g/cm^3 (sample showing an onset of decreasing SSA).

Chemically, as shown by EDX analysis exemplified for PNC_{0h}, the beads predominantly consisted of carbon with some amounts of oxygen (Supporting Information Figure S8). These data were characteristic for all samples. The much higher sensitivity and accuracy of CHNS analysis allow a more precise quantitative analysis. Since EDX did not detect other elements outside the CNHS system except oxygen, we used the latter method to also assess the oxygen content (referred to as ΔO; Table 3). Initially, the novolac beads showed a carbon content of 70.8 mass %, which increased after pyrolysis to 92.6 mass % and decreased after CO_2 activation to 90.7 to 82.1 mass % (with a major decrease of the carbon content $PNC_{2.5h}$). While, after pyrolysis, ΔO was decreased from 20.5 to 5.7 mass %, CO_2 activation led to a slight increase to 7.8−9.0 mass % (for $PNC_{0.25h}$ to PNC_{2h}). The hydrogen content decreased from 6.3 mass % of the polymer beads to a nondetectable level after pyrolysis. The nitrogen content was lowered after the pyrolysis from 2.3 mass % to only ≤0.4 mass %, yet the nitrogen content increased after the CO_2 activation to ≤0.8 mass %, which can be explained by the preferred removal of carbon (i.e., the nitrogen content only increased relatively).

3.3. Supercapacitor Performance in Aqueous and Organic Electrolytes.

Electrochemical characterization (Table 4) of NovoCarb beads as supercapacitor electrodes was carried out for aqueous (1 M Na_2SO_4) and organic electrolyte media (1 M TEA-BF_4 in PC). Aqueous media are highly attractive because of the reduced energy required during supercapacitor manufacturing invested for thorough drying of the electrode materials and the low electrolyte costs.[50] Especially pH-neutral electrolytes are very promising because of their high electrochemical performance stability and beneficial voltage window.[51] Organic electrolytes are currently in widespread use for commercial supercapacitors because of their extended voltage window up to 2.7 V, although ion mobility is lower than in aqueous media.[50] The cyclic voltammograms of the carbon beads (Figure 3A,B) show that even a short physical activation (e.g., $PNC_{0.25h}$) was sufficient to enable enhanced double layer capacitance. As the only exception, the nonactivated pyrolyzed material (PNC_{0h}) did not yield stable electrochemical performance in aqueous media and was deselected for further characterization. In general, longer activation enhanced the SSA and a higher specific capacitance can be seen. The highest capacitance of 127 F/g at 1.2 V was achieved after 1.5 h of CO_2 activation, even though the highest SSA was achieved after 2 h. Obviously, limitations to the achievable specific capacitance of highly porous carbons with high surface area are encountered,[52] such as limited interfacial capacitance in carbon nanopores with very thin walls and incomplete charge screening.[53]

Table 4. Specific Capacitance of the Carbon Beads in Aqueous 1 M Na_2SO_4 and 1 M TEA-BF_4 in PC (n.d., Not Determined; for Comparison, Data for AC Given As Well)

	specific capacitance in aqueous 1 M Na_2SO_4 (F/g)	specific capacitance in 1 M TEA-BF_4 in PC (F/g)
AC	140	103
PNC_{0h}	n.d.	1
$PNC_{0.25h}$	84	44
$PNC_{0.5h}$	89	84
PNC_{1h}	117	112
$PNC_{1.5h}$	127	123
PNC_{2h}	123	123

Like in aqueous media, the CVs showed also the behavior of a near-ideal capacitor in 1 M TEA-BF_4 in PC (Figure 3B) for an activation duration of 0.5 h or longer. A maximum of 123 F/g was measured for $PNC_{1.5h}$ and PNC_{2h} at 2.5 V. All CV were pronouncedly rectangular with a continuous increase in capacitance for higher cell voltages (known as butterfly shaped CV) stemming from electrochemical doping.[39,54] As an exception, the CV of $PNC_{0.25h}$ showed a continuous narrowing and reduced capacitance at higher voltages which was not observed in aqueous media (Figure 3A). This effect can be explained by steric (volumetric) effects as shown by Segalini et al. for nanoporous carbon with a very narrow pore size distribution and an average size of 0.68 nm (TiC-CDC) for 1 M TEA-BF_4 in ACN as electrolyte.[55] For comparison, the ionic diameters of ACN-solvated TEA^+ and BF_4^- are 1.30 and 1.16 nm, respectively, and similar values are expected for PC (1.35 nm for TEA^+ in PC and 1.40 nm for BF^{4-} in PC).[56] Ion electrosorption in pores smaller than this value is accomplished by (partial)[57] desolvation (ionic diameter, 0.67 nm for TEA^+ and 0.45 nm for BF_4^-).[58] Smaller ion diameters are expected for the aqueous media, and, thus, no such effects were seen for $PNC_{0.25h}$ in 1 M Na_2SO_4.[59] In our case, $PNC_{0.25h}$ had an average pore size of 0.6 nm which poses severe accessibility

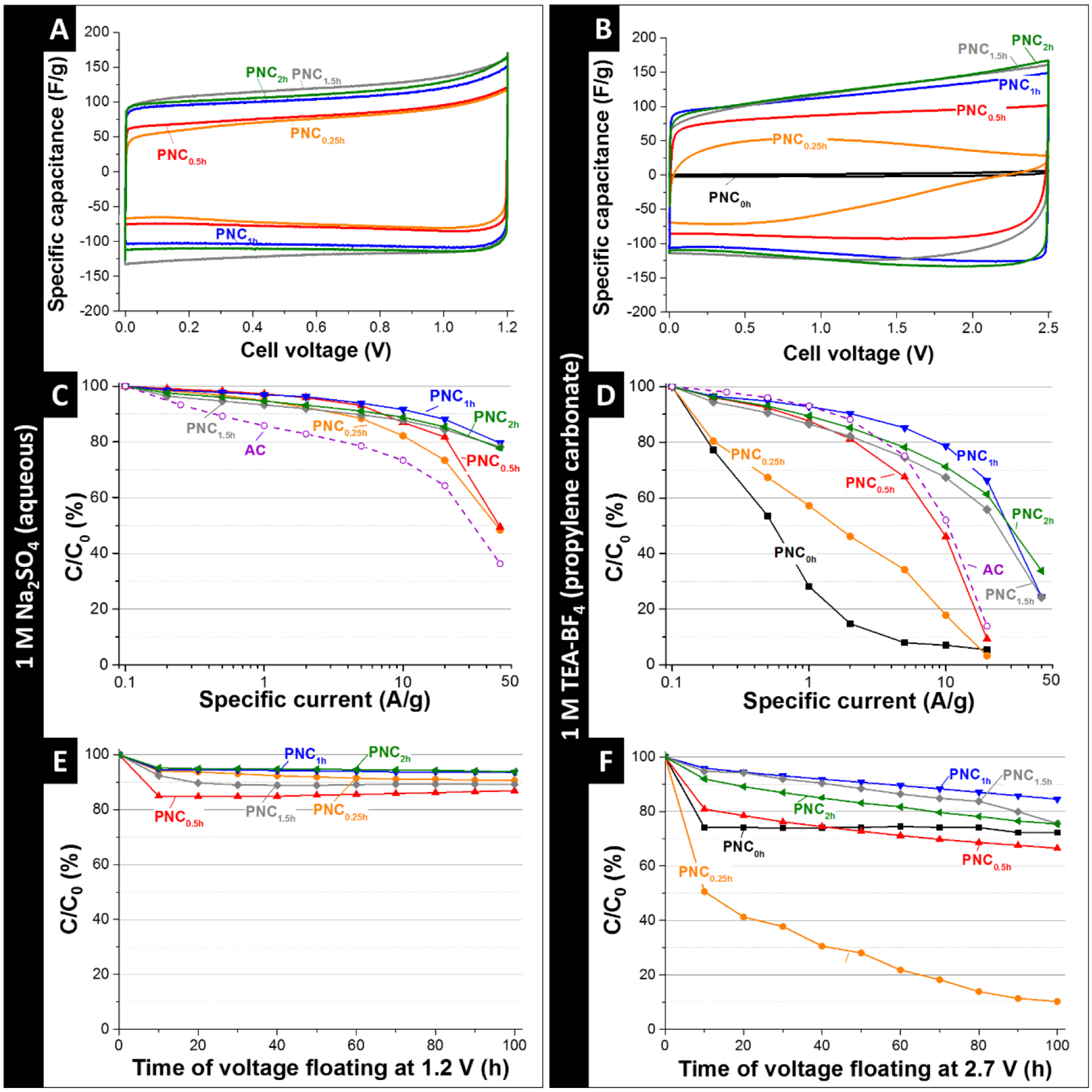

Figure 3. CVs of the carbon bead film electrodes in aqueous 1 M Na_2SO_4 (A) and in 1 M TEA-BF_4 in PC (B) with a scan rate of 5 mV/s. Rate handling of the film electrodes in aqueous 1 M Na_2SO_4 (C) and in 1 M TEA-BF_4 in PC (D) from a range of specific current of 0.1−50 A/g. For comparison, the rate handling ability of a conventional activated carbon (AC) is added as well to panels C and D. Long-time floating stability testing in aqueous 1 M Na_2SO_4 at 1.2 V (E) and in 1 M TEA-BF_4 in PC at 2.7 V (F).

limitations to the electrolyte ions in organic media (Table 1). CO_2 activation for at least 0.5 h was sufficient to yield an average pore size of 0.7 nm or more and no steric hindrance, and resulting CV deformation is observed.

In situ electrochemical dilatometry supports that PNC$_{0.5h}$ suffered from volumetric restrictions to ion electrosorption in sub-nanometer carbon micropores (Supporting Information Figure S9). In particular, we see an increased strain of PNC$_{0.25h}$ when compared to PNC$_{0.5h}$. At 75 C/g, PNC$_{0.25h}$ shows a small expansion of 0.07%, compared to 0.05% of PNC$_{0.5h}$ and the values divert at 175 C/g, namely, 0.29% and 0.22%, respectively. The ion sieving effect leads to a higher desolvation of ions to fit into the pores of PNC$_{0.25h}$ and a higher total strain of the electrode. PNC$_{0h}$ with even smaller pores (average pore size = 0.5 nm) and moderate specific surface area (SSA$_{DFT}$ = 771 m^2/g) yielded a negligible specific capacitance of around 1 F/g (since the ion radius of bare BF_4 is 0.45 nm) and, in comparison, a severely enhanced strain of 0.28% at 75 C/g.[58] These data align well with the increased pore swelling caused by steric effects when the pore size rivals the ion size shown by Hantel et al. for TiC-CDC in 1 M TEA-BF_4 in ACN with in situ electrochemical dilatometry.[60]

All NovoCarb samples showed an excellent rate handling ability in aqueous media with a loss of capacitance of less than 7% at 1 A/g (Figure 3C). Activation for 1 h or longer enabled one to maintain more than 77% of the initial low rate capacitance at a high specific current of 50 A/g. This high power handling ability is also reflected by the very small distortion of CVs at very high scan rates of 1 V/s, as exemplified for PNC$_{2h}$ (Supporting Information Figure S10A). For all activation conditions in aqueous Na_2SO_4, the measured power performance was also superior compared to a conven-

]

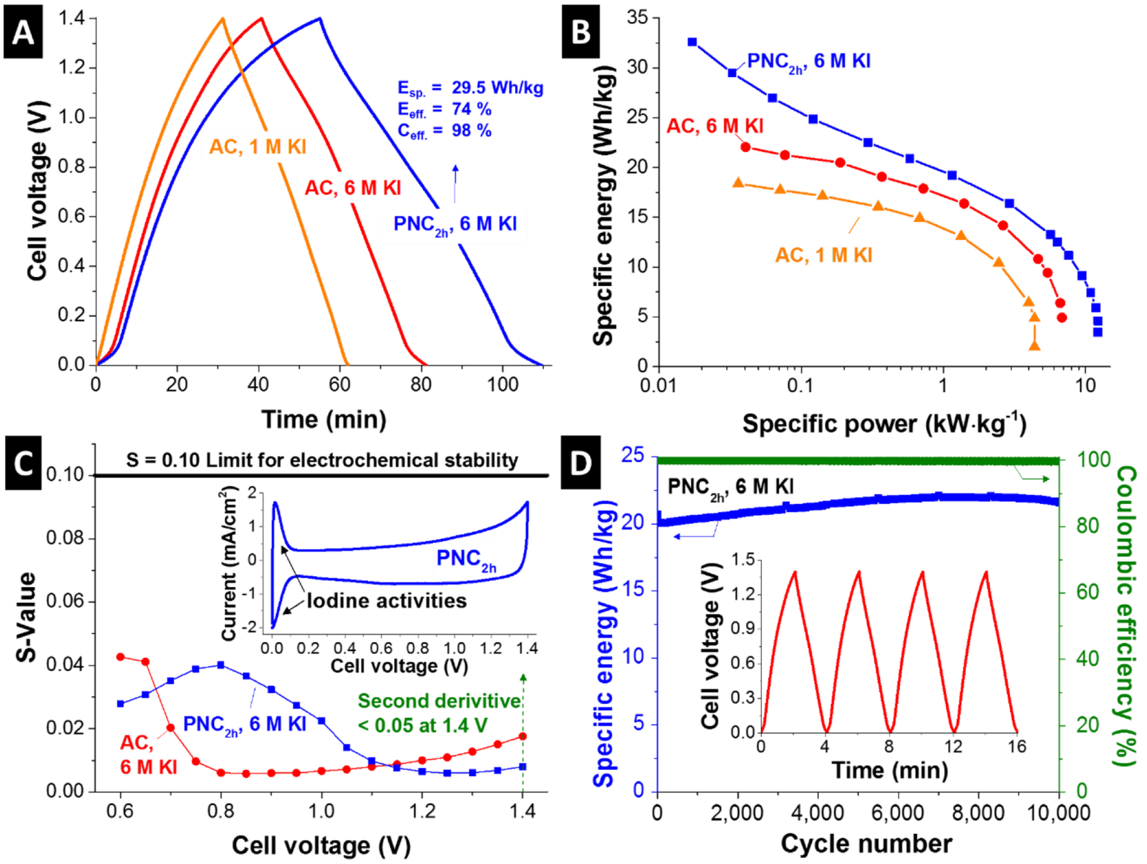

Figure 4. Galvanostatic charge/discharge curve at 50 mA/g (A) and the rate characteristics (B) obtained at various specific power in the cell voltage range from 0 to 1.4 V for different redox electrolyte systems. AC is a standard activated carbon used for the comparison of the performance for 1 and 6 M KI (aqueous). The electrochemical stability window was evaluated by the *S*-value method for 6 M KI with AC or PNC_{2h}. The inset shows the cyclic voltammogram of the cell with PNC_{2h} in 6 M KI at 1 mV/s for the cell stability window of 1.4 V. (C). Cyclic stability testing of PNC_{2h} in 6 M KI in the cell voltage range from 0 to 1.4 V at 1 A/g for 10,000 cycles and galvanostatic charge/discharge curve of the first few cycles (D).

tional nanoporous AC, for which the specific capacitance dropped to 86% at 1 A/g of the initial capacitance and to 73% at 10 A/g. In PC, a much lower overall rate handling is observed in agreement with the much lower ion mobility.[61] Perfectly aligning with the accessibility issues seen from CV and dilatometry, we see a very poor rate handling for PNC_{0h} and $PNC_{0.25h}$ (Figure 3D). On-setting for an activation time of 0.5 h (corresponding to an average pore size of 0.7 nm), we see an enhanced power performance and PNC_{1h} already significantly surpasses the values seen for the activated carbon reference. In detail, PNC_{1h} provided 78% of the initial capacitance at a very high specific current of 10 A/g compared to 52% for AC. The beneficial power handling ability of NovoCarb is also exemplified for PNC_{2h} when sweeping the scan rate in CV up to 1 V/s.

The enhanced power handling ability may relate to the sub-micrometer size of the NovoCarb beads used in this study. This aligns with the conclusions drawn by Perez et al. that nanosizing is an effective tool to enhance the rate handling ability even when comparing materials with virtually identical pore size distribution.[8] Consequently, the improved power performance of NovoCarb beads over micrometer-sized activated carbon is well-explained. When compared to spherical carbide-derived carbon with an average particle diameter of ca. 150 nm, we still see an enhanced performance of NovoCarb. In particular, the mentioned CDC beads material maintained at 20 A/g 80% of the initial low rate capacitance of 110 F/g (in relation to one electrode) in 1 M Na_2SO_4, which is lower than what we obtained for the best-performing NovoCarb beads (i.e., 88% PNC_{1h} with an average bead diameter of 255 nm).[10]

The stability of the NovoCarb is shown in Figure 3E,F for the aqueous and organic electrolytes. Voltage floating is a more demanding benchmarking to survey the electrochemical performance stability compared to voltage cycling.[62] For the aqueous system, a very high electrochemical performance stability was observed with a decrease in capacitance between 6 and 13% after floating at 1.2 V for 100 h. As such, the values stayed above the industry-relevant level of 80% of the initial capacitance.[62] Yet, a significantly higher loss of capacitive energy storage is observed in organic media. Albeit having a vanishing small capacitance of 1 F/g, the nonactivated material PNC_{0h} showed a fair performance stability with a reduction of 27% after 100 h at 2.7 V. Interestingly, $PNC_{0.25h}$ exhibited a drastic performance drop of 90% after 100 h at 2.7 V, while the $PNC_{0.5h}$ maintained 67% of the initial capacitance. The introduction of carbon heteroatoms and active surface sites may have severely reduced the energy storage stability by an enhanced electrolyte degeneration.[63] Longer activation times led to a significantly improved performance stability with capacitive retention between 75 and 85% after 100 h at 2.7 V. Seemingly, the enhanced structural ordering of the carbon and removal of more disordered material as seen from Raman analysis (Supporting Information Figure S6) leads to an improved energy storage capacity retention.

3.4. Electrochemical Performance in an Aqueous Redox Electrolyte. Since the NovoCarb beads exhibit a very high total pore volume with a large fraction of micropores and the potential for facile ion transport, the material is highly attractive for use with redox electrolytes. Besides the pore volume, a highly concentrated redox electrolyte is expected to be advantageous for maximizing redox activity and accomplishing high ion conductivities.[64,65] So far, potassium iodide (KI) had only been explored up to 1 M concentration, yet the low concentrated KI systems have shown already promising performances such as high cyclic lifetime, high energy density, and power density via the variety of halide oxidation states and possibly no need of ion selective membrane through the specific adsorption of the oxidized halide into carbon micropores.[28] The solubility of the KI aqueous solution is very high as compared to other redox electrolyte solutions such as vanadyl sulfate (<3.5 M), potassium ferricyanide (<1.2 M), or hydroquinone solutions (<1 M) at room temperature.[66] For that reason, we provide first data for the potassium iodide system at 6 M concentration and benchmark the performance of PNC_{2h} (i.e., the sample with the largest pore volume) in comparison with conventional AC.

In our experiments, we were able to charge the cells using aqueous KI safely up to 1.4 V cell voltage. Extended *S*-value testing surveyed the entire range of cell voltages up to 1.4 V for the 6 M KI system in AC and PNC_{2h} (Figure 4C). *S*-value testing indicates the onset of enhanced charge transfer related to nonreversible reactions, and values below 0.1 are deemed indicative of stable cell performance.[62] Within the studied range for both molar concentrations of potassium iodide, the second derivative of *S*-values remained below 0.05.

The increase in energy storage capacity at higher concentration can be seen from the galvanostatic charge/discharge profiles in Figure 4A for AC when transitioning from 1 M potassium iodide to 6 M KI. By deriving the specific energy by adequately considering the noncapacitive energy storage mechanism and noncapacitive GCPL shape following the procedure outlined in ref 67 and using eq 3, we calculate for the 1 M KI system in AC a maximum value of 18.4 W·h/kg at a low specific power of 36 W/kg. Note that due to the noncapacitive and nonpseudocapacitive response of the system, values for the specific capacitance (i.e., F/g) are disfavored to avoid misleading data and values are just given for the specific energy. For comparison, 6 M KI yielded at 40 W/kg a maximum specific energy of 22.0 W·h/kg in AC. This performance was severely surpassed when using PNC_{2h} and a specific energy of 29.5 W·h/kg was obtained at 33 W/kg for 6 M KI. This corresponds with a Coulombic efficiency of 98% and an energy efficiency of 74%. For comparison, Laheäär et al. recently reported for a system employing 0.5 M KI and operating at 1.6 V an energy efficiency of 52% and a Coulombic efficiency of 91% (86% and 97%, respectively, at 1.2 V).[67] At even lower specific power (i.e., 17 W/kg), a value of 32.6 W·h/kg was calculated for PNC_{2h} in 6 M KI at 1.4 V, and at a high specific power of 5.7 kW/kg, the system still provided a performance of 13.3 W·h/kg. The PNC_{2h} electrode with 6 M KI maintained about 4.6 W·h/kg at a very high specific power of 12.3 kW/kg. It seems that the system does not show a complete diffusion limited feature of the iodine redox reactions. The high power performance of PNC_{2h} electrode with 6 M KI can be explained by the confinement of redox ions in the micropores which overcome the diffusion limitation through micropores exhibiting pore size smaller than the equivalent diffusion layer.[32] Cyclic stability testing (Figure 4D) showed an excellent stability after 10,000 cycles (virtually no loss in energy storage capacity). The specific energy increased slightly by 4% after 10,000 cycles, due to improved wettability of carbon in aqueous electrolytes after an initial run-in period (conditioning).[4]

3.5. Ragone Plot for Novolac-Derived Carbon Electrodes. The energy vs power performance of the two high energy electrolytes, namely, 1 M TEA-BF_4 in PC (high energy by virtue of the high cell voltage) and aqueous 6 M KI (high energy by virtue of the redox energy storage) is shown for PNC_{2h} and AC (Figure 5). The resulting Ragone chart shows the high potential of novolac-derived carbon beads for electrochemical energy storage, constantly yielding higher power handling and, at the same specific power, higher specific energy when compared to a common activated carbon (Table 5). The zeolite-templated carbons (ZTC) have a SSA similar to that of NovoCarb but have a higher specific capacitance, due to ordered structure and narrow PSD of the ZTCs which makes the pores well-accessible.[68] The main disadvantage of ZTC is the complex synthesis which requires toxic reactants (furfuryl alcohol or acetonitrile) and hydrofluoric acid. The AC, BP2000, activated carbon aerogel, biowaste-derived carbon, and onion-like carbon (OLC) show a lower capacitance than PNC_{2h} due to their lower SSAs. The rate handling behavior of the PNC_{2h} is quite similar to OLC, which is known for its good conductivity which makes it a promising material as a conductive additive.[61] The high rate performance of NovoCarb makes the use of conductive additives redundant. The relative performance of BP2000 at high rates is best, but the specific capacitance of the NovoCarb is still higher. The beneficial performance is particularly attractive when considering the very low raw material costs of the novolac precursor of currently around 3 €/kg (as specified by the manufacturer) and the simple synthesis procedure.

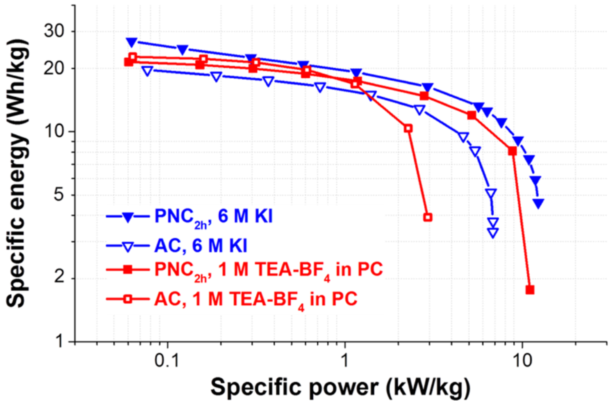

Figure 5. Ragone plot of PNC_{2h} and standard AC with an organic (1 M TEA-BF_4 in PC) and a redox electrolyte (aqueous 6 M KI).

4. CONCLUSIONS

Our work presents a facile synthesis method to obtain ultrasmall spherical carbon particles with a high specific surface and pore volume. A key advantage of our synthesis route is the facile self-emulsifying feature of the novolac−ethanol−water mixture. Therefore, no high shearing forces are needed to produce particles with an average diameter of 300 nm, setting this process apart from the established MAST carbon process.

Table 5. Overview of the Electrochemical Performance of NovoCarb-Material Compared to Other Carbon Materials for Supercapacitor Applications in Organic Media[a]

material	ref	SSA_{BET} (m^2/g)	electrolyte	specific capacitance at 0.1 A/g (F/g)	capacitance loss at 10 A/g (%)
PNC_{2h}	this work	3104	1 M TEA-BF_4 in PC	123	29
zeolite-templated carbon	68	3040	1 M TEA-BF_4 in PC	168	*not reported*
activated carbon (YP-80, Kuraray)	this work	2347	1 M TEA-BF_4 in PC	103	48
biowaste-derived carbon	69	1635	1 M TEA-BF_4 in PC	75	*not reported*
activated carbon aerogel	70	1408	1 M TEA-BF_4 in PC	101	*not reported*
activated carbon black (BP2000)	61	1389	1 M TEA-BF_4 in PC	90	18
activated carbon black (BP2000	61	1389	1 M TEA-BF_4 in ACN	86	9
carbon onions	61	398	1 M TEA-BF_4 in PC	18	28
carbon onions	61	398	1 M TEA-BF_4 in ACN	18	10

[a] The data are arranged by descending BET surface area.

Pyrolyzed material already exhibits a SSA_{DFT} of 771 m^2/g with a total pore volume of 0.26 cm^3/g due to ethanol acting as a pore former. The sub-micrometer spheres are ideal for a physical activation which can further increase the SSA_{DFT} to 2237 m^2/g (total pore volume, 1.71 cm^3/g).

The specific capacitance of the novolac-derived carbon beads can reach approximately 125 F/g in an aqueous or organic electrolyte. The materials showed excellent performance at high scan rates and current densities with capacitance retention of approximately 80% at 50 A/g in aqueous and approximately 30% at 50 A/g in (highly viscous) organic electrolyte. For the redox electrolyte system, the combination of high molar concentration of potassium iodide (i.e., 6 M) and the large pore volume of PNC_{2h} enabled a very high specific energy exceeding 30 W·h/kg. Thereby, it is possible with an aqueous redox electrolyte to reach energy densities similar to that of an organic electrolyte. Due to the adjustability of the porosity via physical activation, novolac-derived carbon beads are highly promising for not only electrochemical energy storage but also for capacitive deionization as well as flow capacitor applications where spherical particles are preferable for the low viscosity.

■ ASSOCIATED CONTENT

Ⓢ Supporting Information

The Supporting Information is available free of charge on the ACS Publications website at DOI: 10.1021/acsami.6b00669.

> Electrode properties, reaction scheme, cell setup, scanning and transmission electron micrographs, combined thermogravimetry with mass spectroscopy data, Raman spectra, skeletal density, elemental analysis, and supplementary electrochemical data (PDF)

■ AUTHOR INFORMATION

Corresponding Author

*E-mail: volker.presser@leibniz-inm.de.

Notes

The authors declare no competing financial interest.

■ ACKNOWLEDGMENTS

We acknowledge funding from the German Federal Ministry for research and Education (BMBF) in support of the nanoEES^{3D} project (Award No. 03EK3013) as part of the strategic funding initiative energy storage framework. We kindly acknowledge the continuing support of Prof. Eduard Arzt (INM). Furthermore, we thank Ralph Schäfer from Allnex Germany GmbH for his help and supply of ALVONOL PN 320. We thank Karl-Peter Schmitt for his support with the hydrothermal process, Robert Drumm for the TGA-MS measurements, Andrea Jung for the CHNS analysis, and Daekyu Kim for the cell assembly (all at INM). This work was supported by the CREATe-Network Project, Horizon 2020 of the European Commission (RISE Project No. 644013). We also thank Dr. Daniel Weingarth, Anna Schreiber, and Marco Zeiger (all at the INM) for helpful discussions and their kind support.

■ REFERENCES

(1) Beguin, F., Frackowiak, E., Eds. *Supercapacitors: Materials, Systems and Applications*. Wiley-VCH Verlag: Weinheim, Germany, 2013; 568 pp.

(2) Simon, P.; Gogotsi, Y. Materials for Electrochemical Capacitors. *Nat. Mater.* **2008**, *7*, 845−854.

(3) Ibrahim, H.; Ilinca, A.; Perron, J. Energy Storage Systems—Characteristics and Comparisons. *Renewable Sustainable Energy Rev.* **2008**, *12* (5), 1221−1250.

(4) Aslan, M.; Weingarth, D.; Jäckel, N.; Atchison, J. S.; Grobelsek, I.; Presser, V. Polyvinylpyrrolidone as Binder for Castable Supercapacitor Electrodes with High Electrochemical Performance in Organic Electrolytes. *J. Power Sources* **2014**, *266*, 374−383.

(5) Inagaki, M.; Konno, H.; Tanaike, O. Carbon Materials for Electrochemical Capacitors. *J. Power Sources* **2010**, *195* (24), 7880−7903.

(6) Zang, L.; Cao, X.; Zhang, Y.; Sun, L.; Qin, C.; Wang, C. Microfluidic Generation of Graphene Beads for Supercapacitor Electrode Materials. *J. Mater. Chem. A* **2015**, *3*, 22088−22093.

(7) Tang, K.; Fu, L.; White, R. J.; Yu, L.; Titirici, M.-M.; Antonietti, M.; Maier, J. Hollow Carbon Nanospheres with Superior Rate Capability for Sodium-Based Batteries. *Adv. Energy Mater.* **2012**, *2* (7), 873−877.

(8) Pérez, C. R.; Yeon, S.-H.; Ségalini, J.; Presser, V.; Taberna, P.-L.; Simon, P.; Gogotsi, Y. Structure and Electrochemical Performance of Carbide-Derived Carbon Nanopowders. *Adv. Funct. Mater.* **2013**, *23* (8), 1081−1089.

(9) Rose, M.; Korenblit, Y.; Kockrick, E.; Borchardt, L.; Oschatz, M.; Kaskel, S.; Yushin, G. Hierarchical Micro- and Mesoporous Carbide-Derived Carbon as a High-Performance Electrode Material in Supercapacitors. *Small* **2011**, *7* (8), 1108−1117.

(10) Oschatz, M.; Zeiger, M.; Jäckel, N.; Strubel, P.; Borchardt, L.; Reinhold, R.; Nickel, W.; Eckert, J.; Presser, V.; Kaskel, S. Emulsion Soft Templating of Carbide-Derived Carbon Nanospheres with Controllable Porosity for Capacitive Electrochemical Energy Storage. *J. Mater. Chem. A* **2015**, *3*, 17983−17990.

(11) Kalpana, D.; Karthikeyan, K.; Renganathan, N. G.; Lee, Y. S. Camphoric Carbon Nanobeads − A New Electrode Material for Supercapacitors. *Electrochem. Commun.* **2008**, *10* (7), 977−979.

(12) Sharon, M.; Mukhopadhyay, K.; Yase, K.; Iijima, S.; Ando, Y.; Zhao, X. Spongy Carbon Nanobeads—A New Material. *Carbon* **1998**, *36* (5−6), 507−511.

(13) Landfester, K. Miniemulsion Polymerization and the Structure of Polymer and Hybrid Nanoparticles. *Angew. Chem., Int. Ed.* **2009**, *48* (25), 4488−4507.

(14) Sanchez-Dominguez, M.; Aubery, C.; Solans, C., New Trends on the Synthesis of Inorganic Nanoparticles Using Microemulsions as Confined Reaction Media. In *Smart Nanoparticles Technology*, Hashim, A., Ed.; InTech Europe: Rijeka, Croatia, 2012; Chapter 9, pp 195−220, DOI: 10.5772/33010.

(15) Yang, J.-B.; Ling, L.-C.; Liu, L.; Kang, F.-Y.; Huang, Z.-H.; Wu, H. Preparation and Properties of Phenolic Resin-Based Activated Carbon Spheres with Controlled Pore Size Distribution. *Carbon* **2002**, *40*, 911−916.

(16) Singh, A.; Lal, D. Microporous Activated Carbon Spheres Prepared from Resole-Type Crosslinked Phenolic Beads by Physical Activation. *J. Appl. Polym. Sci.* **2008**, *110* (5), 3283−3291.

(17) Fang, Y.; Gu, D.; Zou, Y.; Wu, Z.; Li, F.; Che, R.; Deng, Y.; Tu, B.; Zhao, D. A Low-Concentration Hydrothermal Synthesis of Biocompatible Ordered Mesoporous Carbon Nanospheres with Tunable and Uniform Size. *Angew. Chem., Int. Ed.* **2010**, *49* (43), 7987−7991.

(18) Huang, Y.-P.; Hsi, H.-C.; Liu, S.-C. Preparation of Spherical Activated Phenol-Formaldehyde Beads from Bamboo Tar for Adsorption of Toluene. *J. Air Waste Manage. Assoc.* **2013**, *63* (8), 977−983.

(19) Slomkowski, S.; Alemán, J. V.; Gilbert, R. G.; Hess, M.; Horie, K.; Jones, R. G.; Kubisa, P.; Meisel, I.; Mormann, W.; Penczek, S.; Stepto, R. F. T. Terminology of Polymers and Polymerization Processes in Dispersed Systems (IUPAC Recommendations 2011). *Pure Appl. Chem.* **2011**, *83* (12), 2229−2259.

(20) Wan, J.; Wang, S.; Li, C.; Zhou, D.; Chen, J.; Liu, Z.; Yu, L.; Fan, H.; Li, B.-G. Effect of Molecular Weight and Molecular Weight Distribution on Cure Reaction of Novolac with Hexamethylenetetramine and Properties of Related Composites. *Thermochim. Acta* **2012**, *530*, 32−41.

(21) Ahmadpour, A.; Do, D. D. The Preparation of Active Carbons from Coal by Chemical and Physical Activation. *Carbon* **1996**, *34* (4), 471−479.

(22) Bleda-Martínez, M. J.; Maciá-Agulló, J. A.; Lozano-Castelló, D.; Morallón, E.; Cazorla-Amorós, D.; Linares-Solano, A. Role of Surface Chemistry on Electric Double Layer Capacitance of Carbon Materials. *Carbon* **2005**, *43* (13), 2677−2684.

(23) Maciá-Agulló, J. A.; Moore, B. C.; Cazorla-Amorós, D.; Linares-Solano, A. Activation of Coal Tar Pitch Carbon Fibres: Physical Activation vs. Chemical Activation. *Carbon* **2004**, *42* (7), 1367−1370.

(24) Tennison, S. R. Phenolic-Resin-Derived Activated Carbons. *Appl. Catal., A* **1998**, *173* (2), 289−311.

(25) Tennison, S. R.; Kozynchenko, O. P.; Strelko, V. V.; Blackburn, A. J. Porous Carbons. U.S. Patent US 20040024074 A1, 2008

(26) Fernández, J. A.; Tennison, S.; Kozynchenko, O.; Rubiera, F.; Stoeckli, F.; Centeno, T. A. Effect of Mesoporosity on Specific Capacitance of Carbons. *Carbon* **2009**, *47* (6), 1598−1604.

(27) Frackowiak, E.; Meller, M.; Menzel, J.; Gastol, D.; Fic, K. Redox-Active Electrolyte for Supercapacitor Application. *Faraday Discuss.* **2014**, *172*, 179−198.

(28) Frackowiak, E.; Fic, K.; Meller, M.; Lota, G. Electrochemistry Serving People and Nature: High-Energy Ecocapacitors based on Redox-Active Electrolytes. *ChemSusChem* **2012**, *5* (7), 1181−1185.

(29) Akinwolemiwa, B.; Peng, C.; Chen, G. Z. Redox Electrolytes in Supercapacitors. *J. Electrochem. Soc.* **2015**, *162* (5), A5054−A5059.

(30) Roldán, S.; Granda, M.; Menendez, R.; Santamaria, R.; Blanco, C. Mechanisms of Energy Storage in Carbon-Based Supercapacitors Modified with a Quinoid Redox-Active Electrolyte. *J. Phys. Chem. C* **2011**, *115* (35), 17606−17611.

(31) Roldán, S.; Blanco, C.; Granda, M.; Menéndez, R.; Santamaría, R. Towards a Further Generation of High-Energy Carbon-Based Capacitors by Using Redox-Active Electrolytes. *Angew. Chem.* **2011**, *123* (7), 1737−1739.

(32) Narayanan, R.; Bandaru, P. R. High Rate Capacity through Redox Electrolytes Confined in Macroporous Electrodes. *J. Electrochem. Soc.* **2015**, *162* (1), A86−A91.

(33) Schneider, C. A.; Rasband, W. S.; Eliceiri, K. W. NIH Image to ImageJ: 25 years of Image Analysis. *Nat. Methods* **2012**, *9* (7), 671−675.

(34) Presser, V.; McDonough, J.; Yeon, S.-H.; Gogotsi, Y. Effect of Pore Size on Carbon Dioxide Sorption by Carbide Derived Carbon. *Energy Environ. Sci.* **2011**, *4* (8), 3059.

(35) Vishnyakov, A.; Ravikovitch, P. I.; Neimark, A. V. Molecular Level Models for CO_2 Sorption in Nanopores. *Langmuir* **1999**, *15* (25), 8736−8742.

(36) Gor, G. Y.; Thommes, M.; Cychosz, K. A.; Neimark, A. V. Quenched Solid Density Functional Theory Method for Characterization of Mesoporous Carbons by Nitrogen Adsorption. *Carbon* **2012**, *50* (4), 1583−1590.

(37) Brunauer, S.; Emmett, P. H.; Teller, E. Adsorption of Gases in Multimolecular Layers. *J. Am. Chem. Soc.* **1938**, *60* (2), 309−319.

(38) Presser, V.; McDonough, J.; Yeon, S. H.; Gogotsi, Y. Effect of Pore Size on Carbon Dioxide Sorption by Carbide Derived Carbon. *Energy Environ. Sci.* **2011**, *4* (8), 3059−3066.

(39) Weingarth, D.; Zeiger, M.; Jäckel, N.; Aslan, M.; Feng, G.; Presser, V. Graphitization as a Universal Tool to Tailor the Potential-Dependent Capacitance of Carbon Supercapacitors. *Adv. Energy Mater.* **2014**, *4* (13), 1400316.

(40) Chen, L.; Bai, H.; Huang, Z.; Li, L. Mechanism Investigation and Suppression of Self-Discharge in Active Electrolyte Enhanced Supercapacitors. *Energy Environ. Sci.* **2014**, *7* (5), 1750−1759.

(41) Stoller, M. D.; Ruoff, R. S. Best Practice Methods for Determining an Electrode Material's Performance for Ultracapacitors. *Energy Environ. Sci.* **2010**, *3* (9), 1294−1301.

(42) Trick, K. A.; Saliba, T. E. Mechanisms of the Pyrolysis of Phenolic Resin in a Carbon/Phenolic Composite. *Carbon* **1995**, *33* (11), 1509−1515.

(43) Van der Bruggen, B.; Schaep, J.; Wilms, D.; Vandecasteele, C. Influence of Molecular Size, Polarity and Charge on the Retention of Organic Molecules by Nanofiltration. *J. Membr. Sci.* **1999**, *156* (1), 29.

(44) Zickler, G. A.; Smarsly, B.; Gierlinger, N.; Peterlik, H.; Paris, O. A Reconsideration of the Relationship between the Crystallite Size La of Carbons Determined by X-ray Diffraction and Raman Spectroscopy. *Carbon* **2006**, *44* (15), 3239−3246.

(45) Tuinstra, F.; Koenig, J. L. Raman Spectrum of Graphite. *J. Chem. Phys.* **1970**, *53* (3), 1126−1130.

(46) Ferrari, A. C.; Robertson, J. Interpretation of Raman Spectra of Disordered and Amorphous Carbon. *Phys. Rev. B: Condens. Matter Mater. Phys.* **2000**, *61* (20), 14095.

(47) Faber, K.; Badaczewski, F.; Oschatz, M.; Mondin, G.; Nickel, W.; Kaskel, S.; Smarsly, B. M. In-Depth Investigation of the Carbon Microstructure of Silicon Carbide-Derived Carbons by Wide-Angle X-ray Scattering. *J. Phys. Chem. C* **2014**, *118* (29), 15705−15715.

(48) Ferrari, A. C. A Model To Interpret the Raman Spectry of Disordered Amorphous and Nanostructured Carbons. *MRS Online Proc. Libr.* **2001**, *675*, W11.5.1.

(49) Findeisen, E.; Feidenhans'l, R.; Vigild, M. E.; Clausen, K. N.; Hansen, J. B.; Bentzon, M. D.; Goff, J. P. Hydrogen Concentration and Mass Density of Diamondlike Carbon Films Obtained by X-ray and Neutron Reflectivity. *J. Appl. Phys.* **1994**, *76* (8), 4636.

(50) Béguin, F.; Presser, V.; Balducci, A.; Frackowiak, E. Carbons and Electrolytes for Advanced Supercapacitors. *Adv. Mater.* **2014**, *26* (14), 2219−2251.

(51) Fic, K.; Lota, G.; Meller, M.; Frackowiak, E. Novel Insight into Neutral Medium as Electrolyte for High-Voltage Supercapacitors. *Energy Environ. Sci.* **2012**, *5* (2), 5842−5850.

(52) Barbieri, O.; Hahn, M.; Herzog, A.; Kötz, R. Capacitance Limits of High Surface Area Activated Carbons for Double Layer Capacitors. *Carbon* **2005**, *43* (6), 1303−1310.

(53) Stoller, M. D.; Magnuson, C. W.; Zhu, Y.; Murali, S.; Suk, J. W.; Piner, R.; Ruoff, R. S. Interfacial Capacitance of Single Layer Graphene. *Energy Environ. Sci.* **2011**, *4* (11), 4685−4689.

(54) Gerischer, H.; McIntyre, R.; Scherson, D.; Storck, W. Density of the Electronic States of Graphite: Derivation from Differential Capacitance Measurements. *J. Phys. Chem.* **1987**, *91* (7), 1930−1935.

(55) Segalini, J.; Iwama, E.; Taberna, P.-L.; Gogotsi, Y.; Simon, P. Steric Effects in Adsorption of Ions from Mixed Electrolytes into Microporous Carbon. *Electrochem. Commun.* **2012**, *15* (1), 63−65.

(56) Yang, C.-M.; Kim, Y.-J.; Endo, M.; Kanoh, H.; Yudasaka, M.; Iijima, S.; Kaneko, K. Nanowindow-Regulated Specific Capacitance of Supercapacitor Electrodes of Single-Wall Carbon Nanohorns. *J. Am. Chem. Soc.* **2007**, *129* (1), 20−21.

(57) Chmiola, J.; Yushin, G.; Gogotsi, Y.; Portet, C.; Simon, P.; Taberna, P. L. Anomalous Increase in Carbon Capacitance at Pore Sizes Less than 1 nm. *Science* **2006**, *313* (5794), 1760−1763.

(58) Chmiola, J.; Largeot, C.; Taberna, P.-L.; Simon, P.; Gogotsi, Y. Desolvation of Ions in Subnanometer Pores and Its Effect on Capacitance and Double-Layer Theory. *Angew. Chem., Int. Ed.* **2008**, *47* (18), 3392−3395.

(59) Raymundo-Piñero, E.; Kierzek, K.; Machnikowski, J.; Béguin, F. Relationship between the Nanoporous Texture of Activated Carbons and Their Capacitance Properties in Different Electrolytes. *Carbon* **2006**, *44* (12), 2498−2507.

(60) Hantel, M. M.; Presser, V.; Kötz, R.; Gogotsi, Y. In Situ Electrochemical Dilatometry of Carbide-Derived Carbons. *Electrochem. Commun.* **2011**, *13* (11), 1221−1224.

(61) Jäckel, N.; Weingarth, D.; Zeiger, M.; Aslan, M.; Grobelsek, I.; Presser, V. Comparison of Carbon Onions and Carbon Blacks As Conductive Additives for Carbon Supercapacitors in Organic Electrolytes. *J. Power Sources* **2014**, *272* (1), 1122−1133.

(62) Weingarth, D.; Noh, H.; Foelske-Schmitz, A.; Wokaun, A.; Kötz, R. A Reliable Determination Method of Stability Limits for Electrochemical Double Layer Capacitors. *Electrochim. Acta* **2013**, *103*, 119−124.

(63) Cericola, D.; Ruch, P. W.; Foelske-Schmitz, A.; Weingarth, D.; Kötz, R. Effect of Water on the Aging of Activated Carbon Based Electrochemical Double Layer Capacitors during Constant Voltage Load Tests. *Int. J. Electrochem. Sci.* **2011**, *6* (4), 988−996.

(64) Wang, W.; Luo, Q.; Li, B.; Wei, X.; Li, L.; Yang, Z. Recent Progress in Redox Flow Battery Research and Development. *Adv. Funct. Mater.* **2013**, *23* (8), 970−986.

(65) Weber, A. Z.; Mench, M. M.; Meyers, J. P.; Ross, P. N.; Gostick, J. T.; Liu, Q. Redox Flow Batteries: A Review. *J. Appl. Electrochem.* **2011**, *41* (10), 1137−1164.

(66) Rahman, F.; Skyllas-Kazacos, M. Solubility of Vanadyl Sulfate in Concentrated Sulfuric Acid Solutions. *J. Power Sources* **1998**, *72* (2), 105−110.

(67) Laheäär, A.; Przygocki, P.; Abbas, Q.; Béguin, F. Appropriate Methods for Evaluating the Efficiency and Capacitive Behavior of Different Types of Supercapacitors. *Electrochem. Commun.* **2015**, *60*, 21−25.

(68) Nishihara, H.; Itoi, H.; Kogure, T.; Hou, P.-X.; Touhara, H.; Okino, F.; Kyotani, F. Investigation of the Ion Storage/Transfer Behavior in an Electrical Double-Layer Capacitor by Using Ordered Microporous Carbons as Model Materials. *Chem. - Eur. J.* **2009**, *15* (21), 5355−5363.

(69) Ramirez-Castro, C.; Schütter, C.; Passerini, S.; Balducci, A. Microporous Carbonaceous Materials Prepared from Biowaste for Supercapacitor Application. *Electrochim. Acta* **2016**, DOI: 10.1016/j.electacta.2015.12.126.

(70) Fang, B.; Wei, Y. Z.; Maruyama, K.; Kumagai, M. High Capacity Supercapacitors Based on Modified Activated Carbon Aerogel. *J. Appl. Electrochem.* **2005**, *35* (3), 229−233.

Sub-micrometer Novolac-Derived Carbon Beads for High Performance Supercapacitors and Redox Electrolyte Energy Storage

Benjamin Krüner,[1,2] Juhan Lee,[1,2] Nicolas Jäckel,[1,2] Aura Tolosa,[1,2] and Volker Presser[1,2,*]

[1] *INM - Leibniz Institute for New Materials, 66123 Saarbrücken, Germany*

[2] *Department of Materials Science and Engineering, Saarland University, 66123 Saarbrücken, Germany*

* *Corresponding author's eMail: volker.presser@leibniz-inm.de*

Table S1: Electrode properties. Note the reduced active mass per electrode as a result of the increased porosity at comparable electrode thickness.

	Electrode density (mg/cm^3)	**Active mass (mg)**	**Electrode diameter (mm)**	**Electrode thickness (mm)**
PNC_{0h}	611	15.2	12	0.22
$PNC_{0.25h}$	442	8.5	12	0.17
$PNC_{0.5h}$	385	8.7	12	0.20
PNC_{1h}	230	3.9	12	0.15
$PNC_{1.5h}$	169	2.3	12	0.12
PNC_{2h}	161	3.1	12	0.17

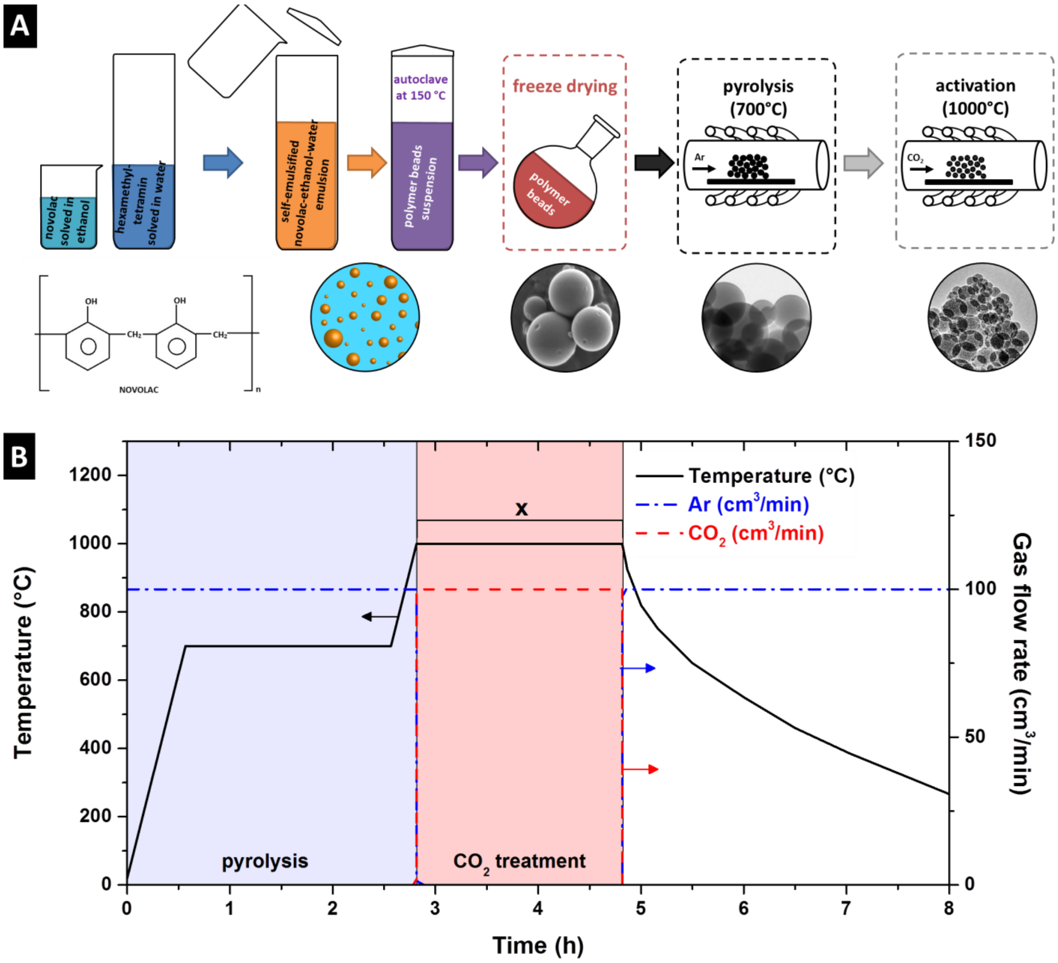

Figure S1: Schematic illustration of the synthesis route (A) and processing conditions of the pyrolysis and CO_2-treatment (B). The parameter X denotes the duration of the CO_2-treatment (physical activation), which was varied for the different experiments.

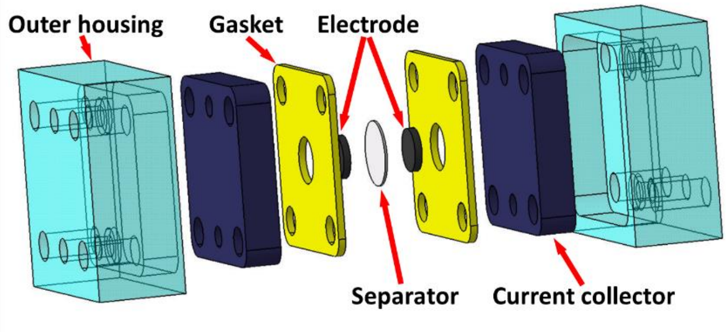

Figure S2: Schematic setup of the redox-electrolyte cell.

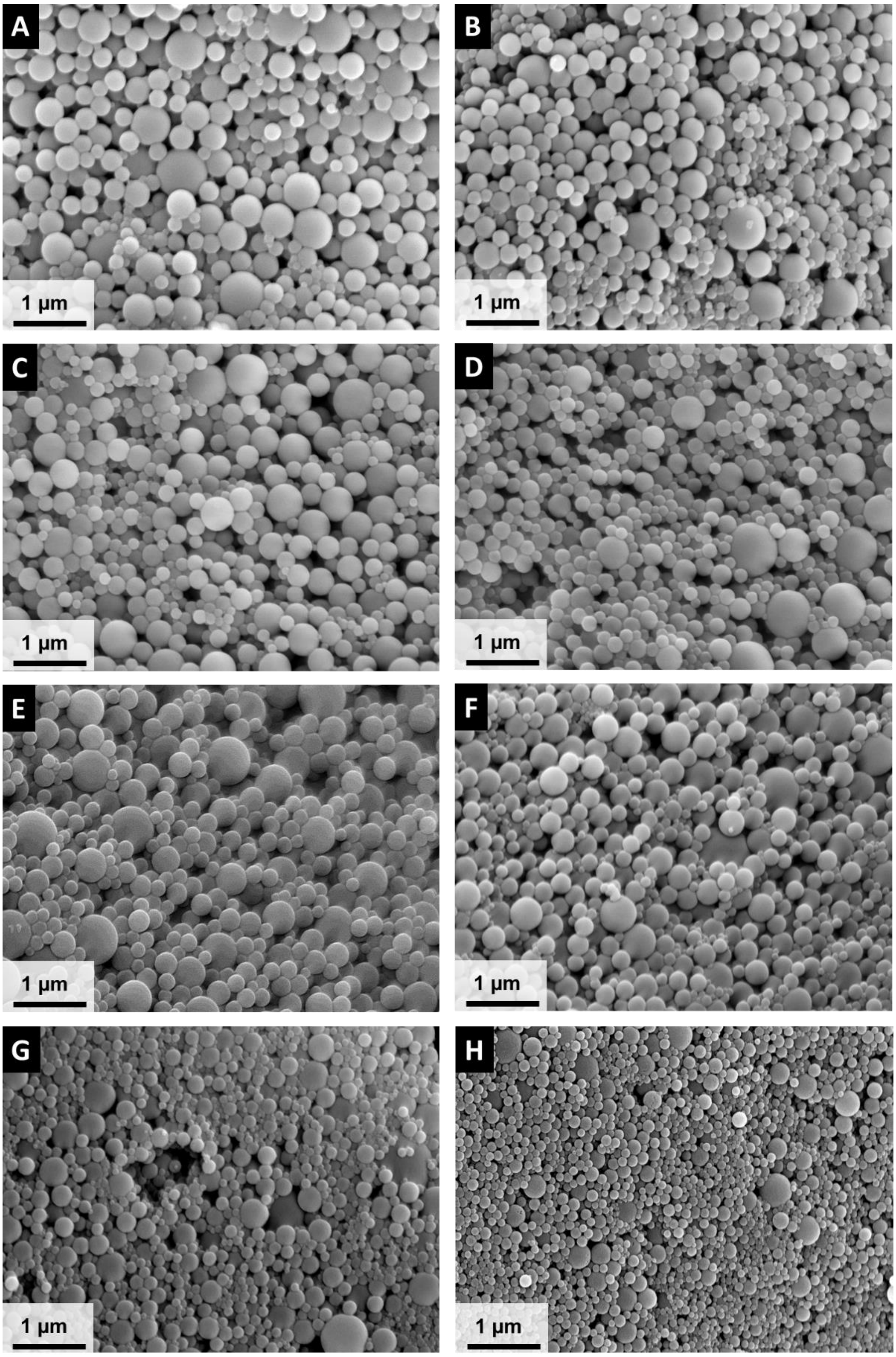

Figure S3: SEM images of PNC_{0h} (A), $\text{PNC}_{0.25h}$ (B), $\text{PNC}_{0.5h}$ (C), PNC_{1h} (D), $\text{PNC}_{1.5h}$ (E), PNC_{2h} (F), $\text{PNC}_{2.5h}$ (G), and PNC_{3h} (H).

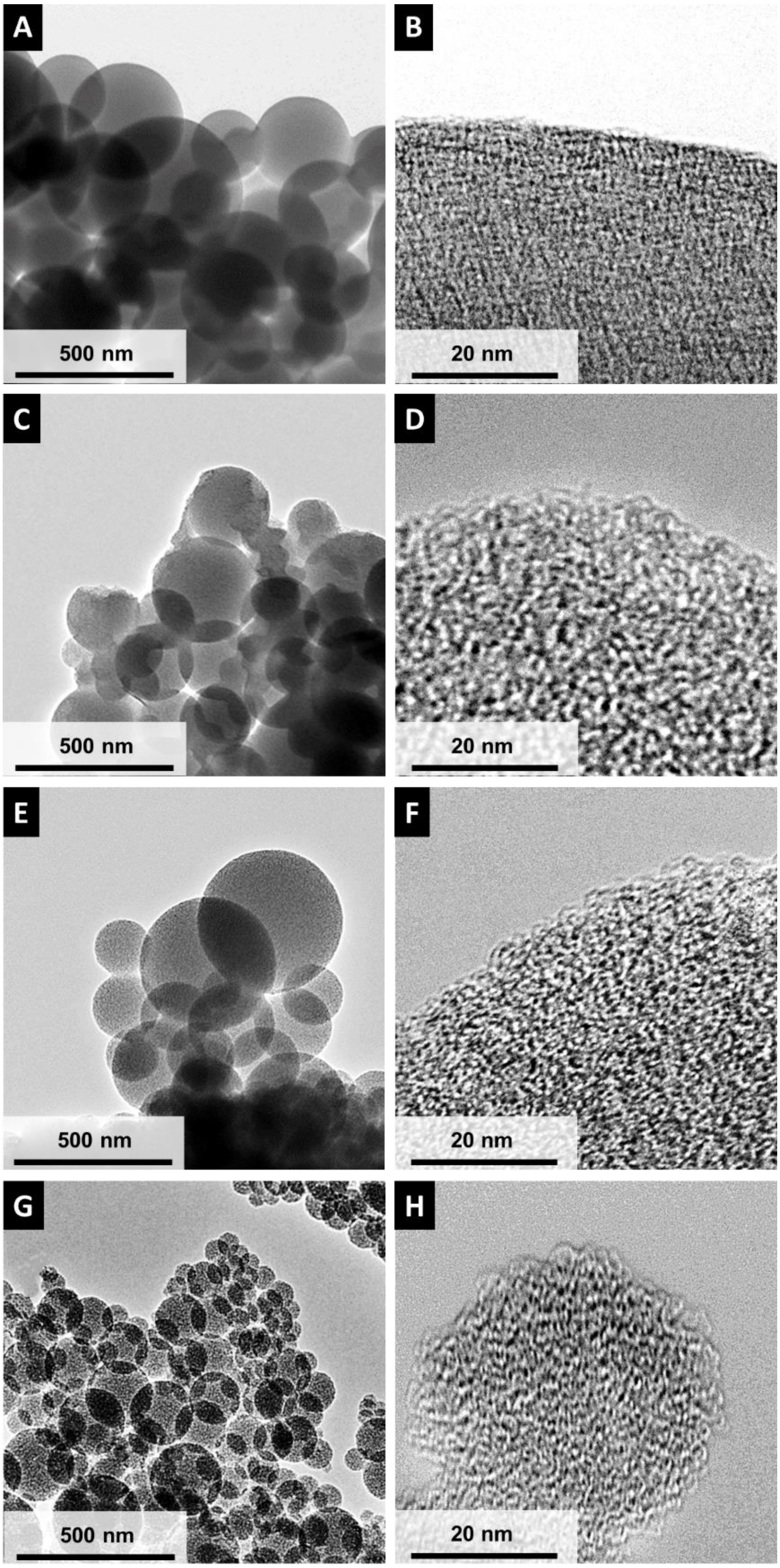

Figure S4: TEM images of the pyrolyzed PNC_{0h} (a, b) and the CO_2 activated PNC_{1h} (c, d), PNC_{2h} (e, f) and PNC_{3h} (g, h).

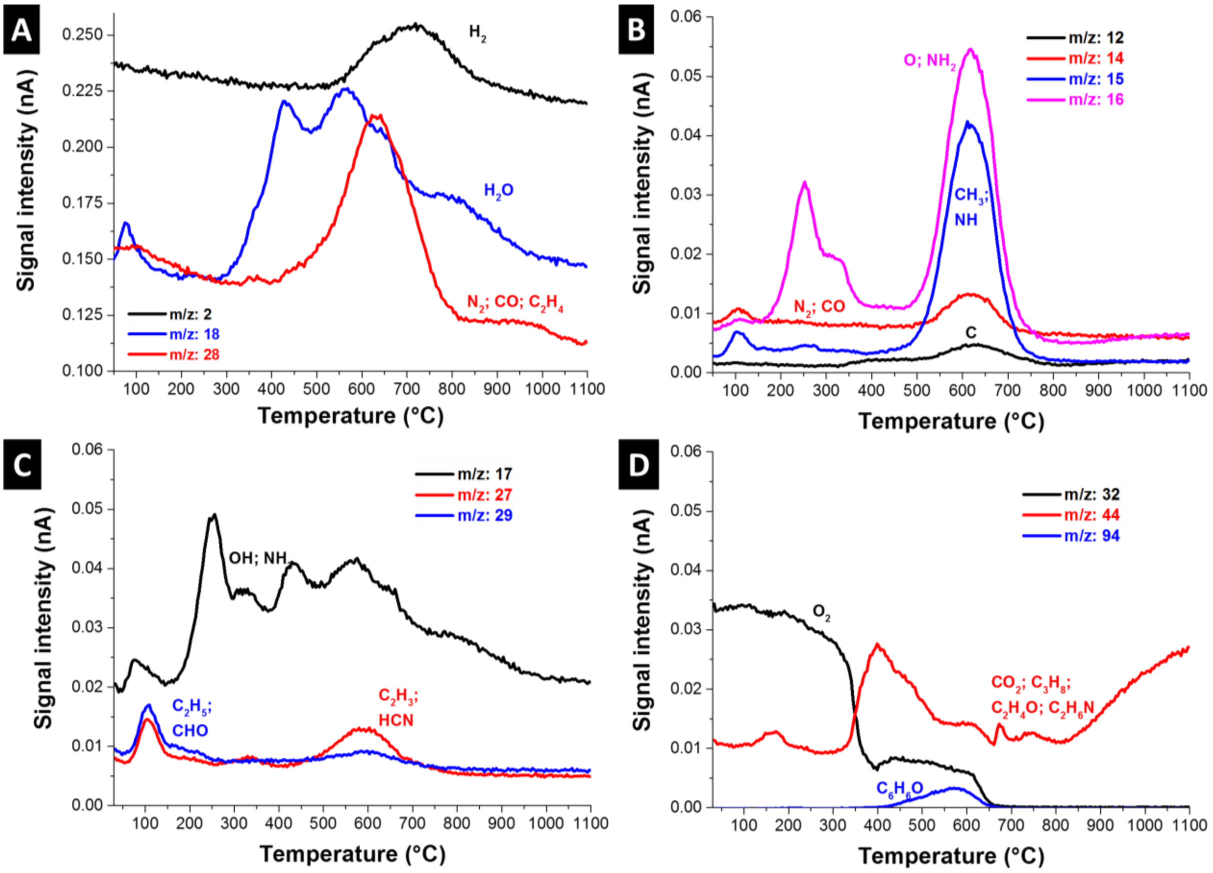

Figure S5: TGA-MS graphs (ionic current vs. temperature) of the pyrolysis of the polymeric beads for the m/z: 2, 18, and 28 (a), m/z: 12, 14, 15, and 16 (b), m/z: 17, 27, and 29 (c), m/z: 32, 44, and 94 (d).

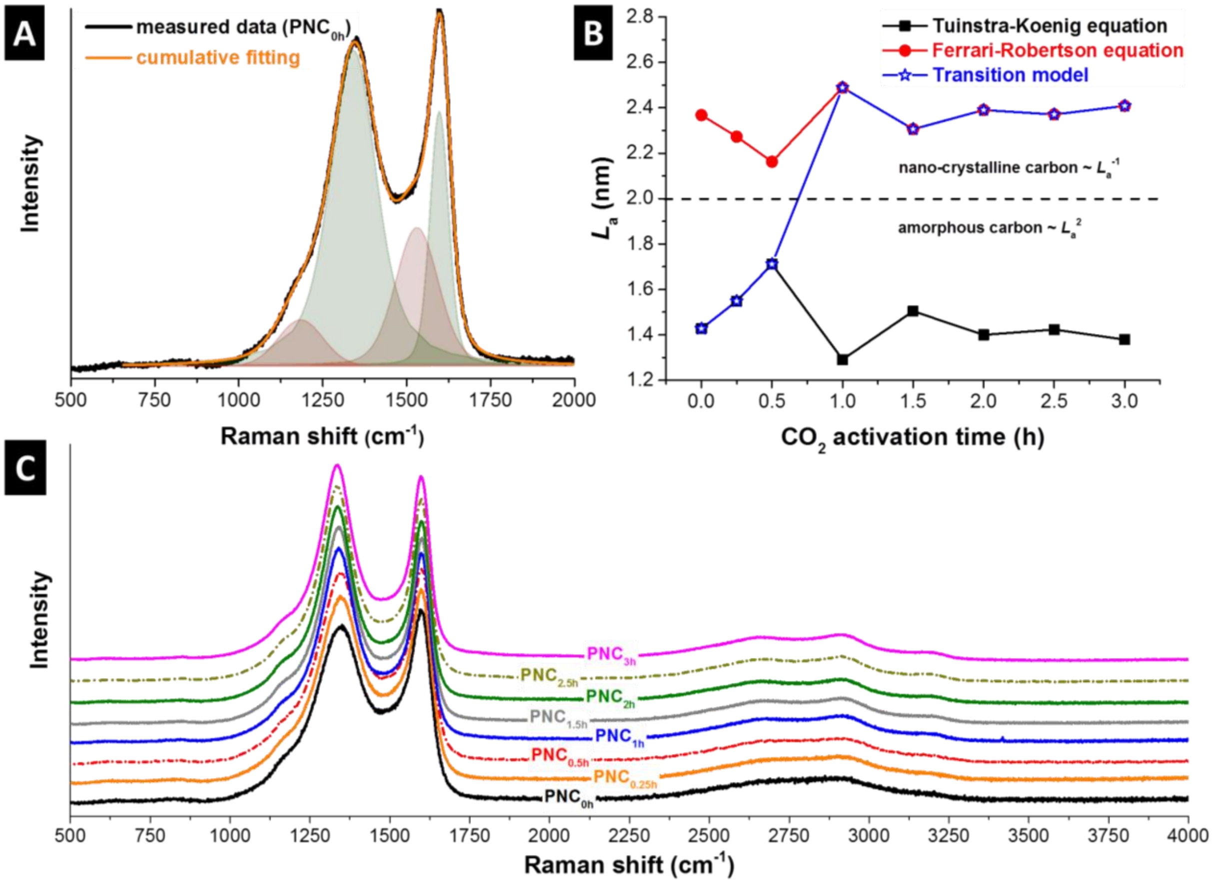

Figure S6: Raman spectra of PN$_{0h}$ showing the two-peak fitting for the D- and G-mode (A) and the average in-plane domain size (L_a) calculated with the Tuinstra-Koenig (black) and Ferrari-Robertson equation (red) and assuming a transition between the two models regarding the L_a values (blue) (B). Raman spectra of the pyrolyzed and activated carbon beads (C). The spectra were off-set by 10% along the *y*-axis for improved visibility.

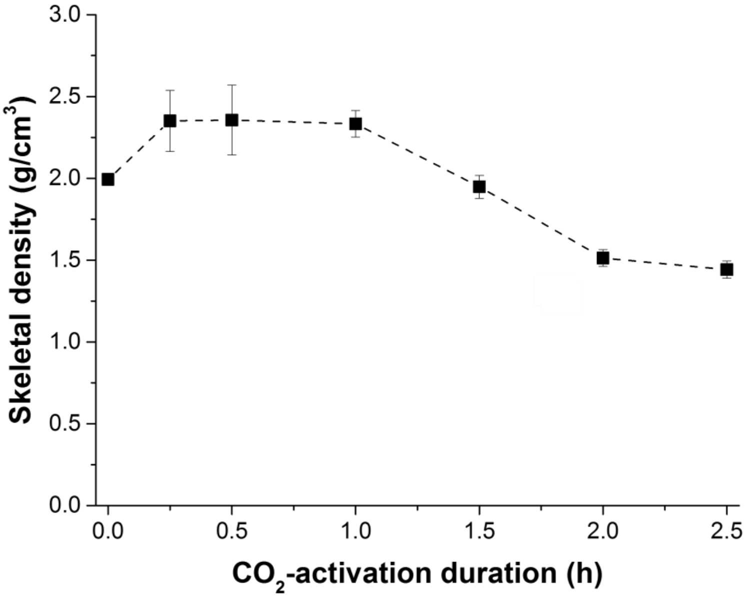

Figure S7: Skeletal density of the carbon beads vs. the CO_2-activation duration measured by pyknometry.

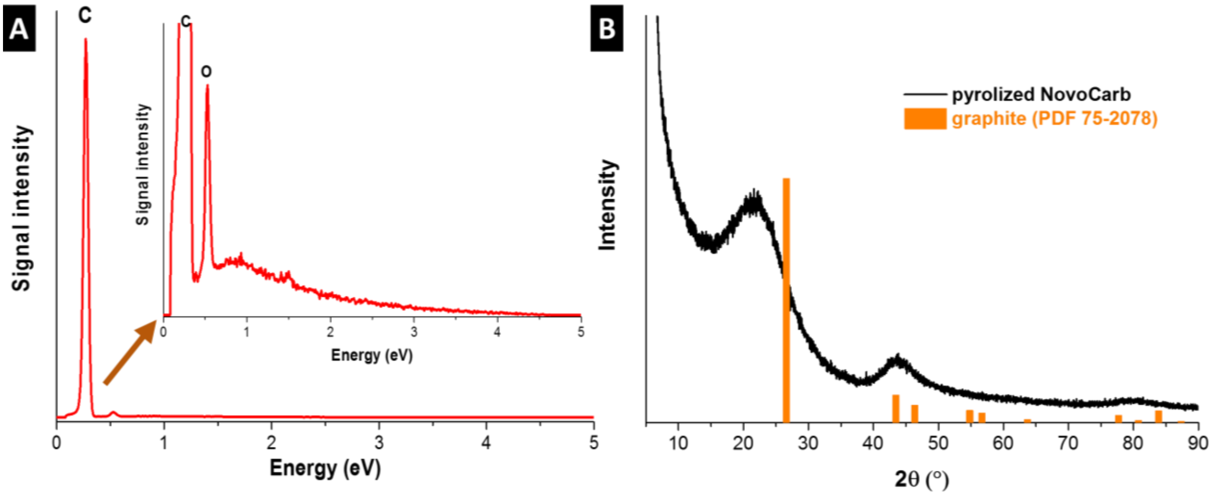

Figure S8: EDX spectra of the pyrolyzed carbon beads (PN$_{0h}$) by an accelerating voltage of 5 keV (A). Only carbon and oxygen can be clearly identified. XRD pattern of the pyrolized NovoCarb (at 1000 °C), which is mainly amorphous (B).

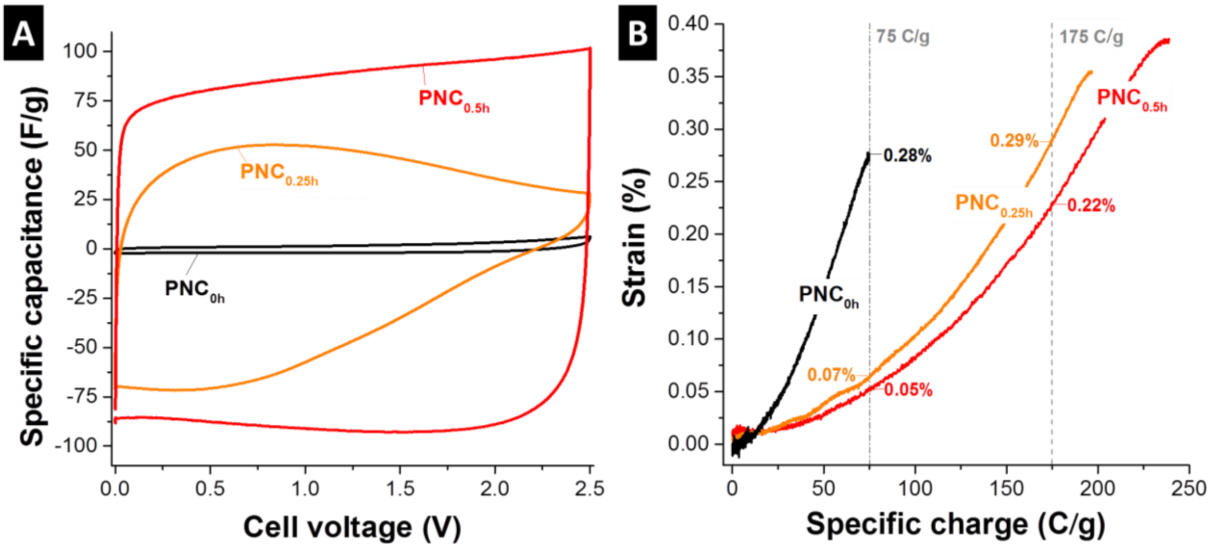

Figure S9: Cyclic voltammograms at 5 mV/s (A) and in-situ dilatometry data (B) of non-activated PNC_{0h} and two activated novolac-derived carbons ($PNC_{0.25h}$ and $PNC_{0.5h}$) in 1 M TEA-BF_4 in PC. The strain data were recorded with a scan rate of 1 mV/s and only data during charging (not discharging) are shown. For a relative comparison, the strain values at 75 C/g and 175 C/g are denoted.

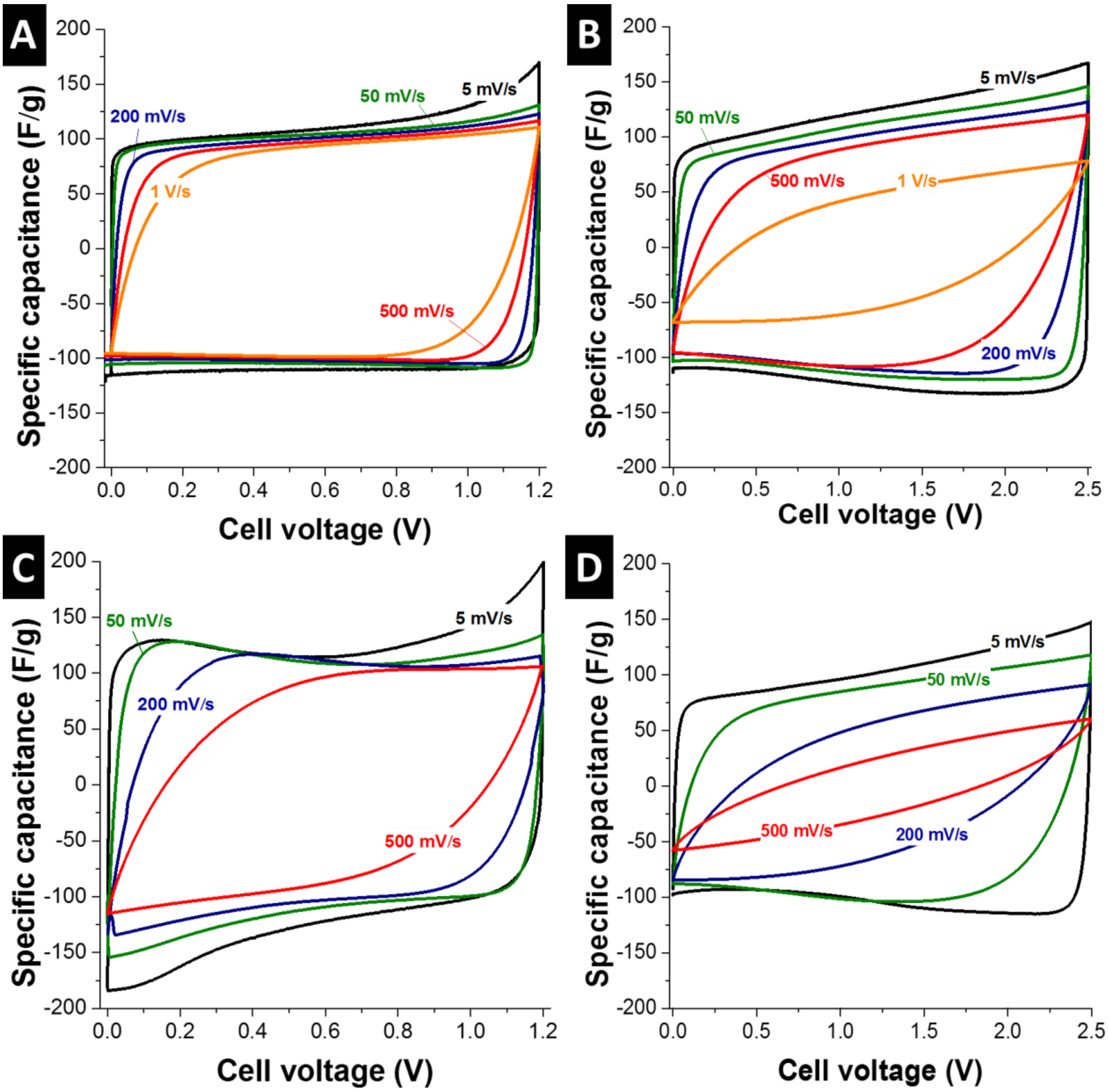

Figure S10: CVs of PNC$_{2h}$ in aqueous 1 M Na_2SO_4 (a) and in 1 M TEA-BF_4 in PC (b) with a scan rate varying from 5 mV/s to 1 V/s and CVs of AC in aqueous 1 M Na_2SO_4 (c) and in 1 M TEA-BF_4 in PC (d) with a scan rate varying from 5 mV/s to 500 mV/s.

4.2. Hydrogen-treated, sub-micrometer carbon beads for fast capacitive deionization with high performance stability

Benjamin Krüner,[1,2] Pattarachai Srimuk,[1,2] Simon Fleischmann,[1,2] Marco Zeiger,[1,2]

Anna Schreiber,[1] Mesut Aslan,[1] Antje Quade,[3] Volker Presser[1,2]

[1] *INM - Leibniz Institute for New Materials, 66123 Saarbrücken, Germany*

[2] *Department of Materials Science and Engineering, Saarland University, 66123 Saarbrücken, Germany*

[3] *Leibniz Institute for Plasma Science and Technology, 17489 Greifswald, Germany*

Krüner, Benjamin et al. (2017) *Carbon*, 117, 46-54
https://doi.org/10.1016/j.carbon.2017.02.054

Own contribution: Design, planning, writing, synthesis of the activated and non-activated carbon beads, SEM, DLS, particle size analysis, TGA coupled with MS analysis, N_2 sorption analysis, Raman analysis, electrochemical analysis for double-layer capacitors, CDI data analysis.

Abstract:

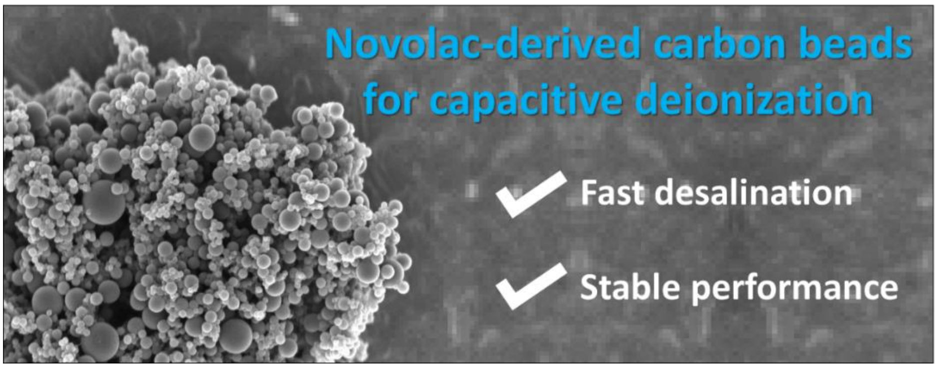

Novolac is a low-cost carbon precursor which can be used to derive nanoporous carbon beads in sub-micrometer size. In this study, we introduce this material as a novel electrode material for capacitive deionization (CDI) with high performance stability and superior desalination rate. The polymer beads were synthesized employing a self-emulsifying system in an autoclave, pyrolyzed under argon, and activated with CO_2, yielding a specific surface area of 1905 $m^2\ g^{-1}$ with a high total pore volume of 1.26 $cm^3\ g^{-1}$. After CO_2 activation, the material shows a salt sorption capacity of ~8 $mg\ g^{-1}$, but the performance is highly influenced by functional groups, causing an inversion peak and fast performance decay. However, de-functionalization via hydrogen treatment is outlined as an effective strategy to improve the CDI performance. After hydrogen treatment of novolac-derived carbon beads, we obtained a salt sorption capacity of 11.5 $mg\ g^{-1}$ with a charge efficiency of more than 80% and a performance stability of around 90% over more than 100 cycles. Particularly attractive for practical application is the very high average salt adsorption rate of 0.104 $mg\ g^{-1}\ s^{-1}$, outperforming commercial activated carbons, which are commonly used for CDI, by at least a factor of two.

Carbon 117 (2017) 46–54

Contents lists available at ScienceDirect

Carbon

journal homepage: www.elsevier.com/locate/carbon

Hydrogen-treated, sub-micrometer carbon beads for fast capacitive deionization with high performance stability

Benjamin Krüner [a, b], Pattarachai Srimuk [a, b], Simon Fleischmann [a, b], Marco Zeiger [a, b], Anna Schreiber [a], Mesut Aslan [a], Antje Quade [c], Volker Presser [a, b, *]

[a] INM - Leibniz Institute for New Materials, 66123, Saarbrücken, Germany
[b] Department of Materials Science and Engineering, Saarland University, 66123, Saarbrücken, Germany
[c] Leibniz Institute for Plasma Science and Technology, 17489, Greifswald, Germany

A R T I C L E I N F O

Article history:
Received 25 December 2016
Received in revised form
16 February 2017
Accepted 17 February 2017
Available online 20 February 2017

Keywords:
Capacitive deionization
Porous carbon
Activated carbon

A B S T R A C T

Novolac is a low-cost carbon precursor which can be used to derive nanoporous carbon beads in sub-micrometer size. In this study, we introduce this material as a novel electrode material for capacitive deionization (CDI) with high performance stability and superior desalination rate. The polymer beads were synthesized employing a self-emulsifying system in an autoclave, pyrolyzed under argon, and activated with CO_2, yielding a specific surface area of 1905 m^2 g^{-1} with a high total pore volume of 1.26 cm^3 g^{-1}. After CO_2 activation, the material shows a salt sorption capacity of ~8 mg g^{-1}, but the performance is highly influenced by functional groups, causing an inversion peak and fast performance decay. However, de-functionalization via hydrogen treatment is outlined as an effective strategy to improve the CDI performance. After hydrogen treatment of novolac-derived carbon beads, we obtained a salt sorption capacity of 11.5 mg g^{-1} with a charge efficiency of more than 80% and a performance stability of around 90% over more than 100 cycles. Particularly attractive for practical application is the very high average salt adsorption rate of 0.104 mg g^{-1} s^{-1}, outperforming commercial activated carbons, which are commonly used for CDI, by at least a factor of two.

1. Introduction

With an increasing population and progressing scarcity of access to clean drinking water, tremendous research efforts have been invested to advance established desalination technologies, such as distillation, reverse osmosis, and electrodialysis [1]. Over the last decades, capacitive deionization (CDI) has emerged as a novel desalination method which is particularly attractive for desalination of brackish water (salt concentration < 170 mM) [2] due to its low energy consumption compared to other techniques [3–5]. CDI operation is based on the reversible electrosorption of ions at the surface of an electrically charged electrode, typically consisting of nanoporous carbon [6]. During the desalination process, ions are removed from the solution by electro-adsorption within the porous electrodes. The electrodes can be regenerated by discharging to electro-desorb the ions, creating an effluent stream with increased salt concentration. In contrast to this conventional CDI process, inversed CDI was recently introduced, in which the surface of the electrode is already charged due to the presence of functional groups [7,8]. Such “chemical charges” [9] can also be employed as an effective tool to enhance the desalination capacity of carbon materials [10].

A key performance parameter for CDI is the salt adsorption capacity (SAC), which is highly dependent on the pore structure [11]. While micropores exhibit the highest differential salt removal capacity (SAC per pore volume), also the contribution of meso- and macropores has to be considered [11]. The latter are of particularly high importance to accomplish fast transport of ions within the electrode, resulting in high deionization rates [6,11]. A suitable way to evaluate the trade-off between SAC and desalination rate has been introduced by Kim and Yoon by so called CDI Ragone plots (also known as Kim-Yoon plots) [12].

The most common electrode materials for CDI are highly porous carbons [3], although hybrid materials [13,14], and non-carbons (like MXenes [15] or metal oxides [16]) have recently also been introduced. Commercially available activated carbon materials

---

* Corresponding author. INM - Leibniz Institute for New Materials, 66123, Saarbrücken, Germany.
E-mail address: volker.presser@leibniz-inm.de (V. Presser).

http://dx.doi.org/10.1016/j.carbon.2017.02.054
0008-6223/© 2017 Elsevier Ltd. All rights reserved.

typically show a SAC of up to 14 mg g^{-1} (MSP-20) in 5 mM saline solution (NaCl, de-aerated) at a cell voltage of 1.2 V [11]. Under these conditions, other common activated carbons (like YP-50F or YP-80F, Kuraray) show a SAC of 9–12 mg g^{-1} which can be increased by CO_2 activation to ~13 mg g^{-1} [6,17]. Further, values up to 21 mg g^{-1} have been reported for highly developed designer carbon (like nitrogen-doped graphene foam) [18].

To further facilitate the technological implementation of CDI, it is particularly necessary to explore low-cost electrode materials. For example, phenolic resins (resol or novolac) derived carbons are a very attractive carbon sources, due to their high carbon yields, availability, and low price (ca. ~3 € kg^{-1}) [19]. In a previous study, we introduced a facile self-emulsifying synthesis for sub-micrometer novolac-derived carbon beads (PNC), which were CO_2-activated and applied for electrochemical energy storage in supercapacitors [19]. In this study, we investigate the CDI performance of novolac-derived carbon beads and present hydrogen treatment as a strategy to improve the CDI performance in three ways: increasing the SAC, charge efficiency, and performance stability. In addition, the salt adsorption rate is superior to other porous carbon materials.

2. Experimental description

2.1. Synthesis of novolac-derived carbon beads

A detailed synthesis outline of the novolac-derived carbon beads is provided in Ref. [19]. In short, novolac (20 g of ALNOVOL PN 320, Allnex Germany) was dissolved in 100 mL ethanol and added to a mixture of 2 g of hexamethylenetetramine (TCI Deutschland) and 500 mL deionized water. The self-emulsified mixture was heated to 150 °C and held at this temperature for 8 h in a 1 L autoclave. The crosslinked polymer particles were freeze-dried and pyrolyzed at 1000 °C for 2 h using a heating rate of 20 °C min^{-1} in a graphite heated furnace (Thermal Technology). The pyrolyzed sample is referred to as “PNC-Pyro”. CO_2 activation was carried out in a rotary quartz-glass tube furnace (HTM Reetz) at 1000 °C for 4 h with a CO_2 flow of 3.6 mL min^{-1}. During heating at 10 °C min^{-1} and during cooling, the furnace was flushed with nitrogen gas. The CO_2 activated sample is denoted “PNC-CO_2”. Carbon de-functionalization was carried out at 1000 °C with a heating rate of 10 °C·min^{-1} in a wolfram heated high temperature furnace (G-2200-91, Thermal Technology) under H_2 flow (~20 mL min^{-1}). The de-functionalized beads are labeled as “PNC-H_2”.

For comparison, also CDI data are shown for commercially available activated carbons (MSP-20 from Maxsorb and YP-80F from Kuraray), which were used as received. For previous CDI work on these two carbons, see Refs. [11,17].

2.2. Materials characterization

The size of the polymer particles in suspension was analyzed via dynamic light scattering (DLS; UPA 150, Microtrac) with a 3 mW diode laser with a wavelength of 780 nm. In addition, scanning electron microscopy (SEM) was carried out with a field emission scanning electron microscope (JEOL JSM-7500F). The diameter of the beads was determined via image analysis with ImageJ 1.47t [20].

Raman spectra were recorded with a Renishaw inVia Raman Microscope operating with a Nd-YAG laser (wavelength: 532 nm; grating: 2400 lines·mm^{-1}; objective: 50×; numeric aperture: 0.9; spectral resolution: ~1.2 cm^{-1}). The incident power on the sample was ~0.02 mW with an acquisition time of 30 s and 10 accumulations were collected. The amorphous contribution, the D- and the G-modes were fitted with OriginPro 9.3 using a total of four Voigt profile functions.

Gas sorption analyses (GSA) with nitrogen were performed with a Quantachrome Autosorb iQ system. The vacuum degassing was carried out at 200 °C for 1 h and afterwards heated up to 300 °C and hold at this temperature for 20 h at a relative pressure of 0.1 Pa to remove volatile surface species. The measurements were performed in liquid nitrogen at −196 °C. The relative pressure of nitrogen was increased from $5 \cdot 10^{-7}$ to 1.0 in 76 steps. A quenched-solid density functional theory (QSDFT) was used to calculate the pore size distribution (PSD) assuming slit-like pores [21–24] and the Brunauer-Emmett-Teller equation (BET) [25] was applied in the linear, low pressure regime of the measured isotherms to obtain the specific surface area (SSA) as well. The total pore volume was extracted at a relative pressure of $p/p_0 = 0.95$. The cumulative pore size corresponding with the half of the pore volume (d_{50} value) is referred to as average pore size [22]. The Quantachrome software ASiQwin 3.0 was used for all GSA calculations.

The carbon samples were also analyzed by thermogravimetric measurement combined with a mass spectrometer (TGA-MS; STA449F3 Jupiter and QMS 403C Aëolos from Netzsch) with a heating rate of 10 °C min^{-1} to 1200 °C in Ar (purity: 5.0).

X-ray photoelectron spectroscopy (XPS) was carried out with an Axis Ultra DLD (Kratos Analytical) with Al K_α radiation (15 kV, 10 mA for general spectra and 15 kV, 15 mA for the highly resolved measured C 1s peak). Data acquisition and processing were carried out using CasaXPS 2.3.15 (Casa Software). After subtraction of Shirley background, the peaks were fitted using Gaussian Lorentzian GL(30) peak shape, for the sp^2-hybridized carbon component an asymmetric line shape was used, which is described in the Doniach–Šunjić function.

The streaming potential was measured with Mütek PCD.03 pH (BTG Instruments). For the measurements, 100 mg of the novolac-derived carbon powder was dispersed in 30 mL deionized water (Milli-Q) with ultrasound and stirred for 10 h. The pH was adjusted with NaOH to a value of 9 and 21 g of the dispersion were titrated with HCl (30 mM) down to a pH of 3.

Contact angle measurements on carbon electrodes were carried out with demineralized water in air using an OC 25 system (Data Physics).

2.3. Electrochemical measurements

Polytetrafluoroethylene (PTFE, 60 mass% in H_2O) was used as binder to prepare free standing electrodes, as detailed in Refs. [26,27]. First, carbon powder was dispersed in ethanol and afterwards the PTFE dispersion was added. The slurry was ground in a mortar during the ethanol evaporation. The resulting carbon paste was rolled out to become a free-standing electrode with a PTFE content of 5 mass% and a final thickness of 110–140 μm. A vacuum furnace with 120 °C and $2 \cdot 10^3$ Pa was used to dry the electrodes for 48 h. For the electrochemical measurements, round electrode discs with a diameter of 10 mm were punched out of the free-standing electrode sheet. A symmetrical two-electrode setup was assembled with custom-built cells [26]. Graphite foils were used as current collector and glass-fiber mats (GF/A, Whatman, GE Healthcare Life Science) with a diameter of 13 mm as separator.

The cyclic voltammetry (CV) and galvanostatic cycling with potential limitation (GCPL) were performed in a symmetric full-cell with an Ag/AgCl reference electrode in aqueous 1 M NaCl with a VMP300 potentiostat/galvanostat from BioLogic. The specific capacitance was calculated with Eq. (1) from CVs and with Eq. (2) for data from GCPLs. For a comparison of different materials, the capacitance was normalized to the active mass of one electrode material [28,29].

$$C_S = \frac{I(t)}{dU(t)/_{dt} \cdot m} \tag{1}$$

C_S: specific capacitance per electrode, $I(t)$: discharge current, $dU(t)/dt$: scan rate, and m: mass of carbon in the electrode.

$$C_S = \frac{4 \cdot Q_{dis}}{U \cdot m} \tag{2}$$

C_S: specific capacitance per electrode, Q_{dis}: charge of the discharging cycle, U: IR-drop corrected cell voltage, and m: mass of carbon in the electrode.

2.4. Capacitive deionization measurements

The free-standing electrodes, which were prepared like the electrodes for electrochemical characterization, where also used for the CDI experiments to obtain a good comparability. The PNC-CO_2 electrodes had a total mass of 291 mg with a thickness of 135 µm for each electrode and a density of 0.34 g cm^{-3}. The mass of both PNC-H_2 electrodes was 331 mg with a thickness of 120 µm and a density of 0.37 g cm^{-3}. The CDI measurements were carried out using a VSP300 potentiostat from Bio-Logic with a CDI device in flow-by mode [30]. A porous spacer (glass fiber pre-filter, Millipore, compressed thickness of a single layer: 380 µm) was used to separate both electrodes. A constant flow rate of 22 mL min^{-1} was adjusted for the experiments. Prior of the CDI test, the dissolved oxygen was removed from the electrolyte via nitrogen gas bubbling (3 h).

The ion adsorption half-cycles were carried out using constant cell voltage of 1.2 V with a holding time of 30 min and the regeneration was accomplished at 0 V also for 30 min. The increase in conductivity in the outlet stream is used to quantify the number of released ions from the initially charged electrodes. The electrolyte for all CDI experiments was 5 mM NaCl in a 10 L electrolyte container which was continuously flushed with nitrogen gas to purge the water from dissolved oxygen. A conductivity meter (Metrohm) and a pH meter were inserted behind the CDI device. The water conductivity was calculated with the following equation:

$$\sigma_W = \frac{e^2}{k_B \cdot T}\left(10^{-pH} \cdot N_A \cdot D_{H_3O^+} + \frac{10^{-14}}{10^{-pH}} \cdot N_A \cdot D_{OH^-}\right) \tag{3}$$

σ_W: conductivity of water, e: elementary charge, k_B: Boltzmann constant, N_A: Avogadro constant, $D_{H_3O^+}$: diffusion coefficient of H_3O^+, D_{OH^-}: diffusion coefficient of OH^-.

The actual conductivity was calculated from the measured conductivity and the water conductivity with Eq. (4).

$$\sigma_n = \sigma_m - \sigma_w \tag{4}$$

σ_n: actual conductivity, σ_m: measured conductivity.

The concentration of the electrolyte in mmol L^{-1} was obtained from actual conductivity in mS cm^{-1} by the following equation, which was fitted to the calibration curve.

$$c = \left(\frac{\sigma_n - 4.5}{121.29}\right)^{1/0.9826} - 0.13 \tag{5}$$

c: concentration.

The salt adsorption capacity (SAC) was calculated for the adsorption and desorption step separately and the average value was normalized to the active mass of the electrodes.

$$SAC = \int c dt \cdot \frac{\dot{v} \cdot M_{NaCl}}{m_{total}} \tag{6}$$

SAC: salt adsorption capacity, t: time of each step (30 min), $\dot{v}$: flow-rate, M_{NaCl}: molar mass of NaCl, m_{total}: active mass of both electrodes.

The charge efficiency was obtained by dividing the charge used for ion sorption by the total charge as followed.

$$\Lambda = \left(SAC \cdot \frac{m_{total}}{M_{NaCl}}\right) \Big/ \left(\int I\, dt \Big/ N_A \cdot e\right) \tag{7}$$

Λ: charge efficiency, I: current.

The mean deionization rate was determined by reducing the integration time of the 15th cycle successively and dividing the SAC by the adsorption time to construct a Kim-Yoon plot (also known as CDI Ragone plot) [12].

3. Results and discussion

3.1. Material characterization

A key feature of novolac-derived carbon beads is their submicrometer diameter. The DLS measurement of the polymer beads in suspension yields a volume weighted average diameter of 244 ± 137 nm, which is similar to the diameter of pyrolyzed PNC beads (302 ± 142 nm) [19], as inferred from SEM image analysis (Fig. 1A-B). The similarity shows also that the beads consisting of nanometer sized primary particles did not agglomerate during the polymerization in the autoclave. The pyrolyzed novolac beads (PNC-Pyro) agglomerated to form micrometer sized particles, as can be seen from Fig. 1B.

After pyrolysis, as-synthesized novolac-derived carbon beads demonstrate microporosity which can be further modified by physical activation, for example, in CO_2 gas [19]. The isotherms and the cumulative pore volume of the three novolac-derived carbons are plotted in Fig. 1B, C and the porosity parameters are given in Table 1. The sample PNC-Pyro has a specific DFT surface area of 641 m^2 g^{-1} and a total pore volume of 0.25 cm^3 g^{-1} with an average pore size of 0.6 nm. Such a low porosity (surface area and pore volume) would be unattractive for CDI [11,30], making an activation process necessary. After CO_2 activation at 1000 °C, the DFT SSA was increased to 1905 m^2 g^{-1} with a pore volume of 1.26 cm^3 g^{-1} and an average pore size of 1.5 nm. The porosity was largely conserved after the H_2 treatment also at 1000 °C, which yielded a DFT SSA of 1755 m^2 g^{-1} with the same pore volume than before. Thereby, the average pore size increased slightly to 1.6 nm, which can be explained with a collapse of microspores and the creation of more mesopores. The hydrogen treatment led to a mass loss of ~7 mass%, which is a consequence of the loss of functional groups and other volatile compounds like adsorbed water.

Novolac-derived carbon is expected to yield nanocrystalline graphitic carbon [19]. The Raman spectra of PNC-Pyro, PNC-CO_2, and PNC-H_2 are shown in Fig. 1E and the fitted values are provided in Table 2. The D- and G-mode of PNC-Pyro is at 1351 cm^{-1} and 1603 cm^{-1} with a full-width at half maximum (FWHM) of 144.8 cm^{-1} and 70.0 cm^{-1}, respectively. The I_D/I_G ratio is 2.78, corresponding to nanocrystalline carbon [31]. The positions of the D- and G-mode are slightly shifted after the CO_2 activation to 1337 cm^{-1} and 1601 cm^{-1} and we also see more narrow peaks ($FWHM_D$: 123.6 cm^{-1}, $FWHM_G$: 62.1 cm^{-1}). The I_D/I_G ratio of PNC-CO_2 increases to 3.35 and is further increased to 3.55 after hydrogen treatment, which is according to the model of Ferrari and Robertson indicating an increase in carbon ordering for crystalline domain sizes below ~2 nm [32]. A higher degree of carbon ordering is also indicated by a decrease of the FWHM ($FWHM_D$: 97.5 cm^{-1}, $FWHM_G$: 53.7 cm^{-1}), while the peak positions remain almost constant (D-mode: 1336 cm^{-1} and G-mode: 1601 cm^{-1}). The higher structural

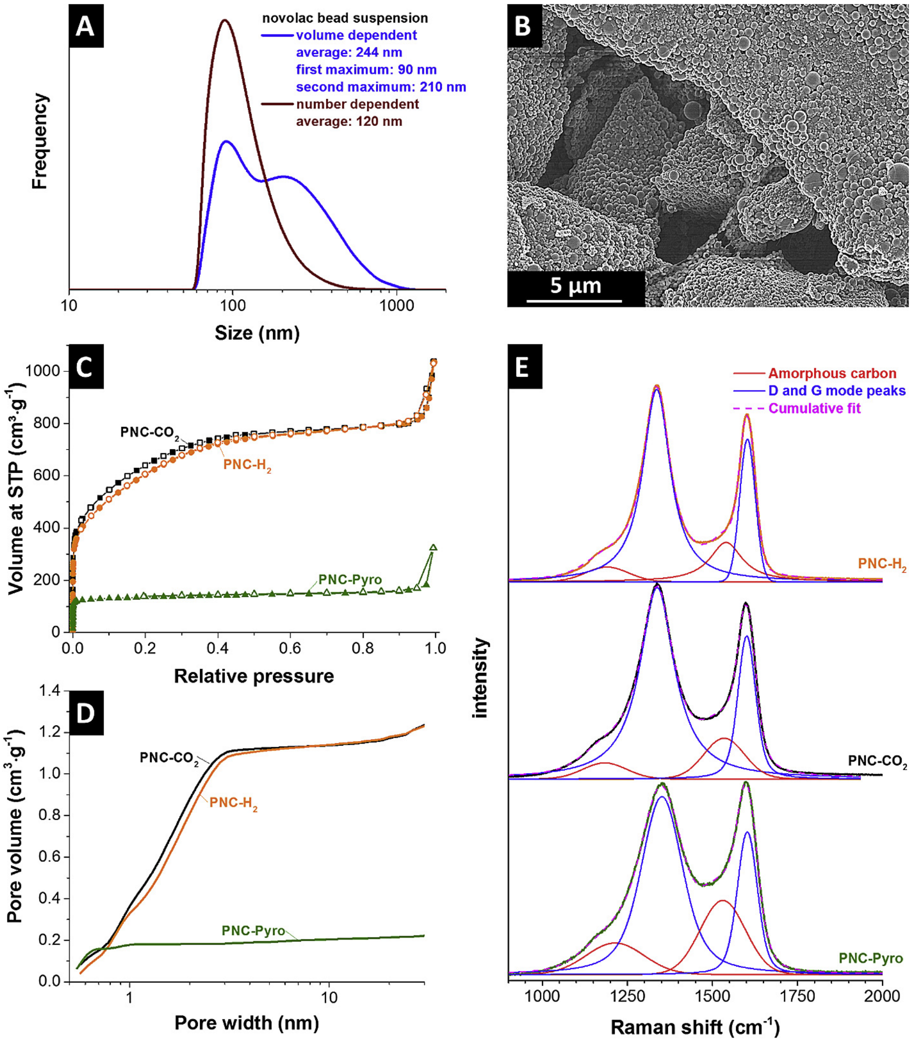

Fig. 1. DLS results of the novolac suspension (A), SEM image of pyrolyzed novolac beads (B), Isotherms of the PNC-Pyro, PNC-CO_2, and PNC-H_2 (C), cumulative pore volume derived from the isotherms (D), fitted Raman spectra of PNC-Pyro, PNC-CO_2, and PNC-H_2 (E). (A colour version of this figure can be viewed online.)

Table 1
Specific surface area (DFT and BET), total pore volume, and average pore size of PNC-Pyro, PNC-CO_2, and PNC-H_2.

	SSA_{DFT} (m^2 g^{-1})	SSA_{BET} (m^2 g^{-1})	Total pore volume (cm^3 g^{-1})	Average pore size (nm)
PNC-Pyro	641	529	0.25	0.6
PNC-CO_2	1905	2317	1.26	1.5
PNC-H_2	1755	2193	1.26	1.6

Table 2
Results of peak fitting of Raman spectra, with D- and G-mode position, the FWHM, and I_D/I_G ratio.

	Mode	Position (cm^{-1})	FWHM (cm^{-1})	I_D/I_G
PNC-Pyro	D	1351	144.8	2.78
	G	1603	70.0	
PNC-CO_2	D	1337	123.6	3.35
	G	1601	62.1	
PNC-H_2	D	1336	97.5	3.55
	G	1603	53.7	

ordering after hydrogen treatment is in agreement with our recent work on hydrogen treatment of activated carbon [33].

Thermogravimetric analysis and mass spectroscopy were utilized to further characterize differences in the samples after pyrolysis, after CO_2 activation, and after H_2 treatment. The TGA curves of PNC-Pyro, PNC-CO_2, and PNC-H_2 in Fig. 2A are very similar up to ~250 °C. Above 250 °C, sample PNC-CO_2 loses more mass than the other two samples due to the loss of carboxylic functional groups, which are released as CO_2 (Fig. 2C). The curve progressions above 700 °C are very similar. At 1200 °C, the residual sample mass of PNC-CO_2 and PNC-H_2 are very comparable (94.4 mass% and 95.1 mass%, respectively). The mass loss behavior can be explained by in situ mass spectroscopy during the TGA experiment, as shown in Fig. 2B–D. PNC-CO_2 shows an increased CO_2 signal intensity (m/z: 44) at approximately 340 °C which can be related to the decomposition of carboxylic functional surface groups [33–35]. PNC-Pyro sample exhibits also a very small increase in the CO_2 signal close to 400 °C related to carboxylic functional groups. Such a peak is absent

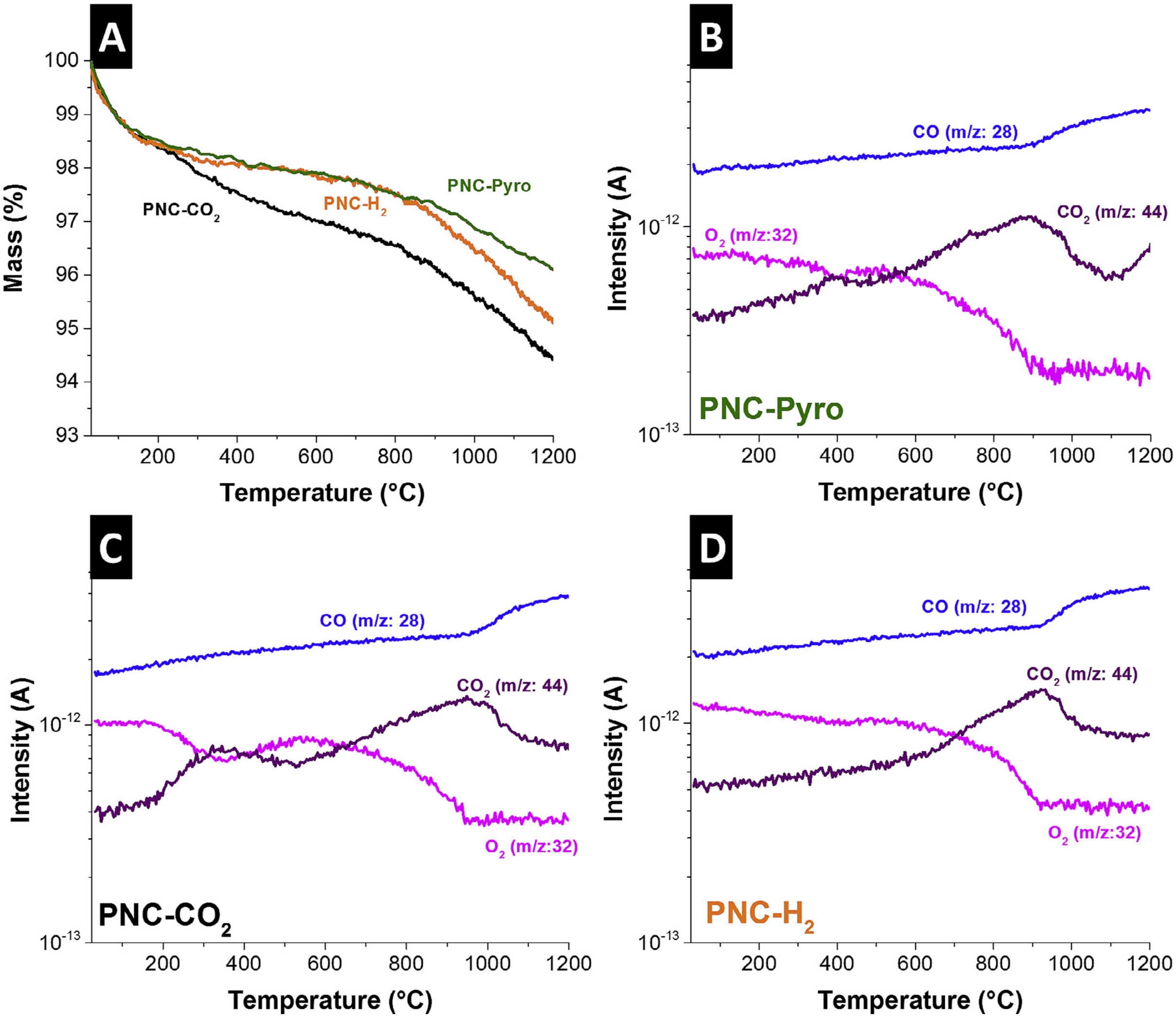

Fig. 2. TGA of all samples (A), ionic current vs. temperature of PNC-Pyro (B), PNC-CO_2 (C), and PNC-H_2 (D). (A colour version of this figure can be viewed online.)

in case of PNC-H_2, indicating effective prior removal of corresponding surface functional groups. Because PNC-Pyro and PNC-CO_2 were produced at 1000 °C, the present functional groups cannot originate directly from the pyrolysis or CO_2 activation at high temperatures. It is more likely that dangling bonds were generated by the activation process and reacted with air, when the samples were removed from the furnace [36]. The samples have another CO_2 peak starting at 600 °C up to 1050 °C. This is mainly a result of the residual trace amounts of oxygen in the system. Above 1000 °C, the CO signal increases due to the Boudouard equilibrium [37].

Further information on the chemical composition of the samples can be gained from X-ray photoelectron spectroscopy. The X-ray photoelectron spectra show that all three samples consist mainly of carbon (Table 3, Fig. 3A-C). PNC-Pyro has a carbon content of 98.0 ± 0.1 atom%, 1.3 ± 0.1 atom% of oxygen, and 0.7 ± 0.1 atom% of nitrogen. No nitrogen was detected after CO_2 activation for either PNC-CO_2 or PNC-H_2, which show, besides carbon, only oxygen 1.1 ± 0.4 atom% for PNC-CO_2 and 0.4 ± 0.1 atom% in PNC-H_2. The highly resolved measured C 1s spectra (Fig. 3A, B) were fitted with four components (sp^2, sp^3, C—O, and Π-Π^* transition). The pyrolyzed novolac shows a C=C sp^2 content of approximately 94.5%, Π-Π^* shake up of 1.9%, and 2.8% of C—C/C—H sp^3. A C—OH(R) functionality is only slightly distinguishable (0.9%). The amount of aliphatic bonded carbon increases by the CO_2 activation to 6.4% and C—O bonds have a portion of 0.8%. Around 89.4% of the C bonds in PNC-CO_2 are sp^2 hybridized and 3.4% are a Π-Π^* shake up [38]. The hydrogen treated sample has a lower amount of sp^2 hybridization (86.3%), but a higher Π-Π^* shake up of 5.8%. The sp^3 hybridization increased to 7.3%, while the C—O bonds are reduced (0.5%). The Π-Π^* transition peak arises from a valence electron at a higher state due to the

Table 3
Chemical composition of the PNC-samples measured with XPS and bonding content of the C 1s peak. “n.d.” stands for “non-detectable”.

	C (atom%)	N (atom%)	O (atom%)	C=C sp^2 (%)	C—C/C—H sp^3 (%)	C—O (%)	Π-Π^* transition (%)
PNC-Pyro	98.0 ± 0.1	1.3 ± 0.1	0.6 ± 0.1	94.5	2.8	0.9	1.9
PNC-CO_2	98.9 ± 0.4	n.d.	1.1 ± 0.4	89.4	6.4	0.8	3.4
PNC-H_2	99.6 ± 0.1	n.d.	0.4 ± 0.1	86.3	7.3	0.5	5.8

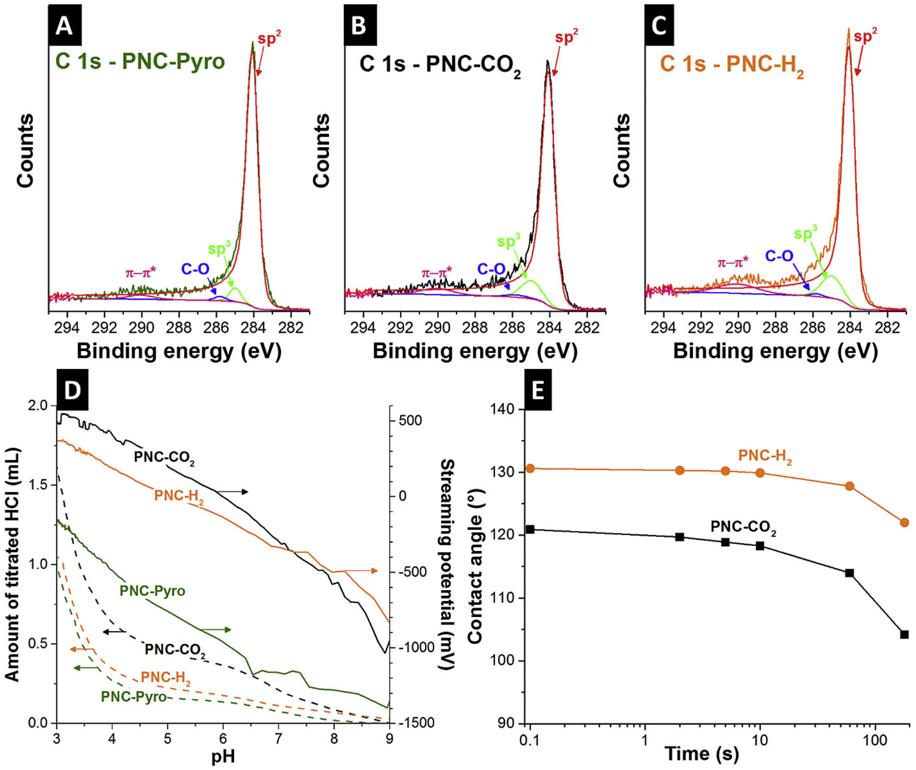

Fig. 3. XPS spectra of the C 1s peak of PNC-Pyro (A), PNC-CO_2 (B), and PNC-H_2 (C). Streaming potential with the consumed amount of HCl of all samples (D). Contact angle measurements using deionized water (E). (A colour version of this figure can be viewed online.)

photoionization process and increased from the PNC-Pyro by the activation and hydrogen treatment, which is an evidence for higher aromatic carbon, due to more combinations of more Π-Π* orbitals [38]. The $C=O$ peak also arises at a similar energy than the Π-Π* shake up peak, but the reduction of the total oxygen of PNC-H_2 makes that contribution insignificant. Because of the low number of heteroatoms in these carbon materials, these values confirm the trend of the Raman and TGA-MS measurements.

To further characterize the nature of surface functionalities, we employed streaming potential measurements. The latter is an efficient tool to characterize the influence of the nature of functional groups and its effects in aqueous media [30]. The consumed amount of HCl solution and the streaming potential are plotted in Fig. 3D. PNC-Pyro consumes the lowest amount of acidic solution, due to its low SSA and the relatively low amount of functional groups [39]. The corresponding streaming potential is always in the negative range and is not reaching the isoelectric point, which indicates the presents of acidic groups. However, the narrow pores might lead to a diffusion limitation, by what the solvent cannot react with all functional groups during the measurement time. The isoelectric point of PNC-CO_2 is at a pH 6.0 and was reduced by the hydrogen treatment to a pH of 5.1, which are reasonable values for activated carbons were carboxylic groups are predominately [40]. The consumed amount of HCl solution was also reduced for PNC-H_2 compared to PNC-CO_2, which means that the amount of surface groups is reduced, due to their similar surface area.

The number of polar functional groups also affects the wetting behavior of the carbon electrodes (Fig. 3E). PNC-CO_2 shows an initial contact angle with Milli-Q water in air of 121°, which increased for PNC-H_2 to 131°. This behavior illustrates the hydrophobic character of these electrodes, which is also influenced by the PTFE-binder [41,42].

3.2. Electrochemical characterization

The electrochemical characterization was performed for PNC-CO_2 and PNC-H_2 since PNC-Pyro has a relatively low SSA, low pore volume, and only very narrow micropores, making it quite unsuitable for supercapacitor or CDI applications. All measurements were carried out in 1 M NaCl to avoid global ion depletion at low molar concentration (which, in case of CDI, does not occur per the constant re-supply of ions of the inflowing stream) [17]. PNC-CO_2 and PNC-H_2 showed a typical rectangular shape of the CVs, as can be seen in Fig. 4A. The specific capacitance of PNC-H_2 (127 F g^{-1}) is almost identical to PNC-CO_2 (124 F g^{-1}). The rate handling ability (Fig. 4B) of both materials was almost identical. Also, the zero charge potentials at 1.2 V measured versus a Ag/AgCl reference are similar with −72 mV (PNC-CO_2) and −74 mV (PNC-H_2) and we see the virtually identical potential development of positively and negatively charged electrodes (inset in Fig. 4B).

3.3. Capacitive deionization performance

All CDI experiments were carried out in 5 mM NaCl in deaerated saline solution at 1.2 V cell voltage as a common setup for assessing the desalination performance [3]. The SAC of PNC-CO_2 drops immediately after the first cycle from 7.8 mg g^{-1} to 5.7 mg g^{-1} due to the rise of an inverse peak, in which ions are adsorbed by surface charges without applying any potential and later on released by a potential (Fig. 5A,C). This peak can be explained by the generation of functional groups, leading to an improved wettability which is an explanation for the SAC increase after the fifth cycle to a maximum of 8.1 mg g^{-1} [17]. After 100 cycles, the SAC has dropped to a value of 5.5 mg g^{-1}, compared to a theoretical value 13.6 mg g^{-1} based on the pore size distribution

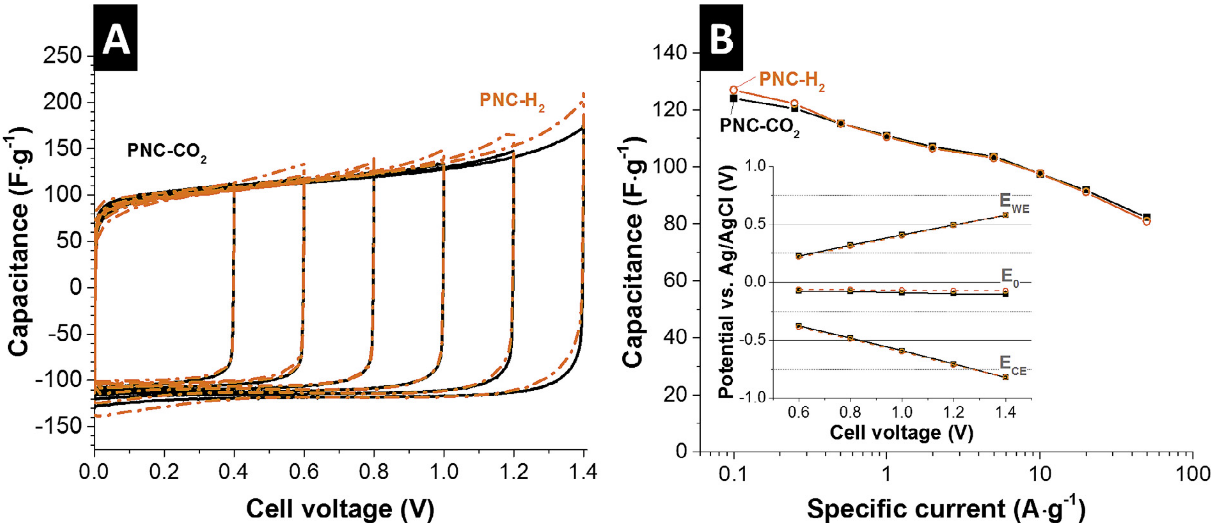

Fig. 4. Cyclic voltammograms of PNC-CO$_2$ and PNC-H$_2$ in aqueous 1 M NaCl (A). Rate handling of the film electrodes from a range of specific current of 0.1–50 A g^{-1} (B). Monitoring of cathode, anode and zero charge potential with different cell potentials (B, inset). (A colour version of this figure can be viewed online.)

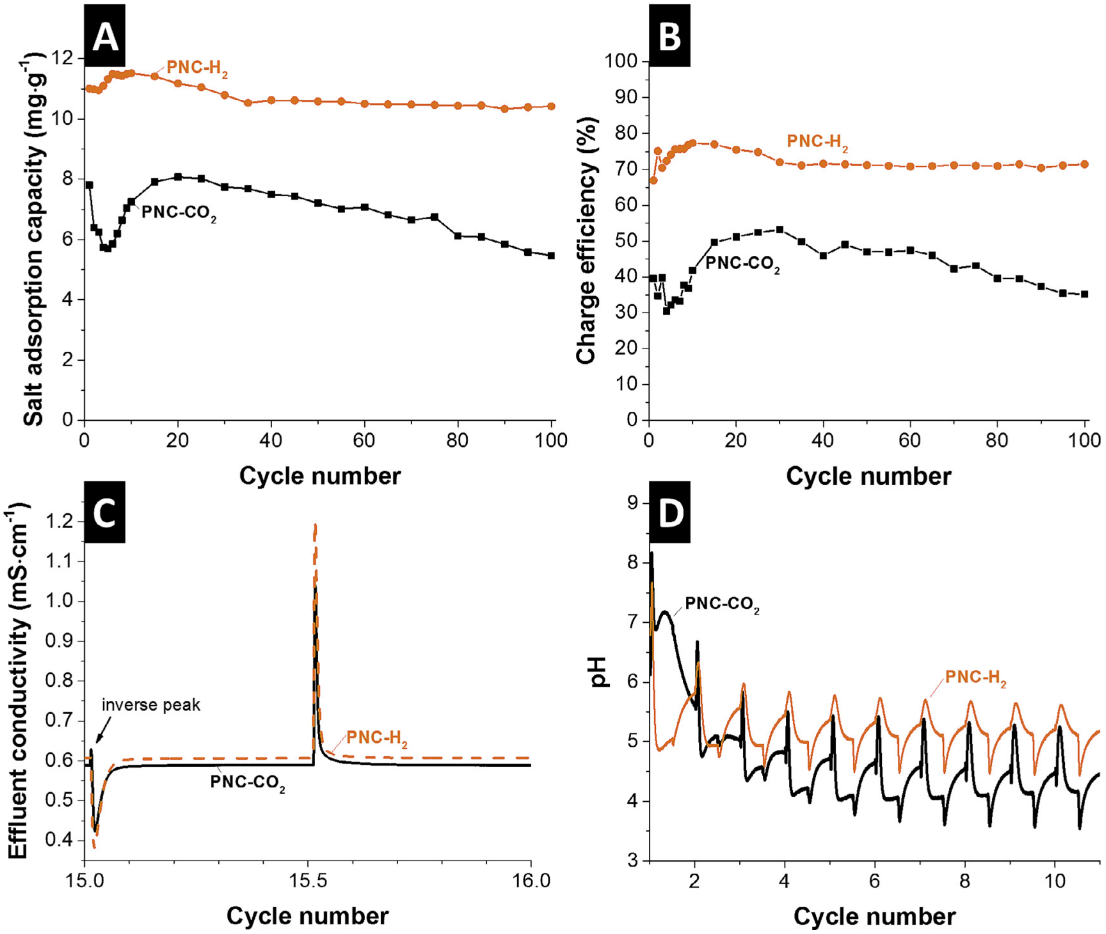

Fig. 5. CDI results from PNC-CO$_2$ and PNC-H$_2$ with salt adsorption capacity over 100 cycles (A), charge efficiency over 100 cycles (B), measured conductivity of the 15th cycle (C), pH of the first 10 cycles (D). (A colour version of this figure can be viewed online.)

(calculated by the predictive CDI tool established in Ref. [11]). The charge efficiency shows a similar pattern, as seen in Fig. 5B, and is 40% at the beginning and drops to 31% in the fourth cycle. Then, the charge efficiency is increasing to approximately 50%, following a pattern comparable to the SAC, but also decreases during the last 70 cycles to 35% after 100 cycles. The low charge efficiency can be explained by electrochemical (Faradaic) side reactions [43–45] indicated by the inversion peak [46] due to the chemical surface charges [9].

The pH over the first ten cycles is plotted in Fig. 5D. Several effects contribute to the measured pH, like the width of the electrochemical operation window, the measurement setup, and the decomposition of water or functional groups [44,45]. As depicted in Fig. 4B, the potential of the negatively polarized electrode at a cell voltage of 1.2 V is in the range of the thermodynamic hydrogen evolution potential [44]. Therefore, it is possible that H_3O^+ is produced during adsorption, reducing the pH value. Even though the system is constantly de-aerated by flushing nitrogen gas through the water reservoir, small amounts of oxygen can still be present at the electrodes. This residual oxygen can electrochemically react with the PNC-CO_2 and PNC-H_2 during the first few cycles [7,47]. In the PNC-CO_2 system, the pH at the adsorption peak drops from 7 to 5.6 during the first cycles and further to 3.6 during desorption of the 10th cycle. This indicates the presence of acidic functional groups which decompose to carbonic acid. The pH of PNC-H_2 is also decreasing, but with a lower amplitude as PNC-CO_2. During the 9th cycle, the pH at the adsorption peak is at 5.7 and at the desorption peak at 4.4, which indicates the presence of fewer acidic groups.

PNC-H_2 shows a more stable CDI performance with significantly higher SAC and charge efficiency (Fig. 5). The SAC is increasing from the first cycle on due to low wettability of the initial carbon for the first 10 cycles to maximum value of 11.5 mg g^{-1} with a charge efficiency of 77%. For comparison: the ideal SAC value based on the carbon pore size distribution (per Ref. [11]) would be very close to 12.6 mg g^{-1}. After 100 cycles, the CDI performance values are slightly reduced to 10.4 mg g^{-1} for the SAC and 71% for the charge efficiency. The inverse peak of PNC-H_2 is negligibly small and is not increasing during the test.

The carboxylic groups are also responsible for the low pH of the PNC-CO_2 system which is the main reason for the low CDI performance. This can be clearly seen from the emergence of an inversion peak during CDI cycling (Fig. 5D). The lower degree of carbon ordering found for PNC-CO_2, as shown by Raman spectroscopy, might also lower the overall CDI stability. In contrast, the hydrogen treatment very effectively reduces the number of functional groups and increases the carbon ordering, which is favorable to achieve stable CDI performance [17,30].

The Kim-Yoon plot (Fig. 6) illustrates the advantage of novolac-derived carbon beads compared to common electrode materials (i.e., commercial activated carbon). MSP-20 shows a very high SAC with 15.2 mg g^{-1}; yet, its relatively narrow pore geometry impedes ion transport, resulting in a maximum average salt adsorption rate (ASAR) of 0.05 mg g^{-1} s^{-1}. A slightly lower rate is displayed by YP-80F with 0.04 mg g^{-1} s^{-1} and a maximum SAC of11.4 mg g^{-1}. These values are in alignment with previous work [11,17,30]. For comparison, PNC-CO_2 displays a maximum ASAR of 0.09 mg g^{-1} s^{-1} and a maximum SAC of 8.1 mg g^{-1} and PNC-H_2 of 0.10 mg g^{-1} s^{-1} (ASAR) and 11.6 mg g^{-1} (SAC). The high rates can be explained by the small particle size of the primary particles (~300 nm) compared to YP-80F or MSP-20 that consists of micrometer sized particles.

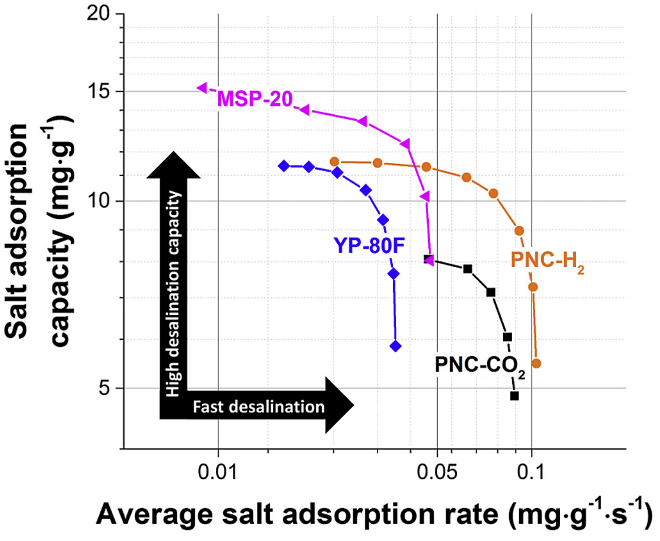

Fig. 6. Kim-Yoon plot of PNC-CO_2, PNC-H_2, YP-80F, and MSP-20. The salt concentration for all experiments was 500 mmol L^{-1} NaCl. Electrode thickness: PNC-CO_2 = 130 μm; PNC-H_2 = 115 μm; YP-80F = 140 μm; MSP-20 = 150 μm. (A colour version of this figure can be viewed online.)

4. Conclusions

Novolac-derived carbons are a promising material for CDI when being activated in CO_2 (to enhance the porosity) and defunctionalized in H_2. Hydrogen treatment was an efficient strategy to reduce the number of carboxylic surface groups, which had a major influence on the CDI performance regarding charge efficiency, SAC, and longtime stability. For an economic, large scale production of these kinds of materials, the combination of pyrolysis, CO_2-activation, and hydrogen treatment in one step should be explored to avoid several heating steps. Yet, the very low cost of the carbon precursor novolac is of practical interest for scaled applications. While the total SAC of PNC-H_2 is comparable to other high performance activated carbon materials (11.5 mg g^{-1}), the mean deionization rate of PNC-H_2 is much higher with a maximum of 0.104 mg g^{-1} s^{-1}. With these metrics, PNC-H_2 is ~3-times faster than YP-80F and ~2-times faster than MSP-20, which are both commonly used commercially available activated carbons. We also showed that hydrogen treatment is an effective strategy to overcome the poor CDI performance stability of PNC-CO_2 to yield a stable long time performance with a decrease smaller than 10% after 100 cycles in de-aerated saline solution.

Acknowledgements

This work was part of the Carbon Metal Oxide Nanohybrid project (CarMON) supported by the by the Leibniz Association (SAW-2017). The authors kindly acknowledge the continuing support of Prof. Eduard Arzt (INM) and thank Ralph Schäfer from Allnex Germany GmbH for supply of ALVONOL PN 320. We thank Robert Drumm (INM) for the TGA-MS measurements, and appreciate Dr. Choonsoo Kim (INM), Juhan Lee (INM), and Mathias Widmaier (Robert Bosch GmbH) for helpful discussions and technical support.

References

[1] M.A. Anderson, A.L. Cudero, J. Palma, Capacitive deionization as an electrochemical means of saving energy and delivering clean water. Comparison to present desalination practices: will it compete? Electrochim. Acta 55 (12) (2010) 3845–3856.
[2] M.E. Suss, S. Porada, X. Sun, P.M. Biesheuvel, J. Yoon, V. Presser, Water desalination via capacitive deionization: what is it and what can we expect from it? Energy Environ. Sci. 8 (8) (2015) 2296–2319.
[3] S. Porada, R. Zhao, A. van der Wal, V. Presser, P.M. Biesheuvel, Review on the science and technology of water desalination by capacitive deionization, Prog. Mater. Sci. 58 (8) (2013) 1388–1442.
[4] R. Zhao, S. Porada, P.M. Biesheuvel, A. van der Wal, Energy consumption in membrane capacitive deionization for different water recoveries and flow rates, and comparison with reverse osmosis, Desalination 330 (0) (2013) 35–41.
[5] A. Hemmatifar, J.W. Palko, M. Stadermann, J.G. Santiago, Energy breakdown in capacitive deionization, Water Res. 104 (2016) 303–311.
[6] Y. Liu, C.Y. Nie, X.J. Liu, X.T. Xu, Z. Sun, L.K. Pan, Review on carbon-based composite materials for capacitive deionization, RSC Adv. 5 (20) (2015) 15205–15225.

[7] X. Gao, A. Omosebi, J. Landon, K.L. Liu, Surface charge enhanced carbon electrodes for stable and efficient capacitive deionization using inverted adsorption-desorption behavior, Energy Environ. Sci. 8 (3) (2015) 897–909.

[8] P.M. Biesheuvel, H.V.M. Hamelers, M.E. Suss, Theory of water desalination by porous electrodes with immobile chemical charge, Colloids Interface Sci. Commun. 9 (2015) 1–5.

[9] P.B. Peters, R. van Roij, M.Z. Bazant, P.M. Biesheuvel, Analysis of electrolyte transport through charged nanopores, Phys. Rev. E 93 (5) (2016) 053108.

[10] X. Gao, S. Porada, A. Omosebi, K.-L. Liu, P.M. Biesheuvel, J. Landon, Complementary surface charge for enhanced capacitive deionization, Water Res. 92 (2016) 275–282.

[11] S. Porada, L.O. Borchardt, M.M. Bryjak, J.S. Atchison, K.J. Keesman, S. Kaskel, P.M. Biesheuvel, V. Presser, Direct prediction of the desalination performance of porous carbon electrodes for capacitive deionization, Energy Environ. Sci. 6 (12) (2013) 3700–3712.

[12] T. Kim, J. Yoon, CDI ragone plot as a functional tool to evaluate desalination performance in capacitive deionization, RSC Adv. 5 (2) (2015) 1456–1461.

[13] J. Lee, S. Kim, C. Kim, J. Yoon, Hybrid capacitive deionization to enhance the desalination performance of capacitive techniques, Energ Environ. Sci. 7 (11) (2014) 3683–3689.

[14] P. Srimuk, L. Ries, M. Zeiger, S. Fleischmann, N. Jäckel, A. Tolosa, B. Krüner, M. Aslan, V. Presser, High performance stability of titania decorated carbon for desalination with capacitive deionization in oxygenated water, RSC Adv. 6 (108) (2016) 106081–106089.

[15] P. Srimuk, F. Kaasik, B. Krüner, A. Tolosa, S. Fleischmann, N. Jäckel, M.C. Tekeli, M. Aslan, M.E. Suss, V. Presser, MXene as a novel intercalation-type pseudocapacitive cathode and anode for capacitive deionization, J. Mater. Chem. A 4 (47) (2016) 18265–18271.

[16] K.C. Smith, R. Dmello, Na-ion desalination (NID) enabled by Na-blocking membranes and symmetric Na-intercalation: porous-electrode modeling, J. Electrochem. Soc. 163 (3) (2016) A530–A539.

[17] M. Aslan, M. Zeiger, N. Jäckel, I. Grobelsek, D. Weingarth, V. Presser, Improved capacitive deionization performance of mixed hydrophobic/hydrophilic activated carbon electrodes, J. Phys. Condens. Matter 28 (11) (2016) 114003.

[18] X. Xu, Z. Sun, D.H.C. Chua, L. Pan, Novel nitrogen doped graphene sponge with ultrahigh capacitive deionization performance, Sci. Rep. 5 (2015) 11225.

[19] B. Krüner, J. Lee, N. Jäckel, A. Tolosa, V. Presser, Sub-micrometer novolac-derived carbon beads for high performance supercapacitors and redox electrolyte energy storage, ACS Appl. Mater. Interfaces 8 (14) (2016) 9104–9115.

[20] C.A. Schneider, W.S. Rasband, K.W. Eliceiri, NIH image to ImageJ 25 years image analysis, Nat. Methods 9 (7) (2012) 671–675.

[21] L.L. He, S.M. Chathoth, Y.B. Melnichenko, V. Presser, J. McDonough, Y. Gogotsi, Small-angle neutron scattering characterization of the structure of nanoporous carbons for energy-related applications, Microporous Mesoporous Mater. 149 (1) (2012) 46–54.

[22] V. Presser, J. McDonough, S.H. Yeon, Y. Gogotsi, Effect of pore size on carbon dioxide sorption by carbide derived carbon, Energy Environ. Sci. 4 (8) (2011) 3059–3066.

[23] C. Prehal, C. Koczwara, N. Jäckel, A. Schreiber, M. Burian, H. Amenitsch, M.A. Hartmann, V. Presser, O. Paris, Quantification of ion confinement and desolvation in nanoporous carbon supercapacitors with modelling and in situ X-ray scattering, Nat. Energy 2 (2017) 16215.

[24] G.Y. Gor, M. Thommes, K.A. Cychosz, A.V. Neimark, Quenched solid density functional theory method for characterization of mesoporous carbons by nitrogen adsorption, Carbon 50 (4) (2012) 1583–1590.

[25] S. Brunauer, P.H. Emmett, E. Teller, Adsorption of gases in multimolecular layers, J. Am. Chem. Soc. 60 (2) (1938) 309–319.

[26] D. Weingarth, M. Zeiger, N. Jäckel, M. Aslan, G. Feng, V. Presser, Graphitization as a universal tool to tailor the potential-dependent capacitance of carbon supercapacitors, Adv. Energy Mater. 4 (13) (2014) 1400316.

[27] N. Jäckel, M. Rodner, A. Schreiber, J. Jeongwook, M. Zeiger, M. Aslan, D. Weingarth, V. Presser, Anomalous or regular capacitance? The influence of pore size dispersity on double-layer formation, J. Power Sources 326 (1) (2016) 660–671.

[28] M.D. Stoller, R.S. Ruoff, Best practice methods for determining an electrode material's performance for ultracapacitors, Energ Environ. Sci. 3 (9) (2010) 1294–1301.

[29] S. Zhang, N. Pan, Supercapacitors performance evaluation, Adv. Energy Mater. 5 (6) (2015) 1401401.

[30] S. Porada, F. Schipper, M. Aslan, M. Antonietti, V. Presser, T.-P. Fellinger, Capacitive deionization with novel biomass-based microporous salt templated heteroatom carbons, ChemSusChem 8 (11) (2015) 1867–1874.

[31] G.A. Zickler, B. Smarsly, N. Gierlinger, H. Peterlik, O. Paris, A reconsideration of the relationship between the crystallite size La of carbons determined by X-ray diffraction and Raman spectroscopy, Carbon 44 (15) (2006) 3239–3246.

[32] A.C. Ferrari, J. Robertson, Interpretation of Raman spectra of disordered and amorphous carbon, Phys. Rev. B 61 (20) (2000) 14095–14107.

[33] M. Widmaier, B. Krüner, N. Jäckel, M. Aslan, S. Fleischmann, C. Engel, V. Presser, Carbon as quasi-reference electrode in unconventional lithium-salt containing electrolytes for hybrid battery/supercapacitor devices, J. Electrochem. Soc. 163 (14) (2016) A2956–A2964.

[34] C. Moreno-castilla, F. Carrasco-marín, F.J. Maldonado-hódar, J. Rivera-utrilla, Effects of non-oxidant and oxidant acid treatments on the surface properties of an activated carbon with very low ash content, Carbon 36 (1) (1998) 145–151.

[35] U. Zielke, K.J. Hüttinger, W.P. Hoffman, Surface-oxidized carbon fibers: I. Surface structure and chemistry, Carbon 34 (8) (1996) 983–998.

[36] K.W. Adu, Q. Li, S.C. Desai, A.N. Sidorov, G.U. Sumanasekera, A.D. Lueking, Morphological, structural, and chemical effects in response of novel carbide derived carbon sensor to NH_3, N_2O, and air, Langmuir 25 (1) (2009) 582–588.

[37] T.F.E. Rhead, R.V. Wheeler, The effect of temperature on the equilibrium $2CO \leftrightarrow CO_2 + C$, J. Chem. Soc. Trans. 97 (0) (1910) 2178–2189.

[38] S.R. Kelemen, K.D. Rose, P.J. Kwiatek, Carbon aromaticity based on XPS II to II* signal intensity, Appl. Surf. Sci. 64 (2) (1993) 167–174.

[39] A.Y. Mottlau, N.E. Fisher, Measurement of pore volume by a titration technique, Anal. Chem. 34 (6) (1962) 714–715.

[40] H. Marsh, Activated Carbon, first ed., Elsevier, Boston, MA, 2006.

[41] A. Kolodziej, K. Fic, E. Frackowiak, Towards sustainable power sources: chitin-bound carbon electrodes for electrochemical capacitors, J. Mater. Chem. A 3 (45) (2015) 22923–22930.

[42] M. Aslan, D. Weingarth, P. Herbeck-Engel, I. Grobelsek, V. Presser, Polyvinylpyrrolidone/polyvinyl butyral composite as a stable binder for castable supercapacitor electrodes in aqueous electrolytes, J. Power Sources 279 (1) (2015) 323–333.

[43] P. Srimuk, M. Zeiger, N. Jäckel, A. Tolosa, B. Krüner, S. Fleischmann, I. Grobelsek, M. Aslan, B. Shvartsev, M.E. Suss, V. Presser, Enhanced performance stability of carbon/titania hybrid electrodes during capacitive deionization of oxygen saturated saline water, Electrochim. Acta 224 (1) (2017) 314–328.

[44] T. Kim, J. Yu, C. Kim, J. Yoon, Hydrogen peroxide generation in flow-mode capacitive deionization, J. Electroanal. Chem. 776 (2016) 101–104.

[45] D. He, C.E. Wong, W. Tang, P. Kovalsky, T.D. Waite, Faradaic reactions in water desalination by batch-mode capacitive deionization, Environ. Sci. Technol. Lett. 3 (5) (2016) 222–226.

[46] X. Gao, A. Omosebi, J. Landon, K. Liu, Enhanced salt removal in an inverted capacitive deionization cell using amine modified microporous carbon cathodes, Environ. Sci. Technol. 49 (18) (2015) 10920–10926.

[47] I. Cohen, E. Avraham, Y. Bouhadana, A. Soffer, D. Aurbach, Long term stability of capacitive de-ionization processes for water desalination: the challenge of positive electrodes corrosion, Electrochim. Acta 106 (0) (2013) 91–100.

4.3. Quantitative information about electrosorption of ionic liquids in carbon nanopores from electrochemical dilatometry and quartz crystal microbalance measurements

Nicolas Jäckel,[1,2] Steffen P. Emge,[3,4] Benjamin Krüner,[1,2] Bernhard Roling,[3]

Volker Presser[1,2]

[1] *INM - Leibniz Institute for New Materials, 66123 Saarbrücken, Germany*

[2] *Department of Materials Science and Engineering, Saarland University, 66123 Saarbrücken, Germany*

[3] *Department of Chemistry, Philipps University of Marburg, 35032 Marburg, Germany*

[4] *Department of Chemistry, University of Cambridge, Cambridge CB2 1EW, United Kingdom*

Jäckel, Nicolas et al. (2017) *The Journal of Physical Chemistry C*, 121 (35), 19120-19128.
https://doi.org/10.1021/acs.jpcc.7b06915

Own contribution: synthesis of the activated carbon beads, N_2 sorption analysis of the carbon powder.

Abstract:

Electrochemical energy storage using nanoporous carbons and ionic liquids enables large cell voltages and is a promising way to increase the energy density of electrical double-layer capacitors. The structure of the double layer in solvent-free electrolytes is fundamentally different from other systems with organic or aqueous solvents. In our study, we investigate the physical behavior of nanoporous carbon electrodes in contact with ionic liquids with a multilength scale approach by combining electrochemical quartz-crystal microbalance and electrochemical dilatometry. Synergistic combination of both in situ methods allows one to correlate system properties on particle and electrode level. We find that the charging mechanism at low charge is characterized by the exchange of more smaller ions by fewer larger ions. At higher charges, the system is changing to preferred counterion adsorption, which is resulting in a strong increase in the electrode volume. The maximum linear strain for a bulk electrode is 2% in our study, which is quite high for a supercapacitor system.

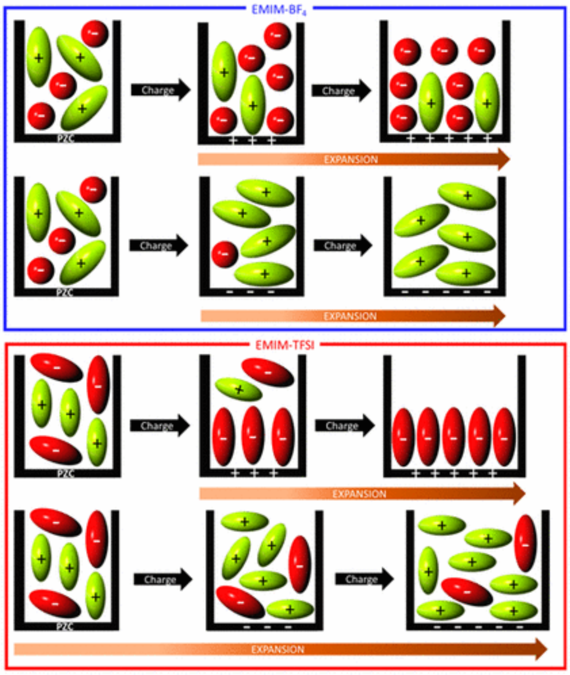

THE JOURNAL OF
PHYSICAL CHEMISTRY C

Article

pubs.acs.org/JPCC

Quantitative Information about Electrosorption of Ionic Liquids in Carbon Nanopores from Electrochemical Dilatometry and Quartz Crystal Microbalance Measurements

Nicolas Jäckel,[†,‡] Steffen Patrick Emge,[§,∥] Benjamin Krüner,[†,‡] Bernhard Roling,[*,§] and Volker Presser[*,†,‡]

[†]INM-Leibniz Institute for New Materials, Saarbrücken 66123, Germany
[‡]Department of Materials Science and Engineering, Saarland University, Saarbrücken 66123, Germany
[§]Department of Chemistry, Philipps-Universität, Marburg 35032, Germany
[∥]Department of Chemistry, University of Cambridge, Cambridge CB2 1EW, United Kingdom

Supporting Information

ABSTRACT: Electrochemical energy storage using nanoporous carbons and ionic liquids enables large cell voltages and is a promising way to increase the energy density of electrical double-layer capacitors. The structure of the double layer in solvent-free electrolytes is fundamentally different from other systems with organic or aqueous solvents. In our study, we investigate the physical behavior of nanoporous carbon electrodes in contact with ionic liquids with a multilength scale approach by combining electrochemical quartz-crystal microbalance and electrochemical dilatometry. Synergistic combination of both in situ methods allows one to correlate system properties on particle and electrode level. We find that the charging mechanism at low charge is characterized by the exchange of more smaller ions by fewer larger ions. At higher charges, the system is changing to preferred counterion adsorption, which is resulting in a strong increase in the electrode volume. The maximum linear strain for a bulk electrode is 2% in our study, which is quite high for a supercapacitor system.

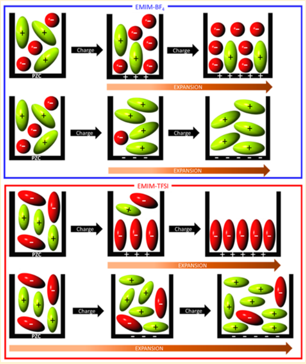

1. INTRODUCTION

Energy storage in electrical double-layer capacitors (EDLCs, also known as supercapacitors or ultracapacitors) via physical ion electrosorption at the electrode/electrolyte interface is highly reversible.[1] To achieve a high energy density, this process requires electrodes with a high surface area, and an enhanced capacitance can be achieved when most of the pores are of similar size as the ion.[2−5] Possible electrolytes are aqueous, organic, or ionic liquids (or mixtures thereof), and depending on the electrolyte, the electrochemical stability window determines the maximum operational cell voltage.[6] Ionic liquids are attractive because their use enables cell voltages above 3 V and very high capacitance of up to 180 F/g.[7−9] Yet, the power output is drastically reduced by the low ion mobility in ionic liquids at room temperature compared to organic electrolytes.[10,11] It is known that, in general, the charging mechanism depends on the pore size, ion size, and applied voltage.[12] Several competing mechanisms, such as bond-length stretching, electrowetting, electrostatic screening, and steric effects, which are all changing according to pore size and amount of functional groups, make a precise prediction of carbon swelling impossible at present.[13]

To devise further ways to enhance supercapacitor performance, it is important to understand the double-layer formation mechanism in nanoconfined spaces, like in (sub)nanometer-sized pores of carbon electrodes. In general, the charge compensation in an electrical double layer can be achieved either by co-ion expulsion, that is, expelling ions of the same charge as the electrode from the interface, or by counterion adsorption, that is, attraction of oppositely charged ions to the interface.[14] To clearly identify the governing mechanism, studies employing different in situ methods have revealed key insights. For example, the ionic liquid spontaneously wets the carbon surface but is unlikely to achieve full wetting. Such partial filling was shown, for example, for microporous activated carbon (YP-50F from Kuraray) in 1-ethyl-3-methylimidazolium bis(trifluoromethylsulfonyl)imide (EMIM-TFSI) and *N*-propyl-*N*-methylpyrrolidinium bis(trifluoromethanesulfonyl)imide (Pyr_{13}-TFSI).[15,16] Further, cations play a dominant role in the double-layer formation, which results in a more pronounced counterion adsorption at negative potentials.[15,17]

Molecular dynamic simulations show that for ionic liquids, counterions can enter the micropores faster than co-ions can exit.[18] For larger pores (i.e., mesopores), the diffusion of cations in confined space is faster than in the bulk electrolyte, and cations also seem to have a higher mobility in micropores.[16,17,19] Additionally, screening effects in highly porous electrodes allow for ions to adsorb in closer proximity

Received: July 14, 2017
Revised: August 15, 2017
Published: August 16, 2017

DOI: 10.1021/acs.jpcc.7b06915
J. Phys. Chem. C 2017, 121, 19120−19128

to the pore walls in nanoconfined spaces as it would be possible on a planar surface.[16] Also, over most potential ranges, the electrical double layer does not contain only counterions, but both kinds of ions influence the structure of the double layer. A significant number of co-ions can remain inside the micropores, and a so-called superionic state of ions is created.[20,21] Calculations and experimental work showed that a preferential adsorption of counterions (permselectivity) will only occur at high voltages of 1.0−1.5 V above the point of zero charge (pzc),[17,22,23] and the ion population in micropores increases up to a certain threshold voltage (i.e., at 1.6 V above pzc) and stays constant for higher voltages.[24]

In the case of ionic liquids, the Gouy−Chapman−Stern model cannot be used to predict electrowetting and the potential-dependent structuring of ions in the double layers at electrified interfaces but a different theoretical approach is required.[25,26] In a simplistic two-dimensional simulation of slit-like pores and ions considered as hard spheres an oscillating behavior of the capacitance was observed.[27,28] This oscillating capacitance vanishes as soon as the pore model is no longer an ideal slit pore with infinitesimally narrow size dispersity, and a broader, more natural pore size distribution is assumed.[29,30] The structural ordering becomes even more complex when taking into account the three-dimensional structure of ionic liquids in confined spaces.[31] In addition, molecular dynamic studies proclaim an exchange of ions with the bulk electrolyte without changing the volume of liquid inside the electrode.[16]

To further advance our nanoscale understanding of the electrical double layer in ionic liquids, a thorough correlation of atomistic/molecular simulations with experimental measurements is required.[32] With state-of-the-art in situ methods a quantification of volumetric changes of carbon particles or bulk electrodes can be monitored. These measurements are usually done by means of electrochemical dilatometry,[33−36] atomic force microscopy,[37,38] or (small-angle) X-ray diffraction.[39] In situ electrochemical dilatometry (eD) has confirmed that the reversible (linear) expansion of microporous carbons in contact with organic electrolytes can range up to several percent.[33−35] In the case of highly porous carbons, ionic liquid ions in nanoconfinement may enable favorable ion packing and crowding,[22,40] causing pore swelling of the electrode material.[41] In all cases of previous dilatometric studies,[42] either with organic electrolytes or with ionic liquids, the expansion for negative potentials exceeds the expansion in the positive potential regime, also at the same charge.[33−35] Moreover, a general trend was observed by an increased expansion for smaller pores,[33,35] and in ionic liquids, the expansion has a linear correlation with the amount of micropores.[42]

It was found that the theoretical expansion according to either ion insertion into bulk electrodes or generated pressure due to crowding of ions in the pores or carbon bond-length variation has been smaller than the measured values on electrodes. This results from the void volume inside the bulk electrode and the possibility of particle rearrangement.[43] To avoid such secondary effects and to gain further insights on the particle level, different measurement techniques should be used. In situ atomic force microscopy (AFM) with ionic liquids evidenced the reversible expansion and compression of porous carbon electrodes.[37,38] The AFM results combined with molecular dynamic calculations showed that cations inside of micropores contribute to increasing pressure to a greater extent than anions, even at the same state of charge.[38] This is in line with the results from eD.[33,42]

Although nanoscale expansions can be tracked by in situ AFM, it remains a very localized probing of single particles.[37,44,45] Therefore, such results cannot be extrapolated directly to the behavior of bulk electrodes with a thickness of a few hundred micrometers and characteristic scales of heterogeneity depending on particle size and the use of binder. The development of noninvasive in situ techniques for the continuous monitoring of mechanical properties of composite electrodes is therefore in high demand. Electrochemical quartz-crystal microbalance (EQCM) measurements are known for very sensitive tracking of mass differences resulting from ion (de)insertion in supercapacitors.[17,20,46−51] In this way, we can quantify the irreversible mass change after cycling or the desolvation of ions in organic electrolytes, that is, stripping off the solvation shell, when approaching narrow pores. To date, there has been only a single paper with EQCM in ionic liquid (EMIM-TFSI) published,[17] but there are no studies comparing in situ measurements with different ionic liquids and a precise description of the charging mechanism depending on the choice of ions.

In our multilength scale approach, we combine EQCM to monitor low mass changes and eD to observe volume changes of the electrode on a bulk level. During EQCM measurements, we monitor simultaneously the charge flow and the mass changes. Since the ionic liquids contain only two mobile ionic species (i.e., one type of cation and one type of anion) with different mass and no solvent molecules, the simultaneous mass and charge measurements allow us to quantify the contribution of counterion and co-ions to the double-layer charge storage. Considering the molar volumes of the ions, we can calculate potential-dependent volume changes due to the ionic liquid ions inside the pores. We show that these volume changes are in good agreement with the measured volumetric expansion from eD measurements. The much wider potential window applied in eD further allows us to see the influence of both ions on the structure of the double layer and the resulting dilatometric behavior.

2. EXPERIMENTAL SECTION

The synthesis of the novolac-derived carbon beads (NovoCarb) is described elsewhere.[52,53] In short, the novolac pellets (20 g) with 10 mass% of methenamine were dissolved in 100 mL of ethanol. The solution was added to 500 mL of water in an autoclave, heated up to 160 °C with a heating rate of 5 °C/min, and held at this temperature for 8 h. The resulting dispersion was freeze dried with liquid nitrogen. The novolac beads were afterward pyrolyzed in a graphite heating furnace (Thermal Technology) in argon atmosphere at 1000 °C with a heating rate of 20 °C/min. CO_2 activation was carried out in a quartz tube furnace (VG Scienta) at 1000 °C for 2 h.

Nitrogen gas sorption measurements were carried out with an Autosorb iQ system (Quantachrome) with liquid nitrogen (−196 °C). The electrode was degassed under vacuum at 150 °C for 10 h; the powder was degassed at 300 °C. Isotherms were recorded at relative pressures (p/p_0) from 5×10^{-7} to 1.0 in 74 steps. The specific surface area (SSA) and pore size distribution were calculated with the ASiQwin software using the quenched-solid density function theory assuming slit pores.[54]

CHNSO analysis was carried out with a Vario Micro Cube (Elementar GmbH). The temperature of the reduction tube was 850 and 1150 °C in the combustion tube. The device was calibrated with sulfanilamide. Oxygen quantification was

DOI: 10.1021/acs.jpcc.7b06915
J. Phys. Chem. C 2017, 121, 19120−19128

Table 1. Physical Properties of the Used Ionic Liquids at 25 °C

	cation size (nm^3)	anion size (nm^3)	conductivity (mS/cm)	density (g/cm^3)	viscosity (cp)	melting point (°C)	ref
EMIM-BF$_4$	0.156 ± 0.018	0.073 ± 0.021	14	1.28	43	+14.85	70−72
EMIM-TFSI	0.156 ± 0.018	0.232 ± 0.015	9.2	1.52	34	−15.15	70,71,73
BMIM-PF$_6$	0.196 ± 0.021	0.109 ± 0.008	1.4	1.36	207	+9.85	69−72

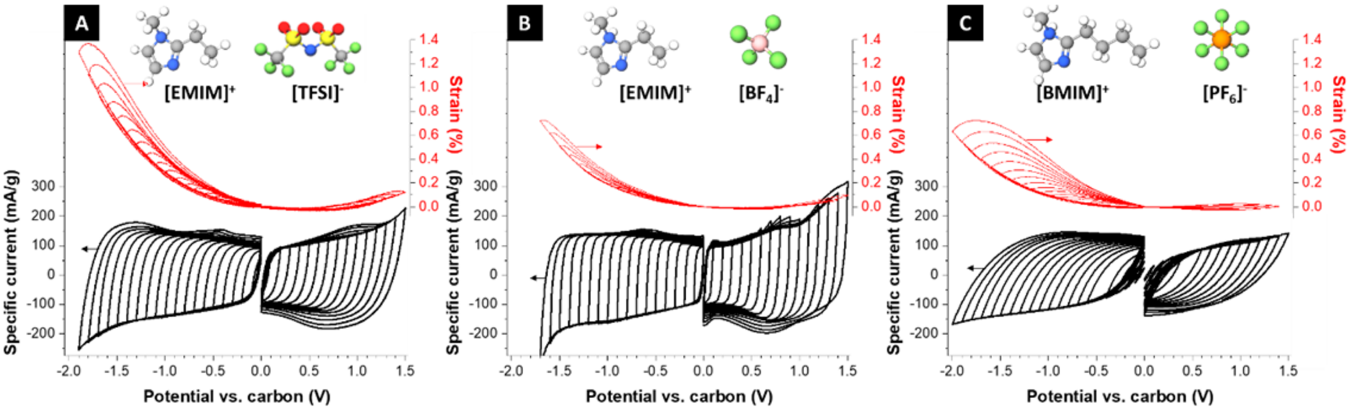

Figure 1. In situ dilatometric measurements of NovoCarb in (A) EMIM-TFSI, (B) EMIM-BF$_4$, and (C) BMIM-PF$_6$ with cyclic voltammetry at 1 mV/s. Electrochemical response of the working electrode (black line) can be simultaneously tracked with the height change (red).

conducted in a rapid OXY Cube with silver crucibles at 1450 °C. The calibration was done with benzoic acid. Room-temperature ionic liquids (RTIL) from Iolitec were degassed under vacuum at 120 °C for 24 h. The three used RTIL 1-ethyl-3-methylimidazolium tetrafluoroborate (EMIM-BF$_4$), 1-ethyl-3-methylimidazolium bis(trifluoromethylsulfonyl)imide (EMIM-TFSI), and 1-butyl-3-methylimidazolium hexafluorophosphate (BMIM-PF$_6$) were stored in an argon-filled glovebox (MBraun, H_2O and O_2 content below 1 ppm).

In situ electrochemical dilatometry was carried out with an ECD-3-nano dilatometer from EL-CELL (setup adopting the design in ref 35 and following the procedure from ref 55). The measurements were conducted at 25.0 ± 0.1 °C in a three-electrode setup. The working electrode with 90 mass % NovoCarb and 10 mass % sodium carboxymethyl cellulose (NaCMC) in water were dropcasted on the platinum current collector and dried at 200 °C for 30 min. The cell contained an oversized activated carbon electrode and a carbon quasi-reference electrode (type YP-50F, Kuraray) and was vacuum backfilled with electrolyte (approximately 0.5 mL) in the glovebox.[56] The working electrode was loaded with a constant force of 1 N, and the strain was tracked with a DP1S displacement transducer (Solartron Metrology, accuracy ±15 nm). After a resting period of 48 h, cyclic voltammograms were recorded at 1 mV/s and galvanostatic data was recorded after an appropriate equilibrium time (10−60 min) at the applied potential. We used a VMP-300 from Bio-Logic.

Electrochemical quartz-crystal microbalance (EQCM) measurements were conducted with RenLux Crystals at 10 MHz resonance frequency with gold-sputtered electrodes and an active surface area of 0.204 cm^2. The electrodes were airbrushed with a suspension of 90 mass % NovoCarb and 10 mass % NaCMC in water on the gold surface at 200 °C and dried afterwards in a vacuum oven at 60 °C for 24 h. According to the electrochemical behavior and the assumption of exclusively capacitive charge, we can calculate the active mass (i.e., carbon mass, m_C) via $m_C = I/(C_C{\cdot}v)$ with the current I during cyclic voltammetry measurements, the calculated capacitance C_C, and the scan rate v. The electrochemical cell TSC surface from RHD Instruments was assembled with the coated quartz crystal as working electrode, a silver wire as quasi-reference electrode, and a gold disc as counter electrode. The cell was filled with electrolyte (approximately 0.6 mL) and sealed in the glovebox. The electrochemical measurements were controlled with an Interface 1000 system from Gamry, while the resonance frequency of the crystal was tracked with a Gamry eQCM 10M. Calculations for the number of ions and the volume changes are presented in the Supporting Information.

3. RESULTS AND DISCUSSION

3.1. Electrode Characterization. The novolac-derived carbon beads (NovoCarb) were produced as described elsewhere.[52,53] This type of porous carbon provides a very narrow pore size distribution[3] with an average pore size of about 1.2 nm, which is larger than the ion size of the used ionic liquids (Table 1). Furthermore, the noncarbon content is about 5 mass % (Supporting Information, Table S1). The quenched-solid DFT specific surface area (QSDFT-SSA) of the dry carbon powder is 1958 m^2/g with a total pore volume of 1.13 cm^3/g and an average pore size of 1.2 nm. The electrodes containing 90 mass% carbon and 10 mass% sodium carboxymethyl cellulose (NaCMC) show a strongly reduced SSA of 1338 m^2/g (−32%) and a pore volume of 0.82 cm^3/g (−27%), whereas the average pore diameter does not change (Supporting Information, Figure S1). The reduced SSA is related to pore blocking effects of the NaCMC binder, which especially blocks subnanometer pores.[57,58]

3.2. Ionic Liquid Properties. We used three room-temperature ionic liquids (RTILs), namely, EMIM-TFSI, EMIM-BF$_4$, and BMIM-PF$_6$, with five different ion species. These ionic liquids differ regarding the sizes, shapes, and masses of the ions. For instance, in the case of EMIM-TFSI, the molar volume and molar mass of the anions are larger than the molar volume and molar mass of the cations, while the situation is reversed in the case of EMIM-BF$_4$ (Table 1). Furthermore, the ionic liquids show distinct transport properties (viscosity and conductivity), which thus lead to different electrochemical properties.[59] Our work critically requires us to stay within a

DOI: 10.1021/acs.jpcc.7b06915
J. Phys. Chem. C 2017, 121, 19120−19128

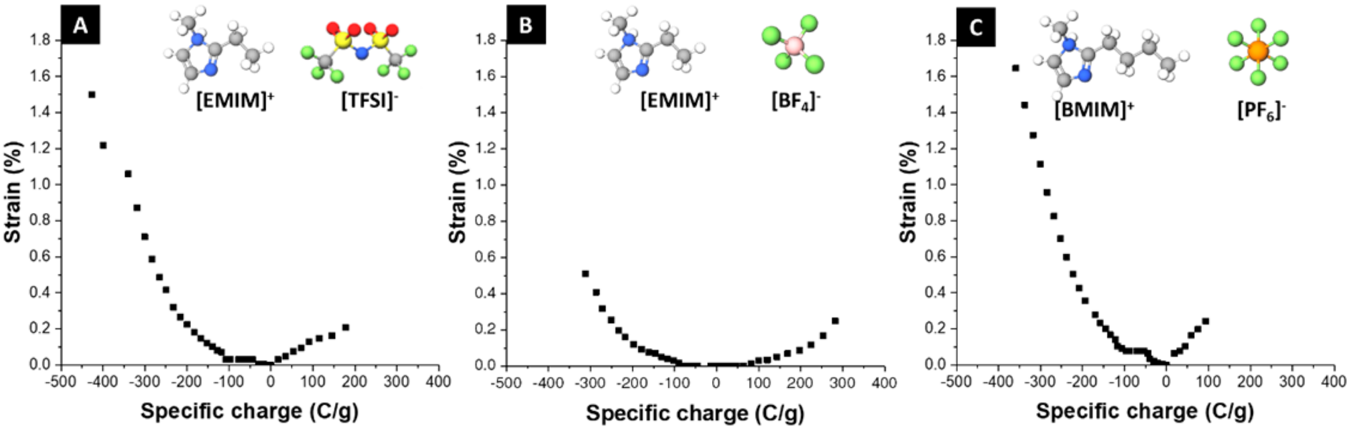

Figure 2. Galvanostatic results of NovoCarb in (A) EMIM-TFSI, (B) EMIM-BF$_4$, and (C) BMIM-PF$_6$ with normalization of charge to the point of zero strain (pzs).

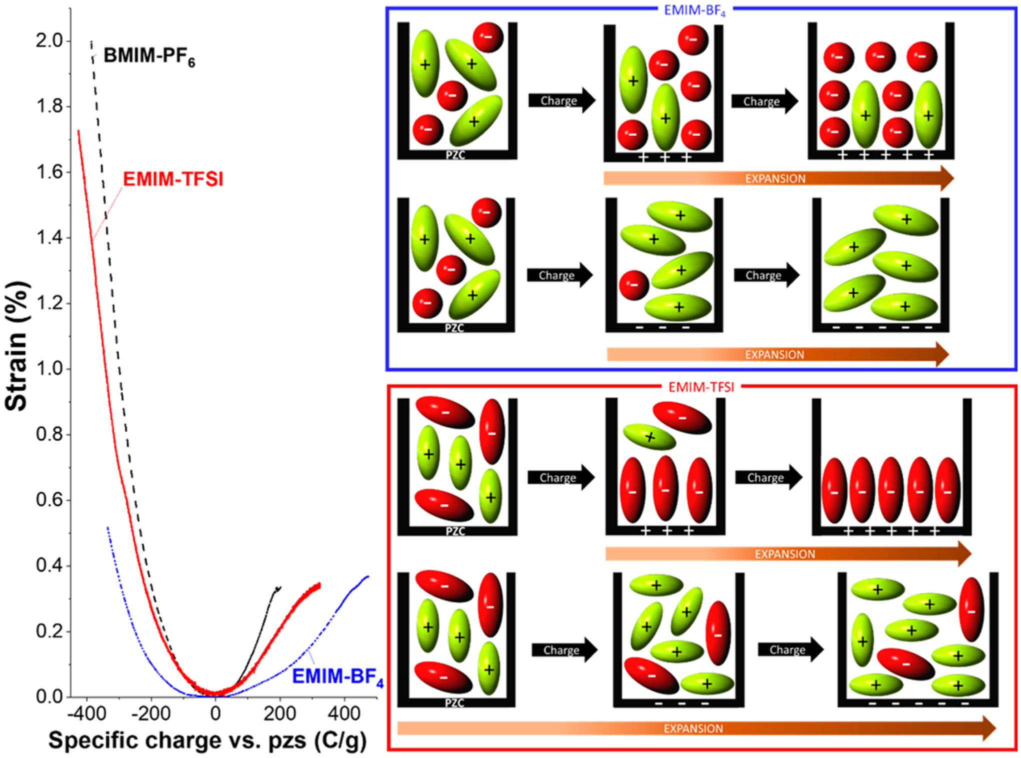

Figure 3. Galvanostatic response of the system at a specific current of 0.1 A/g. Data is derived from the in situ dilatometry system. Charge is normalized to the point of zero strain (pzs) and plotted versus the resulting strain of the working electrode. Schematic drawings show the different charging behavior according to the shape of the adsorbed ions with spherical anions (BF_4^- and PF_6^-) and nonspherical ions ($TFSI^-$). Effect is exaggerated in the drawing to illustrate the trend but not to reproduce the amplitude shown in the eD data. In all cases the smaller ion is more involved in energy storage, which results in either preferred co-ion expulsion or counter-ion adsorption.

stable electrochemical voltage window to avoid any Faradaic reactions at the fluid/solid interface between ionic liquid and carbon electrodes. To find the maximum potential window when using NovoCarb, we conducted cyclic voltammetry at a scan rate of 1 mV/s with increasing voltage window in 100 mV increments (Figure 1).[60] All RTILs were tested until an upper vertex voltage limit of +1.5 V vs carbon. In the cathodic regime, the lower vertex voltage differs with the limits for EMIM-BF$_4$ at −1.6 V vs carbon, for EMIM-TFSI at −1.8 V vs carbon, and for BMIM-PF$_6$ at −2.0 V vs carbon. In accordance with the viscosity and conductivity properties of the different RTILs, a rectangular-shaped cyclic voltammogram (CV) is observed for EMIM-BF$_4$ and EMIM-TFSI, while a more distorted CV with a large resistive knee is seen for BMIM-PF$_6$ because of the 10-fold lower conductivity of the latter (Table 1).

3.3. Electrochemical Dilatometry. Using in situ electrochemical dilatometry (eD) we can simultaneously record the CV and the displacement of the working electrode (Figure 1). This displacement is divided by the thickness of the electrode to obtain the normalized strain values. We can see a clear influence of the RTIL on the expansion of NovoCarb electrodes. The largest expansion of 1.4% is measured for EMIM-TFSI at a negative potential of −1.8 V vs carbon. This is followed by the expansion in EMIM-BF$_4$ (0.8%) and then BMIM-PF$_6$ (0.7%). It can be observed that the expansion is always more pronounced in the negative potential regime.

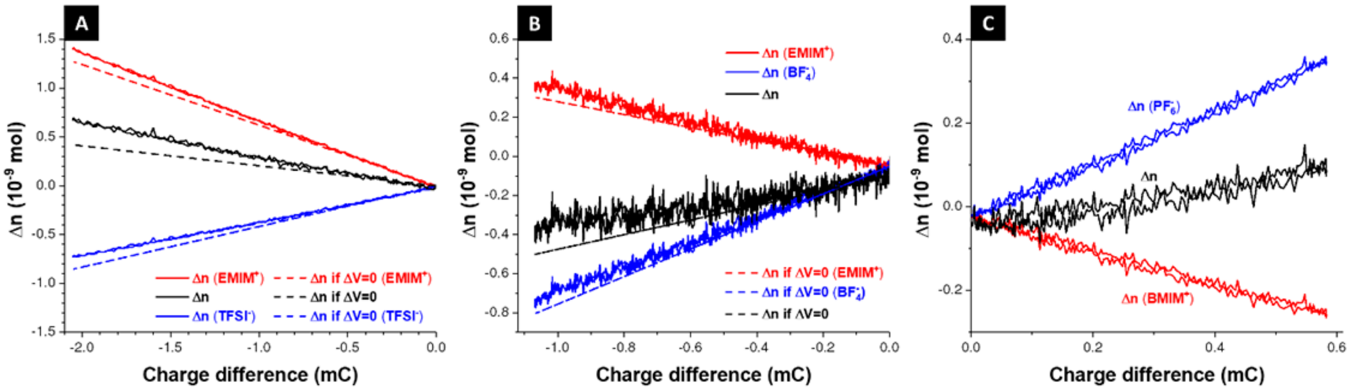

Figure 4. Calculated number of ions in the pores according to the charge difference in (A) EMIM-TFSI, (B) EMIM-BF_4, and (C) BMIM-PF_6. (A and B) Measurements are compared with the calculated changes which would result in a nonvolumetric exchange of ions (dashed lines).

However, the measured expansion cannot solely be related to the electroadsorbing cation, as both EMIM-containing electrolytes drastically differ in expansion depending on the type of anion present. At the most positive potentials (+1.5 V vs carbon), the expansion is largest for the nonspherical $TFSI^-$, which is also the largest anion, followed by PF_6^- and the smallest BF_4^-.

A strain hysteresis occurs during voltage sweeping at 1 mV/s and is enhanced for RTILs with lower ion mobility/higher viscosity as can be seen for BMIM-PF_6. The hysteresis is related to the limited ion migration inside narrow pores and the high viscosity of the used ionic liquids (Table 1). To avoid the strain hysteresis, we conducted galvanostatic measurements with the same voltage steps and an appropriate equilibrium time (Figure 2). The system is quasi-equilibrated at each voltage step, and we can now correlate charge and strain. The curves are normalized to zero charge at the minimum strain measured; we call this point the point of zero strain (pzs). This point is assumed to be close to the point of zero charge (pzc). Therefore, an equal number of cations and anions can be expected in the pores.[15,61] A higher strain is seen again at negative charge compared to positive charge for all RTILs. The smallest expansion is observed for EMIM-BF_4 with 0.25% at +300 C/g and 0.5% at −300 C/g. In the case of EMIM-TFSI, we observe a large strain of 0.7% at negative charges (−300 C/g) compared to a smaller strain of 0.2% at positive charges (+190 C/g). At a positive charge of 100 C/g, the expansion is 0.25% for BMIM-PF_6, 0.13% for EMIM-TFSI and 0.03% for EMIM-BF_4,which shows that in general a larger strain at negative potentials results also in a more pronounced expansion at positive charges. For BMIM-PF_6 the strain at −300 C/g is already 1.1%, which can be explained by the larger volume occupied by the $BMIM^+$ in comparison to $EMIM^+$ (Table 1). The effect of a more pronounced expansion at negative voltages is measured for all RTILs, but it is not fully understood yet.

In the case of EMIM-TFSI, the slope in the strain versus charge plot is smaller than that found for BMIM-PF_6. The higher strain can be correlated to the larger size of $BMIM^+$ (Table 1). It seems likely that the orientation of ions (co-ions and counterions) influences the strain, especially for the nonspherical ions.[62] A parabolic shape in the strain curve is generated by the spherical BF_4^-, whereas a more linear increase in strain can be observed for $TFSI^-$ and for the PF_6^- that is paired with the $BMIM^+$ cation. Hence, for the two $EMIM^+$-containing electrolytes, the strain at −300 C/g differs, with 0.5% for EMIM-BF_4 and 0.7% for EMIM-TFSI.[42] Moreover, the total charge values also strongly differ, which is related to the slightly different voltage windows and the surface coverage per ion, which is changing in the case of nonspherical ions (Figure 3).[62,63] The higher total charge values for EMIM-TFSI and EMIM-BF_4 in comparison to BMIM-PF_6, which has the largest cation and a spherical anion, are related to the bare ion size and the volume occupied by each ion (Table 1). Hence, we would expect higher energy E for higher potentials or larger cell voltages according to $E = 1/2CV^2$ (with capacitance C and cell voltage V), but the size of the adsorbed ions seems to have a greater impact on the possible surface charge.

The electrochemical stability of ionic liquids in the literature does not show a clear trend.[4,60,64,65] The different pzs (+0.2 V vs carbon for EMIM-BF_4 and 0.7 V vs carbon for EMIM-TFSI) might have an influence on the preferred electrosorption of ions, but there might be also a steric hindrance according to the different shapes of the ions.[66] In the case of EMIM-TFSI, both ions are nonspherical and can be approximated as cylindrically shaped. In confinement of nanometer-sized pores, these ions might slide easier along each other than spherical ions.[26,42] Nonspherical ions may create a steric barrier for other ions to slide along each other by generating the double layer inside the small pores due to their larger diameter in the x−y direction, and the shape of the double layer is more affected by the larger nonspherical ions (Figure 3). In our case, the strain created at the highest potential is similar for all three types of anions within a margin of about 0.3% (Figure 3). This is counter-intuitive considering the different sizes of the ions, but considering the vastly different charges a direct comparison is not possible this way.

In general, we observe a larger strain at negative polarization compared to positive potentials. The expansion is not only related to the bare ion size as described above for EMIM-TFSI and EMIM-BF_4. Even at the same amount of charge, the expansion differs for the same type of counterion, which is ascribed to an influence of the co-ions.

3.4. Electrochemical Quartz-Crystal Microbalance (EQCM).

To better understand the charging mechanism in the carbon nanopores, we conducted electrochemical quartz-crystal microbalance (EQCM) measurements. We note that in the EQCM experiments the electrodes are much thinner compared to the bulk electrodes in electrochemical dilatometry. This results in a more flooded electrode (the amount of electrolyte in comparison to the mass of electrode) and faster charge transport in the electrolyte but should not affect the charging mechanism of the nanopores in the quasi-equilibrated

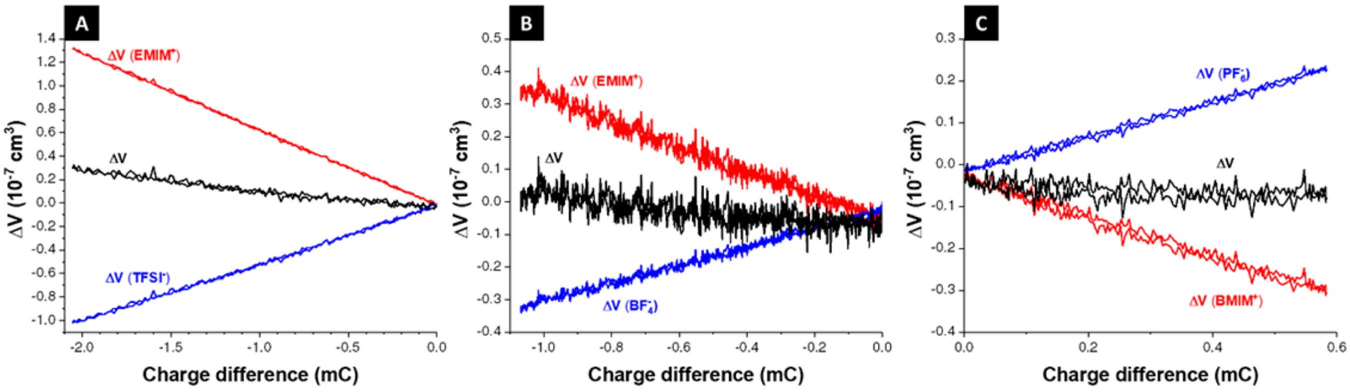

Figure 5. Calculation of volumetric changes ΔV according to the changes of number of ions Δn in the double layer in (A) EMIM-TFSI, (B) EMIM-BF_4, and (C) BMIM-PF_6. All graphs are plotted versus the charge difference for each system. Black line is the total volumetric change according to the sum of anion and cation expulsion and/or adsorption.

state. The thickness of the active mass should be in a range where the full width at half-maximum (fwhm) of the resonance peak does not change significantly. A change of the fwhm indicates viscoelastic behavior of the electrodes, and in this case, the origin of the frequency changes would not be exclusively related to mass changes. Consequently, the Sauerbrey equation would not be applicable.[47,49,67,68] However, in our measurements, the viscoelastic effects were small, since the fwhm of the resonance peak changed only by about 50−100 Hz, whereas the frequency shift was about 300−700 Hz (Supporting Information, Figure S2).

Gravimetric in situ measurements of the electrodes with adsorbed ions can be used to calculate the change of the number of ions in the pores. In all cases, the mass of the electrode is highest at the highest potential (Supporting Information, Figure S3). The different masses of cations and anions allow us to track adsorbing and desorbing ions in the pores, even if there is just a 1:1 exchange of cations and anions. A higher mass at positive potential results from a larger number of ions in the pores or is just a result of ion swapping if the mass difference of cation and anion is large. A clear differentiation of the changes in ion population is possible when calculating the change in the number of ions as described in the Supporting Information. We see that for EMIM-TFSI, more cations enter the pores than anions are ejected when applying a negative potential (Figure 4A). Accordingly, the total number of ions (Δn) increases. This is in contrast to the measured and simulated behavior of supercapacitors with aqueous or organic electrolytes.[5,14,20,32] This implies that the absence of a solvation shell leads to a different double-layer structure in the nanoconfined space.[22,26] We see a stronger increase in the number of cations $\Delta n(\mathrm{EMIM}^+)$ compared to the decrease of anions $\Delta n(\mathrm{TFSI}^-)$ for negative polarization. Thus, the charge storage is dominated by the insertion or expulsion of the smaller ion (i.e., EMIM^+, Figure 4A). This charge storage mechanism leads only to a small increase of the volume for negative polarization (Figure 5A).

The mechanism changes when using EMIM-BF_4 or BMIM-PF_6 as electrolyte (Figure 4B and 4C). In the case of these ionic liquids, the sizes of the spherical anions are smaller compared to the sizes of the cations. When the electrode is charged negatively, the number of anions decreases more strongly than the number of cations increases. This mechanism leads also to an almost constant volume of the ionic liquids within the pores (Figure 5B and 5C).

3.5. Multilength Scale Behavior. The EQCM results in the previous subsection reveal that movement of smaller ions is the dominating part of the charging mechanism at lower surface charges. We see at larger potentials an increase of the amount of counterion adsorption (Figure 3) due to the strong depletion of the smaller ions and the need of further surface charge compensation. Considering the theoretical volume of each ion,[69,70] we can estimate the volume change of the ionic liquid inside the porous electrode (Figure 4) for the low charges in the EQCM measurements. Since we have different sized ions, the structure of the electric double layer can change without yielding strong volumetric changes. The volumetric ratio of EMIM^+ to BF_4^- is, for example, more than 2:1; accordingly, two BF_4^- ions occupy the same volume as just one EMIM^+ (Table 1).

The chosen potential window for the eD measurements is much wider, so we can see the effect of ion swapping without volumetric changes and then a drastic increase in strain according to crowding the pores with counterions to compensate for the higher surface charge. In contrast to systems with solvated ions, where the total number of ions in the pore is constant,[5] we can see a crowding of pores which get filled with more ions to compensate for the surface charge. For EMIM-BF_4, the volume neutral ion swapping occurs at very low charge difference according to EQCM measurements and confirmed by eD where no strain is measured for low charges until −70 C/g (Figure 2B). This means that more BF_4^- migrates than EMIM^+ since two anions fit into the space of one cation. When applying more negative potentials, the strain increases, as seen by eD. Hence, the slope in EMIM-BF_4 is much smaller compared to EMIM-TFSI, which is caused by the size difference of anions and the fact that the smaller ions are more involved in the charge compensation. For BMIM-PF_6, the mechanism of charge storage is similar to EMIM-BF_4 without any significant volumetric change around the pzc (Figure 5C) due to the larger BMIM^+ being exchanged for more of the smaller PF_6^- ions (volumetric ratio BMIM^+ to PF_6^- is 1.8:1). The volume increases for more negative charges, where the amount of counterion adsorption increases. Considering that BMIM^+ is the largest ion in this study, the expected volumetric changes are highest, too. Moreover, the strain at the most negative charge is less for the quasi-equilibrated state (Figure 2C) in comparison to the dynamic measurement in Figure 3, which is related to the very high viscosity of this IL.

DOI: 10.1021/acs.jpcc.7b06915
J. Phys. Chem. C 2017, 121, 19120−19128

In summary, we see at first always smaller ions are being exchanged for fewer large ions until a critical point is reached, where the mechanism due to strong diminution of co-ions must change to a larger amount of counterion adsorption. This aligns with the dilatometer measurements, where no strain was measured (up to ±100 C/g for EMIM-BF_4), while for higher negative charges the increased counterion adsorption causes the slope to rise (Figure 3).

A rigorous quantification is difficult since the pores are not completely filled without an applied voltage and secondary effects like electrowetting may occur.[15] In the absence of solvent molecules, ideal RTIL counterion adsorption must cause an increase in the volume of the electrical double layer and a crowding of ions in the pores.[17,22,26] For potentials far from pzc, counterion adsorption dominates as the charging mechanism and the slope of volume expansion increases for larger ions since each ion occupies a larger volume fraction inside a narrow pore (Figure 3). However, the expansion differs for EMIM-TFSI and EMIM-BF_4 even though both systems employ the same cation. This must be related to strong ion−ion interactions and a non-negligible number of the co-ions are involved in the charging mechanism. According to the shape and degree of freedom, also the adsorption sites inside of micropores might differ strongly (Figure 3).[41,42] The spherical anions seem to create less strain compared to the cylindrical $TFSI^-$, which also might be caused by a lower degree of freedom and a larger steric hindrance as co-ion in the double layer.[66]

4. CONCLUSIONS

We present a systematic study on capacitive energy storage at a microporous carbon surface with different ionic liquids. The electrochemical properties at the fluid/solid interface were investigated in situ by a multilength scale approach. Electrochemical dilatometry on bulk electrodes and electrochemical quartz-crystal microbalance on thin electrodes were used to fundamentally understand the charging mechanism and the resulting bulk behavior. Close to the potential of zero charge, smaller ions are more involved in the charging mechanism. Since more smaller ions are exchanged by less larger ions, the charging takes place at almost constant volume. For potentials far from the pzc, the mechanism changes to a preferred counterion adsorption due to depletion of co-ions. Moreover, a spherical anion creates less strain compared to a nonspherical one, which might be caused by a lower degree of freedom and a larger steric hindrance as co-ion in the electrical double layer.

■ ASSOCIATED CONTENT

Ⓢ Supporting Information

The Supporting Information is available free of charge on the ACS Publications website at DOI: 10.1021/acs.jpcc.7b06915.

> Description of quantification of ions, clarification of volumetric changes, supporting Information for gas sorption analysis, supporting Information on EQCM measurements, chemical analysis via CHNSO analysis (PDF)

■ AUTHOR INFORMATION

Corresponding Authors

*E-mail: roling@staff.uni-marburg.de.
*E-mail: volker.presser@leibniz-inm.de.

ORCID

Volker Presser: 0000-0003-2181-0590

Notes

The authors declare no competing financial interest.

■ ACKNOWLEDGMENTS

The authors thank Prof. Eduard Arzt (INM) for his continuing support. N.J. and V.P. acknowledge funding from the German-Israeli Foundation for Scientific Research and Development (GIF) via Research Grant Agreement No. 1-1237-302.5/2014. B.K. and V.P. acknowledge support by the Minerva Foundation via the Award for Research Cooperation and High Excellence in Science Award (ARCHES). We appreciate the discussions with Simon Fleischmann (INM) and Prof. Mikhael Levi (Bar-Ilan University). B.R. and S.E. acknowledge financial support of this work by the Federal State of Hesse within the LOEWE program of excellence (project initiative STORE-E).

■ REFERENCES

(1) Simon, P.; Gogotsi, Y. Materials for Electrochemical Capacitors. *Nat. Mater.* **2008**, *7*, 845−854.

(2) Salanne, M.; Rotenberg, B.; Naoi, K.; Kaneko, K.; Taberna, P. L.; Grey, C. P.; Dunn, B.; Simon, P. Efficient Storage Mechanisms for Building Better Supercapacitors. *Nat. Energy* **2016**, *1*, 16070.

(3) Jäckel, N.; Simon, P.; Gogotsi, Y.; Presser, V. The Increase in Capacitance by Subnanometer Pores in Carbon. *ACS Energy Lett.* **2016**, *1*, 1262−1265.

(4) Pohlmann, S.; Kühnel, R.-S.; Centeno, T. A.; Balducci, A. The Influence of Anion−Cation Combinations on the Physicochemical Properties of Advanced Electrolytes for Supercapacitors and the Capacitance of Activated Carbons. *ChemElectroChem* **2014**, *1*, 1301−1311.

(5) Prehal, C.; Koczwara, C.; Jäckel, N.; Schreiber, A.; Burian, M.; Amenitsch, H.; Hartmann, M. A.; Presser, V.; Paris, O. Quantification of Ion Confinement and Desolvation in Nanoporous Carbon Supercapacitors with Modelling and in Situ X-Ray Scattering. *Nat. Energy* **2017**, *2*, 16215.

(6) Beguin, F.; Presser, V.; Balducci, A.; Frackowiak, E. *Adv. Mater.* **2014**, *26*, 2219−2251.

(7) Zhong, C.; Deng, Y.; Hu, W.; Qiao, J.; Zhang, L.; Zhang, J. A Review of Electrolyte Materials and Compositions for Electrochemical Supercapacitors. *Chem. Soc. Rev.* **2015**, *44*, 7484−539.

(8) Redondo, E.; Tsai, W.-Y.; Daffos, B.; Taberna, P.-L.; Simon, P.; Goikolea, E.; Mysyk, R. Outstanding Room-Temperature Capacitance of Biomass-Derived Microporous Carbons in Ionic Liquid Electrolyte. *Electrochem. Commun.* **2017**, *79*, 5−8.

(9) Salanne, M. Ionic Liquids for Supercapacitor Applications. *Top. Curr. Chem.* **2017**, *375*, 63.

(10) Brandt, A.; Balducci, A. Theoretical and Practical Energy Limitations of Organic and Ionic Liquid-Based Electrolytes for High Voltage Electrochemical Double Layer Capacitors. *J. Power Sources* **2014**, *250*, 343−351.

(11) Burt, R.; Breitsprecher, K.; Daffos, B.; Taberna, P. L.; Simon, P.; Birkett, G.; Zhao, X. S.; Holm, C.; Salanne, M. Capacitance of Nanoporous Carbon-Based Supercapacitors Is a Trade-Off between the Concentration and the Separability of the Ions. *J. Phys. Chem. Lett.* **2016**, *7*, 4015−4021.

(12) Forse, A. C.; Merlet, C.; Griffin, J. M.; Grey, C. P. New Perspectives on the Charging Mechanisms of Supercapacitors. *J. Am. Chem. Soc.* **2016**, *138*, 5731−44.

(13) Rochester, C. C.; Pruessner, G.; Kornyshev, A. A. Statistical Mechanics of 'Unwanted Electroactuation' in Nanoporous Supercapacitors. *Electrochim. Acta* **2015**, *174*, 978−984.

(14) Griffin, J. M.; Forse, A. C.; Wang, H.; Trease, N. M.; Taberna, P. L.; Simon, P.; Grey, C. P. Ion Counting in Supercapacitor Electrodes Using Nmr Spectroscopy. *Faraday Discuss.* **2015**, *176*, 49−68.

(15) Forse, A. C.; Griffin, J. M.; Merlet, C.; Bayley, P. M.; Wang, H.; Simon, P.; Grey, C. P. Nmr Study of Ion Dynamics and Charge Storage in Ionic Liquid Supercapacitors. *J. Am. Chem. Soc.* **2015**, *137*, 7231−42.

(16) Merlet, C.; Rotenberg, B.; Madden, P. A.; Taberna, P. L.; Simon, P.; Gogotsi, Y.; Salanne, M. On the Molecular Origin of Supercapacitance in Nanoporous Carbon Electrodes. *Nat. Mater.* **2012**, *11*, 306−10.

(17) Tsai, W.-Y.; Taberna, P.-L.; Simon, P. Electrochemical Quartz Crystal Microbalance (Eqcm) Study of Ion Dynamics in Nanoporous Carbons. *J. Am. Chem. Soc.* **2014**, *136*, 8722−8728.

(18) Pean, C.; Rotenberg, B.; Simon, P.; Salanne, M. Understanding the Different (Dis)Charging Steps of Supercapacitors: Influence of Potential and Solvation. *Electrochim. Acta* **2016**, *206*, 504−512.

(19) Chathoth, S. M.; Mamontov, E.; Dai, S.; Wang, X.; Fulvio, P. F.; Wesolowski, D. J. Fast Diffusion in a Room Temperature Ionic Liquid Confined in Mesoporous Carbon. *Epl-Europhys. Lett.* **2012**, *97*, 66004.

(20) Griffin, J. M.; Forse, A. C.; Tsai, W. Y.; Taberna, P. L.; Simon, P.; Grey, C. P. In Situ Nmr and Electrochemical Quartz Crystal Microbalance Techniques Reveal the Structure of the Electrical Double Layer in Supercapacitors. *Nat. Mater.* **2015**, *14*, 812−9.

(21) Kondrat, S.; Kornyshev, A. Superionic State in Double-Layer Capacitors with Nanoporous Electrodes. *J. Phys.: Condens. Matter* **2011**, *23*, 022201.

(22) Bazant, M. Z.; Storey, B. D.; Kornyshev, A. A. Double Layer in Ionic Liquids: Overscreening Versus Crowding. *Phys. Rev. Lett.* **2011**, *106*, 046102.

(23) He, Y.; Huang, J.; Sumpter, B. G.; Kornyshev, A. A.; Qiao, R. Dynamic Charge Storage in Ionic Liquids-Filled Nanopores: Insight from a Computational Cyclic Voltammetry Study. *J. Phys. Chem. Lett.* **2015**, *6*, 22−30.

(24) Kondrat, S.; Georgi, N.; Fedorov, M. V.; Kornyshev, A. A. A Superionic State in Nano-Porous Double-Layer Capacitors: Insights from Monte Carlo Simulations. *Phys. Chem. Chem. Phys.* **2011**, *13*, 11359−66.

(25) Kornyshev, A. A. Double-Layer in Ionic Liquids: Paradigm Change? *J. Phys. Chem. B* **2007**, *111*, 5545−5557.

(26) Fedorov, M. V.; Kornyshev, A. A. Ionic Liquids at Electrified Interfaces. *Chem. Rev.* **2014**, *114*, 2978−3036.

(27) Jiang, D.; Jin, Z.; Wu, J. Oscillation of Capacitance inside Nanopores. *Nano Lett.* **2011**, *11*, 5373−5377.

(28) Ma, K.; Wang, X.; Forsman, J.; Woodward, C. E. Molecular Dynamic Simulations of Ionic Liquid's Structural Variations from Three to One Layers inside a Series of Slit and Cylindrical Nanopores. *J. Phys. Chem. C* **2017**, *121*, 13539−13548.

(29) Eikerling, M.; Kornyshev, A. A.; Lust, E. Optimized Structure of Nanoporous Carbon-Based Double-Layer Capacitors. *J. Electrochem. Soc.* **2005**, *152*, E24−E33.

(30) Kondrat, S.; Perez, C. R.; Presser, V.; Gogotsi, Y.; Kornyshev, A. A. Effect of Pore Size and Its Dispersity on the Energy Storage in Nanoporous Supercapacitors. *Energy Environ. Sci.* **2012**, *5*, 6474−6479.

(31) Kornyshev, A. A.; Qiao, R. Three-Dimensional Double Layers. *J. Phys. Chem. C* **2014**, *118*, 18285−18290.

(32) Forse, A. C.; Griffin, J. M.; Merlet, C.; Carretero-Gonzalez, J.; Raji, A.-R. O.; Trease, N. M.; Grey, C. P. Direct Observation of Ion Dynamics in Supercapacitor Electrodes Using In situ Diffusion Nmr Spectroscopy. *Nat. Energy* **2017**, *2*, 16216.

(33) Hantel, M. M.; Presser, V.; Kötz, R.; Gogotsi, Y. In Situ Electrochemical Dilatometry of Carbide-Derived Carbons. *Electrochem. Commun.* **2011**, *13*, 1221−1224.

(34) Hahn, M.; Barbieri, O.; Campana, F. P.; Kötz, R.; Gallay, R. Carbon Based Double Layer Capacitors with Aprotic Electrolyte Solutions: The Possible Role of Intercalation/Insertion Processes. *Appl. Phys. A: Mater. Sci. Process.* **2006**, *82*, 633−638.

(35) Hahn, M.; Barbieri, O.; Gallay, R.; Kötz, R. A Dilatometric Study of the Voltage Limitation of Carbonaceous Electrodes in Aprotic Edlc Type Electrolytes by Charge-Induced Strain. *Carbon* **2006**, *44*, 2523−2533.

(36) Ruch, P. W.; Hahn, M.; Cericola, D.; Menzel, A.; Kötz, R.; Wokaun, A. A Dilatometric and Small-Angle X-Ray Scattering Study of the Electrochemical Activation of Mesophase Pitch-Derived Carbon in Non-Aqueous Electrolyte Solution. *Carbon* **2010**, *48*, 1880−1888.

(37) Arruda, T. M.; Heon, M.; Presser, V.; Hillesheim, P. C.; Dai, S.; Gogotsi, Y.; Kalinin, S. V.; Balke, N. In Situ Tracking of the Nanoscale Expansion of Porous Carbon Electrodes. *Energy Environ. Sci.* **2013**, *6*, 225−231.

(38) Black, J. M.; Feng, G.; Fulvio, P. F.; Hillesheim, P. C.; Dai, S.; Gogotsi, Y.; Cummings, P. T.; Kalinin, S. V.; Balke, N. Strain-Based in Situ Study of Anion and Cation Insertion into Porous Carbon Electrodes with Different Pore Sizes. *Adv. Energy Mater.* **2014**, *4*, 1300683.

(39) Hantel, M. M.; Kaspar, T.; Nesper, R.; Wokaun, A.; Kötz, R. Persistent Electrochemical Pillaring of Graphene Ensembles. *Electrochem. Commun.* **2013**, *34*, 189−191.

(40) Wang, X.; Zhou, H.; Sheridan, E.; Walmsley, J. C.; Ren, D.; Chen, D. Geometrically Confined Favourable Ion Packing for High Gravimetric Capacitance in Carbon-Ionic Liquid Supercapacitors. *Energy Environ. Sci.* **2016**, *9*, 232−239.

(41) Kaasik, F.; Tamm, T.; Hantel, M. M.; Perre, E.; Aabloo, A.; Lust, E.; Bazant, M. Z.; Presser, V. Anisometric Charge Dependent Swelling of Porous Carbon in an Ionic Liquid. *Electrochem. Commun.* **2013**, *34*, 196−199.

(42) Hantel, M. M.; Weingarth, D.; Kötz, R. Parameters Determining Dimensional Changes of Porous Carbons During Capacitive Charging. *Carbon* **2014**, *69*, 275−286.

(43) Hantel, M. M.; Nesper, R.; Wokaun, A.; Kötz, R. In-Situ Xrd and Dilatometry Investigation of the Formation of Pillared Graphene Via Electrochemical Activation of Partially Reduced Graphite Oxide. *Electrochim. Acta* **2014**, *134*, 459−470.

(44) Black, J. M.; Okatan, M. B.; Feng, G.; Cummings, P. T.; Kalinin, S. V.; Balke, N. Topological Defects in Electric Double Layers of Ionic Liquids at Carbon Interfaces. *Nano Energy* **2015**, *15*, 737−745.

(45) Balke, N.; Jesse, S.; Carmichael, B.; Okatan, M. B.; Kravchenko, I. I.; Kalinin, S. V.; Tselev, A. Quantification of in-Contact Probe-Sample Electrostatic Forces with Dynamic Atomic Force Microscopy. *Nanotechnology* **2017**, *28*, 065704.

(46) Pean, C.; Daffos, B.; Rotenberg, B.; Levitz, P.; Haefele, M.; Taberna, P. L.; Simon, P.; Salanne, M. Confinement, Desolvation, and Electrosorption Effects on the Diffusion of Ions in Nanoporous Carbon Electrodes. *J. Am. Chem. Soc.* **2015**, *137*, 12627−32.

(47) Levi, M. D.; Daikhin, L.; Aurbach, D.; Presser, V. Quartz Crystal Microbalance with Dissipation Monitoring (Eqcm-D) for in-Situ Studies of Electrodes for Supercapacitors and Batteries: A Mini-Review. *Electrochem. Commun.* **2016**, *67*, 16−21.

(48) Levi, M. D.; Levy, N.; Sigalov, S.; Salitra, G.; Aurbach, D.; Maier, J. Electrochemical Quartz Crystal Microbalance (Eqcm) Studies of Ions and Solvents Insertion into Highly Porous Activated Carbons. *J. Am. Chem. Soc.* **2010**, *132*, 13220−13222.

(49) Levi, M. D.; Shpigel, N.; Sigalov, S.; Dargel, V.; Daikhin, L.; Aurbach, D. In Situ Porous Structure Characterization of Electrodes for Energy Storage and Conversion by Eqcm-D: A Review. *Electrochim. Acta* **2017**, *232*, 271−284.

(50) Levi, M. D.; Salitra, G.; Levy, N.; Aurbach, D.; Maier, J. Application of a Quartz-Crystal Microbalance to Measure Ionic Fluxes in Microporous Carbons for Energy Storage. *Nat. Mater.* **2009**, *8*, 872−875.

(51) Sigalov, S.; Levi, M. D.; Daikhin, L.; Salitra, G.; Aurbach, D. Electrochemical Quartz Crystal Admittance Studies of Ion Adsorption on Nanoporous Composite Carbon Electrodes in Aprotic Solutions. *J. Solid State Electrochem.* **2014**, *18*, 1335−1344.

(52) Krüner, B.; Lee, J.; Jäckel, N.; Tolosa, A.; Presser, V. Sub-Micrometer Novolac-Derived Carbon Beads for High Performance Supercapacitors and Redox Electrolyte Energy Storage. *ACS Appl. Mater. Interfaces* **2016**, *8*, 9104−9115.

(53) Krüner, B.; Srimuk, P.; Fleischmann, S.; Zeiger, M.; Schreiber, A.; Aslan, M.; Quade, A.; Presser, V. Hydrogen-Treated, Sub-

Micrometer Carbon Beads for Fast Capacitive Deionization with High Performance Stability. *Carbon* **2017**, *117*, 46−54.

(54) Gor, G. Y.; Thommes, M.; Cychosz, K. A.; Neimark, A. V. Quenched Solid Density Functional Theory Method for Characterization of Mesoporous Carbons by Nitrogen Adsorption. *Carbon* **2012**, *50*, 1583−1590.

(55) Jäckel, N.; Krüner, B.; van Aken, K. L.; Alhabeb, M.; Anasori, B.; Kaasik, F.; Gogotsi, Y.; Presser, V. Electrochemical in Situ Tracking of Volumetric Changes in Two-Dimensional Metal Carbides (Mxenes) in Ionic Liquids. *ACS Appl. Mater. Interfaces* **2016**, *8*, 32089−32093.

(56) Weingarth, D.; Foelske-Schmitz, A.; Wokaun, A.; Kötz, R. Ptfe Bound Activated Carbon—a Quasi-Reference Electrode for Ionic Liquids. *Electrochem. Commun.* **2012**, *18*, 116−118.

(57) Kumagai, S.; Mukaiyachi, K.; Tashima, D. Rate and Cycle Performances of Supercapacitors with Different Electrode Thickness Using Non-Aqueous Electrolyte. *J. Energy Stor.* **2015**, *3*, 10−17.

(58) Varzi, A.; Raccichini, R.; Marinaro, M.; Wohlfahrt-Mehrens, M.; Passerini, S. Probing the Characteristics of Casein as Green Binder for Non-Aqueous Electrochemical Double Layer Capacitors' Electrodes. *J. Power Sources* **2016**, *326*, 672−679.

(59) Jäckel, N.; Rodner, M.; Schreiber, A.; Jeongwook, J.; Zeiger, M.; Aslan, M.; Weingarth, D.; Presser, V. Anomalous or Regular Capacitance? The Influence of Pore Size Dispersity on Double-Layer Formation. *J. Power Sources* **2016**, *326*, 660−671.

(60) Weingarth, D.; Noh, H.; Foelske-Schmitz, A.; Wokaun, A.; Kötz, R. A Reliable Determination Method of Stability Limits for Electrochemical Double Layer Capacitors. *Electrochim. Acta* **2013**, *103*, 119−124.

(61) Nanjundiah, C.; McDevitt, S. F.; Koch, V. R. Differential Capacitance Measurements in Solvent-Free Ionic Liquids at Hg and C Interfaces. *J. Electrochem. Soc.* **1997**, *144*, 3392−3397.

(62) Baldelli, S. Surface Structure at the Ionic Liquid−Electrified Metal Interface. *Acc. Chem. Res.* **2008**, *41*, 421−431.

(63) Rivera-Rubero, S.; Baldelli, S. Surface Spectroscopy of Room-Temperature Ionic Liquids on a Platinum Electrode: A Sum Frequency Generation Study. *J. Phys. Chem. B* **2004**, *108*, 15133−15140.

(64) Mousavi, M. P. S.; Dittmer, A. J.; Wilson, B. E.; Hu, J.; Stein, A.; Bühlmann, P. Unbiased Quantification of the Electrochemical Stability Limits of Electrolytes and Ionic Liquids. *J. Electrochem. Soc.* **2015**, *162*, A2250−A2258.

(65) Brandt, A.; Pohlmann, S.; Varzi, A.; Balducci, A.; Passerini, S. Ionic Liquids in Supercapacitors. *MRS Bull.* **2013**, *38*, 554−559.

(66) Segalini, J.; Iwama, E.; Taberna, P.-L.; Gogotsi, Y.; Simon, P. Steric Effects in Adsorption of Ions from Mixed Electrolytes into Microporous Carbon. *Electrochem. Commun.* **2012**, *15*, 63−65.

(67) Sauerbrey, G. Verwendung Von Schwingquarzen Zur Wägung Dünner Schichten Und Zur Mikrowägung. *Eur. Phys. J. A* **1959**, *155*, 206−222.

(68) Shpigel, N. In Situ Hydrodynamic Spectroscopy for Structure Characterization of Porous Energy Storage Electrodes. *Nat. Mater.* **2016**, *15*, 570−575.

(69) Slattery, J. M.; Daguenet, C.; Dyson, P. J.; Schubert, T. J. S.; Krossing, I. How to Predict the Physical Properties of Ionic Liquids: A Volume-Based Approach. *Angew. Chem., Int. Ed.* **2007**, *46*, 5384−5388.

(70) Zhang, S.; Sun, N.; He, X.; Lu, X.; Zhang, X. Physical Properties of Ionic Liquids: Database and Evaluation. *J. Phys. Chem. Ref. Data* **2006**, *35*, 1475−1517.

(71) Krossing, I.; Slattery, J. M.; Daguenet, C.; Dyson, P. J.; Oleinikova, A.; Weingärtner, H. Why Are Ionic Liquids Liquid? A Simple Explanation Based on Lattice and Solvation Energies. *J. Am. Chem. Soc.* **2006**, *128*, 13427−13434.

(72) Resende Prado, C. E.; Gomide Freitas, L. C. Molecular Dynamics Simulation of the Room-Temperature Ionic Liquid 1-Butyl-3-Methylimidazolium Tetrafluoroborate. *J. Mol. Struct.: THEOCHEM* **2007**, *847*, 93−100.

(73) Largeot, C.; Portet, C.; Chmiola, J.; Taberna, P.-L.; Gogotsi, Y.; Simon, P. Relation between the Ion Size and Pore Size for an Electric Double-Layer Capacitor. *J. Am. Chem. Soc.* **2008**, *130*, 2730−2731.

Quantitative Information about Electrosorption of Ionic Liquids in Carbon Nanopores from Electrochemical Dilatometry and Quartz Crystal Microbalance Measurements

Nicolas Jäckel,[1,2] Steffen Patrick Emge,[3,4] Benjamin Krüner,[1,2]
Bernhard Roling,[3,*] and Volker Presser[1,2,*]

[1]… INM - Leibniz Institute for New Materials, Saarbrücken, Germany
[2]… Department of Materials Science and Engineering, Saarland University, Saarbrücken, Germany
[3]… Department of Chemistry, Philipps-Universität, Marburg, Germany
[4]… Department of Chemistry, University of Cambridge, Cambridge, United Kingdom
*… Corresponding author's email address: roling@staff.uni-marburg.de (BR), volker.presser@leibniz-inm.de (VP)

Supporting Information

1. Quantification of ions

To calculate the number of ions in the double-layer we expect an exclusive capacitive energy storage behavior. The surface charge Q is balanced by adsorption of counter-ions or expulsion of co-ions via:

$$Q = -F(\Delta n_+ - \Delta n_-) \tag{S1}$$

with the Faradaic Constant F and the change in number of cations Δn_+ and the change in number of anions Δn_-. All used ionic liquids contain single charged (monovalent) ions and we can simplify the equation by calculating the difference x between co-ions and counter-ions:

$$-\frac{Q}{F} = \Delta n_+ - \Delta n_- = -x \tag{S2}$$

The total change of number of ions Δn is the sum of the changes of co-ions and counter-ions:

$$\Delta n = \Delta n_+ + \Delta n_- \tag{S3}$$

Since there are only monovalent ions *Eq. (S3)*, we can write the following:

$$\Delta n = 2\Delta n_+ + x \tag{S4}$$

The mass change according to the Sauerbrey equation $\Delta m = k \cdot \Delta f$ is linear related to the change in frequency.[1] Assuming only ion adsorption and desorption [2] we can correlate the mass change with the change in number of ions and mass of ion M as:

$$\Delta m = \Delta n_+ \cdot M_+ + \Delta n_- \cdot M_- \tag{S5}$$

By combination of *Eq. (S3)-(S5)*, we can calculate the change in number of a single type of ions as:

$$\Delta m = \Delta n_+ * M_+ + (\Delta n_+ + x) * M_- \tag{S6}$$

$$\Delta m = \Delta n_+ * (M_+ + M_-) + x * M_- \tag{S7}$$

$$\Delta n_+ = \frac{\Delta m - x * M_-}{M_+ + M_-} \tag{S8}$$

2. Volumetric changes

The changes in volume related to the changes in number of ions in the pores are correlated by the molar volume of the ions V_m and the Avogadro constant N_A

$$V_m = V \cdot N_A \tag{S9}$$

Since the volumes of the ions are quite different there are possible changes of ions in the pores without any volumetric changes. If we know the free of volumetric change state of (dis-)charging we can calculate the number of ions which is related to the occurring volumetric change. If we assume $\Delta V=0$, then we see:

$$\Delta V = 0 = \Delta V_+ + \Delta V_- = \Delta n_{0+} V_{m+} + \Delta n_{0-} V_{m-} \tag{S10}$$

$$\Delta n_{0-} = \frac{Q * V_{m+}}{F(\Delta V_{m-} * V_{m+})} \tag{S11}$$

$$\Delta n_{0+} = \frac{Q}{F} - \Delta n_{0-} \tag{S12}$$

with Δn_0 is the number of ions which can be exchanged without any volumetric changes.

3. Gas sorption analysis

Nitrogen gas sorption measurements were carried out on the dry NovoCarb powder and the electrode containing 10 mass% NaCMC. The resulting quenched-solid density functional theory (QSDFT) plots show a decreased total pore volume in the electrode (**Fig. S1A**). This is resulted from the pore blocking of the binder, which is especially pronounced for the smallest pores below 1 nm as seen when normalizing the total pore volume to 100 % (**Fig. S1B**). Hence, the average pore volume stays constant.

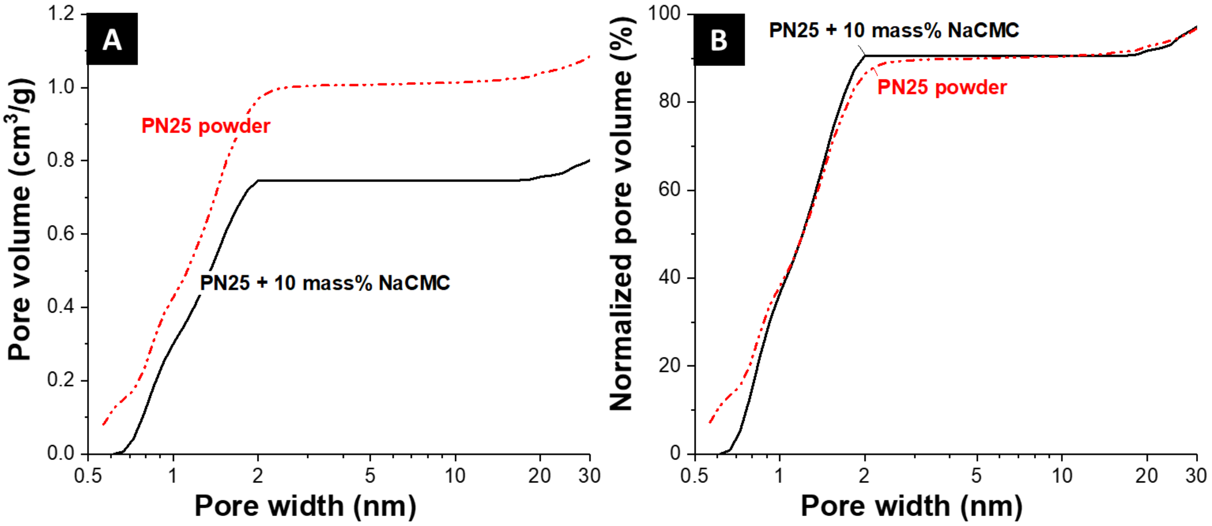

Figure S1: Cumulative pore volume for dry powder (red line, dashed) and electrode containing 10 mass% NaCMC (black line, solid).

4. EQCM measurements

The EQCM measurements for all three ionic liquids show changes in frequency Δ*f* and changes in FWHM of the peaks (dissipation Δ*W*) when applying a potential. To avoid any viscoelastic influence of the electrode on the frequency changes the change in dissipation must be much lower than the changes in peak shift Δ*f*.[3] This is confirmed by our measurements where the change in W is 3-10 times less than the change in frequency (**Fig. S2**). The signal is smoothed with a 20-point Savitzy-Golay filter.

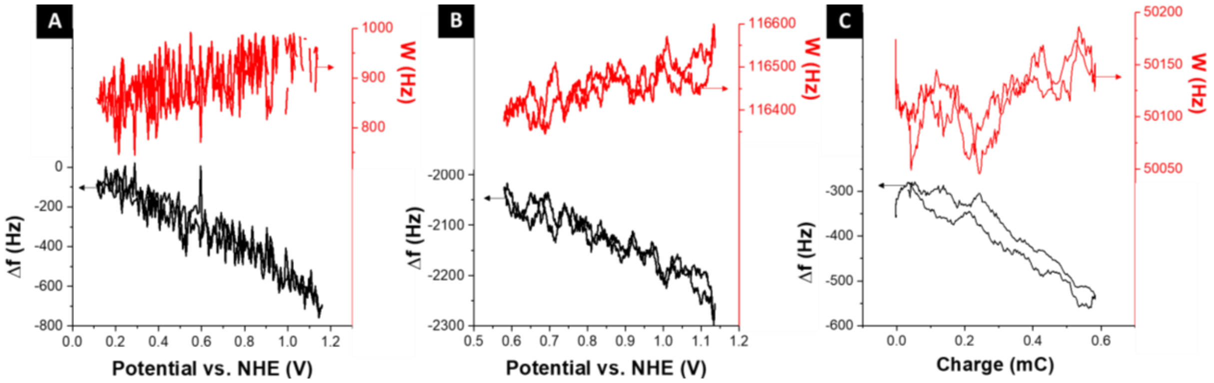

Figure S2: Change in frequency Δf and dissipation W according to the applied voltage (A,B) or to the charge (C) in (A) EMIM-TFSI, (B) EMIM-BF$_4$, and (C) BMIM-PF$_6$.

With cyclic voltammetry, the change in mass of the working electrode Δ*m* can be traced in situ with the electrochemical response of the system. In all cases the mass increased when applying positive potentials (**Fig. S3**).

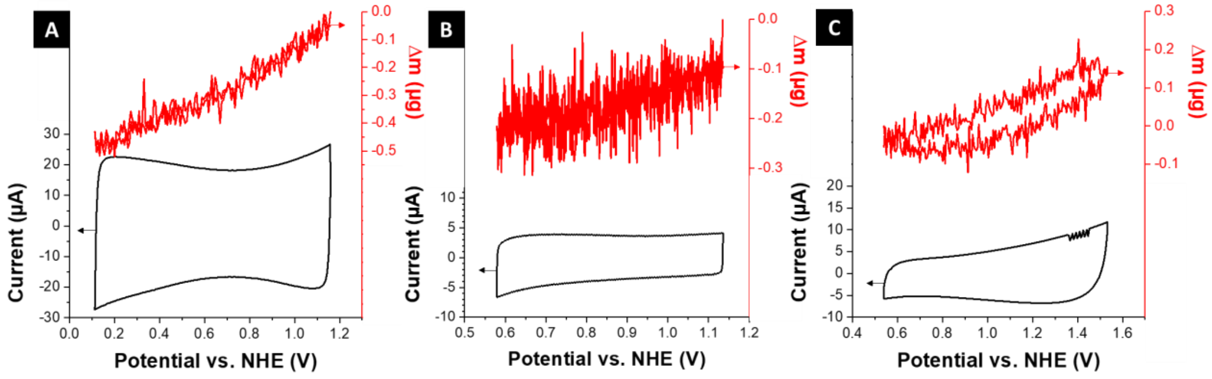

Figure S3: In situ tracing of mass changes of the working electrode (red line) and the electrochemical response (black line) of the thin EQCM electrodes in (A) EMIM-TFSI, (B) EMIM-BF$_4$, and (C) BMIM-PF$_6$.

The measured changes in mass are correlated to the change in number of adsorbed ions on the working electrode. Since we know the volume of each ion,[4] a direct calculation of volumetric changes according to the composition of the double-layer is possible (**Fig. 5**).

5. Chemical analysis

Table S1: Chemical analysis of the dry carbon powder via CHNSO analysis.

Carbon (mass%)	Hydrogen (mass%)	Nitrogen (mass%)	Sulfur (mass%)	Oxygen (mass%)
94.1±1.3	0.5±0.1	0.7±0.1	Not detectable	2.8±0.5

References

1. Shpigel, N., et al., In Situ Hydrodynamic Spectroscopy for Structure Characterization of Porous Energy Storage Electrodes. *Nat. Mater.* **2016**, *15*, 570-575.
2. Levi, M. D.; Sigalov, S.; Salitra, G.; Aurbach, D.; Maier, J., The Effect of Specific Adsorption of Cations and Their Size on the Charge-Compensation Mechanism in Carbon Micropores: The Role of Anion Desorption. *ChemPhysChem* **2011**, *12*, 854-862.
3. Sigalov, S.; Levi, M. D.; Daikhin, L.; Salitra, G.; Aurbach, D., Electrochemical Quartz Crystal Admittance Studies of Ion Adsorption on Nanoporous Composite Carbon Electrodes in Aprotic Solutions. *J. Solid State Electrochem.* **2013**, *18*, 1335-1344.
4. Krossing, I.; Slattery, J. M.; Daguenet, C.; Dyson, P. J.; Oleinikova, A.; Weingärtner, H., Why Are Ionic Liquids Liquid? A Simple Explanation Based on Lattice and Solvation Energies. *J. Am. Chem. Soc.* **2006**, *128*, 13427-13434.

4.4. Nitrogen-containing novolac-derived carbon beads as electrode material for supercapacitors

Benjamin Krüner,[1,2] Anna Schreiber,[1] Aura Tolosa,[1,2] Antje Quade,[3] Felix Badaczewski,[4] Torben Pfaff,[4] Bernd M. Smarsly,[4] Volker Presser[1,2]

[1] *INM - Leibniz Institute for New Materials, 66123 Saarbrücken, Germany*

[2] *Department of Materials Science and Engineering, Saarland University, 66123 Saarbrücken, Germany*

[3] *Leibniz Institute for Plasma Science and Technology, 17489 Greifswald, Germany*

[4] *Institute of Physical Chemistry, Justus-Liebig University Giessen, 35392 Giessen, Germany*

Krüner, Benjamin et al. (2018) *Carbon*, 132, 220-231.
https://doi.org/10.1016/j.carbon.2018.02.029

Own contribution: Design, planning, writing, synthesis of the activated and non-activated carbon beads, SEM, particle size analysis, TGA coupled with MS analysis, CO_2 and N_2 sorption analysis, Raman analysis, electrochemical analysis for double-layer capacitors.

Abstract:

We pyrolyzed and activated novolac beads in one single step with ammonia at different temperatures (750–950 °C), which leads to a highly porous carbon with nitrogen-doping. The chemical and physical properties were characterized and correlated with the electrochemical performance as supercapacitor electrodes. The average pore size varied at 0.6–1.4 nm dependent on the synthesis temperatures. Three different electrolytes (aqueous, organic, and an ionic liquid) were tested. The specific capacitance in a symmetrical supercapacitor reached up to 173 $F \cdot g^{-1}$ and was strongly dependent on the porosity of the electrode material and the kind of electrolyte. We found that the presence of nitrogen enhanced the electrochemical performance stability and led to a high specific energy of 50 $Wh \cdot kg^{-1}$ using an ionic liquid as electrolyte.

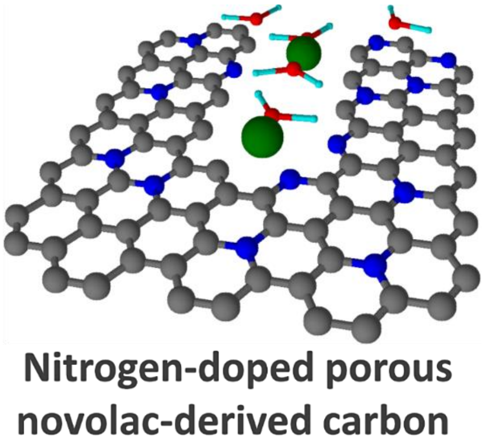

Carbon 132 (2018) 220–231

Contents lists available at ScienceDirect

Carbon

journal homepage: www.elsevier.com/locate/carbon

Nitrogen-containing novolac-derived carbon beads as electrode material for supercapacitors

Benjamin Krüner [a, b], Anna Schreiber [a], Aura Tolosa [a, b], Antje Quade [c], Felix Badaczewski [d], Torben Pfaff [d], Bernd M. Smarsly [d], Volker Presser [a, b, *]

[a] *INM - Leibniz Institute for New Materials, Campus D2 2, 66123 Saarbrücken, Germany*
[b] *Department of Materials Science and Engineering, Saarland University, Campus D2 2, 66123 Saarbrücken, Germany*
[c] *Leibniz Institute for Plasma Science and Technology, Felix-Hausdorff-Straße 2, 17489 Greifswald, Germany*
[d] *Institute of Physical Chemistry, Justus-Liebig University Giessen, Heinrich-Buff-Ring 58, 35392 Giessen, Germany*

ARTICLE INFO

Article history:
Received 25 December 2017
Received in revised form
26 January 2018
Accepted 4 February 2018
Available online 7 February 2018

Keywords:
Porous carbon
Nitrogen-doping
Supercapacitor
Electrochemical energy storage

ABSTRACT

We pyrolyzed and activated novolac beads in one single step with ammonia at different temperatures (750–950 °C), which leads to a highly porous carbon with nitrogen-doping. The chemical and physical properties were characterized and correlated with the electrochemical performance as supercapacitor electrodes. The average pore size varied at 0.6–1.4 nm dependent on the synthesis temperatures. Three different electrolytes (aqueous, organic, and an ionic liquid) were tested. The specific capacitance in a symmetrical supercapacitor reached up to 173 $\mathrm{F\,g^{-1}}$ and was strongly dependent on the porosity of the electrode material and the kind of electrolyte. We found that the presence of nitrogen enhanced the electrochemical performance stability and led to a high specific energy of 50 $\mathrm{Wh \cdot kg^{-1}}$ using an ionic liquid as electrolyte.

1. Introduction

Porous carbon materials are attractive for many applications like catalysis [1], gas storage [2,3], energy storage [4], or water treatment [5,6]. To enhance the electrical conductivity and overall performance, nitrogen-doped porous carbons have been developed [7–10]. A particularly promising technology for rapid and highly efficient energy storage is the electrical double-layer capacitor, also known as supercapacitor [11]. The latter uses highly porous carbons as electrode material and stores energy by fast ion electrosorption [12]. Supercapacitors are characterized by a high specific power due to fast interfacial processes, but suffer from relatively low specific energies compared to batteries [4]. It was shown that nitrogen-doping in graphene can improve the specific capacitance by modifying the electronic structure of the material [13,14]. Therefore, it is promising to implement this enhanced electrochemical performance via nitrogen-doping to nanoporous carbon materials [15,16]. Salinas-Torres et al. investigated the influence of different nitrogen groups and showed that aniline groups on porous carbon electrodes can improve specific capacitance more than pyrrolic or graphitic nitrogen groups [17]. Aniline groups also led to a lower capacitance retention over time when operating in an organic electrolyte because they facilitate the electrolyte decomposition, which leads to pore blocking [17,18]. A similar effect was observed for carbons with a high amount of oxygen-containing functional groups [19,20].

The synthesis strategies to introduce nitrogen in porous carbons can be classified into two distinct groups [21]. The first approach is the direct synthesis from nitrogen-containing precursors, like melamine resin [22–24], polypyrrole [25], glucosamine [9], bean shells [26], or other biomasses [27,28]. The porosity of these materials is often accomplished by a templating route or activation step at high temperatures. The pyrolysis and the activation at high temperatures increase the porosity, but also often reduce the amount of nitrogen in the structure [21]. Chen et al. showed by the pyrolysis of polypyrrole that a higher temperature (500–1100 °C) leads to a higher ratio of graphitic and pyrrolic nitrogen, while the total amount of nitrogen was reduced from 12 at% to 5 at% [25]. The second approach to produce nitrogen-containing carbon materials is a post-treatment of a porous carbon with nitrogen-containing compounds, like NH_3 [29], HCN [30], urea [31], or HNO_3 [32,33] in a gaseous or liquid phase. This approach often forms nitrogen

---

[*] Corresponding author. INM - Leibniz Institute for New Materials, Campus D2 2, 66123 Saarbrücken, Germany.
E-mail address: volker.presser@leibniz-inm.de (V. Presser).

https://doi.org/10.1016/j.carbon.2018.02.029

functionalities instead of leading to actual nitrogen-doping of the carbon structure [21,29,33,34]. A treatment at high temperatures leads to a decomposition of ammonia to NH_2 and NH [30]. These radicals can further react with carbon and form nitrogen functionalities, which decompose at high temperatures to HNC or other components like CH_4 leading to an increase in porosity [29,35,36].

A new method to produce nitrogen-enriched carbons was introduced by Wang et al. in 2013 by the direct pyrolysis of a phenolic resin in ammonia [37]. Ammonia is reacting during the pyrolysis with the polymer which leads to nitrogen-doping and at higher temperatures, the NH_3 decomposition activates the carbon as well. By this way, high surface area and nitrogen-doping are accomplished at the same time. The carbon precursor used by Wang et al. was combined with a block-copolymer as soft-template to produce mesopores. Micropores were created by carbon reacting with ammonia at high temperatures of 700–850 °C. This procedure led to a specific surface area (BET) of 795–1415 $m^2\,g^{-1}$ and a total pore volume of 0.69–1.20 $cm^3\,g^{-1}$. The nitrogen content produced by this method was 7.1–9.1 at%. The type of nitrogen groups (i.e., pyridinic-type, amide or imine, pyrrolic-type or pyridonic-type, graphitic-type, and pyridine N-oxide) was identified with X-ray photoelectron spectroscopy (XPS) and varied depending on the holding time at high temperatures. The presence of ammonia during the pyrolysis eliminates the need for a nitrogen-containing precursor, additional activation, or post-treatments. The materials were also tested in a symmetrical supercapacitor using 1 M tetraethylammonium tetrafluoroborate (TEA-BF_4) in propylene carbonate (PC) as electrolyte, achieving a specific capacitance of 76 $F\,g^{-1}$ [37].

In a previous study, we introduced the synthesis of submicrometer sized novolac-derived carbon beads, which were physically activated and used for energy storage (supercapacitors, lithium-sulfur batteries) and water treatment (capacitive deionization) [38–41]. We now applied the method of Wang et al. [37] to our novolac beads to effectively synthesize nanoporous, nitrogen-doped carbon beads in one step at high temperatures. We varied the synthesis temperature in presence of ammonia from 750 °C to 950 °C, which resulted in different microporous carbon. These materials were characterized via temperature-programmed desorption (TPD) and XPS to identify the nitrogen groups, which have a major influence on the electrochemical stability of the supercapacitors. We also studied the influence of the temperature and ammonia during the pyrolysis on the non-graphitic structure of the materials with Raman spectroscopy and wide-angle X-ray scattering (WAXS). Additionally, we benchmarked the nitrogen-containing novolac-derived carbon beads as electrode materials for supercapacitors in an aqueous electrolyte, an organic electrolyte, and an ionic liquid. Our work gives further insights into the impact of the nitrogen-doping on the carbon material properties and electrochemical performance, especially in ionic liquids.

2. Experimental description

2.1. Synthesis of novolac-derived carbon beads

The novolac beads were prepared with a method described before [38,40]. In short, 20 g of the novolac (Alnovol PN 320 from Allnex) was dissolved in 100 mL ethanol together with 2 g of hexamethyl tetralin as crosslinker. The solution was added to 500 mL deionized water in an autoclave and heated to 150 °C for 8 h. The resulting suspension was freeze-dried with liquid nitrogen to avoid strong agglomeration.

1 g of the dried polymer powder was placed in a quartz glass crucible for the temperature treatment in an argon/ammonia atmosphere. The argon gas (purity: 4.6) constantly flowed at 50 $cm^3\,min^{-1}$ and the ammonia (purity: 5.0) flow of 20 $cm^3\,min^{-1}$ was added during the heating and holding time. The heating rate was 1 °C min^{-1} and the target temperature of 750 °C, 850 °C, or 950 °C was held for 3 h. The ammonia flow was switched off during the cooling of the quartz tube furnace (Carbolite Gero). One sample was prepared without the addition of ammonia as reference (pyrolysis temperature: 950 °C).

2.2. Material characterization

The porosity of the powder and electrode samples was analyzed via CO_2 and N_2 gas sorption analysis (GSA) with a Quantachrome Autosorb iQ system. The powder samples were degassed at 200 °C for 1 h and heated to 300 °C at a relative pressure of 0.1 Pa and kept at this temperature up to 20 h to remove volatile molecules from the samples. The electrode samples were only degassed at a maximum temperature of 150 °C with the same procedure. The N_2 measurements were performed at −196 °C and the CO_2 measurements at 0 °C. The relative pressure for the nitrogen isotherms was varied between $5\cdot10^{-6}$ and 1 in 73 steps for measurements with N_2 and between $2\cdot10^{-3}$ and 1 relative pressure in 40 steps for measurements with CO_2. A quenched-solid density functional theory (QSDFT) kernel assuming slit-like pores was applied to obtain the pore size distribution and specific surface area (SSA) above 0.9 nm from the N_2 isotherms and a non-local density functional theory (NLDFT) kernel for deconvolution of the CO_2 isotherms for pore sizes below 0.9 nm [42–44]. The average pore size was obtained by the d_{50} value and relates to the pore size of half of the cumulative pore volume at 10 nm. The Brunauer-Emmett-Teller (BET) equation was also applied in the linear part of the isotherms to obtain the SSA_{BET}. The calculations were carried out with the software ASiQwin 3.01 [45].

Scanning electron microscopy (SEM) was performed with a field emission scanning electron microscope (JEOL JSM-7500F). The samples were fixed to a steel holder with carbon tape. The particle size was determined by measuring 100 beads from the SEM images by ImageJ software [46]. Transmission electron microscopy (TEM) was performed with a JEOL JEM-2100F system at 200 kV. The samples were prepared by sonication in ethanol and drop casting in copper grids with carbon film.

Raman spectra were measured with a Nd-YAG laser with a wavelength of 532 nm and a grating of 2400 lines. The objective had a 50 times enlargement and the numeric aperture was 0.9 with a spectral resolution of ~1.2 cm^{-1}. The laser power was approximately 0.02 mW. An acquisition time of 30 s was chosen, and 10 accumulations were recorded. The Raman spectra were fitted with four Voigt profile functions between 500 and 2000 cm^{-1} and the Tuinstra-Koenig (Eq. (1)) and Ferrari-Robertson equations (Eq. (2)) were used to calculate the average graphene layer extent L_a.

$$L_a = \frac{C_\lambda}{I_D/I_G} \tag{1}$$

with $C_{(532\ nm)}$ of 4.956 nm ($C_\lambda = 0.033\ \lambda_L$ - 12.6 nm; with the wavelength of the laser λ_L) [47].

$$L_a = \sqrt{\frac{I_D/I_G}{C'_\lambda}} \tag{2}$$

with $C'_{(532\ nm)}$ of 0.6195 nm^{-2} ($C'_\lambda = C_\lambda/8$) [48].

A X'Pert Pro powder diffractometer from PANalytical (θ-θ geometry) with Cu-K_α radiation (0.15418 nm) at 40 kV and 40 mA was used for WAXS measurements in an angular range of $2\theta = 10$–100°. The powder samples were flattened on a silicon single-crystal sample holder to a thickness of 1 mm and measured at room temperature. We used a 4° anti-scatter slit and an automatic divergence slit, affording a fixed irradiated length of 7 mm on the sample surface. A step size of 0.1° and a scanning speed of 0.03 $^\circ s^{-1}$ were chosen for the measurements.

The software Wolfram Mathematica 11.0 (Wolfram Research) and CarbX (Justus-Liebig University Giessen) were used for the fitting of the WAXS data [49]. The WAXS data were fitted applying the algorithm by Ruland and Smarsly [50,51]. The starting values of the parameters were determined manually in CarbX and then the fit was optimized using the NonlinearModelFit operation implemented in Mathematica 11.0. The experimental data were not altered for the fitting, that is, no background subtraction was applied. The values for the concentration of nitrogen, oxygen, and non-organized carbon were fixed to the results of the elemental analysis.

The chemical composition was characterized with a CHNS analyzer from Vario Micro Cube from Elementar calibrated with sulfanilamide. The reduction tube had a temperature of 850 °C and the combustion tube of 1150 °C.

A thermogravimetric measurement coupled with mass spectrometry (TGA-MS) was carried out up to 1400 °C with a heating rate of 10 $^\circ C \cdot min^{-1}$ in argon with a STA449F3 Jupiter and QMS 403C Aëolos from Netzsch.

The functional groups and the chemical composition were also studied with X-ray photoelectron spectroscopy (XPS). We used an Axis Ultra DLD (Kratos Analytical) with Al-K_α radiation (15 kV, 10 mA for general spectra and 15 kV, 15 mA for highly resolved measured C 1s and N 1s peaks). Data analysis was performed with CasaXPS 2.3.15 from Casa Software. After subtraction of the Shirley background the peaks were fitted using a Gaussian-Lorentzian GL(30) peak shape. The full-width-at-half-maximum (FWHM) of the carbon peaks was kept constant for the fitting. An asymmetric line shape was used for the sp^2 component, which is described by the Doniach-Šunjić function [52,53].

2.3. Electrochemical measurements

Free-standing electrodes were prepared from the electrode materials with 5 mass% polytetrafluoroethylene (PTFE) using a 60 mass% PTFE suspension in water from Sigma-Aldrich [54]. We dispersed the carbon powder in ethanol before the PTFE suspension was added in a mortar. The resulting dough was rolled out to a thickness of 120–190 μm and dried at 120 °C at $2 \cdot 10^3$ Pa for 48 h. Disc electrodes with a diameter of 6–8 mm were punched out of the electrode sheets. The samples were analyzed in a symmetrical full-cell with a spectator reference electrode and a half-cell setup with an oversized carbon counter electrode (>10 times heavier than the working electrode; composed of YP-80F from Kuraray) in custom-built cells (see Ref. [54] for cell design). The reference electrode for the organic electrolyte (1 M tetraethylammonium tetrafluoroborate in acetonitrile, TEA-BF_4 in ACN) and the ionic liquid (1-ethyl-3-methylimidazolium tetrafluoroborate, EMIM-BF_4) was YP-50F from Kuraray and the current collector was a carbon-coated alumina foil (Zflo 2653, Coveris Advanced Coatings). The reference electrode for the aqueous 1 M NaCl system was Ag/AgCl and the current collector was graphite foil. Glass-fiber mats (GF/A from Whatman, GE Healthcare Life Science) were used as separator for all electrochemical measurements, which were carried out using a potentiostat/galvanostat VMP300 from Bio-Logic. The cyclic voltammetry (CV) was conducted at 10 $mV\,s^{-1}$ and the galvanostatic cycling with potential limitation (GCPL) with a 10 min holding step at each potential for the half-cells. The specific capacitance was calculated following Eq. (3):

$$C_{sp} = \frac{\int_{t_0}^{t_{end}} I\,dt}{U \cdot m} \tag{3}$$

with specific capacitance C_{sp}, starting time of discharge t_0, end of discharge time t_{end}, applied potential difference U, discharge current I and active mass of the working electrode m.

The specific capacitance of the full-cells was calculated with Eq. (4), where the specific capacitance C_{sp} is multiplied with the factor of 4 for the comparison with the half-cell results and the IR-drop is subtracted from the applied voltage U_{IR}.

$$C_{sp} = \frac{4 \cdot \int_{t_0}^{t_{end}} I\,dt}{U_{IR} \cdot m} \tag{4}$$

The performance stability was surveyed with voltage floating with the symmetric full-cell at high cell voltages (1.2 V for aqueous electrolyte, 2.7 V for organic electrolyte, and 3.2 V for the ionic liquid) for 100 h. The specific capacitance was measured via GCPL at 1 $A\,g^{-1}$ every 10 h.

We compared our electrochemical measurements with the CO_2 activated novolac-derived carbon beads (PNC-CO_2; activated for 1 h) and two commercial activated carbons (YP-80F and Kynol-5092-20) which were characterized in previous works (Ref. [38,55–57]).

3. Results and discussion

3.1. Material characterization

The spherical shape of the primary particles is clearly seen from electron micrographs displayed in Fig. 1. The beads of the sample pyrolyzed in argon, NC-950, have a number-dependent average size of 230 ± 103 nm (volume-dependent: ca. 426 nm), which is similar to the reported value from our previous work (Ref. [38]). The activation with ammonia (N-NC-950) decreases the number-dependent average primary particle size to 177 ± 80 nm (volume-dependent: 333 nm). The reduction of the particle size was also observed for highly CO_2-activated novolac-derived carbon beads [38]. The TEM images in Fig. 1C+F show that there is no ordered carbon structure.

The nitrogen sorption data of the samples pyrolyzed in argon (NC-950) and ammonia (N-NC-750, N-NC-850, and N-NC-950) are presented in Fig. 2A and show the characteristics of a type I isotherm, indicative of micropores [58]. The pore size distribution, which results from the CO_2 and N_2 GSA measurements, is plotted in Fig. 2B and the extracted data are shown in Table 1. The patterns show pores below 2 nm (micropores), which are inside the beads, and mesopores, which are interparticle pores resulting from the agglomeration of the beads. The non-activated material NC-950 shows a sub-nanometer porosity with an average pore size of 0.55 nm and a SSA_{DFT} of 616 $m^2\,g^{-1}$. The treatment with ammonia increases the average pore size as well as the surface area. N-NC-750 has an average pore size of 0.60 nm with a SSA_{DFT} of 865 $m^2\,g^{-1}$. By increasing the temperature, the activation degree increases as well. The mass loss increases from 45 mass% for NC-950 to 53 mass % for N-NC-750 and up to 86 mass% for N-NC-950. The latter sample presents the largest average pore size of 1.43 nm, SSA_{DFT} of 1827 $m^2\,g^{-1}$, and total pore volume of 1.32 $cm^3\,g^{-1}$.

On the Raman spectra (Fig. 2C + D), peak fitting was performed (Table 2), obtaining the position of the D-mode at 1332-1349 cm^{-1} and of the G-mode at 1602-1605 cm^{-1}. These findings are indicative of nanocrystalline or non-graphitic carbon [59]. The full-width-at-

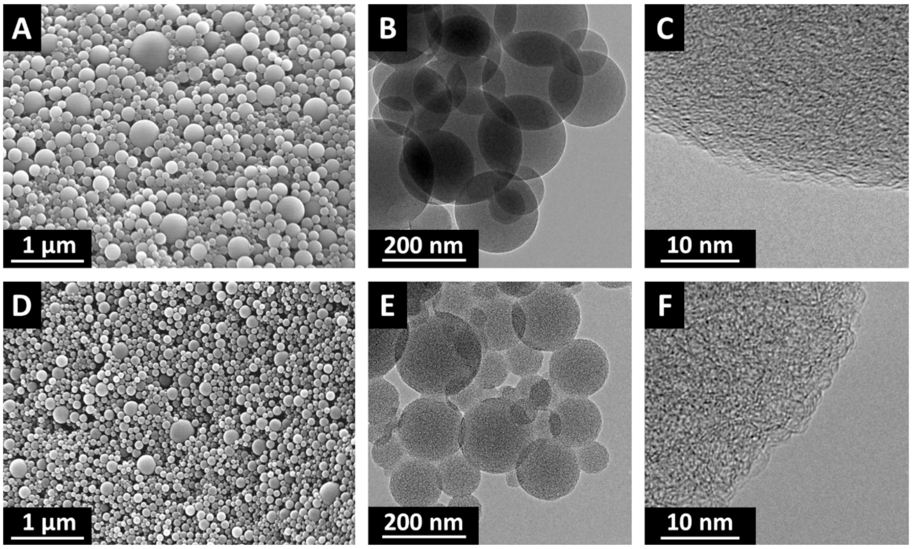

Fig. 1. SEM and TEM figures of NC-950 (A–C) and N-NC-950 (D–F).

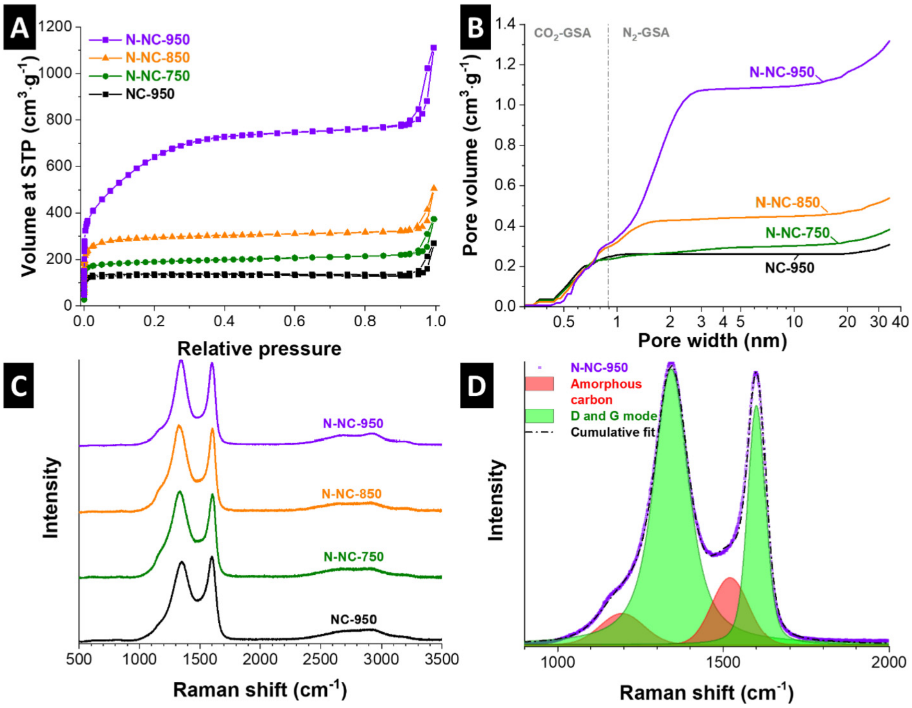

Fig. 2. Nitrogen sorption isotherms at STP (standard temperature and pressure; A) and pore size distributions obtained by the combination of the nitrogen and CO_2 sorption measurements (B) of NC-950, N-NC-750, N-NC-850, and N-NC-950. Raman spectra of these samples (C) and fitted Raman spectrum of N-NC-950 (D). (A colour version of this figure can be viewed online.)

Table 1
Mass loss during pyrolysis. Porosity data obtained by CO_2 and N_2 sorption of the powder samples of NC-950, N-NC-750, N-NC-850, and N-NC-950.

	Mass loss (mass%)	SSA_{DFT} ($m^2\ g^{-1}$)	SSA_{BET} ($m^2\ g^{-1}$)	Total pore volume ($cm^3\ g^{-1}$)	Pore volume at 10 nm ($cm^3\ g^{-1}$)	Average pore size (nm)
NC-950	45	616	536	0.31	0.26	0.55
N-NC-750	53	865	742	0.38	0.30	0.60
N-NC-850	66	1159	1145	0.54	0.45	0.73
N-NC-950	86	1827	2358	1.32	1.09	1.43

half-maximum (FWHM) and the I_D/I_G ratio decrease with an increasing activation degree. NC-950 has the widest FWHM for the D- and G-mode with 171 cm^{-1} and 73 cm^{-1}, respectively. The ammonia-treated samples have a narrower FWHM ranging from 152 cm^{-1} to 126 cm^{-1} for the D-mode and from 64 cm^{-1} to 63 cm^{-1} for the G-mode and there is a decrease when increasing the synthesis temperature. N-NC-750 and N-NC-850 have I_D/I_G ratios of 2.73 and 2.72, respectively, which are lower than NC-950 with 2.90 even though they were produced at lower temperatures. It seems that the removal of carbon by the activation with ammonia is stronger for less ordered carbon. N-NC-950 has the lowest I_D/I_G ratio of 2.63 due to its high synthesis temperature and the activation with ammonia. With the I_D/I_G ratios it is possible to estimate the average graphene layer extent (L_a) using the Tuinstra-Koenig and Ferrari-Robertson equation [59,60]. The Tuinstra-Koenig relation is in general valid for an average graphene layer extent above 2 nm; yet, when we apply this equation to our samples, we obtain values of 1.71–1.88 nm. A similar issue occurs when we use the Ferrari-Robertson relation, were we obtained L_a values of 2.06–2.16 nm even though the model is valid for amorphous carbon materials with a L_a below 2 nm [59]. These findings show that both models (Tuinstra-Koenig and Ferrari-Robertson) are not suitable for the analysis of the studied carbon materials. Yet, Faber et al. stated that the real limiting value for L_a is 3 nm instead of 2 nm, which would make the Ferrari-Robertson relation valid for the samples in this study [48]. Therefore, we also applied a model from Ruland and Smarsly to fit the WAXS data, which gives us a further understanding of the carbon structure [50,51].

The non-graphitic nature of novolac-derived carbons is confirmed with WAXS (Fig. 3A). Three X-ray reflections can be observed at a scattering vector $s = (2\ \sin(\theta)/\lambda)$ of 0.27 $Å^{-1}$ ($2\theta = 23°$), 0.48 $Å^{-1}$ ($2\theta = 44°$), and 0.83 $Å^{-1}$ ($2\theta = 80°$), which relate to the (002), (10), and (11) plane of non-graphitic carbon, respectively. NC-950, N-NC-750, and N-NC-850 have very similar scattering patterns and we see the typical broad reflections for a turbostratic stacking of sp^2 carbon [61]. The high degree of activation of N-NC-950 led to a reduction of the first (002) peak, because the large porosity hinders the ordering of several graphitic sheets. The WAXS patterns were all fitted with the parameters for non-graphitic carbon materials listed in Table 3 [50,51]. The fitted average graphene layer extent L_a obtained from WAXS analysis are in the same range as the values which were calculated using the Tuinstra-Koenig or Ferrari-Robertson equation from our Raman data. The low carbon ordering is also in alignment with the TEM images in Fig. 1. N-NC-750 has the smallest L_a of 1.1 nm; L_a is increased at higher synthesis temperatures to 1.7 nm for N-NC-850 and 2.4 nm for N-NC-950. The latter value is even larger than for the pyrolyzed sample without nitrogen (NC-950) with only 2.0 nm.

In addition to L_a, additional structural parameters can be obtained from the WAXS analysis, namely the average C-C bond length (l_{CC}), the average stack height (L_c), and the average interlayer spacing (a_3). The values for l_{CC} of NC-950 and N-NC-950 are both 0.141 nm, which corresponds to the value for l_{CC} in graphite (0.142 nm) [62]. N-NC-750 and N-NC-850 have a higher level of nitrogen-doping and an almost identical value for l_{CC} of 0.142 nm. The L_c of the samples NC-950, N-NC-750, and N-NC-850 are very similar and range from 0.9 nm to 1.1 nm. This finding shows that the precursor is not easily graphitizable. N-NC-950 has an even lower L_c of 0.8 nm because its high porosity prevents further stacking [48,61]. The average interlayer spacing a_3 of NC-950 (0.385 nm) is reduced for the sample N-NC-950 to 0.364 nm due to stronger van-der-Waals interactions caused by the presence of nitrogen [61]. For comparison: graphite has a much lower a_3 value of 0.335 nm [63]. Also, the number of graphene layers per stack (N^*) was calculated via dividing L_c by a_3 [51] and is reduced after the NH_3 treatment from 2.4 (NC-950) to 2.2 (N-NC-950). The samples produced at lower temperatures with ammonia have the highest N^* of 2.7 (N-NC-750) and 2.9 (N-NC-850).

The elemental analysis in Table 4 shows a significant number of heteroatoms within the porous carbon materials. NC-950 has the highest carbon content of 91.5 mass%. The ammonia-activated samples have a carbon content of 84.4–86.5 mass%. The hydrogen content of the pyrolyzed samples is 1–2 mass% and the oxygen content (ΔO), which was obtained by the difference of the initial mass and the measured elements, is about 6.4–7.6 mass%. The sample NC-950 was pyrolyzed under Ar atmosphere and contains no measurable nitrogen. N-NC-750 has the highest nitrogen content of 7.1 ± 1.8 mass%. By increasing the temperature, the nitrogen content decreases to 6.5 ± 0.8 mass% for N-NC-850 and 4.9 ± 2.0 mass% for N-NC-950. As expected, samples treated at higher temperatures show a lower amount of nitrogen, because nitrogen groups desorb at high temperatures [64–66].

The identity of the functional groups in the samples was studied by TGA-MS and XPS. The TGA curve in Fig. 3B shows the mass loss of the four samples normalized to the value at 150 °C (i.e., after removal of adsorbed surface water). The mass loss of all samples increases when the measurement temperature exceeds the synthesis temperature. The sample NC-950 presents the highest mass loss at the beginning and a total mass loss at 1200 °C of 6.6 mass%. The ammonia-treated samples N-NC-750, N-NC-850, and N-NC-950 are initially more stable, but reach higher total mass loss values at 1200 °C, namely, 8.9 mass%, 7.4 mass%, and 5.2 mass% for N-NC-750, N-NC-850, and N-NC-950, respectively. The latter was also the ammonia-treated sample with the lowest amount of nitrogen.

Online monitoring the evolving gas species via mass spectrometry during heating (Fig. 3C-F) provides more information about the character of the heteroatoms in the porous materials. Decomposition products of nitrogen functional groups are N_2, NH_3, HCN, their fragments, and NO when we assume the presence of oxygen groups [29,67,68]. A complication is that CO and N_2 have the same mass of 28 g mol^{-1}, which is also the desorbing signal with the highest intensity. Residual oxygen in the argon flow also burns

Table 2
Peak characteristics of the D- and G-mode of the Raman spectra.

		Position (cm^{-1})	FWHM (cm^{-1})	I_D/I_G	L_a (nm) Tuinstra-Koenig	L_a (nm) Ferrari-Robertson
NC-950	D-mode	1349	171	2.90	1.71	2.16
	G-mode	1603	73			
N-NC-750	D-mode	1334	152	2.73	1.82	2.10
	G-mode	1605	64			
N-NC-850	D-mode	1332	146	2.72	1.82	2.10
	G-mode	1603	64			
N-NC-950	D-mode	1344	126	2.63	1.88	2.06
	G-mode	1602	63			

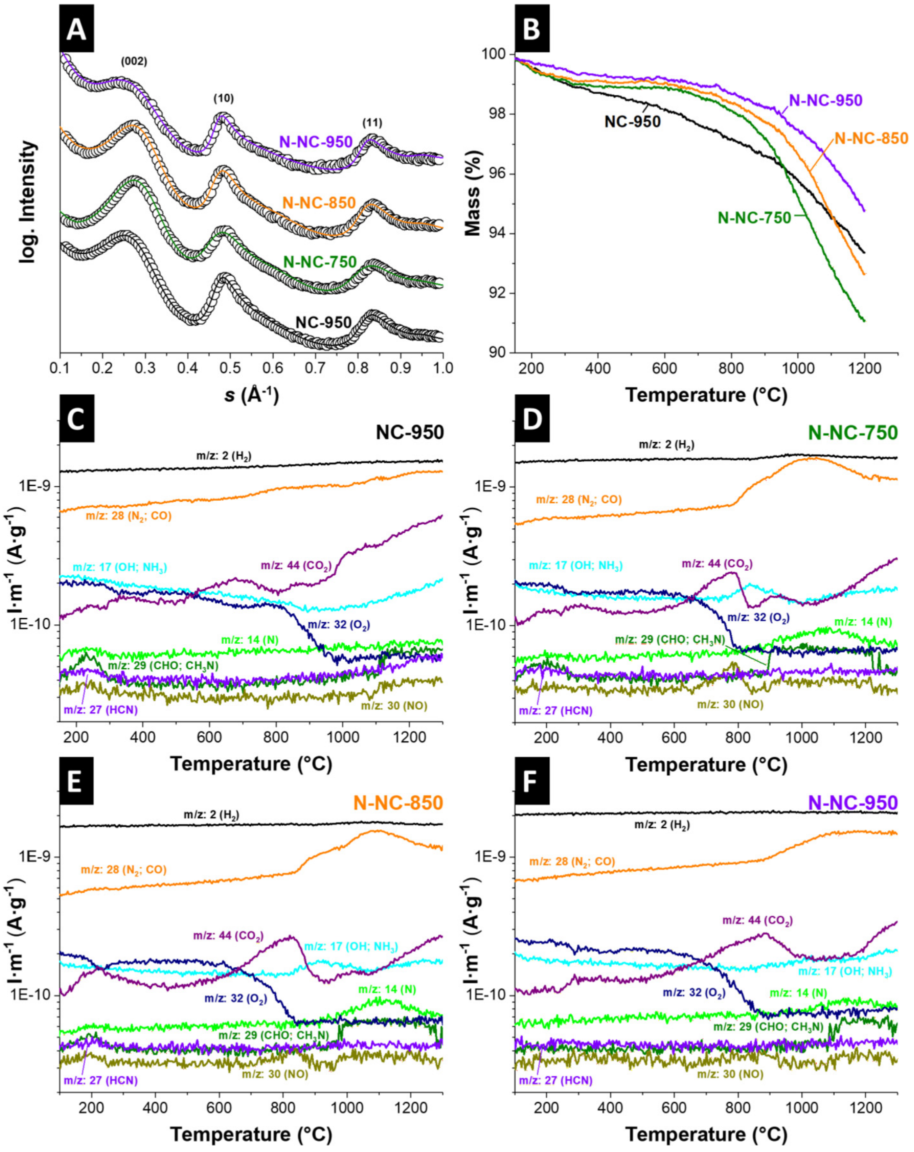

Fig. 3. X-ray diffractograms (A) and TGA curve (B) of the carbon samples after the pyrolysis in argon and ammonia. Mass spectra of the TGA-MS measurements of each sample to identify functional groups (C–F). (A colour version of this figure can be viewed online.)

Table 3
Structural parameters obtained from the WAXS data fits including the errors of each parameter based on the work of Faber et al. [51].

Parameter	Comment	NC-950	N-NC-750	N-NC-850	N-NC-950	Error (%)
L_a (nm)	Average graphene layer extent	2.0	1.1	1.7	2.4	±10-15
l_{cc} (nm)	Average C-C bond length	0.141	0.142	0.142	0.141	±0.2–0.4
σ_1	Standard deviation of the first-neighbor distribution	0.12	0.13	0.13	0.10	±5-12
L_c (nm)	Average stack height	0.9	1.0	1.1	0.8	±10-15
κ_c	Polydispersity of stack height	0.47	0.32	0.31	0.11	±10-15
a_3 (nm)	Average interlayer spacing	0.385	0.370	0.374	0.364	±1-2
σ_3 (nm)	Standard deviation of interlayer spacing	0.89	0.94	0.96	0.66	±10
N^*	Number of graphene layers per stack	2.4	2.7	2.9	2.2	±10-15

the carbon, producing CO and CO_2, which are influenced by the Boudouard equilibrium [69]. No nitrogen was detected for NC-950 and this sample is also the only one where no intensive peak ranging from 900 to 1200 °C is occurring. The mass-to-charge value of 14 corresponding with nitrogen is increasing in that temperature range. The mass-to-charge value of 28 has two maxima for N-NC-

Table 4
Elemental composition of the CHNS analysis of NC-950, N-NC-750, N-NC-850, and N-NC-950 (n.d.: not detectable). Sulfur was always below the limit of detection.

	C		H		N		ΔO	
	(mass%)	(at%)	(mass%)	(at%)	(mass%)	(at%)	(mass%)	(at%)
Polymer beads	73.0 ± 0.2	46.1 ± 0.1	5.8 ± 0.1	43.7 ± 0.8	1.9 ± 0.1	1.0 ± 0.1	19.3 ± 0.4	9.2 ± 0.2
NC-950	91.5 ± 1.1	84.8 ± 1.0	0.9 ± 0.1	9.9 ± 1.1	n.d.	n.d.	7.6 ± 1.2	5.3 ± 0.8
N-NC-750	84.4 ± 4.0	70.1 ± 3.3	2.1 ± 0.2	20.8 ± 2.0	7.1 ± 1.8	5.1 ± 1.3	6.4 ± 6.0	4.0 ± 3.7
N-NC-850	84.4 ± 2.6	70.8 ± 2.2	2.0 ± 0.3	20.0 ± 3.0	6.5 ± 0.8	4.7 ± 0.6	7.1 ± 3.7	4.5 ± 2.3
N-NC-950	86.5 ± 0.6	79.04 ± 0.5	1.1 ± 0.1	12.0 ± 1.1	4.9 ± 2.0	3.8 ± 1.6	7.5 ± 2.7	5.1 ± 1.9

750 at ~900 °C and at ~1020 °C. These two maxima shift for the samples treated at higher temperatures to ~960 °C and ~1090 °C for N-NC-850. Due to the steep decrease of the CO_2 signal at ~900 °C and 960 °C, it is likely that the first maximum is more influenced by CO. The sample N-NC-950 has only one broad signal with a maximum at ~1100 °C. The decomposition of nitrogen at high temperatures is an indicator for pyridine groups or graphitic nitrogen, since they only contain one nitrogen atom [29]. N-NC-750 and N-NC-850 show a peak for the NH_3 group (m/z: 17) at around 840 °C and 920 °C, which occurs most probably from protonated aniline or amide structures [29].

Nitrogen groups can also rearrange during the TGA-MS measurement depending on the heating rate and experimental pressure conditions [67]. HCN is produced as decomposition of pyrrolic nitrogen forming pyridinic nitrogen at temperatures of about 200 °C, which can further react towards graphitic nitrogen at higher temperatures [67]. For N-NC-750, only a low amount of the m/z of 27 can be detected at around 200 °C. Another minor desorption group has the mass-to-charge ratio of 30 at around 800 °C, which can be related to NO. Its intensity is reduced by increasing the ammonia-treatment temperature.

The samples were also characterized by XPS and the results are listed in Table 5. The chemical composition obtained by the XPS is a bit different compared to the values from CHNS analysis. One reason for that is that hydrogen cannot be detected by XPS. Also, the extreme surface-sensitivity of XPS limits the information depth to a few nanometers. All XPS measurements were also carried out in high vacuum, whereby volatile components evaporate and thereby avoided detection. Nevertheless, CHNS analysis and XPS yield similar trends. NC-950 and N-NC-950 have the highest amount of carbon (96.6 ± 1.7 at% and 96.7 ± 0.1 at%), since they both were synthesized at the highest temperatures. NC-950 shows no detectable amount of nitrogen for the CHNS and XPS analysis and has a relatively high amount of oxygen. The nitrogen content is decreasing for the ammonia-treated samples when the temperature is increased. NC-950 and N-NC-750 have according to XPS the highest oxygen content of 3.4 ± 1.7 at% and 3.8 ± 0.3 at%, while N-NC-850 and N-NC-950 contain less oxygen with 1.1 ± 0.1 at% and 1.3 ± 0.1 at%, respectively.

Table 5
Chemical composition measured with XPS and bonding content of the C 1s and N 1s peak (n.d.: not detectable).

	C (at%)	N (at%)	O (at%)	N1 (%)	N2 (%)	N3 (%)
NC-950	96.6 ± 1.7	n.d.	3.4 ± 1.7	n.d.	n.d.	n.d.
N-NC-750	91.3 ± 0.8	4.9 ± 0.5	3.8 ± 0.3	43.8	33.2	23.0
N-NC-850	95.1 ± 0.1	3.8 ± 0.2	1.1 ± 0.1	40.0	32.3	27.7
N-NC-950	96.7 ± 0.1	2.1 ± 0.1	1.3 ± 0.1	34.3	28.0	37.7
	C=C sp^2 (%)	C-C/C-H sp^3 (%)	C-N (%)	C-O (%)	C=O/N-C- (%)	Π-Π* transition (%)
NC-950	92.9	3.6	0	2.2	0	1.3
N-NC-750	92.5	3.3	2.8	0.4	0.9	0.2
N-NC-850	88.0	6.4	2.0	0.3	1.0	2.4
N-NC-950	82.5	9.5	1.2	2.3	1.0	3.6

The spectra of the C 1s peaks of all samples are plotted in Fig. 4A-D. NC-950 has the highest C=C sp^2 ratio with 92.9%. The addition of ammonia and the higher treatment temperature lead to a decrease in the sp^2 component to 82.5% for N-NC-950, which indicates that the radicals of the ammonia react more strongly with the sp^2 than with the sp^3 hybridized carbon. The structural difference between the non-graphitic samples NC-950 and N-NC-950 is a slight increase in L_a and N^* even though the C=C sp^2 ratio of the N-NC-950 is lower. The pyrolyzed sample (NC-950) shows no C-N bonds, since no nitrogen was detected. The ammonia-treated samples show such C-N bonds and their ratio is decreasing with an increasing temperature from 2.8% for N-NC-750 to 1.2% for N-NC-950.

The identity of the nitrogen groups can be further clarified from analyzing the N 1s peak position in the XPS spectra [67,68,70]. The N 1s peak is plotted in Fig. 4E and was fitted with three peaks (N1, N2, and N3). The N1 peak has in our study an energy of 397.7 eV which can be related to pyridinic nitrogen [67,70]. The energy of the second peak (N2) is 399.5 eV and can be related to pyrrolic nitrogen, amide, amine, or nitrile [70]. The nitrile group is unlikely to remain on the surface after a NH_3 treatment at high temperatures [29,71]. Therefore, the N2 signal represents a mixture of pyrrolic nitrogen, amide, and amine. The TGA-MS results show also that these groups can be present in low amounts on the carbon surfaces. The nitrogen component with the highest energy is the N3 at 401.1 eV, which relates to graphitic nitrogen [67,70]. By comparing their amounts, we see that the N1 and N2 intensities are reduced from 43.8% to 34.3%, and from 33.2% to 28.0% after increasing the temperature of the ammonia treatment. Concurrently, the relative content of N3 increased from 23.0% to 37.7%. Possibly the total nitrogen content was reduced when the treatment temperature was increased, but a higher temperature leads also to a higher content of graphitic nitrogen in the carbon structure.

3.2. Electrochemical characterization

The samples were first tested in a half-cell setup with 1 M TEA-BF_4 in ACN as electrolyte with activated carbon as oversized counter and reference electrode. The CV and the specific capacitance obtained by GCPL measurements are plotted in Fig. 5 and key performance data are provided in Table 6. The pyrolyzed sample (NC-950) has almost no capacitance (4 F g^{-1} at −1 V vs. carbon) in the negative potential range, because the average pore size of ~0.6 nm is smaller than the solvated (1.3 nm) and non-solvated size (0.67 nm) of TEA^+ in ACN [72]. The BF_4^- ion is smaller than the cation and we can assume 1.1 nm for the solvated and 0.45 nm for the non-solvated anion [72]. Therefore, the capacitance at a positive potential is higher with 36 F g^{-1} at 1.2 V vs. carbon. Such steric effects are often observed when nanoporous carbon materials are used as electrodes for supercapacitors [38,73–75]. The activated N-NC-750 material shows these effects even more clearly with its average pore size of 0.6–0.8 nm, whereby the non-solvated BF_4^- can

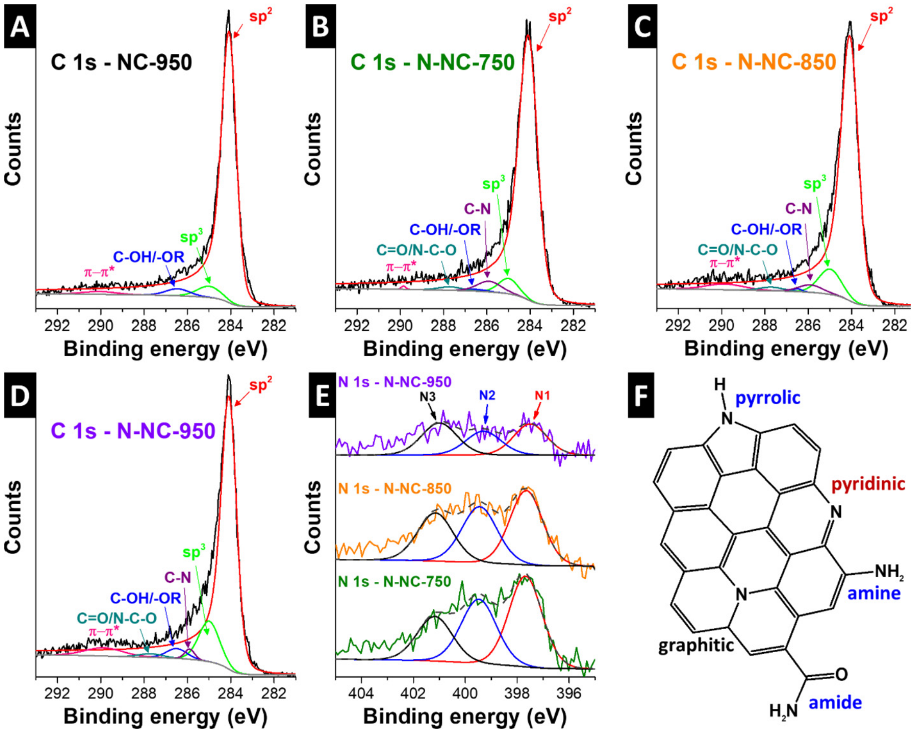

Fig. 4. XPS spectra of the C 1s peak of NC-950 (A), N-NC-750 (B), N-NC-850 (C), and N-NC-950 (D) and of the N 1s peak of the nitrogen containing samples (E). Structural formula of the five identified nitrogen groups in a graphitic structure (F). (A colour version of this figure can be viewed online.)

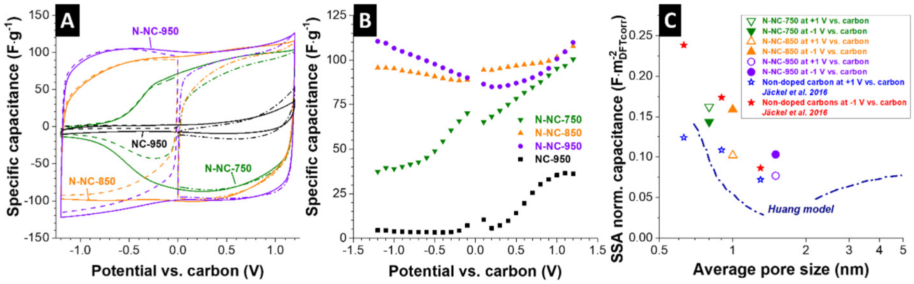

Fig. 5. Cyclic voltammetry at a scan rate of 10 mV s^{-1} with discontinuous lines for only positive or negative potential and continuous lines for the whole potential window measured in 1 M TEA-BF$_4$ in ACN (A). Specific capacitance of the samples measured with galvanostatic charge/discharge cycling at a specific current of 0.2 A g^{-1} (B). Surface area normalized capacitance versus the average pore size with a comparison with data from the literature and a model from Huang et al. (C) [73,76,77]. (A colour version of this figure can be viewed online.)

Table 6
Overview of the supercapacitor performance of the nitrogen containing novolac-derived carbon beads in a half-cell configuration versus carbon in 1 M TEA-BF$_4$ in acetonitrile. SSA$_{DFT}$ of the electrodes as well as the accessible SSA$_{DFT}$ for each ion and the average pore size of the electrodes obtained by CO$_2$ and N$_2$ GSA measurements.

	Specific capacitance (F·g^{-1})						SSA$_{DFT}$ electrode (m^2 g^{-1})	Accessible SSA$_{DFT}$ for TEA$^+$ (m^2 g^{-1})	Accessible SSA$_{DFT}$ for BF$_4^-$ (m^2 g^{-1})	Average pore size (nm)
	At −0.1 V	At −1.0 V	At −1.2 V	At +0.1 V	At +1.0 V	At +1.2 V				
NC-950	7	4	4	10	35	36	–	–	–	–
N-NC-750	70	39	37	65	95	100	692	272	586	0.8
N-NC-850	89	95	96	94	102	108	1108	598	999	1.0
N-NC-950	90	107	111	86	101	110	1319	1036	1313	1.5

partially fit inside some of the pores. This results in a rectangular shape of the CV on the positive potential and a specific capacitance of 100 F g^{-1} at +1.2 V vs. carbon.

For negative potentials, steric ion hindrance becomes noticeable, where the rectangular shape is obtained only for a very low negative potential. The average pore size of the N-NC-750 is similar to the non-solvated cation size. It is likely that only the smaller anions exit the pores at low negative potentials, similar to what was reported for ionic liquids in small pores at low potentials [39]. These effects lead to a decrease of the specific capacitance for N-NC-750 (Fig. 5B) when a higher negative potential is applied. The specific capacitance at −0.1 V vs. carbon is 70 F g^{-1} and reduced to

$37\ F\ g^{-1}$ at −1.2 V vs. carbon.

The slightly higher average pore size of 0.8 nm of N-NC-850 improves the ion accessibility significantly. A rectangular shape of the CVs at a positive and negative potential was obtained, because the pores are larger than both non-solvated ions. Nevertheless, the specific capacitance at the positive potential is slightly higher ($108\ F\ g^{-1}$) than on the negative side ($96\ F\ g^{-1}$). This can also be explained by a smaller ion size of the BF_4^- and its lower space requirement. A larger number of anions than cations can therefore fit inside the pores [73]. A further increase in the specific surface area by the activation leads to an expected higher specific capacitance, which was obtained for N-NC-950. The capacitance of N-NC-950 at −1.2 V and +1.2 V vs. carbon is similar to $111\ F\ g^{-1}$ and $110\ F\ g^{-1}$. A minimum of capacitance of $85\ F\ g^{-1}$ is measured at 0.2 V vs. carbon, which correlates to the point of zero charge (PZC), where the total surface charge is compensated [39].

The capacitance of porous carbon depends on the pore size and may additionally be increased via Faradaic reactions of the nitrogen groups with the electrolyte. To gain more insights in these influencing parameters, we have normalized the measured capacitance by the accessible surface area and plotted these values versus the average pore size in Fig. 5C [73,76]. To obtain a reasonable value for the surface area, we carried out CO_2 and N_2 sorption measurements. The average pore size of the electrodes is slightly larger compared to the powder due to the blocking of small pores which also reduces the SSA [55]. The accessible SSA_{DFT} of the electrodes was calculated by subtracting the surface area at 0.4 nm for the BF_4^- and at 0.6 nm for the TEA^+ due to their ionic radius (Table 6). As seen from Fig. 5C, N-doped carbon and non-doped carbon from previous work yield very similar results for different average pore sizes. The data also align with the work from Huang et al. who calculated an increase of the capacity for smaller pores from theoretical considerations [77]. Thereby, it is implied that pore size is the more determining parameter for the resulting capacitance compared to the presence or absence of nitrogen in nanoporous carbon.

We further characterized the electrochemical performance of the electrode materials in a symmetrical full-cell with 1 M $TEA\text{-}BF_4$ in ACN as electrolyte. The resulting specific capacitances are listed in Table 7 (including the SSA_{BET} of the electrodes for comparison) and plotted in Fig. 6. The non-activated NC-950 has a negligible specific capacitance below $1\ F\ g^{-1}$. The specific capacitance of N-NC-750 was $56\ F\ g^{-1}$, which is between the values measured for positive ($100\ F\ g^{-1}$) and negative ($37\ F\ g^{-1}$) polarization in the half-cell setup. N-NC-850 shows very similar specific capacitance values in the full-cell of $92\ F\ g^{-1}$ and the half-cell at negative potential of $96\ F\ g^{-1}$. The same was found for N-NC-950 with $105\ F\ g^{-1}$ in the symmetrical full-cell. In a symmetric full-cell, the electrode with the smaller capacitance is limiting the device performance.

We further quantified the rate handling ability for full-cells in the specific current range of $0.05–100\ A\ g^{-1}$ and the data are shown in Fig. 6B. NC-950 exhibits the narrowest pores and the poorest power performance. By increasing the average pore size of the nitrogen-containing novolac-derived carbon beads, also the normalized capacitance at high rates increases. The ion transport is significantly enhanced with increasing pore size. For comparison, CO_2-activated novolac derived carbon beads (PNC-CO_2) and two commercial activated carbon materials (YP-80F and Kynol-5092-20) were tested under the same conditions. Further information on the chemical composition and pore structure of these materials is found in Refs. [38,55–57]. Very similar to N-NC-950 with $105\ F\ g^{-1}$, the specific capacitance of PNC-CO_2 and YP-80F is $107\ F\ g^{-1}$ and $108\ F\ g^{-1}$, respectively, even though the surface area of the latter two is much higher (up to $2105\ m^2\ g^{-1}$) [57]. At a specific current of $10\ A\ g^{-1}$, the YP-80F electrodes had the highest residual capacitance of 89%, while the N-NC-950 and the PNC-CO_2 have a residual capacitance of 80%. Only by increasing the measurement rate to very high specific currents, the advantage of the small primary particle size of both novolac-derived carbon beads becomes clear. At $100\ A\ g^{-1}$, the capacitance loss of YP-80F is 92%, while the N-NC-950 has a loss of 79% and the PNC-CO_2 only of 52%. Seemingly, the nitrogen functional groups hinder the ion transport at high rate, which results in a better performance of the CO_2-activated beads at very high rates with an even smaller average pore size of 1.1 nm and similar SSA [38].

The performance stability was quantified with voltage holding at a high cell voltage of 2.7 V for 100 h and the results are plotted in Fig. 6D. The NC-950 shows a large relative increase of the normalized capacitance after a holding time of 10 h, because of the enhanced penetration of the ions in the very small pores; yet, we note that the specific capacitance is negligible to start with. N-NC-750 shows also an increase of the normalized capacitance after 20 h. After 30 h of voltage holding, the capacitance of N-NC-750 decreases very fast, which can be explained with the asymmetric voltage profile seen in Fig. 6C. Since the cations cannot easily fit inside the pores, the potential value at the negative electrode is much higher (−1.73 V vs. carbon) than at the positive electrode (+0.67 V vs. carbon; measured at a cell voltage of 2.5 V). Therefore, the potential at the negative electrode is higher than the stability window of −1.7 V vs. carbon for this electrolyte [78]. N-NC-750 has the less negative PZC of the nitrogen-containing carbons of −0.08 V and the PZC for N-NC-850 is more negative with −0.27 V vs. carbon. N-NC-950 has a PZC of −0.13 V vs. carbon which is similar than the value obtained by the half-cell measurements. N-NC-850 and N-NC-950 have a relatively symmetrical potential distribution of both electrodes (Fig. 6C). Besides NC-950 and N-NC-750, all the other samples show no increase of the capacitance by the voltage holding experiment, because their pores were large enough for the ions.

The loss of capacitance in a supercapacitor is often related to the electrochemical degradation of the electrolyte with functional groups on the carbon surface. The products of the decomposition of the electrolyte can block pores and reduce the accessible surface area [19]. Therefore, a lower amount of functional groups is preferable to obtain good performance longevity [19,79]. The CO_2 activated novolac-derived carbon beads (PNC-CO_2) have a relatively high amount of carboxylic groups, which are formed after the synthesis by a reaction of surface active sides with oxygen and moisture from the environment [40]. These groups might be the reason for the fast decrease of the capacitance during the voltage holding experiment. The presence of these unfavorable functional groups is reduced by the NH_3 treatment and increases the stability to 86% after 100 h of voltage holding for N-NC-950, which is like the stability of the commercial YP-80F with 88%. Kynol-5092-20 shows

Table 7

Overview of the supercapacitor performance of the nitrogen containing novolac-derived carbon beads in 1 M $TEA\text{-}BF_4$ in acetonitrile and the comparison with other carbon-based electrode materials for supercapacitors. SSA_{BET} of the electrodes measured via N_2 GSA.

	1 M $TEA\text{-}BF_4$ in acetonitrile			SSA_{BET} of the electrode ($m^2\ g^{-1}$)
	Capacitance at $0.05\ A\ g^{-1}$ ($F\ g^{-1}$)	Capacitance loss at $10\ A\ g^{-1}$ (%)	Capacitance loss at $100\ A\ g^{-1}$ (%)	
NC-950	0.3	>95	–	–
N-NC-750	56	69	–	–
N-NC-850	92	23	–	634
N-NC-950	105	20	79	1615
PNC-CO_2	107	20	52	1784
YP-80F	108	11	92	2105
Kynol-5092-20	118	67	–	2070

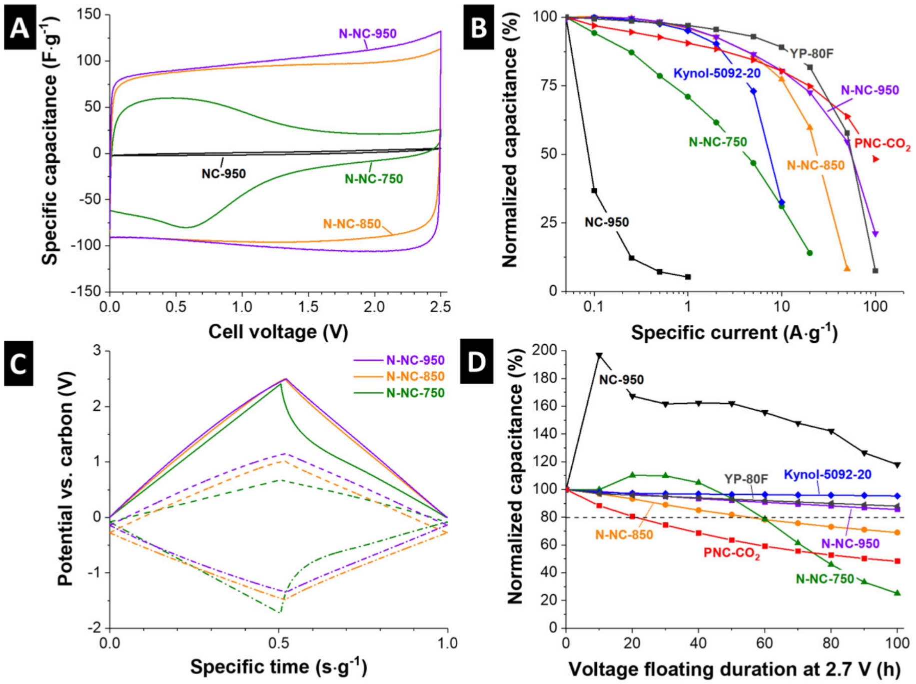

Fig. 6. Cyclic voltammograms of NC-950, N-NC-750, N-NC-850, and N-NC-950 measured in a symmetrical full-cell in 1 M TEA-BF$_4$ in acetonitrile measured with scan rate of 10 mV s^{-1} (A). Rate handling measured in GCPL mode with the samples and other materials from the literature as comparison (B). Voltage distribution in a symmetrical cell measured with the use of a carbon spectator electrode (C). Performance stability assessed via voltage floating of the samples with other materials as comparison (D). (A colour version of this figure can be viewed online.)

the highest residual capacitance of 95% after the holding experiment, aligning with the absence of any binder and a low oxygen content of 1.5 mass% [57]. This is an indicator for a small number of functional groups.

The material with the highest porosity and highest specific capacitance (N-NC-950) for the organic electrolyte was also tested in an aqueous electrolyte (1 M NaCl) and in a neat ionic liquid (EMIM-BF$_4$). The CVs in Fig. 7A show the typical rectangular shape of a supercapacitor for all electrolytes. The specific capacitance for the aqueous electrolyte is 134 F g^{-1} at the beginning and increases after the voltage floating experiment at 1.2 V to 173 F g^{-1}. This effect can be explained by improved wetting [80]. The specific capacitance with the ionic liquid is 136 F g^{-1}. A small peak at around a cell voltage of 1.5 V is noticeable during the discharging, which is a result of the reversible reaction of the EMIM-BF$_4$ [78,81]. The ionic liquid showed an excellent stability of 95% after a voltage floating at 3.2 V for 100 h (Fig. 7B).

The high stability and the high potential for the ionic liquid leads to a high specific energy of 48 Wh·kg^{-1}, as can be seen from the Ragone plot provided in Fig. 7C. The organic electrolyte has a maximum energy of 22 Wh·kg^{-1}. A comparison with the literature shows that even higher specific energies can be achieved for nitrogen-containing porous carbon materials with supercapacitor using ionic liquids (like 64 Wh·kg^{-1} for lignin-urea derived carbon with EMIM-BF$_4$; Ref. [27]). The performance of the organic electrolyte is only outperforming the ionic liquid for very high specific powers (>14 kW kg^{-1}). The aqueous electrolyte has the lowest specific energy of 9 Wh kg^{-1}.

4. Conclusions

In this study, we showed that the addition of ammonia during the pyrolysis of a carbon precursor like the novolac beads is a facile method to combine the pyrolysis, the activation of the material, and the introduction of nitrogen heteroatoms in one step. Thereby, no nitrogen-containing precursor or follow-up treatment is necessary to produce nitrogen-doped porous carbon materials. The nitrogen content and the kind of nitrogen group are mainly influenced by the reaction temperature. By increasing the temperature from 750 °C to 950 °C, the nitrogen content is reduced from 7.1 mass% to 4.9 mass%. The relative amount of graphitic nitrogen in the carbon structure increases while other pyridinic and pyrrolic nitrogen groups are reduced when the synthesis is carried out at higher temperatures. These temperatures and the presence of ammonia as well lead to a more ordered non-graphitic structure, which was shown by the Raman and WAXS results.

The obtained materials showed a promising performance as electrode material for supercapacitors reaching a specific energy of up to 50 Wh kg^{-1} using ionic liquids as electrolyte. By comparing the surface-normalized capacitance of the nitrogen-containing carbon beads with other porous carbon materials, we saw that the capacitance is mainly influenced by the pore size distribution. Our work also shows the influence of functional groups on the electrochemical stability with certain electrolytes. Some materials might work very well for only few electrolytes. For example, the CO$_2$-activated novolac-derived carbon beads are a good and stable material for a supercapacitor with an aqueous electrolyte or TEA-BF$_4$ in propylene carbonate (PC) [38], but it has a very low stability in TEA-BF$_4$ in ACN due to the high amount of carboxylic groups. The treatment with ammonia leads to different heteroatoms and functional groups that increase the stability in this electrolyte even though the specific capacitance and the performance at high scan rates is not improved. Therefore, the physical activation of carbon with ammonia is an interesting alternative. It combines the activation of the carbon material with heteroatom doping, which might be also interesting for other applications like catalysis or electrochemical water treatment.

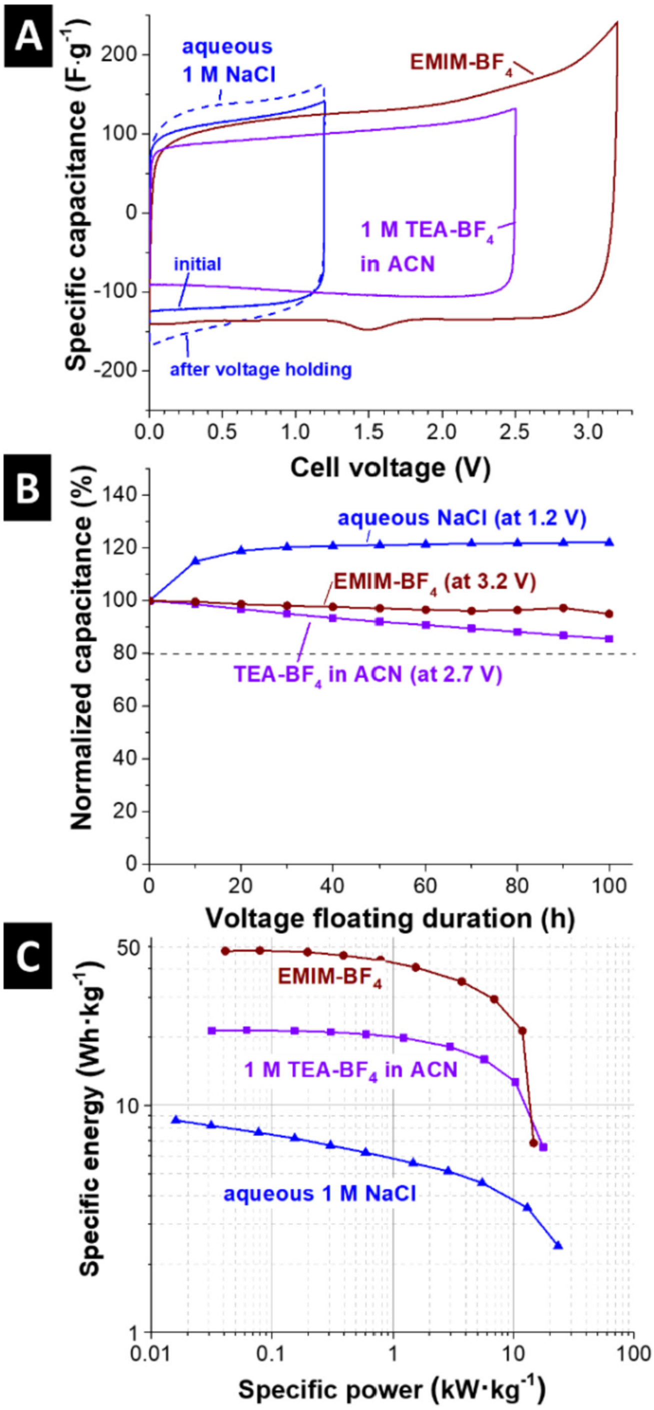

Fig. 7. Cyclic voltammogram at 10 mV s^{-1} (A) and longtime stability test (B) of N-NC-950 with three different electrolytes (1 M aqueous NaCl, 1 M TEA-BF$_4$ in acetonitrile, and neat EMIM-BF$_4$). Ragone plot of the aqueous electrolyte, organic electrolyte, and ionic liquid with N-NC-950 (C). (A colour version of this figure can be viewed online.)

Acknowledgements

This work was part of the Carbon Metal Oxide Nanohybrid project (CarMON) supported by the by the Leibniz Association (SAW-2017). B.K. and V.P. also acknowledge support by the Minerva Foundation via the Award for Research Cooperation and High Excellence in Science Award (ARCHES). FB and BS acknowledge financial support from the DFG via GrK (Research training groups) 2204 "Substitute Materials for sustainable Energy Technologies". The authors kindly acknowledge the continuing support of Prof. Eduard Arzt (INM). We thank Ralph Schäfer (Allnex Germany GmbH) for supply of ALVONOL PN 320, Andrea Jung (INM) for the CHNS analysis, and Robert Drumm (INM) for the TGA-MS measurements. We also thank Mesut Aslan, Choonsoo Kim, Nicolas Jäckel, Tobias Dörr, and Pattarachai Srimuk (all INM) for their input and support.

References

[1] A. Taguchi, F. Schüth, Ordered mesoporous materials in catalysis, Microporous Mesoporous Mater. 77 (1) (2005) 1–45.
[2] L. Schlapbach, A. Züttel, Hydrogen-storage materials for mobile applications, Nature 414 (6861) (2001) 353–358.
[3] R.E. Morris, P.S. Wheatley, Gasspeicherung in nanoporösen materialien, Angew. Chem. 120 (27) (2008) 5044–5059.
[4] P. Simon, Y. Gogotsi, Materials for electrochemical capacitors, Nat. Mater. 7 (11) (2008) 845–854.
[5] S. Porada, L. Weinstein, R. Dash, A. Van Der Wal, M. Bryjak, Y. Gogotsi, P. Biesheuvel, Water desalination using capacitive deionization with microporous carbon electrodes, ACS Appl. Mater. Interfaces 4 (3) (2012) 1194–1199.
[6] K.-J. Choi, S.-G. Kim, S.-H. Kim, Removal of antibiotics by coagulation and granular activated carbon filtration, J. Hazard Mater. 151 (1) (2008) 38–43.
[7] Y. Deng, Y. Xie, K. Zou, X. Ji, Review on recent advances in nitrogen-doped carbons: preparations and applications in supercapacitors, J. Mater. Chem. 4 (4) (2016) 1144–1173.
[8] K. Gong, F. Du, Z. Xia, M. Durstock, L. Dai, Nitrogen-doped carbon nanotube arrays with high electrocatalytic activity for oxygen reduction, Science 323 (5915) (2009) 760–764.
[9] S. Porada, F. Schipper, M. Aslan, M. Antonietti, V. Presser, T.P. Fellinger, Capacitive deionization using biomass-based microporous salt-templated heteroatom-doped carbons, ChemSusChem 8 (11) (2015) 1867–1874.
[10] J. Przepiórski, M. Skrodzewicz, A. Morawski, High temperature ammonia treatment of activated carbon for enhancement of CO_2 adsorption, Appl. Surf. Sci. 225 (1) (2004) 235–242.
[11] B.E. Conway, Electrochemical Supercapacitors, Springer, Berlin, 1999.
[12] F. Béguin, V. Presser, A. Balducci, E. Frackowiak, Carbons and electrolytes for advanced supercapacitors, Adv. Mater. 26 (14) (2014) 2219–2251.
[13] H.M. Jeong, J.W. Lee, W.H. Shin, Y.J. Choi, H.J. Shin, J.K. Kang, J.W. Choi, Nitrogen-doped graphene for high-performance ultracapacitors and the importance of nitrogen-doped sites at basal planes, Nano Lett. 11 (6) (2011) 2472–2477.
[14] E. Paek, A.J. Pak, K.E. Kweon, G.S. Hwang, On the origin of the enhanced supercapacitor performance of nitrogen-doped graphene, J. Phys. Chem. C 117 (11) (2013) 5610–5616.
[15] A. Borenstein, O. Hanna, R. Attias, S. Luski, T. Brousse, D. Aurbach, Carbon-based composite materials for supercapacitor electrodes: a review, J. Mater. Chem. (5) (2017) 12653–12672.
[16] G. Lota, B. Grzyb, H. Machnikowska, J. Machnikowski, E. Frackowiak, Effect of nitrogen in carbon electrode on the supercapacitor performance, Chem. Phys. Lett. 404 (1) (2005) 53–58.
[17] D. Salinas-Torres, S. Shiraishi, E. Morallon, D. Cazorla-Amorós, Improvement of carbon materials performance by nitrogen functional groups in electrochemical capacitors in organic electrolyte at severe conditions, Carbon 82 (2015) 205–213.
[18] A.K. Kinage, P.P. Upare, A.B. Shivarkar, S.P. Gupte, Highly regio-selective synthesis of β-amino alcohol by reaction with aniline and propylene carbonate in self solvent system over large pore zeolite catalyst, Green Sustain. Chem. 01 (03) (2011) 76–84.
[19] P. Azaïs, L. Duclaux, P. Florian, D. Massiot, M.-A. Lillo-Rodenas, A. Linares-Solano, J.-P. Peres, C. Jehoulet, F. Béguin, Causes of supercapacitors ageing in organic electrolyte, J. Power Sources 171 (2) (2007) 1046–1053.
[20] D. Cazorla-Amorós, D. Lozano-Castelló, E. Morallón, M.J. Bleda-Martínez, A. Linares-Solano, S. Shiraishi, Measuring cycle efficiency and capacitance of chemically activated carbons in propylene carbonate, Carbon 48 (5) (2010) 1451–1456.
[21] W. Shen, W. Fan, Nitrogen-containing porous carbons: synthesis and application, J. Mater. Chem. 1 (4) (2013) 999–1013.
[22] D. Hulicova, J. Yamashita, Y. Soneda, H. Hatori, M. Kodama, Supercapacitors prepared from melamine-based carbon, Chem. Mater. 17 (5) (2005) 1241–1247.
[23] Z. Liu, K. Xiao, H. Guo, X. Ning, A. Hu, Q. Tang, B. Fan, Y. Zhu, X. Chen, Nitrogen-doped worm-like graphitized hierarchical porous carbon designed for enhancing area-normalized capacitance of electrical double layer supercapacitors, Carbon 117 (2017) 163–173.
[24] N.A. Travlou, T.J. Bandosz, N-doped polymeric resin-derived porous carbons as efficient ammonia removal and detection media, Carbon 117 (2017) 228–239.
[25] L.-F. Chen, X.-D. Zhang, H.-W. Liang, M. Kong, Q.-F. Guan, P. Chen, Z.-Y. Wu, S.-H. Yu, Synthesis of nitrogen-doped porous carbon nanofibers as an efficient

electrode material for supercapacitors, ACS Nano 6 (8) (2012) 7092–7102.

[26] G. Xu, J. Han, B. Ding, P. Nie, J. Pan, H. Dou, H. Li, X. Zhang, Biomass-derived porous carbon materials with sulfur and nitrogen dual-doping for energy storage, Green Chem. 17 (3) (2015) 1668–1674.

[27] C. Schneidermann, N. Jäckel, S. Oswald, L. Giebeler, V. Presser, L. Borchardt, Solvent-free mechanochemical synthesis of nitrogen-doped nanoporous carbon for electrochemical energy storage, ChemSusChem 10 (11) (2017) 2416–2424.

[28] X. Liu, Y. Zhou, W. Zhou, L. Li, S. Huang, S. Chen, Biomass-derived nitrogen self-doped porous carbon as effective metal-free catalysts for oxygen reduction reaction, Nanoscale 7 (14) (2015) 6136–6142.

[29] C.L. Mangun, K.R. Benak, J. Economy, K.L. Foster, Surface chemistry, Pore Sizes and Adsorption Properties of activated carbon fibers and precursors treated with ammonia, Carbon 39 (12) (2001) 1809–1820.

[30] B. Stöhr, H. Boehm, R. Schlögl, Enhancement of the catalytic activity of activated carbons in oxidation reactions by thermal treatment with ammonia or hydrogen cyanide and observation of a ssuperoxide species as a possible intermediate, Carbon 29 (6) (1991) 707–720.

[31] S. Bashkova, T.J. Bandosz, The effects of urea modification and heat treatment on the process of NO_2 removal by wood-based activated carbon, J. Colloid Interface Sci. 333 (1) (2009) 97–103.

[32] J.S. Noh, J.A. Schwarz, Effect of HNO_3 treatment on the surface acidity of activated carbons, Carbon 28 (5) (1990) 675–682.

[33] M. Widmaier, B. Krüner, N. Jäckel, M. Aslan, S. Fleischmann, C. Engel, V. Presser, Carbon as quasi-reference electrode in unconventional lithium-salt containing electrolytes for hybrid battery/supercapacitor devices, J. Electrochem. Soc. 163 (14) (2016) A2956–A2964.

[34] S. Kundu, W. Xia, W. Busser, M. Becker, D.A. Schmidt, M. Havenith, M. Muhler, The formation of nitrogen-containing functional groups on carbon nanotube surfaces: a quantitative XPS and TPD study, Phys. Chem. Chem. Phys. 12 (17) (2010) 4351–4359.

[35] H.P. Boehm, G. Mair, T. Stoehr, A.R. De Rincón, B. Tereczki, Carbon as a catalyst in oxidation reactions and hydrogen halide elimination reactions, Fuel 63 (8) (1984) 1061–1063.

[36] U. Świetlik, B. Grzyb, K. Torchała, G. Gryglewicz, J. Machnikowski, High temperature ammonia treatment of pitch particulates and fibers for nitrogen enriched microporous carbons, Fuel Process. Technol. 119 (2014) 211–217.

[37] X. Wang, C.-G. Liu, D. Neff, P.F. Fulvio, R.T. Mayes, A. Zhamu, Q. Fang, G. Chen, H.M. Meyer, B.Z. Jang, Nitrogen-enriched ordered mesoporous carbons through direct pyrolysis in ammonia with enhanced capacitive performance, J. Mater. Chem. 1 (27) (2013) 7920–7926.

[38] B. Krüner, J. Lee, N. Jäckel, A. Tolosa, V. Presser, Sub-micrometer novolac-derived carbon beads for high performance supercapacitors and redox electrolyte energy storage, ACS Appl. Mater. Interfaces 8 (14) (2016) 9104–9115.

[39] N. Jäckel, S.P. Emge, B. Krüner, B. Roling, V. Presser, Quantitative information about electrosorption of ionic liquids in carbon nanopores from electrochemical dilatometry and quartz crystal microbalance measurements, J. Phys. Chem. C 121 (35) (2017) 19120–19128.

[40] B. Krüner, P. Srimuk, S. Fleischmann, M. Zeiger, A. Schreiber, M. Aslan, A. Quade, V. Presser, Hydrogen-treated, sub-micrometer carbon beads for fast capacitive deionization with high performance stability, Carbon 117 (2017) 46–54.

[41] S. Choudhury, B. Krüner, P. Massuti-Ballester, A. Tolosa, C. Prehal, I. Grobelsek, O. Paris, L. Borchardt, V. Presser, Microporous novolac-derived carbon beads/sulfur hybrid cathode for lithium-sulfur batteries, J. Power Sources 357 (2017) 198–208.

[42] V. Presser, J. McDonough, S.-H. Yeon, Y. Gogotsi, Effect of pore size on carbon dioxide sorption by carbide derived carbon, Energy Environ. Sci. 4 (8) (2011) 3059–3066.

[43] A. Vishnyakov, P.I. Ravikovitch, A.V. Neimark, Molecular level models for CO_2 sorption in nanopores, Langmuir 15 (25) (1999) 8736–8742.

[44] G.Y. Gor, M. Thommes, K.A. Cychosz, A.V. Neimark, Quenched solid density functional theory method for characterization of mesoporous carbons by nitrogen adsorption, Carbon 50 (4) (2012) 1583–1590.

[45] S. Brunauer, P.H. Emmett, E. Teller, Adsorption of gases in multimolecular layers, J. Am. Chem. Soc. 60 (2) (1938) 309–319.

[46] C.A. Schneider, W.S. Rasband, K.W. Eliceiri, NIH image to ImageJ: 25 Years of image analysis, Br. J. Pharmacol. 9 (7) (2012) 671.

[47] M. Matthews, M. Pimenta, G. Dresselhaus, M. Dresselhaus, M. Endo, Origin of dispersive effects of the Raman D band in carbon materials, Phys. Rev. B 59 (10) (1999) R6585.

[48] K. Faber, F. Badaczewski, M. Oschatz, G. Mondin, W. Nickel, S. Kaskel, B.M. Smarsly, In-depth investigation of the carbon microstructure of silicon carbide-derived carbons by wide-angle X-ray scattering, J. Phys. Chem. C 118 (29) (2014) 15705–15715.

[49] T. Pfaff, M. Simmermacher, B.M. Smarsly, CarbX: a program for the evaluation of wide-angle X-ray scattering data of non-graphitic carbons, J. Appl. Crystallogr. 51 (2018) 219–229.

[50] W. Ruland, B. Smarsly, X-ray scattering of non-graphitic carbon: an improved method of evaluation, J. Appl. Crystallogr. 35 (5) (2002) 624–633.

[51] K. Faber, F. Badaczewski, W. Ruland, B.M. Smarsly, Investigation of the microstructure of disordered, non-graphitic carbons by an advanced analysis method for wide-angle X-ray scattering, Z. Anorg. Allg. Chem. 640 (15) (2014) 3107–3117.

[52] S. Doniach, M. Sunjic, Many-electron singularity in X-ray photoemission and X-ray line spectra from metals, J. Phys. C Solid State Phys. 3 (2) (1970) 285–291.

[53] S. Evans, Curve synthesis and optimization procedures for X-ray photoelectron spectroscopy, Surf. Interface Anal. 17 (2) (1991) 85–93.

[54] D. Weingarth, M. Zeiger, N. Jäckel, M. Aslan, G. Feng, V. Presser, Graphitization as a universal tool to tailor the potential-dependent capacitance of carbon supercapacitors, Adv. Energy Mater. 4 (13) (2014).

[55] N. Jäckel, D. Weingarth, M. Zeiger, M. Aslan, I. Grobelsek, V. Presser, Comparison of carbon onions and carbon blacks as conductive additives for carbon supercapacitors in organic electrolytes, J. Power Sources 272 (2014) 1122–1133.

[56] N. Jäckel, D. Weingarth, A. Schreiber, B. Krüner, M. Zeiger, A. Tolosa, M. Aslan, V. Presser, Performance evaluation of conductive additives for activated carbon supercapacitors in organic electrolyte, Electrochim. Acta 191 (2016) 284–298.

[57] C. Kim, P. Srimuk, J. Lee, S. Fleischmann, M. Aslan, V. Presser, Influence of pore structure and cell voltage of activated carbon cloth as a versatile electrode material for capacitive deionization, Carbon 122 (2017) 329–335.

[58] M. Thommes, K. Kaneko, A.V. Neimark, J.P. Olivier, F. Rodriguez-Reinoso, J. Rouquerol, K.S.W. Sing, Physisorption of gases, with special reference to the evaluation of surface area and pore size distribution, Pure Appl. Chem. 87 (9–10) (2015) 1051–1069.

[59] A.C. Ferrari, J. Robertson, Interpretation of Raman spectra of disordered and amorphous carbon, Phys. Rev. B 61 (20) (2000) 14095.

[60] F. Tuinstra, J.L. Koenig, Raman spectrum of graphite, J. Chem. Phys. 53 (3) (1970) 1126–1130.

[61] M. Einert, C. Wessel, F. Badaczewski, T. Leichtweiß, C. Eufinger, J. Janek, J. Yuan, M. Antonietti, B.M. Smarsly, Nitrogen-doped carbon electrodes: influence of microstructure and nitrogen configuration on the electrical conductivity of carbonized polyacrylonitrile and poly (ionic liquid) blends, Macromol. Chem. Phys. 216 (19) (2015) 1930–1944.

[62] J. Bernal, The structure of graphite, proceedings of the royal society of London. Series a, Contain. Pap. a Math. Phys. Character 106 (740) (1924) 749–773.

[63] R.E. Franklin, The structure of graphitic carbons, Acta Crystallogr. 4 (3) (1951) 253–261.

[64] R. Jansen, H. Van Bekkum, Amination and ammoxidation of activated carbons, Carbon 32 (8) (1994) 1507–1516.

[65] G.S. Szymański, T. Grzybek, H. Papp, Influence of nitrogen surface functionalities on the catalytic activity of activated carbon in low temperature SCR of NO_x with NH_3, Catal. Today 90 (1) (2004) 51–59.

[66] S. Zhang, S. Tsuzuki, K. Ueno, K. Dokko, M. Watanabe, Upper limit of nitrogen content in carbon materials, Angew. Chem. Int. Ed. 54 (4) (2015) 1302–1306.

[67] R. Arrigo, M. Hävecker, R. Schlögl, D.S. Su, Dynamic surface rearrangement and thermal stability of nitrogen functional groups on carbon nanotubes, Chem. Commun. (40) (2008) 4891–4893.

[68] J.-P. Boudou, P. Parent, F. Suarez-Garcia, S. Villar-Rodil, A. Martínez-Alonso, J. Tascón, Nitrogen in aramid-based activated carbon fibers by TPD, XPS and XANES, Carbon 44 (12) (2006) 2452–2462.

[69] T.F.E. Rhead, R.V. Wheeler, The effect of temperature on the equilibrium $2\,CO \rightleftharpoons CO_2 + C$, J. Chem. Soc. Trans. 97 (1910) 2178–2189.

[70] Y. Zhao, X. Liu, Y. Han, Microporous carbonaceous adsorbents for CO_2 separation via selective adsorption, RSC Adv. 5 (38) (2015) 30310–30330.

[71] C. Jones, E. Sammann, The effect of low power plasmas on carbon fibre surfaces, Carbon 28 (4) (1990) 509–514.

[72] M. Hantel, D. Weingarth, R. Kötz, Parameters determining dimensional changes of porous carbons during capacitive charging, Carbon 69 (2014) 275–286.

[73] N. Jäckel, M. Rodner, A. Schreiber, J. Jeongwook, M. Zeiger, M. Aslan, D. Weingarth, V. Presser, Anomalous or regular Capacitance? The influence of pore size dispersity on double-layer formation, J. Power Sources 326 (2016) 660–671.

[74] J. Segalini, E. Iwama, P.-L. Taberna, Y. Gogotsi, P. Simon, Steric effects in adsorption of ions from mixed electrolytes into microporous carbon, Electrochem. Commun. 15 (1) (2012) 63–65.

[75] S. Sigalov, M.D. Levi, G. Salitra, D. Aurbach, A. Jänes, E. Lust, I.C. Halalay, Selective adsorption of multivalent ions into TiC-derived nanoporous carbon, Carbon 50 (10) (2012) 3957–3960.

[76] N. Jäckel, P. Simon, Y. Gogotsi, V. Presser, Increase in capacitance by subnanometer pores in carbon, ACS Energy Lett. 1 (6) (2016) 1262–1265.

[77] J. Huang, B.G. Sumpter, V. Meunier, G. Yushin, C. Portet, Y. Gogotsi, Curvature effects in carbon nanomaterials: exohedral versus endohedral supercapacitors, J. Mater. Res. 25 (8) (2010) 1525–1531.

[78] D. Weingarth, H. Noh, A. Foelske-Schmitz, A. Wokaun, R. Kötz, A reliable determination method of stability limits for electrochemical double layer capacitors, Electrochim. Acta 103 (2013) 119–124.

[79] D. Weingarth, A. Foelske-Schmitz, R. Kötz, Cycle versus voltage hold–which is the better stability test for electrochemical double layer capacitors? J. Power Sources 225 (2013) 84–88.

[80] B. Krüner, C. Odenwald, A. Tolosa, A. Schreiber, M. Aslan, G. Kickelbick, V. Presser, Carbide-derived carbon beads with tunable nanopores from continuously produced polysilsesquioxanes for supercapacitor electrodes, Sustain. Energy Fuel. 1 (7) (2017) 1588–1600.

[81] J.-K. Ewert, D. Weingarth, C. Denner, M. Friedrich, M. Zeiger, A. Schreiber, N. Jäckel, V. Presser, R. Kempe, Enhanced capacitance of nitrogen-doped hierarchically porous carbide-derived carbon in matched ionic liquids, J. Mater. Chem. 3 (37) (2015) 18906–18912.

4.5. Carbide-derived carbon beads with tunable nanopores from continuously produced polysilsesquioxanes for supercapacitor electrodes

Benjamin Krüner,[1,2,†] Christina Odenwald,[3,†] Aura Tolosa,[1,2] Anna Schreiber,[1] Mesut Aslan,[1] Guido Kickelbick,[3] Volker Presser[1,2]

[1] *INM - Leibniz Institute for New Materials, 66123 Saarbrücken, Germany*

[2] *Department of Materials Science and Engineering, Saarland University, 66123 Saarbrücken, Germany*

[3] *Inorganic Solid State Chemistry, Saarland University, 66123 Saarbrücken, Germany*

[†] *these authors contributed equally*

Krüner, Benjamin et al. (2017) *Sustainable Energy & Fuels*, 1 (7), 1588-1600.
https://doi.org/10.1039/C7SE00265C

<u>Own contribution</u>: Design, planning, writing, pyrolysis, chlorine gas treatment, SEM, particle size analysis, EDX analysis, TGA coupled with MS analysis, N_2 sorption analysis, Raman analysis, XRD, electrochemical analysis for double-layer capacitors.

<u>Abstract:</u>

The MicroJet reactor technique is an excellent continuous method to produce spherical and homogeneous organically modified silica (ORMOSIL) particles in a large scale (10–15 g min^{-1}). We applied this method to manufacture polyorganosilsesquioxanes with different ratios of phenyl and vinyl functional groups, which were later pyrolyzed to obtain silicon oxycarbides. Such polymer-derived ceramic (PDC) materials are highly suited as precursor for carbide-derived carbon (CDC) synthesis. Chlorine etching of PDC at high temperatures removed silicon and oxygen, yielding the formation of nanoporous carbon. Pure poly(phenyl-silsesquioxane) spheres lost their shape during the thermal process by undergoing further condensation reactions. Yet, the spherical shape was conserved during thermal processing after adding vinyl functionalities. The ratio of vinyl and phenyl functionalities controlled the pore structure and the total CDC yield, enabling an increase from 2 mass% to 22 mass%. The total pore volume varied between 1.3-2.1 $cm^3\ g^{-1}$ and the specific surface area between 2014–2114 $m^2\ g^{-1}$. The high surface area and large pore volume makes these materials attractive for high power supercapacitor electrodes. The specific capacitance of the best sample at low rates in 1 M tetraethylammonium tetrafluoroborate in acetonitrile was 116 F g^{-1} (at 5 mA g^{-1}) and still 80 F g^{-1} at very high rates (at 100 A g^{-1}).

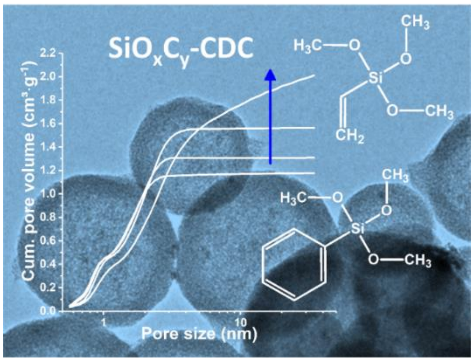

Sustainable
Energy & Fuels

ROYAL SOCIETY
OF CHEMISTRY

PAPER

View Article Online
View Journal | View Issue

Cite this: *Sustainable Energy Fuels*, 2017, **1**, 1588

Carbide-derived carbon beads with tunable nanopores from continuously produced polysilsesquioxanes for supercapacitor electrodes†

Benjamin Krüner, ‡[ab] Christina Odenwald,‡[c] Aura Tolosa, [ab] Anna Schreiber,[a]
Mesut Aslan,[a] Guido Kickelbick *[c] and Volker Presser *[ab]

The MicroJet reactor technique is an excellent continuous method to produce spherical and homogeneous organically modified silica (ORMOSIL) particles in a large scale (10–15 g min^{-1}). We applied this method to manufacture polyorganosilsesquioxanes with different ratios of phenyl and vinyl functional groups, which were later pyrolyzed to obtain silicon oxycarbides. Such polymer-derived ceramic (PDC) materials are highly suited as precursor for carbide-derived carbon (CDC) synthesis. Chlorine etching of PDC at high temperatures removed silicon and oxygen, yielding the formation of nanoporous carbon. Pure poly(phenyl-silsesquioxane) spheres lost their shape during the thermal process by undergoing further condensation reactions. Yet, the spherical shape was conserved during thermal processing after adding vinyl functionalities. The ratio of vinyl and phenyl functionalities controlled the pore structure and the total CDC yield, enabling an increase from 2 mass% to 22 mass%. The total pore volume varied between 1.3-2.1 cm^3 g^{-1} and the specific surface area between 2014–2114 m^2 g^{-1}. The high surface area and large pore volume makes these materials attractive for high power supercapacitor electrodes. The specific capacitance of the best sample at low rates in 1 M tetraethylammonium tetrafluoroborate in acetonitrile was 116 F g^{-1} (at 5 mA g^{-1}) and still 80 F g^{-1} at very high rates (at 100 A g^{-1}).

Received 23rd May 2017
Accepted 15th July 2017

DOI: 10.1039/c7se00265c

rsc.li/sustainable-energy

1. Introduction

Highly porous carbon materials are attractive for many applications such as gas storage,[1,2] catalysis,[3] or electrochemical energy storage.[4] Electrical double-layer capacitors, also known as supercapacitors, are particularly efficient energy storage devices, capitalizing on rapid and reversible ion electrosorption.[5] Due to fast polarization, it is possible to achieve a high specific power, but only a moderate specific energy.[4] Beside high power ratings, supercapacitors exhibit a very long lifetime and high Coulombic efficiency.[6]

Carbide-derived carbons (CDCs) are a broad family of carbon materials,[7] which can be obtained from metal carbides,[8] carbonitrides,[9] or oxycarbides.[10,11] Depending on the precursor and the synthesis temperatures it is possible to produce CDC materials with different pore architectures[11] and carbon structures.[12] Oxycarbides, like SiOC, are promising precursors to synthesize highly porous CDCs with a high BET specific surface area (SSA) of 3089 m^2 g^{-1} and a large pore volume of 1.8 cm^3 g^{-1}.[13] SiOC-CDC micrometer-sized particles have been obtained from commercial polymethyl- and polymethylphenylsilsesquioxanes by pyrolysis of monoliths, followed by chlorine etching at 1200 °C of the grinded monoliths.[10] Thereby, it was possible to obtain BET SSA up to 2600 m^2 g^{-1} and a total pore volume up to 1.7 cm^3 g^{-1}. Polymethylsilsesquioxane can also be used in an emulsion process to obtain spherical particles with a diameter of 50–600 nm, 1–10 μm, and 10–100 μm, which were successfully converted to polymer-derived ceramics (PDCs).[14] Sub-micrometer CDCs with a diameter of 20–200 nm and a SSA of ~2300 m^3 g^{-1} were successfully obtained by emulsion soft templating using a commercial allylhydriopolycarbosilane precursor.[15] The specific capacitance of this material in 1 M tetraethylammonium tetrafluoroborate (TEA-BF$_4$) in acetonitrile (ACN) was 130 F g^{-1} and 110 F g^{-1} in aqueous 1 M Na$_2$SO$_4$.[15] The small size of the individual particles is beneficial to achieve a high power within supercapacitor applications. Yet, a disadvantage of the mentioned methods to produce PDC precursors for CDC synthesis is the need to add a hazardous metal crosslinking agent like hydrogen hexachloroplatinate(IV),[15] zirconium acteylacetonate,[16] or zinc acetylacetonate.[13] The crosslinking agent is necessary because the oligomers can melt before converted to PDCs.[13]

---

[a] *INM – Leibniz Institute for New Materials, 66123 Saarbrücken, Germany. E-mail: volker.presser@leibniz-inm.de*

[b] *Department of Materials Science and Engineering, Saarland University, 66123 Saarbrücken, Germany*

[c] *Inorganic Solid State Chemistry, Saarland University, 66123 Saarbrücken, Germany. E-mail: guido.kickelbick@uni-saarland.de*

† Electronic supplementary information (ESI) available. See DOI: 10.1039/c7se00265c

‡ These authors contributed equally

Wet chemical preparation methods for the synthesis of defined nano- and microparticles are commonly used as batch processes which exhibit several disadvantages like a variation in the product quality from batch-to-batch and a limited and complex scale-up. Continuous preparation methods offer in general a better controllability and reproducibility and are attractive for industrial scale production.[17,18] There are few continuous pathways to obtain spherical particles from oxycarbides. For example, electrospraying yields spherical particles and can be carried out with a commercial polymethylphenylsilsesquioxane.[13] The diameter of these particles was 1–6 μm, which is significant larger than soft-templated emulsion beads. The BET SSA of these micrometer spheres was up to ~2230 $m^2\ g^{-1}$ and the specific capacitance was 112 F g^{-1} for 1 M TEA-BF_4 in ACN.

An advanced continuous method is the MicroJet reactor technique.[19] Thereby, two reagent solutions are forced with high pressure through micro-nozzles into the reactor which is exposed to a constant gas flow. A fast and homogenous mixing is obtained due to the high shear forces that are generated by the impinging jets. The gas flow pushes the products out of the reactor into a reservoir, which also effectively avoids clogging. The MicroJet reactor technique was already used to synthesize inorganic nanoparticles, such as TiO_2,[20] $BaSO_4$,[21] ZnO, Fe_3O_4, or $CaHPO_4$.[22]

In this work, we synthesized for the first time polyorganosilsesquioxane spheres with different ratios of phenyl and vinyl groups from organotrialkoxysilanes by using a MicroJet reactor. Poly(benzyl)silsesquioxane or poly(phenyl)silsesquioxane beads obtained by a sol–gel process have a softening point at ~50 °C and ~140 °C.[23,24] This property makes them unsuitable to produce PDCs that conserve the initial shape during pyrolysis. By adding vinyl groups to the system, it was possible to obtain a higher condensation degree and to conserve the spherical shape of the particles after the pyrolysis to obtain SiOC-PDCs. Afterwards the samples were treated in chlorine gas to obtain highly porous SiOC-CDCs. The variation of the organic groups of the silanes has a strong influence for the yield and porosity of the CDCs, which relates directly to the rate performance in the supercapacitor.

2. Experimental description

2.1. Materials

Phenyltrimethoxysilane (PTMS; 97%) and vinyltrimethoxysilane (VTMS; 99%) were obtained from ABCR GmbH. Ammonia (25%) was purchased from VWR International GmbH. All chemicals were used as received.

2.1.1. Synthesis of siloxane beads. For the synthesis of the polymer microparticles, two precursor solutions (A and B) were used as schematically shown in Fig. 1. Solution A was prepared by dissolving the respective amount of trialkoxysilane(s) in methanol (MeOH) followed by the addition of an aqueous solution of HCl (Table 1). A prehydrolization of the silane(s) was performed by stirring the solution overnight at room temperature. For solution B, we used an aqueous solution of ammonia (2.2 mol L^{-1}).

The particles were synthesized at room temperature in a MicroJet reactor of stainless steel (Synthesechemie Dr. Penth GmbH). The precursor solutions A and B were transported through the system with two HPLC-pumps (LaPrep P110 preparative HPLC pumps, VWR International GmbH) with a flow rate of 250 mL min^{-1}. The solutions were forced through opposing nozzles (nozzle diameter 300 μm) into a reaction chamber where they collide as impinging jets and a fast mixing occurs effected by the high jet velocities. A nitrogen gas flow helped to transport the product out of the reactor and avoided clogging. The outlet tube was 1.5 mm in diameter and *ca.* 85 cm in length. The product suspension was collected in a polyethylene flask. The particles were isolated by centrifugation (8000 rpm, 7012 G, 10 min) and dried in vacuum at 30 °C.

2.1.2. Pyrolysis and chlorine treatment. The polymer beads were pyrolyzed in a graphite heated furnace (Thermal Technology) in an argon atmosphere (flow rate: 50 $cm^3\ min^{-1}$) at 1200 °C for 2 h with a heating rate of 2 °C min^{-1}. The resulting polymer-derived ceramic samples were labelled with the ending SiOC in the following. The materials were then transferred to a quartz tube furnace (Carbolite Gero) and heated to 1200 °C with a rate of 15 °C min^{-1}. An argon flow (50 $cm^3\ min^{-1}$) was constantly supplied and the chlorine flow (10 $cm^3\ min^{-1}$) was added when the target temperature (1200 °C) was reached

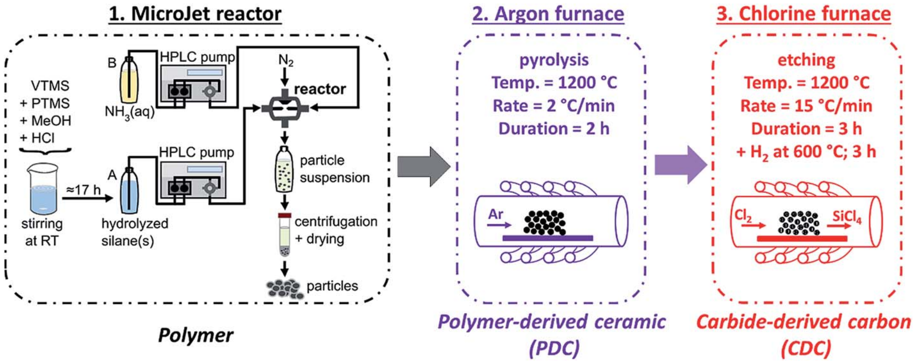

Fig. 1 Schematic overview of the synthesis method: (1) the production of the polymer beads with the MicroJet reactor, (2) the pyrolysis, and (3) the chlorine treatment. VTMS: vinyltrimethoxysilane; PTMS: phenyltrimethoxysilane; MeOH: methyl alcohol; RT: room temperature; (A and B): solution A or solution B; HPLC: high performance liquid chromatography.

Table 1 Compositions of precursor solutions A and B that were used for the synthesis of polysilsesquioxane microparticles. VTMS: vinyltrimethoxysilane; PTMS: phenyltrimethoxysilane; MeOH: methyl alcohol

	Solution A					Solution B
	$n_{(\mathrm{VTMS})}$ (mmol)	$n_{(\mathrm{PTMS})}$ (mmol)	$n_{(\mathrm{MeOH})}$ (mol)	$n_{(\mathrm{H_2O})}$ (mol)	$n_{(\mathrm{HCl})}$ (mmol)	$C_{(\mathrm{NH_3})}$ (mol L^{-1})
Vi-$SiO_{1.5}$	138.8	—	3.2	2.8	0.03	2.2
$Ph_{0.25}Vi_{0.75}$-$SiO_{1.5}$	104.1	34.7	2.8	2.8	0.03	2.2
$Ph_{0.5}Vi_{0.5}$-$SiO_{1.5}$	69.4	69.4	3.0	2.8	0.03	2.2
$Ph_{0.75}Vi_{0.25}$-$SiO_{1.5}$	34.7	104.1	3.2	2.8	0.03	2.2

(holding time: 3 h). Afterwards chlorine gas was switched off and the furnace was cooled to 600 °C under argon flow and hold at that temperature for 3 h under inlet of additional hydrogen (10 cm^3 min^{-1}) to remove residual chlorine from the sample. The cooling from 600 °C to room temperature was carried out in argon atmosphere. The carbide-derived carbon materials are referred to as CDC.

2.2. Material characterization

Solid-state CP-MAS NMR spectra were recorded at 25 °C using a Bruker AV400WB spectrometer (^{13}C 100.62 MHz, ^{29}Si 79.50 MHz). A contact time of 2.0 ms and a variable power contact time (ramp 10050) were used. The spin rate was 13 kHz and the delay time 3–6 s. For ^{13}C NMR, adamantane, and for ^{29}Si NMR, octakis(trimethylsiloxy)silsesquioxane was used as external standards. The intensity of all NMR spectra was normalized.

Fourier transform infrared (FT-IR) spectroscopy was applied on the dried polysilsesquioxane samples in attenuated total reflectance (ATR) mode on a Vertex 70 spectrometer (Bruker Optics). The measurements were accomplished in the wave number range of 500–4500 cm^{-1} and under ambient air. For each spectrum, 32 scans were averaged with a spectral resolution of 4 cm^{-1}.

The XRD patterns were measured with a D8 Advance diffractometer (Bruker AXS) using Cu-K$_\alpha$ radiation (40 kV and 40 mA) and a Goebel mirror with point focus and a two-dimensional X-ray detector (Vantec-500). The sample holder was a sapphire single crystal.

Raman spectroscopy was carried out with a Renishaw inVia Raman microscope with a wavelength of 532 nm and a grating of 2400 lines mm^{-1}. The spectral resolution was 1.2 cm^{-1}, the numeric aperture 0.9, and the incident power on the sample ~0.02 mW. A spectrum was recorded for 30 s and averaged over 10 accumulations. The D- and G-mode with the amorphous contribution of carbon in the Raman spectra were fitted using five Voigt functions for the SiOCs and four Voigt functions for the CDCs.

The thermogravimetric measurements combined with a mass spectrometer (TGA-MS) were carried out with a STA449F3 Jupiter and QMS 403C Aëolos from Netzsch. The heating rate for the measurement was 10 °C min^{-1} to 1200 °C in Argon (purity: 5.0).

Scanning electron microscopy (SEM) was performed in a field emission scanning electron microscope JSM-7500F from JEOL. The samples were sputtered with gold to increase the surface conductivity. The size of 150 individual spheres was measured to obtain an average diameter with the image analysis software ImageJ.[25] A X-MAX silicon detector from Oxford Instruments was used to perform the energy dispersive X-ray spectroscopy (EDX) attached to the SEM chamber. The operating voltage for the SEM and EDX was 5 kV.

High-resolution transmission electron microscopy (TEM) was executed with a JEM-2100F from JEOL at 200 kV. The polymer samples were dispersed and sonicated in water to deposit them on a lacey carbon film on a copper grid (Gatan). Ethanol was used instead of water to perform this step for the CDCs.

Nitrogen gas sorption analysis (N_2 GSA) was performed with an Autosorb iQ system from Quantachrome. The samples were degassed at 100 mbar at 200 °C for 1 h and at 300 °C for 20 h. The temperature during the measurement was −196 °C and the relative pressure was varied between 5×10^{-7} to 1.0 in 76 steps. A quenched-solid density functional theory (QSDFT) kernel assuming slit-like pores (QSDFT) was applied to obtain the pore size distribution from the adsorption isotherms.[26] The Brunauer–Emmett–Teller (BET) surface area was calculated with the BET equation in the linear region of the isotherm between 0.02 and 0.3 partial pressure.[27] The value of the total pore volume was obtained by the adsorbed volume at a relative pressure of 0.95 and the average pore size (d_{50}) represents the pore size with a half of the total pore volume.[11] The data analysis of the nitrogen sorption isotherms was performed with ASiQwin 3.0 from Quantachrome.

Contact angle measurements of the CDC electrodes were carried out with an OC 25 system from Data Physics with demineralized water (volume per drop: 3 μL) in air.

2.3. Electrochemical measurements

Free-standing carbon electrodes were prepared by dispersing the CDC powder in ethanol and adding 5 mass% of polytetrafluoroethylene binder (PTFE, 60 mass% in water, Sigma-Aldrich). The slurry was crushed in a mortar until a doughy carbon paste was formed, which was rolled with a rolling machine from MTI Corporation to a thickness of ~110 μm. The electrodes were dried for 48 h at 120 °C in a vacuum oven at 2×10^3 Pa. For electrochemical measurements, electrode discs with a diameter of 8 mm were punched out (geometrical information about the electrodes is given in ESI, Table S1†). Custom-built symmetrical two-electrode cells were assembled with carbon-coated aluminum current collectors (type Zflo 2653, Coveris

Advanced Coatings) for the organic electrolyte (1 M TEA-BF_4 in ACN; BASF, battery grade).[28] Graphite foil current collectors were used for the aqueous electrolyte (1 M Na_2SO_4 prepared with Milli-Q water; pH 5.2). A glass fiber separator (GF/A from Whatman) with a diameter of 13 mm was used between the electrodes. The cell for the organic electrolyte was placed in a vacuum oven (2×10^3 Pa) at 120 °C for 16 h.

All electrochemical measurements were carried out in a climate chamber (Binder) at 25 ± 1 °C with a VMP300 potentiostat/galvanostat from BioLogic. Electrochemical impedance spectra were recorded in a symmetrical full cell for 100 kHz to 100 mHz at 0 V with ten points per decade and averaged over five measurements. The electrical serial resistance (ESR) and the electrical distribution resistance (EDR) were normalized to the geometrical area of the electrode. The capacitance from cyclic voltammograms (CV) was calculated with eqn (1) and from galvanostatic cycling with potential limitation (GCPL) with eqn (2). The specific capacitance was normalized to the active mass (95%) of one electrode. The IR-drop of the GCPL measurements was obtained after a resting time of 10 s. The electrochemical performance is benchmarked against PTFE bonded film electrodes from YP-80F (Kuraray Co.), which is referred to as AC (activated carbon).

$$C_S = \frac{4I(t)}{dU(t)/dt \times m} \tag{1}$$

C_S: specific capacitance per electrode, $I(t)$: current, $dU(t)/dt$: scan rate, and m: mass of carbon in the electrode.

$$C_S = \frac{4Q_{dis}}{Um} \tag{2}$$

C_S: specific capacitance per electrode, Q_{dis}: charge of the discharging cycle, U: IR-drop corrected cell voltage, and m: mass of carbon in the electrode.

Stability testing *via* voltage floating for 100 h was also conducted in the climate chamber at 25 °C at 1.4 V for the aqueous and 2.7 V for the organic electrolyte. Every 10 h, galvanostatic cycling was performed at a cell voltage of 1.2 V (aqueous) or 2.5 V (organic). After voltage floating, the electrodes with the aqueous electrolyte were washed with Milli-Q water for further post mortem analysis.

3. Results and discussion

3.1. Particle characterization

FT-IR measurements of the polymer particles confirm the presence of the desired organic groups (Fig. S1†). All samples exhibit peaks from the inorganic backbone in the range of 935–1230 cm^{-1} from –Si–O–Si– vibrations. In addition, the samples show vibration bands from the organic groups. At 2800–3095 cm^{-1}, in each spectrum C–H stretching vibrations are present and at 1600 cm^{-1} peaks from C═C vibrations. Samples with phenyl groups show characteristic signals from Si–C-vibrations at 1430 cm^{-1} and 1130 cm^{-1}. Samples that contain vinyl groups also show well-defined modes at 1275 cm^{-1} from Si–C vibrations and peaks at 1410 cm^{-1} that can be assigned to ═CH_2 bending vibrations.[29–31] The increasing vinyl content of the samples $Ph_{0.75}Vi_{0.25}$-$SiO_{1.5}$, $Ph_{0.5}Vi_{0.5}$-$SiO_{1.5}$, $Ph_{0.25}Vi_{0.75}$-$SiO_{1.50}$, and Vinyl-$SiO_{1.5}$ is reflected by the increasing intensity of the Si-vinyl vibration (1275 cm^{-1}) compared to the Si-phenyl vibration (1430 cm^{-1}).

^{13}C NMR spectra (Fig. 2A) of the prepared polysilsesquioxane particles show characteristic signals for the vinyl and phenyl groups. For the samples with both organic groups overlapping peaks were obtained. Samples exhibit no or only weak signals from residual alkoxy groups (at *ca.* 60 ppm), which suggests that almost all alkoxy groups were hydrolyzed during polymerization and that in T^2 units OH-groups are present in addition to the vinyl and phenyl groups. ^{29}Si NMR spectra (Fig. 2B) give important information about the network structure. The peaks at ≈ −73 ppm and ≈ −82 ppm of the organically modified silica (ORMOSIL) particles can be assigned to T^2 and T^3 species, meaning silicon atoms that are connected to the network with two or three bonds. The spectra also show that the T^2 to T^3 ratio decrease with an increasing vinyl content. This behavior confirms the incorporation of vinyl groups into the network, which leads to an enhanced cross-linking that is desired to obtain a better thermal stability.

The XRD pattern of the mixed polymers in Fig. 2C show a shift of very broad peaks to higher 2θ values with an increasing amount of vinyl groups. Polyphenylsiloxanes can have a ladder like structure and two peaks in the XRD pattern can be identified with the plane-to-plane peak at ~7.3° 2θ and the chain-to-chain peak of the Si–O–Si frame at ~18.8° 2θ.[32] Polyvinylsiloxanes with a ladder structure exhibit a plain-to-plain peak at ~10° 2θ.[33] The corresponding chain-to-chain peak is at around 23° 2θ due to the lower required space of the vinyl group compared to the phenyl group.[33] The measured peak positions of the Vi-$SiO_{1.5}$ is similar to the reported values in the literature.[33] The three samples with mixtures synthesized with different ratios of phenyl- and vinyltrimethoxysilane show peaks in between the pure polyphenyl- and polyvinylsiloxanes, which indicates a homogeneous mixture. From the peak width, it is possible to estimate domain sizes by use of the Scherer equation which were below 5 nm.[34] These small domain sizes point out the mainly amorphous character of the synthesized polymers. The absence of long-range order can also be seen in the transmission electron micrographs in the ESI, Fig. S2.†

The pyrolysis of the polysiloxanes was monitored with TGA-MS (Fig. 2D and E, ESI Fig. S1C and D†). All four polymers show a degradation of the ladder structure around 560 °C (Fig 2D), which would be an untypical degradation behavior for a cage structure.[35] The mass loss of the vinyl-polymer is the lowest and the mass loss increases constantly with the amount of added phenyl-groups. The mass spectra of the most important evolving groups are plotted in Fig. 2E, while all relevant leaving groups of $Ph_{0.5}Vi_{0.5}$-$SiO_{1.5}$ are displayed in the ESI (Fig. S1C and D†). The mass spectra in Fig. 2E identify evolving groups during heating. Water (*m*/*z*: 18) is removed from the samples in two main temperature regimes: first, between 135 °C and 430 °C, and second, at temperatures from 450 °C to 800 °C, where also the other organic groups are being removed. Samples with more phenyl groups (*m*/*z*: 78 at ~570 °C) or vinyl groups (*m*/*z*: 28 at ~550 °C) show a larger loss of these functional groups. The

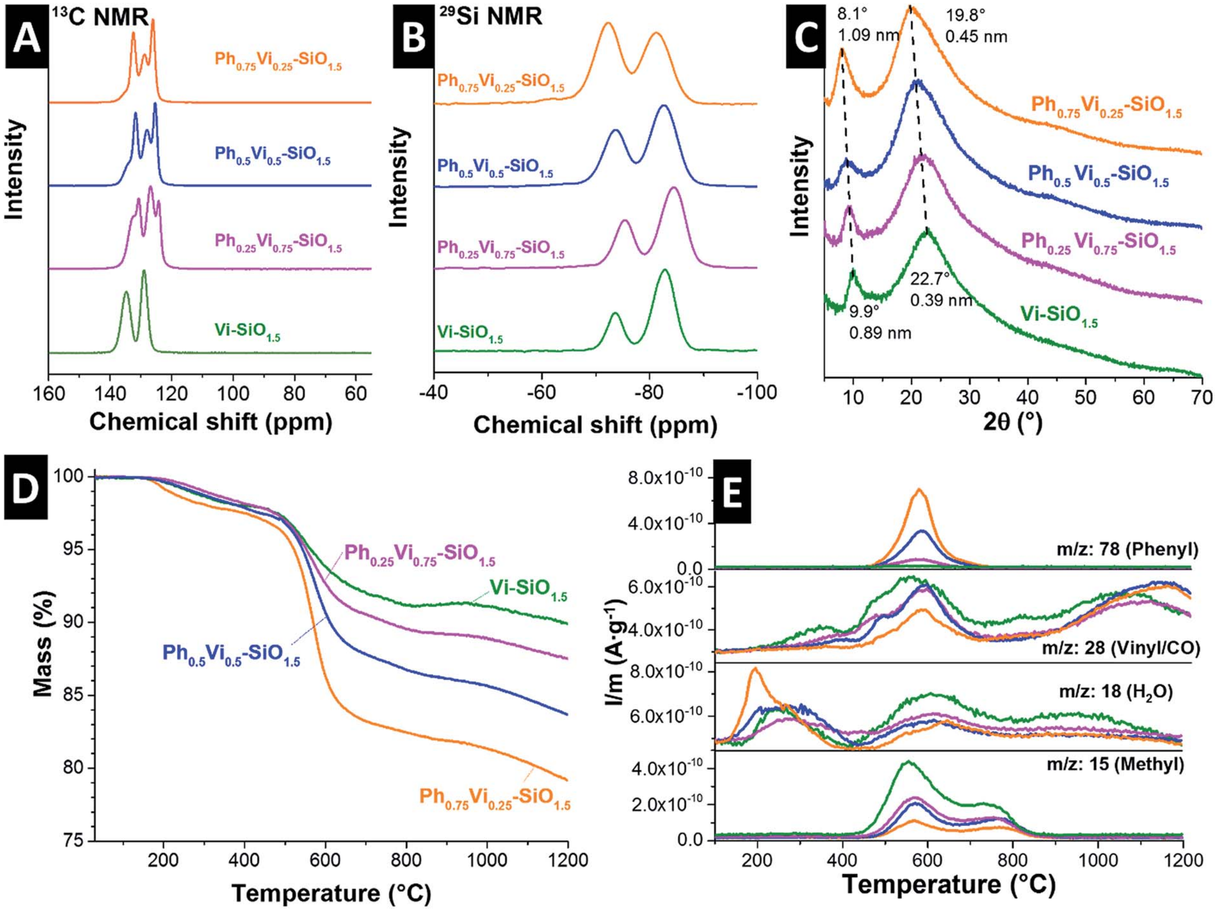

Fig. 2 Solid-state ^{13}C NMR (A), ^{29}Si NMR (B), and XRD pattern (C) of the four polymer beads. TGA curve of the pyrolysis process (D) and the corresponding mass spectra of selected leaving groups (E).

atomic mass of 28 can also be related to carbon monoxide, which is formed at higher temperatures (>900 °C) with residual oxygen. Another major leaving group is the methyl group formed by the decomposition of organic chains from the vinyl groups, which shows two peaks at 550 °C and 750 °C.

3.2. Properties of the polymer-derived ceramics and carbide-derived carbons

The chemical composition of the SiOCs is denoted in Table 2. Of our samples, the carbon content of the Vi-SiOC is the lowest with 32.2 ± 4.8 mass% and increases with an increasing amount of phenyl groups to 50.8 ± 1.8 mass% for $Ph_{0.5}Vi_{0.5}$-SiOC. Yet, the carbon content is not increasing when the amount of phenyl groups is increased from 50% to 75%, which can be explained with the higher mass loss of $Ph_{75}Vi_{25}$-SiOC.

As can be seen from our EDX results (Table 2), the removal of silicon and oxygen by chlorine treatment at high temperatures was successful and we only found a low amount of residual silicon and oxygen. The mass losses after pyrolysis and chlorine treatment of samples with different ratios of phenyl and vinyl functional groups are quite different (Table 3). The sample Vi-SiOC had the lowest mass loss after pyrolysis of only 11 mass% and shows the highest mass loss after the etching of 97.6 mass%. The total yield of Vi-SiOC-CDCs synthesis amounts to only 2.2 mass%. The addition of phenyl groups increases the total yield to 21.9 mass%, which can be explained by the higher carbon and aromatic content introduced by the phenyl groups.

The Raman spectra and XRD pattern of the SiOCs and CDCs with different ratios of vinyl- and phenyltrimethoxysilanes are very similar; therefore, Fig. 3 only depicts data for the $Ph_{0.5}Vi_{0.5}$-SiOC samples (and the remaining Raman spectra and XRD patterns are found in ESI, Fig. S3†). The SiOC Raman spectra (Fig. 3A) show the presence of incompletely graphitic carbon,

Table 2 Chemical composition of all SiOCs and CDCs measured with EDX

	C (mass%)	O (mass%)	Si (mass%)
Vi-SiOC	32.2 ± 4.8	31.5 ± 4.0	36.3 ± 8.2
$Ph_{0.25}Vi_{0.75}$-SiOC	41.9 ± 2.4	26.2 ± 1.6	31.9 ± 4.0
$Ph_{0.5}Vi_{0.5}$-SiOC	50.8 ± 1.8	25.2 ± 0.8	24.0 ± 2.5
$Ph_{0.75}Vi_{0.25}$-SiOC	50.2 ± 1.5	25.9 ± 1.0	23.9 ± 2.4
Vi-SiOC-CDC	97.9 ± 0.3	1.9 ± 0.3	0.3 ± 0.1
$Ph_{0.25}Vi_{0.75}$-SiOC-CDC	98.4 ± 0.7	1.3 ± 0.4	0.4 ± 0.3
$Ph_{0.5}Vi_{0.5}$-SiOC-CDC	98.4 ± 0.2	1.4 ± 0.1	0.2 ± 0.1
$Ph_{0.75}Vi_{0.25}$-SiOC-CDC	97.1 ± 0.4	2.9 ± 0.4	n.d.

Table 3 Mass loss by pyrolysis and chlorine treatment

	Mass loss after pyrolysis (mass%)	Mass loss after chlorine gas treatment (mass%)	Total mass loss (mass%)
Vi-SiOC-CDC	11.0	97.6	97.8
$Ph_{0.25}Vi_{0.75}$-SiOC-CDC	13.0	85.1	87.1
$Ph_{0.5}Vi_{0.5}$-SiOC-CDC	15.0	76.1	79.6
$Ph_{0.75}Vi_{0.25}$-SiOC-CDC	20.7	72.4	78.1

Table 4 Fitted values of the D- and G-mode from the Raman spectroscopy of all SiOCs and CDCs

	Mode	Position (cm^{-1})	FWHM (cm^{-1})	I_D/I_G
Vi-SiOC	D	1334	181	4.27
	G	1587	111	
$Ph_{0.25}Vi_{0.75}$-SiOC	D	1331	162	4.67
	G	1601	67	
$Ph_{0.5}Vi_{0.5}$-SiOC	D	1333	159	4.58
	G	1603	62	
$Ph_{0.75}Vi_{0.25}$-SiOC	D	1324	167	4.40
	G	1599	66	
Vi-SiOC-CDC	D	1333	85	2.80
	G	1593	65	
$Ph_{0.25}Vi_{0.75}$-SiOC-CDC	D	1337	89	2.40
	G	1597	66	
$Ph_{0.5}Vi_{0.5}$-SiOC-CDC	D	1337	84	2.55
	G	1596	68	
$Ph_{0.75}Vi_{0.25}$-SiOC-CDC	D	1339	76	2.56
	G	1601	67	

due to the position of the D- and G-mode at 1331 cm^{-1} and 1603 cm^{-1}. The Vi-SiOC shows a higher amount of amorphous carbon than the other SiOC samples, which can be recognized by having a look to the broader full-width at half-maximum (FWHM) of 181 cm^{-1} and 111 cm^{-1}, compared to 159 cm^{-1} and 62 cm^{-1} of $Ph_{0.5}Vi_{0.5}$-SiOC (Table 4). The I_D/I_G ratios of the SiOCs ranged between 4.27 and 4.67.

The Raman spectra of the CDCs (Fig. 3A) show nanocrystalline graphitic carbon nature. This can also be recognized by the position of the D- and G-mode at 1337 cm^{-1} and 1596 cm^{-1}.[36] The FWHM decreased significantly to 84 cm^{-1} for the D-mode and 68 cm^{-1} for the G-mode. The I_D/I_G ratios of the CDCs are lower (2.40–2.80) compared to the SiOCs. It appears that the amount of amorphous carbon is reduced by comparing the SiOC with the CDC. Yet, it is reasonable to assume that amorphous carbon formed by the pyrolysis did not entirely disappear after the chlorine gas treatment. Instead, additional nanocrystalline carbon is formed by the chlorine treatment at 1200 °C by converting the SiOC to CDC; this leads to a relative lower amount of the amorphous phase compared to the carbon with more structural ordering.[37,38] Due to the high temperature during the CDC formation, the carbon of all CDCs has a similar (narrow) FWHM and positions of the D- and G-mode (Table 4).

The XRD pattern of the SiOC in Fig. 3B show mainly two broad signals at 22° 2θ and 44° 2θ. The broad peak at 22° 2θ is related to the short-range order of SiO_4 tetrahedra and the 44° 2θ is related to (101)-graphite. The results from EDX, Raman spectroscopy, and XRD show that all PDCs contain amorphous silicon oxide and carbon, which is consistent with the literature.[39,40] The XRD pattern of the CDCs in Fig. 3B show no signal related to amorphous silicon oxide; only the peak at 44° 2θ from (101)-graphite is visible. The results of Raman spectroscopy and the X-ray diffraction indicate only carbons are present in the CDC.

Fig. 4 illustrates the morphology of the CDCs by SEM and TEM images. The average diameters of the particles obtained by the SEM images are given in Table 5. The Vi-SiOC-CDCs are the smallest with the narrowest distribution wide (0.68 ± 0.09 μm). Particles with vinyl and phenyl groups are larger and have a broader size distribution of 2.20 ± 0.48 μm ($Ph_{0.25}Vi_{0.75}$-SiOC-CDC), 2.54 ± 0.58 μm ($Ph_{0.5}Vi_{0.5}$-SiOC-CDC), and 1.81 ± 0.28 μm ($Ph_{0.75}Vi_{0.25}$-SiOC-CDC). The broad size distribution of the particles favors effective packing in the electrode, which may benefit the electrical conductivity. On the surface of the particles, small fractures are noticeable where the particles were agglomerated. The TEM images of all CDC samples show disordered carbon, which is consistent with the XRD pattern (Fig. 3B).

$Ph_{0.75}Vi_{0.25}$-SiOC-CDC, $Ph_{0.5}Vi_{0.5}$-SiOC-CDC, and $Ph_{0.25}Vi_{0.75}$-SiOC-CDC have a type I isotherm resulting from a high amount

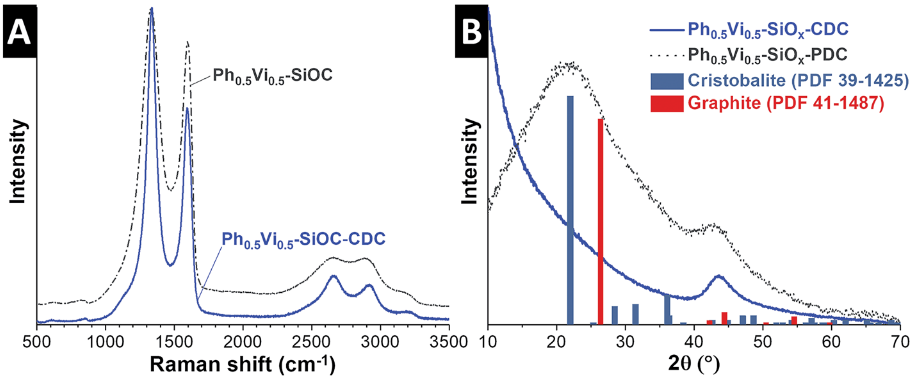

Fig. 3 Raman spectra (A) and XRD pattern (B) of the SiOC and CDC from $Ph_{0.5}Vi_{0.5}$-SiOC.

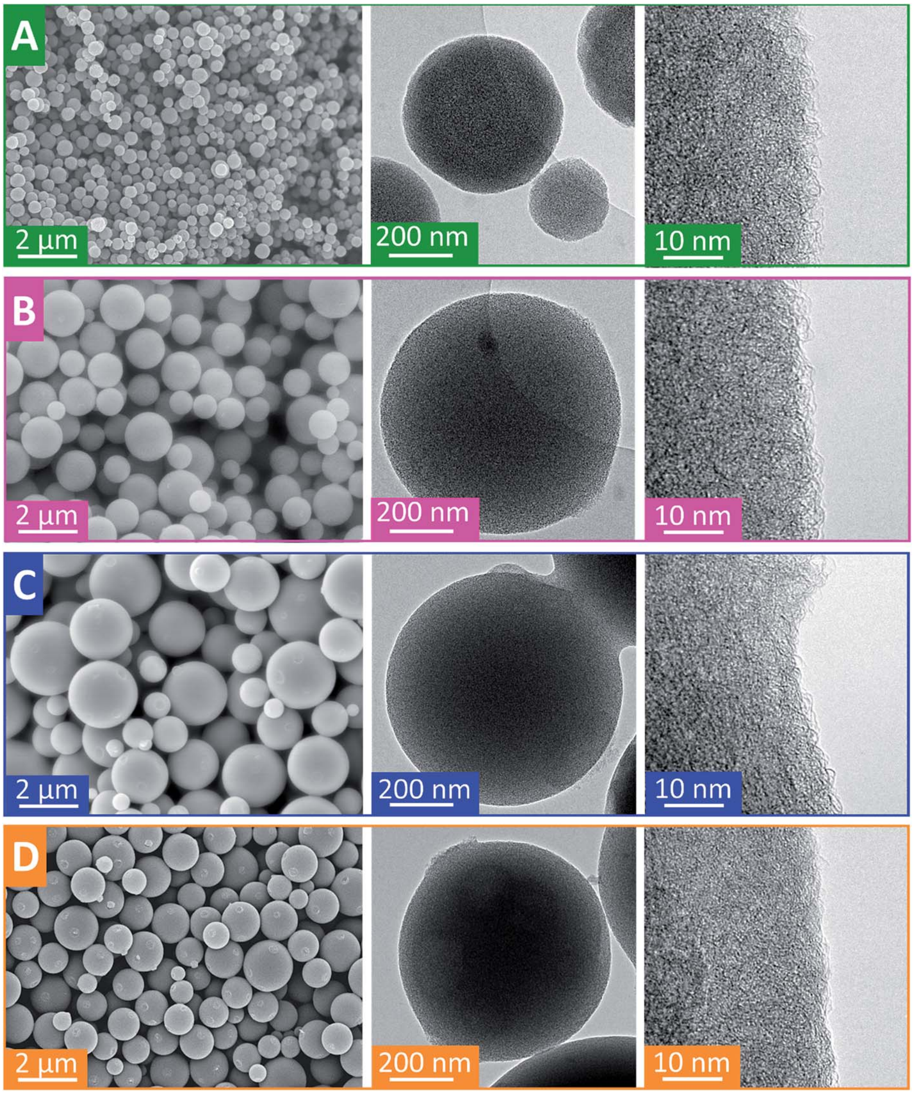

Fig. 4 Scanning and transmission electron micrographs of Vi-SiOC-CDC (A), $Ph_{0.25}Vi_{0.75}$-SiOC-CDC (B), $Ph_{0.5}Vi_{0.5}$-SiOC-CDC (C), and $Ph_{0.75}Vi_{0.25}$-SiOC-CDC (D).

of micropores measured with N_2 GSA in Fig. 5A. Only Vi-SiOC-CDC has a type IV isotherm because it has also a high amount of mesopores, which increase the pore volume. Therefore, Vi-SiOC-CDC shows the highest total pore volume with 2.06 cm^3 g^{-1}. The total pore volume is steadily reduced by adding a higher amount of phenyl groups to the siloxane to 1.67 cm^3 g^{-1} for $Ph_{0.25}Vi_{0.75}$-SiOC-CDC, 1.40 cm^3 g^{-1} for $Ph_{0.5}Vi_{0.5}$-SiOC-CDC, and 1.27 cm^3 g^{-1} for $Ph_{0.75}Vi_{0.25}$-SiOC-CDC. Also, the average pore size was reduced from 2.9 nm to 1.4 nm. Yet, the DFT SSA remains rather constant with values between 2014 m² g^{-1} and 2198 m² g^{-1}. In Table 5, we provide values obtained from the N_2 GSA. We clearly see that the CDC porosity can be modified in a controllable way by adjusting the functional groups of the silanes which were used as precursor.

Table 5 Volume depended average particle size obtained by SEM images and porosity of the carbide-derived carbons measured with nitrogen gas sorption

	Average particle size (µm)	SSA_{DFT} (m^2 g^{-1})	SSA_{BET} (m^2 g^{-1})	Total pore volume (cm^3 g^{-1})	Average pore size (nm)
Vi-SiOC-CDC	0.68 ± 0.09	2044	2473	2.06	2.9
$Ph_{0.25}Vi_{0.75}$-SiOC-CDC	2.20 ± 0.48	2198	2905	1.67	1.7
$Ph_{0.5}Vi_{0.5}$-SiOC-CDC	2.54 ± 0.58	2114	2729	1.40	1.5
$Ph_{0.75}Vi_{0.25}$-SiOC-CDC	1.81 ± 0.28	2014	2554	1.27	1.4

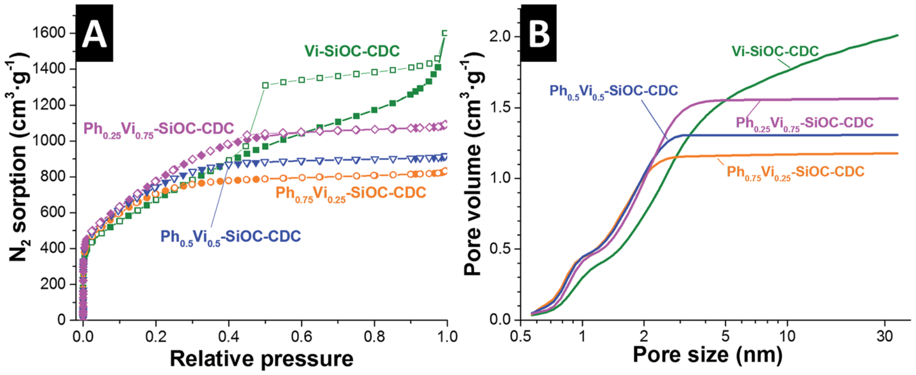

Fig. 5 Nitrogen gas sorption isotherms recorded at −196 °C of the CDC samples (A) and the corresponding pore size distributions applying a QSDFT model assuming slit-like pores (B).

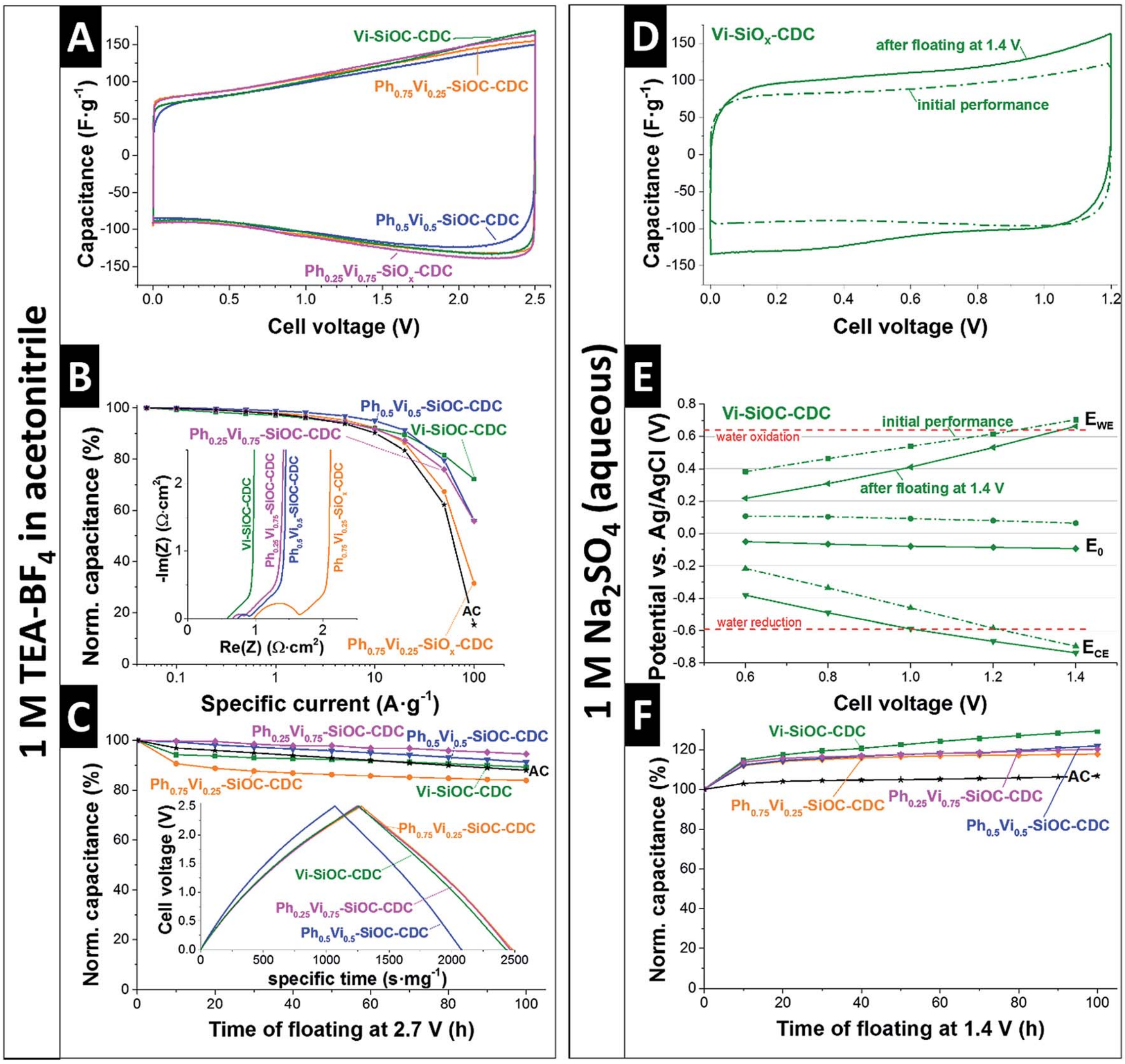

Fig. 6 Cyclic voltammograms (A), rate handling behavior with Nyquist plot as inset (B), and the stability test operating with voltage floating at 2.7 V including the GCPL curve to 2.5 V at 0.05 A g^{-1} as inset (C) of the CDCs in TEA-BF_4 in ACN. Cyclic voltammograms (D) of Vi-SiOC-CDC before and after the voltage floating test at 1.4 V (F), and monitored potentials of the positive and negative electrode including the zero-charge potential (E) in aqueous Na_2SO_4.

3.3. Supercapacitor performance

The electrochemical performance of the SiOC-CDC electrodes was tested in a symmetrical supercapacitor cell using the most commonly used organic electrolyte (1 M in TEA-BF_4 in ACN). The CVs with the organic electrolyte in Fig. 6A shows a typical rectangular shape, typical for nanoporous carbon.[28] A significant difference of the mass-normalized CVs of the different samples is not distinguishable. The specific capacitances measured in GCPL mode are denoted in Table 6. $Ph_{0.25}Vi_{0.75}$-SiOC-CDC has a slightly higher specific capacitance in TEA-BF_4 in ACN with 116 F g^{-1} than the other materials (Vi-SiOC-CDC: 111 F g^{-1}; $Ph_{0.5}Vi_{0.5}$-SiOC-CDC: 106 F g^{-1}; $Ph_{0.75}Vi_{0.25}$-SiOC-CDC: 112 F g^{-1}). Commercial microporous activated carbon (AC; see ref. 41 for AC properties) has a similar specific capacitance of 110 F g^{-1} under the same measurement conditions. The variable porosity of the SiOC-CDCs influences the rate handling behavior much stronger than the total capacitance plotted in Fig. 6B. While the AC has only a residual capacitance of 15% at an ultrahigh specific current of 100 A g^{-1}, the sample $Ph_{0.75}Vi_{0.25}$-SiOC-CDC retains twice as much capacitance under the same conditions (31%). With an increasing mesoporous fraction and an increasing pore volume, the capacitance retention at 100 A g^{-1} increases to 56% for $Ph_{0.5}Vi_{0.5}$-SiOC-CDC and $Ph_{0.25}Vi_{0.75}$-SiOC-CDC and to up to 72% for Vi-SiOC-CDC. We can explain the superior power handling ability of Vi-SiOC-CDC also by the smaller particle size.[42] In Table 6, we see a comparison of the performance of the MicroJet SiOC-CDCs with literature values. There is a clear advantage of the MicroJet SiOC-CDCs of retaining a high specific capacitance at high specific currents (10 A g^{-1} or 100 A g^{-1}). Even materials optimized for high power handling, such as electrospun CDC fiber mats,[13] show a higher capacitance loss at 10 A g^{-1} or 100 A g^{-1} than electrodes made from Vi-SiOC-CDC when using a similar thickness and measurement conditions. The Coulombic efficiencies are plotted in the ESI (Fig. S4A†) and we see all values approaching 99% at around 1 A g^{-1}.

Table 7 ESR and EDR obtained from EIS in 1 M TEA-BF_4 in ACN

	ESR (Ω cm^2)	EDR (Ω cm^2)
Vi-SiOC-CDC	0.59	0.35
$Ph_{0.25}Vi_{0.75}$-SiOC-CDC	0.66	0.51
$Ph_{0.5}Vi_{0.5}$-SiOC-CDC	0.74	0.49
$Ph_{0.75}Vi_{0.25}$-SiOC-CDC	0.98	0.44

The rate handling ability is influenced by the resistance of the electrodes. Using electrochemical impedance spectroscopy (EIS), we quantified the electrical serial resistance (ESR) and electrical distribution resistance (EDR), as seen in Table 7. Vi-SiOC-CDC, which shows the best rate behavior, has the lowest ESR with 0.59 Ω cm^2. $Ph_{0.25}Vi_{0.75}$-SiOC-CDC and $Ph_{0.5}Vi_{0.5}$-SiOC-CDC have a slightly higher ESR of 0.66 Ω cm^2 and 0.74 Ω cm^2, respectively. $Ph_{0.75}Vi_{0.25}$-SiOC-CDC, which was also the CDC with the lowest performance at high rates has the highest ESR of 0.98 Ω cm^2. An increasing ESR value correlates with a reduced performance at high specific currents. The EDR value of Vi-SiOC-CDC is also the lowest with 0.35 Ω cm^2. The other EDR values are very close and vary in the range of 0.44–0.51 Ω cm^2 without a systematic trend.

Also, the performance stability of the system is very high, as can be seen in Fig. 6C. After voltage floating at 2.7 V for 100 h in 1 M TEA-BF_4 in ACN, all materials show a residual specific capacitance between 84% and 95%. The commercial AC has a similar residual capacitance of 89%.[41] Yet, a comparison with literature values is difficult because the electrochemical stability is influenced by the carbon structure,[41] presence and type of functional groups,[41] the electrochemical operation window,[43] measurement conditions,[44] and other cell components like the current collector.[45]

In addition to a common organic electrolyte, we also benchmarked the supercapacitor performance in an aqueous medium. We see important differences of the supercapacitor performance by using an aqueous electrolyte as compared to

Table 6 Overview of the supercapacitor performance of the SiOC-CDCs in 1 M TEA-BF_4 in ACN and aqueous 1 M Na_2SO_4 and the comparison with other carbon-based electrode materials for supercapacitors (n.r.: not reported)

	1 M TEA-BF_4 in ACN			Aqueous 1 M Na_2SO_4			
	Low-rate capacitance (F g^{-1})	Capacitance loss at 10 A g^{-1} (%)	Capacitance loss at 100 A g^{-1} (%)	Initial specific capacitance (F g^{-1})	After floating, specific capacitance (F g^{-1})	SSA_{DFT} (m^2 g^{-1})	Ref.
Vi-SiOC-CDC	111 (at 0.05 A g^{-1})	8	28	98	126	2044	This work
$Ph_{0.25}Vi_{0.75}$-SiOC-CDC	116 (at 0.05 A g^{-1})	8	44	113	135	2198	This work
$Ph_{0.5}Vi_{0.5}$-SiOC-CDC	106 (at 0.05 A g^{-1})	5	44	116	135	2114	This work
$Ph_{0.75}Vi_{0.25}$-SiOC-CDC	112 (at 0.05 A g^{-1})	8	69	104	123	2014	This work
AC	110 (at 0.05 A g^{-1})	10	85	143	152	1756	This work
Emulsion CDC-NS-70-30	130 (at 0.05 A g^{-1})	8	n.r.	103	n.r.	2298	Ref. 15
Electro-sprayed SiOC-CDC beads	117 (at 0.1 A g^{-1})	20	95	n.r.	n.r.	2227	Ref. 13
Electrospun SiOC-CDC fiber mat	130 (at 0.1 A g^{-1})	14	37	n.r.	n.r.	2394	Ref. 13
Activated carbon black (BP2000)	86 (at 0.1 A g^{-1})	9	n.r.	n.r.	n.r.	1389	Ref. 55
Carbon onions	24 (at 0.1 A g^{-1})	10	n.r.	n.r.	n.r.	404	Ref. 59
N-doped activated Lignin-derived carbon	147 (at 0.1 A g^{-1})	19	n.r.	n.r.	n.r.	2353	Ref. 60

the organic electrolyte. The initial CV of Vi-SiOC-CDC in Fig. 6D shows a typical rectangular shape of a supercapacitor with a relatively low specific capacitance of only 98 F g^{-1}. All other CVs are very similar (ESI, Fig. S4†). The capacitance was not reduced after voltage floating at 1.4 V for 100 h; yet, the specific capacitance of Vi-SiOC-CDC increased to 126 F g^{-1} instead of an assumed loss of capacitance (Fig. 6F). It was already shown that aqueous supercapacitors with Na_2SO_4 can have a very high stability at high potentials which exceed the thermodynamic stability window of water of 1.2 V.[46] The improved performance after floating can be related to (i) progressing wetting,[47–50] and (ii) reversible faradaic redox-reactions of oxygen functional groups,[51] and reversible hydrogen reaction.[52–54]

A three-electrode cell with an Ag/AgCl reference electrode provides information about the potential development in the symmetrical setup (Fig. 6E). The initial electrodes have a zero-charge potential of +64 mV *versus* Ag/AgCl at a cell voltage of 1.4 V. The potential at the positive electrode is 0.70 V *versus* Ag/AgCl, exceeding the thermodynamic water oxidation of 0.64 V *versus* Ag/AgCl.[46] Also, the potential at the negative electrode is at −0.70 V *versus* Ag/AgCl below the limit of water reduction at −0.59 V *versus* Ag/AgCl.[46] The high potential at the positive electrode leads to the assumption that an irreversible oxidation of the carbon took place during the voltage holding at 1.4 V. The zero-charge potential was reduced from +64 mV to −93 mV *versus* Ag/AgCl after the longtime test which can be explained with an increase of oxygen containing functional groups on the carbon surface introduced by the oxidation at high cell voltages.

The aqueous Vi-SiOC-CDC cell was disassembled after the stability test to perform a post mortem analysis *via* gas sorption analysis, EDX, and contact angle measurements. By comparing the nitrogen sorption isotherms of the powder (Fig. 5A) with the isotherms of the electrodes (Fig. 7A) it is striking that the porosity is reduced. The addition of PTFE-binder leads to a smaller porosity due to an additional mass and pore blocking.[55] By comparing the isotherms of the initial electrode with the electrodes after the voltage floating in Fig. 7A, a significant pore volume loss is evident. Table S2† (ESI) supplies the detailed values obtained from the isotherms. The DFT surface area was reduced from 1756 $m^2 g^{-1}$ to 980 $m^2 g^{-1}$ at the negative and 897 $m^2 g^{-1}$ at the positive electrode. The total pore volume also decreased from 1.83 $m^2 g^{-1}$ to 1.23 $m^2 g^{-1}$ at the negative, and 1.19 $m^2 g^{-1}$ at the positive side, which might also be influenced by residual salt from the electrolyte. We see from the normalized pore size distribution in Fig. 7B (*i.e.*, normalized to 100%) that the pore volume is reduced mainly in the micropore range. The reduction of the micropores explains the loss of surface area of 49% compared to a relative low reduction of the total pore volume of 35% of the positive electrode. This is an indication for surface functionalities which block small micropores for N_2 during the GSA measurement. The increase of oxygen content further supports this assumption (Fig. 7D).

Post mortem EDX analysis was conducted, showing an increase in the oxygen-to-carbon ratio from 0.055 of the initial electrode to 0.075 on the negative, and 0.115 on the positive electrode after the voltage floating (ESI, Table S3†). The increase

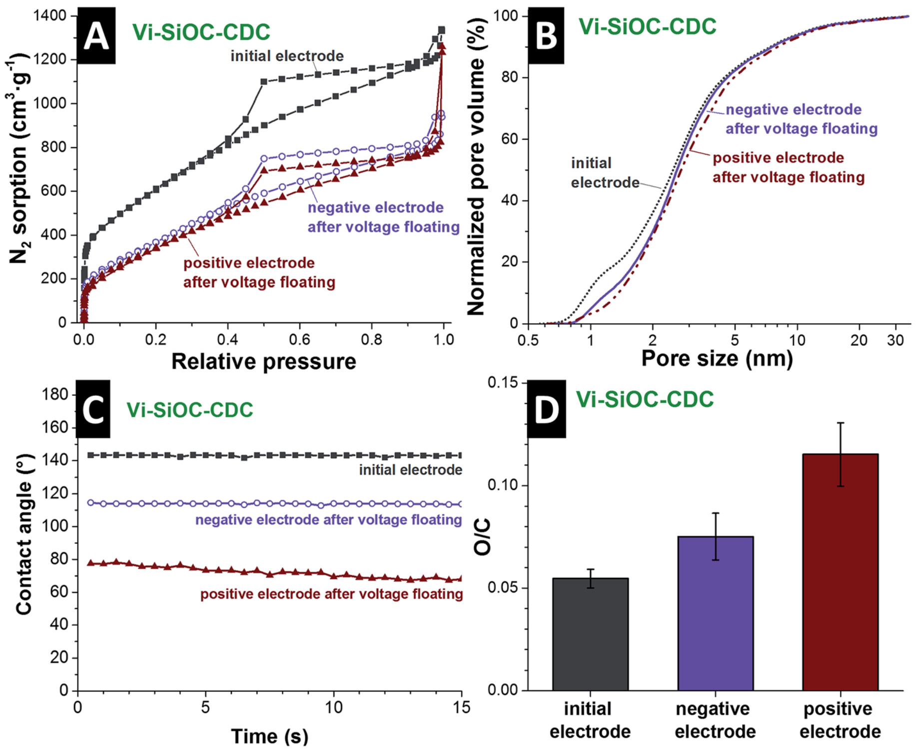

Fig. 7 Post mortem analysis of the Vi-SiOC-CDC electrodes after the voltage floating in aqueous 1 M Na_2SO_4 at 1.4 V cell voltage compared to the initial electrodes. N_2 gas sorption isotherms (A), normalized pore size distribution (B), contact angle (C), and the oxygen/carbon ratio measured *via* EDX (D).

of oxygen-containing functional groups also influences the wetting behavior of the electrodes (Fig. 7C). Initially, the Vi-SiOC-CDC electrode exhibits a contact angle with water of 143° after 1 s. This is relatively high compared to other highly porous carbon materials, like the AC with an initial contact angle of 63° (ref. 56) or CO_2-activated novolac-derived carbons with 121° (ref. 57). The contact angle of the negative electrode after the voltage floating is reduced to 114°. At the positive electrode, oxidation mainly takes place during electrochemical operation, leading to an even lower contact angle of 77° after 1 s and faster water absorption. Besides functional surface groups of the carbon, the contact angle is also influenced by the hydrophobic character of the PTFE-binder,[58] which allows only a relative comparison of the samples. The oxidation of the carbon surface and the permanent operation during the testing led to an increase of the wettability of the carbon. Thereby, we enabled enhanced access for the aqueous electrolyte to the surface of the CDCs, which led to an increase of the capacitance after the voltage floating of 16–29%.

4. Conclusions

In this study, phenyl- and vinyltrimethoxysilane mixtures with four different ratios were used to synthesize polysiloxane polymer beads. The MicroJet reactor technique allows continuous manufacturing of polysiloxanes beads with a constant quality at rates of 10–15 g min^{-1}. These beads were found as highly suited for pyrolysis, to obtain SiOC, and chlorine gas treatment, to obtain CDC by removal of non-carbon elements and still conserving the spherical morphology. An increase of phenyl groups increased the total yield after pyrolysis and etching from 2.2 mass% to 21.9 mass%, which is relevant for the economic efficiency to produce highly porous carbon materials. A possible way to increase the yield might be the use of organic functional groups with a higher amount of carbon, like naphthyl or anthracenyl groups. Also, the combination of the pyrolysis and chlorine treatment should be considered to improve the process.

By varying the ratio of phenyl and vinyl groups it was possible to produce highly porous CDCs with DFT SSA ranging between 2014-2198 m^2 g^{-1} with a total pore volume in the range of 1.27–2.06 cm^3 g^{-1} without any additional activation step. A higher amount of vinyl groups leads to a higher total pore volume. The increased mesoporosity influences mainly the rate handling behavior of the supercapacitor, while the specific capacitance at low ranges (5 mA g^{-1}) is in 1 M TEA-BF_4 in ACN very similar for all synthesized CDCs (106–116 F g^{-1}). The highest residual capacitance of 72% at high current rates (100 A g^{-1}) was also obtained from the sample with the highest amount of mesopores.

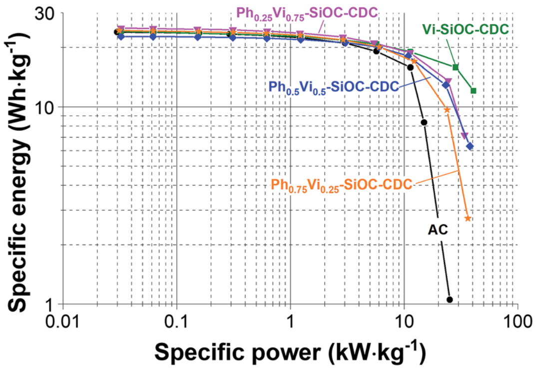

Fig. 8 Ragone chart of the four spherical CDC materials and the AC as comparison, measured in 1 M TEA-BF_4 in ACN (electrode thickness: 110–130 μm).

The Ragone chart (Fig. 8) illustrates the specific energy of the CDC materials of 25 W h kg^{-1} at low specific powers and the excellent performance at high specific power. In the best case (Vi-SiOC-CDC), the specific energy only decreases slightly to 12 W h kg^{-1} at high specific powers of 41 kW kg^{-1}. For comparison: AC shows a very low rate handling ability with only 1 W h kg^{-1} at 25 kW kg^{-1} (which is lower than any of the samples studied in this work). The low wettability of the relatively graphitic carbons is unfavorable for aqueous electrolytes, but a long-time testing shows an increase of the specific capacitance of almost 30% when floated at 1.4 V for 100 h. Functional groups are formed by the operation, which improves the wettability as well as the specific capacitance.

In conclusion, the high porosity of the SiOC-CDCs is attractive for electrochemical energy storage with supercapacitors. The excellent rate handling behavior and the high stability in organic electrolyte documents suitability for common supercapacitors.

Acknowledgements

The INM authors kindly acknowledge the continuing support of Prof. Eduard Arzt (INM). We also thank Robert Drumm (INM) for the TGA-MS, Dr Ingrid Grobelsek (INM) for the help with the SEM, Dr Michael Zimmer (UdS) for CP-MAS NMR, and Juhan Lee, Simon Fleischmann, and Nicolas Jäckel (all INM) for fruitful discussions and their support. The INM acknowledges funding from the German Federal Ministry for Research and Education (BMBF) in support of the nanoEES^{3D} project (award number 03EK3013) as part of the strategic funding initiative energy storage framework.

References

1 L. Schlapbach and A. Züttel, Hydrogen-Storage Materials for Mobile Applications, *Nature*, 2001, **414**(6861), 353–358.
2 R. E. Morris and P. S. Wheatley, Gasspeicherung in Nanoporösen Materialien, *Angew. Chem.*, 2008, **120**(27), 5044–5059.
3 A. Taguchi and F. Schüth, Ordered Mesoporous Materials in Catalysis, *Microporous Mesoporous Mater.*, 2005, **77**(1), 1–45.
4 P. Simon and Y. Gogotsi, Materials for Electrochemical Capacitors, *Nat. Mater.*, 2008, **7**(11), 845–854.
5 M. Lu, F. Beguin, E. Frackowiak, *Supercapacitors: Materials, Systems and Applications*, John Wiley & Sons, 2013.
6 M. Salanne, B. Rotenberg, K. Naoi, K. Kaneko, P.-L. Taberna, C. P. Grey, B. Dunn and P. Simon, Efficient Storage

Mechanisms for Building Better Supercapacitors, *Nat. Energy*, 2016, **1**, 16070.

7 V. Presser, M. Heon and Y. Gogotsi, Carbide-Derived Carbons–From Porous Networks to Nanotubes and Graphene, *Adv. Funct. Mater.*, 2011, **21**(5), 810–833.

8 R. Dash, G. Yushin and Y. Gogotsi, Synthesis, Structure and Porosity Analysis of Microporous and Mesoporous Carbon Derived from Zirconium Carbide, *Microporous Mesoporous Mater.*, 2005, **86**(1), 50–57.

9 S.-H. Yeon, P. Reddington, Y. Gogotsi, J. E. Fischer, C. Vakifahmetoglu and P. Colombo, Carbide-Derived-Carbons with Hierarchical Porosity from a Preceramic Polymer, *Carbon*, 2010, **48**(1), 201–210.

10 C. Vakifahmetoglu, V. Presser, S.-H. Yeon, P. Colombo and Y. Gogotsi, Enhanced Hydrogen and Methane Gas Storage of Silicon Oxycarbide Derived Carbon, *Microporous Mesoporous Mater.*, 2011, **144**(1), 105–112.

11 V. Presser, J. McDonough, S.-H. Yeon and Y. Gogotsi, Effect of Pore Size on Carbon Dioxide Sorption by Carbide Derived Carbon, *Energy Environ. Sci.*, 2011, **4**(8), 3059–3066.

12 S. Welz, M. J. McNallan and Y. Gogotsi, Carbon Structures in Silicon Carbide Derived Carbon, *J. Mater. Process. Technol.*, 2006, **179**(1), 11–22.

13 A. Tolosa, B. Krüner, N. Jäckel, M. Aslan, C. Vakifahmetoglu and V. Presser, Electrospinning and Electrospraying of Silicon Oxycarbide-Derived Nanoporous Carbon for Supercapacitor Electrodes, *J. Power Sources*, 2016, **313**, 178–188.

14 V. Bakumov, M. Schwarz and E. Kroke, Emulsion Processing and Size Control of Polymer-Derived Spherical Si/C/O Ceramic Particles, *Soft Mater.*, 2007, **4**(2–4), 287–299.

15 M. Oschatz, M. Zeiger, N. Jäckel, P. Strubel, L. Borchardt, R. Reinhold, W. Nickel, J. Eckert, V. Presser and S. Kaskel, Emulsion Soft Templating of Carbide-Derived Carbon Nanospheres with Controllable Porosity for Capacitive Electrochemical Energy Storage, *J. Mater. Chem. A*, 2015, **3**(35), 17983–17990.

16 A. Guo, M. Roso, M. Modesti, J. Liu and P. Colombo, Preceramic Polymer-Derived SiOC Fibers by Electrospinning, *J. Appl. Polym. Sci.*, 2014, **131**(3), 39836.

17 S. A. Khan, A. Günther, M. A. Schmidt and K. F. Jensen, Microfluidic Synthesis of Colloidal Silica, *Langmuir*, 2004, **20**(20), 8604–8611.

18 N. Jongen, M. Donnet, P. Bowen, J. Lemaître, H. Hofmann, R. Schenk, C. Hofmann, M. Aoun-Habbache, S. Guillemet-Fritsch and J. Sarrias, Development of a Continuous Segmented Flow Tubular Reactor and the "Scale-out" Concept–In Search of Perfect Powders, *Chem. Eng. Technol.*, 2003, **26**(3), 303–305.

19 B. Penth, Kontinuierliche Fällung von Nanoskaligen Produkten in Mikroreaktoren, German Patent DE102006004350 A1, 2007.

20 B. Dittert, A. Gavrilović, S. Schwarz, P. Angerer, H. Steiner and R. Schöftner, Phase Content Controlled TiO_2 Nanoparticles using the MicroJetReactor Technology, *J. Eur. Ceram. Soc.*, 2011, **31**(14), 2475–2480.

21 A. Rüfer, K. Räuchle, F. Krahl and W. Reschetilowski, Kontinuierliche Darstellung von Bariumsulfat-Nanopartikeln im MicroJet-Reaktor, *Chem. Ing. Tech.*, 2009, **81**(12), 1949–1954.

22 A. Betke and G. Kickelbick, Bottom-Up, Wet Chemical Technique for the Continuous Synthesis of Inorganic Nanoparticles, *Inorganics*, 2014, **2**(1), 1–15.

23 A. Matsuda, T. Sasaki, K. Hasegawa, M. Tatsumisago and T. Minami, Thermal Softening Behavior of Poly (Phenylsilsesquioxane) and Poly (Benzylsilsesquioxane) Particles, *J. Ceram. Soc. Jpn.*, 2000, **108**(1261), 830–835.

24 K. Katagiri, K. Hasegawa, A. Matsuda, M. Tatsumisago and T. Minami, Preparation of Transparent Thick Films by Electrophoretic Sol-Gel Deposition Using Phenyltriethoxysilane-Derived Particles, *J. Am. Ceram. Soc.*, 1998, **81**(9), 2501–2503.

25 C. A. Schneider, W. S. Rasband and K. W. Eliceiri, NIH Image to ImageJ: 25 Years of Image Analysis, *Nat. Methods*, 2012, **9**(7), 671.

26 G. Y. Gor, M. Thommes, K. A. Cychosz and A. V. Neimark, Quenched Solid Density Functional Theory Method for Characterization of Mesoporous Carbons by Nitrogen Adsorption, *Carbon*, 2012, **50**(4), 1583–1590.

27 S. Brunauer, P. H. Emmett and E. Teller, Adsorption of Gases in Multimolecular Layers, *J. Am. Chem. Soc.*, 1938, **60**(2), 309–319.

28 D. Weingarth, M. Zeiger, N. Jäckel, M. Aslan, G. Feng and V. Presser, Graphitization as a Universal Tool to Tailor the Potential-Dependent Capacitance of Carbon Supercapacitors, *Adv. Energy Mater.*, 2014, **4**(13), 1400316.

29 R. K. Sharma, S. Das and A. Maitra, Surface Modified Ormosil Nanoparticles, *J. Colloid Interface Sci.*, 2004, **277**(2), 342–346.

30 A. Arkhireeva and J. N. Hay, Synthesis of Sub-200 nm Silsesquioxane Particles using a Modified Stöber Sol–Gel Route, *J. Mater. Chem.*, 2003, **13**(12), 3122–3127.

31 J. Macan, K. Tadanaga and M. Tatsumisago, Influence of Copolymerization with Alkyltrialkoxysilanes on Condensation and Thermal Behaviour of Poly (Phenylsilsesquioxane) Particles, *J. Sol-Gel Sci. Technol.*, 2010, **53**(1), 31–37.

32 J. F. Brown Jr, L. H. Vogt Jr, A. Katchman, J. W. Eustance, K. M. Kiser and K. W. Krantz, Double Chain Polymers of Phenylsilsesquioxane, *J. Am. Chem. Soc.*, 1960, **82**(23), 6194–6195.

33 Z. Li, X. Cao, H. Xu, P. Xie, M. Cao and R. Zhang, Synthesis and Characterization of Reactive Ladderlike Polyallylsilsesquioxane and Polyvinylsilsesquioxane, *React. Funct. Polym.*, 1999, **39**(1), 1–7.

34 P. Scherrer, Bestimmung der Größe und der inneren Struktur von Kolloidteilchen mittels Röntgenstrahlen, *Nachrichten von der Gesellschaft der Wissenschaften zu Göttingen*, 1918, **2**, 3.

35 S.-S. Choi, A. S. Lee, S. S. Hwang and K.-Y. Baek, Structural Control of Fully Condensed Polysilsesquioxanes: Ladderlike vs Cage Structured Polyphenylsilsesquioxanes, *Macromolecules*, 2015, **48**(17), 6063–6070.

36 A. C. Ferrari and J. Robertson, Interpretation of Raman Spectra of Disordered and Amorphous Carbon, *Phys. Rev. B: Condens. Matter Mater. Phys.*, 2000, **61**(20), 14095.

37 V. Presser, L. Zhang, J. J. Niu, J. McDonough, C. Perez, H. Fong and Y. Gogotsi, Flexible Nano-felts of Carbide-Derived Carbon with Ultra-high Power Handling Capability, *Adv. Energy Mater.*, 2011, **1**(3), 423–430.

38 Y. Gao, V. Presser, L. Zhang, J. J. Niu, J. K. McDonough, C. R. Pérez, H. Lin, H. Fong and Y. Gogotsi, High Power Supercapacitor Electrodes Based on Flexible TiC-CDC Nano-felts, *J. Power Sources*, 2012, **201**, 368–375.

39 A. Scarmi, G. D. Sorarù and R. Raj, The Role of Carbon in Unexpected Visco (an) Elastic Behavior of Amorphous Silicon Oxycarbide Above 1273K, *J. Non-Cryst. Solids*, 2005, **351**(27), 2238–2243.

40 H.-J. Kleebe and Y. D. Blum, SiOC Ceramic with High Excess Free Carbon, *J. Eur. Ceram. Soc.*, 2008, **28**(5), 1037–1042.

41 N. Jäckel, D. Weingarth, A. Schreiber, B. Krüner, M. Zeiger, A. Tolosa, M. Aslan and V. Presser, Performance Evaluation of Conductive Additives for Activated Carbon Supercapacitors in Organic Electrolyte, *Electrochim. Acta*, 2016, **191**, 284–298.

42 C. R. Pérez, S. H. Yeon, J. Ségalini, V. Presser, P. L. Taberna, P. Simon and Y. Gogotsi, Structure and Electrochemical Performance of Carbide-Derived Carbon Nanopowders, *Adv. Funct. Mater.*, 2013, **23**(8), 1081–1089.

43 D. Weingarth, H. Noh, A. Foelske-Schmitz, A. Wokaun and R. Kötz, A Reliable Determination Method of Stability Limits for Electrochemical Double Layer Capacitors, *Electrochim. Acta*, 2013, **103**, 119–124.

44 D. Weingarth, A. Foelske-Schmitz and R. Kötz, Cycle versus Voltage Hold–Which is the better Stability Test for Electrochemical Double Layer Capacitors?, *J. Power Sources*, 2013, **225**, 84–88.

45 J. Busom, A. Schreiber, A. Tolosa, N. Jäckel, I. Grobelsek, N. J. Peter and V. Presser, Sputtering of Sub-Micrometer Aluminum Layers as Compact, High-Performance, Light-Weight Current Collector for Supercapacitors, *J. Power Sources*, 2016, **329**, 432–440.

46 M. Bichat, E. Raymundo-Piñero and F. Béguin, High Voltage Supercapacitor Built with Seaweed Carbons in Neutral Aqueous Electrolyte, *Carbon*, 2010, **48**(15), 4351–4361.

47 J. Lee, D. Weingarth, I. Grobelsek and V. Presser, Use of Surfactants for Continuous Operation of Aqueous Electrochemical Flow Capacitors, *Energy Technol.*, 2016, **4**(1), 75–84.

48 K. Fic, G. Lota and E. Frackowiak, Effect of Surfactants on Capacitance Properties of Carbon Electrodes, *Electrochim. Acta*, 2012, **60**, 206–212.

49 M. Aslan, D. Weingarth, P. Herbeck-Engel, I. Grobelsek and V. Presser, Polyvinylpyrrolidone/Polyvinyl Butyral Composite as a Stable Binder for Castable Supercapacitor Electrodes in Aqueous Electrolytes, *J. Power Sources*, 2015, **279**, 323–333.

50 J. Lee, S. Kim and J. Yoon, Rocking Chair Desalination Battery Based on Prussian Blue Electrodes, *ACS Omega*, 2017, **2**(4), 1653–1659.

51 K. Fic, M. Meller, J. Menzel and E. Frackowiak, Around the Thermodynamic Limitations of Supercapacitors Operating in Aqueous Electrolytes, *Electrochim. Acta*, 2016, **206**, 496–503.

52 E. Frackowiak and F. Beguin, Electrochemical Storage of Energy in Carbon Nanotubes and Nanostructured Carbons, *Carbon*, 2002, **40**(10), 1775–1787.

53 J. Lee, A. Tolosa, B. Krüner, N. Jäckel, S. Fleischmann, M. Zeiger, D. Kim and V. Presser, Asymmetric Tin–Vanadium Redox Electrolyte for Hybrid Energy Storage with Nanoporous Carbon Electrodes, *Sustainable Energy Fuels*, 2017, **1**, 9.

54 J. Lee, B. Krüner, A. Tolosa, S. Sathyamoorthi, D. Kim, S. Choudhury, K.-H. Seo and V. Presser, Tin/Vanadium Redox Electrolyte for Battery-like Energy Storage Capacity Combined with Supercapacitor-like Power Handling, *Energy Environ. Sci.*, 2016, **9**(11), 3392–3398.

55 N. Jäckel, D. Weingarth, M. Zeiger, M. Aslan, I. Grobelsek and V. Presser, Comparison of Carbon Onions and Carbon Blacks as Conductive Additives for Carbon Supercapacitors in Organic Electrolytes, *J. Power Sources*, 2014, **272**, 1122–1133.

56 M. Aslan, M. Zeiger, N. Jäckel, I. Grobelsek, D. Weingarth and V. Presser, Improved Capacitive Deionization Performance of Mixed Hydrophobic/Hydrophilic Activated Carbon Electrodes, *J. Phys.: Condens. Matter*, 2016, **28**(11), 114003.

57 B. Krüner, P. Srimuk, S. Fleischmann, M. Zeiger, A. Schreiber, M. Aslan, A. Quade and V. Presser, Hydrogen-treated, Sub-micrometer Carbon Beads for Fast Capacitive Deionization with High Performance Stability, *Carbon*, 2017, **117**, 46–54.

58 A. Kolodziej, K. Fic and E. Frackowiak, Towards Sustainable Power Sources: Chitin-Bound Carbon Electrodes for Electrochemical Capacitors, *J. Mater. Chemi. A*, 2015, **3**(45), 22923–22930.

59 M. Zeiger, N. Jäckel, D. Weingarth and V. Presser, Vacuum or Flowing Argon: What is the Best Synthesis Atmosphere for Nanodiamond-Derived Carbon Onions for Supercapacitor Electrodes?, *Carbon*, 2015, **94**, 507–517.

60 C. Schneidermann, N. Jäckel, S. Oswald, L. Giebeler, V. Presser and L. Borchardt, Solvent-Free Mechanochemical Synthesis of Nitrogen-Doped Nanoporous Carbon for Electrochemical Energy Storage, *ChemSusChem*, 2017, **10**(11), 2416–2424.

Electronic Supplementary Material (ESI) for Sustainable Energy & Fuels.

SUPPORTING INFORMATION

Carbide-derived carbon beads with tunable nanopores from continuously produced polysilsesquioxanes for supercapacitor electrodes

Benjamin Krüner,[1,2,ᶦ] Christina Odenwald,[3,ᶦ] Aura Tolosa,[1,2] Anna Schreiber,[1]
Mesut Aslan,[1] Guido Kickelbick,[3,*] and Volker Presser[1,2,*]

[1] *INM - Leibniz Institute for New Materials, 66123 Saarbrücken, Germany*

[2] *Department of Materials Science and Engineering, Saarland University, 66123 Saarbrücken, Germany*

[3] *Inorganic Solid State Chemistry, Saarland University, 66123 Saarbrücken, Germany*

ᶦ *these authors contributed equally*

* *Corresponding authors' eMails:*
guido.kickelbick@uni-saarland.de *(G. Kickelbick);* volker.presser@leibniz-inm.de *(V. Presser)*

Table S1: Properties of the PTFE-bound electrodes.

	Electrode density ($mg \cdot cm^{-3}$)	Active mass of one electrode (mg)	Electrode disc diameter (mm)	Electrode thickness (µm)
1 M TEA-BF_4 in acetonitrile				
Vi-SiOC-CDC	197	1.15	8	122
$Ph_{0.25}Vi_{0.75}$-SiOC-CDC	372	2.33	8	131
$Ph_{0.5}Vi_{0.5}$-SiOC-CDC	452	2.51	8	116
$Ph_{0.75}Vi_{0.25}$-SiOC-CDC	438	2.41	8	115
AC	435	2.27	8	109
Aqueous 1 M Na_2SO_4				
Vi-SiOC-CDC	206	1.47	8	150
$Ph_{0.25}Vi_{0.75}$-SiOC-CDC	377	2.24	8	124
$Ph_{0.5}Vi_{0.5}$-SiOC-CDC	450	2.51	8	117
$Ph_{0.75}Vi_{0.25}$-SiOC-CDC	432	2.44	8	118

Table S2: Porosity of the Vi-SiOC-CDC electrodes measured with nitrogen gas sorption.

	SSA_{DFT} ($m^2 \cdot g^{-1}$)	SSA_{DFT} loss after voltage floating (%)	SSA_{BET} ($m^2 \cdot g^{-1}$)	Total pore volume ($cm^3 \cdot g^{-1}$)	Total pore volume loss after voltage floating (%)	Average pore size (nm)
Vi-SiOC-CDC initial electrode	1756	-	2287	1.83	-	2.5
Vi-SiOC-CDC negative electrode	980	44	1515	1.23	34	2.6
Vi-SiOC-CDC positive electrode	897	49	1403	1.19	35	2.8

Table S3: EDX element analysis of Vinyl-SiOC-CDC electrodes before the electrochemical testing and after the voltage floating at 1.4 V for 100 h in aqueous 1 M Na_2SO_4. Values below the detection limit are denoted n.d. (not detected).

	C (mass%)	O (mass%)	Si (mass%)	F (mass%)	Na (mass%)	S (mass%)	Cl (mass%)
Vi-SiOC-CDC initial electrode	89.5±0.6	4.1±0.3	3.5±0.3	2.9±0.3	n.d.	n.d.	n.d.
Vi-SiOC-CDC positive electrode	81.3±1.3	7.4±1.0	1.6±0.3	3.5±1.1	4.6±0.6	0.7±0.2	0.9±0.2
Vi-SiOC-CDC negative electrode	81.3±0.5	4.4±0.8	2.2±0.1	6.6±1.6	4.4±0.4	0.5±0.1	0.7±0.1

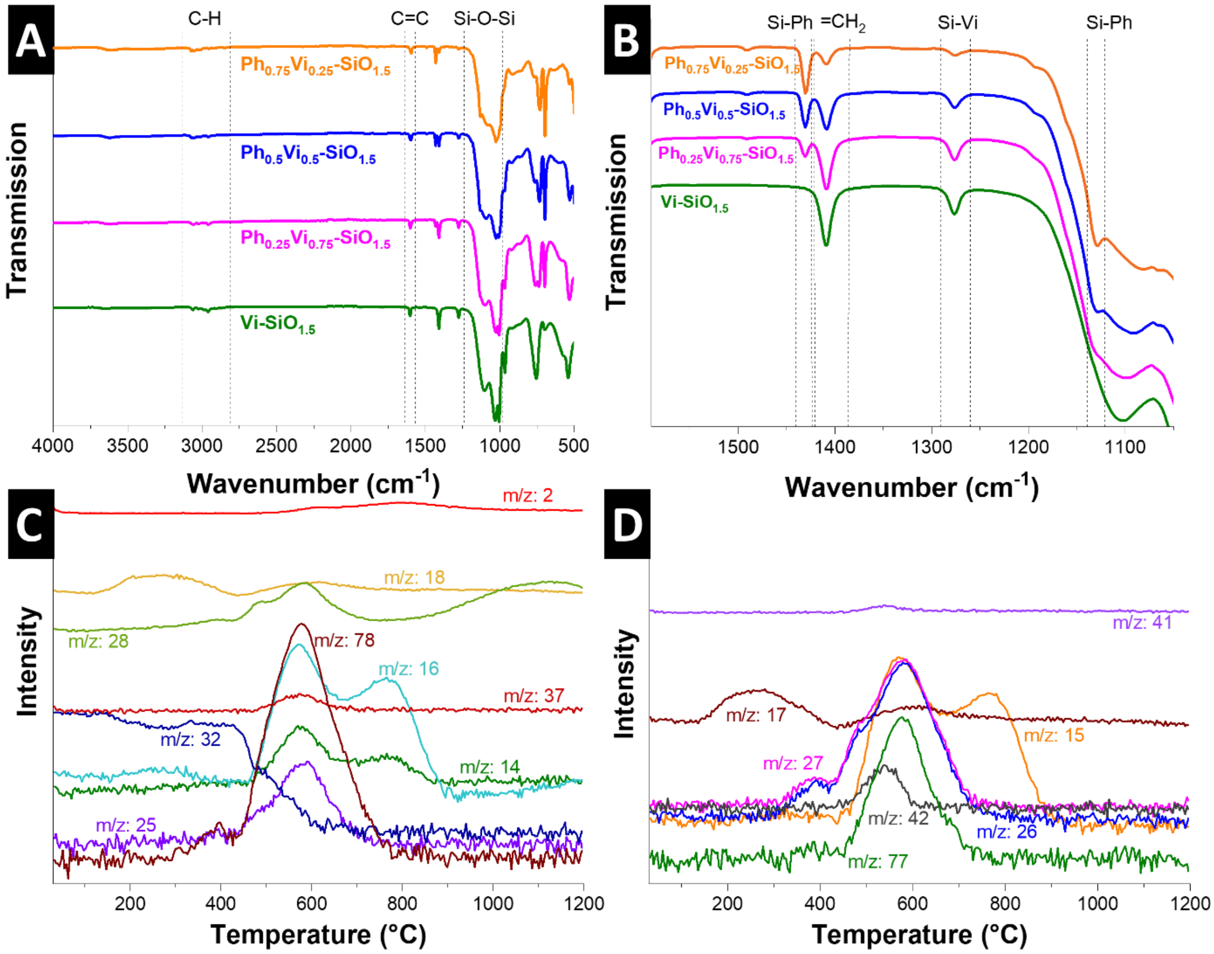

Figure S1: Overview of the FT-IR spectra of the four polymer beads (A) and detailed spectra in the range of 1000-1600 cm^{-1} (B). The corresponding mass spectra of $Ph_{0.5}Vi_{0.5}$-$SiO_{1.5}$ to the thermogram shown in Fig. 2D of relevant evolving groups (C) and (D).

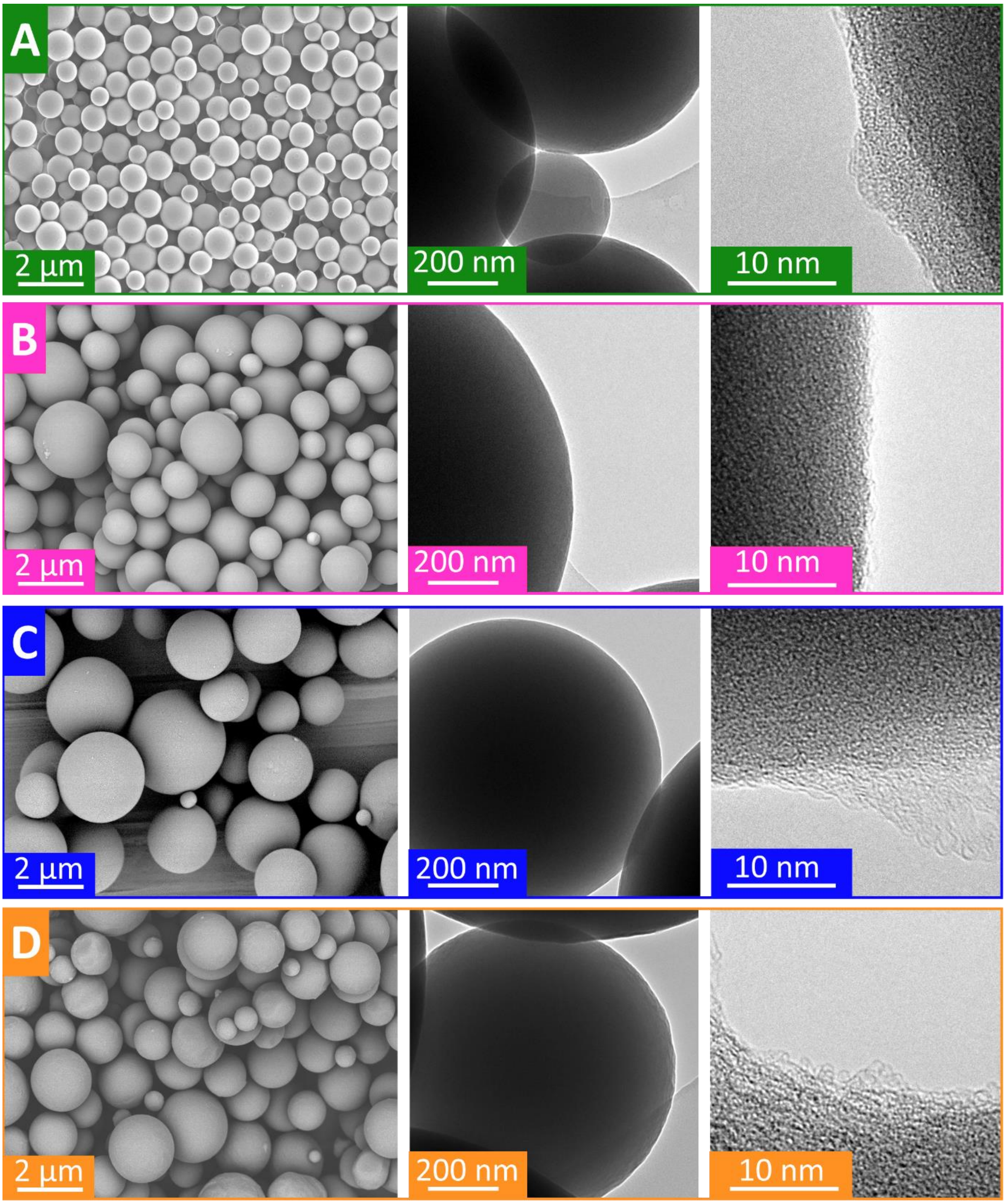

Figure S2: Scanning and transmission electron micrographs of the polymer beads Vi-$SiO_{1.5}$ (A), $Ph_{0.25}Vi_{0.75}$-$SiO_{1.5}$ (B), $Ph_{0.5}Vi_{0.5}$-$SiO_{1.5}$ (C), and $Ph_{0.75}Vi_{0.25}$-$SiO_{1.5}$ (D).

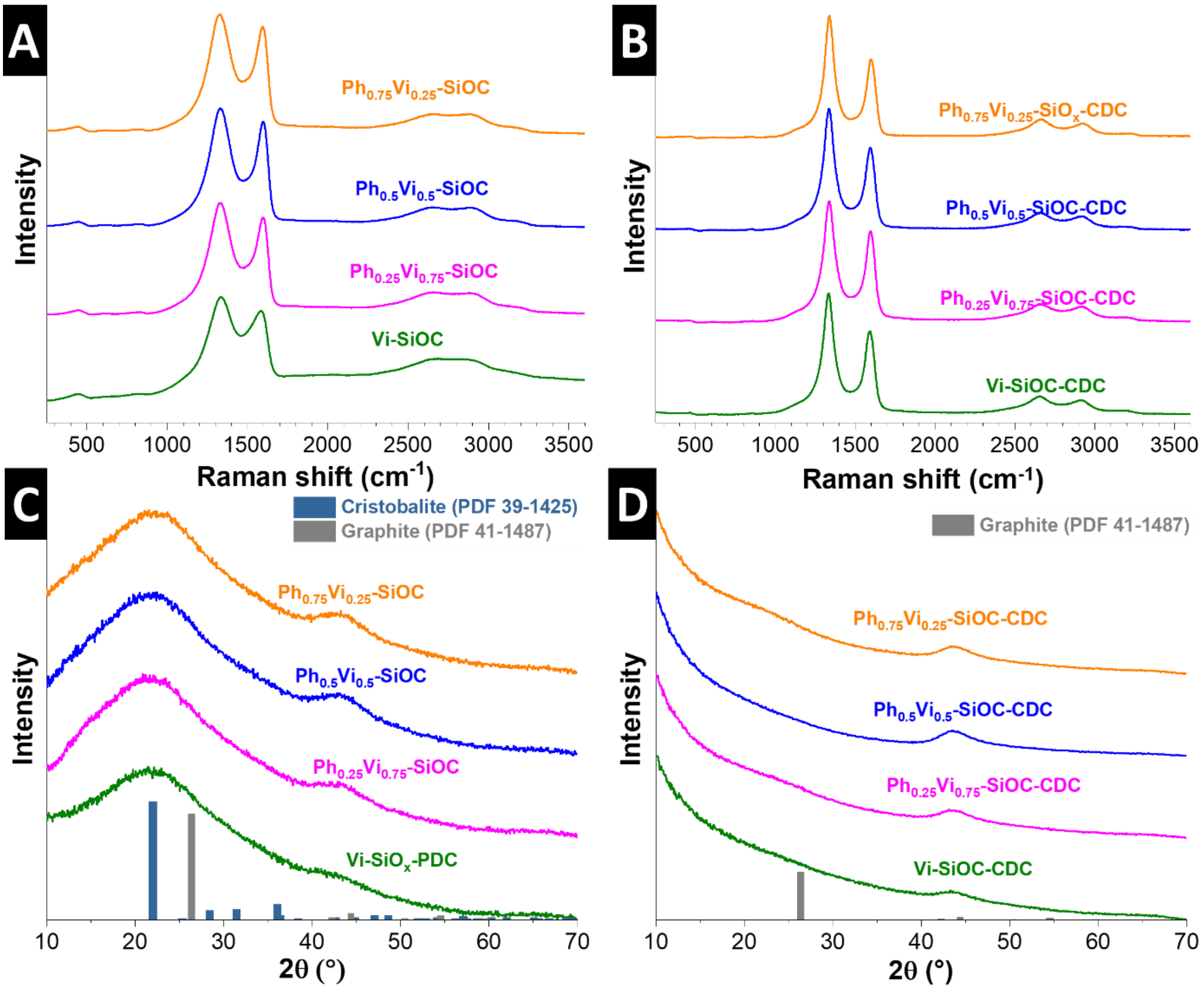

Figure S3: Raman spectra of PDCs (A) and CDCs (B). XRD pattern of PDCs (C) and CDCs (D).

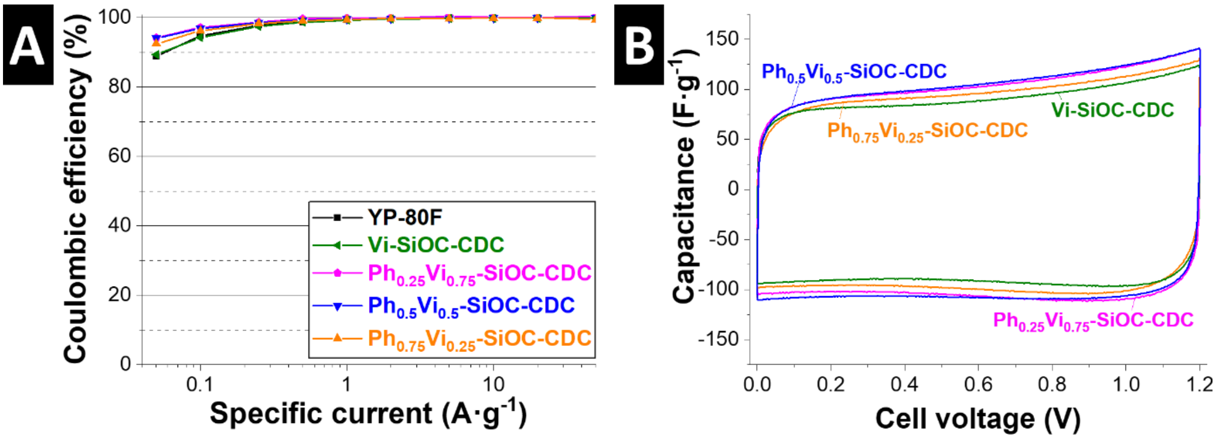

Figure S4: Coulombic efficiencies of all CDC materials including the AC in TEA-BF_4 in ACN (A) and cyclic voltammograms of all CDC samples in aqueous 1 M Na_2SO_4 (B) up to a cell voltage of 1.2 V.

4.6. Influence of nitrogen-doping for carbide-derived carbons on the supercapacitor performance in an organic electrolyte and an ionic liquid

Benjamin Krüner,[1,2] **Christina Odenwald,**[3] **Antje Quade,**[4] **Guido Kickelbick,**[3]

Volker Presser[1,2]

[1] *INM - Leibniz Institute for New Materials, 66123 Saarbrücken, Germany*

[2] *Department of Materials Science and Engineering, Saarland University, 66123 Saarbrücken, Germany*

[3] *Inorganic Solid State Chemistry, Saarland University, 66123 Saarbrücken, Germany*

[4] *Leibniz Institute for Plasma Science and Technology, 17489 Greifswald, Germany*

Krüner, Benjamin et al. (2018) *Batteries & Supercaps*.
https://doi.org/10.1002/batt.201800051

Own contribution: Design, planning, writing, pyrolysis, chlorine gas treatment, SEM, particle size analysis, EDX analysis, TGA coupled with MS analysis, CO_2 and N_2 sorption analysis, Raman analysis, XRD, electrochemical analysis for double-layer capacitors.

Abstract:

We investigated the influence of nitrogen groups on the electrochemical performance of carbide-derived carbons by using materials with a similar pore structure with and without a nitrogen-doping. These materials were tested in a half-cell and full-cell supercapacitor using a conventional organic electrolyte (1 M tetraethylammonium tetrafluoroborate in acetonitrile) and an ionic liquid (1-ethyl-3-methylimidazolium tetrafluoroborate). We found that the nitrogen-groups with a content of 1-7 mass% have no systematic influence on the energy storage capacity but a stronger impact on the rate handling ability. The highest specific capacitance in a half-cell supercapacitor at a negative potential was 215 F/g in EMIM-BF_4. Using the best-performing carbide-derived carbon with and without nitrogen-doping (i.e., by using a synthesis temperature of 800 °C), the full-cell performance was 174 F/g, which results in the high specific energy of 61 Wh/kg in EMIM-BF_4. For the same materials, the corresponding specific energy was about 30 Wh/kg when using the organic electrolyte.

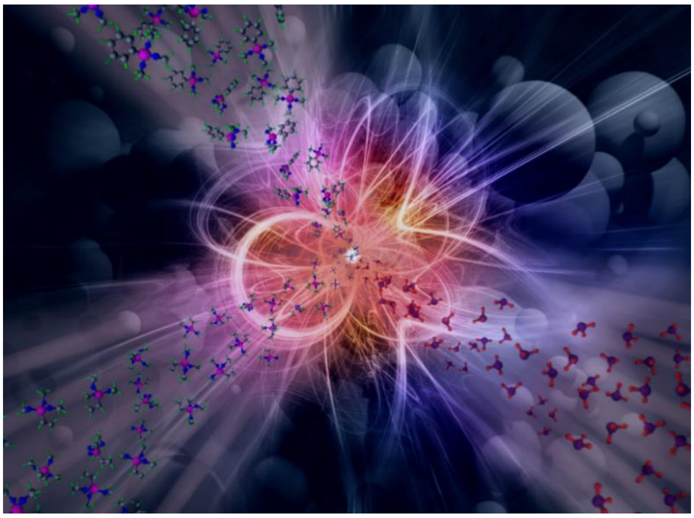

ChemPubSoc Europe
DOI: 10.1002/batt.201800051
BATTERIES & SUPERCAPS
Articles

Influence of Nitrogen-Doping for Carbide-Derived Carbons on the Supercapacitor Performance in an Organic Electrolyte and an Ionic Liquid

Benjamin Krüner,[a] Christina Odenwald,[b] Antje Quade,[c] Guido Kickelbick,*[b] and Volker Presser*[a]

We investigated the influence of nitrogen groups on the electrochemical performance of carbide-derived carbons by comparing materials with a similar pore structure with and without nitrogen-doping. These materials were tested in a half-cell and full-cell supercapacitor setup with a conventional organic electrolyte (1 M tetraethylammonium tetrafluoroborate in acetonitrile) and an ionic liquid (1-ethyl-3-methylimidazolium tetrafluoroborate). Varying the nitrogen content in the range of 1–7 mass% had no systematic influence on the energy storage capacity but a stronger impact on the rate handling ability. The highest specific capacitance in a half-cell supercapacitor at a negative potential was 215 F/g in EMIM-BF_4. Using the best-performing carbide-derived carbon with and without nitrogen-doping (i.e., by applying a synthesis temperature of 800 °C), the full-cell performance was 174 F/g, which results in a high specific energy of 61 Wh/kg in EMIM-BF_4. For the same materials, the corresponding specific energy was about 30 Wh/kg when using the organic electrolyte.

1. Introduction

Supercapacitors are electrochemical energy storage devices for high power applications with long cycling stability.[1–3] The most common type of supercapacitor is the electrical double-layer capacitor (EDLC) where the charge is stored by electrosorption of ions from an electrolyte on a high surface area electrode.[1] Electrodes for EDLCs are usually carbon-based, and various materials have been explored, including activated carbons,[4–6] salt-templated carbons,[7–9] graphene,[10] carbon-nanotubes,[11] carbon onions,[12,13] and carbide-derived carbons (CDC).[14,15] Especially nanoporous carbons with a high surface area are well suited to provide high specific energy and power.[3,16] One way to further increase the energy storage capacity of a porous carbon electrode is to choose an average pore size close to the diameter of the bare ion.[17–19] This effect can be explained by the partial desolvation of the ions in aqueous or organic electrolytes and the resulting more space-effective arrangement of ions within nanopores.[18–22]

Beyond the design of carbon materials with an optimized porosity, there are other ways to enhance the energy storage capacity of supercapacitors.[1,16,23] Examples include the use of ionic liquids[1,7] or redox electrolytes,[5,24–27] and the addition of a redox-active material like metal oxides[28–31] or heteroatom doping.[32] Especially the use of ionic liquids as an electrolyte for supercapacitors is promising because the significantly enhanced potential window leads to a large increase of the specific energy (the latter scales with the square of the voltage).[1] Along with this line of research, Ewert et al. reported that nitrogen-doping of CDC leads to an enhanced specific capacitance for certain ionic liquids, such as EMIM-BF_4, while there was no enhancement for organic electrolytes based on acetonitrile as the solvent.[32] Also, other groups investigated nitrogen-doped carbon materials made from different precursors and reported high specific energy of up to 64 Wh/kg (measured at a cell voltage of 3.2 V).[6,7,33,34] Yan et al. used EMIM-BF_4 as the electrolyte and different micro- and mesoporous carbons as the electrodes in symmetric full-cells.[7] The specific capacitance and rate capability of these porous carbon materials with and without nitrogen-doping (up to 6 mass%) were quite similar, but there was an improvement of the rate capability for the nitrogen-containing electrodes.[7] Yet, the comparison of half-cell and full-cell data complicates the identification of underlying energy storage mechanisms during ion electrosorption, and our understanding of the general role of nitrogen in different forms (pyridinic, graphitic, etc.) remains limited at present.

Due to the influence of the pore size distribution on the double-layer capacitance,[20] it is necessary to produce carbon materials with a similar porosity to investigate the contribution of the nitrogen groups. In a previous study, we applied the MicroJet reactor technique to produce SiOC-CDC and varied the ratio of silanes with different organic groups.[35] Thereby, it

---

[a] B. Krüner, Prof. Dr. V. Presser
INM – Leibniz Institute for New Materials
66123 Saarbrücken, Germany
Department of Materials Science and Engineering
Saarland University
66123 Saarbrücken, Germany
E-mail: volker.presser@leibniz-inm.de
[b] C. Odenwald, Prof. Dr. G. Kickelbick
Inorganic Solid State Chemistry
Saarland University
66123 Saarbrücken, Germany
E-mail: guido.kickelbick@uni-saarland.de
[c] Dr. A. Quade
Leibniz Institute for Plasma Science and Technology
Felix-Hausdorff-Straße 2
17489 Greifswald, Germany

Supporting information for this article is available on the WWW under https://doi.org/10.1002/batt.201800051 was possible to adjust the porosity of the highly porous carbon material. The continuous MicroJet technique ensures a constant quality of polysilsesquioxane beads with homogeneous particle size. In the present study, we used a similar approach but varied the organic group to introduce nitrogen via silane to the ceramic material. Nitrogen in the carbide can still be found in the CDC material after chlorine gas treatment, as we know from previous work.[32] We produced CDCs also with another silane to obtain porous carbon materials without nitrogen with a similar pore size distribution (average pore size of 1.6–1.9 nm and 94–99 % of the pore volume relates to pores smaller than 5 nm). Thereby, our materials cover the range of nitrogen concentration of 0–7 mass %. The materials were tested as electrodes for supercapacitors in half-cell and full-cell configuration in 1 M TEA-BF_4 in acetonitrile (ACN) and neat ionic liquid (EMIM-BF_4).

Experimental

Materials and Material Synthesis

Vinyltrimethoxysilane (VTMS) and 4-phenylbutyltrimethoxysilane (PBTMS) were obtained from ABCR. [3-(phenylamino)propyl]trimethoxysilane (PAPTMS) was purchased from Sigma-Aldrich. The structural formulae of the silanes precursors are shown in the *Supporting Information*, Figure S1. Ammonia was purchased from VWR International. All chemicals were used as received.

The polymer spheres were produced by mixing the precursor solutions A1/A2 and B in a microreactor. Solution A1 contained VTMS (37.04 g, 250 mmol) and PAPTMS (12.81 g, 50 mmol) dissolved in methanol (307.58 g, 9.6 mol). For the A2 solution, PBTMS (12.76 g, 50 mmol) was used instead of PAPTMS. The alkoxysilanes were partly hydrolyzed by adding aqueous HCl (150 mL of a 0.55 mmol/L solution) and stirring at room temperature for 16 h.[36] The solution B was an aqueous solution of ammonia (2.2 mol/L).

The synthesis of similar particles with the same technical setup is described in detail in previous work.[35,36] In short: two HPLC pumps (LaPrep P110 preparative HPLC pumps, VWR International) transport solution A1 or A2 and solution B at a rate of 250 mL/min (pressure of 3–4 MPa) to the MicroJet reactor (Synthesechemie Dr. Penth GmbH). The solutions enter the reactor chamber through narrow nozzles (300 μm in diameter) from opposing sites and collide inside as fine impinging jets. A fast mixing takes place before a support gas flow forces the suspension out of the microreactor in vertical direction out to a collecting vessel. The particles were separated by centrifugation (8000 rpm, 7012 G, 10 min) and dried in vacuum at room temperature. The reactor system was flushed with methanol between the production of different samples.

The pyrolysis of the polysilsesquioxane beads was carried out in a graphite heated furnace (LHTG from Carbolite Gero) in a nitrogen atmosphere with a gas flow of 150 L/h. The target temperature of 1000 °C was reached with a heating rate of 300 °C/h, and we used a holding time of 2 h. A mass of 1.5 g of the obtained polymer-derived ceramic (PDC) was transferred to a graphite crucible and placed in a quartz tube furnace from Carbolite Gero. The chlorine gas treatment to produce carbide-derived carbon (CDC) spheres was performed at 600 °C, 800 °C, or 1000 °C for 5 h with a chlorine gas flow of 10 cm^3/min. The quartz tube furnace was constantly supplied with argon (flow: 50 cm^3/min) during the chlorine gas treatment including the heating and cooling step. A hydrogen treatment at 600 °C for 3 h was conducted after the chlorination step to remove residual chlorine from the surface. We labeled the three non-doped SiOC-CDC materials as CDC-600, CDC-800, and CDC-1000, depending on the chlorination temperature. Accordingly, we labeled the nitrogen-containing CDCs as N-CDC-600, N-CDC-800, and N-CDC-1000.

Material Characterization

The carbon beads were analyzed with a field emission scanning electron microscope (SEM) Jeol JSM-7500F at 3 kV and a high-resolution transmission electron microscopy (TEM) Jeol JEM-2100F at 200 kV. We quantified the bead diameter of 150 individual particles with the image analysis software ImageJ.[37] For TEM measurements, the samples were dispersed and sonicated in ethanol to deposit them on a lacey carbon film on a copper grid from Gatan.

The porosity of the mainly microporous materials was analyzed via nitrogen gas sorption analysis (N_2 GSA) and carbon dioxide gas sorption analysis (CO_2 GSA) with an Autosorb iQ system from Quantachrome. The powder samples were outgassed before the measurement at 10 kPa at 200 °C for 1 h and at 300 °C for 20 h. To avoid any issue with the presence of the polymer binder polytetrafluoroethylene (PTFE), the electrodes were pretreated at 10 kPa first at 100 °C for 1 h and then at 150 °C for 20 h. The N_2 GSA measurements were carried out in a relative pressure range from $5 \cdot 10^{-6}$ to 1 at −196 °C. The measurement temperature for the CO_2 GSA was 0 °C, and the relative pressure was in the range of $7 \cdot 10^{-5}$ to $1 \cdot 10^{-2}$. The specific surface area was calculated with the Brunauer-Emmett-Teller equation in the linear regime of the N_2 isotherm.[38] We further analyzed the pore structure by applying a quenched-solid density functional theory (QSDFT) kernel assuming slit-like carbon nanopores.[39] A non-local density functional theory (NLDFT) assuming the same pore geometry was used to deconvolute the CO_2 isotherm.[40] The BET and DFT calculations were performed with the software ASiQwin from Quantachrome. The pore size distributions obtained from N_2 and CO_2 GSA measurements were combined with a cross-over point at 0.9 nm to obtain a pore size distribution in the range from 0.35 nm to 35 nm.[41] The total pore volume and the SSA_{DFT} values were obtained by combining the pore size distribution data of the CO_2 and N_2 GSA measurements; the average pore size corresponds to the pore diameter of the half of the total pore volume (d_{50}) of the cumulative pore size distribution.[41] For all GSA measurements, a sufficient time at each pressure increment was obtained so that a near-equilibrium was obtained, which is important to obtain a reliable combined pore size distribution pattern (as pointed out by Lobato et al.[42]).

The structure of the carbon materials was investigated via Raman spectroscopy. We used a Renishaw inVia Raman microscope with a wavelength of 532 nm and a grating of 2400 lines/mm. The spectral resolution was 1.2 cm^{-1}, the numeric aperture 0.75, and the incident power on the sample ~0.2 mW. The recording time was 30 s, and 10 accumulations were accomplished. Four Voigt functions were chosen to fit the D- and G-mode of the Raman spectra.

The chemical composition was quantified with a CHNS analyzer Vario Micro Cube from Elementar. The temperature for the tube was 850 °C and for the combustion tube 1150 °C. The equipment was calibrated with sulfanilamide. The oxygen content was obtained with a rapid OXY cube from Elementar. The analysis temperature was 1450 °C, and it was calibrated with benzoic acid.

The chemical composition of the materials was also quantified by use of X-ray photoelectron spectroscopy (XPS). We used an Axis Ultra DLD from Kratos Analytical with Al K_α radiation at a high voltage 15 kV and current of 10 mA to acquire survey spectra at a pass energy of 80 eV. The current was increased to 15 mA for the highly resolved measurement of the C 1s and N 1s peaks at a pass energy of 10 eV. The XPS spectra were analyzed with the software CasaXPS and charged corrected by shifting all peaks to the aliphatic C 1s spectral component set to a binding energy of 285 eV. The Shirley background was subtracted before fitting the peaks with a Gaussian-Lorentzian (GL(30)) profile function. The carbon peaks were fitted with a constant full-width-at-half-maximum (FWHM). An asymmetric line shape was used for the sp^2-hybridized carbon component, which is well-described by the Doniach-Šunjić function.[43,44]

Electrochemical Measurements

The synthesized carbon powders were mixed with 5 mass% of PTFE binder (60 mass% in water, Sigma-Aldrich) and crushed in a mortar to form a doughy paste. The carbon paste was rolled to free-standing films with a thickness of ~100 µm and we dried the electrodes at 120 °C and 2 kPa for 48 h. Discs with a diameter of 10 mm and a mass of 2–4 mg were punched from the casted electrodes for the electrochemical measurements. The electrodes were tested in a half-cell figuration with YP-80F as a counter electrode (>5 times heavier) and YP-50F from Kuraray as a reference electrode in a custom-built cell.[45] For electrochemical characterization, we used either an organic electrolyte (1 M tetraethylammonium tetrafluoroborate, TEA-BF_4, in acetonitrile, ACN) or a neat ionic liquid (1-ethyl-3-methylimidazolium tetrafluoroborate, EMIM-BF_4). The cells were loaded with the electrolyte in an argon-filled glove box (O_2, $H_2O \leq 1$ ppm) and placed in a vacuum oven (2 kPa) at 120 °C to remove adsorbed moisture for 16 h. A carbon coated aluminum foil (Zflo 2653, Coveris Advanced Coatings) was used as a current collector, and we employed a glass-fiber mat (GF/A from Whatman, GE Healthcare Life Science) as a separator for all measurements with a potentiostat/galvanostat VMP300 from Bio-Logic. The cyclic voltammetry (CV) was conducted at 10 mV/s and the galvanostatic cycling with potential limitation (GCPL) with a 10 min holding step at each potential for the half-cells. The specific capacitance was calculated following Eq. (1):

$$C_{sp} = \frac{\int_{t_0}^{t_{end}} I dt}{\Delta U \cdot m} \tag{1}$$

with specific capacitance C_{sp}, starting time of discharge t_0, end of discharge time t_{end}, applied potential difference ΔU, discharge current I and active mass of the working electrode m.

The limits for the positive and negative potential window of the samples CDC-800 and N-CDC-800 were investigated in the organic electrolyte and ionic liquid via S-value analysis in a half-cell configuration. The cyclic voltammetry was tested in a potential range of ±(0.2–2.5) V vs. carbon with intervals of 0.05 V and a scan rate of 1 mV/s. The S-values were calculated with Eq. (2).

$$S = \frac{Q_{charge}}{Q_{discharge}} - 1 \tag{2}$$

with S for S-value, Q_{charge} and $Q_{discharge}$ for the charge during charge and discharge.

Was also measured the sample with the highest specific capacitance with and without nitrogen in a symmetrical full-cell supercapacitor device with YP-50F from Kuraray as a quasi-reference.[46] The capacitance from cyclic voltammograms was calculated with Eq. (3) and from GCPL cycling with Eq. (4). The IR-drop of the GCPL measurements was obtained after a resting time of 10 s.

$$C_{sp} = \frac{4 \cdot I}{\frac{dU}{dt} \cdot m} \tag{3}$$

with C_{sp} as the specific capacitance per electrode, I as the current, dU/dt as the scan rate, and m as the mass of carbon in the electrode (e.g., mass of the electrode without the polymer binder).

$$C_{sp} = \frac{4 \cdot Q_{discharge}}{U \cdot m} \tag{4}$$

with C_{sp} as the specific capacitance per electrode, $Q_{discharge}$ as the charge of the discharging half-cycle, U as the IR-drop corrected cell voltage, and m as the mass of carbon in the electrode.

Stability testing via voltage floating[47] for 100 h was also conducted in a temperature-controlled environment at 25 °C at 2.7 V for the organic electrolyte and 3.2 V for the ionic liquid. These cell voltages were chosen based on the results of the S-value analysis. Every 10 h, galvanostatic cycling was performed at a cell voltage of 2.5 V (organic solvent-based electrolyte) or 3.2 V (ionic liquid).

2. Results and Discussion

2.1. Characterization of the Carbide-Derived Carbon Beads

The spherical shape of the synthesized materials after chlorine gas treatment is exemplified for CDC-800 and N-CDC-800 by scanning and transmission electron micrographs (Figure 1). SEM images of the other samples are shown in Figure S2. Transmission electron micrographs (Figure 1C,D,G,H) document the disordered nature of the carbon structure. Quantitative SEM image analysis revealed no major influence of the chlorination temperature on the volume dependent sphere diameter which all are about 1–2 µm (Table S1). All samples showed a mass loss of 24% after the pyrolysis, and 91–95% of the residual mass is lost after the chlorine gas treatment (Table S1). Thereby, when we compare the initial and final mass, there is a mass loss of 93–96%, which aligns with the low amount of aromatic groups in the precursor.[35]

We used a combination of CO_2 and N_2 gas sorption to characterize the micro- and mesopores of the samples (Figure 2, Table 1, Figure S3, S4).[20,41] All samples showed a well-developed porosity after chlorine gas treatment with a predominance of micropores, as inferred from the type I nitrogen sorption isotherms (Figure 2A,B).[48] Only the data of sample CDC-1000 shows a type IV isotherm with a large hysteresis caused by mesopores.[48] In accordance with previous works,[49,50] we see the lowest SSA_{DFT} for samples produced at 600 °C with 1740 m^2/g for CDC-600 and 1416 m^2/g for N-CDC-600. By increasing the annealing temperature to 800 °C during the chlorine gas treatment, the SSA_{DFT} of the resulting CDC material increased to 2163 m^2/g for CDC-800 and 2133 m^2/g for N-CDC-800. A further increase of the synthesis temperature increased the SSA_{DFT} to 2320 m^2/g for CDC-1000 and 2206 m^2/g for N-CDC-1000. In addition to the surface area, also the total

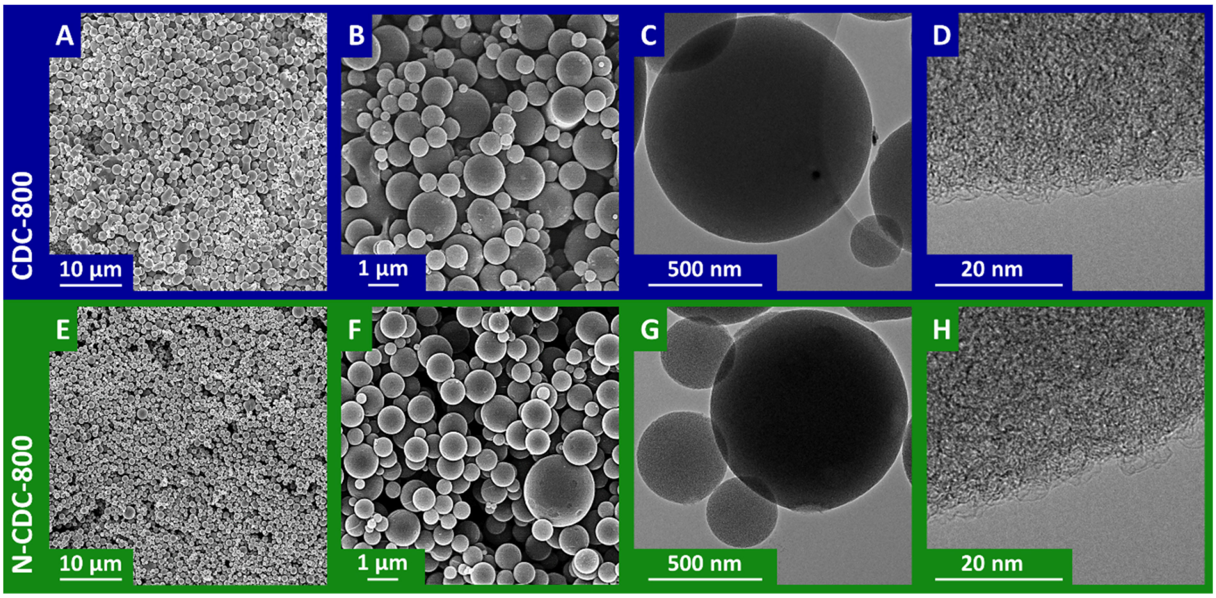

Figure 1. Scanning and transmission electron micrographs of A)-D) CDC-800 and E)-H) N-CDC-800.

Table 1. Porosity data of the powder and the electrode samples obtained by gas sorption analysis with CO_2 and N_2.

	powder				electrode					
	SSA_{DFT} [m^2/g]	SSA_{BET} [m^2/g]	Pore volume [cm^3/g]	Average pore size [nm]	SSA_{DFT} [m^2/g]	SSA_{BET} [m^2/g]	Pore volume [cm^3/g]	Cation accessible SSA_{DFT} [m^2/g]	Anion accessible SSA_{DFT} [m^2/g]	Average pore size [nm]
CDC-600	1740	1965	1.17	1.69	1446	1796	1.02	1095	1401	1.74
CDC-800	2163	2955	1.54	1.66	1966	2512	1.34	1555	1938	1.69
CDC-1000	2320	2430	1.73	1.85	2066	2485	1.53	1614	2030	1.90
N-CDC-600	1416	1644	0.92	1.69	1441	1432	0.89	1058	1377	1.61
N-CDC-800	2133	2771	1.57	1.86	1915	2334	1.36	1498	1886	1.84
N-CDC-1000	2206	2530	1.57	1.85	1908	2293	1.39	1498	1893	1.88

pore volume increased with the synthesis temperature in the range of 0.92–1.73 cm^3/g (Table 1) which agrees to previous works on CDC synthesis.[49,51]

Albeit some differences in total pore volume and total surface area, all samples showed a very similar pore size distribution, which can be best seen when normalizing the latter to the maximum pore volume. As seen from Figure S4, the average pore sizes of all samples range within a narrow range of 1.7–1.9 nm. When transforming the carbon powder into composite film electrodes, the presence of polymer binder reduces the overall porosity.[52,53] As seen from Table 1, about 11 % of the total pore volume and about 9 % of the total surface area are lost when comparing the dry carbon powder with the composite film electrodes. Yet, as required for this study, the average pore size is only marginally affected with values of 1.6–1.9 nm, and the pore size distribution pattern of all CDC and N-CDC samples remain highly similar.

The elemental analysis of the samples is summarized in Table 2 and was measured via chemical analysis (CHNS/O) and X-ray photoelectron spectroscopy (XPS). The carbon content of

Table 2. Chemical composition by CHNS/O analysis and XPS.

	Chemical analysis (CHNS/O)				XPS		
	C [mass %]	H [mass %]	N [mass %]	O [mass %]	C [mass %]	N [mass %]	O [mass %]
CDC-600	94.6 ± 1.3	1.1 ± 1.0	0.4 ± 0.1	3.8 ± 0.3	97.6	0.0	2.4
CDC-800	93.1 ± 1.9	0.6 ± 0.1	0.5 ± 0.2	6.2 ± 0.4	97.7	0.0	2.3
CDC-1000	93.1 ± 0.2	n.d.[a]	0.6 ± 0.1	4.4 ± 0.9	98.3	0.0	1.7
N-CDC-600	85.0 ± 0.6	1.1 ± 0.1	7.0 ± 0.1	5.0 ± 0.2	88.5	4.5	7.0
N-CDC-800	89.9 ± 1.0	0.7 ± 0.1	3.7 ± 0.1	5.5 ± 0.4	94.9	2.7	2.4
N-CDC-1000	92.1 ± 0.2	0.5 ± 0.1	1.2 ± 0.2	5.5 ± 0.1	96.5	0.9	2.5

[a] n.d.: not detectable.

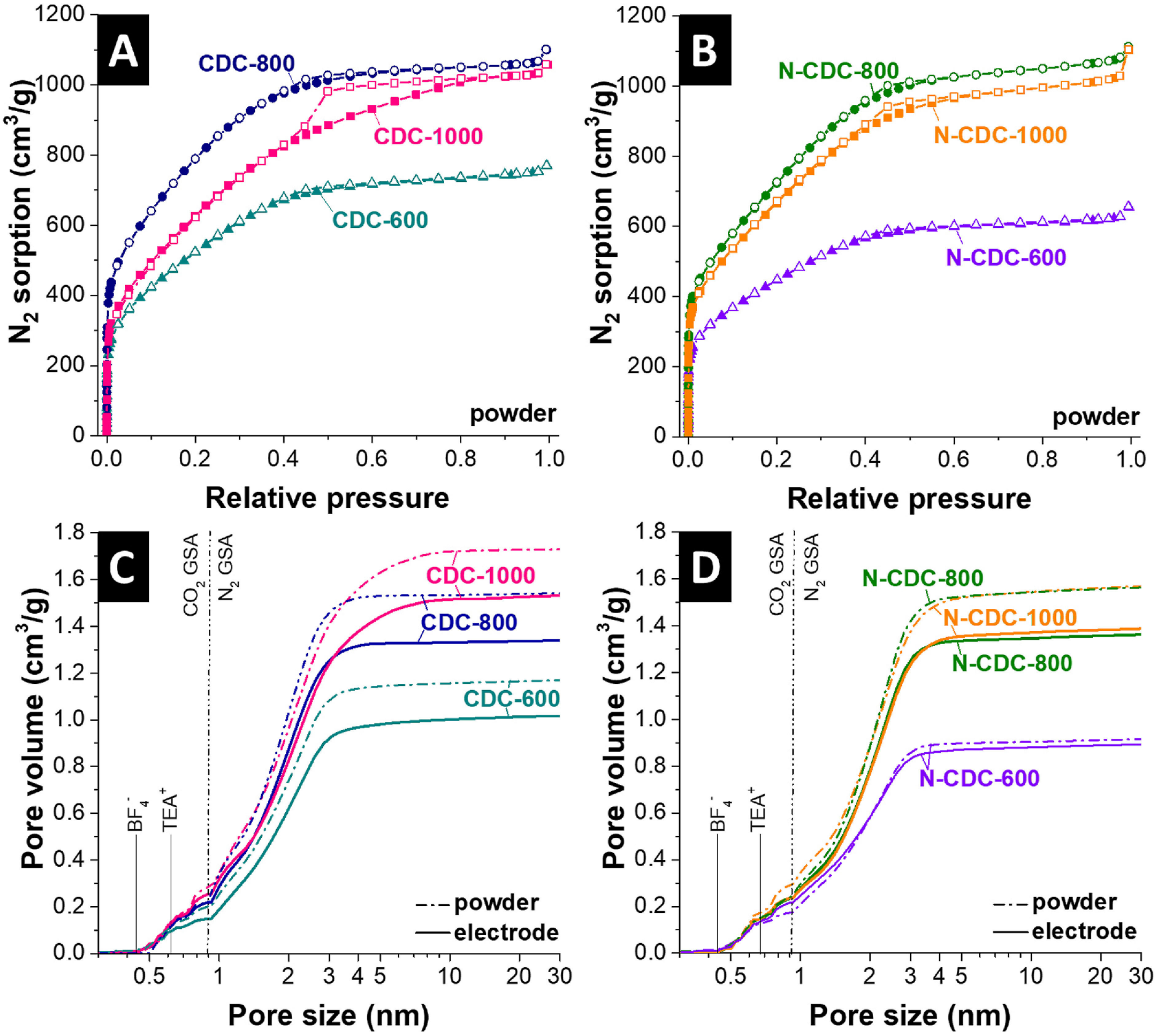

Figure 2. Pore analysis of carbide-derived carbon samples with nitrogen-doping (A,C) and without nitrogen-doping (B,D). A), B) Nitrogen sorption isotherms of the carbon powder materials recorded at −196 °C. C), D) Cumulative pore size distribution of the carbon powder materials and the electrodes (i.e., carbon plus 5 mass% polytetrafluoroethylene binder). The ionic diameter of the TEA^+ and BF_4^- is added to the pore size distributions in (C,D).

all CDC samples exceeds 93 mass%, and the hydrogen content is lowered for increased synthesis temperature from around 1 mass% for 600 °C to a not detectable value for 1000 °C. The oxygen content of all samples is in the range of 4–6 mass%. A low amount of nitrogen (~0.5 mass%) is also detectable for the CDC samples without nitrogen in the precursor. This nitrogen could be introduced to the samples during the particle synthesis were NH_3 served as a catalyst or during the pyrolysis in a nitrogen atmosphere, as reported in earlier work.[54] All N-CDC samples show a nitrogen content ranging from 1–7 mass% and both the nitrogen and hydrogen content are reduced when using a higher synthesis temperature. The sample N-CDC-600 has a nitrogen content of 7 mass%, which is reduced to 4 mass% for N-CDC-800 and to 1 mass% for N-CDC-1000.

Although chemical data and XPS analysis are intrinsically different regarding the sampling depth and the overall detection sensitivity,[55] we also see a reduced nitrogen content with an increasing synthesis temperature in the XPS data. The N1s peak of the XPS spectra can be fitted to identify the nitrogen groups, and we used 4 peaks (N1, N2, N3, and N4) which can be related to different nitrogen groups (Figure 3). The N1 species has a typical binding energy of around 398 eV which indicates pyridinic nitrogen.[56,57] The binding energy of N2 is 400.7 eV and relates to pyrrolic nitrogen, amide, amine, or nitrile.[57] Nitrogen surface groups like amide, amine, or nitrile are unlikely due to the origin of nitrogen in the precursor and the absence of an additional post-synthesis treatment with nitrogen. Therefore, we can assume that N2 peaks are mainly obtained by pyrrolic nitrogen. Graphitic nitrogen (N3) shows a characteristic binding energy of 402 eV.[56,57] A fourth nitrogen peak (N4) was identified for the samples N-CDC-800 and N-CDC-1000 at approximately 404 eV, which relates to nitrogen bonded to oxygen (pyridine oxide).[57] Figure 3B displays the relative bond content of the four identified nitrogen groups. An increasing synthesis temperature reduces the amount of

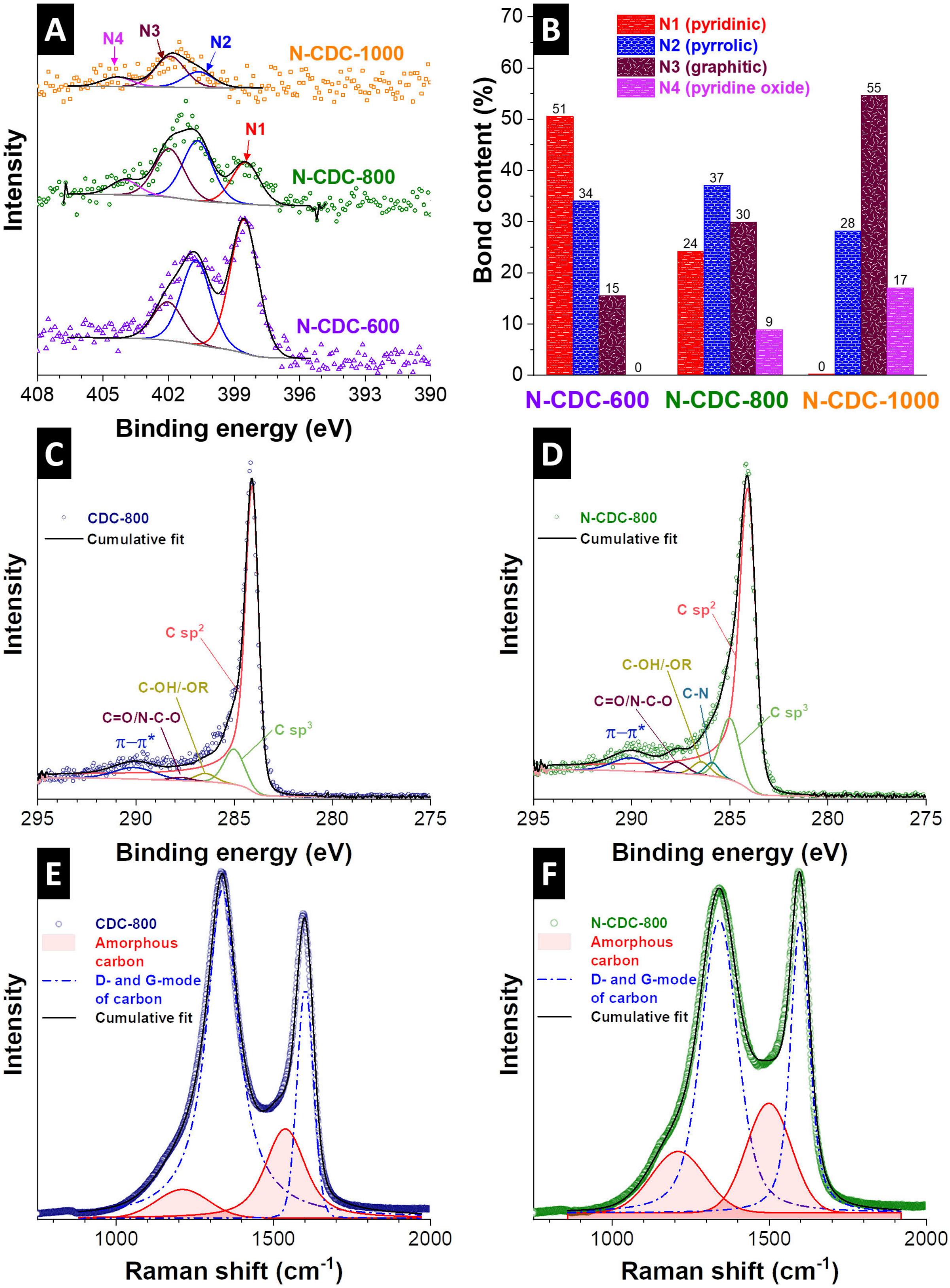

Figure 3. A) XPS N 1s spectra and peak fitting of all nitrogen-doped samples and B) bond content of the nitrogen groups. XPS C 1s spectra and peak fitting of C) CDC-800 and D) N-CDC-800. Raman spectra and peak fitting of E) CDC-800 and F) N-CDC-800.

pyridinic nitrogen from 51 % to 0 %, while the relative amount of graphitic nitrogen and pyridine oxide increases from 15 % to 55 % and from 0 % to 17 %. The pyridinic groups are released at lower temperatures and can be converted to graphitic nitrogen at higher temperatures, which explains the relative increase of the groups with higher binding energy.[6] The relative amount of pyrrolic nitrogen remained rather constant for all samples in the range of 28–37 %.

The carbon bonding can be characterized by analysis of the XPS C1s spectra (Figure 3C,D, and Figure S5, Table S2). Peak fitting shows that most of the carbon is sp^2-hybridized and the CDC samples have with 83–92 % a slightly higher relative amount of the latter bonding type than N-CDC samples with 78–85 %. An increase in the synthesis temperature reduces the sp^2-hybridized carbon content, while the sp^3-hybridized carbon content increases up to 9–11 %. The N-CDC samples show in addition to C–C and C–O bonds also C–N bonds due to the nitrogen-doping in the range of 1.6-2.5 % and the sample with the lowest nitrogen content N-CDC-1000 has the lowest amount of C–N bonds as well.

We further characterized the carbon structure by use of Raman spectroscopy (Figure 3E,F, and Figure S6). The D- and G-modes were fitted with Voigt functions, and the obtained values are listed in Table 3. The D-mode for the CDC is located between 1330–1338 cm^{-1}, while the G-mode is found between 1599–1602 cm^{-1}. The nitrogen-doped CDCs have a similar position of the D-mode (1339–1342 cm^{-1}) and G-mode (1596–1604 cm^{-1}). The position of the D- and G-mode indicate that the carbon of all samples is incompletely graphitic (nanocrystalline).[58] Higher synthesis temperatures lead to a higher degree of carbon ordering, as can be seen from a reduced full-width at half-maximum (FWHM) for all samples. When comparing the FWHMs of the CDC and N-CDC samples produced at the same temperature, there is an increased FWHM for the nitrogen-containing samples in alignment with previous work.[59,60]

Table 3. Fitted values of the D- and G- mode from the Raman spectroscopy of all CDC and N-CDC samples.

		Position [cm^{-1}]	FWHM [cm^{-1}]
CDC-600	D-mode	1330	130
	G-mode	1599	59
CDC-800	D-mode	1338	122
	G-mode	1602	62
CDC-1000	D-mode	1338	100
	G-mode	1600	67
N-CDC-600	D-mode	1342	159
	G-mode	1604	61
N-CDC-800	D-mode	1341	136
	G-mode	1598	72
N-CDC-1000	D-mode	1339	122
	G-mode	1596	68

2.2. Supercapacitor Performance in an Organic Electrolyte

We conducted half-cell measurements for all CDC materials with carbon as a quasi-reference electrode. The cyclic voltammograms in Figure 4A + B show the typical rectangular shape of a supercapacitor with an increased capacitance at higher potentials. This increased differential capacitance yields a characteristic butterfly-like shape and can be explained by the increased charge carrier density when the non-metallic carbon is being charged.[45,61–63] Values of the specific capacitance obtained at ±1 V vs. carbon are listed in Table 4, and we have identified the lowest specific capacitance for CDC-600 at −1 V vs. carbon with 116 F/g and 146 F/g at +1 V vs. carbon. CDC-800 and CDC-1000 have very similar specific capacitances of 143 F/g and 135 F/g, respectively, at −1 V vs. carbon and 144 F/g and 150 F/g, respectively, at +1 V vs. carbon. The specific capacitance at negative polarization is lower compared to the values obtained from positive polarization due to the larger ionic diameter of the TEA^+ ion (0.67 nm non-solvated) compared to the BF_4^- (0.45 nm non-solvated).[64] The nitrogen-containing CDCs have in general a higher specific capacitance at the negative potential vs. carbon. N-CDC-600 has a very similar specific capacitance at ±1 V vs. carbon (118 F/g and 120 F/g), and the largest specific capacitance in the organic electrolyte was obtained for N-CDC-800 with 151 F/g at −1 V vs. carbon and 143 F/g at +1 V vs. carbon (Table 4).

We determined the electrochemical stability window of N-CDC-800 and CDC-800 by using the S-value analysis (Figure 4E + F). The S-value (stability value) is the ratio of invested charge during charging and recovered charge during discharging [Eq. (2)].[65] Weingarth et al. proposed that the electrochemical stability window limit is reached when the second derivative of the S-value over the potential (d^2S/dU^2) exceeds 5 %.[65] This definition is of particular use for a system that shows an exponential increase in the non-reversible charge at a certain potential limit. Using this criterion, we have identified a potential limit of -1.75 ± 0.05 V vs. carbon for both CDC-800 and N-CDC-800 in 1 M TEA-BF_4 in ACN. This value is close to the literature value of -1.7 ± 0.1 V vs. carbon.[65] The more monotonic shape of the S-curve for positive polarization shown in

Table 4. Half-cell capacitance of the CDC materials with and without nitrogen-doping in 1 M TEA-BF_4 in ACN at ±1.0 V vs. carbon and in EMIM-BF_4 at ±1.0 V and ±1.5 V vs. carbon.

	Specific capacitance [F/g]					
	1 M TEA-BF_4 in ACN		EMIM-BF_4			
	at −1.0 V	at +1.0 V	at −1.0 V	at +1.0 V	at −1.5 V	at +1.5 V
CDC-600	116	146	127	125	158	139
CDC-800	143	144	145	157	184	155
CDC-1000	135	150	135	159	176	162
N-CDC-600	118	120	146	124	171	134
N-CDC-800	151	143	169	174	215	173
N-CDC-1000	145	138	150	168	211	172

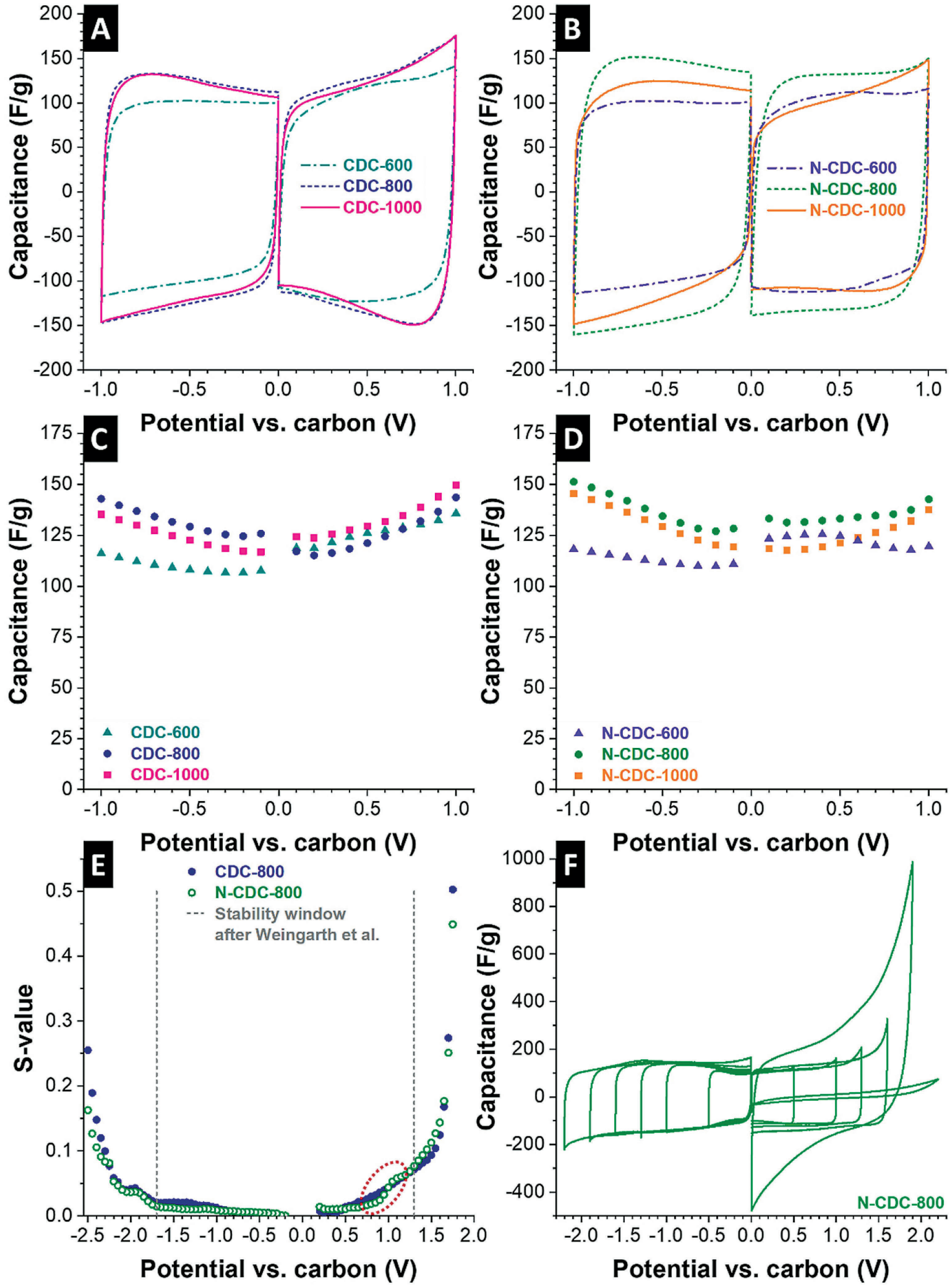

Figure 4. Electrochemical characterization of carbon materials without nitrogen-doping (A,C) and with nitrogen-doping (B,D,F) and S-value analysis of CDC-800 and N-CDC-800 (E,F) in a half-cell configuration in 1 M TEA-BF_4 in ACN. A), B) Cyclic voltammetry measured at a scan rate of 10 mV/s in the potential range of ±1.0 V vs. carbon. C)-D) Capacitance obtained by galvanostatic charge/discharge cycling at a specific current of 0.2 A/g. E) S-value analysis measured by cyclic voltammetry at a scan rate of 1 mV/s and the stability windows after Weingarth et al. (Ref.[65]). F) Selected cyclic voltammograms from the S-value analysis of N-CDC-800.

Figure 4E makes the direct application of $d^2S/dU^2 > 0.05$ more difficult; in fact, the 5% limit is reached already at around +1 V vs. carbon. An increased slope of the S-value can also be caused by (incompletely) reversible Faradaic reactions without leading immediately to escalating electrochemical degradation.[66] From the literature, we would expect the upper limit of the electrochemical stability window at +1.3 V vs. carbon.[65] For CDC-800 and N-CDC-800, we observed the onset of an escalating increase in non-reversible charge above +1.3 V to +1.5 V vs. carbon (Figure 4E). This range also coincides with the stability criterion of $S > 0.1$ as defined by Xu et al. (where the S-value is called the R-value; Ref.[67]). In addition, N-CDC-800 shows a first rapid increase of the S-value at around +0.95 V vs. carbon which may indicate an early onset of the electrolyte degradation aided by the presence of nitrogen, which can be observed at large potentials. Figure 4F shows selected cyclic voltammograms of N-CDC-800 recorded during the S-value analysis, where the electrolyte decomposition can be observed at large potentials. It is also noticeable that the specific capacitance is dramatically reduced at even higher potentials (+2.2 V vs. carbon).

In addition to the half-cell experiments, we conducted symmetrical full-cell measurements with the samples CDC-800 and N-CDC-800. The cyclic voltammograms show the typical rectangular shape of an electrical double-layer capacitor (Figure 5A). The specific capacitance of N-CDC-800 at a low specific current (0.05 A/g) is 139 F/g, which is slightly lower than the value obtained by the half-cell experiment. The sample CDC-800 without nitrogen has a very similar specific capacitance of 135 F/g at the same specific current. The rate capability analysis is seen in Figure 5B and reveals at a high specific current of 100 A/g a lower specific capacitance of N-CDC-800 (20 F/g) compared to CDC-800 (86 F/g). This observation aligns with the strong correlation between ion mobility and the resulting rate capability of nanoporous carbons.[7] In the case of nitrogen-doping, there is an increased interaction strength between the pore wall and ions, which reduces the ion mobility.[7,68,69] Thereby, the relaxation time of the ions in the micropores increases which leads to a lower rate capability of the nitrogen-doped CDCs.

The performance stability of the nitrogen-containing sample is also reduced (Figure 5D): while CDC-800 retained 89% of its initial capacitance after voltage floating at 2.7 V for 100 h, the capacitance of N-CDC-800 decayed rapidly. The reduced stability seems to align with the reduced electrochemical stability window as seen from the increased slope of N-CDC-800 in the S-value analysis at around +1 V vs. carbon. The full-cell experiments show that the additional nitrogen-doping does not improve the specific capacitance in organic electrolyte TEA-BF$_4$ in ACN significantly and reduce the rate handling capability and performance stability.

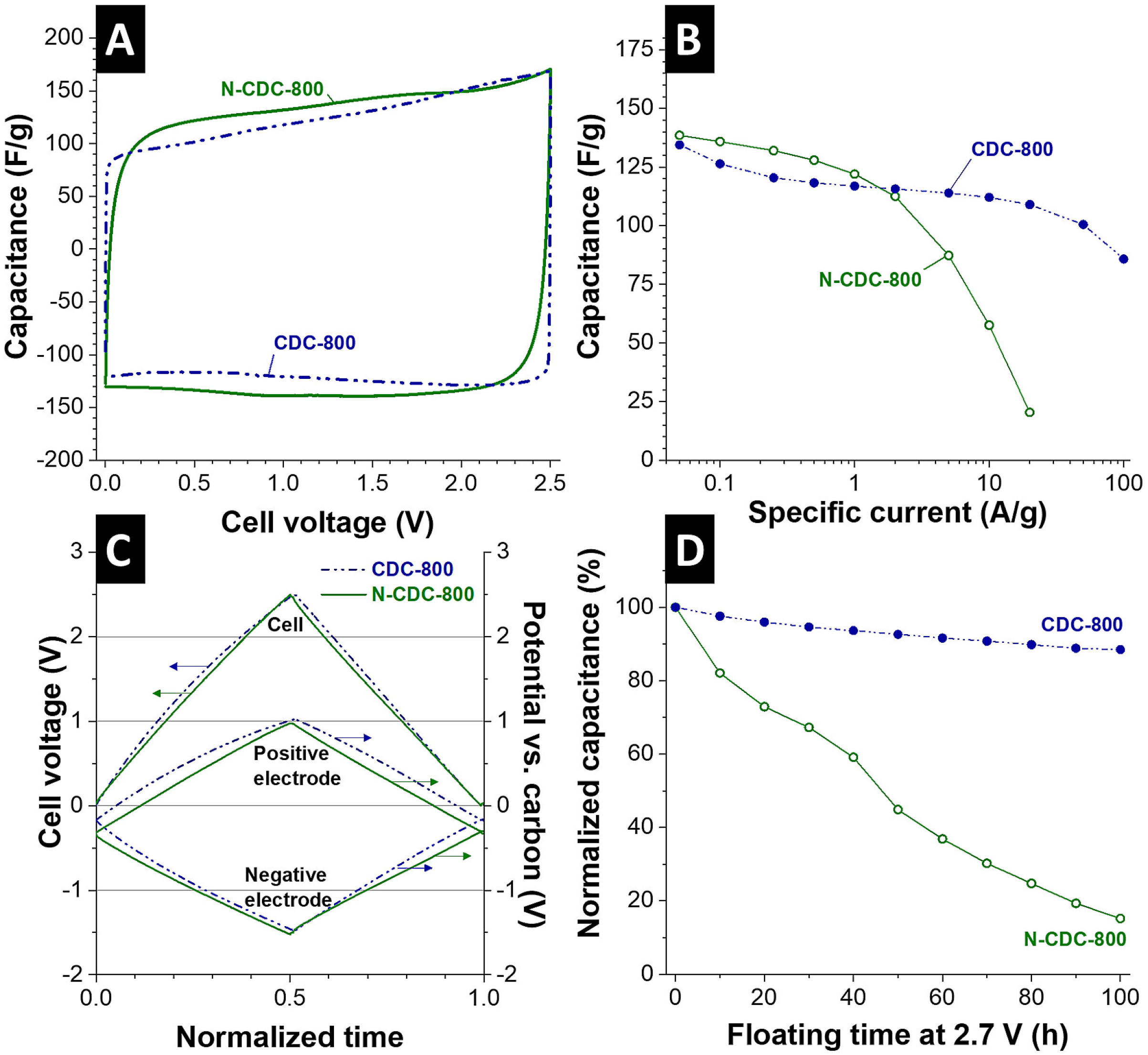

Figure 5. Results of the full-cell supercapacitor measurements with 1 M TEA-BF$_4$ in ACN. A) Cyclic voltammetry at a scan rate of 10 mV/s, B) galvanostatic charge/discharge rate handling measurement, C) cell voltage and electrode potential distribution during galvanostatic charge/discharge cycling at 0.1 A/g, D) performance stability characterization by floating at a cell voltage of 2.7 V.

2.3. Supercapacitor Performance in Ionic Liquid

We further characterized the CDC materials with and without nitrogen-doping as electrodes using the ionic liquid EMIM-BF_4. The results of the half-cell measurements vs. carbon are presented in Figure 6 and in Table 4. The electric response depicted in the cyclic voltammograms in the negative potential range retains the typical rectangular shape of an electrical double-layer capacitor for all samples with an increased capacitance at higher potentials.[45,61] The specific capacitance in the ionic liquid is in general for all CDCs higher at a negative polarization with an almost linear increase with the potential.

During positive polarization, we see for CDC-600 and N-CDC-600 a rectangular shape without any peaks and a linear increase of the capacitance with the potential. All other samples show to a different degree the emergence of a peak at around +1 V vs. carbon during charging and at +0.7 V vs. carbon during discharging. The area of these peaks is much larger for

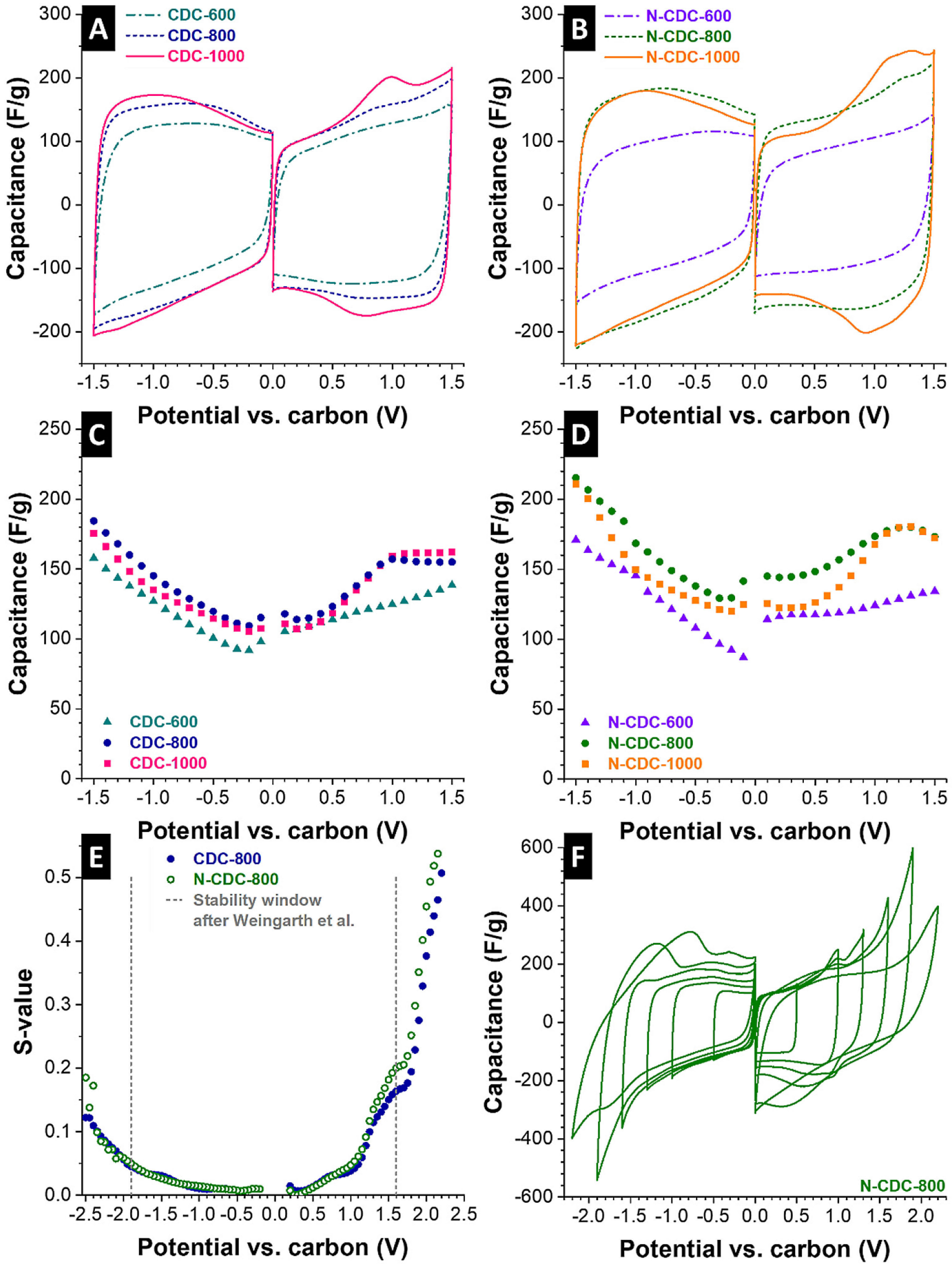

Figure 6. Electrochemical characterization of carbon materials without nitrogen-doping (A, C) and with nitrogen-doping (B,D,F) and S-value analysis of CDC-800 and N-CDC-800 (E, F) in a half-cell configuration in the ionic liquid EMIM-BF_4. A), B) Cyclic voltammetry measured at a scan rate of 10 mV/s in the potential range of ±1.5 V vs. carbon. C)-D) Capacitance obtained by galvanostatic charge/discharge cycling at a specific current of 0.2 A/g. E) S-value analysis measured by cyclic voltammetry at a scan rate of 1 mV/s and the stability windows after Weingarth et al. (Ref.[65]). F) Selected cyclic voltammograms from S-value analysis of N-CDC-800.

the samples produced at 1000 °C and very small for CDC-800 and N-CDC-800. Similar peaks have been reported for EMIM-BF_4 in the literature before, but the origin of this electrochemical signal is not often discussed.[70,71] Intercalation of the BF_4^- as the origin of these peaks is unlikely since it only occurs at much higher potentials for graphitic carbon.[72] A highly irreversible decomposition of BF_4^- can also not cause the highly reversible current peaks.[71] In less pure systems, peaks may also occur because of parasitic side-reactions, as shown by the Kötz group.[64] However, if our system were plagued by impurity-related issues, we would see this redox peak for all samples. The presence of nitrogen in the material also cannot explain the peaks because the samples with the lowest amount of nitrogen show the largest peaks.

A reasonable explanation for the peak was provided by Yan et al. by assuming conformational changes of the ionic liquid inside the micropores during electrochemical cycling.[7] Accordingly, we can relate the higher current signal relates to a better ion packing. This explanation is further supported by our previous work on the use of electrochemical dilatometry (eD) and quartz crystal microbalance measurements (EQCM) to explain the electrosorption of EMIM-BF_4 in microporous carbons.[70] The enhanced volume expansion found in the latter study aligns with highly mobile BF_4^- anions being electro-adsorbed during positive polarization while more of the less mobile $EMIM^+$ cations remain inside the pores.[70] Possibly, the larger $EMIM^+$ leave the micropore confinement more easily at high positive potential when the pore diameter is larger. The free space can be filled by electro-adsorption of additional anions, and the enhanced number of charge carriers induces the peak seen in the CVs at potentials larger than 1 V vs. carbon. This explains why we see the peak very clearly for CDC-1000 and N-CDC-1000 because these samples have a broader pore size distribution with larger average pore size. Samples synthesized at lower temperatures, however, show no visible peak (CDC-600 and N-CDC-600) or only a small peak (CDC-800 and N-CDC-800).

The specific capacitance measured by galvanostatic charge/discharge cycling shows a maximum at +1 V vs. carbon for CDC-800 (157 F/g) and at +1.5 V vs. carbon for N-CDC-800 (180 F/g), which aligns with the data obtained by cyclic voltammetry. During negative polarization, we see even higher capacitance values in EMIM-BF_4 with 184 F/g for CDC-800 and 215 F/g for N-CDC-800 (both values at −1.5 V vs. carbon). A summary of all specific capacitances measured in the half-cell with EMIM-BF_4 is provided in Table 4.

We also tested the electrochemical stability window of CDC-800 and N-CDC-800 using the ionic liquid electrolyte (Figure 6E+F). The S-value pattern for the non-doped and the nitrogen-doped materials are quite similar for both negative and positive polarization (Figure 6E). The electrochemical stability window is characterized by an exponential current increase.[65] We subtract the restored charge for the calculation of S-value. Hence, if the reaction is reversible, we do not expect the exponential S-value increase. The irreversible reaction will cause the exponential S-value increase. The stability criterion from Weingarth et al. ($d^2S/dU^2 < 0.05$) is reached for CDC-800 at −2.00 ± 0.05 V vs. carbon and for N-CDC-800 at −2.10 ± 0.05 V vs. carbon, which are close to the literature value of −1.9 ± 0.1 V vs. carbon.[65] During positive polarization, the sample N-CDC-800 exceeds a value of 0.05 for d^2S/dU^2 already at +0.5 V vs. carbon. The S-values further show a significant increase at +1.15 ± 0.05 V and +1.60 ± 0.05 V vs. carbon. The latter value is also similar to the electrochemical stability window of +1.6 ± 0.1 V vs. carbon typically found in the literature.[65] The increased S-value below +1.5 V vs. carbon may align with incompletely reversible Faradaic reactions, which were also observed in the cyclic voltammograms (Figure 6A+B+F). While the criterion of exceeding the stability window when reaching a value of 0.05 for d^2S/dU^2 is a highly useful tool, our data also show that S-value analysis may be more complex, and it is important to consider the general development of arising incompletely recoverable charge at different potentials. This is also why voltage floating experiments are important to further investigate practical limitations for the performance stability.

The materials CDC-800 and N-CDC-800 were further tested in a symmetrical full-cell setup with EMIM-BF_4 (Figure 7). We chose these two samples because of the promising electrochemical performance in half-cell configuration and for comparability with the full-cell data using 1 M TEA-BF_4 (Figure 5). The CV in Figure 7A shows at a low scan rate a higher specific capacitance for the nitrogen-doped sample compared to the non-doped sample. Galvanostatic charge/discharge cycling measurements yield for CDC-800 a specific capacitance of 164 F/g at 0.05 A/g, while the nitrogen-doped N-CDC-800 has a higher initial capacitance of 174 F/g at the same specific current. The capacitance of N-CDC-800 is being reduced more pronouncedly compared to CDC-800 when increasing the applied current. For example, at a high specific current of 10 A/g, the electrode with N-CDC-800 retains only a specific capacitance of 24 F/g (14%) while CDC-800 still provides 102 F/g (62%) at the same current. As seen from these data, we noticed the same trend of reduced high rate performance of nitrogen-doped CDC for operation with the ionic liquid as we did when using the organic electrolyte. Therefore, we also suspect the reduced ion mobility to be caused by an increased interaction strength between the pore walls and the ions since the pore size distribution is highly comparable for all samples.

Stability testing was performed at a floating cell voltage of 3.2 V (Figure 7D). In general, EMIM-BF_4 has a maximum potential window of 3.5 V but is limited to +1.6 V vs. carbon for the positive electrode.[65] Therefore, we chose a maximum cell voltage of 3.2 V for the full-cell measurements. Our data show a slightly better electrochemical stability of the nitrogen-doped sample: after 100 h at 3.2 V, the nitrogen-doped sample retains 78% of the initial capacitance, while 70% is retained for CDC-800.

3. Conclusions

The doping of SiOC-CDC beads with nitrogen can be obtained by adding nitrogen groups to the precursor. The resulting nitrogen content depends on the chlorine gas treatment

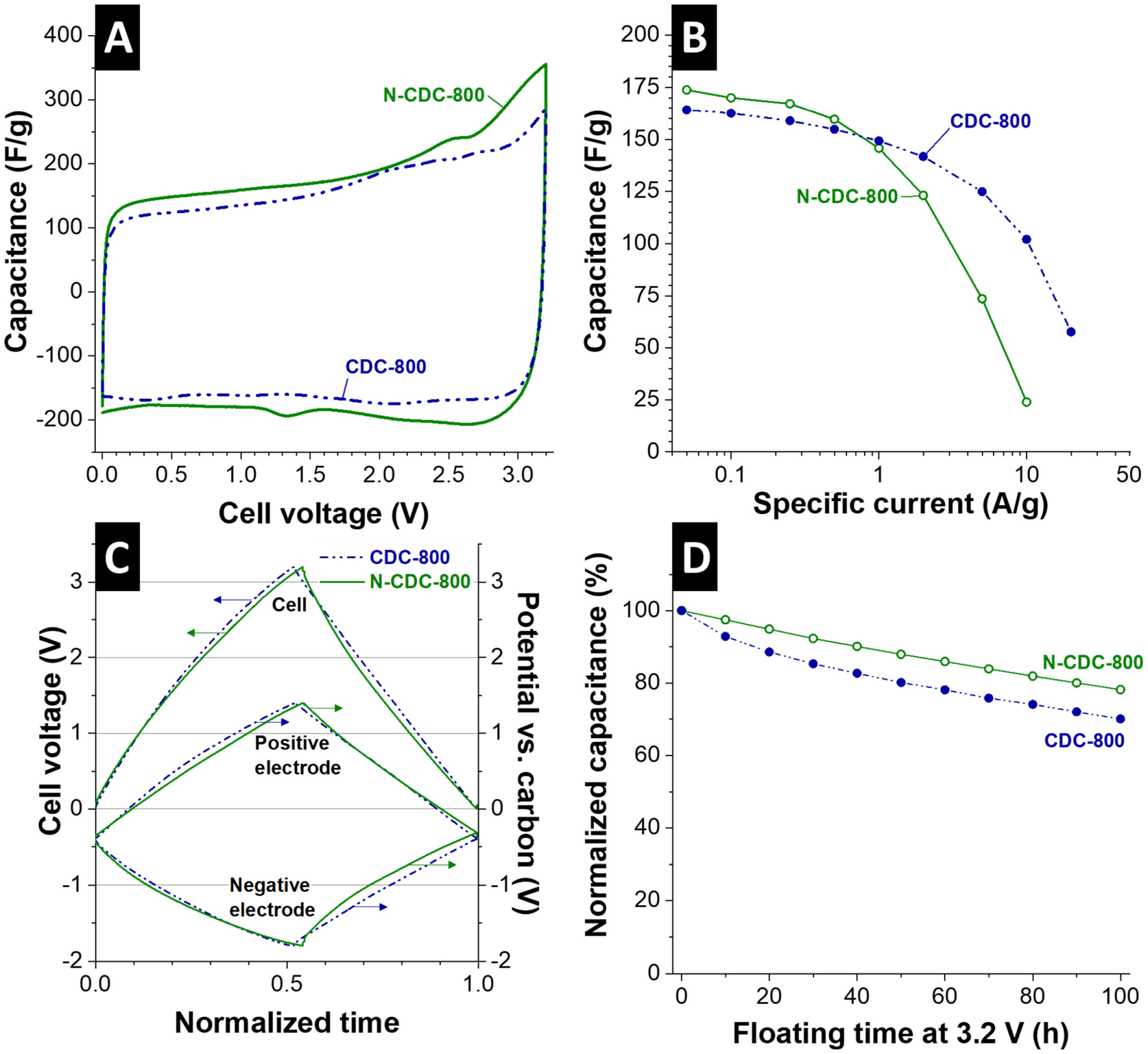

Figure 7. Results of the full-cell supercapacitor measurements with the ionic liquid EMIM-BF_4. A) Cyclic voltammetry at a scan rate of 10 mV/s, B) galvanostatic charge/discharge rate handling measurement. C) Cell voltage and electrode potential distribution during galvanostatic charge/discharge cycling at 0.1 A/g. D) Performance stability characterization by floating at a cell voltage of 3.2 V.

temperature: a low temperature of 600 °C led to a nitrogen content of 7 mass%, while the sample produced at a higher temperature only had a nitrogen content from 1–4 mass%. The nitrogen groups for the sample N-CDC-600 were mainly pyridinic, which were removed at high temperatures.

We investigated the electrochemical performance of the CDCs with a similar pore structure in an organic electrolyte (TEA-BF_4 in ACN) and an ionic liquid (EMIM-BF_4). Using a half-cell setup, we observed that the nitrogen groups did not systematically yield a higher capacitance; instead, the pore structure seemed to have a larger influence on the electrochemical performance. The measurements in a symmetrical full-cell showed that the nitrogen-doped samples have a slightly higher specific capacitance in the organic electrolyte and the ionic liquid at low specific currents. However, when increasing the charge/discharge rate, the specific capacitance decreases more pronouncedly for the nitrogen-doped samples compared to the non-doped samples. This effect may be caused by stronger interaction between the in-pore ions with the pore wall in the presence of nitrogen compared to nitrogen-free CDC.

The different electrochemical full-cell performances of the CDC and N-CDC materials produced by the MicroJet reactor technique are compared in a Ragone plot depicted in Figure 8. N-CDC-800 in EMIM-BF_4 has the highest specific energy of 62 Wh/kg, but the non-doped CDC-800 provides a higher specific power. The organic electrolyte has a lower specific energy of ~30 Wh/kg which is mostly related to the lower maximum cell voltage of 2.7 V. The lower viscosity of the organic electrolyte combined with the non-doped CDC-800 shows the highest specific energy combined with high specific powers (12 Wh/kg at 44 kW/kg).

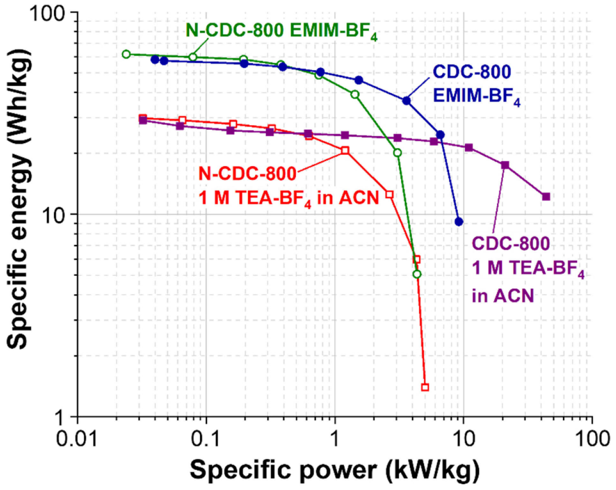

Figure 8. Ragone plot of the carbide-derived carbon materials synthesized at 800 °C with and without nitrogen-doping measured in a symmetrical full-cell supercapacitor in the organic electrolyte 1 M TEA-BF$_4$ in ACN and an ionic liquid EMIM-BF$_4$.

Acknowledgements

The INM authors kindly acknowledge the continuing support of Eduard Arzt (INM). This work was part of the Carbon Metal Oxide Nanohybrid project (CarMON) supported by the Leibniz Association (SAW-2017). We also thank Aura Tolosa, Nicolas Jäckel, and Juhan Lee (all at INM) for fruitful discussions and technical support.

Conflict of Interest

The authors declare no conflict of interest.

Keywords: carbide-derived carbon · carbon · nitrogen-doping · sol-gel processes · supercapacitors

[1] F. Beguin, V. Presser, A. Balducci, E. Frackowiak, *Adv. Mater.* **2014**, *26*, 2219–2251.
[2] P. Simon, Y. Gogotsi, B. Dunn, *Science.* **2014**, *343*, 1210–1211.
[3] P. Simon, Y. Gogotsi, *Nat. Mater.* **2008**, *7*, 845–854.
[4] D. Qu, H. Shi, *J. Power Sources.* **1998**, *74*, 99–107.
[5] B. Krüner, J. Lee, N. Jäckel, A. Tolosa, V. Presser, *ACS Appl. Mater. Interfaces.* **2016**, *8*, 9104–9115.
[6] B. Krüner, A. Schreiber, A. Tolosa, A. Quade, F. Badaczewski, T. Pfaff, B. M. Smarsly, V. Presser, *Carbon.* **2018**, *132*, 220–231.
[7] R. Yan, M. Antonietti, M. Oschatz, *Adv. Energy Mater.* **2018**, 1800026.
[8] T.-P. Fellinger, A. Thomas, J. Yuan, M. Antonietti, *Adv. Mater.* **2013**, *25*, 5838–5855.
[9] N. Fechler, T.-P. Fellinger, M. Antonietti, *Adv. Mater.* **2013**, *25*, 75–79.
[10] Y. Wang, Z. Shi, Y. Huang, Y. Ma, C. Wang, M. Chen, Y. Chen, *J. Phys. Chem. C.* **2009**, *113*, 13103–13107.
[11] K. H. An, W. S. Kim, Y. S. Park, J. M. Moon, D. J. Bae, S. C. Lim, Y. S. Lee, Y. H. Lee, *Adv. Funct. Mater.* **2001**, *11*, 387–392.
[12] D. Pech, M. Brunet, H. Durou, P. Huang, V. Mochalin, Y. Gogotsi, P. L. Taberna, P. Simon, *Nat. Nanotechnol.* **2010**, *5*, 651.
[13] M. Zeiger, N. Jäckel, D. Weingarth, V. Presser, *Carbon.* **2015**, *94*, 507–517.
[14] V. Presser, M. Heon, Y. Gogotsi, *Adv. Funct. Mater.* **2011**, *21*, 810–833.
[15] M. Oschatz, S. Boukhalfa, W. Nickel, J. P. Hofmann, C. Fischer, G. Yushin, S. Kaskel, *Carbon.* **2017**, *113*, 283–291.
[16] M. Salanne, B. Rotenberg, K. Naoi, K. Kaneko, P. L. Taberna, C. P. Grey, B. Dunn, P. Simon, *Nat. Energy.* **2016**, *1*, 16070.
[17] C. Largeot, C. Portet, J. Chmiola, P.-L. Taberna, Y. Gogotsi, P. Simon, *J. Am. Chem. Soc.* **2008**, *130*, 2730–2731.
[18] E. Raymundo-Pinero, K. Kierzek, J. Machnikowski, F. Beguin, *Carbon.* **2006**, *44*, 2498–2507.
[19] J. Chmiola, G. Yushin, Y. Gogotsi, C. Portet, P. Simon, P.-L. Taberna, *Science.* **2006**, *313*, 1760–1763.
[20] N. Jäckel, M. Rodner, A. Schreiber, J. Jeongwook, M. Zeiger, M. Aslan, D. Weingarth, V. Presser, *J. Power Sources.* **2016**, *326*, 660–671.
[21] B. Kastening, S. Spinzig, *J. Electroanal. Chem. Interfacial Electrochem.* **1986**, *214*, 295–302.
[22] N. Jäckel, P. Simon, Y. Gogotsi, V. Presser, *ACS Energy Lett.* **2016**, *1*, 1262–1265.
[23] S. Zhang, N. Pan, *Adv. Energy Mater.* **2015**, *5*, 1401401.
[24] J. Lee, B. Krüner, A. Tolosa, S. Sathyamoorthi, D. Kim, S. Choudhury, K.-H. Seo, V. Presser, *Energy Environ. Sci.* **2016**, *9*, 3392–3398.
[25] E. Frackowiak, K. Fic, M. Meller, G. Lota, *ChemSusChem.* **2012**, *5*, 1181–1185.
[26] B. Akinwolemiwa, G. Chen, *Curr. Top. Electrochem.* **2017**, *19*, 47–65.
[27] E. Frackowiak, M. Meller, J. Menzel, D. Gastol, K. Fic, *Faraday Discuss.* **2014**, *172*, 179–198.
[28] S. Fleischmann, M. Zeiger, N. Jäckel, B. Krüner, V. Lemkova, M. Widmaier, V. Presser, *J. Mater. Chem. A.* **2017**, *5*, 13039–13051.
[29] J. S. Daubert, N. P. Lewis, H. N. Gotsch, J. Z. Mundy, D. N. Monroe, E. C. Dickey, M. D. Losego, G. N. Parsons, *Chem. Mater.* **2015**, *27*, 6524–6534.
[30] M. Zeiger, S. Fleischmann, B. Krüner, A. Tolosa, S. Bechtel, M. Baltes, A. Schreiber, R. Moroni, S. Vierrath, S. Thiele, *RSC Adv.* **2016**, *6*, 107163–107179.
[31] S. Fleischmann, A. Tolosa, V. Presser, *Chem. Eur. J.* **2018**, DOI:10.1002/chem.201800772.
[32] J. K. Ewert, D. Weingarth, C. Denner, M. Friedrich, M. Zeiger, A. Schreiber, N. Jäckel, V. Presser, R. Kemp, e *J. Mater. Chem. A.* **2015**, *3*, 18906–18912.
[33] C. Schneidermann, N. Jäckel, S. Oswald, L. Giebeler, V. Presser, L. Borchardt, *ChemSusChem.* **2017**, *10*, 2416–2424.
[34] J. Pu, C. Li, L. Tang, T. Li, L. Ling, K. Zhang, Y. Xu, Q. Li, Y. Yao, *Carbon.* **2015**, *94*, 650–660.
[35] B. Krüner, C. Odenwald, A. Tolosa, A. Schreiber, M. Aslan, G. Kickelbick, V. Presser, *Sustainable Energy Fuels.* **2017**, *1*, 1588–1600.
[36] C. Odenwald, G. Kickelbick *J. Sol-Gel Sci. Technol.* **2018**, DOI:10.1007/s10971-10018-14626-x.
[37] C. A. Schneider, W. S. Rasband, K. W. Eliceiri, *Nat. Methods.* **2012**, *9*, 671.
[38] S. Brunauer, P. H. Emmett, E. Teller, *J. Am. Chem. Soc.* **1938**, *60*, 309–319.
[39] G. Y. Gor, M. Thommes, K. A. Cychosz, A. V. Neimark, *Carbon.* **2012**, *50*, 1583–1590.
[40] A. Vishnyakov, P. I. Ravikovitch, A. V. Neimark, *Langmuir.* **1999**, *15*, 8736–8742.
[41] V. Presser, J. McDonough, S.-H. Yeon, Y. Gogotsi, *Energy Environ. Sci.* **2011**, *4*, 3059–3066.
[42] B. Lobato, L. Suárez, L. Guardia, T. A. Centeno, *Carbon.* **2017**, *122*, 434–445.
[43] S. Doniach, M. Sunjic, *J. Phys. C: Solid State Phys.* **1970**, *3*, 285–291.
[44] S. Evans, *Surf. Interface Anal.* **1991**, *17*, 85–93.
[45] D. Weingarth, M. Zeiger, N. Jäckel, M. Aslan, G. Feng, V. Presser, *Adv. Energy Mater.* **2014**, *4*, 1400316.
[46] D. Weingarth, A. Foelske-Schmitz, A. Wokaun, R. Kötz, *Electrochem. Commun.* **2012**, *18*, 116–118.
[47] D. Weingarth, A. Foelske-Schmitz, R. Kötz, *J. Power Sources.* **2013**, *225*, 84–88.
[48] M. Thommes, K. Kaneko, A. V. Neimark, J. P. Olivier, F. Rodriguez-Reinoso, J. Rouquerol, K. S. W. Sing, *Pure Appl. Chem.* **2015**, *87*, 1051–1069.
[49] R. Dash, J. Chmiola, G. Yushin, Y. Gogotsi, G. Laudisio, J. Singer, J. Fischer, S. Kucheyev, *Carbon.* **2006**, *44*, 2489–2497.
[50] G. Laudisio, R. K. Dash, J. P. Singer, G. Yushin, Y. Gogotsi, J. E. Fischer, *Langmuir.* **2006**, *22*, 8945–8950.
[51] Y. Gogotsi, A. Nikitin, H. Ye, W. Zhou, J. E. Fischer, B. Yi, H. C. Foley, M. W. Barsoum, *Nat. Mater.* **2003**, *2*, 591.
[52] M. Aslan, D. Weingarth, N. Jäckel, J. S. Atchison, I. Grobelsek, V. Presser, *J. Power Sources.* **2014**, *266*, 374–383.
[53] B. Dyatkin, V. Presser, M. Heon, M. R. Lukatskaya, M. Beidaghi, Y. Gogotsi, *ChemSusChem.* **2013**, *6*, 2269–2280.
[54] C. R. Perez, S.-H. Yeon, J. Segalini, V. Presser, P.-L. Taberna, P. Simon, Y. Gogotsi, *Adv. Funct. Mater.* **2013**, *23*, 1081–1089.
[55] J. Zemek, J. Zalman, A. Luches, *Appl. Surf. Sci.* **1998**, *133*, 27–32.

[56] R. Arrigo, M. Hävecker, R. Schlögl, D. S. Su, *Chem. Commun.* **2008**, 4891–4893.
[57] Y. Zhao, X. Liu, Y. Han, *RSC Adv.* **2015**, *5*, 30310–30330.
[58] A. C. Ferrari, J. Robertson, *Phys. Rev. B.* **2000**, *61*, 14095.
[59] Z. R. Ismagilov, A. E. Shalagina, O. Y. Podyacheva, A. V. Ischenko, L. S. Kibis, A. I. Boronin, Y. A. Chesalov, D. I. Kochubey, A. I. Romanenko, O. B. Anikeeva, T. I. Buryakov, E. N. Tkachev, *Carbon.* **2009**, *47*, 1922–1929.
[60] J. D. Wiggins-Camacho, K. J. Stevenson, *J. Phys. Chem. C.* **2009**, *113*, 19082–19090.
[61] P. W. Ruch, R. Kötz, A. Wokaun, *Electrochim. Acta.* **2009**, *54*, 4451–4458.
[62] H. Gerischer, R. McIntyre, D. Scherson, W. Storck, *J. Phys. Chem.* **1987**, *91*, 1930–1935.
[63] H. Gerischer, *J. Phys. Chem.* **1985**, *89*, 4249–4251.
[64] M. M. Hantel, D. Weingarth, R. Kötz, *Carbon.* **2014**, *69*, 275–286.
[65] D. Weingarth, H. Noh, A. Foelske-Schmitz, A. Wokaun, R. Kötz, *Electrochim. Acta.* **2013**, *103*, 119–124.
[66] J. Lee, P. Srimuk, K. Aristizabal, C. Kim, S. Choudhury, Y. C. Nah, F. Mücklich, V. Presser, *J. Electrochem. Soc.* **2017**, *10*, 3611–3623.
[67] K. Xu, S. P. Ding, T. R. Jow, *ChemSusChem* **1999**, *146*, 4172–4178.
[68] R. Singh, J. Monk, F. R. Hung, *J. Phys. Chem. C.* **2011**, *115*, 16544–16554.
[69] R. Singh, N. N. Rajput, X. He, J. Monk, F. R. Hung, *Phys. Chem. Chem. Phys.* **2013**, *15*, 16090–16103.
[70] N. Jäckel, S. P. Emge, B. Krüner, B. Roling, V. Presser, *J. Phys. Chem. C.* **2017**, *121*, 19120–19128.
[71] T. Romann, O. Oll, P. Pikma, H. Tamme, E. Lust, *Electrochim. Acta.* **2014**, *125*, 183–190.
[72] P. W. Ruch, M. Hahn, F. Rosciano, M. Holzapfel, H. Kaiser, W. Scheifele, B. Schmitt, P. Novák, R. Kötz, A. Wokaun, *Electrochim. Acta.* **2007**, *53*, 1074–1082.

Manuscript received: June 28, 2018
Version of record online: [redacted] [redacted], [redacted]

Supporting Information

Influence of Nitrogen-Doping for Carbide-Derived Carbons on the Supercapacitor Performance in an Organic Electrolyte and an Ionic Liquid

Benjamin Krüner, Christina Odenwald, Antje Quade, Guido Kickelbick,* and Volker Presser*

Table S1: Mass losses after the pyrolysis and the chlorine treatment together with the average diameter of the CDC beads.

	Mass loss after pyrolysis (%)	Mass loss after chlorine gas treatment (%)	Total mass loss (%)	Number-dependent average diameter (nm)	Volume-dependent average diameter (nm)
CDC-600	24	91	93	1025±445	1831±445
CDC-800	24	95	96	884±459	1625±459
CDC-1000	24	95	96	1001±458	1826±458
N-CDC-600	24	92	94	839±229	1379±229
N-CDC-800	24	93	95	707±281	1261±281
N-CDC-1000	24	94	95	832±255	1305±255

Table S2: Bonding content of the fitted C 1s peak measured with XPS.

	sp^2 C (%)	sp^3 C (%)	C-N (%)	C-OH (%)	C=O/N-C-O (%)	π-π* (%)
CDC-600	92.4	2.3	-	1.9	0.5	2.8
CDC-800	82.7	8.6	-	2.0	0.8	5.8
CDC-1000	83.0	8.9	-	1.8	0.7	5.6
N-CDC-600	85.2	7.9	2.5	0.8	1.5	2.1
N-CDC-800	77.9	11.4	1.8	2.2	2.2	4.6
N-CDC-1000	77.7	10.2	1.6	2.9	1.9	5.8

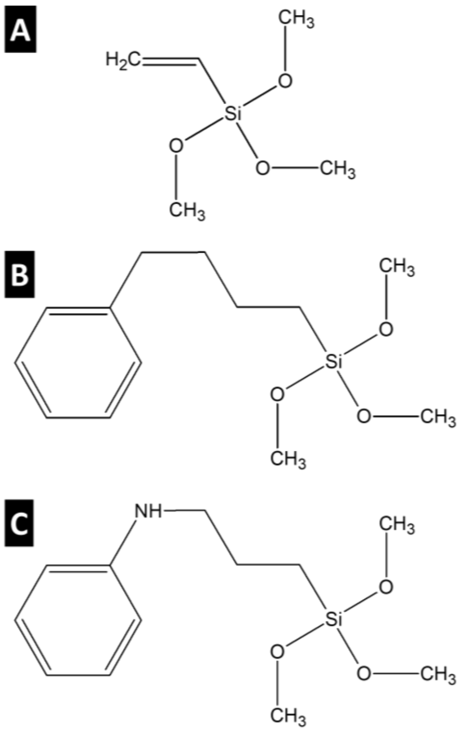

Figure S1: Structural formula of (A) vinyltrimethoxysilane (VTMS), (B) 4-phenylbutyltrimethoxysilane (PBTMS), and (C) [3-(phenylamino)propyl]trimethoxysilane (PAPTMS).

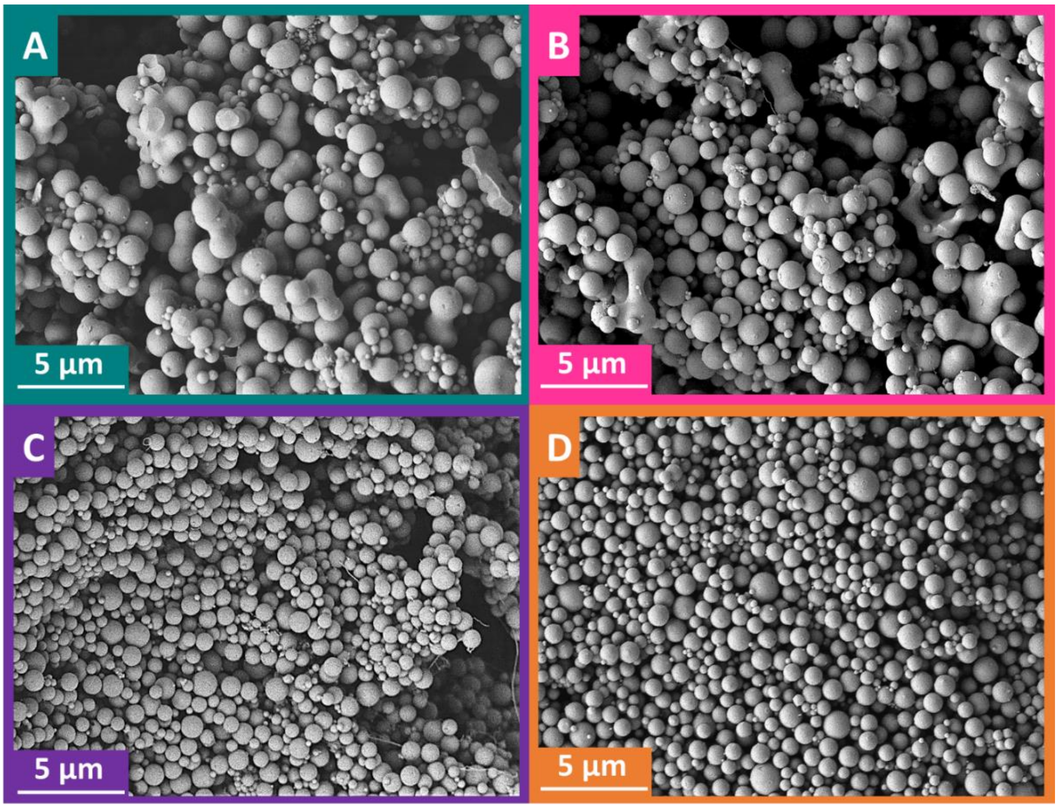

Figure S2: Scanning electron micrographs of (A) CDC-600, (B) CDC-1000, (C) N-CDC-600, and (D) N-CDC-1000.

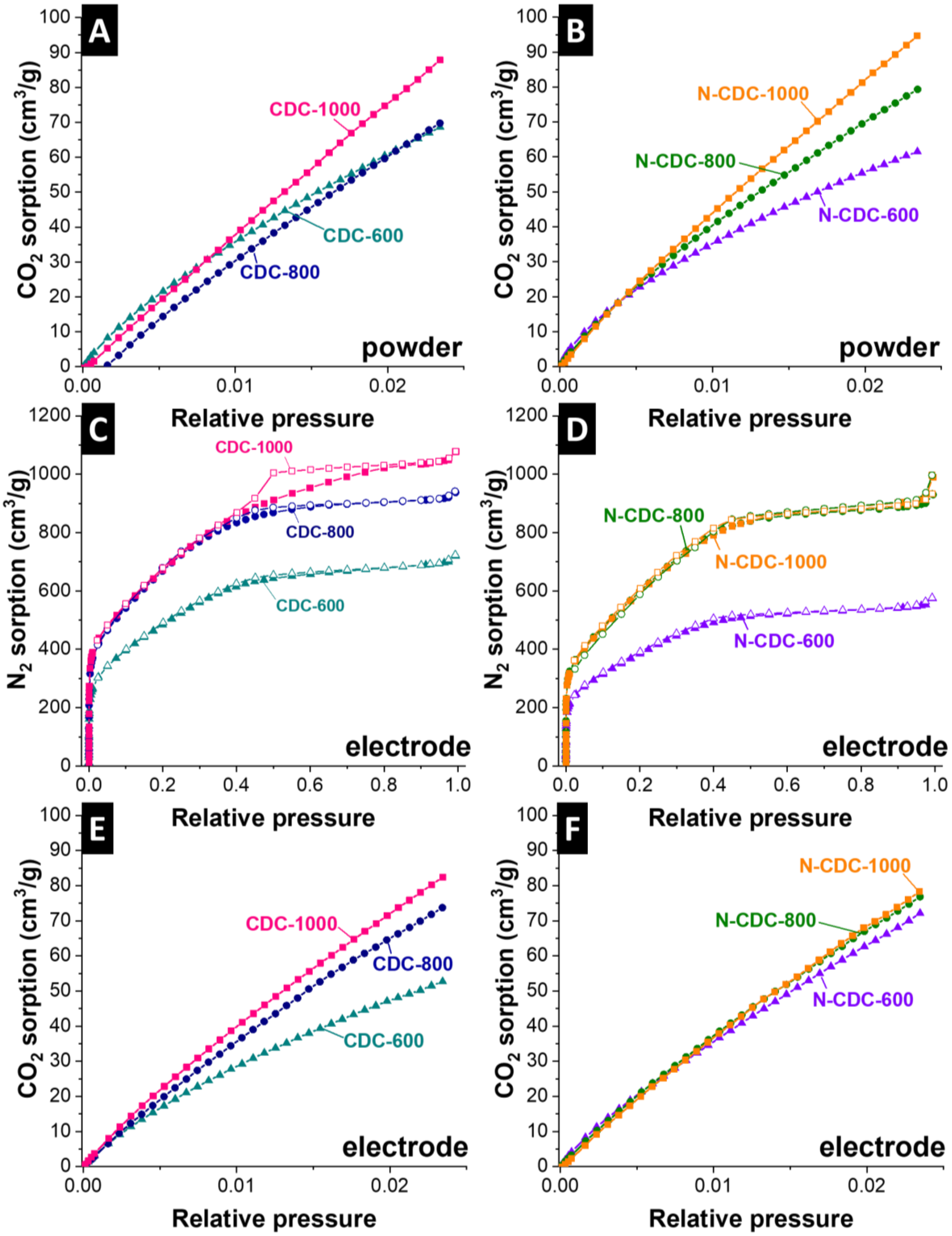

Figure S3: (A,B,E,F) CO$_2$ gas sorption isotherms recorded at 0 °C and (C,D) nitrogen gas sorption isotherms recorded at -196 °C of the carbide-derived carbons with and without nitrogen doping measured as (A,B) powder material or as (C,D,E,F) electrode (i.e., consolidated with 5 mass% of polytetrafluoroethylene).

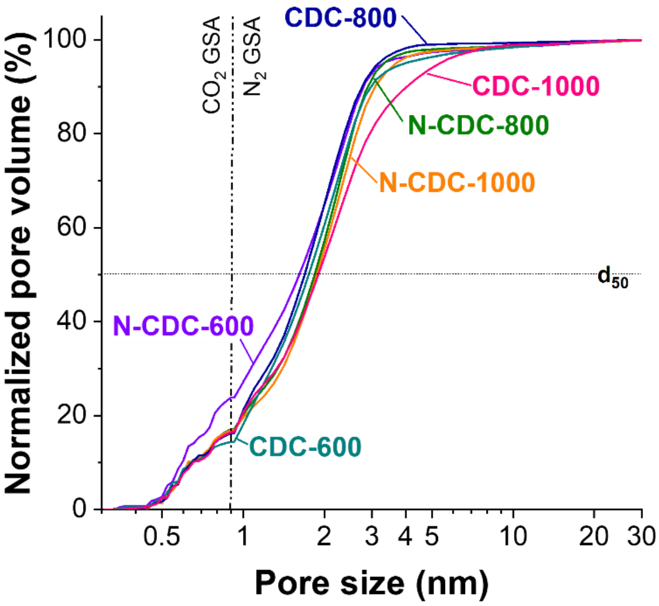

Figure S4: Comparison of the normalized pore size distribution of all materials used as electrodes. The value of d_{50} relates to the volume-weighted average pore size.

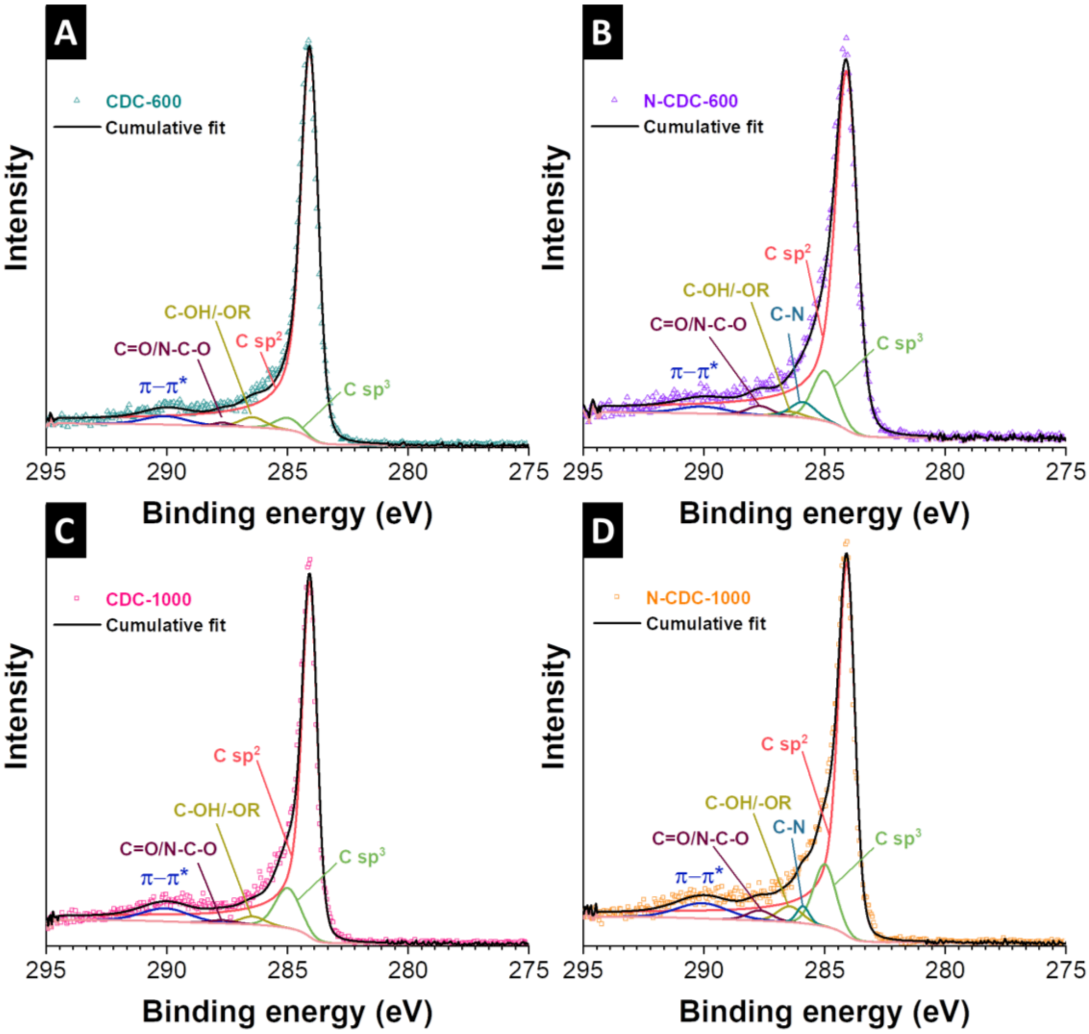

Figure S5: X-ray photoelectron spectra showing the C 1s peaks of the samples (A) CDC-600, (B) N-CDC-600, (C) CDC-1000, and (D) N-CDC-1000.

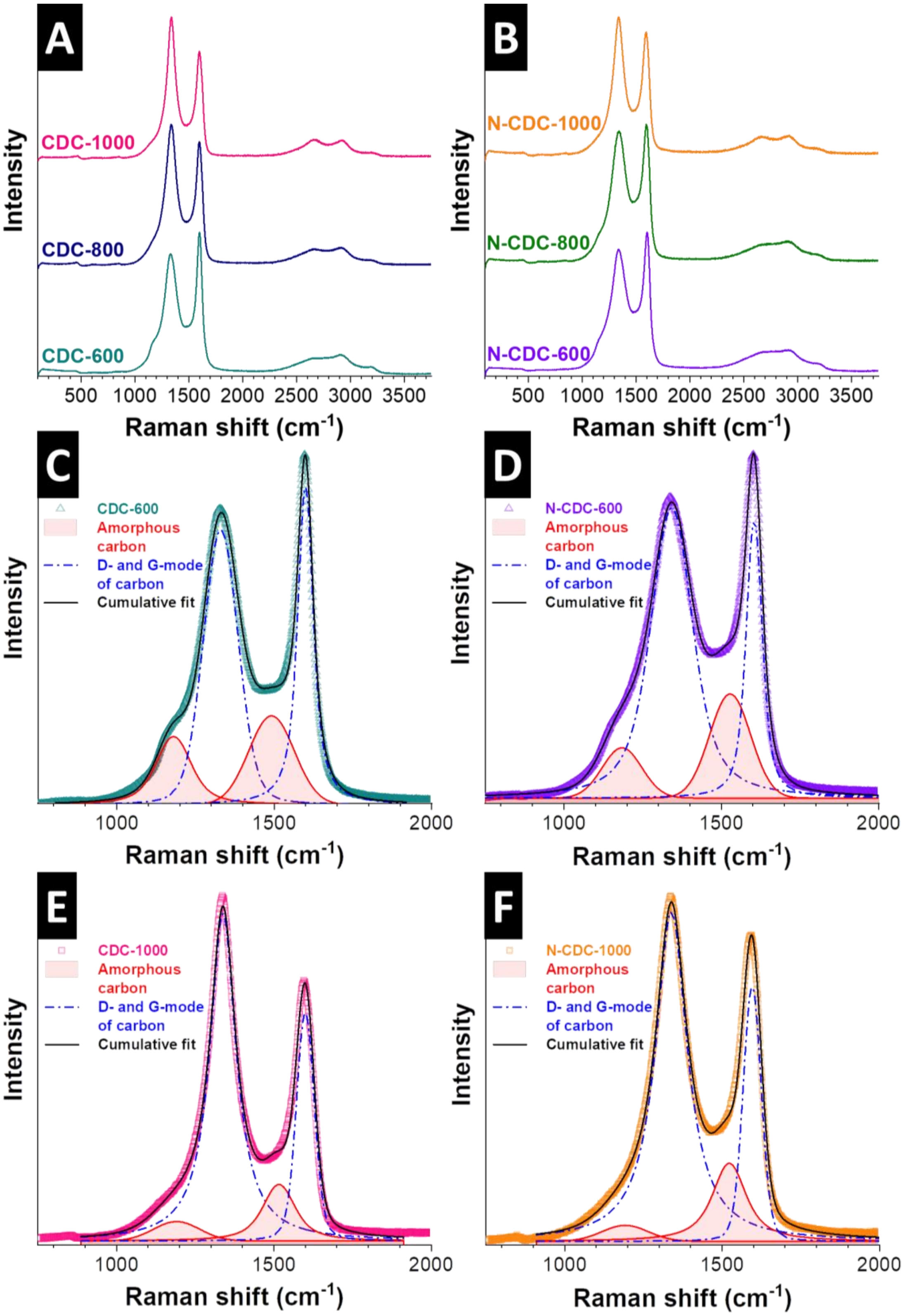

Figure S6: Raman spectra of the samples CDC-600, CDC-800, and CDC-1000 (A) and of the samples N-CDC-600, N-CDC-800, and N-CDC-1000 (B). Fitted Raman spectra of the samples (C) CDC-600, (D) N-CDC-600, (E) CDC-1000, and (F) N-CDC-1000.

4.7. Silicon oxycarbide beads from continuously produced polysilsesquioxane as stable anode material for Li-ion batteries

Benjamin Krüner,[1,2] Christina Odenwald,[3] Nicolas Jäckel,[2] Aura Tolosa,[1,2]

Guido Kickelbick,[3] Volker Presser[1,2]

[1] *INM - Leibniz Institute for New Materials, 66123 Saarbrücken, Germany*

[2] *Department of Materials Science and Engineering, Saarland University, 66123 Saarbrücken, Germany*

[3] *Inorganic Solid State Chemistry, Saarland University, 66123 Saarbrücken, Germany*

Krüner, Benjamin et al. (2018) *ACS Applied Energy Materials*, 1 (6), 2961-2970.
https://doi.org/10.1021/acsaem.8b00716

Own contribution: Design, planning, writing, pyrolysis, SEM, particle size analysis, EDX analysis, N_2 sorption analysis, Raman analysis, NMR data analysis, XRD, electrochemical analysis for Li-ion batteries.

Abstract:

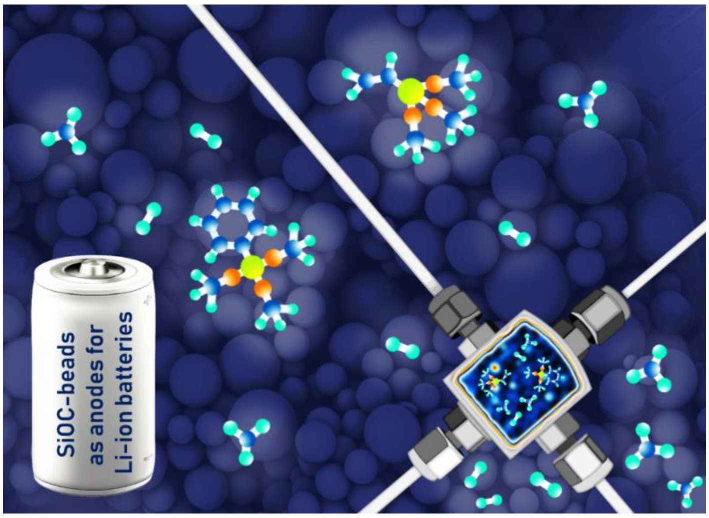

Silicon oxycarbides are promising anode materials for lithium-ion batteries. In this study, we used the continuous MicroJet reactor technique to produce organically modified silica spheres (ORMOSIL) which were pyrolyzed to obtain silicon oxycarbides. The continuous technique allows the production of large quantities with a constant quality. Different silanes were used to produce the silicon oxycarbides with different compositions. Thereby, the amount of silicon/carbon bonds, as well as the free carbon content, were modified. Electrochemical testing was carried out in 1 M $LiPF_6$ in ethylene carbonate/dimethyl carbonate. A mixture of vinyl- and phenyltrimethoxysilane was identified as the best anode material with a stable performance due to the increased carbon content. The first-cycle delithiation capacity of the most stable material was 922 mAh/g and the capacity retention after 100 cycles was 83% (767 mAh/g).

ACS APPLIED ENERGY MATERIALS

Article

Cite This: *ACS Appl. Energy Mater.* 2018, 1, 2961−2970

www.acsaem.org

Silicon Oxycarbide Beads from Continuously Produced Polysilsesquioxane as Stable Anode Material for Lithium-Ion Batteries

Benjamin Krüner,[†,‡] Christina Odenwald,[§] Nicolas Jäckel,[†,‡] Aura Tolosa,[†,‡] Guido Kickelbick,[*,§] and Volker Presser[*,†,‡]

[†]INM—Leibniz Institute for New Materials, 66123 Saarbrücken, Germany
[‡]Department of Materials Science and Engineering, Saarland University, 66123 Saarbrücken, Germany
[§]Inorganic Solid State Chemistry, Saarland University, 66123 Saarbrücken, Germany

Supporting Information

ABSTRACT: Silicon oxycarbides are promising anode materials for lithium-ion batteries. In this study, we used the continuous MicroJet reactor technique to produce organically modified silica (ORMOSIL) spheres which were pyrolyzed to obtain silicon oxycarbides. The continuous technique allows the production of large quantities with a constant quality. Different alkoxysilanes were used to produce the silicon oxycarbides with different compositions. Thereby, the amounts of silicon−carbon bonds, as well as the free carbon content, were modified. Electrochemical testing was carried out in 1 M $LiPF_6$ in ethylene carbonate/dimethyl carbonate. A mixture of vinyl- and phenyltrimethoxysilane was identified as the best anode material with a stable performance due to the increased carbon content. The first-cycle delithiation capacity of the most stable material was 922 mA h/g, and the capacity retention after 100 cycles was 83% (767 mA h/g).

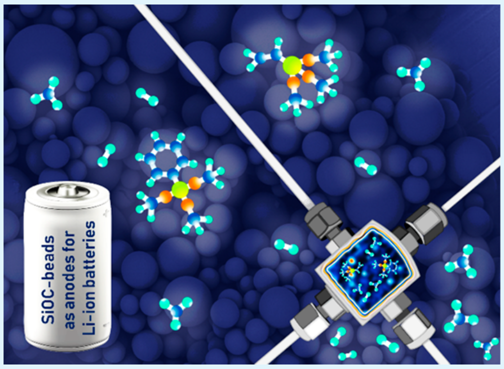

KEYWORDS: *polymer-derived ceramic, silicon oxycarbide, sol−gel, Li-ion battery, anode material, polysilsesquioxane*

1. INTRODUCTION

Lithium-ion batteries (LIBs) are a key technology for today's mobile computing and for the transition of our fleet of internal combustion vehicles to electric cars.[1,2] The constantly growing requirements for energy storage, power handling, safety, and costs are at the core of research activities on next-generation LIB electrode materials.[3,4] Graphite is a common anode material with a theoretical capacity of 372 mA h/g when fully lithiated (LiC_6).[4] A much higher theoretical capacity of 4200 mA h/g is known for silicon, which creates an alloy with lithium.[4] However, the use of silicon remains limited because of the large volume expansion during charging and discharging, causing structural deterioration and poor performance stability of the electrode material.[4−7] The use of nanoparticles and composite or hybrid materials with carbon can reduce the fast capacity fading of silicon-based Li-ion batteries,[6,8−11] but the performance stability remains unsatisfactory.

An alternative to the direct use of silicon is the use of silicon oxycarbides (SiOCs) for LIB anodes. This material can be produced on a large scale by the pyrolysis of polysilsesquioxanes.[12−15] Such SiOC materials belong to the family of polymer-derived ceramics (PDCs) and consist of nanodomains of $SiO_{4-x}C_x$ tetrahedra which are surrounded by free carbon. The encapsulating of the silica domains by graphene cages results in a viscoelastic behavior of the SiOCs, which is beneficial for the large expansion and contraction during the lithiation and delithiation.[16,17] The theoretical capacity of these SiOC materials is between 372 and 1300 mA h/g depending on the composition, which is lower than for SiO_2 (1784 mA h/g).[4,7,14,18] The alloying reaction forming Li_2O is not completely reversible; correspondingly, the Coulombic efficiency of the first cycle is in the range from about 40% to 70% and depends on the chemical composition and the structure, which is influenced by the pyrolysis conditions.[13,14,19,20] For example, Kaspar et al. investigated different pyrolysis temperatures of 900−2000 °C to produce SiOC for Li-ion batteries, and the best Coulombic efficiency was obtained for the material synthesized at 1100 °C.[13] The formation of larger graphitic domains at this temperature leads to improved electrical conductivity and is below the crystallization temperature of SiC (>1200 °C).[21] These domains of free carbon improve the electrical conductivity of the ceramic and reduce the capacity fading of the anode material.[22] The SiOC ceramics with a low amount of free carbon (~8 wt %) have a low conductivity of about 10^{-5} S/m which can increase to ~2 S/m for a high content of free carbon (~54 wt %), measured at a high pressure

Received: May 4, 2018
Accepted: June 1, 2018
Published: June 1, 2018

DOI: 10.1021/acsaem.8b00716
ACS Appl. Energy Mater. 2018, 1, 2961−2970

of 1 MPa.[22] These values are still low for use as electrodes, and it is necessary to improve the conductivity further by adding a conductive additive, such as carbon black.

The importance of silicon−carbon bonds for the electrochemical performance was shown, for example, by Graczyk-Zajac et al. using polysiloxanes pyrolyzed in an argon atmosphere or in an oxidizing CO_2 atmosphere.[19] The ^{29}Si NMR data of the oxidized sample documented the absence of silicon−carbon bonds after the pyrolysis, while the content of free carbon was about 37 wt %.[19] The sample pyrolyzed in argon contained units of C_2SiO_2, $CSiO_3$, and SiO_4, along with 47 wt % free carbon. Both electrode materials had a similar initial capacity of ∼1500 mA h/g during the cathodic sweep, but the reversible capacity was much higher for the sample treated in argon (800 mA h/g) compared to the other material (600 mA h/g). The long-time stability of the SiOC with silicon−carbon bonds was higher compared to that of the oxidized SiOC. Nevertheless, the reversible capacity after 100 cycles was only 55% of the initial capacity, and the largest capacity fade occurs already after 20 cycles. In another study, Pradeep et al. synthesized a SiOC aerogel which had a capacity retention of almost 80% after 100 cycles, but the overall specific capacity was rather low (450 mA h/g).[23] Many other publications of SiOCs as anode material for Li-ion batteries report even less than 100 cycles at low rate, by which measure it is difficult to assess the actual performance stability.[12,22,24]

In this study, we investigate three SiOC bead materials obtained from methyltrimethoxysilane, vinyltrimethoxysilane, and a mixture of vinyltrimethoxysilane with phenyltrimethoxysilane. Wilamowska-Zawlocka et al. used similar precursors for the synthesis of SiOC as LIB anodes, but they used a batch method which resulted in large particles which were ball-milled to obtain particles of around 10 μm.[20] In contrast to previous work, we produced polysilsesquioxane with a spherical shape and by use of the continuous MicroJet reactor.[25,26] The voids between the spherical particles may partially buffer the volume expansion and improve the performance stability of the LIB.[10,11] Our approach does not need any cross-linking agent to maintain the sphere morphology, and the continuous process allows the production of large amounts with constant quality. The absence of a cross-linker is expected to enhance the purity of the resulting SiOC material.[15,27]

We analyzed the SiOC beads among others with electron microscopy, X-ray diffraction, Raman spectroscopy, solid-state NMR, and Fourier-transform infrared spectroscopy. This array of analytical tools helped us to clarify the correlation between structural properties and the resulting electrochemical performance when used as an anode for Li-ion batteries. The electrochemical performance in 1 M $LiPF_6$ in ethylene carbonate/dimethyl carbonate was characterized with a focus on the long-time stability.

2. EXPERIMENTAL DESCRIPTION

2.1. Synthesis of Siloxane Beads and Pyrolysis. Methyltrimethoxysilane (MTMS; 97%), vinyltrimethoxysilane (VTMS; 99%), and phenyltrimethoxysilane (PTMS; 97%) were purchased from ABCR. The diluted ammonia (25%) was obtained from VWR. All chemicals were used as received.

The synthesis of the polysiloxane microparticles is described in detail in our previous publications.[25,26] An overview of the synthesis steps is provided in the Figure 1. In short, the silanes were dissolved in methanol and aqueous HCl and prehydrolyzed at room temperature overnight. The silane solution was mixed with an ammonia solution with a concentration of 2.2 M in a microreactor (MicroJet reactor, Synthesechemie Dr. Penth GmbH) at 20 °C. The composition of the used silane solution is listed in Table 1. Two HPLC pumps (LaPrep P110 preparative HPLC pumps, VWR; flow rate, 250 mL/min) transport the precursor solutions through opposing horizontal nozzles (300 μm in diameter) in the mixing chamber where they collide as fine impinging jets, and a fast mixing occurs. A gas flow (N_2, 0.8 MPa) orthogonal to the feeding jets supports the transfer of the product suspension out of the reactor. The suspension was collected, and the particles were centrifuged (8000 rpm, 7012*g*, 10 min) and dried in vacuum at room temperature.

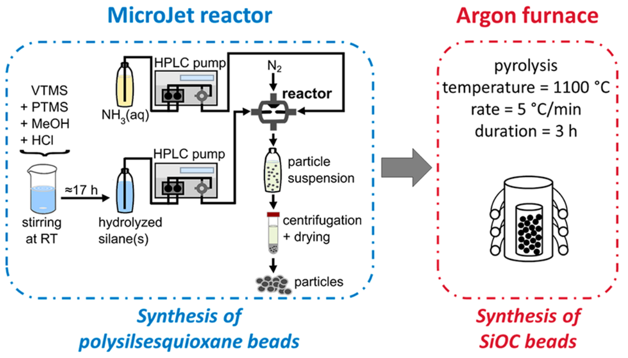

Figure 1. Schematic synthesis using the MicroJet reactor to obtain polysilsesquioxane beads which are transformed to silicon oxycarbide beads via thermal treatment in argon. The scheme was modified and is reproduced with permission.[26] Copyright 2017 Royal Society of Chemistry.

The three different types of polysiloxane particles were pyrolyzed in a graphite furnace (LHTG, Carbolite Gero) in an argon atmosphere at 1100 °C for 3 h with a heating rate of 300 °C/h. The pyrolysis temperature of 1100 °C was chosen to yield graphitic carbon which improves the conductivity, but to stay below the temperature regime of silicon carbide crystallization.[13]

2.2. Electrode Preparation. The pyrolyzed SiOC beads were mixed with 5 wt % of carbon black (CB; C-Nergy Super C65 from Imerys Graphite & Carbon). We chose 5 wt % sodium carboxymethylcellulose (NaCMC) as the binder because it is superior to polyvinylidene fluoride (PVdF) for silicon and silicon oxide electrodes, and the use of water as solvent is less hazardous than *N*-methyl-2-pyrrolidone (NMP).[28−30] A solution of NaCMC in water (1 wt %) was used to prepare a suspension of SiOC and CB which was coated with a doctor blade (layer thickness: 200 μm) on a copper foil as a current collector and dried at 80 °C for 24 h.

2.3. Material Characterization. Electron microscopy was performed with a field emission scanning electron microscopy (SEM) JSM-7500F instrument from JEOL and a high-resolution transmission electron microscopy (TEM) JEM-2100F instrument from JEOL as well. A thin platinum layer was sputtered onto the SEM samples to increase the surface conductivity, and 175 beads were analyzed with the software ImageJ to obtain the average diameter.[31] For TEM, the samples were dispersed and sonicated in ethanol to deposit them on a lacey carbon film on a copper grid from Gatan. The TEM was operated using a voltage of 200 kV under vacuum.

The chemical composition of the silicon oxycarbides was quantified with energy-dispersive X-ray spectroscopy (EDX). This X-MAX silicon detector from Oxford Instruments was attached to the SEM chamber. The electron beam for the EDX had a voltage of 5 kV, and the samples were sputtered with a thin layer of gold. A total of 20 EDX spectra were recorded, and the average composition was used to calculate the theoretical formula for the SiOCs.

Nitrogen gas sorption analysis (GSA) was carried out to measure the specific surface area (SSA) with an Autosorb iQ system from Quantachrome. The samples were outgassed at 300 °C for up to 20 h, and the measurements were performed at −196 °C in the relative pressure range from 2×10^{-4} to 1.0. The linear regime of the isotherm was analyzed with the Brunauer−Emmett−Teller equation to calculate the specific surface area.[32] The skeletal density of the silicon

Table 1. Compositions of Precursor Silane Solutions and Ammonia Solution That Were Used for the Synthesis of Polysilsesquioxane Microparticles

	silane solution						
sample	$n_{(\mathrm{MTMS})}$ (mmol)	$n_{(\mathrm{VTMS})}$ (mmol)	$n_{(\mathrm{PTMS})}$ (mmol)	$n_{(\mathrm{MeOH})}$ (mol)	$n_{(\mathrm{H_2O})}$ (mol)	$n_{(\mathrm{HCl})}$ (mmol)	ammonia solution $c_{(\mathrm{NH_3})}$ (mol/L)
Me-SiOC	69.4			2.8	2.8	0.01	2.2
Vi-SiOC		277.6		6.4	5.6	0.06	2.2
Vi-Ph-SiOC		83.3	16.7	6.4	11.1	0.01	2.2

oxycarbide beads was measured by helium pycnometry (AccuPyc 1330 pycnometer from Micromeritics; He purity, 5.0).

The solid-state NMR measurements were performed on a Bruker AV400WB spectrometer. The samples were packed in zirconia rotors that were spun at 13 kHz under nitrogen or compressed air flow. The spectra were recorded with single pulse excitation under the following conditions: ^{29}Si frequency, 79.5 MHz; $\pi/4$ pulse length, 3.8 μs; recycle delay, 10 s, >10^3 scans. ^{13}C frequency, 100.7 MHz; $\pi/4$ pulse length, 3.5 μs; recycle delay, 10 s, >10^3 scans. Adamantane (for ^{13}C) and octakis(trimethylsiloxy)silsesquioxane (for ^{29}Si) were used as the external standards. The ^{29}Si NMR spectra were fitted with 4 Voigt functions to quantify the SiO_4, $CSiO_3$, C_2SiO_2, and C_3SiO units. The Fourier-transform infrared spectroscopy (FT-IR) was measured with a diamond total attenuated reflectance crystal (ATR; Tensor 27 system from Bruker AXS). The spectra were integrated over 28 scans.

X-ray diffraction was carried out with a D8 Discover diffractometer from Bruker AXS. Cu Kα radiation was chosen with a Lynxeye detector in a Bragg−Brentano configuration. We carried out Raman spectroscopy to investigate the structure of the SiOC beads with a Renishaw inVia Raman microscope. The wavelength of the laser was 532 nm, and a grating of 2400 lines/mm was used. The spectral resolution was 1.2 cm^{-1}, the numeric aperture 0.75, and the incident power on the sample ~0.2 mW.

The conductivity of the powder was measured in a custom-built device seen in the Supporting Information, Figure S1, and the two-point-probe was operated with a Keithley 199 System DMM/scanner. The diameter of the pressure cell was 13 mm, and a powder mass of 50 mg was filled in the cell. The powder was contacted with copper foil, and a pressure of 1 MPa was applied during the measurement with a Zwick Roell Xforce HP system.

2.4. Electrochemical Measurements. Electrode disks with a diameter of 1.42 cm were punched out and placed in a CR2032 coin cell. The electrodes had a thickness after drying of approximately 100 μm while the mass loading (SiOC with carbon black and binder) was 1.9 mg/cm^2. A glass fiber mat (GF/D from Whatman, GE Healthcare Life Science) was used as a separator, and a lithium disk (diameter: 15.6 mm) served as the counter electrode in a two-electrode setup. Lithium hexafluorophosphate ($LiPF_6$) in electrochemical grade ethylene carbonate/dimethyl carbonate (EC/DMC 1:1 by volume; LP30) with a concentration of 1 M from BASF served as the electrolyte.

An Astrol BatSmall battery analyzer was used for the galvanostatic measurements. The cell voltage was applied between +0.01 and +3.0 V versus Li/Li$^+$. For characterization of the rate handling, the first 5 cycles were conducted with a specific current of 35 mA/g, which corresponds to a C-rate of 0.05C when we assume a specific capacity of 700 mA h/g. The specific current was increased to 70 mA/g (0.1C) for 20 cycles, 140 mA/g (0.2C), 350 mA/g (0.5C), 700 mA/g (1C), and 1400 mA/g (2C) for 10 cycles each. Afterward, the specific current was reduced to 70 mA/g for the last cycles. The long-time stability test was carried out using a specific current of 70 mA/g. The specific capacity C_{sp} was calculated with eq 1 with I for the current, dt for the time per charging or discharging step, and m_{SiOC} for the active mass of the electrode (i.e., 90 wt % of SiOC).

$$C_{\mathrm{sp}} = \frac{\int_{t_0}^{t_1} I\,\mathrm{d}t}{m_{\mathrm{SiOC}}} \tag{1}$$

The cyclic voltammograms were recorded with a Squidstat Prime potentiostat from Admiral Instruments with a scan rate of 0.1 mV/s in the same potential window as the galvanostatic measurements.

3. RESULTS AND DISCUSSION

3.1. Material Characterization. The TEM images in Figure 2 show the synthesized spherical particles after pyrolysis. The average volume-dependent diameter of the beads is 0.9−2.4 μm, while Me-SiOC has the smallest and Vi-SiOC the largest size within that range. The particle size distributions are plotted in the Supporting Information, Figure S2A. These values, together with the specific surface area, the skeletal density, and the mass loss during pyrolysis, are listed in Table 2. The skeletal density of the SiOCs is in the range 2.16−2.36 g/cm^3, which is similar to values for SiOC ceramics found in the literature (1.9−2.3 g/cm^3).[33,34]

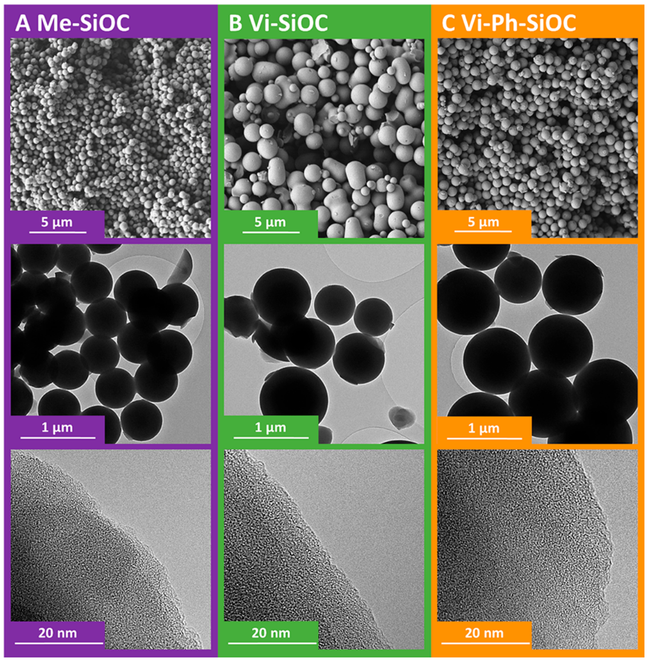

Figure 2. Scanning and transmission electron micrographs of the pyrolyzed SiOC samples. (A) Me-SiOC, (B) Vi-SiOC, and (C) Vi-Ph-SiOC.

The pyrolysis of the polysilsesquioxane particles leads to a mass loss of 29 wt % for Me-SiOC, 12 wt % for Vi-Ph-SiOC, and 10 wt % for Vi-SiOC. The small methyl groups tend to decompose more easily which explains the higher mass loss. The phenyl groups have a higher molar mass than the vinyl and methyl groups, and we observed correspondingly a larger mass loss for Vi-Ph-SiOC compared to Vi-SiOC.[26] The mass loss also reflects the specific surface area because the decomposition of organic components produces pores. Nitrogen gas sorption was carried out to measure the specific surface area, and the

Table 2. Mass Loss after the Pyrolysis, Average Diameter, Skeletal Density, Measured Specific Surface Area, and Calculated External Surface Area of the SiOC Beads

sample	mass loss (wt %)	number-dependent average diameter (nm)	volume-dependent average diameter (nm)	skeletal density (cm^3/g)	SSA_{BET} (m^2/g)	$SSA_{external}$ (m^2/g)
Me-SiOC	29	576 ± 77	903 ± 77	2.36	6.0	2.8
Vi-SiOC	10	1365 ± 509	2366 ± 509	2.20	3.1	1.2
Vi-Ph-SiOC	12	776 ± 156	1244 ± 156	2.16	4.7	2.2

Table 3. Chemical Composition Measured with EDX and the Theoretical Formula of the SiOC Calculated by the EDX and the Specific Conductivity of Powder of SiOC Beads and Carbon Black (C65) Compacted with 1 MPa Compression Force

sample	Si (wt %)	O (wt %)	C (wt %)	Si (atom %)	O (atom %)	C (atom %)	formula via EDX	specific conductivity (S/m)
Me-SiOC	37.9 ± 5.1	40.0 ± 1.5	22.1 ± 4.4	23.9 ± 4.1	44.0 ± 1.6	32.1 ± 5.0	$SiO_{1.84}C_{0.08} + C_{1.26}$	$<3 \times 10^{-6}$
Vi-SiOC	38.9 ± 3.0	29.6 ± 1.8	31.5 ± 1.3	23.7 ± 2.3	31.6 ± 1.4	44.8 ± 1.1	$SiO_{1.33}C_{0.33} + C_{1.56}$	$(7.3 \pm 0.1) \times 10^{-6}$
Vi-Ph-SiOC	30.6 ± 2.2	29.4 ± 0.8	40.0 ± 1.5	17.5 ± 1.5	29.4 ± 0.5	53.2 ± 1.2	$SiO_{1.68}C_{0.16} + C_{2.89}$	$(1.2 \pm 0.1) \times 10^{-2}$
carbon black			>98			>98	C	2264 ± 22

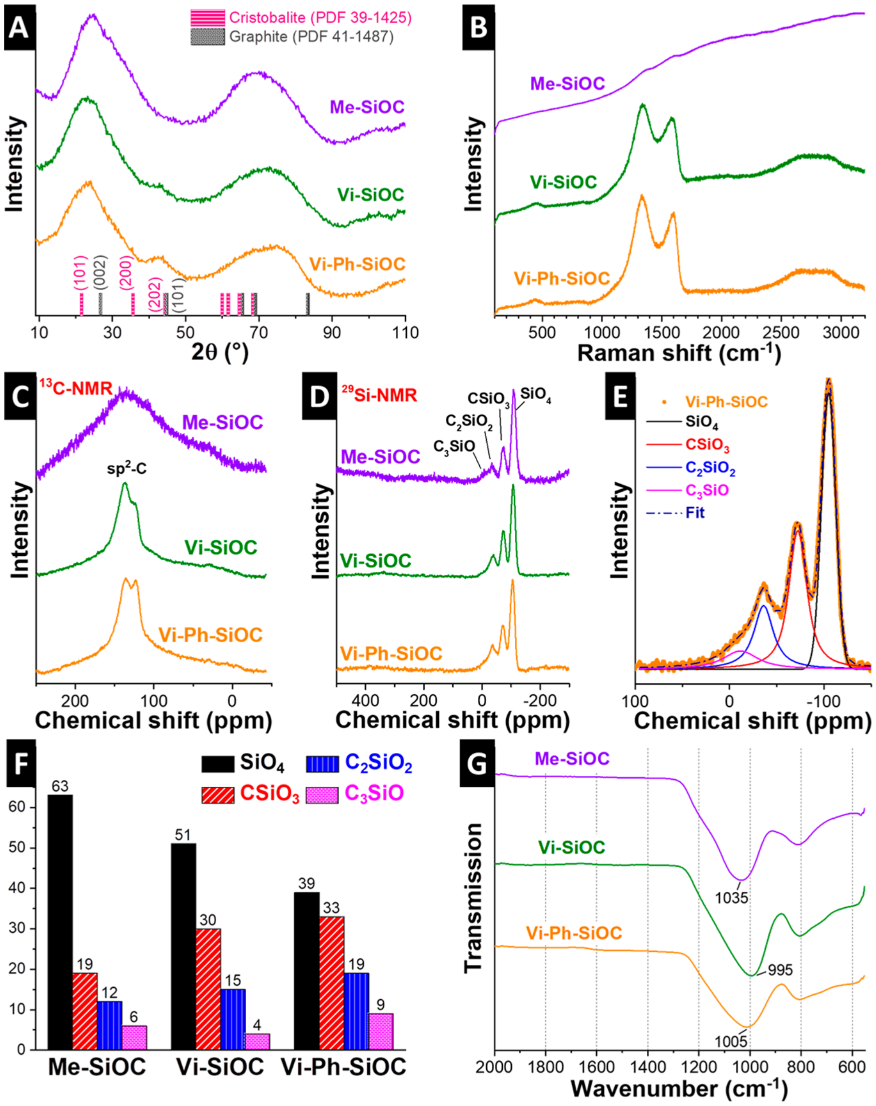

Figure 3. Material characterization of the pyrolyzed SiOC samples. (A) X-ray diffractograms. (B) Raman spectra. (C) ^{13}C NMR. (D) ^{29}Si NMR. (E) ^{29}Si NMR peak deconvolution for Vi-Ph-SiOC. (F) Contributions of the measured Si-bonds. (G) FT-IR spectra.

isotherms are plotted in the Supporting Information (Figure S2B). Me-SiOC and Vi-Ph-SiOC have an SSA_{BET} of 6 and 5 m^2/g, respectively. The sample with the lowest mass loss was Vi-SiOC which also shows the lowest surface area (3 m^2/g). While these values were obtained from gas sorption measurements, we can also calculate the external specific surface area using the volume-dependent average diameter (d) and the skeletal density (ρ) of the ceramic particles with eq 2:

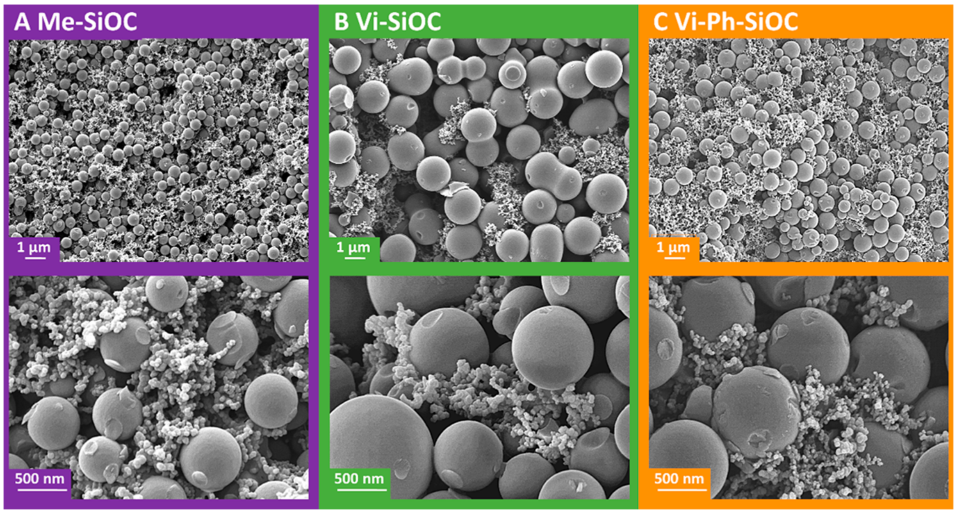

Figure 4. Scanning electron micrographs of the electrodes coated on a nickel current collector with 5 wt % NaCMC (binder) and 5 wt % carbon black (conductive additive). (A) Me-SiOC, (B) Vi-SiOC, and (C) Vi-Ph-SiOC.

$$\mathrm{SSA}_{\mathrm{external}} = \frac{\pi d^2}{\rho d^3 \frac{1}{6}\pi} = \frac{6}{\rho d} \qquad (2)$$

As seen from Table 2, the external specific surface area of the particles is approximately half of the measured $\mathrm{SSA_{BET}}$. Accordingly, all beads have internal pores in addition to the external surface. Overall, the specific surface area of our SiOC beads is very small compared to those of mesoporous SiOC aerogels with around 200 m^2/g.[19,23]

The chemical composition of the SiOC materials was quantified via EDX. As can be seen from Table 3, the material with the lowest carbon amount in the precursor had also the lowest amount of carbon in the ceramic. This finding aligns with previous reports.[26,35] Me-SiOC had a carbon content of 22 wt %, while Vi-SiOC and Vi-Ph-SiOC had 32 and 40 wt % of carbon, respectively. The chemical composition also allows the calculation of the theoretical formula $SiO_{2-2x}C_x + yC_{\mathrm{free}}$.[36] The samples with a higher overall carbon content also have a higher content of free carbon, which is known to surround the silica domains. Me-SiOC has 1.26 parts of C_{free} corresponding to one $SiO_{2-2x}C_x$ unit, which increases for Vi-SiOC to 1.56 and for Vi-Ph-SiOC to 2.89.

The TEM images in Figure 2 show the morphology and the structure of the beads. At high magnifications, we see the nonordered structure of the silicon oxycarbides which were pyrolyzed at 1100 °C. This maximum temperature remains below the temperature at which the formation of crystalline carbides is expected.[13,17] The domain size was estimated from XRD data (Figure 3A) by applying the Scherrer equation and assuming a SiO_2 and graphite phase.[37] The domain size of the SiO_2 and graphite phase for Me-SiOC, Vi-SiOC, and Vi-Ph-SiOC is around 1 nm. Fewer than six unit cells of crystalline SiO_2 with a volume of approximately $0.5 \times 0.5 \times 0.7$ nm^3 can fit into a volume of 1 nm^3 assuming a crystalline structure with SiO_4 tetrahedrons and a Si−O distance of 0.16 nm.[38] A significant difference in the XRD pattern of Vi-SiOC and Vi-Ph-SiOC is an increased peak intensity at 43° 2θ. These two materials have a larger amount of carbon, and the observed peaks align with the (101) plane of incompletely graphitic carbon. The incompletely graphitic nature of carbon is also confirmed with Raman spectroscopy where we observed a characteristic D-mode at 1340 cm^{-1} and a G-mode at 1600 cm^{-1} (Figure 3B).[39,40] In the case of the Raman spectrum of Me-SiOC, the D-mode and the G-mode are overlaid by a large fluorescence background.

The ^{13}C and ^{29}Si solid-state NMR spectra give further insights into the chemical structure of the SiOC samples (Figure 3C−F). Me-SiOC has only one very broad peak for the chemical shift of ^{13}C at +130 ppm, which indicates the formation of aromatic carbon groups.[40−43] After the pyrolysis at 1100 °C, there is no signal from the methyl group at around −5 ppm.[42,43] The data of Vi-SiOC and Vi-Ph-SiOC show a larger signal for sp^2-conjugated carbon, which is split into two peaks at 123 and 136 ppm. These signals relate to aromatic carbon.[42,43]

The carbon/silicon and silicon/oxide bonds were further investigated with ^{29}Si NMR (Figure 3D). The presence of SiO_4 groups is documented by a peak at a chemical shift of −105 ppm. This signal is reduced when the silicon atoms are bound to carbon atoms as well. $CSiO_3$ units have a shift of −73 ppm, C_2SiO_2 units of −35 ppm, and C_3SiO units of −11 ppm.[19,44] We deconvoluted these contributions by fitting four Voigt functions (Figure 3F). SiO_4 units are dominant in all samples, and we see the largest contributions thereof for Me-SiOC (63%), which has also the lowest amount of silicon−carbon bonds. There are fewer SiO_4 units in Vi-SiOC (51%) and even less for Vi-Ph-SiOC (39%). The number of silicon−carbon bonds increases with the amount of carbon. Vi-Ph-SiOC has the highest amount of $CSiO_3$, C_2SiO_2, and C_3SiO units (in total 61%). Vi-SiOC has a similar amount of silicon atoms only bound to oxygen, as silicon atoms bound to oxygen and carbon at the same time.

The FT-IR spectra provide further information about the structure of the pyrolyzed SiOC materials. Peaks in the range 1000−1100 cm^{-1} relate to an antisymmetric stretching mode Si−O−Si network.[45] A shift toward lower wavenumbers of the latter occurs when carbon atoms are introduced to the structure (Figure 3G).[19,45] This mode is at 1035 cm^{-1} for Me-SiOC, and the downshift becomes larger for a higher amount of carbon. Accordingly, Vi-SiOC and Vi-Ph-SiOC exhibit a Si−O−Si stretching mode at 995 and 1005 cm^{-1}, respectively. Another peak is observed at 810 cm^{-1} for all samples, which indicates Si−C or C−O bonds.[45,46]

The electrical conductivity of the SiOC powders was measured at a pressure of 1 MPa and is listed in Table 3.

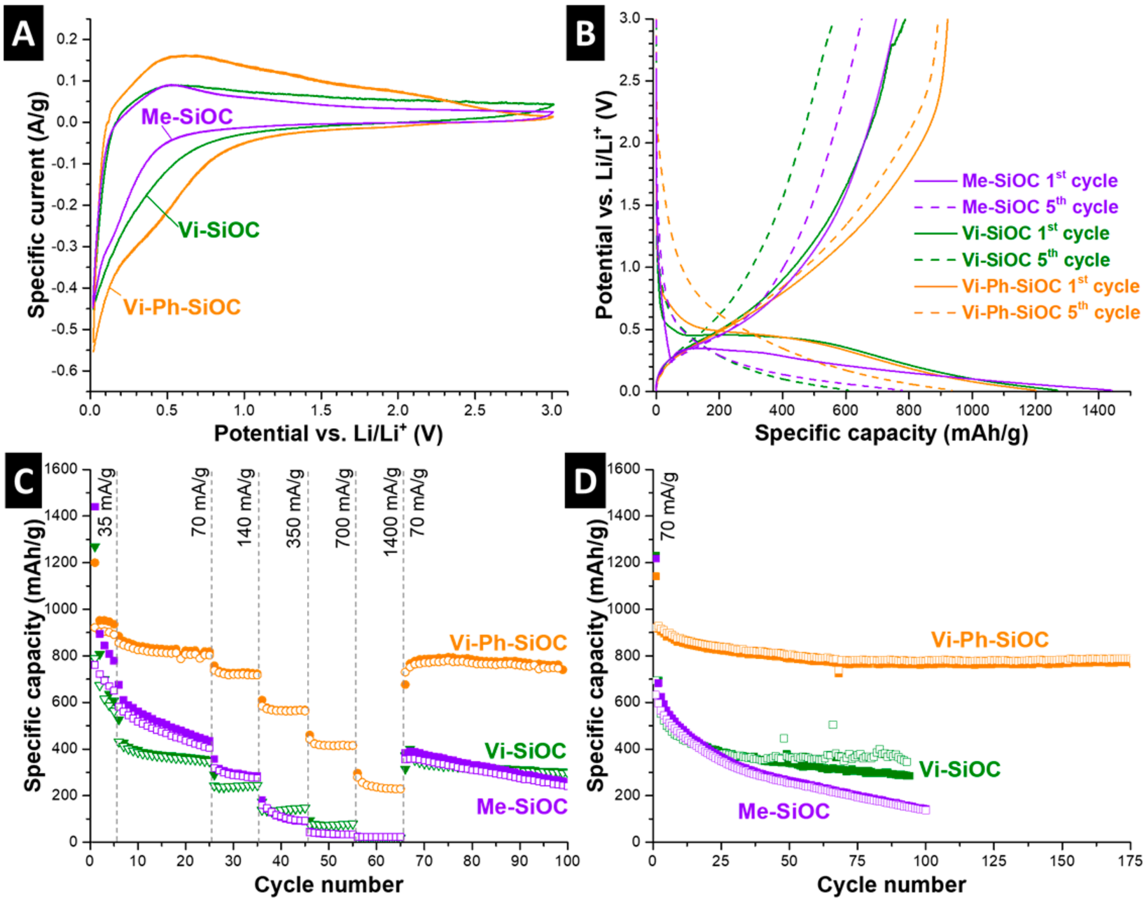

Figure 5. Electrochemical characterization of pyrolyzed Me-SiOC, Vi-SiOC, and Vi-Ph-SiO using 1 M LiPF$_6$ in EC/DMC. (A) Cyclic voltammograms of the 5th cycle at 0.1 mV/s. (B) Galvanostatic charge/discharge profiles of the 1st and 5th cycle at 35 mA/g. (C) Rate capability at 35−1400 mA/g. (D) Performance stability at 70 mA/g.

The conductivity of Me-SiOC was below the limit of detection of 3×10^{-6} S/m. Vi-SiOC had a low conductivity of $(7.3 \pm 0.1) \times 10^{-6}$ S/m, and Vi-Ph-SiOC had the value of $(1.2 \pm 0.1) \times 10^{-2}$ S/m due to the higher amount of carbon in the sample. An increase of the conductivity of SiOCs with an increasing amount of free carbon was also observed by Kasper et al. and was found beneficial for the use in LIBs.[22,47] Although the electrical conductivity of Vi-Ph-SiOC beads was much larger compared to those of the other materials, it is still low compared to those of other electrode materials; accordingly, we added carbon black (C65 with a conductivity of 2264 ± 22 S/m) to all electrodes.

3.2. Electrochemical Characterization of SiOC Beads as Anodes for Li-Ion Batteries. For electrochemical measurements, the pyrolyzed SiOC beads were mixed with NaCMC binder and carbon black. The resulting cast electrodes show a homogeneous distribution for all three types of material (Figure 4). The carbon black particles percolate well between the SiOC beads to guarantee a sufficient electrical conductivity.[48] The specific capacity was normalized to the amount of silicon oxycarbide.[13,19,22,27]

First, we determined the possible contribution of carbon black to the measured specific capacity at 0.1 mV/s in the used potential range (from +0.01 to +3.0 V versus Li/Li$^+$). The cyclic voltammograms and the voltage profile of an electrode only composed of carbon black are provided in the Supporting Information, Figure S3. The first lithiation cycle at 35 mA/g of carbon black electrodes provides a specific capacity of 480 mA h/g, and the first delithiation capacity is about 250 mA h/g. The latter value remains stable during four subsequent charge/discharge cycles. In our SiOC electrodes, we admixed only 5 wt % of carbon black. Therefore, the contribution of carbon black to the measured specific capacity of our SiOC materials is around 13 mA h/g. This contribution is minor compared to the high specific capacity of the SiOC (>700 mA h/g).

The cyclic voltammograms for the fifth cycle were recorded at 0.1 mV/s in a potential range from +0.01 to +3.0 V versus Li/Li$^+$ and plotted in Figure 5A. The data show a cathodic lithiation peak below 1 V versus Li/Li$^+$. Vi-Ph-SiOC shows the largest specific current response and, thereby, the largest specific capacity. This is in agreement with the study of Wilamowska-Zawlocka et al. showing that a mixture of vinyl with phenyl groups with the ratio of 1:2 yielded the best performance for SiOC materials.[20] The extraction of the Li$^+$ out of the SiOC occurs at around +0.6 V versus Li/Li$^+$. Similar potentials for the lithiation (discharging) and delithiation (charging) are seen in the galvanostatic charge/discharge profiles shown in Figure 5B. As common for LIB anodes, the first-cycle lithiation capacity is much larger than the following, which is partially attributed to the reduction of the electrolyte below 1 V versus Li/Li$^+$ forming the solid−electrolyte interphase (SEI).[7] The first delithiation of the Vi-Ph-SiOC yielded a specific capacity of 922 mA h/g, which slightly reduced to 892 mA h/g for the fifth cycle. Me-SiOC and Vi-SiOC have a higher specific capacity of 1440 mA h/g and 1269 mA h/g during the first lithiation cycle (Figure 5C,D) because

DOI: 10.1021/acsaem.8b00716
ACS Appl. Energy Mater. 2018, 1, 2961−2970

Table 4. Electrochemical Performance[a] of the SiOC Beads Compared with the Literature

				specific capacity (mA h/g)							
				1st cycle		5th cycle		100th cycle			
sample	electrode	carbon content (wt %)	potential vs Li/Li$^+$ (V)	L	D	L	D	L	D	capacity retention (%)	ref
Me-SiOC	90 wt % SiOC; 5 wt % NaCMC; 5 wt % carbon black	22	0.01−3	1440	761	779	650	258	241	32	this work
Vi-SiOC	90 wt % SiOC; 5 wt % NaCMC; 5 wt % carbon black	32	0.01−3	1269	789	608	563	302	299	38	this work
Vi-Ph-SiOC	90 wt % SiOC; 5 wt % NaCMC; 5 wt % carbon black	40	0.01−3	1200	922	936	892	762	747	83	this work
carbon black (C65)	95 wt % carbon black; 5 wt % NaCMC	98	0.01−3	479	251	272	251	282	279	111	this work
PhTES:VTES 2:1 sol−gel particles	85 wt % SiOC; 10 wt % PVdF; 5 wt % carbon black	39	0.005−3	1462	900				558 (134 cycles)	62	20
electrospun Sn/SiOC fibers (0.05Sn-1200)	free-standing electrode	41	0.01−3	1075	840	804	801		509	61	15
SiOC-1100 °C microparticles	85 wt % SiOC; 10 wt % PVdF; 5 wt % carbon black	42	0.005−3	866	532						13
SiOC-1000 °C (PD2) microparticles	85 wt % SiOC; 10 wt % PVdF; 5 wt % carbon black	55	0−3	898	568						14
PR/DVB SiOC	85 wt % SiOC; 10 wt % PVdF; 5 wt % carbon black	59	0.005−3	791	504				338 (60 cycles)	67	22
PR SiOC	85 wt % SiOC; 10 wt % PVdF; 5 wt % carbon black	51	0.005−3	872	536				304 (60 cycles)	57	22
SR/RR SiOC	85 wt % SiOC; 10 wt % PVdF; 5 wt % carbon black	39	0.005−3	1178	683				90 (60 cycles)	14	22
PB-SiOC microparticles	85 wt % SiOC; 7.5 wt % PVdF; 7.5 wt % carbon black	72	0−3	867	608	∼570	∼560		∼550 (50 cycles)	90	12
SiOC-Ar aerogels	85 wt % SiOC; 10 wt % PVdF; 5 wt % carbon black	>47	0.005−3	∼1500	∼780		∼660		∼430	55	19
SiOC aerogels	85 wt % SiOC; 10 wt % PVdF; 5 wt % carbon black	43	0.005−3	∼1160	∼580			∼420	∼450	78	23
SiOC−CNT composite	80 wt % SiOC/CNT; 10 wt % PAA; 10 wt % carbon black	>16	0.01−2.5	1255	842				686 (40 cycles)	82	24
porous Si/C	75 wt % Si/C; 5 wt % carbon black; 20 wt % NaCMC	66	0.005−3	1190	∼750	636		∼630		84	53

[a] L, lithiation; D, delithiation; PVdF, polyvinylidene difluoride; PAA, poly(acrylic acid). The capacity retention is calculated from the difference between the first and last reported cycle in the respective studies.

of the higher amount of silicon oxide in the silicon oxycarbide.[14,20,22] However, the higher initial lithiation capacity cannot be maintained during delithiation. Me-SiOC and Vi-SiOC have a specific capacity of only 761 and 789 mA h/g, respectively, in the first delithiation cycle. Possibly more significant Li_2O formation occurs for Me-SiOC and Vi-SiOC.[7,49] Me-SiOC has a higher initial specific capacity than Vi-SiOC, but the long-time performance stability is better for Vi-SiOC (Figure 5D). This is because of the higher amount of free carbon in the structure and more silicon−carbon bonds. The performance of Me-SiOC and Vi-SiOC in $LiPF_6$ in EC/DMC is relatively low at high rates. Both materials have a specific capacity below 200 mA h/g at a specific current of 350 mA/g (corresponds to ∼0.5C). The higher content of free carbon in Vi-SiOC improves the specific capacity at high rates (700 mA/g; ∼1C) with around 75 mA h/g compared to 35 mA h/g of Me-SiOC.[22]

Vi-Ph-SiOC shows a superior electrochemical performance at high specific currents as well as very high performance stability among all SiOC anode materials in $LiPF_6$ in EC/DMC. By increasing the specific current to 70 mA/g, the specific capacity reduces from 936 (5th lithiation) to 885 (6th lithiation) mA h/g. Vi-Ph-SiOC still provided a specific capacity of 610 mA h/g measured at 350 mA/g (36th lithiation) and at the highest measured rate of 1400 mA/g still 116 mA h/g (56th lithiation). This performance is accomplished even with the low specific surface area of only 5 m^2/g. Thereby, there is a lack of a large pore volume of intraparticle pores which would contribute toward fast ion transport kinetics. For example, Pradeep et al. synthesized a mesoporous SiOC aerogel with a specific surface area of more than 200 m^2/g.[23] They obtained a high rate capability by a porous structure with a specific capacity of 600 mA h/g at 360 mA/g (0.5C), which is similar to our results.[23] At even higher C-rates (720 mA/g; 1C), the latter material provided still a specific capacity of ∼500 mA h/g; however, the mesopores of the aerogel had a diameter of 24 nm which is much smaller than the diameter (∼1 μm) of the SiOC beads from this study. The reduction of the diffusion length for the Li through the SiOC to a nanometer range is beneficial for very high C-rates (>1C) when considering the low diffusion coefficient of Li-ions in SiOCs in the range 10^{-9}−10^{-11} cm^2/s; for comparison, the Li-ion diffusion coefficients of amorphous Si films is 10^{-10}−10^{-11} cm^2/s, of Si nanowires is 10^{-10} cm^2/s, and of nano-Si is 10^{-12}−$10^{-13}$$cm^2/s$.[47,50−52] When we returned for operation of the Vi-Ph-SiOC beads to a lower specific current (70 mA/g) after 50 cycles, a specific charge capacity of about 800 mA h/g was re-established. The specific capacity of Me-SiOC and Vi-SiOC was also reaching a similar value for the specific capacity after the rate performance test.

The coin cells were disassembled after the rate capability test to investigate the morphology of the beads with TEM (see the Supporting Information, Figure S4). As can be seen from the electron micrographs, the SiOC beads conserved their shape after 100 cycles, and the spherical carbon black particles remain well-distributed throughout the electrode. The absence of visible structural changes of the electrode material encourages further characterization of the long-time performance; accordingly, we carried out performance stability tests at 0.1C (70 mA/g). After 100 cycles (Figure 5D), Vi-Ph-SiOC still provides a lithiation capacity of 764 mA h/g and a delithiation capacity of 778 mA h/g, which corresponds to 84% compared to the first lithiation. The specific capacitance remained stable from the 100th onward until the end of the testing procedure (175th cycle) at a value of 773 mA h/g for the lithiation capacity and a delithiation capacity of 789 mA h/g. We see a similar pattern compared to the rate capability data where Me-SiOC and Vi-SiOC have lower stability compared to Vi-Ph-SiOC. The performance stability of the samples Me-SiOC and Vi-SiOC measured only at low C-rates is lower after the same number of cycles compared to the samples which were also cycled at high C-rates. The performance stability of Vi-Ph-SiOC is similar for both measurement methods because of its high reversibility. Graczyk-Zajac et al. showed that the presence of silicon−carbon bonds improves the stability of SiOC anode materials.[19] Since all of our materials have silicon−carbon bonds in different amounts we conclude that a high amount of silicon−carbon bonds combined with a higher free carbon content is beneficial for a high performance stability.

Our data on SiOC as the LIB anode in 1 M $LiPF_6$ in EC/DMC is compared to the literature data in Table 4. A direct comparison is complicated by the influence of silicon oxycarbide structure, type and amount of the binder and the conductive additive, number of charge/discharge cycles, charge/discharge rates, and the voltage window. Nevertheless, Table 4 shows that Vi-Ph-SiOC has a higher specific capacity after the long-time experiment than all other silicon oxycarbides which we found in the literature. Our material also provides a higher specific capacity than the sol−gel-produced particles from Wilamowska-Zawlocka et al. using similar precursors for their synthesis.[20] The capacity retention of Vi-Ph-SiOC after 100 cycles is 83% higher than most other materials. The high performance stability originates from the high amount of carbon (especially free carbon) and possibly with carbon/silicon bonds, which leads to a higher reversible capacity. The spherical shape of the particles may also benefit the compensation of volume expansion which occurs during the alloying reaction.

4. CONCLUSIONS

Three types of spherical SiOC materials were synthesized with a MicroJet reactor by use of methyltrimethoxysilane, vinyltrimethoxysilane, and a mixture of vinyltrimethoxysilane with phenyltrimethoxysilane. Thereby, no additional cross-linking agent, which could cause impurities, was needed to preserve the morphology of the particles. The use of the MicroJet reactor to produce beads is also beneficial because the particles have a similar size, and the volumetric changes during lithiation and delithiation are equally distributed.

By choice of the precursor, it was possible to influence the amount of silicon−carbon bonds as well as the content of free carbon. Both parameters are important for the synthesis of SiOC anode materials for Li-ion batteries with high capacity and performance stability. The mixture of vinyl and phenyl groups provided the best electrochemical performance (922 mA h/g for first delithiation) and a high specific delithiation capacity after 100 cycles of 677 mA h/g was obtained. A mixture of phenyl and vinyl groups showed for the resulting SiOC materials the best performance in our study. Future optimization of the power-handling ability of the SiOC beads may be further promoted by additional mesopores by adding a template to the silane solution which decomposes during the pyrolysis.

ASSOCIATED CONTENT

Supporting Information

The Supporting Information is available free of charge on the ACS Publications website at DOI: 10.1021/acsaem.8b00716.

> Images of the conductivity-probe setup, supplementary data on particle size distribution, nitrogen gas sorption isotherms, electrochemical characterization of carbon black (used as a conductive additive), and post-mortem TEM images of the SiOC beads after the electrochemical measurements (PDF)

AUTHOR INFORMATION

Corresponding Authors

*E-mail: guido.kickelbick@uni-saarland.de.
*E-mail: volker.presser@leibniz-inm.de.

ORCID

Guido Kickelbick: 0000-0001-6813-9269
Volker Presser: 0000-0003-2181-0590

Notes

The authors declare no competing financial interest.

ACKNOWLEDGMENTS

The INM authors kindly acknowledge the continuing support of Eduard Arzt (INM). We also thank Simon Fleischmann, Ingrid Grobelsek, Hwirim Shim, and Robert Drumm (all INM) for technical support and discussions and Michael Zimmer (Saarland University) for the NMR measurements. We also acknowledge the kind support of the INM workshop for the design and construction of the conductivity-probe setup.

REFERENCES

(1) Diouf, B.; Pode, R. Potential of Lithium-Ion Batteries in Renewable Energy. *Renewable Energy* **2015**, *76*, 375−380.

(2) Dunn, J. B.; Gaines, L.; Kelly, J. C.; James, C.; Gallagher, K. G. The Significance of Li-ion Batteries in Electric Vehicle Life-cycle Energy and Emissions and Recycling's Role in its Reduction. *Energy Environ. Sci.* **2015**, *8* (1), 158−168.

(3) Nitta, N.; Wu, F.; Lee, J. T.; Yushin, G. Li-ion Battery Materials: Present and Future. *Mater. Today* **2015**, *18* (5), 252−264.

(4) Li, H.; Wang, Z.; Chen, L.; Huang, X. Research on Advanced Materials for Li-Ion Batteries. *Adv. Mater.* **2009**, *21* (45), 4593−4607.

(5) Boukamp, B. A.; Lesh, G. C.; Huggins, R. A. All-Solid Lithium Electrodes with Mixed-Conductor Matrix. *J. Electrochem. Soc.* **1981**, *128* (4), 725−729.

(6) Kasavajjula, U.; Wang, C.; Appleby, A. J. Nano-and Bulk-Silicon-Based Insertion Anodes for Lithium-ion Secondary Cells. *J. Power Sources* **2007**, *163* (2), 1003−1039.

(7) Zhang, W.-J. A Review of the Electrochemical Performance of Alloy Anodes for Lithium-ion Batteries. *J. Power Sources* **2011**, *196* (1), 13−24.

(8) Dash, R.; Pannala, S. Theoretical Limits of Energy Density in Silicon-Carbon Composite Anode Based Lithium Ion Batteries. *Sci. Rep.* **2016**, *6*, 27449.

(9) Szczech, J. R.; Jin, S. Nanostructured Silicon for High Capacity Lithium Battery Anodes. *Energy Environ. Sci.* **2011**, *4* (1), 56−72.

(10) Ma, X.; Liu, M.; Gan, L.; Tripathi, P. K.; Zhao, Y.; Zhu, D.; Xu, Z.; Chen, L. Novel mesoporous Si@C microspheres as anodes for lithium-ion batteries. *Phys. Chem. Chem. Phys.* **2014**, *16* (9), 4135−4142.

(11) Liu, M.; Ma, X.; Gan, L.; Xu, Z.; Zhu, D.; Chen, L. A facile synthesis of a novel mesoporous Ge@C sphere anode with stable and high capacity for lithium ion batteries. *J. Mater. Chem. A* **2014**, *2* (40), 17107−17114.

(12) Fukui, H.; Ohsuka, H.; Hino, T.; Kanamura, K. A Si-O-C Composite Anode: High Capability and Proposed Mechanism of Lithium Storage Associated with Microstructural Characteristics. *ACS Appl. Mater. Interfaces* **2010**, *2* (4), 998−1008.

(13) Kaspar, J.; Graczyk-Zajac, M.; Riedel, R. Lithium Insertion into Carbon-rich SiOC Ceramics: Influence of Pyrolysis Temperature on Electrochemical Properties. *J. Power Sources* **2013**, *244*, 450−455.

(14) Pradeep, V. S.; Graczyk-Zajac, M.; Riedel, R.; Soraru, G. D. New Insights in to the Lithium Storage Mechanism in Polymer Derived SiOC Anode Materials. Electrochim. *Electrochim. Acta* **2014**, *119*, 78−85.

(15) Tolosa, A.; Widmaier, M.; Krüner, B.; Griffin, J. M.; Presser, V. Continuous Silicon Oxycarbide Fiber Mats with Tin Nanoparticles as a High Capacity Anode for Lithium-Ion Batteries. *Sustainable Energy Fuels* **2018**, *2* (1), 215−228.

(16) Scarmi, A.; Sorarù, G. D.; Raj, R. The Role of Carbon in Unexpected Visco (An) Elastic Behavior of Amorphous Silicon Oxycarbide Above 1273 K. *J. Non-Cryst. Solids* **2005**, *351* (27−29), 2238−2243.

(17) Kleebe, H.-J.; Blum, Y. D. SiOC Ceramic with High Excess Free Carbon. *J. Eur. Ceram. Soc.* **2008**, *28* (5), 1037−1042.

(18) Guo, B.; Shu, J.; Wang, Z.; Yang, H.; Shi, L.; Liu, Y.; Chen, L. Electrochemical Reduction of Nano-SiO_2 in Hard Carbon as Anode Material for Lithium Ion Batteries. *Electrochem. Commun.* **2008**, *10* (12), 1876−1878.

(19) Graczyk-Zajac, M.; Vrankovic, D.; Waleska, P.; Hess, C.; Sasikumar, P. V.; Lauterbach, S.; Kleebe, H.-J.; Sorarù, G. D. The Li-storage Capacity of SiOC Glasses with and without Mixed Silicon Oxycarbide Bonds. *J. Mater. Chem. A* **2018**, *6* (1), 93−103.

(20) Wilamowska-Zawlocka, M.; Puczkarski, P.; Grabowska, Z.; Kaspar, J.; Graczyk-Zajac, M.; Riedel, R.; Sorarù, G. D. Silicon Oxycarbide Ceramics as Anodes for Lithium Ion Batteries: Influence of Carbon Content on Lithium Storage Capacity. *RSC Adv.* **2016**, *6* (106), 104597−104607.

(21) Rouxel, T.; Massouras, G.; Sorarù, G.-D. High Temperature Behavior of a Gel-derived SiOC Glass: Elasticity and Viscosity. *J. Sol-Gel Sci. Technol.* **1999**, *14* (1), 87−94.

(22) Kaspar, J.; Graczyk-Zajac, M.; Choudhury, S.; Riedel, R. Impact of the Electrical Conductivity on the Lithium Capacity of Polymer-derived Silicon Oxycarbide (SiOC) Ceramics. *Electrochim. Acta* **2016**, *216*, 196−202.

(23) Pradeep, V. S.; Ayana, D. G.; Graczyk-Zajac, M.; Soraru, G. D.; Riedel, R. High Rate Capability of SiOC Ceramic Aerogels with Tailored Porosity as Anode Materials for Li-ion Batteries. *Electrochim. Acta* **2015**, *157*, 41−45.

(24) Bhandavat, R.; Singh, G. Stable and Efficient Li-ion Battery Anodes Prepared from Polymer-derived Silicon Oxycarbide−Carbon Nanotube Shell/Core Composites. *J. Phys. Chem. C* **2013**, *117* (23), 11899−11905.

(25) Odenwald, C.; Kickelbick, G. Additive-free Continuous Synthesis of Silica and ORMOSIL Micro-and Nanoparticles Applying a MicroJet Reactor. *J. Sol-Gel Sci. Technol.* **2018**, DOI: 10.1007/s10971-018-4626-x.

(26) Krüner, B.; Odenwald, C.; Tolosa, A.; Schreiber, A.; Aslan, M.; Kickelbick, G.; Presser, V. Carbide-derived Carbon Beads with Tunable Nanopores from Continuously Produced Polysilsesquioxanes for Supercapacitor Electrodes. *Sustainable Energy Fuels* **2017**, *1* (7), 1588−1600.

(27) Kaspar, J.; Terzioglu, C.; Ionescu, E.; Graczyk-Zajac, M.; Hapis, S.; Kleebe, H. J.; Riedel, R. Stable SiOC/Sn Nanocomposite Anodes for Lithium-Ion Batteries with Outstanding Cycling Stability. *Adv. Funct. Mater.* **2014**, *24* (26), 4097−4104.

(28) Magasinski, A.; Zdyrko, B.; Kovalenko, I.; Hertzberg, B.; Burtovyy, R.; Huebner, C. F.; Fuller, T. F.; Luzinov, I.; Yushin, G. Toward Efficient Binders for Li-Ion Battery Si-Based Anodes: Polyacrylic Acid. *ACS Appl. Mater. Interfaces* **2010**, *2* (11), 3004−3010.

(29) Chou, S. L.; Pan, Y.; Wang, J. Z.; Liu, H. K.; Dou, S. X. Small Things Make a Big Difference: Binder Effects on the Performance of

Li and Na Batteries. *Phys. Chem. Chem. Phys.* **2014**, *16* (38), 20347−20359.

(30) Komaba, S.; Shimomura, K.; Yabuuchi, N.; Ozeki, T.; Yui, H.; Konno, K. Study on Polymer Binders for High-Capacity SiO Negative Electrode of Li-Ion Batteries. *J. Phys. Chem. C* **2011**, *115* (27), 13487−13495.

(31) Schneider, C. A.; Rasband, W. S.; Eliceiri, K. W. NIH Image to ImageJ: 25 Years of Image Analysis. *Nat. Methods* **2012**, *9* (7), 671.

(32) Brunauer, S.; Emmett, P. H.; Teller, E. Adsorption of Gases in Multimolecular Layers. *J. Am. Chem. Soc.* **1938**, *60* (2), 309−319.

(33) Vakifahmetoglu, C.; Zeydanli, D.; Innocentini, M. D.; Ribeiro, F. D.; Lasso, P. R.; Soraru, G. D. Gradient-Hierarchic-Aligned Porosity SiOC Ceramics. *Sci. Rep.* **2017**, *7*, 41049.

(34) Zanchetta, E.; Cattaldo, M.; Franchin, G.; Schwentenwein, M.; Homa, J.; Brusatin, G.; Colombo, P. Stereolithography of SiOC Ceramic Microcomponents. *Adv. Mater.* **2016**, *28* (2), 370−376.

(35) Bujalski, D. R.; Grigoras, S.; Wieber, G. M.; Zank, G. A. Stoichiometry Control of SiOC Ceramics by Siloxane Polymer Functionality. *J. Mater. Chem.* **1998**, *8* (6), 1427−1433.

(36) Soraru, G. D.; D'Andrea, G.; Campostrini, R.; Babonneau, F.; Mariotto, G. Structural Characterization and High-Temperature Behavior of Silicon Oxycarbide Glasses Prepared from Sol-Gel Precursors Containing Si-H Bonds. *J. Am. Ceram. Soc.* **1995**, *78* (2), 379−387.

(37) Scherrer, P. Bestimmung der Größe und der inneren Struktur von Kolloidteilchen mittels Röntgenstrahlen. *Nachr. Ges. Wiss. Göttingen* **1918**, *2*, 98−100.

(38) Wright, A. F.; Leadbetter, A. J. The Structures of the β-Cristobalite Phases of SiO_2 and $AlPO_4$. *Philos. Mag.* **1975**, *31* (6), 1391−1401.

(39) Ferrari, A. C.; Robertson, J. Interpretation of Raman Spectra of Disordered and Amorphous Carbon. *Phys. Rev. B: Condens. Matter Mater. Phys.* **2000**, *61* (20), 14095.

(40) Kleebe, H.-J.; Gregori, G.; Babonneau, F.; Blum, Y. D.; MacQueen, D. B.; Masse, S. Evolution of C-Rich SiOC Ceramics. *Z. Metallkd.* **2006**, *97* (6), 699−709.

(41) Trimmel, G.; Badheka, R.; Babonneau, F.; Latournerie, J.; Dempsey, P.; Bahloul-Houlier, D.; Parmentier, J.; Soraru, G. D. Solid State NMR and TG/MS Study on the Transformation of Methyl Groups During Pyrolysis of Preceramic Precursors to SiOC Glasses. *J. Sol-Gel Sci. Technol.* **2003**, *26* (1−3), 279−283.

(42) Brus, J.; Kolář, F.; Machovič, V.; Svıtilová, J. Structure of Silicon Oxycarbide Glasses Derived from Poly (Methylsiloxane) and Poly [Methyl(Phenyl)siloxane] Precursors. *J. Non-Cryst. Solids* **2001**, *289* (1−3), 62−74.

(43) Sitarz, M.; Czosnek, C.; Jelen, P.; Odziomek, M.; Olejniczak, Z.; Kozanecki, M.; Janik, J. F. SiOC Glasses Produced from Silsesquioxanes by the Aerosol-assisted Vapor Synthesis Method. *Spectrochim. Acta, Part A* **2013**, *112*, 440−445.

(44) Widgeon, S. J.; Sen, S.; Mera, G.; Ionescu, E.; Riedel, R.; Navrotsky, A. ^{29}Si and ^{13}C Solid-state NMR Spectroscopic Study of Nanometer-scale Structure and Mass Fractal Characteristics of Amorphous Polymer Derived Silicon Oxycarbide Ceramics. *Chem. Mater.* **2010**, *22* (23), 6221−6228.

(45) Grill, A.; Neumayer, D. A. Structure of Low Dielectric Constant to Extreme Low Dielectric Constant SiCOH Films: Fourier Transform Infrared Spectroscopy Characterization. *J. Appl. Phys.* **2003**, *94* (10), 6697−6707.

(46) Oh, T.; Choi, C. K. Comparison Between SiOC Thin Films Fabricated by Using Plasma Enhance Chemical Vapor Deposition and SiO_2 Thin Films by Using Fourier Transform Infrared Spectroscopy. *J. Korean Phys. Soc.* **2010**, *56* (4), 1150−1155.

(47) Kaspar, J.; Graczyk-Zajac, M.; Riedel, R. Determination of the chemical diffusion coefficient of Li-ions in carbon-rich silicon oxycarbide anodes by electro-analytical methods. *Electrochim. Acta* **2014**, *115*, 665−670.

(48) Pandolfo, A. G.; Wilson, G. J.; Huynh, T. D.; Hollenkamp, A. F. The Influence of Conductive Additives and Inter-Particle Voids in Carbon EDLC Electrodes. *Fuel Cells* **2010**, *10* (5), 856−864.

(49) Miyachi, M.; Yamamoto, H.; Kawai, H.; Ohta, T.; Shirakata, M. Analysis of SiO Anodes for Lithium-ion Batteries. *J. Electrochem. Soc.* **2005**, *152* (10), A2089−A2091.

(50) Ding, N.; Xu, J.; Yao, Y. X.; Wegner, G.; Fang, X.; Chen, C. H.; Lieberwirth, I. Determination of the diffusion coefficient of lithium ions in nano-Si. *Solid State Ionics* **2009**, *180* (2), 222−225.

(51) Ruffo, R.; Hong, S. S.; Chan, C. K.; Huggins, R. A.; Cui, Y. Impedance Analysis of Silicon Nanowire Lithium Ion Battery Anodes. *J. Phys. Chem. C* **2009**, *113* (26), 11390−11398.

(52) Xie, J.; Imanishi, N.; Zhang, T.; Hirano, A.; Takeda, Y.; Yamamoto, O. Li-ion diffusion in amorphous Si films prepared by RF magnetron sputtering: A comparison of using liquid and polymer electrolytes. *Mater. Chem. Phys.* **2010**, *120* (2), 421−425.

(53) Li, X.; Yan, P.; Xiao, X.; Woo, J. H.; Wang, C.; Liu, J.; Zhang, J.-G. Design of Porous Si/C−Graphite Electrodes with Long Cycle Stability and Controlled Swelling. *Energy Environ. Sci.* **2017**, *10* (6), 1427−1434.

Supporting Information

Silicon Oxycarbide Beads from Continuously Produced Polysilsesquioxane as Stable Anode Material for Lithium-ion Batteries

Benjamin Krüner,[1,2] Christina Odenwald,[3] Nicolas Jäckel,[1,2]
Aura Tolosa,[1,2] Guido Kickelbick,[3,*] and Volker Presser[1,2,*]

[1] *INM - Leibniz Institute for New Materials, 66123 Saarbrücken, Germany*

[2] *Department of Materials Science and Engineering, Saarland University, 66123 Saarbrücken, Germany*

[3] *Inorganic Solid State Chemistry, Saarland University, 66123 Saarbrücken, Germany*

* *Corresponding authors' eMails:*

guido.kickelbick@uni-saarland.de *(G. Kickelbick)*; volker.presser@leibniz-inm.de *(V. Presser)*

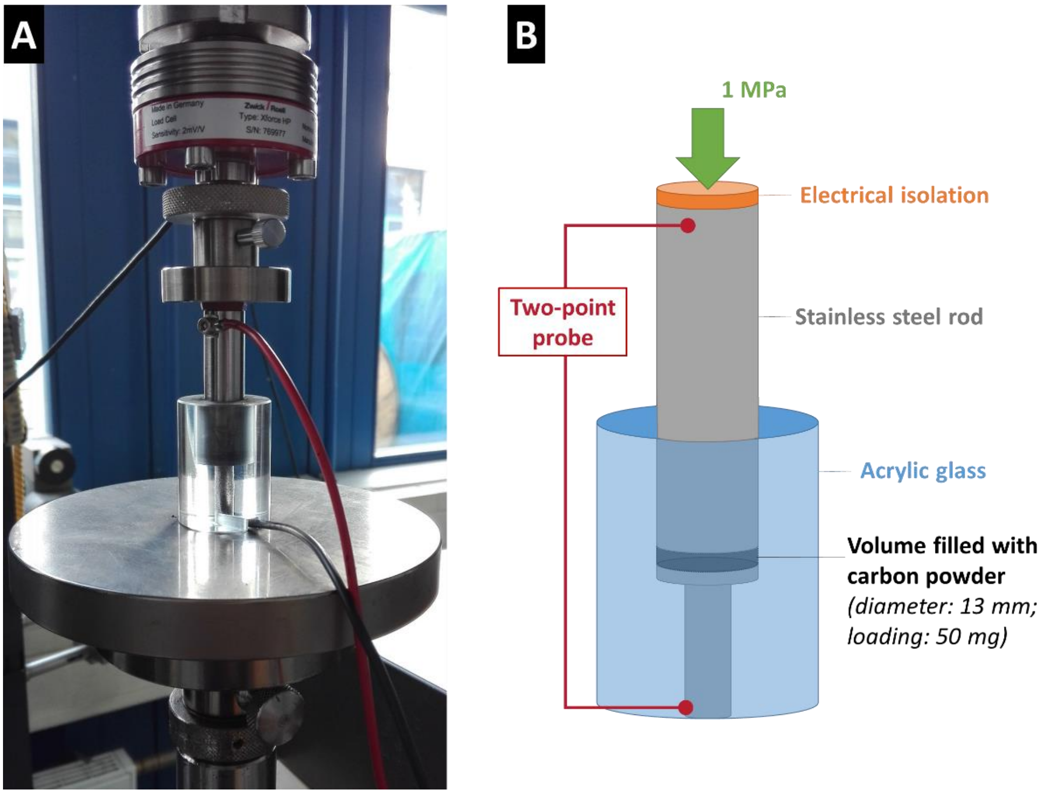

Figure S1: (A) Photograph of the custom-built conductivity probe setup and the corresponding (B) schematic setup.

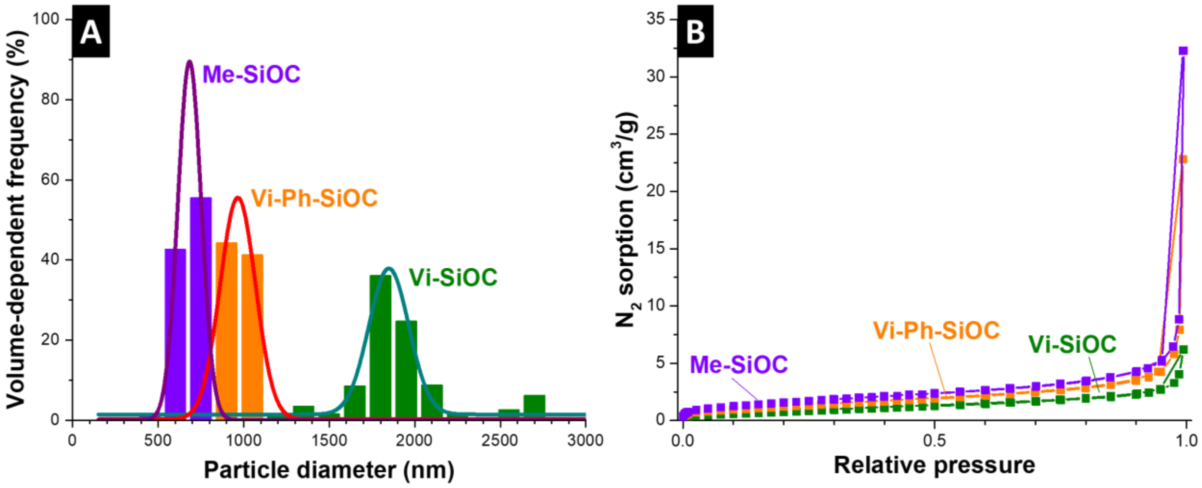

Figure S2: (A) Particle size distribution obtained by the analysis of SEM images and (B) nitrogen sorption isotherms at -196 °C of the samples Me-SiOC, Vi-SiOC, and Vi-Ph-SiOC.

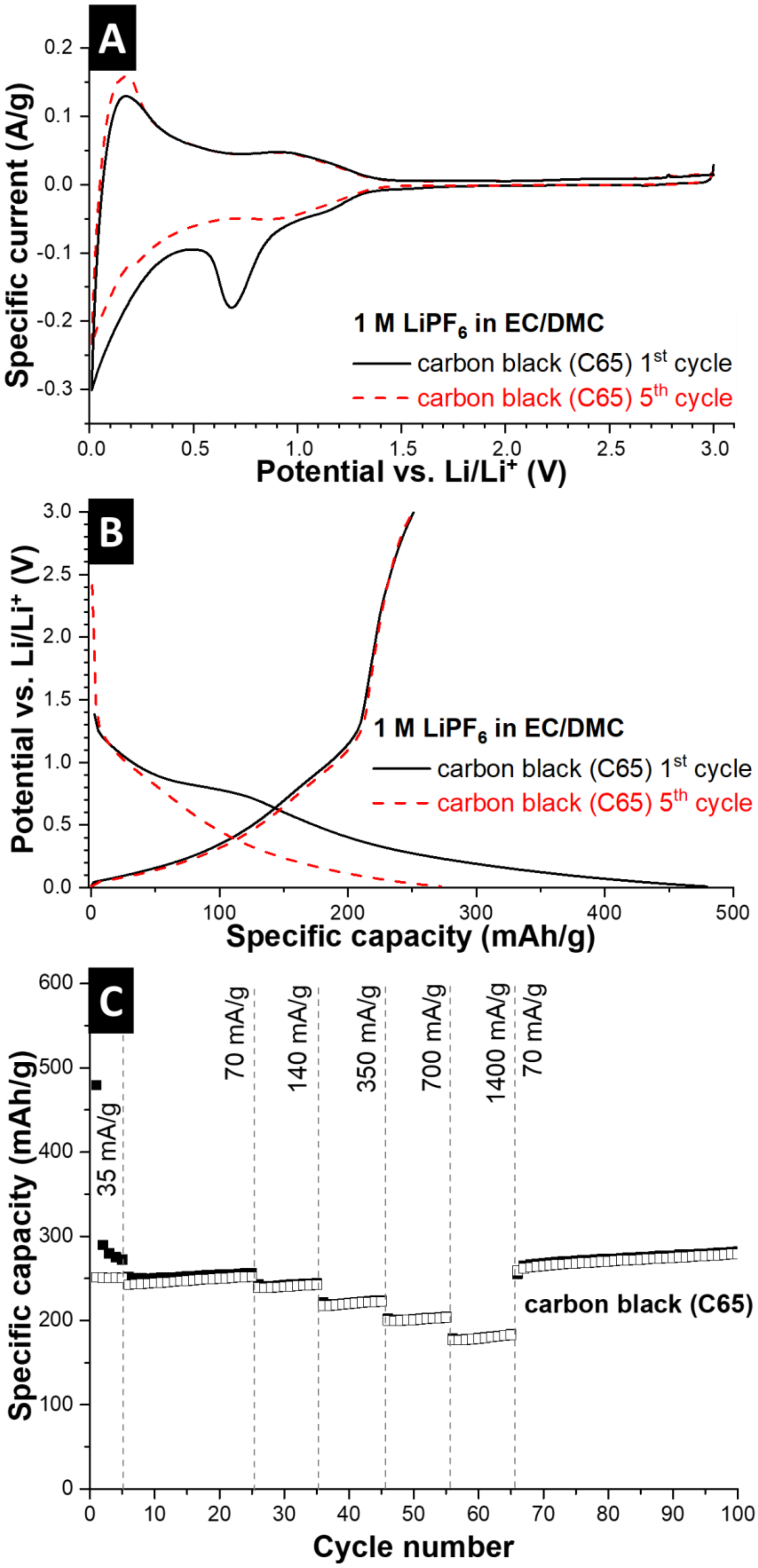

Figure S3: Electrochemical characterization of the carbon black (C65) using 1 M $LiPF_6$ in EC/DMC. (A) Cyclic voltammograms at 0.1 mV/s, (B) galvanostatic charge/discharge profiles at 35 mA/g of the 1st and 5th cycle, and (C) rate capability at 35-1400 mA/g.

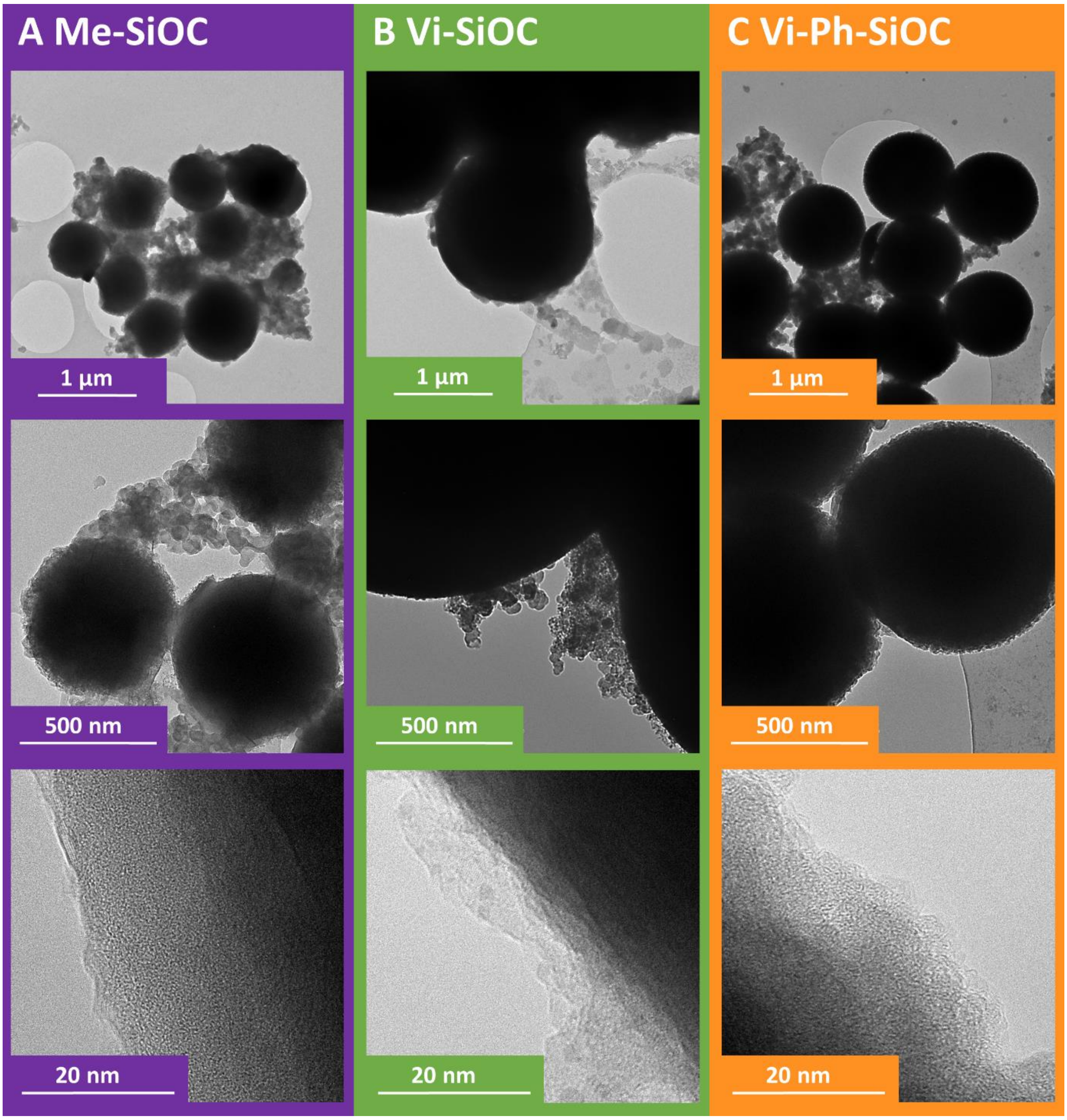

Figure S4: Post-mortem transmission electron micrographs of the SiOC electrodes after the rate capability tests. (A) Me-SiOC, (B) Vi-SiOC, and (C) Vi-Ph-SiOC.

4.8. Microporous novolac-derived carbon beads/sulfur hybrid cathode for lithium-sulfur batteries

Soumyadip Choudhury,[1,ƚ] Benjamin Krüner,[1,2,ƚ] Pau Massuti-Ballester,[2] Aura Tolosa,[1,2] Christian Prehal,[3] Ingrid Grobelsek,[1] Oskar Paris,[3] Lars Borchardt,[4] Volker Presser[1,2]

[1] *INM - Leibniz Institute for New Materials, 66123 Saarbrücken, Germany*

[2] *Department of Materials Science and Engineering, Saarland University, 66123 Saarbrücken, Germany*

[3] *Institute of Physics, Montanuniversität Leoben, 8700 Leoben, Austria*

[4] *Department of Inorganic Chemistry, Technische Universität Dresden, 01069 Dresden, Germany*

[ƚ] these authors contributed equally

Choudhury, Soumyadip et al. (2017) *Journal of Power Sources*, 357, 198-208.
https://doi.org/10.1016/j.jpowsour.2017.05.005

Own contribution: Design, planning, writing, synthesis of the activated and non-activated carbon beads, N_2 sorption analysis, Raman analysis, XRD.

Abstract:

Novolac-derived nanoporous carbon beads were used as conductive matrix for lithium-sulfur battery cathodes. We employed a facile self-emulsifying synthesis to obtain sub-micrometer novolac-derived carbon beads with nanopores. After pyrolysis, the carbon beads showed already a specific surface area of 640 $m^2\,g^{-1}$ which was increased to 2080 $m^2\,g^{-1}$ after physical activation. The non-activated and the activated carbon beads represent nanoporous carbon with a medium and a high surface area, respectively. This allows us to assess the influence of the porosity on the electrochemical performance of lithium-sulfur battery cathodes. The carbon/sulfur hybrids were obtained from two different approaches of sulfur infiltration: melt-infusion of sulfur (annealing) and in situ formation of sulfur from sodium thiosulfate. The best performance (~880 mAh g_{sulfur}^{-1} at low charge rate; 5th cycle) and high performance stability (>600 mAh g_{sulfur}^{-1} after 100 cycles) were found for the activated carbon beads when using melt infusion of sulfur.

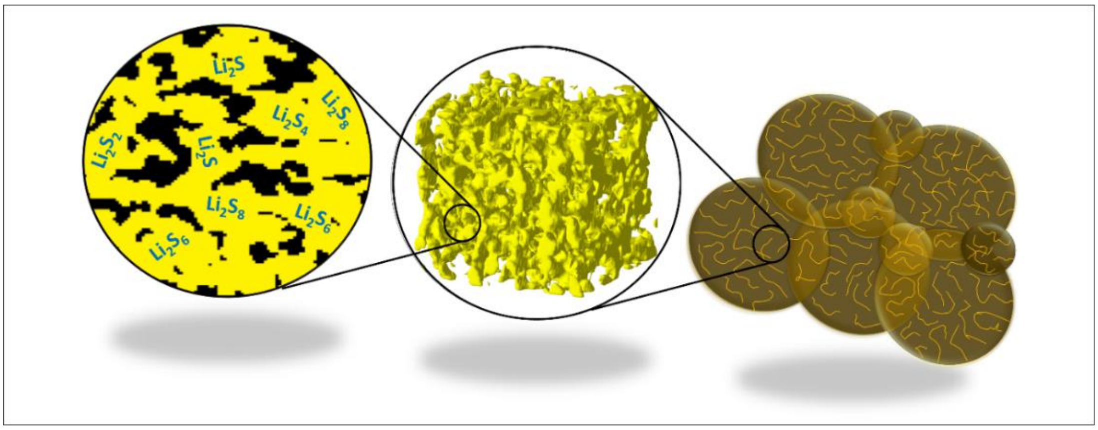

Journal of Power Sources 357 (2017) 198–208

Contents lists available at ScienceDirect

Journal of Power Sources

journal homepage: www.elsevier.com/locate/jpowsour

Microporous novolac-derived carbon beads/sulfur hybrid cathode for lithium-sulfur batteries

Soumyadip Choudhury [a, 1], Benjamin Krüner [a, b, 1], Pau Massuti-Ballester [b], Aura Tolosa [a, b], Christian Prehal [c], Ingrid Grobelsek [a], Oskar Paris [c], Lars Borchardt [d], Volker Presser [a, b, *]

[a] INM - Leibniz Institute for New Materials, 66123, Saarbrücken, Germany
[b] Department of Materials Science and Engineering, Saarland University, 66123, Saarbrücken, Germany
[c] Institute of Physics, Montanuniversitaet Leoben, 8700, Leoben, Austria
[d] Department of Inorganic Chemistry, Technische Universität Dresden, 01069, Dresden, Germany

HIGHLIGHTS

- Template-free synthesis of nanoporous carbon beads.
- Highly porous and conducting carbon beads employed as sulfur host for Li-S battery.
- Promising electrochemical performance as Li-S battery cathode.

GRAPHICAL ABSTRACT

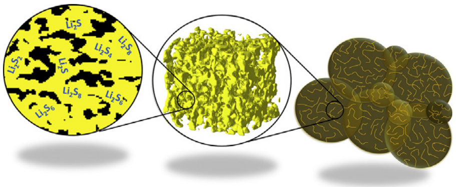

ARTICLE INFO

Article history:
Received 17 March 2017
Received in revised form
25 April 2017
Accepted 3 May 2017
Available online 9 May 2017

Keywords:
Porous carbon
Activation
Hybrid material
Lithium-sulfur batteries

ABSTRACT

Novolac-derived nanoporous carbon beads were used as conductive matrix for lithium-sulfur battery cathodes. We employed a facile self-emulsifying synthesis to obtain sub-micrometer novolac-derived carbon beads with nanopores. After pyrolysis, the carbon beads showed already a specific surface area of 640 m^2 g^{-1} which was increased to 2080 m^2 g^{-1} after physical activation. The non-activated and the activated carbon beads represent nanoporous carbon with a medium and a high surface area, respectively. This allows us to assess the influence of the porosity on the electrochemical performance of lithium-sulfur battery cathodes. The carbon/sulfur hybrids were obtained from two different approaches of sulfur infiltration: melt-infusion of sulfur (annealing) and in situ formation of sulfur from sodium thiosulfate. The best performance (~880 mAh g_{sulfur}^{-1} at low charge rate; 5th cycle) and high performance stability (>600 mAh g_{sulfur}^{-1} after 100 cycles) were found for the activated carbon beads when using melt infusion of sulfur.

1. Introduction

The demand for electrochemical energy storage devices has increased over the past decades, strongly driven by the pressure towards renewable energies and increasing electro mobility applications [1,2]. Efficient storage of renewable energy with intermittent generation requires advanced battery technology [3]. In recent years, research has been dedicated to fabricate batteries with high energy storage capacity, such as Li-ion [4], Li-air [5,6], and Zn air [7,8]. Although possessing very high theoretical specific energy (>20 kWh kg^{-1}), Li-air systems still require optimized gas diffusion membranes and redox catalysts to achieve high cycle stability and high energy efficiency [9]. Also, sodium-ion batteries are attractive to replace metallic lithium and to enable sustainable

---

[*] Corresponding author. INM - Leibniz Institute for New Materials, 66123, Saarbrücken, Germany.
E-mail address: volker.presser@leibniz-inm.de (V. Presser).

[1] These authors contributed equally.

http://dx.doi.org/10.1016/j.jpowsour.2017.05.005
0378-7753/© 2017 Elsevier B.V. All rights reserved.

large scale energy storage technologies [10,11].

A very promising battery system is lithium-sulfur (Li-S) due to the high theoretical specific capacity (1675 mAh g^{-1}), the cost-attractive electrode materials, and the high natural abundance of sulfur [12–14]. To exploit these beneficial properties, it is important to complement sulfur with an electrically conductive matrix. Carbon materials are the most attractive candidates for sulfur composite electrodes because of their high electrical conductivity, low density, structural flexibility, and tunable porosity [12,15]. A highly porous carbon material is beneficial to accommodate sulfur, to trap dissolved polysulfides, to minimize sulfur leaching, and to compensate the volume expansion during charge-discharge cycling [12]. Employing an optimized pore architecture of the carbon matrix material is important to achieve a high electrochemical performance [12]. A high pore volume generally favors high sulfur loadings, and also provides space for Li^+ facile migration [16]. When sulfur is confined in small micropores (~0.5 nm), only smaller molecules occur (i.e., $S_{2\text{-}4}$) [17], because access for larger sulfur molecules (S_6 or S_8) with a diameter of 0.76–0.84 nm is restricted. Nanoconfinement within micropores can also prevent the formation of soluble polysulfides [17]. The trapping of polysulfides inside the micropores improves the long-time stability, which is one of the crucial challenges for Li-S batteries.

Previous studies have shown that neither completely microporous nor solely mesoporous carbon can suffice both requirements of high sulfur loading and control of polysulfide leaching [18–20]. Therefore, an optimized pore architecture of carbon can be beneficial [18]. For example, Li et al. designed an ordered core-shell architecture of porous carbon where a mesoporous core is surrounded by a microporous shell; in this architecture, the core ensures sufficient sulfur loading and a high utilization of the active material, while the shell serves as a physical barrier and stabilizes the cycle performance of the cell [18]. Therefore, hierarchical porous carbons are attractive Li-S cathode materials [12,21].

Spherical carbon particles filled with sulfur have been developed by several research groups aiming for high packing densities of hybrid particles, thereby increasing the energy density of the cathode [22–24]. For example, Schuster et al. developed bimodal mesoporous carbon particles via a two-step method [22]. They synthesized a silica structure, which was infiltrated with phenolic resin as source of carbon. As a result, porous carbon with a bimodal porous structure was obtained by removing the silica fraction by washing with hydrofluoric acid. Zhang et al. reported on double-shelled hollow carbon spheres using polysaccharides as carbon precursor and SnO_2 as hard template, which was finally removed with hydrochloric acid [23]. With this complex design of porous carbon, a high loading with sulfur was achieved along with a suppression of polysulfide migration. Further, Jayaprakash et al. reported on hollow spherical carbon/sulfur composites using a silica hard template and pitch as a low-cost carbon precursor [24].

The motivation of this work is to develop a time- and resource-efficient synthesis for spherical carbon particles. In our approach, we avoid the use of a template for the synthesis of microporous carbon beads. We utilize a facile method to synthesize sub-micrometer novolac-derived carbon beads from an inexpensive precursor with a self-emulsifying system and evaluated its performance as host material for Li-S battery cathodes. Already after pyrolysis at 1000 °C, the carbon beads show a micropore volume of 0.25 cm^3 g^{-1}. Further physical activation in CO_2 enhances the porosity, yielding a specific surface area (SSA) of up to 2237 m^2 g^{-1} with a tunable average pore size ranging between 0.5 nm and 2.2 nm depending on the degree of activation [25]. In recent studies, the small diameter of the primary particles have already proven to be beneficial if applied as supercapacitor electrode materials and for high electrochemical water desalination rates in capacitive deionization processes [26].

In the present study, we compared non-activated beads with very small micropores (average pore size: 0.6 nm; pore volume: 0.25 cm^3 g^{-1}) and a highly-activated sample with larger micropores (average pore size: 1.5 nm; pore volume: 1.45 cm^3 g^{-1}). By this way, we will investigate the influence of inner porosity (i.e., pores within the beads) and of small micropores for carbon/sulfur hybrid electrodes. We compare two different synthesis methods (melt infiltration and in situ formation of sulfur from $Na_2S_2O_3$) to produce sulfur-carbon electrodes and with two different microporous carbons.

2. Experimental description

2.1. Materials

Novolac pellets (ALNOVOL PN 320) were obtained from Allnex. Battery-grade conductive carbon black (C65) was received from Imerys. Hexamethylenetetramine, sodium thiosulfate pentahydrate ($Na_2S_2O_3 \cdot 5H_2O$), elemental sulfur (S_8), polyvinylidene fluoride (PVDF) powder (molecular mass ca. 534,000 g mol^{-1}), *N*-methyl-2-pyrrolidone (NMP), bis(trifluoromethane)-sulfonimide lithium salt (LiTFSI), 1,2-dimethoxyethane (DME), 1,3-dioxolane (DOL), and lithium nitrate ($LiNO_3$) were purchased from Sigma Aldrich and used without any further purification. Nickel foil with a thickness of 13 μm was procured from Carl Schlenk. Electrochemical grade high purity (99.9%) lithium was purchased from PI-KEM. Trilayer porous polyolefine separator was obtained from Celgard and we used non-woven polypropylene separators from Freudenberg.

2.2. Synthesis of the carbon beads

The synthesis of the novolac-derived carbon beads was introduced by us and outlined in a previous publication (Ref. [25]). In short, 20 g of the novolac and 2 g of hexamethylenetetramine was dissolved in 100 mL ethanol. The solution was added to 500 mL of deionized water (Milli-Q) whereby the self-emulsifying solution arises, which was crosslinked in an autoclave (150 °C for 8 h). The dispersion was freeze-dried and pyrolyzed in argon at 1000 °C (Thermal Technology; heating rate 20 °C min^{-1}) for 2 h; the pyrolyzed sample is referred to as PNC. The beads were activated with CO_2 at 1000 °C for 2.5 h in a rotary quartz-glass tube furnace (HTM Reetz; heating rate: 10 °C min^{-1}, CO_2 flow: 987 mL min^{-1}). The tube was flushed with nitrogen during heating and cooling. The activated carbon beads are referred to as PNC_{act}.

2.3. Synthesis for sulfur/carbon bead hybrid

As schematically depicted in Fig. 1, we used two different approaches to synthesize hybrids of carbon beads and sulfur: (i) mechanical melt mixing of sulfur with carbon beads and (ii) in situ formation of sulfur nanoparticles on the carbon surface. These two approaches were applied to non-activated (PNC) and activated (PNC_{act}) carbon beads.

Mechanical melt mixing was performed as follows: 65 mass% elemental sulfur (S_8) was added to 35 mass% of carbon beads. To obtain a uniform mixture both components were mixed in a mortar and afterwards ball-milled. The carbon-sulfur composite powder was thermally treated at 155 °C for 5 h in an argon atmosphere. Using this treatment, sulfur melts and attains minimum viscosity [27]; as a result, the melt was distributed to all accessible surface area and a uniform coverage of sulfur was achieved (Fig. 1D,F) [28].

In the other approach, 1.55 g of sodium thiosulfate was first dissolved in 40 mL of water. Afterwards, 100 mg of either non-

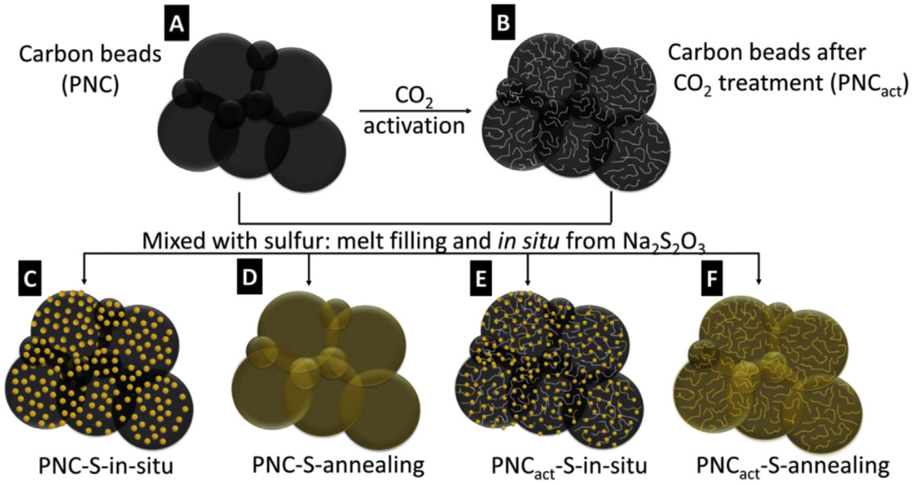

Fig. 1. Schematic image of the (A) pyrolyzed and (B) activated carbon beads and their mixtures with sulfur; (C) in situ method applied on pyrolyzed carbon beads, (D) melt infusion technique applied on pyrolyzed carbon beads, and (E, F) adopted on CO_2-activated carbon beads.

activated or activated carbon beads were added with subsequent sonication for 30 min under ice water. In the next step, 2.5 mL of 5 M HCl was added dropwise to the dispersion to form sulfur nanoparticles. After 2 h reaction time, the mixture was filtered through a 0.2 μm hydrophilic PVDF membrane. It was washed with copious amount of water till pH 7 was achieved and then dried at 80 °C under vacuum for 12 h. The resulting materials are labelled: PNC-S-annealing, PNC-S-in-situ, PNC_{act}-S-annealing, and PNC_{act}-S-in-situ.

2.4. Electrode casting

For electrode manufacturing four sets of sulfur/carbon bead hybrid materials were mixed in a ball mill with 10 mass% conductive carbon black (C-Nergy Super C65, Imerys). For electrode casting, we added 8 mass% of PVDF binder in NMP to attain the desired slurry viscosity. The slurry was coated on a nickel current collector by doctor-blade casting method with a gate height of 300 μm. Afterwards, the electrodes were dried in an oven operated under vacuum at 60 °C for 12 h to remove any remaining traces of solvent. In the dry state, each electrode had a thickness of 80–90 μm with mass loading of 3–4 mg cm^{-2} (corresponding sulfur loading: 2–3 mg cm^{-2}; ~60 mass%). This mass loading is at the level to attain the required areal capacity desired for applications in electrically driven vehicles [29].

2.5. Material characterization

2.5.1. Gas sorption analysis (GSA)

The porosity of the materials was quantified with N_2 gas sorption analysis (GSA; Quantachrome Autosorb iQ). Before the measurement, the samples were degassed at 100 mbar and 200 °C for 1 h and at 300 °C for 20 h. The N_2 sorption analysis was carried out in liquid nitrogen at −196 °C. The relative pressure varied between $5 \cdot 10^{-7}$ to 1.0 in 76 steps. We used a quenched-solid density functional theory (QSDFT) kernel assuming slit-like pores (QSDFT) for the N_2 isotherm to obtain the pore size distribution [30,31]. The Brunauer-Emmett-Teller (BET) equation was used in the linear region of the isotherm between 0.1 and 0.3 partial pressure to calculate the BET specific surface area (BET SSA) [32]. The total pore volume corresponds to the adsorbed volume at a relative pressure (p/p_0) of 0.95. The average pore size was obtained by the d_{50} value (pore size corresponding with half of the pore volume) [33]. The calculations were carried out with ASiQwin 3.0 from Quantachrome.

2.5.2. Small angle X-ray scattering (SAXS)

SAXS measurements of activated and non-activated novolac-derived carbon beads were conducted using a laboratory SAXS instrument (Nanostar, Bruker AXS) using Cu-Kα radiation and a Vantec-2000 area detector. The azimuthally averaged SAXS patterns were corrected for instrument background taking transmission and measurement time into account, and normalize to sample thickness [34]. Using real-space pore models generated from SAXS [35–37], pore size distributions (PSDs) can be calculated directly from the SAXS data. In short, the mathematical concept of Gaussian random fields (GRFs) was used to generate a three-dimensional model of the carbon nanopore structure. Hereby, parameters containing the statistical information about the pore morphology are obtained from a model fit to the measured SAXS intensities [35], which were further used to create the 3D pore model. A pore size distribution was then extracted from this model by calculating a histogram of all normal distances within the pore space. The calculated cumulative PSDs from SAXS were finally normalized to the maximum cumulative pore volume found by nitrogen gas sorption analysis.

2.5.3. X-ray diffraction and Raman spectroscopy

Phase analysis was carried out with X-ray diffraction (XRD) and Raman spectroscopy. A D8 Advance diffractometer (Bruker AXS) with Cu-Kα radiation (40 kV, 40 mA) was used in point focus mode with a Goebel mirror and a 2D detector (Vantec-500). The samples were placed on a sapphire single crystal, which was wobbling during the measurement to obtain a better orientational averaging. The Raman spectra were recorded with a Renishaw inVia Raman microscope using laser power of 0.2 mW with an excitation wavelength of 632.8 nm and a grating of 1800 lines mm^{-1}.

2.5.4. Thermogravimetric analysis

To estimate the loading of sulfur in each carbon-sulfur hybrid, we employed thermogravimetric analysis (TGA). Sulfur sublimes completely when heated to 450 °C at normal pressure, TGA of the carbon-sulfur hybrids were performed using a Netzsch Libra TG 209 F1 in the temperature range of 30–550 °C with a heating rate of 10 °C min^{-1} under a continuous flow of argon.

2.5.5. CHNS elemental analysis

The chemical composition was further investigated with CHNS elemental analysis with a Vario Micro Cube system (Elementar

Analysensysteme). After combustion, the samples were measured under oxygen atmosphere at 1150 °C in a tin holder. The CHNS analyzer was calibrated with sulfanilic acid (41.6 mass% C, 4.1 mass % H, 8.1 mass% N, 18.5 mass% S).

2.5.6. Scanning electron microscopy (SEM) and energy dispersive X-ray spectroscopy (EDX)

The SEM images and the EDX mapping were carried out with a field emission scanning electron microscope (SEM; JSM-7500F from Jeol) with operating voltage of 1.5 kV and 3 kV. An energy dispersive X-ray detector with an X-Max Silicon detector (Oxford Instruments) was used for the detection of generated X-rays at 6 kV.

2.5.7. High-resolution transmission electron microscopy (TEM) and energy dispersive X-ray spectroscopy (EDX)

TEM was carried out using a JEOL JEM-2100F system operating at 200 kV in vacuum. EDX mapping was performed using a Thermo Scientific MC100021 detector attached to the TEM chamber also with 200 kV and acquisition time for mapping was 10 min. The powder samples were dispersed and sonicated in ethanol and deposited on a lacey carbon film on a copper grid (Gatan).

2.5.8. Conductivity measurements

For measurements of the electrical conductivity, the samples were prepared on to 50 μm thin polyimide film using the same slurries for electrode casting keeping the same thickness of electrode layer. Sheet resistance measurements were made with a custom-built spring-loaded four-point probe with blunt gold contacts (tip diameter: 1.5 mm, tip distance: 3 mm). For better statistics, sheet resistance at four different points were recorded for each sample.

2.6. Electrochemical analyses

The carbon-sulfur electrodes were used to build 2032 coin cells (two-electrode setup) for galvanostatic charge-discharge measurements and custom-built three-electrode cells (see Ref. [38]) for cyclic voltammetry. In all our coin cells carbon-sulfur hybrid cathodes of 14.2 mm diameter were used as working electrode (cathode) and a lithium disc of 15.6 mm diameter as counter electrode. During cell assembly, 50 μL of electrolyte (1 M LiTFSI + 0.25 M $LiNO_3$ in 1:1 DME/DOL by volume) was added to the separators. The electrolyte-to-sulfur ratio plays a crucial role in controlling the ultimate cell performance [39]. Our cell has a sulfur loading of 3 mg cm^{-2} and an electrolyte/sulfur ratio of 10.8 mL g^{-1}. Cyclic voltammetry was carried out with a cathode of 10 mm in diameter, using a lithium disc (13 mm diameter) as the counter electrode and 60 μL of the electrolyte was inserted into the separator. Additionally, a thin wire of lithium was inserted from the side into the electrolyte reservoir as the reference electrode. Before placing the lithium reference electrode, we inserted a piece of glass fiber separator (Whatman GF/A) to avoid the electrical contact with the working and counter electrode assembly. Unlike the galvanostatic charge-discharge measurements, an additional electrolyte amount of 20 μL was used to ensure proper wetting of the entire cell. Cyclic voltammetry was performed in VMP-300 potentiostat-galvanostat (from Biologic) within the potential range of 1 V–3 V vs. Li/Li^+ at a scan rate of 100 μV s^{-1} (equivalent to 0.2C). Galvanostatic charge/discharge tests were carried out in Astrol BatSmall battery analyzer at a constant current rate of 336 mA g^{-1} (0.2C) for charging and 168 mA g^{-1} (0.1C) for discharging in the potential window of 1.8 V–2.6 V. For rate capability measurements, the coin cells were subjected to different scan rates from 0.1C (discharge)/0.2C (charge) for 20 cycles, 0.2C (discharge)/0.4C (charge) for the next 10 cycles, 0.5C (discharge)/1C (charge) for further 10 cycles, 1C (discharge)/2C (charge), and again 0.1C (discharge)/0.2C (charge) for the final 20 charging-discharging cycles. We also evaluated the cathode performance at high C-rates (i.e., discharged with 1C and charged with 2C) for 500 cycles. The capacity obtained during discharge and charge is normalized to the sulfur mass. In all our galvanostatic charge-discharge experiments, the charging rate was two times of the discharge rate.

3. Results and discussion

3.1. Pore structure

Based on our previous work, we have chosen PNC because of its microporosity [25,26]. The nitrogen sorption isotherm of PNC (Fig. 2A) confirms the absence of mesopores and the volume of micropores is further increased by physical activation with CO_2 at 1000 °C. Following the Boudouard equation, injected CO_2 reacts with carbon to form carbon monoxide ($C(solid)+CO_2(gas) \rightarrow 2CO(gas)$), leading to an increase in porosity [40]. A steep increase of the isotherms above a relative pressure of 0.95 is caused by interparticle pores [25]. By applying a QSDFT model assuming slit pores, we calculated the pore size distributions (Fig. 2B). PNC shows a DFT SSA of 640 m^2 g^{-1} with pores exclusively smaller than 0.6 nm, which is notably smaller than the diameter of S_6 or S_8 molecules (0.76 nm or 0.84 nm) [17]. Therefore, only smaller polysulfides will be able to infiltrate these small pores. The activation process broadened the pore size distribution yielding a DFT SSA of 2080 m^2 g^{-1} and a total pore volume of 1.45 cm^3 g^{-1}. The average pore size increased to 1.5 nm, which enables access to the micropores for larger polysulfides. This corresponds to an increase in DFT SSA of 324% and an increase in pore volume of 580% via physical activation in CO_2. The yield of carbon after the pyrolysis of the polymer is around 55 mass%. The activation reduces the total yield to approximately 15 mass% compared to the polymer beads which were pyrolyzed.

In addition to gas sorption, we also characterized the pore structure by small angle X-ray scattering (SAXS). The measured SAXS intensities of PNC and PNC_{act} as a function of the scattering vector length Q are given in Fig. 2C. The power law intensity decay at the smallest Q-values is influenced by the scattering contribution of the carbon bead surface [41]. The rest of the curve contains information about pore size, pore shape, and possible correlations (i.e., ordering effects) between the nanopores [35,42]. Since the SAXS intensity I(Q) is related to structural features with a size being roughly proportional to π/Q, the calculated pore size distribution pattern do not account for pores larger than about 5 nm. In contrast, nitrogen gas sorption provided information on the pore size distribution within the range of 0.5–35 nm. Following the procedure and correlation function from previous work [35], 3D pore structures were generated from which pore size distributions were derived (Fig. 2D–E). The carbons differ mainly regarding the pore volume fraction and the mean pore size. In good agreement with the gas sorption data, the CO_2 activated sample (PNC_{act}) exhibits a higher pore volume, surface area, and a larger mean pore size. The cumulative PSDs generated for PNC and PNC_{act} from SAXS reproduce the pattern obtained from gas sorption (Fig. 2B). Although the size distributions obtained from SAXS are slightly broader, the average pore width is similar (Table 1). The SAXS data validate the PSDs obtained from nitrogen sorption analysis and the 3D model visualizes the increase in pore volume (i.e., reduced carbon mass per unit volume; Fig. 2D–E).

3.2. Chemical composition, structure, and electrical conductivity

The sulfur content of the hybrid materials was quantified by

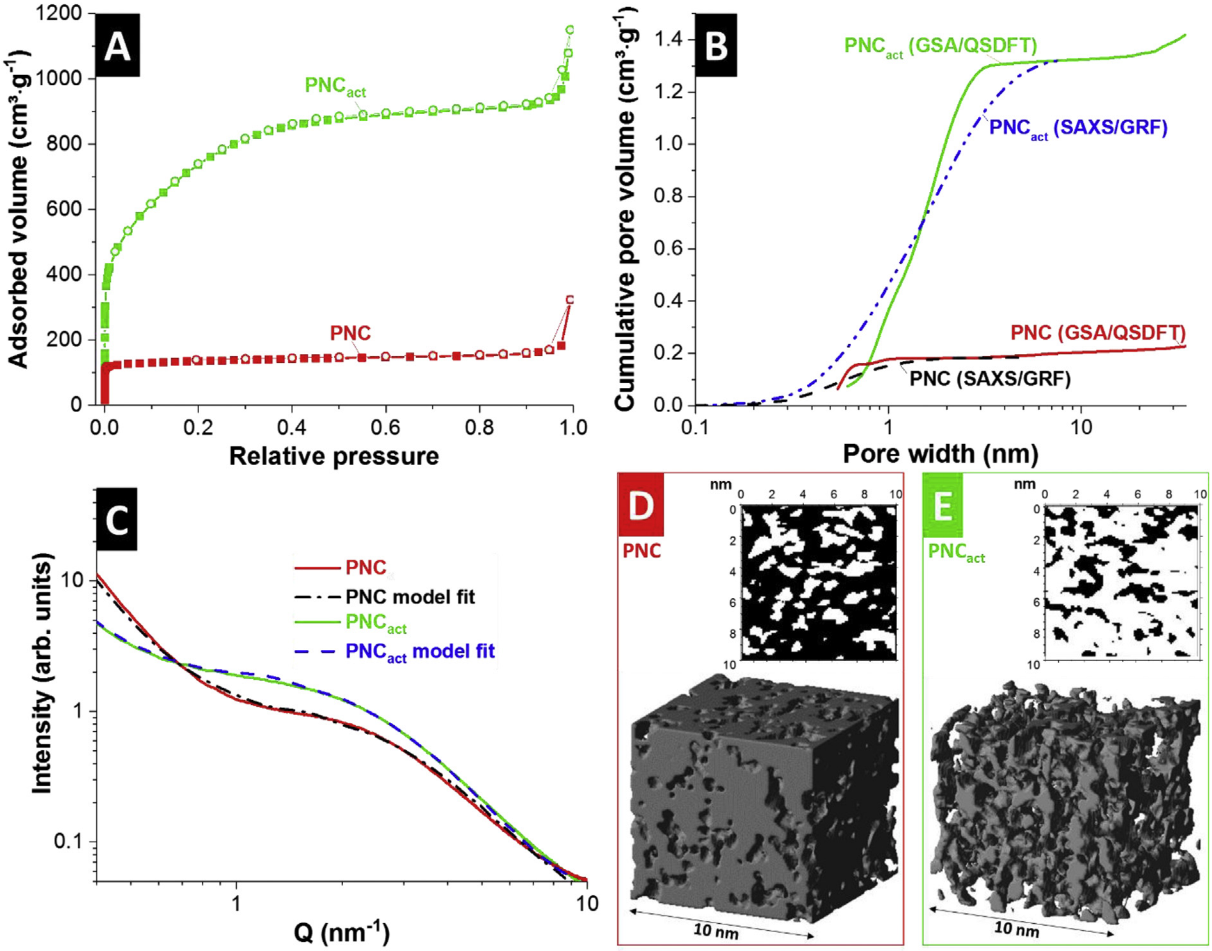

Fig. 2. (A) Nitrogen sorption isotherms of PNC and PNC_{act} at −196 °C. (B) Calculated pore size distribution pattern derived from nitrogen gas sorption and small angle X-ray scattering (SAXS). The latter are fitted to the maximum pore volume derived from gas sorption. (C) Measured and fitted SAXS data. (D–E) 3D pore models and cross section of the pyrolyzed (D; PNC) and activated carbon beads (E; PNC_{act}) simulated from the SAXS measurements.

Table 1
Specific surface area, total pore volume, and average pore size obtained from nitrogen gas sorption analysis (GSA) and calculated average pore size from small angle X-ray scattering (SAXS).

	DFT SSA ($m^2\ g^{-1}$)	BET SSA ($m^2\ g^{-1}$)	Pore volume ($cm^3\ g^{-1}$)	Average pore size (nm)	
				GSA	SAXS
PNC	641	529	0.25	0.6	0.6
PNC_{act}	2080	2698	1.45	1.5	1.4

thermogravimetry from the mass loss between 100 °C and 500 °C (Fig. 3A). The sulfur content of the PNC-S-in-situ and PNC_{act}-S-in-situ was 57.2 mass% and 61.2 mass%, respectively, and the sulfur annealing approach yielded consistently higher sulfur loadings (namely, 68.7–69.5 mass%; Table 2). A lower sulfur loading from the in situ approach is explained by the incomplete filling of the nanopores of hydrophobic carbon by the aqueous sulfur precursor. The measured sulfur contents align with the results from CHNS-analysis (Table 2). The latter data also indicate consistently higher oxygen contents of the in situ approach (i.e., above 4 mass%) compared to the annealing route (i.e., below 1 mass%). There are more evident differences in the thermograms between PNC/sulfur and PNC_{act}/sulfur compared to the difference between the in situ and sulfur annealing approach. The maximum mass loss shifts towards higher temperatures for PNC_{act}. As mentioned above carbon activation has led to a severe increase of the inner porosity of PNC (Table 1) and sulfur confined inside the nanopores requires higher thermal energy to be mobilized [43].

The presence of nitrogen and oxygen has been reported to minimize the rate of capacity decay by anchoring the long chain polysulfides. Hydroxyl and epoxy groups of carbon surfaces may control the shuttle-effect and dissolution of polysulfides [44]. Zhang et al. explained by X-ray absorption spectroscopy and ab-initio calculations that epoxy and hydroxyl groups can enhance the binding of S to carbon due to the induced ripples by these functional groups. Nitrogen-doped carbons are also often reported as polysulfide immobilizer, leading to an enhanced capacity retention [45–47].

The PNC-S-annealing and PNC-S-in-situ samples show three distinct Raman peaks at 156, 219, and 473 cm^{-1} related to the vibrations of the sulfur-sulfur bonds (Fig. 3B) [48]. For both non-activated PNC/sulfur hybrid samples, the sulfur peaks are more

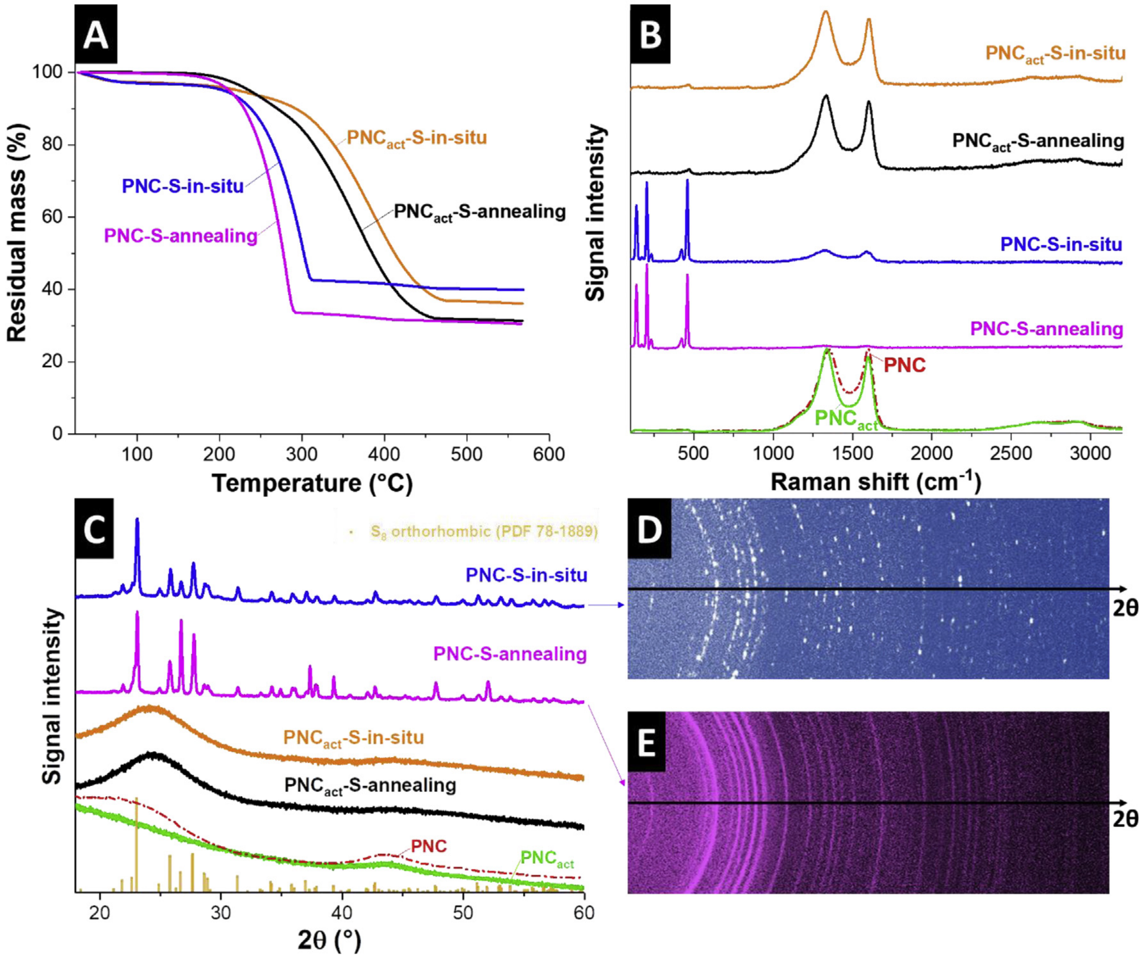

Fig. 3. (A) Thermogravimetry of the hybrid samples carried out in argon to obtain the sulfur content. (B) Raman spectra and (C) X-ray diffraction pattern of the hybrid samples, PNC, and PNC$_{act}$. (D–E) 2D X-ray diffraction pattern of PNC-S-annealing (D) and PNC-S-in-situ (E).

Table 2
Chemical composition obtained from TGA and CHNS-analysis. ΔO is calculated from the difference of S-, C, H-, and N-content to 100%.

	TGA	CHNS				
	S (mass%)	S (mass%)	C (mass%)	H (mass%)	N (mass%)	ΔO (mass%)
PNC-S-in-situ	57.2	55.8 ± 0.3	39.1 ± 0.2	≤0.4	≤0.6	Δ4.1
PNC-S-annealing	69.5	68.7 ± 0.8	30.1 ± 0.6	≤0.2	≤0.3	Δ0.7
PNC$_{act}$-S-in-situ	61.2	58.5 ± 2.6	33.6 ± 1.3	≤0.4	≤0.4	Δ7.1
PNC$_{act}$-S-annealing	68.7	69.5 ± 0.3	30.2 ± 0.5	≤0.2	≤0.4	Δ0

pronounced than the D- and G-modes of carbon because of the high localization of sulfur clusters on the exterior surfaces. PNC$_{act}$/sulfur hybrids show only a small Raman signal of sulfur at approximately 470 cm^{-1}. The PNC$_{act}$-S-in-situ sample shows a carbon-related D-mode at 1333 cm^{-1} with a full width at half maximum (FWHM) of 115 cm^{-1} and the G-mode at 1604 cm^{-1} (FWHM: 59 cm^{-1}). These values are similar to the sample PNC$_{act}$-S-annealing since the carbon was not changed (D-mode: 1329 cm^{-1}; FWHM D-mode: 119 cm^{-1}; G-mode: 1603 cm^{-1}; FWHM G-mode: 61 cm^{-1}). In alignment with our previous work [25], we confirmed an decrease in FWHM after PNC activation (Table 3).

As can be seen from Fig. 3C, PNC shows X-ray reflections typical for highly disordered carbon with broad carbon-related peaks at 23° 2θ and 44° 2θ. The lower signal intensity after activation originates from the creating of a larger pore volume and the removal of carbon, as can be seen from the 3D model in Fig. 2D and E. The X-ray diffractograms of PNC-S-in-situ and PNC-S-annealing (Fig. 3C) show sharp reflections of crystalline orthorhombic sulfur (α-sulfur), which is the stable modification at room temperature [49]. These PNC samples have the major fraction of pores below 0.7 nm, which are too small for the formation of crystalline sulfur (puckered S$_8$ rings), because the S$_8$ rings cannot penetrate into these small micropores. This result shows that sulfur is preferably located at the exterior surfaces of the PNC carbon beads. The 2D diffraction pattern of the sample PNC-S-annealing (Fig. 3E) shows homogeneous Debye rings, indicating a high number of statistically

Table 3
Fitted position and full width at half maximum (FWHM) for the carbon D- and G-modes of the Raman spectra.

	D-mode		G-mode	
	Position (cm^{-1})	FWHM (cm^{-1})	Position (cm^{-1})	FWHM (cm^{-1})
PNC-S-in-situ	1321	162	1590	77
PNC-S-annealing	1322	142	1592	75
PNC$_{act}$-S-in-situ	1333	115	1604	59
PNC$_{act}$-S-annealing	1329	119	1603	61

distributed sulfur crystals. In contrast, the 2D diffraction pattern of PNC-S-in-situ exhibit spotted Debye rings, which indicates the presence of fewer crystals. In both samples, the average domain size of sulfur is (at least) in the range of 50–100 nm. These rather large domain sizes point out that a part of the sulfur cannot be within the carbon particles. X-ray diffraction pattern of PNC$_{act}$/sulfur hybrids show a broad peak at 24° 2θ as a superimposition of amorphous carbon and sulfur. Evidently, in situ synthesis and sulfur annealing do not yield crystalline sulfur for PNC$_{act}$ because of the high confinement of sulfur in carbon micropores [27].

Elemental mapping with EDX (carried out in a scanning electron microscope) shows an inhomogeneous distribution of sulfur within the carbon for PNC-S-in-situ and PNC-S-annealing (Fig. 4A–B). In these samples, sulfur is mostly found between the carbon particles which have an average diameter of 302 ± 142 nm [25]. This is in agreement with the X-ray and Raman results, where non-activated PNC exhibited crystalline sulfur (Fig. 3). PNC-S-in-situ also shows fiber-like agglomerates of sulfur between the carbon particles (Fig. 4A). For PNC$_{act}$-S-in-situ and PNC$_{act}$-S-annealing, sulfur is much more homogenously distributed and the high amount of sulfur inside the carbon beads is seen from the elemental distribution maps (Fig. 4C–D).

The findings from SEM-EDX agree with elemental distribution mappings obtained from transmission electron microscope (Fig. 5).

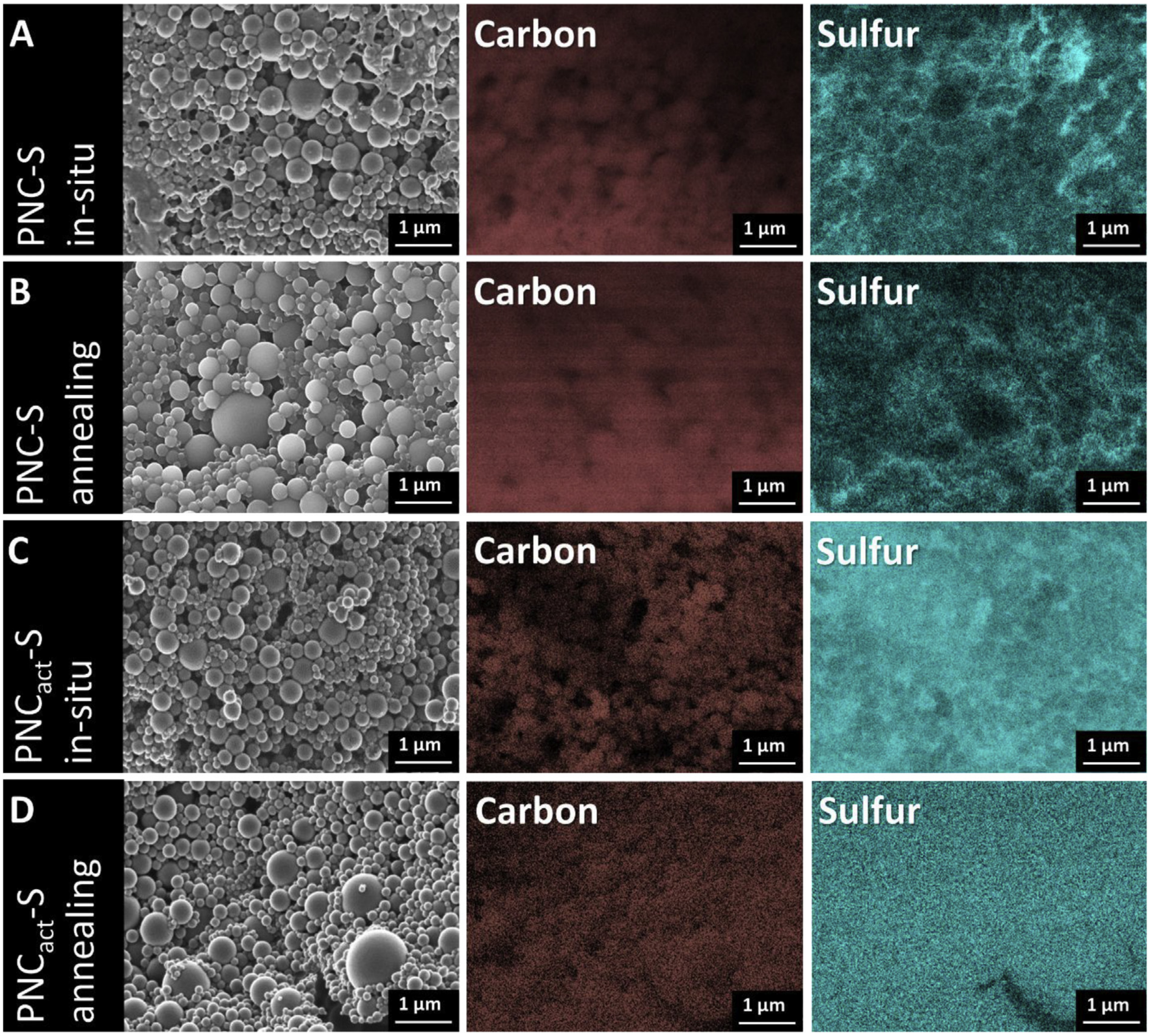

Fig. 4. SEM images and EDX mapping of carbon and sulfur of PNC-S-in-situ (A), PNC-S-annealing (B), PNC$_{act}$-S-in-situ (C), and PNC$_{act}$-S-annealing (D).

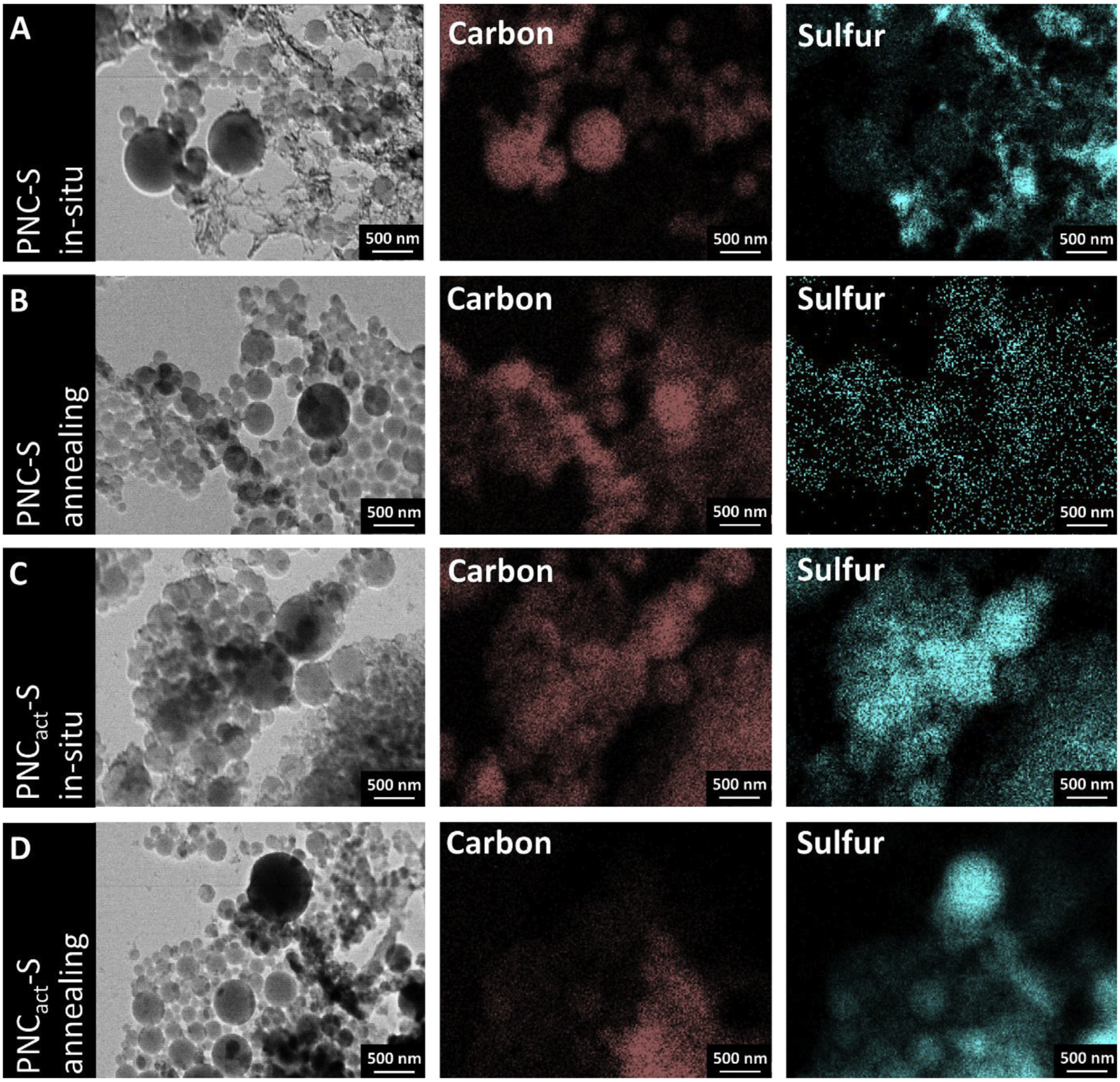

Fig. 5. TEM images and EDX mapping of carbon and sulfur of PNC-S-in-situ (A), PNC-S-annealing (B), PNC_{act}-S-in-situ (C), and PNC_{act}-S-annealing (D).

PNC-S-in-situ (Fig. 5A) shows sulfur and carbon particles which are separated from each other. The sulfur distribution of PNC-S-annealing (Fig. 5B) is more homogeneous, but the sulfur content inside the particles is low. Both PNC_{act} samples (Fig. 5C–D) show a more overlapping sulfur and carbon distribution; therefore, we conclude that sulfur is more evenly distributed throughout the carbon particles, by filling intra-particle micropores.

Sheet resistance measurements of the 80–90 μm (dry) thick electrodes coated on polyimide foil are found in Table 4. Using a four-point-probe, the measured electrical conductivity of the samples showed little difference, with values around 0.2 S cm^{-1}. A somewhat enhanced conductivity was found for PNC_{act}-S-annealing (0.36 S cm^{-1}). The measured values are in accordance with the often-reported values of conductivity of the carbon-sulfur hybrids (Ref. [27,50]) and relate to the entire film electrode (i.e., including binder and carbon black additive).

Table 4
Electrical conductivity measured via four-point-probe of all carbon-sulfur hybrids.

Sample	Conductivity (S cm^{-1})
PNC-S-in-situ	0.25
PNC-S-annealing	0.22
PNC_{act}-S-in-situ	0.22
PNC_{act}-S-annealing	0.36

3.3. Electrochemical performance

Cyclic voltammograms (CV) of the 1st, 5th, and 10th cycle are shown for all samples in Fig. 6A–D. During discharging of PNC_{act}-S-annealing, a peak at 2.41 V in the first cycle is related to the reduction of elemental sulfur to a Li-polysulfide (Li_2S_{4-8}) [24,51]. A small shift of the peak position in subsequent cycles to ca. 2.38 V occurs because of the stabilization of the cell and the formation of solid electrolyte interphase [12,13]. The peak at 2.13 V, which shifts to 2.07 V, originates from the further reduction to Li_2S_2 and Li_2S [14]. During charging, only one oxidation peak is visible at ca. 2.5 V.

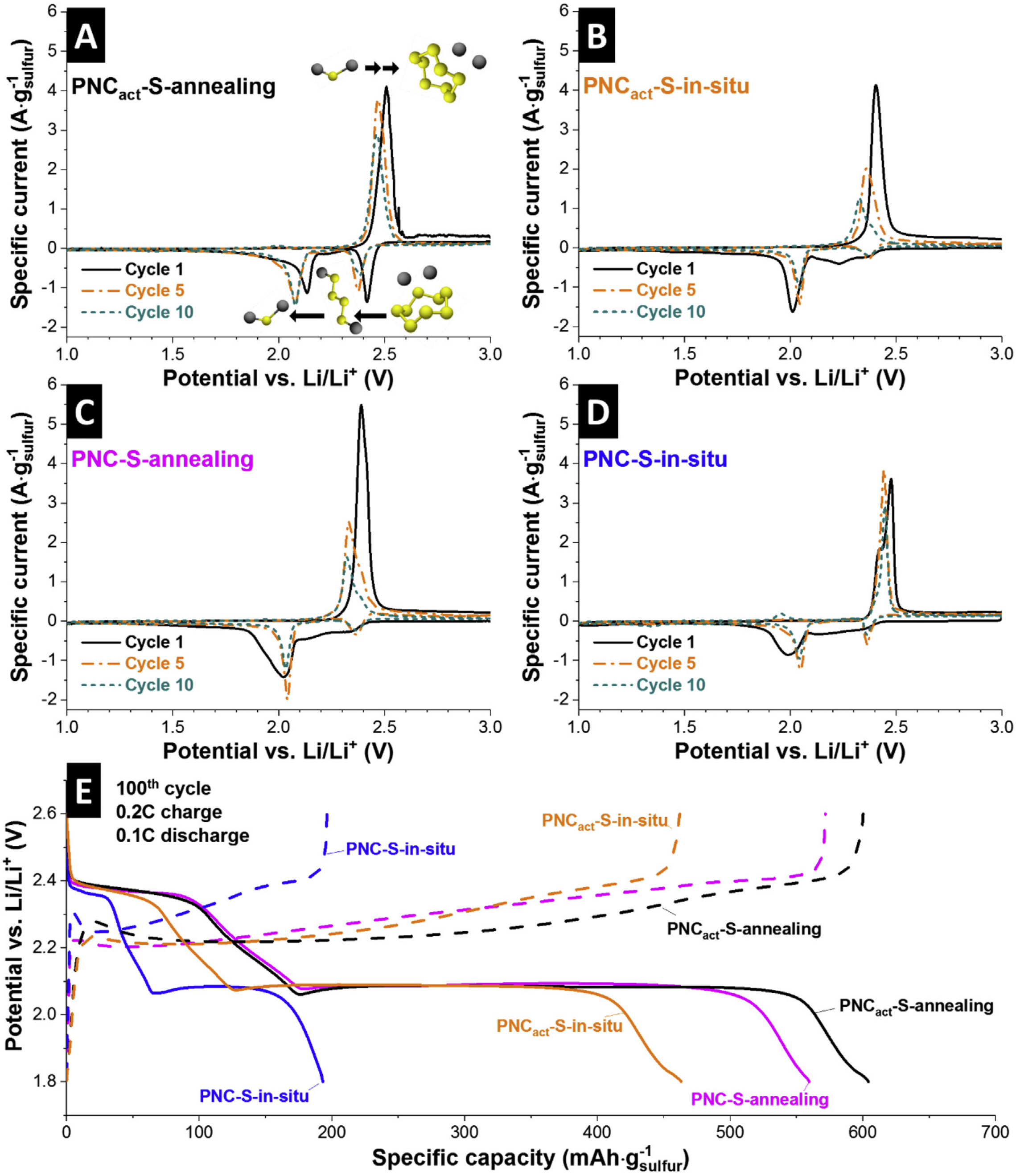

Fig. 6. Electrochemical performance of the samples in a Li-S battery. Cyclic voltammogram of PNC$_{act}$-S-annealing (A), PNC$_{act}$-S-in-situ (B), PNC-S-annealing (C), and PNC-S-in-situ (D). Voltage profiles of the 100th cycle at low rates (discharge: 0.1C and charge: 0.2C) of all samples (E).

This results from the overlap of two peaks, which correlate with the formation of larger polysulfides (Li_2S_{4-8}) and metallic lithium/elemental sulfur until all Li polysulfides are consumed at 2.50 V [52]. This peak shifts to 2.46 V in subsequent cycles [53,54]. The cyclic voltammograms of the other samples show similar shift of the reaction peak to similar potentials. All peak voltages correlate with the plateaus in the voltage profiles at the 100th cycle of cells measured with 0.1C discharge and 0.2C charge rate (Fig. 6E).

As can be seen from the cycle performance in Fig. 7, there is a rather sharp capacity drop during the first few cycles. This initial and irreversible capacity loss is due to the reorganization of active sulfur inside the carbon matrix which is often termed as activation and stabilization of the cell [18]. Thereafter, the capacity values become more stable for continued cycling. The highest specific capacity after 100 cycles (normalized to sulfur mass) is seen for PNC$_{act}$-S-annealing (600 mAh g^{-1}) followed by PNC-S-annealing (572 mAh g^{-1}) and PNC$_{act}$-S-in-situ (462 mAh g^{-1}).

The rate capability tests at multiple C-rates were performed in 2032 coin cells for all four types of carbon-sulfur hybrids (Fig. 7B). To assess power handling, we performed charge/discharge cycles at low C-rate (0.2C charge and 0.1C discharge) and raised the C-rates progressively up to 2C charge and 1C discharge and then brought back to low C-rate (0.2C charge and 0.1C discharge). The sample PNC$_{act}$-S-annealing showed the highest residual discharge capacity of 344 mAh g^{-1} at the highest C-rate (54% compared to lowest C-rate capacity). PNC$_{act}$-S-in-situ and PNC-S-annealing have a similar

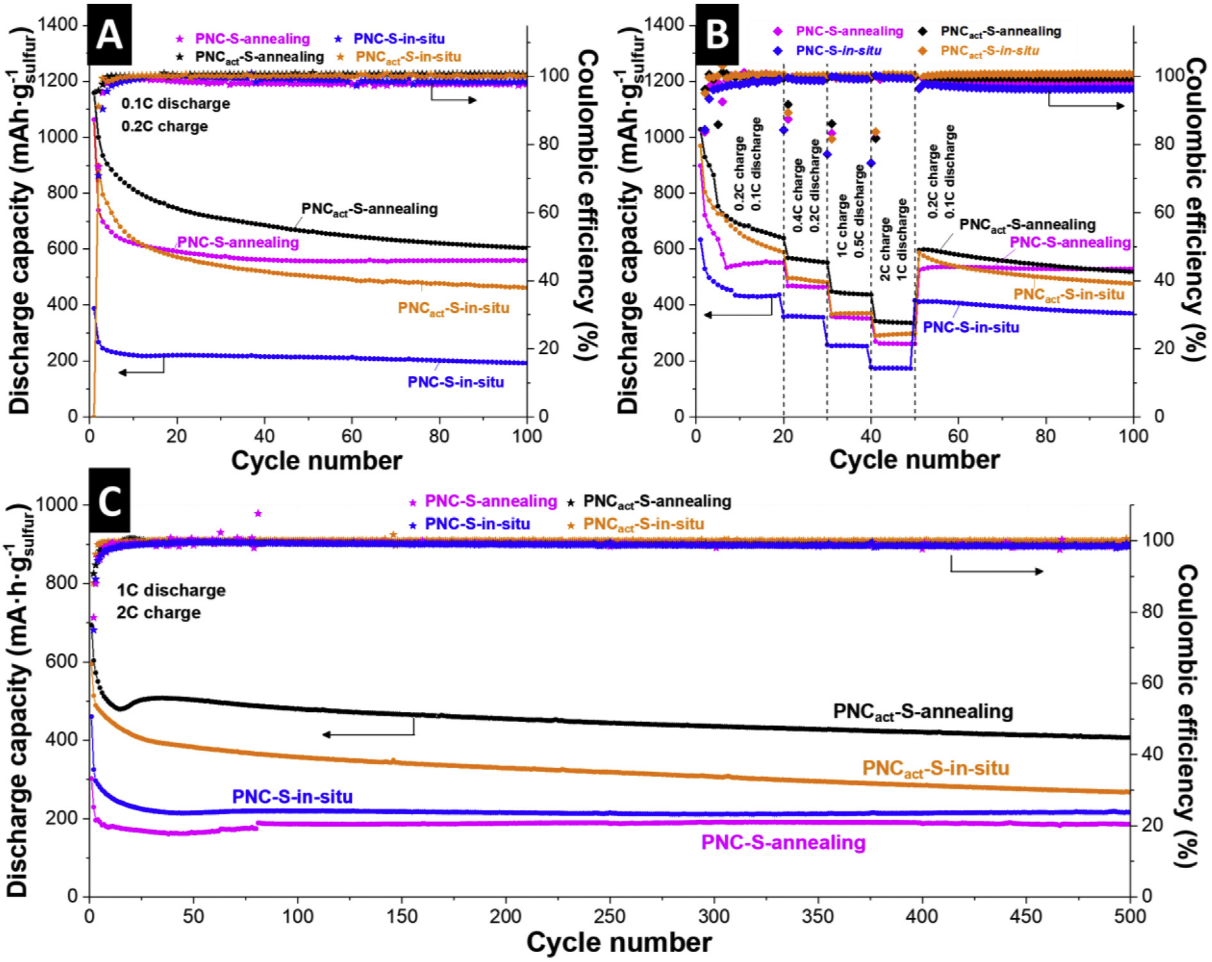

Fig. 7. Electrochemical performance of the samples in a Li-S battery. (A) Charge-discharge performance at low rates (discharge: 0.1C and charge: 0.2C) of all samples for 100 cycles. (B) Rate handling ability of all samples. (C) Performance stability benchmarking of tested all materials at high rates (discharge: 1C; charge: 2C) for 500 cycles.

rate behavior when they were first operating at low C-rates followed by high C-rates with 291 mAh g^{-1} and 271 mAh g^{-1} (=49% compared to lowest C-rate capacity). The poorest discharge capacity of 178 mAh g^{-1} (=41% compared to lowest C-rate capacity) was obtained from PNC-S-in-situ.

We also benchmarked the long-term cycle performance (Fig. 7C) at 2C for charging (equivalent to 3350 mAh g^{-1} with respect to sulfur) and for discharging 1C (equivalent to 1675 mAh g^{-1} with respect to sulfur). The results after a certain number of cycles are summarized in Table 5. Among all four carbon-sulfur hybrids, PNC$_{act}$-S-annealing demonstrated the highest initial specific discharge capacity of 800 mAh g^{-1}, yielding 410 mAh g^{-1} after 500 cycles.

The beneficial performance of electrodes obtained from sulfur melt infiltration can be explained by the low water wettability of the carbon beads [26] because the in situ formation of sulfur is carried out in an aqueous solution. Thereby, the carbon beads were incompletely decorated with sulfur, which leads to a low connectivity of carbon and sulfur (as seen from elemental mapping; Figs. 4–5). The hydrophobic character of elemental sulfur [55] facilitates covering the available surfaces of carbon in the molten state efficiently.

By comparison of PNC with PNC$_{act}$ for each synthesis approach, the activated samples show a higher electrochemical performance namely, higher specific capacity, better rate capability, and enhanced performance stability (Fig. 7). The results from material characterization (Raman, XRD, EDX) illustrate that the filling of the micropores with sulfur was possible only for the activated samples. The non-activated samples have residual sulfur in-between the carbon beads only, which leads to lower electrochemical

Table 5
Specific discharge capacity of all four hybrid electrodes after 5, 50, 100, and 500 cycles in the potential window of 1.8–2.6 V at low and high discharge/charge rates.

	Specific capacity (mAh·g$^{-1}_{sulfur}$) discharge: 0.1C; charge: 0.2C			Specific capacity (mAh·g$^{-1}_{sulfur}$) discharge: 1C; charge: 2C			
	Cycle 5	Cycle 50	Cycle 100	Cycle 5	Cycle 50	Cycle 100	Cycle 500
PNC-S-in-situ	233	213	193	281	215	220	216
PNC-S-annealing	661	558	560	191	164	186	186
PNC$_{act}$-S-in-situ	731	504	462	476	382	357	267
PNC$_{act}$-S-annealing	884	662	604	534	504	480	407

performance. Some of this sulfur can be considered as dead mass, which is only partially contributing to the overall performance of the battery. In general, we see that PNC_{act} yields higher discharge capacities than PNC when comparing samples from in situ sulfur synthesis and sulfur annealing separately. Both, the type of carbon nanopore architecture and way of sulfur hybridization, play key roles for the resulting electrochemical performance.

4. Conclusions

In this study, we fabricated spherical, microporous carbons by a template-free emulsion technique. The surface area, pore size, and pore volume of carbon were tuned by physical activation method. The carbon beads with an average pore size of 0.6 nm and 1.5 nm for the non-activated and activated carbons, respectively, were employed to embed sulfur via two different filling strategies to obtain carbon/sulfur hybrids. We used sulfur filling via melt infiltration and in situ formation of sulfur from aqueous $Na_2S_2O_3$. The non-activated carbon beads with pores smaller than 1 nm were unfavorable to achieve a high loading with sulfur. Therefore, sulfur is accumulated around carbon beads, whereby it is not fully being active in the electrochemical reaction in the Li-S battery.

The sulfur filling in the activated samples was achieved with melt infiltration and in situ sulfur formation. At low rate and when considering the rate handling, the electrochemical performance of the melt infiltrated cathodes was superior to the cathodes obtained from the in situ approach. The hydrophobic character of carbon leads to an incomplete wetting during the in situ formation of sulfur from aqueous $Na_2S_2O_3$. Therefore, it is likely that the pores inside the carbon beads are less efficiently filled with sulfur generated from the aqueous sulfur precursor. The melt infiltrated carbon benefits from the hydrophobic behavior and creates a homogeneous hybrid carbon-sulfur cathode for Li-S batteries.

Acknowledgements

L.B. gratefully acknowledge funding from the German Federal Ministry for Research and Education (BMBF) in support of the Mechanocarb project (award number 03SF0498). The INM authors kindly acknowledge the continuing support of Prof. Eduard Arzt (INM). We thank Ralph Schäfer (Allnex) for the supply of the novolac and Anna Schreiber (INM) for her kind support and helpful discussions.

References

[1] M. Armand, J.M. Tarascon, Nature 451 (2008) 652–657.
[2] P.G. Bruce, S.A. Freunberger, L.J. Hardwick, J.-M. Tarascon, Nat. Mater. 11 (2012) 19–29.
[3] Z. Yang, J. Zhang, M.C.W. Kintner-Meyer, X. Lu, D. Choi, J.P. Lemmon, J. Liu, Chem. Rev. 111 (2011) 3577–3613.
[4] N. Nitta, F. Wu, J.T. Lee, G. Yushin, Mater. Today 18 (2015) 252–264.
[5] P. Stevens, G. Toussaint, G. Caillon, P. Viaud, P. Vinatier, C. Cantau, O. Fichet, C. Sarrazin, M. Mallouki, ECS Trans. 28 (2010) 1–12.
[6] G. Girishkumar, B. McCloskey, A.C. Luntz, S. Swanson, W. Wilcke, J. Phys. Chem. Lett. 1 (2010) 2193–2203.
[7] M. Xu, D.G. Ivey, Z. Xie, W. Qu, J. Power Sources 283 (2015) 358–371.
[8] J.-S. Lee, S. Tai Kim, R. Cao, N.-S. Choi, M. Liu, K.T. Lee, J. Cho, Adv. Energy Mater. 1 (2011) 34–50.
[9] K.-N. Jung, J. Kim, Y. Yamauchi, M.-S. Park, J.-W. Lee, J.H. Kim, J. Mater. Chem. A 4 (2016) 14050–14068.
[10] J.-Y. Hwang, S.-T. Myung, Y.-K. Sun, Chem. Soc. Rev. (2017), http://dx.doi.org/10.1039/c6cs00776g.
[11] B. Jache, P. Adelhelm, Angew. Chem. Int. Ed. 53 (2014) 10169–10173.
[12] L. Borchardt, M. Oschatz, S. Kaskel, Chem. - A Eur. J. 22 (2016) 7324–7351.
[13] A. Manthiram, S.-H. Chung, C. Zu, Adv. Mater. 27 (2015) 1980–2006.
[14] M. Wild, L. O'Neill, T. Zhang, R. Purkayastha, G. Minton, M. Marinescu, G.J. Offer, Energ Environ. Sci. 8 (2015) 3477–3494.
[15] L. Borchardt, H. Althues, S. Kaskel, Curr. Opin. Green Sustain. Chem. (2017), http://dx.doi.org/10.1016/j.cogsc.2017.02.008.
[16] X. Li, Y. Cao, W. Qi, L.V. Saraf, J. Xiao, Z. Nie, J. Mietek, J.-G. Zhang, B. Schwenzer, J. Liu, J. Mater. Chem. 21 (2011) 16603–16610.
[17] S. Xin, L. Gu, N.-H. Zhao, Y.-X. Yin, L.-J. Zhou, Y.-G. Guo, L.-J. Wan, J. Am. Chem. Soc. 134 (2012) 18510–18513.
[18] Z. Li, Y. Jiang, L. Yuan, Z. Yi, C. Wu, Y. Liu, P. Strasser, Y. Huang, Acs Nano 8 (2014) 9295–9303.
[19] R. Sahore, L.P. Estevez, A. Ramanujapuram, F.J. DiSalvo, E.P. Giannelis, J. Power Sources 297 (2015) 188–194.
[20] J. Zhang, H. Ye, Y. Yin, Y. Guo, J. Energy Chem. 23 (2014) 308–314.
[21] A. Petzold, A. Juhl, J. Scholz, B. Ufer, G. Goerigk, M. Froba, M. Ballauff, S. Mascotto, Langmuir 32 (2016) 2780–2786.
[22] J. Schuster, G. He, B. Mandlmeier, T. Yim, K.T. Lee, T. Bein, L.F. Nazar, Angew. Chem. Int. Ed. 51 (2012) 3591–3595.
[23] C. Zhang, H.B. Wu, C. Yuan, Z. Guo, X.W. Lou, Angew. Chem. 124 (2012) 9730–9733.
[24] N. Jayaprakash, J. Shen, S.S. Moganty, A. Corona, L.A. Archer, Angew. Chem. Int. Ed. 50 (2011) 5904–5908.
[25] B. Krüner, J. Lee, N. Jäckel, A. Tolosa, V. Presser, ACS Appl. Mater. Interfaces 8 (2016) 9104–9115.
[26] B. Krüner, P. Srimuk, S. Fleischmann, M. Zeiger, A. Schreiber, M. Aslan, A. Quade, V. Presser, Carbon 117 (2017) 46–54.
[27] X. Ji, K.T. Lee, L.F. Nazar, Nat. Mater. 8 (2009) 500–506.
[28] X. Jia, C. Zhang, J. Liu, W. Lv, D.-W. Wang, Y. Tao, Z. Li, X. Zheng, J.-S. Yu, Q.-H. Yang, Nanoscale 8 (2016) 4447–4451.
[29] D. Lv, J. Zheng, Q. Li, X. Xie, S. Ferrara, Z. Nie, L.B. Mehdi, N.D. Browning, J.-G. Zhang, G.L. Graff, J. Liu, J. Xiao, Adv. Energy Mater. 5 (2015) 1402290.
[30] G.Y. Gor, M. Thommes, K.A. Cychosz, A.V. Neimark, Carbon 50 (2012) 1583–1590.
[31] A. Vishnyakov, P.I. Ravikovitch, A.V. Neimark, Langmuir 15 (1999) 8736–8742.
[32] S. Brunauer, P.H. Emmett, E. Teller, J. Am. Chem. Soc. 60 (1938) 309–319.
[33] V. Presser, J. McDonough, S.H. Yeon, Y. Gogotsi, Energ Environ. Sci. 4 (2011) 3059–3066.
[34] D. Orthaber, A. Bergmann, O. Glatter, J. Appl. Crystallogr. 33 (2000) 218–225.
[35] C. Prehal, C. Koczwara, N. Jäckel, A. Schreiber, M. Burian, H. Amenitsch, M.A. Hartmann, V. Presser, O. Paris, Nat. Energy 2 (2017) 16215.
[36] N.F. Berk, Phys. Rev. Lett. 58 (1987) 2718–2721.
[37] C.J. Gommes, A.P. Roberts, Phys. Rev. E 77 (2008) 041409.
[38] D. Weingarth, M. Zeiger, N. Jäckel, M. Aslan, G. Feng, V. Presser, Adv. Energy Mater. 4 (2014) 1400316.
[39] S. Zhang, Energies 5 (2012) 5190.
[40] A. Ahmadpour, D.D. Do, Carbon 34 (1996) 471–479.
[41] A. Gibaud, J.S. Xue, J.R. Dahn, Carbon 34 (1996) 499–503.
[42] C. Prehal, D. Weingarth, E. Perre, R.T. Lechner, H. Amenitsch, O. Paris, V. Presser, Energ Environ. Sci. 8 (2015) 1725–1735.
[43] G. Li, J. Sun, W. Hou, S. Jiang, Y. Huang, J. Geng, Nat. Commun. 7 (2016) 10601.
[44] L. Ji, M. Rao, H. Zheng, L. Zhang, Y. Li, W. Duan, J. Guo, E.J. Cairns, Y. Zhang, J. Am. Chem. Soc. 133 (2011) 18522–18525.
[45] S. Niu, W. Lv, G. Zhou, Y. He, B. Li, Q.-H. Yang, F. Kang, Chem. Commun. 51 (2015) 17720–17723.
[46] Z. Yang, Y. Dai, S. Wang, H. Cheng, J. Yu, RSC Adv. 5 (2015) 78017–78025.
[47] C. Wang, F. Zhang, X. Wang, G. Huang, D. Yuan, D. Yin, Y. Cheng, L. Wang, RSC Adv. 6 (2016) 76568–76574.
[48] A.T. Ward, J. Phys. Chem. 72 (1968) 4133–4139.
[49] N.A. Cañas, S. Wolf, N. Wagner, K.A. Friedrich, J. Power Sources 226 (2013) 313–319.
[50] S. Choudhury, M. Zeiger, P. Massuti-Ballester, S. Fleischmann, P. Formanek, L. Borchardt, V. Presser, Sustain. Energy & Fuels 1 (2017) 84–94.
[51] X. Tao, X. Chen, Y. Xia, H. Huang, Y. Gan, R. Wu, F. Chen, W. Zhang, J. Mater. Chem. A 1 (2013) 3295–3301.
[52] A. Manthiram, Y. Fu, S.-H. Chung, C. Zu, Y.-S. Su, Chem. Rev. 114 (2014) 11751–11787.
[53] C. Barchasz, F. Molton, C. Duboc, J.-C. Leprêtre, S. Patoux, F. Alloin, Anal. Chem. 84 (2012) 3973–3980.
[54] J. Kim, D.-J. Lee, H.-G. Jung, Y.-K. Sun, J. Hassoun, B. Scrosati, Adv. Funct. Mater. 23 (2013) 1076–1080.
[55] E. Chibowski, K. Terpilowski, J. Colloid Interface Sci. 319 (2008) 505–513.

4.9. Gyroidal porous carbon activated with NH_3 or CO_2 as lithium−sulfur battery cathodes

Benjamin Krüner,[1,2] Tobias S. Dörr,[1,2] Hwirim Shim,[1,2]Joachim Sann,[3] Jürgen Janek,[3]

Volker Presser[1,2]

[1] *INM - Leibniz Institute for New Materials, 66123 Saarbrücken, Germany*

[2] *Department of Materials Science and Engineering, Saarland University, 66123 Saarbrücken, Germany*

[3] *Institute of Physical Chemistry & Center for Materials Research, Justus-Liebig University Giessen, 35392 Giessen, Germany*

Krüner, Benjamin et al. (2018) *Batteries & Supercaps*.
https://doi.org/10.1002/batt.201800013

Own contribution: Design, planning, writing, pyrolysis and activation of the gyroidal carbons, CO_2 and N_2 sorption analysis, Raman analysis, XRD, electrochemical analysis for Li-sulfur batteries.

Abstract:

Ordered mesoporous carbon materials, prepared from co-assembly of a block copolymer and a commercial resol, were investigated as a sulfur host for LiS-battery cathodes. We studied two activation methods for such carbons, namely annealing in ammonia (NH_3) and carbon dioxide (CO_2). We found that both activation environments drastically increased the specific surface area and establish a micro- and mesoporous pore structure. Treatment with NH_3 also introduced nitrogen groups, which increased the initial specific capacity. The non-activated carbon yielded carbon/sulfur cathodes with an initial capacity of ~900 mAh/g_{sulfur} (150 mAh/g_{sulfur} after 100 cycles). The initial capacity was increased to 1300 mAh/g_{sulfur} for the NH_3 activated sample but with poor cycling stability. Enhanced performance stability was found for the CO_2 treated sample with an initial capacity of 1100 mAh/g_{sulfur} (700 mAh/g_{sulfur} after 100 cycles).

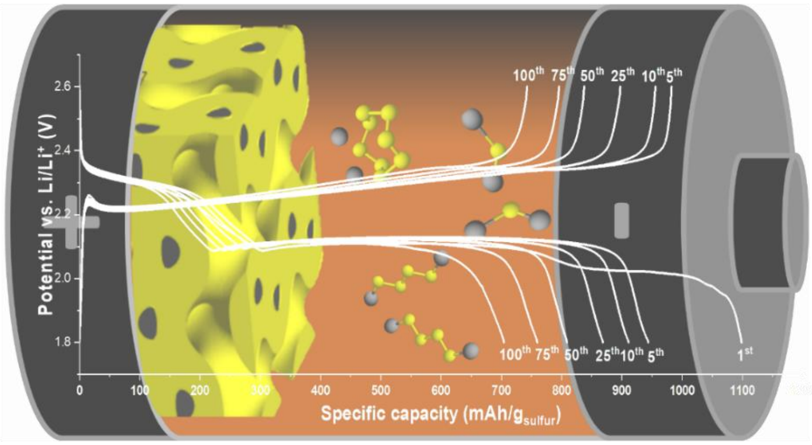

Gyroidal Porous Carbon Activated with NH_3 or CO_2 as Lithium–Sulfur Battery Cathodes

Benjamin Krüner,[a, b] Tobias S. Dörr,[a, b] Hwirim Shim,[a, b] Joachim Sann,[c] Jürgen Janek,[c] and Volker Presser*[a, b]

Ordered mesoporous carbon materials, prepared from co-assembly of a block copolymer and a commercial resol, were investigated as a sulfur host for LiS-battery cathodes. We studied two activation methods for such carbons, namely annealing in ammonia (NH_3) and carbon dioxide (CO_2). We found that both activation environments drastically increased the specific surface area and establish a micro- and mesoporous pore structure. Treatment with NH_3 also introduced nitrogen groups, which increased the initial specific capacity. The non-activated carbon yielded carbon/sulfur cathodes with an initial capacity of ~900 mAh/g_{sulfur} (150 mAh/g_{sulfur} after 100 cycles). The initial capacity was increased to 1300 mAh/g_{sulfur} for the NH_3 activated sample but with poor cycling stability. Enhanced performance stability was found for the CO_2 treated sample with an initial capacity of 1100 mAh/g_{sulfur} (700 mAh/g_{sulfur} after 100 cycles).

1. Introduction

Lithium-sulfur batteries (LiS) with their high theoretic specific capacity of 1672 mAh/g_{sulfur} are promising for advanced energy storage considering that sulfur is an abundant, cheap, and low-toxic resource.[1–4] Sulfur itself shows a very low electrical conductivity; LiS cathodes, therefore, require hybridization of sulfur with a conductive matrix material, such as carbon.[2,4] Various microporous,[5,6] mesoporous,[7–10] and hierarchical porous carbon composites[11–13] have been reported as highly conductive matrices to encapsulate the sulfur. An advanced pore structure can increase the performance of LiS-batteries and reduce the sulfur shuttling, which is one of the main reasons for the LiS-battery degradation.[14] Especially microporous and hierarchical porous carbons reduce polysulfide shuttling due to the confinement of the polysulfides to nanopores.[2,11–13,15,16] There are many different synthesis methods to produce advanced pore structures, like soft-templating, hard-templating, in-situ-templating, or using biomass precursors.[14] The material properties and pore structures will depend on the choice of synthesis method and the set of employed process parameters.

In 2015, Werner et al.[17] and Choudhury et al.[18] synthesized ordered gyroidal mesoporous carbons for LiS-batteries with promising performance owed to the homogeneous winding pore structure. Werner et al. used a triblock terpolymer poly(isoprene)-block-poly(styrene)-block-poly(ethylene oxide) (ISO) and either phenol-formaldehyde resin or oligomeric resorcinol-formaldehyde to produce different gyroidal mesoporous structures by co-assembly, followed by carbonization in argon at 900–1600 °C.[17,19] An additional removal of a template to produce the ordered mesopores is unnecessary, because the ISO decomposes at high temperatures. They also carried out physical activation of carbon with CO_2 to create suitable micropores that encapsulate the sulfur. This hierarchical activated carbon was used to produce a carbon/sulfur (ratio 1:1) hybrid electrode with a specific capacity of 830 mAh/g_{sulfur} after 100 cycles.[17] Choudhury et al. produced gyroidal carbon by co-assembly of poly(styrene)-block-poly(4-vinylpyridine) block copolymer (PS-b-P4VP) with 3-pentadecylphenol (PDP).[18] They selectively removed the PDP with ethanol and backfilled the structure by a resorcinol-formaldehyde solution which was cross-linked and carbonized at 900 °C. The carbon was melt-infiltrated with sulfur in a ratio of 1:2. The initial specific capacity of the LiS-battery was around 600 mAh/g_{sulfur} and decreased to ~450 mAh/g_{sulfur} after 100 cycles measured at low C-rates (i.e., 0.2C for charging and 0.1 for discharging) in a potential window of 1.8-2.6 V.

Next to an ordered pore structure, also nitrogen groups are reported to reduce sulfur shuttling because of strong N–S bonding.[16,20–24] Nitrogen can also enhance the activity towards sulfur reduction and, thereby, provides a higher initial capacity.[23,25,26] The many methods to produce nitrogen-doped porous carbon mainly follow two approaches:[27] either direct pyrolysis of nitrogen-containing precursors (e.g., melamine resin,[28–31] polypyrrole,[32] or biomass[33]) or post-synthesis treatment of carbon with nitrogen-containing compounds (e.g., NH_3,[34] HCN,[35] or HNO_3[36,37]). One disadvantage of the direct use of nitrogen-containing precursors is that the functional groups may be released at high pyrolysis temperatures.[30] In

---

[a] *B. Krüner, T. S. Dörr, H. Shim, Prof. V. Presser*
INM-Leibniz Institute for New Materials, 66123 Saarbrücken, Germany
E-mail: volker.presser@leibniz-inm.de
[b] *B. Krüner, T. S. Dörr, H. Shim, Prof. V. Presser*
Department of Materials Science and Engineering, Saarland University, 66123 Saarbrücken, Germany
[c] *Dr. J. Sann, Prof. Dr. J. Janek*
Institute of Physical Chemistry & Center for Materials Research, Justus-Liebig University Giessen,
35392 Giessen, Germany

Supporting Information and the ORCID identification number(s) for the author(s) of this article can be found under: https://doi.org/10.1002/batt.201800013 contrast, post-synthesis treatments are an elegant way to modify a given material without changing the initial reaction parameters. However, this approach might form additional functional surface groups instead of actual nitrogen doping.[27,34,37] Wang et al. combined block copolymer co-assembly using a commercial Pluronic F127 and an in-situ doping during pyrolysis in ammoniacal atmosphere.[38] They obtained a mesoporous carbon containing up to 9 at% nitrogen in the form of pyridine, pyrrole, pyridone, and quaternary nitrogen groups after the treatment at 850 °C.[38] The resulting material showed a BET surface area of around 1400 m^2/g with an average pore diameter of 7 nm and was used as an electrode for supercapacitors. We applied the in-situ doping during pyrolysis in NH_3 to sub-micrometer sized novolac beads in a previous study.[39] Thereby, it was possible to achieve microporous carbon beads with a nitrogen content of 5–7 mass% depending on the target temperature (750–950 °C).

In this study, we combine the beneficial pore size of a mesoporous carbon prepared by co-assembly of an optimized ISO block copolymer with in-situ activation upon pyrolysis. We synthesized three different samples: a mainly mesoporous carbon (pyrolyzed in argon), hierarchic (meso- and microporous) carbon obtained after CO_2 activation, and a hierarchic N-doped-carbon via activation in NH_3. The homogeneous pore structure produced by the co-assembly makes this material attractive for fundamental investigations. The three carbons were used for carbon/sulfur hybrid LiS-battery cathodes to compare the influence of the two different activation methods on the electrochemical performance. Our work used a commercially available resol as the carbon source and a constant sulfur-to-carbon ratio of 2:1 considering industrial requirements.

Experimental Section

Materials

For the synthesis of ISO, benzene (99 %, Alfa Aesar), *n*-buthyllithium (nBuLi, 2.5 M in hexane, Alfa Aesar), 1,1-diphenylethylene (DPE, 98 %, Alfa Aesar), isoprene (99 %, < 1000 ppm p-tert-butylcatechol, Sigma Aldrich), sec-butyllithium (secBuLi, 1.4 M in cyclohexane, Sigma Aldrich), styrene (ReagentPlus, stabilized, Sigma Aldrich), calcium hydride (CaH_2, 1–20 mm granules, 88–98 %, Alfa Aesar), ethylene oxide (EO, 99,8 %, Praxair), potassium (98 %, pieces in mineral oil, Fisher Scientific), naphthalene (99 %, Fisher Scientific), tetrahydrofuran (THF, 99 %, < 1000 ppm Stabilizer, Alfa Aesar), chloroform ($CHCl_3$, 99,8 %, ACS, Alfa Aesar), methanol (MeOH, 99 % AlfaAesar), hydrochloric acid (HCl, reagent grade, 37 %, Sigma Aldrich), deuterochloroform ($CDCl_3$, 99.8 atom% D, Sigma Aldrich), and absolute tetrahydrofuran (THF_{abs}, 99.85 %, extra dry, non-stabilized, Acros Organics) were used as received, or purified as described below. The commercial phenolic resol (Phenodur PR 373) was obtained from Allnex. Elemental sulfur, polyvinylidene fluoride (PVDF) powder (molecular mass ca. 534.000 g/mol), *N*-methyl-2-pyrrolidone (NMP), bis(trifluoromethane)-sulfonimide lithium salt (LiTFSI), 1,2-dimethoxyethane (DME), 1,3-dioxolane (DOL), and lithium nitrate ($LiNO_3$) were purchased from Sigma Aldrich. The battery-grade conductive carbon black (C65) was obtained from Imerys Graphite & Carbon and the nickel foil (thickness of 13 nm) from Carl Schlenk. Electrochemical grade high purity (99.9 %) lithium was purchased from PI-KEM. Trilayer porous polyolefin separator (type 2325) was obtained from Celgard, and we used non-woven polypropylene separators from Freudenberg.

Synthesis

Poly(isoprene)-block-poly(styrene)-block-poly(ethylene oxide) (ISO) terpolymer was synthesized via living sequential anionic polymerization.[40,41] All chemicals were first purified by either nBuLi or CaH_2 and distilled under a reduced atmosphere. Sequential polymerization of the first two blocks was performed in benzene at room temperature using secBuLi as an initiator. The living poly(isoprene)-block-poly(styrene) was end-capped by ethylene oxide, deactivated by MeOH/HCl, and washed several times with MilliQ water. After drying in vacuum at 90 °C, the polymer was dissolved in THF and reactivated by potassium naphthalenide, and the last block was prepared. The final ISO was precipitated from $CHCl_3$ in an aliquot of MeOH, filtrated, and stored at 6 °C.

The ISO/resol hybrids were synthesized by a modified synthesis previously reported by Werner et al. (Ref. [19]). Briefly, a 4.0 mass% ISO in THF:$CHCl_3$ (1:1 by mass) stock solution was combined with 12.5 mass% resol (in THF) solution. The optimized structure was achieved with an ISO-to-resol mass ratio of 1:0.734 and a stirring time of 24 h. The mixture was then placed on a hotplate under a glass dome at 35 °C for 2 d for the evaporation-induced self-assembly (EISA). The resulting rubber-like hybrids were further aged successively from 90 °C to 130 °C to remove residual solvents and promote cross-linking.

The different activated mesoporous carbons were obtained by heating the ISO/resol hybrids in different atmospheres (Ar: G^A-C-Ar, CO_2: G^A-C-CO_2 and NH_3: G^A-C-NH_3) at 5 °C/min to 850 °C. The argon flow for all samples was constant with 50 cm^3/min, and CO_2 or NH_3 was added to the inert gas. G^A-C-Ar was held for 3 h at 850 °C only in Ar. The sample G^A-C-CO_2 was heated in Ar and annealed for 3 h at a temperature of 850 °C with an additional CO_2 gas flow of 100 cm^3/min. G^A-C-NH_3 was also heated in a mixed Ar/NH_3 atmosphere with an NH_3 gas flow of 20 cm^3/min while the argon flow was maintained at 50 cm^3/min. This sample was held for 2.25 h at 850 °C in that specific gas mixture. Different annealing times for the heat treatment were necessary to achieve similar surface areas and allow the best comparability between the samples. The cooling was always carried out in an inert argon atmosphere. The carbon monoliths were ground in a mortar, and the particle size was reduced with a BeadBug Microtube homogenizer to a few micrometers.

Using melt infiltration, the carbon/sulfur hybrids were synthesized (G^A-C-Ar/S, G^A-C-CO_2/S, and G^A-C-NH_3/S). The samples were homogenized in a mortar with sulfur and annealed at 155 °C for 5 h. Sulfur has its lowest viscosity at this temperature, and capillary forces assist the sulfur transport into the carbon pores.[7]

Material Characterization

The synthesized ISO terpolymer was characterized by gel permeation chromatography (GPC) and ^{1}H nuclear magnetic resonance (NMR) spectroscopy. The molecular weight (M_W) and polydispersity (PDI) of the terminated polyisoprene (PI) block (taken from the reaction during synthesis) was determined using a WATERS ambient-temperature GPC system equipped with a WATER 2410 differential refractive index (RI) detector and a sample concentration of 1 mg/mL in THF. ^{1}H-NMR spectra after each polymerization step were recorded with a Bruker Advance III HD Nanobay equipped with a SampleXpress autosampler and a BBFO probe for 5 mm tubes. The samples were dissolved in $CDCl_3$ and measured at 300 MHz. The final M_W of the polymer was determined by normalization of the PI ^{1}H-NMR signal to the M_W determined by GPC. The overall polydispersity index (PDI) was further analyzed by GPC of the terminated terpolymer.

For small-angle X-ray scattering (SAXS) of the powdered sample after melt infiltration, an adequate piece of the polymer/resol hybrid or the monolithic carbon disc was sealed in polyimide tape. The measurements were performed on a Xenocs XEUSS 2.0, equipped with a Dectris Pilatus 1 M detector (detector distance of 250 cm) and a Cu-K$_\alpha$ source (154 pm). Calibration of the device was conducted with silver behenate, and total radial integration (with masking the primary beam) was performed for the 1D pattern.

We used for scanning electron microscopy (SEM) a JSM-7500F (Jeol) field emission scanning electron microscope with an operating voltage of 5 kV. Transmission electron microscopy (TEM) was carried out with a JEM-2100F (Jeol) and a high beam voltage of 200 kV. Energy dispersive X-ray spectroscopy (EDX) mapping was done at the TEM at 200 kV with an attached detector from Thermo Scientific (MC100021).

The porosity of the carbon materials was quantified by use of N_2 and CO_2 gas sorption analysis (Quantachrome Autosorb iQ). The samples were degassed at 300 °C for 20 h in a vacuum of 10 kPa to remove volatile components from the surface. The nitrogen measurements were performed in liquid nitrogen (−196 °C) with a relative pressure between $5\cdot10^{-7}$ and 1.0 in 76 steps. The CO_2 measurements were conducted at 0 °C with a relative pressure between $7\cdot10^{-5}$ and 0.024 in 40 steps. A mixed quenched-solid density functional theory (QSDFT) assuming slit-like and cylindrical pores was applied to obtain the pore size distribution and specific surface area (SSA) above 0.9 nm from the N_2 isotherm and a non-local density functional theory (NLDFT) for deconvolution of the CO_2 isotherms for pore sizes below 0.9 nm.[42–44] We also used the Brunauer-Emmett-Teller (BET) equation in the linear part of the isotherm to obtain the SSA$_{BET}$.[45] The calculations were carried out with the ASiQwin software.

X-ray photoelectron spectroscopy (XPS) measurements were conducted in a PHI Versaprobe II Scanning ESCA Microprobe (Physical Electronics) using a monochromatized Al-K$_\alpha$ X-ray source (beam diameter 50 μm, X-ray power of 12.5 W). The analyzer pass energy for detail spectra was set to 11.75 eV with a step time of 50 ms and a step size of 0.1 eV. For the measurement, the sample was mounted on insulating tape and flooded with slow electrons and argon ions using the built-in ion sputter and electron guns to compensate the surface charge. Data evaluation was performed using CasaXPS software. The samples were already electronically conductive, were grounded during measurement with no further charge neutralization, and no further calibration was applied to the data. The analyzer itself was calibrated to a C1s C–C binding energy of 284.8 eV.

The chemical composition of the carbon/sulfur hybrids was determined with CHNS and O elemental analysis and thermogravimetric analysis (TGA). A vario MICRO cube system (Elementar Analysensysteme) oxidized the samples at 1150 °C in a tin sample holder, and the system was calibrated with sulfanilic acid (41.6 mass% C, 4.1 mass% H, 8.1 mass% N, 18.5 mass% S). The oxygen content was measured with a rapid OXY cube from Elementar at a pyrolysis temperature of 1450 °C. The device was calibrated with benzoic acid. The TGA measurements were performed with a Netzsch Libra TG 209 F1 in the temperature range from 25 °C to 700 °C with a heating rate of 10 °C/min under a constant flow of synthetic air.

Phase analysis was carried out with X-ray diffraction (XRD) and Raman spectroscopy. A D8 Advance diffractometer (Bruker AXS) with Cu-K$_\alpha$ radiation (40 kV, 40 mA) was used in point focus mode with a Goebel mirror and a 2D detector (Vantec-500). The samples were placed on a sapphire single crystal.

The Raman spectra were recorded with a Renishaw inVia system using laser power of 0.2 mW on the sample with an excitation wavelength of 632.8 nm, a grating of 1800 lines/mm, a recording time of 10 s per step, and 50 accumulations to reduce the signal to noise ratio. The D- and G-modes were fitted with four Voigt peaks.

Electrochemical Measurements

The sulfur-infiltrated carbon samples were mixed with 10 mass% carbon black (C65) and 8 mass% PVdF (dissolved in NMP). The suspension was treated with a magnetic stirrer for 1 d and then coated on the nickel foil with a doctor blade (wet thickness: 200 μm). The electrodes were dried for ~16 h in the fume hood at room temperature and afterward heated to 80 °C in an oven for 8 h do evaporate any residual solvent. Then, electrode discs with a diameter of 14.2 mm were punched out and placed in a CR2032 coin cell in a two-electrode setup. A lithium disc with a diameter of 15.6 mm was used as a counter electrode with one Celgard 2325 separator. The amount of electrolyte is important for the performance of LiS-batteries.[46] Therefore, we used for the electrolyte (1 M LiTFSI + 0.25 M $LiNO_3$ in 1 : 1 DME/DOL by volume) a ratio to sulfur of 10.7 mL/g$_{sulfur}$. The electrolyte was pipetted onto the electrode, and the Celgard 2325 separator was placed on it. The sealed coin cells were tested with a battery analyzer from Astrol (BatSmall) in galvanostatic charge/discharge mode at a constant current of 336 mA/g$_{electrode}$ (0.2C) for charging and 168 mA/g$_{electrode}$ (0.1C) for discharging in the potential window of 1.8 V to 2.6 V vs. Li/Li$^+$. The charging rate was twice as large as the discharging rate. For rate capability measurements, the coin cells were measured at different rates from 0.1C (discharge)/0.2C (charge) for 20 cycles, 0.2C (discharge)/0.4C (charge) for the next 10 cycles, 0.5C (discharge)/1C (charge) for further 10 cycles, 1C (discharge)/2C (charge), and again 0.1C (discharge)/0.2C (charge) for the final 20 charging-discharging cycles. We normalized the capacity to the mass of sulfur or the mass of the electrodes, as seen from the labels "g$_{sulfur}$" or "g$_{electrode}$".

2. Results and Discussion

2.1. Material Characterization of the Three Gyroidal Materials

The simplified preparation of our different activated mesoporous carbon/sulfur hybrids is shown in Figure 1. The poly (isoprene)-block-poly(styrene)-block-poly(ethylene oxide) (ISO) comprises 31 vol%, 65 vol% and 4 vol% polyisoprene (PI), polystyrene (PS) and poly(ethylene oxide) (PEO), respectively, and has a PDI of $D_P = 1.09$ at a total M_W of 51000 g/mol. In a first step, we selectively swelled the hydrophilic PEO by a commercial resol (see Supporting Information, Figures S1–S2). Through the evaporation-induced self-assembly (EISA) process, the mixture separated into phase-pure microdomains of each block. The resulting ISO/resol hybrid was pyrolyzed in different atmospheres to archive either mainly mesoporous carbon (argon; sample: G^A-C-Ar) or hierarchically meso- and microporous carbon (CO_2; sample: G^A-C-CO_2, and NH_3; sample: G^A-C-NH_3). These carbons served as a conductive host material for the following melt-infiltration of sulfur.

Electron micrographs of the non-activated carbon (G^A-C-Ar) are shown in Figure 2A–D. We did not observe noticeable

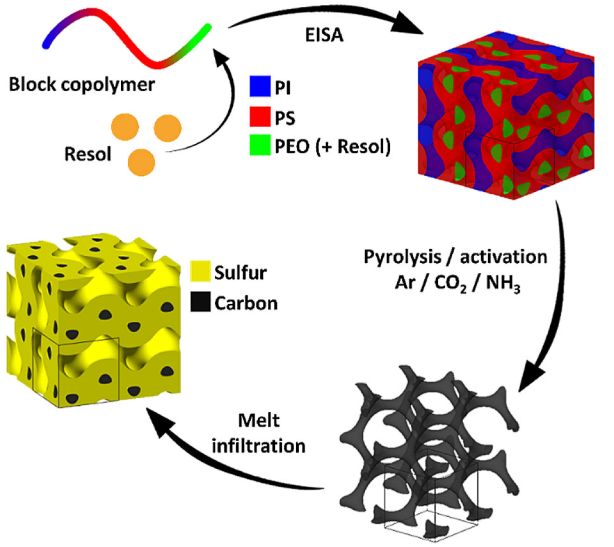

Figure 1. Schematic illustration of the synthesis of the gyroidal carbon/sulfur hybrid materials, by co-assembly, pyrolysis in Ar, CO_2, or NH_3, and melt infiltration with sulfur.

differences in the structure and morphology in the SEM images after the different activation conditions. By optimization of the preparation process and the ISO-to-resol ratio, we ensured a high degree of near- and long-range order of the resulting pore system. Estimated from electron micrograph, we determined homogenously distributed pores with an average pore size of 20 nm. The material shows no long-range ordering or highly crystalline structure, as can be seen from high-resolution TEM images (Figure 2D).

Results of the SAXS measurement of the ISO/resol hybrid and the various activated mesoporous carbon samples are provided in Figure 2E. From the first order diffraction (q^*), we calculated the expected peak positions for allowed q/q^* ratios of the alternating gyroid (G^A) morphology ($q/q^*=1, \sqrt{3}, \sqrt{4}, \sqrt{5}, \ldots$) and give the fits above the corresponding pattern as triangles.[47] The ISO/resol hybrid with its low electron density difference of the components shows blurred peaks which are consistent with the G^A morphology and well preserved during pyrolysis in first and second order diffraction for the activated mesoporous carbons. From q^*, the periodicity (d_{100}) was calculated to 50.4 nm for the ISO/resol hybrid, which shrinks during heat treatment by around 30% to 35.1 nm for G^A-C-Ar. The shift towards higher q^* values for the CO_2 and NH_3 activated carbons indicates a decreasing value for d_{100}. After activation, additional micropores blur the initially sharp interface boundaries (air/carbon), which results in peak broadening and no clear d_{100} peak can be identified.

We used nitrogen gas sorption at −196 °C and carbon dioxide gas sorption at 0 °C to characterize the porosity of our materials (Table 1). The nitrogen sorption isotherms of G^A-C-CO_2

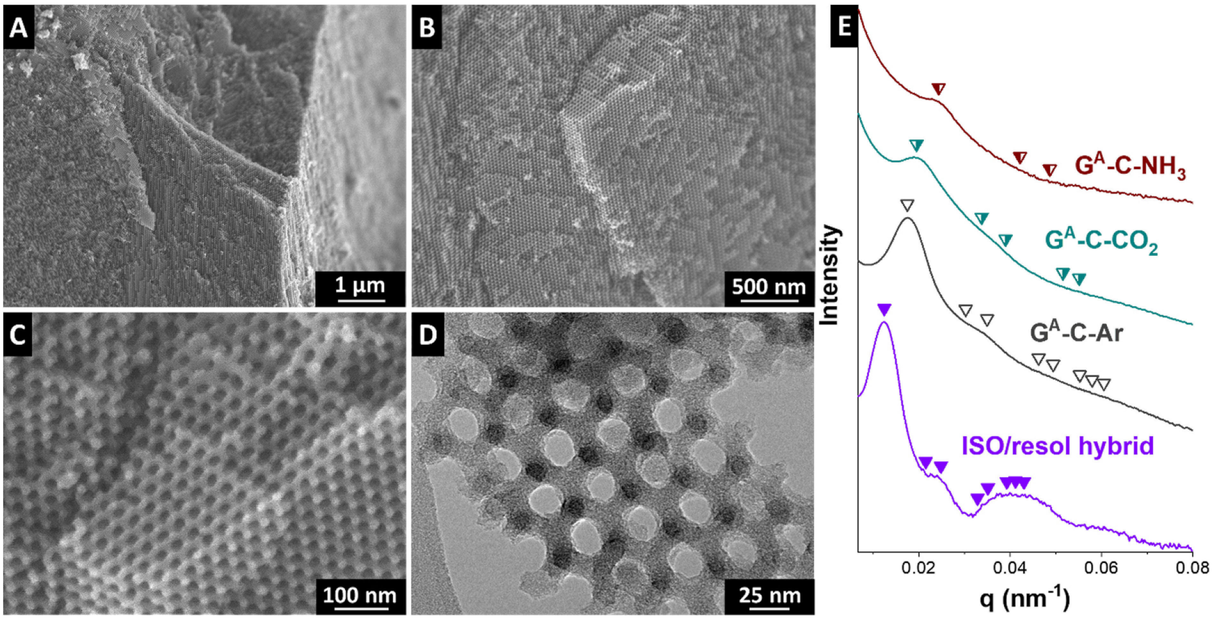

Figure 2. (A–C) SEM images of G^A-C-Ar. (D) TEM image of G^A-C-Ar. (E) SAXS pattern of the ISO/resol hybrid, G^A-C-Ar, G^A-C-CO_2, and G^A-C-NH_3.

Table 1. Porosity data of the three samples obtained by the combination of CO_2 and N_2 gas sorption.

Sample	SSA_{BET} [m^2/g]	SSA_{DFT} [m^2/g]	Micropore volume [cm^3/g]	Micropore volume [%]	Total pore volume [cm^3/g]	Average micropore size [nm]	Average mesopore size [nm]
G^A-C-Ar	197	739	0.17	22	0.78	0.55	21.2
G^A-C-CO_2	1264	1530	0.43	33	1.29	0.62	22.7
G^A-C-NH_3	1191	1328	0.37	25	1.49	0.80	18.6

and G^A-C-NH$_3$ are very similar and a mix of Type I(a) and Type II with Type H4 hysteresis loops, typical for micro-mesoporous carbons (Figure 3A).[48] In comparison, the sample G^A-C-NH$_3$ shows lower adsorption in the low-pressure range and higher adsorption in the high-pressure range. This aligns with the calculated surface area of 1264 m^2/g SSA$_{BET}$ for G^A-C-CO$_2$ and of 1191 m^2/g SSA$_{BET}$ for G^A-C-NH$_3$. The nitrogen sorption isotherm of G^A-C-Ar shows a low nitrogen adsorption capacity in the low-pressure range, aligning with a low SSA$_{BET}$ of 197 m^2/g. To investigate sub-nanometer pores more accurately, we also conducted CO$_2$ sorption analysis (Figure 3B). As seen from these data, there is significant CO$_2$ adsorption of G^A-C-Ar with an amplitude like G^A-C-NH$_3$. We used the NLDFT model assuming slit pores for deconvolution of the CO$_2$ isotherms and calculated

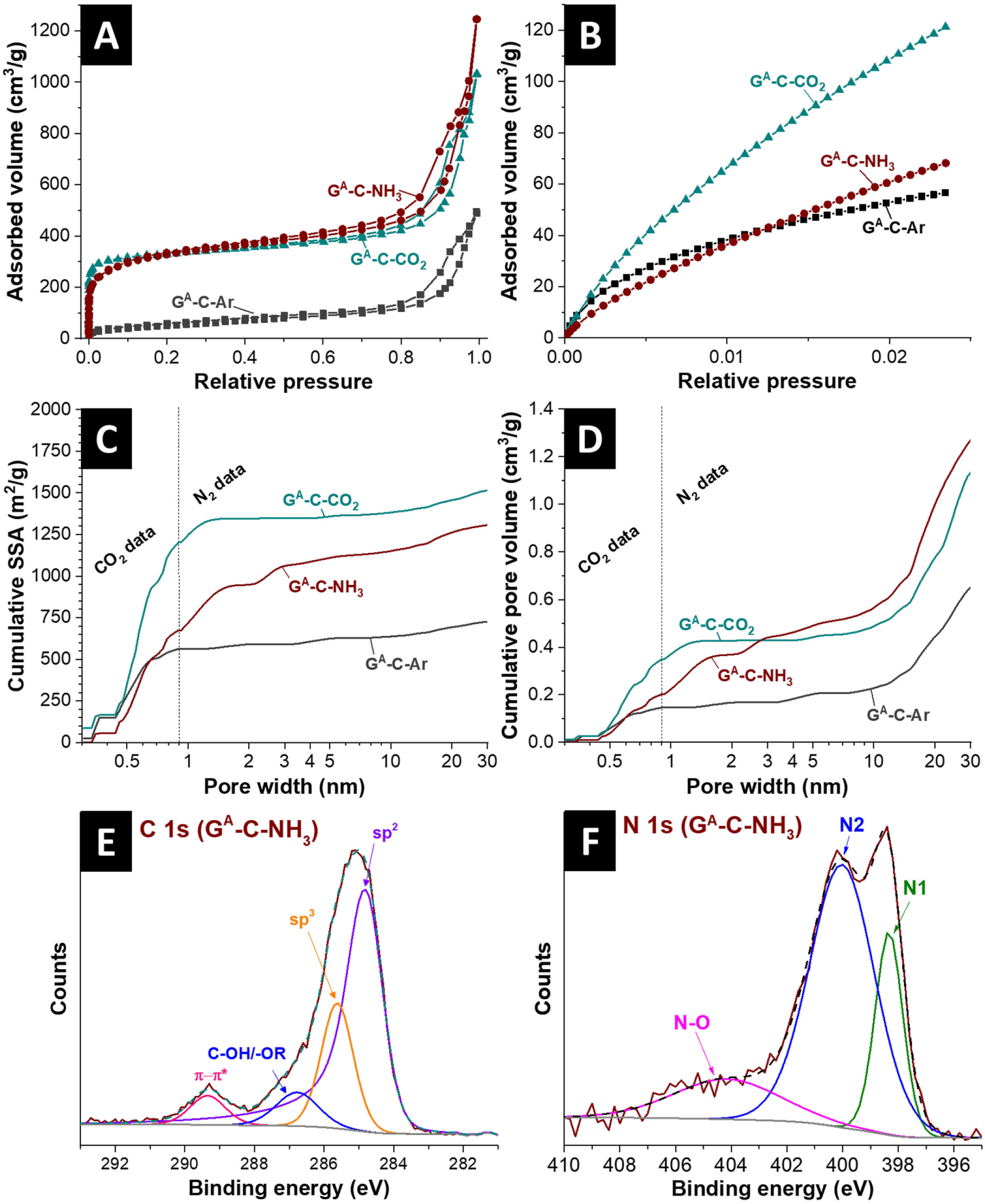

Figure 3. (A) Nitrogen and (B) carbon dioxide sorption isotherm with the combined pore size distribution of G^A-C-Ar, G^A-C-CO$_2$, and G^A-C-NH$_3$. (C) Cumulative SSA and (D) cumulative pore volume calculated with density functional theory kernels. (E) C 1s and (F) N 1s signal of the XPS measurements sample G^A-C-NH$_3$.

the pore size distribution up to 0.9 nm for all samples. For larger pores, we used data from the N_2 sorption isotherms and employed a QSDFT kernel. The resulting pore size distributions are shown in Figure 3C–D. The lowest SSA_{DFT} has G^A-C-Ar with 739 m^2/g, followed by G^A-C-NH_3 with 1328 m^2/g, and G^A-C-CO_2 with 1530 m^2/g. G^A-C-Ar also has the lowest pore volume of all materials with 0.78 cm^3/g and its average micropore size is 0.55 nm, while the mesopores have an average diameter of 21.2 nm. The micropore volume of G^A-C-CO_2 is the highest with 0.43 cm^3/g, and the total pore volume is 1.29 cm^3/g. The micropores of G^A-C-CO_2 are very small with an average value of 0.62 nm, while the mesopores are the largest in average with 22.7 nm. The activation with ammonia leads to a broader pore size distribution which results in a larger average micropore size of 0.80 nm and the largest total pore volume of all three materials with 1.49 cm^3/g.

The results of the elemental analysis (CHNOS) of the carbon materials are summarized in Table 2. G^A-C-Ar and G^A-C-CO_2 have a very similar chemical composition: both mainly contain carbon (94 mass%) and oxygen (4 mass%), with negligible amounts of hydrogen and nitrogen. The NH_3 activation introduced around 7 mass% nitrogen and increased the oxygen content to 9 mass%. The latter value is close to the composition of nitrogen-containing novolac-derived carbon beads which were produced under similar conditions in a previous study.[39]

We also quantified the chemical composition by XPS (Table 3). The high surface sensitivity of XPS indicates that the higher oxygen content of G^A-C-CO_2 aligns with the larger amount of oxygen-containing functional groups at the activated surface. G^A-C-NH_3 has a lower total amount of heteroatoms from XPS compared to the CHNS and O analyses, but a surplus of oxygen compared to nitrogen. The C 1s and N 1s spectra of G^A-C-NH_3 are plotted in Figure 3E–F. Deconvolution of the N 1s signal allows the identification of nitrogen-containing groups.[49–51] We assign around 22% to pyridinic groups with its typical binding energy of 398 eV (N1).[50,51] 60% of nitrogen groups have a binding energy of 400 eV with a broadened signal, typical for pyrrolic, amine, and amide groups.[51] Graphitic nitrogen groups have a binding energy of ~401 eV, and a minor fraction of these groups might be present as well.[50,51] A third kind of nitrogen group with a binding energy of 404 eV can be quantified with 18%, which relates to oxygen-bound nitrogen-like pyridine oxide.[51] The high amount of oxygen found in the chemical analysis aligns with this assumption. The absence of larger fractions graphitic nitrogen is in contrast to previous works where ammonia annealing was used to implement graphitic nitrogen groups in activated phenolic resins (novolac).[38,39]

To further analyze the carbon structure, we applied Raman spectroscopy (Figure 4B). The positions as well as the full-width at half-maximum (FWHM) of the D- and G-mode and the I_D/I_G-ratios are listed in Table 4. The G-mode of all three samples is at 1593–1605 cm^{-1}, and the I_D/I_G-ratio ranges from 1.53 to 1.89, indicative of nanocrystalline graphitic carbon.[52,53] The sample G^A-C-Ar shows broader peaks ($FWHM_D$: 155 cm^{-1} and $FWHM_G$: 76 cm^{-1}) due to a higher amount of amorphous carbon in the structure, which is in good agreement with TEM images seen in Figure 2.[54] The samples G^A-C-CO_2 and G^A-C-NH_3 show narrower peaks because the activation with carbon dioxide ($FWHM_D$: 135 cm^{-1} and $FWHM_G$: 70 cm^{-1}) and ammonia ($FWHM_D$: 124 cm^{-1} and $FWHM_G$: 61 cm^{-1}) prefers the removal of amorphous and less ordered carbon.[6,39]

Table 4. Peak characteristics of the D- and G-mode of the Raman spectra.

Sample		Position [cm^{-1}]	FWHM [cm^{-1}]	I_D/I_G
G^A-C-Ar	D-mode	1316	155	1.67
	G-mode	1593	76	
G^A-C-CO_2	D-mode	1324	135	1.53
	G-mode	1600	70	
G^A-C-NH_3	D-mode	1326	126	1.89
	G-mode	1605	61	

The incompletely graphitic structure of the gyroidal carbons was confirmed with XRD (Figure 4C). Only the X-ray reflections

Table 2. Elemental composition of chemical analysis and the TGA measurements of the carbon samples and the carbon/sulfur hybrids (n.d.: not detected).

Sample	CHNOS analysis C [mass%]	H [mass%]	N [mass%]	S [mass%]	O [mass%]	TGA S [mass%]
G^A-C-Ar	93.5 ± 0.3	1.4 ± 0.9	0.5 ± 0.1	n.d.	4.6 ± 0.2	–
G^A-C-CO_2	94.3 ± 0.8	1.1 ± 0.1	0.3 ± 0.1	n.d.	4.3 ± 1.0	–
G^A-C-NH_3	82.5 ± 0.1	1.8 ± 0.1	6.5 ± 0.1	n.d.	9.2 ± 0.1	–
G^A-C-Ar/S	29.0 ± 0.3	0.5 ± 0.1	0.2 ± 0.1	67.3 ± 0.8	3.0 ± 0.5	68.1
G^A-C-CO_2/S	29.1 ± 0.5	0.5 ± 0.3	0.2 ± 0.1	67.6 ± 0.5	2.7 ± 0.7	67.1
G^A-C-NH_3/S	25.8 ± 0.3	0.4 ± 0.1	2.0 ± 0.1	67.8 ± 0.6	4.1 ± 0.9	67.5

Table 3. Chemical composition of the NC-carbon samples measured with XPS (normalized to 100%) and bonding content of the N 1s peak (n.d.: not detectable).

Sample	C [mass%]	N [mass%]	O [mass%]	N1 at 398 eV [%]	N2 at 400 eV [%]	N–O at 404 eV [%]
G^A-C-Ar	93.3	n.d.	6.7	n.d.	n.d.	n.d.
G^A-C-CO_2	82.3	n.d.	17.7	n.d.	n.d.	n.d.
G^A-C-NH_3	86.0	5.0	9.0	21.6	60.3	18.1

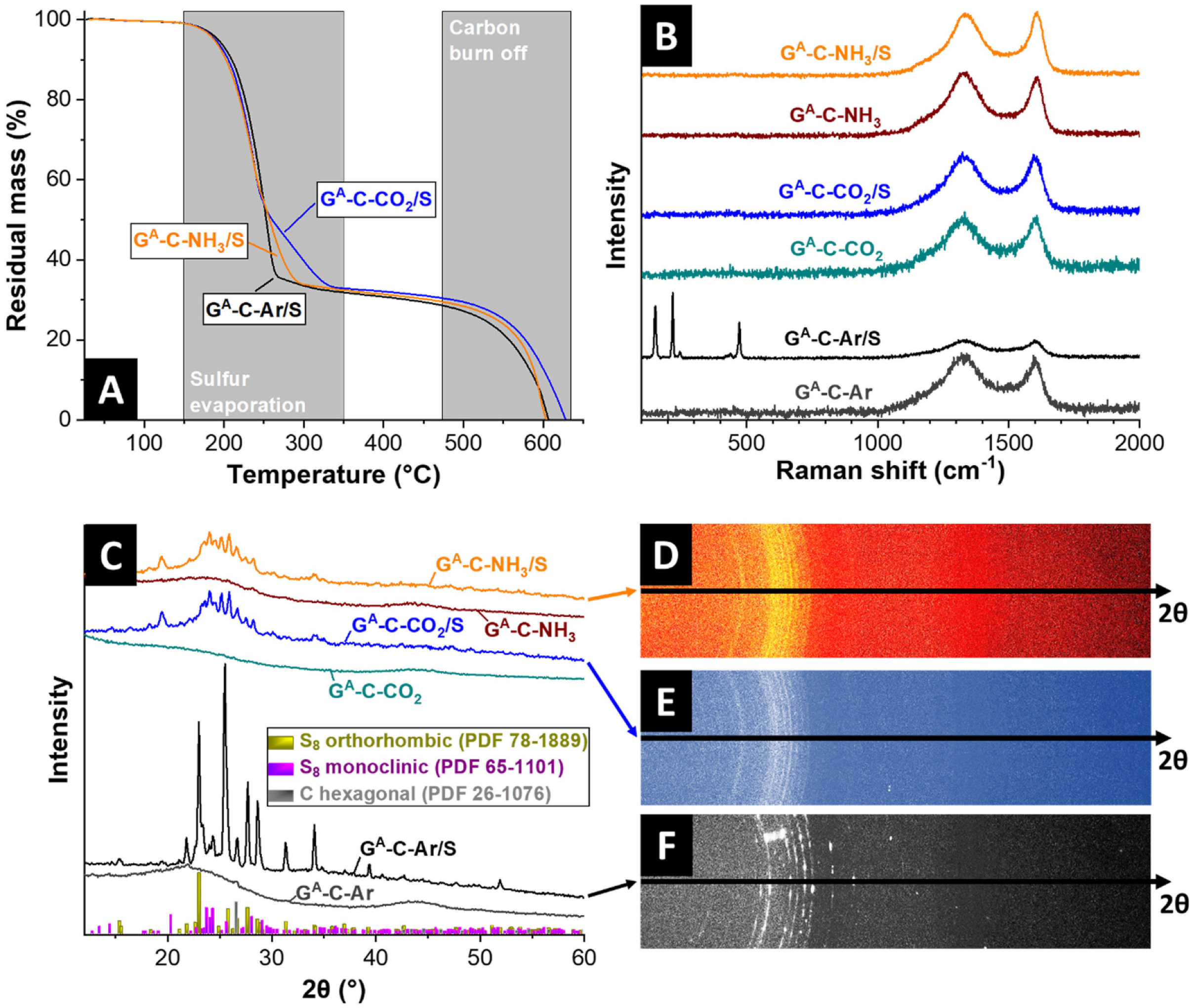

Figure 4. (A) Thermogravimetric analysis of the carbon/sulfur hybrids measured in synthetic air, (B) Raman spectra, and (C) XRD pattern of the carbon and the carbon/sulfur samples including the 2D XRD pattern (D–F).

of the (002) plane at 23° 2θ, and (110) plane at 44° 2θ of carbon can be observed for all samples.[53,55] The reflections of G^A-C-Ar are more intense than for the other two samples, even though the Raman spectra showed that all three materials have a similar carbon structure. This can be explained by the higher porosity of the CO_2 and NH_3 activated samples, which reduces the stacking of graphene layers and the overall signal strength.[53]

2.2. Characterization of the Carbon/Sulfur Hybrids

We choose melt infiltration to prepare the carbon/sulfur hybrid electrodes based on our previous experience with microporous carbons.[6] The TGA data in Figure 4A confirm an average sulfur content of 66.6 mass% by the mass loss due to the evaporation of the sulfur in the range from 200 °C to 350 °C. This sulfur loading was corroborated by the chemical analysis where the samples showed values of 67.3–67.8 mass% (Table 3). Based on these values, the amount of electrolyte was calculated, and the performance of the LiS-battery was normalized to the sulfur mass. The TGA data also give insights into the nanoconfinement of sulfur. The curve of G^A-C-Ar/S exhibits only one single step for the sulfur evaporation, while G^A-C-CO_2/S and G^A-C-NH_3/S data have a lower slope at higher temperatures (~275 °C). Sulfur confined in micropores evaporates at higher temperatures compared to bulk sulfur.[15] Since TGA measurements were carried out in synthetic air, the carbon burn-off is identical from 500 °C. Note that all samples achieve finally complete volatilization (i.e., 100 % mass loss), which confirms the absence of incombustible (inorganic) impurities in the samples.

The position and FWHM of the carbon-related D- and G-modes were not affected after sulfur infiltration since the temperature of 155 °C is too low to change the carbon structure (Figure 4B). The lower intensity of the carbon signal in G^A-C-Ar/S results from the high signal strength of crystalline sulfur below 500 cm^{-1}. The other two hierarchically porous samples have no observable sulfur signals, which indicates homogeneously confined sulfur inside the pores. The crystalline nature of sulfur was further investigated by XRD (Figure 4C–F). In all three carbon/sulfur samples, typical crystalline sulfur diffractions are obvious. While the sample G^A-C-Ar/S showed the presence of orthorhombic and monoclinic sulfur, the sulfur inside G^{A}-C-CO$_2$/S and G^{A}-C-NH$_3$/S is only monoclinic. Sulfur forms first a monoclinic phase when it solidifies which converts to an orthorhombic stricter later. The mesoporous confinement of the carbon hinders the formation of such an orthorhombic crystal structure, as it is the case for G^{A}-C-Ar/S where sulfur is additionally located outside the mesopores. The sample G^{A}-C-Ar/S has also sulfur which is not confined to the mesopores which can faster convert to orthorhombic sulfur. Using the Scherrer equation, it is possible to estimate the average domain size of the sulfur crystals.[56] The orthorhombic sulfur in the sample G^{A}-C-Ar/S shows no peak broadening beyond from finite domain sizes; therefore, these crystals must be larger than 100–200 nm and cannot completely fit into the gyroidal structure. The presence of large sulfur crystals is confirmed from the spotted Debye rings seen in the 2D diffraction pattern (Figure 4F). The average domain size of the sulfur in G^{A}-C-CO$_2$/S and G^{A}-C-NH$_3$/S is approximately 60 nm, which is larger than the pore diameter of around 20 nm. Therefore, sulfur crystals are predominating growing among the mesopores. Besides the sulfur peaks from G^{A}-C-CO$_2$/S and G^{A}-C-NH$_3$/S, we observed also a broad amorphous peak, which can only partly be related to non-graphitic carbon. These large reflections occur due to sulfur within the micropores, unable to grow to large crystals due to the confinement.[6] By having a look at the 2D diffraction pattern of G^{A}-C-CO$_2$/S and G^{A}-C-NH$_3$/S, we see complete Debye rings of the sulfur phase, which indicates a very homogeneous distribution of the sulfur in the carbon pores.

The distribution of the elements was visualized by a TEM-EDX mapping (Figure 5). G^{A}-C-Ar/S shows an overlapping of the carbon and sulfur mapping in the entire analyzed area, but the intensity of carbon and sulfur is different at certain locations (Figure 5). This inhomogeneous intensity distribution indicates that the sulfur is not filling the pores completely and is also found on the external surface in large amounts. External sulfur aligns also with the large sulfur domain sizes calculated from XRD. The samples G^{A}-C-CO$_2$/S and G^{A}-C-NH$_3$/S show a very homogeneous carbon and sulfur distribution, supporting the XRD data and the conclusion of sulfur confinement within the pores.

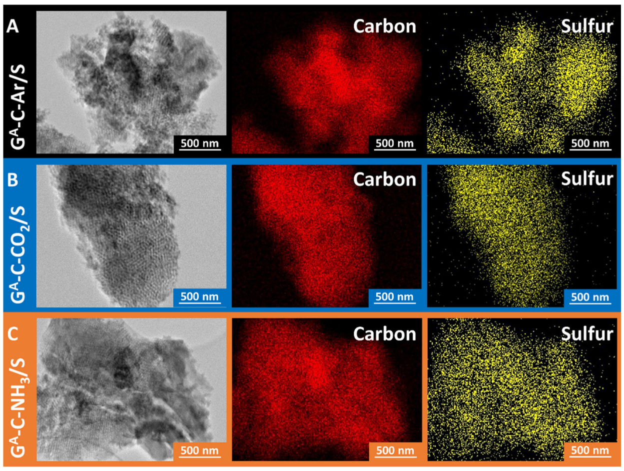

Figure 5. TEM images of the samples (A) G^{A}-C-Ar/S, (B) G^{A}-C-CO$_2$/S, and (C) G^{A}-C-NH$_3$/S including EDX mapping of carbon and sulfur.

2.3. Electrochemical Characterization

The carbon/sulfur hybrids were tested as LiS-battery cathodes at low C-rates (0.1C discharge, 0.2C charge). The discharge capacity and the Coulombic efficiency of these measurements with the voltage profile of selected cycles are plotted in Figure 6. Initially, G^{A}-C-Ar/S shows a high capacity of more than 700 mAh/g$_{sulfur}$ for the first few cycles, followed by a rapid decrease, and reaching 151 mAh/g$_{sulfur}$ after 100 cycles. Since sulfur was incompletely filling the micro- and mesopores, it is likely that polysulfides are easily dissolved in the electrolyte, which results in stronger sulfur shuttling. It is also likely that the electron transfer from the carbon towards the sulfur is hindered, due to the low accessible surface area. We also see distinct features in the measured voltage profile shown in Figure 6B. Usually, two plateaus are expected for LiS-batteries during discharge in the range of 2.3-2.4 V and at ~2.1 V vs. Li/Li^{+} (as was seen for G^{A}-C-CO$_2$/S, Figure 6C). The first plateau at 2.3-2.4 V occurs from the reduction of elemental sulfur to large Li-polysulfides (Li$_2$S$_{4\text{-}8}$).[57,58] The second plateau is related to the further reduction to small Li-polysulfides (Li$_2$S$_2$ and Li$_2$S).[57,58] The voltage profile of the sample G^{A}-C-Ar/S shows a first plateau in the range of 2.2-2.3 V vs. Li/Li^{+}, then a decrease to almost 1.8 V vs. Li/Li^{+} which indicates the formation of small polysulfides, followed by a potential increase. During the discharge of the cell, the potential is increasing again and reaches around 2.1 V vs. Li/Li^{+}, which is characteristic for the reaction of larger polysulfides. Sulfur, which is not confined to the carbon pores, is expected to react completely before the sulfur within the pores becomes accessible. This is well visible for G^{A}-C-Ar/S, where the sulfur is not homogeneously distributed because the mesopores cannot accommodate the large sulfur content. This finding is supported by XRD result, where the orthorhombic structure indicates the formation of much larger crystals, which do not fit inside the pores. From a practical application point of view, however, such high sulfur mass loadings are desirable.[2] Sulfur inside the porous carbon is most probably only accessible for the electrolyte when the sulfur on the outside of the particles has been dissolved. The larger polysulfides then increase the potential in the voltage profile by reacting to smaller units. This behavior is reduced when the LiS cell is running for a larger number of cycles because more pathways are generated, and a lower capacity is obtained due to polysulfide shuttling.

The G^{A}-C-CO$_2$/S samples show typical LiS-battery voltage profiles with the two plateaus for the reduction of sulfur towards Li$_2$S for all cycles (Figure 6). The initial specific capacity of 1098 mAh/g$_{sulfur}$ remains above 800 mAh/g$_{sulfur}$ after 50 cycles and above 700 mAh/g$_{sulfur}$ after 100 cycles measured with a C-rate of 0.1C for the discharging and 0.2C for the charging step.

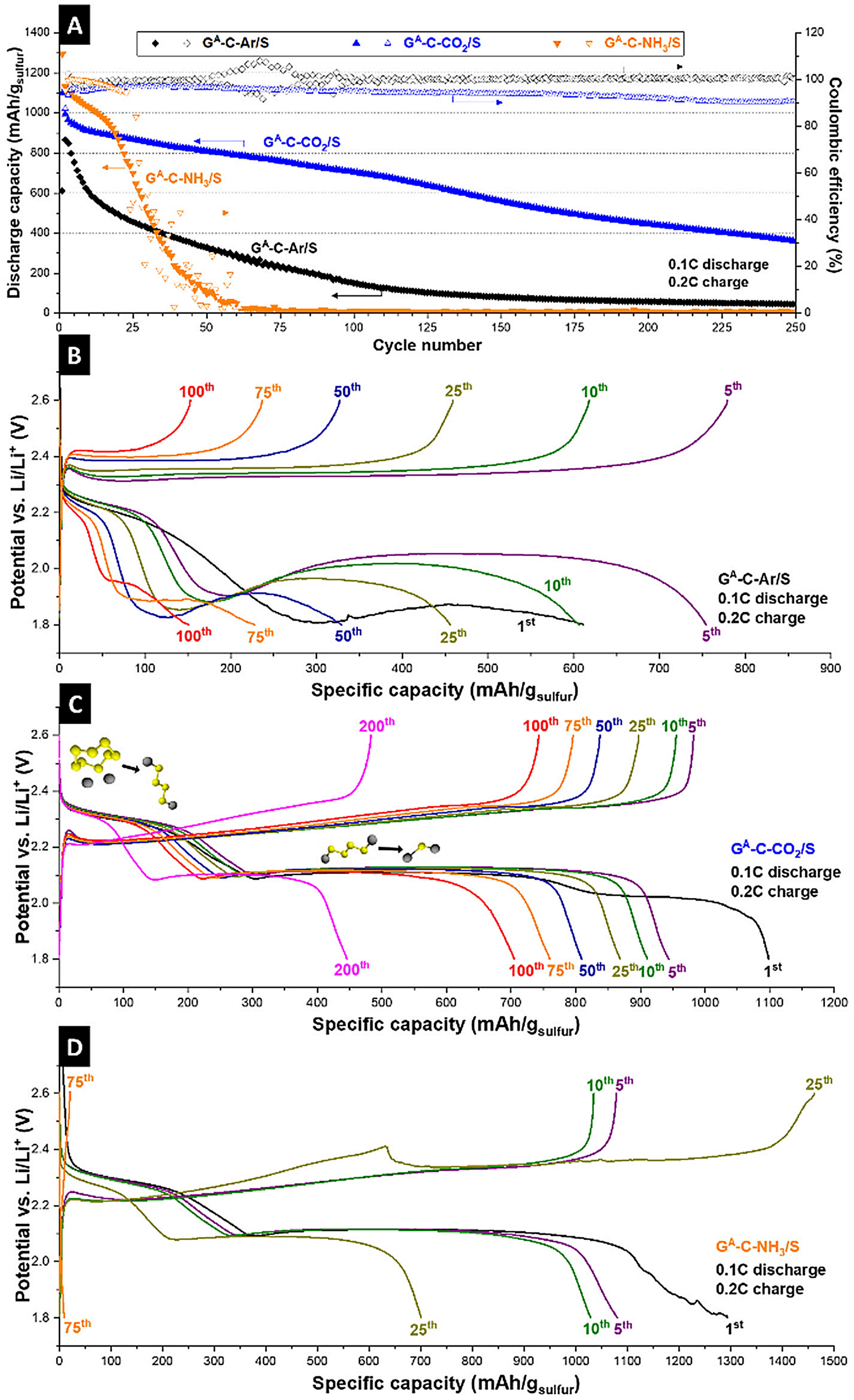

Figure 6. (A) Electrochemical performance of the LiS-batteries at low C-rates (0.1C discharge and 0.2C charge) and (B–D) corresponding voltage profiles of selected cycles.

After 100 cycles, the capacity fade increases and a specific capacity of about 450 mAh/g_{sulfur} is reached after 200 cycles.

G^A-C-NH_3/S shows among all samples the highest initial specific capacity of about 1300 mAh/g_{sulfur}, corresponding to 78 % of the theoretical specific capacity (Figure 6D). After 10 cycles, the capacity is still above 1000 mAh/g_{sulfur}, which is higher than the capacity for G^A-C-CO_2/S. After the 20th cycle, capacity and Coulombic efficiency decreases significantly. The voltage profile for the 25th charging cycle in Figure 6D shows a large plateau at 2.3-2.4 V vs. Li/Li^+. This region shows a large energy consumption and we assume the decomposition of nitrogen groups.

The discharge specific capacity after 50 cycles is 100 mAh/g_{sulfur} and only ~10 mAh/g_{sulfur} after 75 cycles. Seemingly, nitrogen groups enable a higher specific capacity initially because of the affinity of sulfur towards the carbon surface in good agreement with previous works.[23,25,26,61] Yet, this performance cannot be maintained for a large number of cycles. It is likely that degradation of nitrogen- and oxygen-containing functional groups (mainly pyrrolic, amine, and amide groups) causes the poor long-time electrochemical performance. Other studies which propose that nitrogen groups enhance the electrochemical performance of LiS-batteries often have graphitic or pyridinic nitrogen and only low amount of amorphous carbon in contrast to our mainly non-graphitic carbon host.[23,25,62–64] These features might be crucial for nitrogen-doped carbon materials for LiS-batteries.

To have better understanding on the performance stability, we carried out post-mortem XPS, TEM, and EDX mapping measurements of the cathode after the long-time stability test at low C-rates. The XPS spectra (Supporting Information, Figure S4) show that a solid electrolyte interphase (SEI) was formed. The binding energies of the C1s, N1s, F1s, Li1s, and O1s in Figure S4 fit the energies found in the literature for SEI components like LiTFSI, Li_2CO_3, or polysulfides.[59,60] The TEM images (Figure S5) show that the gyroidal structure was maintained after the electrochemical measurements. A TEM-EDX mapping was conducted (Figure S6), which shows that carbon, sulfur, nitrogen, and oxygen remain well distributed in the sample. The measured nitrogen is not only related to nitrogen functional groups but also to the SEI which contains decomposed products of the electrolyte.

An overview of the LiS-performance data normalized to the mass of sulfur and the whole electrode mass with values from the literature is given in Table 5. We choose only carbon/sulfur materials which were produced with similar synthesis conditions (melt infiltration) and measured under comparable conditions (e.g., same electrolyte and similar potential window). Other sulfur infiltration methods like the in-situ formation from $Na_2S_2O_3$ also show high specific capacities of >1300 mAh/g_{sulfur} for the first cycle with a quite stable performance.[65] The carbon host can only be compared when the same infiltration method is used because it has a significant influence on the performance.[6,66] Another approach to producing stable LiS-batteries can be achieved by C/Li_2S-hybrids instead C/S-hybrids.[67] Such system can reach a specific capacity of >1100 mAh/g_{sulfur} (~800 mAh/g_{sulfur} after 100 cycles with a sulfur loading of ~61 mass%).[67] The comparison of different C/S-hybrid cathode materials measured at similar conditions in Table 5 shows improved performance for the activated gyroidal carbons. The gyroidal carbon materials used by Werner et al. show higher stability normalized to the amount of sulfur (810 mAh/g_{sulfur} after 100 cycles), but this study used a low carbon to sulfur ratio of only 1:1.[2,17] Even though the sulfur content was relatively low, a relatively high specific capacity normalized to the electrode of 365 mAh/$g_{electrode}$ after 100 cycles was reported,[17] which is lower compared to G^A-C-CO_2/S after 100 cycles (387 mAh/g). The high electrode normalized specific capacity of Werner et al. was reached because they were not using additional conductive additives for the low C-rate measurements even though the sulfur content was relatively low.[17] Nevertheless, conductive additives are necessary to reach high C-rates and to enhance the overall performance.[68] The gyroidal-templated carbon material from Choudhury et al. has a relatively low electrode normalized specific capacity of 236 mAh/$g_{electrode}$ after 100 cycles.[18] Other comparable microporous and mesoporous materials from the literature show after 100 cycles a lower specific capacity than the G^A-C-CO_2/S

Table 5. Specific discharge capacity of all three hybrid electrodes after 1, 5, and 100 cycles at low discharge/charge rates with a comparison of other carbon materials for LiS-batteries from the literature.[a]

Electrode material	Porosity type	SSA_{BET} [m^2/g]	Potential vs. Li/Li^+ [V]	Specific capacity [mAh/g][b]						Ref.
				1st cycle		5th cycle		100th cycle		
				per sulfur	per electrode	per sulfur	per electrode	per sulfur	per electrode	
G^A-C-Ar/S	mesoporous	197	1.8–2.6	611	336	754	414	151	83	this work
G^A-C-CO_2/S	micro- & mesoporous	1264	1.8–2.6	1098	603	944	519	704	387	this work
G^A-C-NH_3/S	micro- & mesoporous	1191	1.8–2.6	1294	711	1080	593	9	5	this work
G^AMC-15-900 °C	mesoporous	600	1.5–2.8	1392	626	1070	482	728	328	[17]
aG^DMC-15-CO_2-10 h	micro- & mesoporous	2030	1.5–2.8	1700	765	1130	509	810	365	[17]
Gyroid-templated-C	micro- & mesoporous	885	1.8–2.6	580	319	590	324	430	236	[18]
PNC-S-annealed	microporous	529	1.8–2.6	1063	601	661	374	560	317	[6]
PNC_{act}-S-annealed	microporous	2700	1.8–2.6	1159	656	662	375	604	342	[6]
OLC-S-1	mesoporous	400	1.8–2.6	950	530	730	407	670	374	[66]
Carbon aerogel	micro- & mesoporous	1395	1.8–2.8	910	364	800	320	600	240	[71]
BCP templated carbon	micro- & mesoporous	630	1.8–2.6	1050	568	800	433	530	287	[72]
Kroll-C/S_53	micro- & mesoporous	1990	1.8–2.6	1089	577	~1000	530	817 (80th cycle)	433 (80th cycle)	[9]

[a] The specific capacity is normalized to the mass of sulfur and to the mass of the whole electrode. [b] Discharge: 0.1C; charge: 0.2C

material; the latter had a capacity of 704 mAh/g_{sulfur}, which corresponds to 387 mAh/$g_{electrode}$ (cycled at 0.1C for discharging and 0.2C for charging).

The performance of the gyroidal carbon materials was also investigated at higher charge and discharge rates (Figure 7).

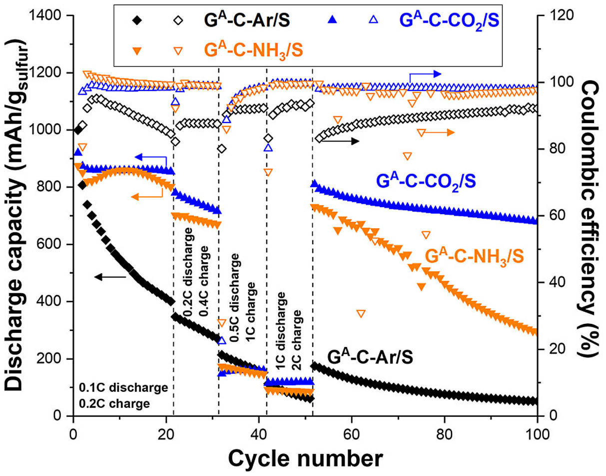

Figure 7. Electrochemical performance of G^A-C-Ar/S, G^A-C-CO_2/S, and G^A-C-NH_3/S at different rates.

The sample G^A-C-Ar/S does provide stable performance, yet only a small effect of scan rates is seen for the specific capacity. The specific capacity of G^A-C-NH_3/S and G^A-C-CO_2/S slightly reduces at 0.2C (discharge) and 0.4C (charge), but there is a large performance drop below 200 mAh/g_{sulfur} at higher C-rates. It is likely that the crystalline sulfur within the mesopores hinders the intrapore mass transport. At low rates, this issue is not a limiting factor because the system is given sufficient time for sulfide dissolution. At high rates, the sulfur in the mesopores cannot be fully capitalized on; therefore, activated and non-activated materials show a similar performance. By reducing the C-rate again to the initial charge/discharge rate, the high specific capacity with a stable performance is restored, especially for G^A-C-CO_2/S.

Electrochemical impedance spectroscopy of the initial cells at 2.6 V vs. Li/Li^+ was carried out, and the Nyquist plot is shown in the Supporting Information, Figure S3. The Ohmic resistance (R_0) is influenced by the electrolyte resistance, the current collector, and the cell design and all material showed a very similar value for R_0.[69,70] This relates to the use of the same setup and cell design for all measurements. The charge transfer resistance (R_{ct}) in the medium-to-high-frequency range correlates to the electrochemical kinetics and is also similar for all three hybrid cathode materials.[69,70] The R_{ct} for G^A-C-CO_2/S is slightly smaller compared to the value of G^A-C-Ar/S and G^A-C-NH_3/S which is in line with the similar performance at high C-rates (1C discharge and 2C charge), where G^A-C-CO_2/S also performs better.

3. Conclusions

In this study, we prepared ordered porous carbons by co-assembly of a commercial resol with an ISO block copolymer. The latter was pyrolyzed and in-situ activated in different atmospheres, namely Ar, CO_2, or NH_3. All samples had micro- and mesopores, with the smallest volume of micropores and smallest total pore volume after treatment just in argon (G^A-C-Ar; non-activated sample). Larger pore volumes were obtained after activation with CO_2 (G^A-C-CO_2) or NH_3 (G^A-C-NH_3). We hybridized all samples with sulfur using melt infiltration to test the resulting materials as cathodes for LiS-batteries. The pore structure of the non-activated sample was not suitable to achieve a homogeneous phase distribution. The ammonia activation increased microporosity and formed nitrogen functionalities, identified by XPS as pyridinic, pyrrolic, amine, and amide groups. These groups lead to a superior initial capacity (~1300 mAh/g_{sulfur} in the 1st cycle), but simultaneously drastically reducing the long-term stability. The activation with CO_2 did not change the chemical composition much compared to the non-activated argon sample but enhanced the total pore volume and the microporosity. Thereby, it was possible to obtain a homogeneous carbon/sulfur hybrid by melt infiltration. This cathode material showed a slightly lower initial capacity of 1100 mAh/g_{sulfur}, but rather stable performance with a specific capacity of more than 700 mAh/g_{sulfur} after 100 cycles. While NH_3 treatment did introduce nitrogen to our samples, it failed to generate graphitic nitrogen. Thereby, we see a severe drop in performance and poor cycling stability of the sample G^A-C-NH_3. Obviously, the pore structure is of high importance for the performance of LiS-batteries. We also see that nitrogen-doping may enhance the initial capacity, but there may be a poor performance stability depending on the type of nitrogen.

Acknowledgements

This project was supported by the INM FOCUS project funding (POLION). J.S. and J.J. acknowledge support by the Center for Materials Research at JLU Gießen. The authors kindly acknowledge the continuing support of Eduard Arzt (INM). We thank Ralph Schäfer from Allnex Germany GmbH for the supply of Phenodur, Andrea Jung (INM) for the CHNS and O analysis, and Peng Zhang (INM) for the SAXS measurements. We also acknowledge the help from Ingrid Grobelsek (INM) regarding the XRD analysis, we thank Nicolas Jäckel (INM) for discussions, and we are grateful to Lars Borchardt (TU Dresden) for support and discussions.

Conflict of Interest

The authors declare no conflict of interest.

Keywords: activation · carbon · energy storage · lithium-sulfur battery · self-assembly

[1] M. Wild, L. O'Neill, T. Zhang, R. Purkayastha, G. Minton, M. Marinescu, G. Offer, *Energy Environ. Sci.* **2015**, *8*, 3477–3494.
[2] L. Borchardt, M. Oschatz, S. Kaskel, *Chem. – Eur. J.* **2016**, *22*, 7324–7351.
[3] S. Pelletier, O. Jabali, G. Laporte, M. Veneroni, *Trans. Res. Part B: Method.* **2017**, *103*, 158–187.
[4] L. Medenbach, P. Adelhelm, *Top. Curr. Chem.* **2017**, *375*, 81.
[5] Z. Li, X. Li, Y. Liao, X. Li, W. Li, *J. Power Sources* **2016**, *334*, 23–30.
[6] S. Choudhury, B. Krüner, P. Massuti-Ballester, A. Tolosa, C. Prehal, I. Grobelsek, O. Paris, L. Borchardt, V. Presser, *J. Power Sources* **2017**, *357*, 198–208.
[7] X. Ji, K. T. Lee, L. F. Nazar, *Nat. Mater.* **2009**, *8*, 500–506.
[8] J. Song, T. Xu, M. L. Gordin, P. Zhu, D. Lv, Y. B. Jiang, Y. Chen, Y. Duan, D. Wang, *Adv. Funct. Mater.* **2014**, *24*, 1243–1250.
[9] M. Oschatz, S. Thieme, L. Borchardt, M. R. Lohe, T. Biemelt, J. Brückner, H. Althues, S. Kaskel, *Chem. Commun.* **2013**, *49*, 5832–5834.
[10] A. Schneider, C. Suchomski, H. Sommer, J. Janek, T. Brezesinski, *J. Mater. Chem. A* **2015**, *3*, 20482–20486.
[11] G. Xu, B. Ding, P. Nie, L. Shen, H. Dou, X. Zhang, *ACS Appl. Mater. Interfaces* **2013**, *6*, 194–199.
[12] J.-J. Kim, H. S. Kim, J. Ahn, K. J. Lee, W. C. Yoo, Y.-E. Sung, *J. Power Sources* **2016**, *306*, 617–622.
[13] C. Reitz, B. Breitung, A. Schneider, D. Wang, M. von der Lehr, T. Leichtweiss, J. r. Janek, H. Hahn, T. Brezesinski, *ACS Appl. Mater. Interfaces* **2016**, *8*, 10274–10282.
[14] T. Wang, K. Kretschmer, S. Choi, H. Pang, H. Xue, G. Wang, *Small Methods.* **2017**, *1*, 1700089.
[15] C. Fu, B. M. Wong, K. N. Bozhilov, J. Guo, *Chem. Sci.* **2016**, *7*, 1224–1232.
[16] A. Schneider, J. Janek, T. Brezesinski, *Phys. Chem. Chem. Phys.* **2017**, *19*, 8349–8355.
[17] J. r. G. Werner, S. S. Johnson, V. Vijay, U. Wiesner, *Chem. Mater.* **2015**, *27*, 3349–3357.
[18] S. Choudhury, M. Agrawal, P. Formanek, D. Jehnichen, D. Fischer, B. Krause, V. Albrecht, M. Stamm, L. Ionov, *ACS Nano.* **2015**, *9*, 6147–6157.
[19] J. r. G. Werner, T. N. Hoheisel, U. Wiesner, *ACS Nano.* **2013**, *8*, 731–743.
[20] J. Song, M. L. Gordin, T. Xu, S. Chen, Z. Yu, H. Sohn, J. Lu, Y. Ren, Y. Duan, D. Wang, *Angew. Chem. Int. Ed.* **2015**, *54*, 4325–4329.
[21] C. Wang, K. Su, W. Wan, H. Guo, H. Zhou, J. Chen, X. Zhang, Y. Huang, *J. Mater. Chem. A* **2014**, *2*, 5018–5023.
[22] F. Sun, J. Wang, H. Chen, W. Li, W. Qiao, D. Long, L. Ling, *ACS Appl. Mater. Interfaces* **2013**, *5*, 5630–5638.
[23] S. Niu, G. Zhou, W. Lv, H. Shi, C. Luo, Y. He, B. Li, Q.-H. Yang, F. Kang, *Carbon.* **2016**, *109*, 1–6.
[24] F. Hippauf, W. Nickel, G. P. Hao, K. Schwedtmann, L. Giebeler, S. Oswald, L. Borchardt, S. Doerfler, J. J. Weigand, S. Kaskel, *Adv. Mater. Interfaces* **2016**, *3*, 1600508.
[25] X. G. Sun, X. Wang, R. T. Mayes, S. Dai, *ChemSusChem.* **2012**, *5*, 2079–2085.
[26] X. Wang, Z. Zhang, Y. Qu, Y. Lai, J. Li, *J. Power Sources* **2014**, *256*, 361–368.
[27] W. Shen, W. Fan, *J. Mater. Chem. A* **2013**, *1*, 999–1013.
[28] Z. Liu, K. Xiao, H. Guo, X. Ning, A. Hu, Q. Tang, B. Fan, Y. Zhu, X. Chen, *Carbon.* **2017**, *117*, 163–173.
[29] N. A. Travlou, T. J. Bandosz, *Carbon.* **2017**, *117*, 228–239.
[30] Y. Wu, S. Fang, Y. Jiang, *J. Mater. Chem.* **1998**, *8*, 2223–2227.
[31] Z. Wang, L. Sun, F. Xu, X. Peng, Y. Zou, H. Chu, L. Ouyang, M. Zhu, *RSC Adv.* **2016**, *6*, 1422–1427.
[32] L.-F. Chen, X.-D. Zhang, H.-W. Liang, M. Kong, Q.-F. Guan, P. Chen, Z.-Y. Wu, S.-H. Yu, *ACS Nano.* **2012**, *6*, 7092–7102.
[33] X. Liu, Y. Zhou, W. Zhou, L. Li, S. Huang, S. Chen, *Nanoscale.* **2015**, *7*, 6136–6142.
[34] C. L. Mangun, K. R. Benak, J. Economy, K. L. Foster, *Carbon.* **2001**, *39*, 1809–1820.
[35] B. Stöhr, H. Boehm, R. Schlögl, *Carbon.* **1991**, *29*, 707–720.
[36] J. S. Noh, J. A. Schwarz, *Carbon.* **1990**, *28*, 675–682.
[37] M. Widmaier, B. Krüner, N. Jäckel, M. Aslan, S. Fleischmann, C. Engel, V. Presser, *J. Electrochem. Soc.* **2016**, *163*, A2956–A2964.
[38] X. Wang, C.-G. Liu, D. Neff, P. F. Fulvio, R. T. Mayes, A. Zhamu, Q. Fang, G. Chen, H. M. Meyer, B. Z. Jang, *J. Mater. Chem. A* **2013**, *1*, 7920–7926.
[39] B. Krüner, A. Schreiber, A. Tolosa, A. Quade, F. Badaczewski, T. Pfaff, B. M. Smarsly, V. Presser, *Carbon.* **2018**, *132*, 220–231.
[40] M. A. Hillmyer, F. S. Bates, *Macromolecules.* **1996**, *29*, 6994–7002.
[41] J. Chatterjee, S. Jain, F. S. Bates, *Macromolecules.* **2007**, *40*, 2882–2896.
[42] V. Presser, J. McDonough, S.-H. Yeon, Y. Gogotsi, *Energy Environ. Sci.* **2011**, *4*, 3059–3066.
[43] A. Vishnyakov, P. I. Ravikovitch, A. V. Neimark, *Langmuir.* **1999**, *15*, 8736–8742.
[44] G. Y. Gor, M. Thommes, K. A. Cychosz, A. V. Neimark, *Carbon.* **2012**, *50*, 1583–1590.
[45] S. Brunauer, P. H. Emmett, E. Teller, *J. Amer. Chem. Soc.* **1938**, *60*, 309–319.
[46] S. S. Zhang, *Energies.* **2012**, *5*, 5190–5197.
[47] T. H. Epps, E. W. Cochran, C. M. Hardy, T. S. Bailey, R. S. Waletzko, F. S. Bates, *Macromolecules.* **2004**, *37*, 7085–7088.
[48] M. Thommes, K. Kaneko, A. V. Neimark, J. P. Olivier, F. Rodriguez-Reinoso, J. Rouquerol, K. S. Sing, *Pure Appl. Chem.* **2015**, *87*, 1051–1069.
[49] J.-P. Boudou, P. Parent, F. Suarez-Garcia, S. Villar-Rodil, A. Martínez-Alonso, J. Tascón, *Carbon.* **2006**, *44*, 2452–2462.
[50] R. Arrigo, M. Hävecker, R. Schlögl, D. S. Su, *Chem. Commun.* **2008**, 4891–4893.
[51] Y. Zhao, X. Liu, Y. Han, *RSC Adv.* **2015**, *5*, 30310–30330.
[52] A. C. Ferrari, J. Robertson, *Phys. Rev. B* **2000**, *61*, 14095.
[53] K. Faber, F. Badaczewski, M. Oschatz, G. Mondin, W. Nickel, S. Kaskel, B. M. Smarsly, *J. Phys. Chem. C* **2014**, *118*, 15705–15715.
[54] P. K. Chu, L. Li, *Mater. Chem. Phys.* **2006**, *96*, 253–277.
[55] P. Debye, P. Scherrer, *Nachrichten von der Gesellschaft der Wissenschaften zu Göttingen, Mathematisch-Physikalische Klasse* **1917**, *1917*, 180–188.
[56] P. Scherrer, *Nachrichten von der Gesellschaft der Wissenschaften zu Göttingen* **1918**, *2*, 98–100.
[57] J. Kulisch, H. Sommer, T. Brezesinski, J. Janek, *Phys. Chem. Chem. Phys.* **2014**, *16*, 18765–18771.
[58] N. Jayaprakash, J. Shen, S. S. Moganty, A. Corona, L. A. Archer, *Angew. Chem.* **2011**, *123*, 6026–6030.
[59] E. Markevich, G. Salitra, A. Rosenman, Y. Talyosef, F. Chesneau, D. Aurbach, *J. Mater. Chem. A* **2015**, *3*, 19873–19883.
[60] H. Metelmann, Justus-Liebig-Universität Gießen, **2017**.
[61] Y. Qiu, W. Li, W. Zhao, G. Li, Y. Hou, M. Liu, L. Zhou, F. Ye, H. Li, Z. Wei, *Nano Lett.* **2014**, *14*, 4821–4827.
[62] L. Chen, Y. Liu, M. Ashuri, C. Liu, L. L. Shaw, *J. Mater. Chem. A* **2014**, *2*, 18026–18032.
[63] Q. Li, Z. Zhang, Z. Guo, Y. Lai, K. Zhang, J. Li, *Carbon.* **2014**, *78*, 1–9.
[64] G. Zhou, Y. Zhao, A. Manthiram, *Adv. Energy Mater.* **2015**, *5*, 1402263.
[65] B. Papandrea, X. Xu, Y. Xu, C.-Y. Chen, Z. Lin, G. Wang, Y. Luo, M. Liu, Y. Huang, L. Mai, X. Duan, *Nano Res.* **2016**, *9*, 240–248.
[66] S. Choudhury, M. Zeiger, P. Massuti-Ballester, S. Fleischmann, P. Formanek, L. Borchardt, V. Presser, *Sustainable Energy & Fuels.* **2017**, *1*, 84–94.
[67] G. Tan, R. Xu, Z. Xing, Y. Yuan, J. Lu, J. Wen, C. Liu, L. Ma, C. Zhan, Q. Liu, T. Wu, Z. Jian, R. Shahbazian-Yassar, Y. Ren, D. J. Miller, L. A. Curtiss, X. Ji, K. Amine, *Nat. Energy* **2017**, *2*, 17090.
[68] A. Jozwiuk, H. Sommer, J. Janek, T. Brezesinski, *J. Power Sources* **2015**, *296*, 454–461.
[69] N. A. Cañas, K. Hirose, B. Pascucci, N. Wagner, K. A. Friedrich, R. Hiesgen, *Electrochim. Acta* **2013**, *97*, 42–51.
[70] J. Zhang, Y. Shi, Y. Ding, L. Peng, W. Zhang, G. Yu, *Adv. Energy Mater.* **2017**, *7*, 1602876.
[71] K. Balakumar, N. Kalaiselvi, *RSC Adv.* **2015**, *5*, 34008–34018.
[72] S. Choudhury, D. Fischer, P. Formanek, M. Stamm, L. Ionov, *Adv. Mater. Interfaces* **2018**, *5*, 1701116.

Manuscript received: February 23, 2018
Version of record online: April 26, 2018

Supporting Information

Gyroidal porous carbon activated with NH_3 or CO_2 as lithium-sulfur battery cathodes

Benjamin Krüner,[1,2] Tobias S. Dörr,[1,2] Hwirim Shim,[1,2]
Joachim Sann,[3] Jürgen Janek,[3] Volker Presser[1,2,*]

[1] *INM - Leibniz Institute for New Materials, 66123 Saarbrücken, Germany*

[2] *Department of Materials Science and Engineering, Saarland University, 66123 Saarbrücken, Germany*

[3] *Institute of Physical Chemistry & Center for Materials Research, Justus-Liebig University Giessen, 35392 Giessen, Germany*

* *Corresponding author's eMail: volker.presser@leibniz-inm.de*

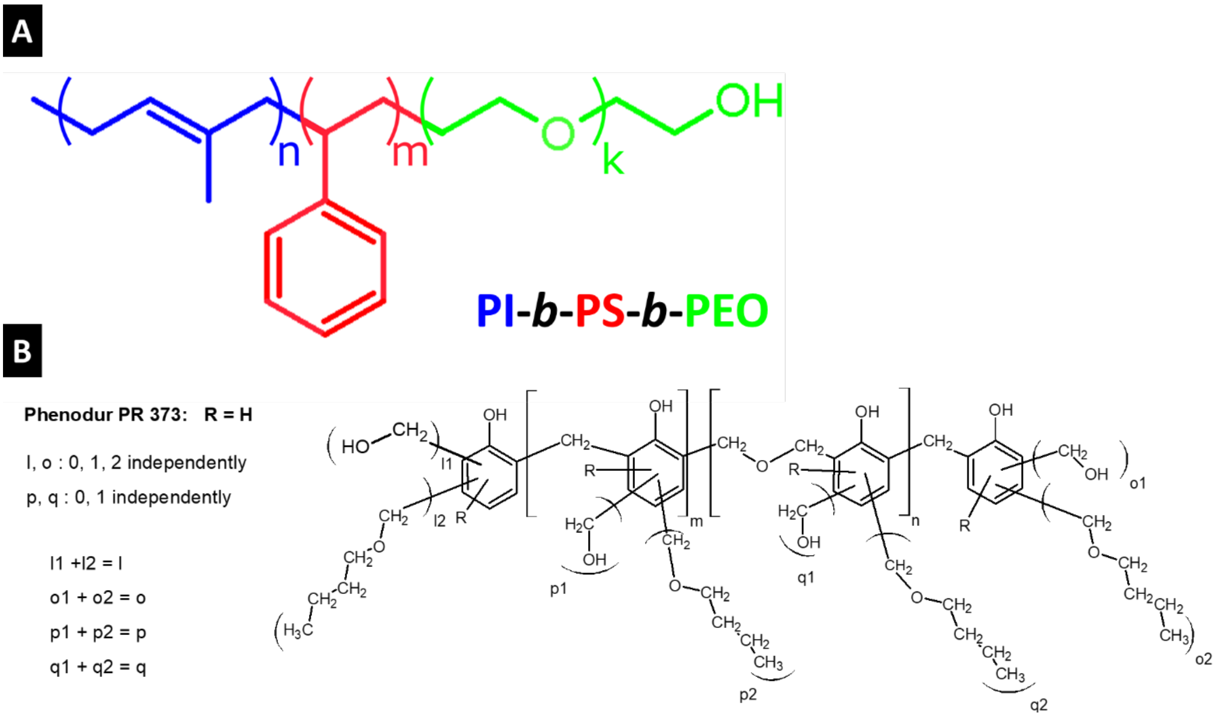

Figure S1: Structural formula of (A) the triblock terpolymer poly(isoprene)-block-poly(styrene)-block-poly(ethylene oxide) (ISO) and (B) the commercial resol.

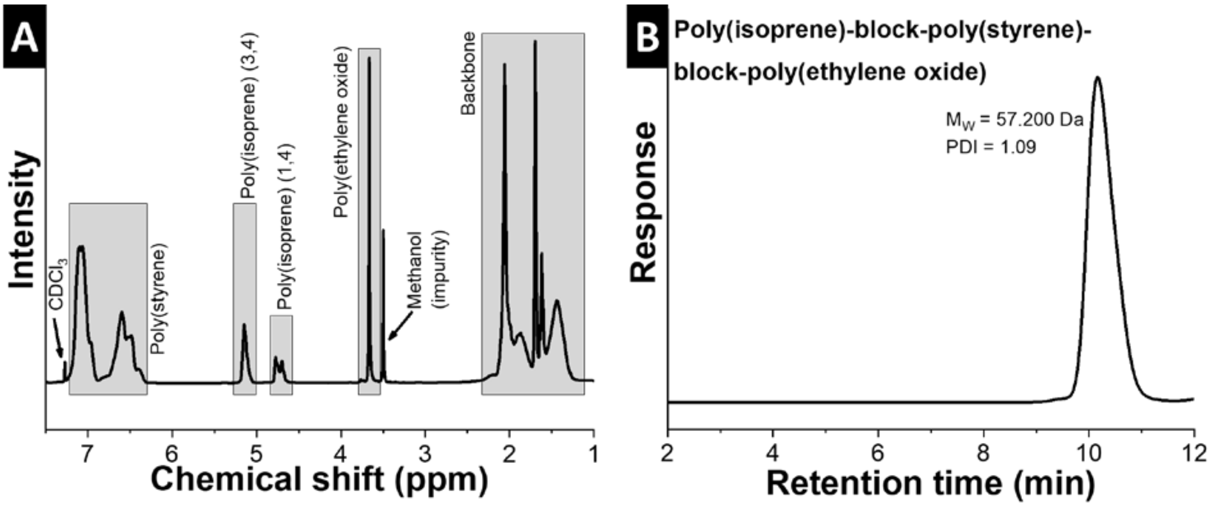

Figure S2: (A) ^{1}H-NMR and (B) HPLC chromatogram of ISO. PDI: polydispersity index.

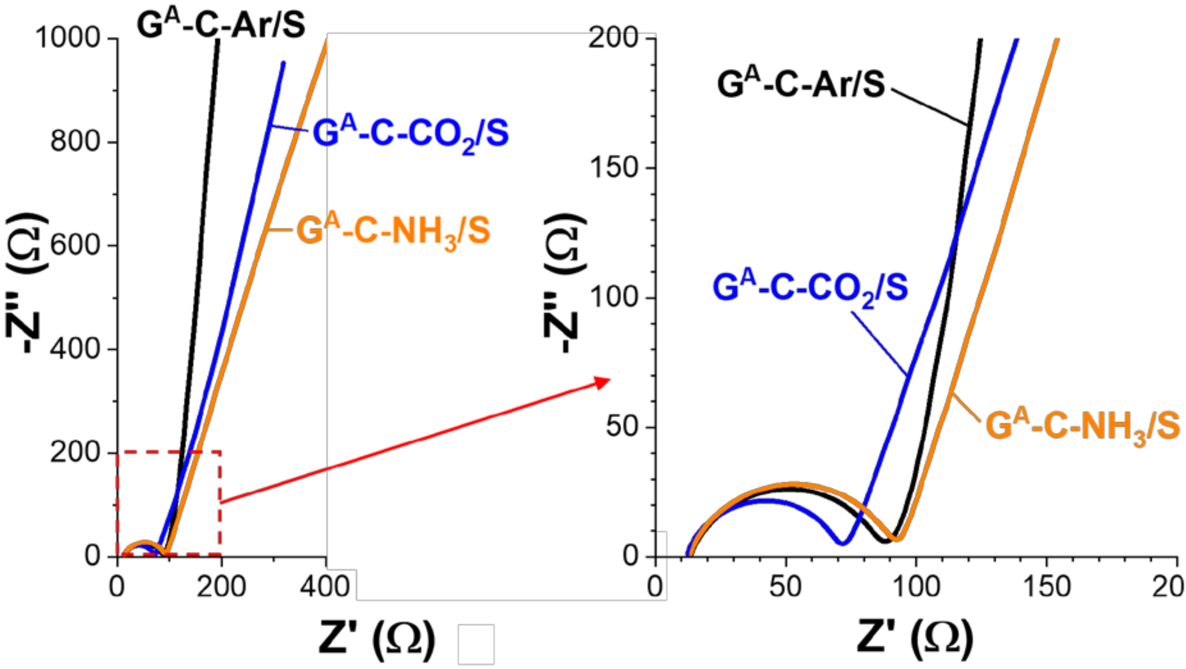

Figure S3: Nyquist plot obtained by electrochemical impedance spectroscopy measurements of the initial LiS-cells carried out at 2.6 V vs. Li/Li^+.

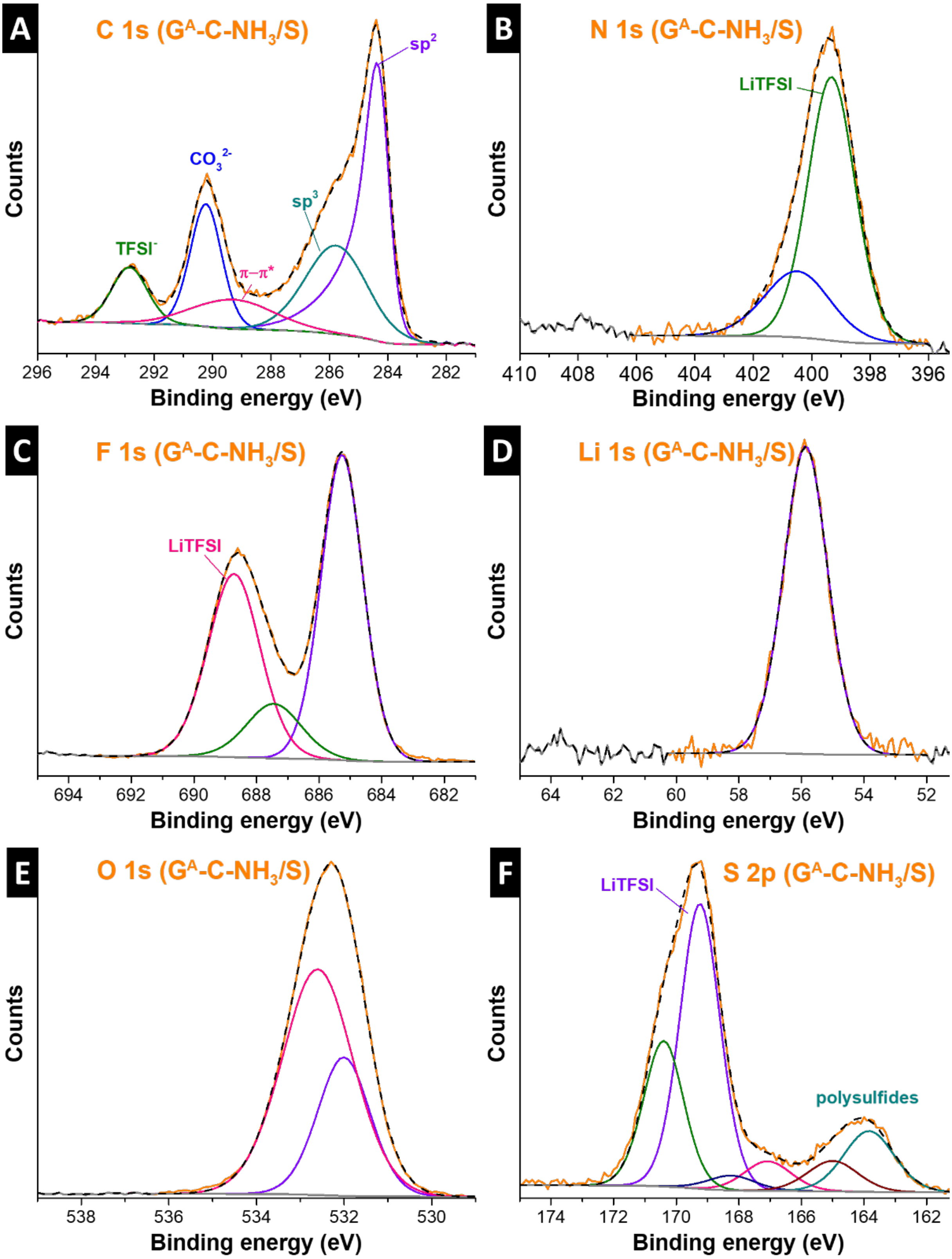

Figure S4: XPS spectra of C1s, N1s, F1s, Li1s, O1s, and S2p of the sample G^A-C-NH_3/S after the long-time performance stability measurements at low C-rates (0.1C discharge; 0.2C charge).

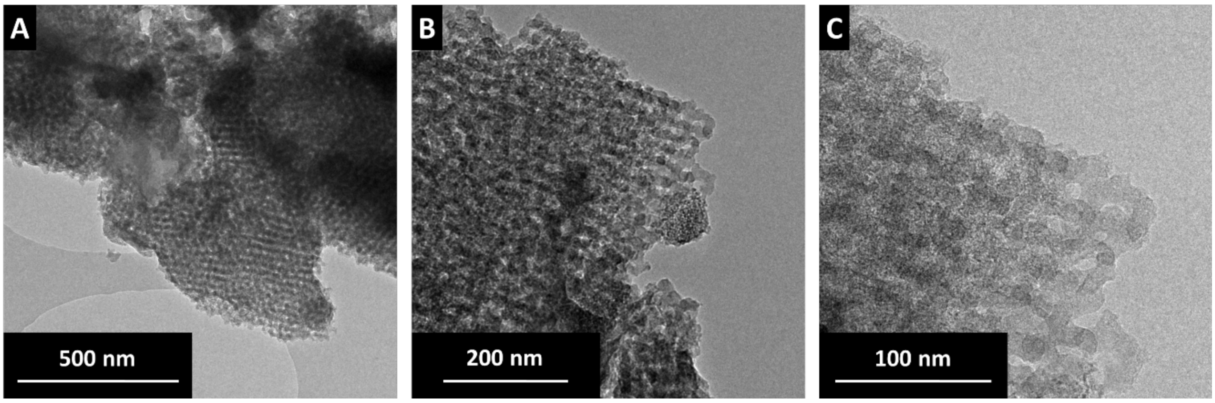

Figure S5: TEM images of the sample G^A-C-NH_3/S after the long-time performance stability measurements at low C-rates (0.1C discharge; 0.2C charge).

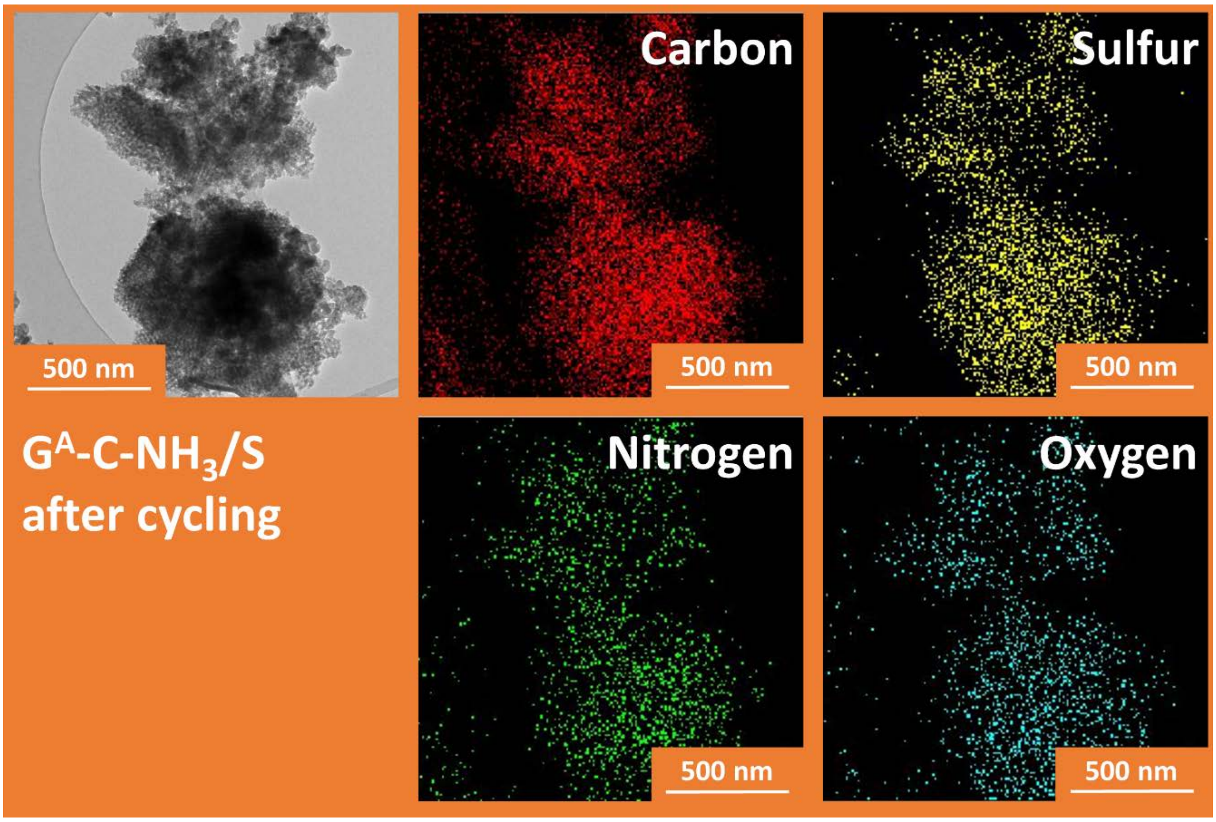

Figure S6: EDX-TEM mapping of the sample G^A-C-NH_3/S after the long-time performance stability measurements at low C-rates (0.1C discharge; 0.2C charge).

5. Conclusions

This thesis has investigated several methods to create nanoporous carbon materials from selected organic and inorganic precursors. To achieve a high pore volume, all carbon precursors undergo massive mass loss after activation or thermal treatment with chlorine gas. **Fig. 14** illustrates the increase in total pore volume and SSA$_{DFT}$ with an increasing total mass loss for the novolac-derived carbons and the SiOC-CDC.

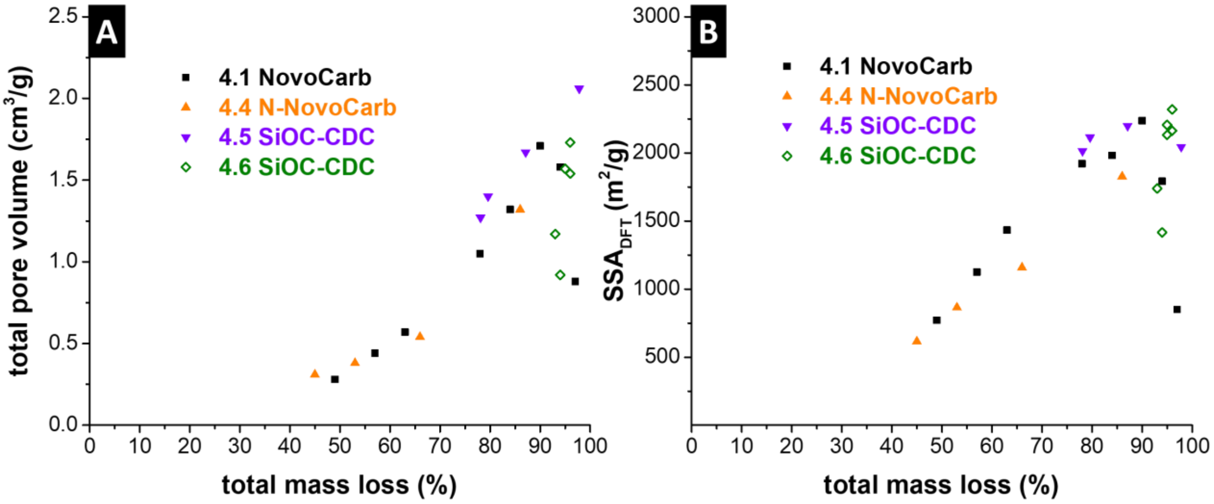

Figure 14: Comparison of different polymer-derived carbon materials produced in this work regarding the porosity (A: total pore volume; B: SSA$_{DFT}$) and the total mass loss.[88, 169, 172, 175]

The porosity of the investigated materials increases until a mass loss of about 90 %. The total pore volume and SSA$_{DFT}$ of the novolac-derived carbons are reduced when the mass loss exceeds >90 %. The SiOC-CDC, which were produced by the VTMS, had a high mass loss of 98 % and showed the highest total pore volume, but its SSA$_{DFT}$ was not much higher compared to the other SiOC-CDC materials of that study. Nitrogen-doped SiOC-CDC also showed a large total mass loss due to the high amount of VTMS.

The high porosity of the produced carbon materials makes them attractive for use as electrical double-layer capacitors. All materials were tested in a symmetrical supercapacitor with several electrolytes, and the best performance of these studies can be compared in a Ragone plot (**Fig. 15**). The specific energy depends on the cell voltage squared, and a comparison of the materials strongly depends on the electrochemical stability window of the electrolyte. Aqueous electrolytes have a relatively narrow electrochemical stability window (~1.2 V) in a symmetrical supercapacitor. Nevertheless, using an aqueous redox electrolyte (KI) achieved a high specific energy of 33 Wh/kg at only 1.4 V, which is comparable to the performance of an organic electrolyte operating at 2.5 V. The performance of the samples in the redox electrolyte is similar to the performance of the commercial organic electrolytes using the novolac-derived carbon beads as an electrode material. The CDCs showed for the organic electrolyte even higher specific energy at high specific powers due to the higher pore volume, larger average pore size, and more ordered structure of the carbon. A higher specific energy up to 61 Wh/kg was achieved by using an ionic liquid with a high cell voltage of 3.2 V. The nitrogen groups in novolac-derived carbons and SiOC-CDC did not significantly increase the specific energy. A comparison of the samples with and without nitrogen showed that the nitrogen groups reduce the rate handling capability in organic electrolytes and ionic liquids.

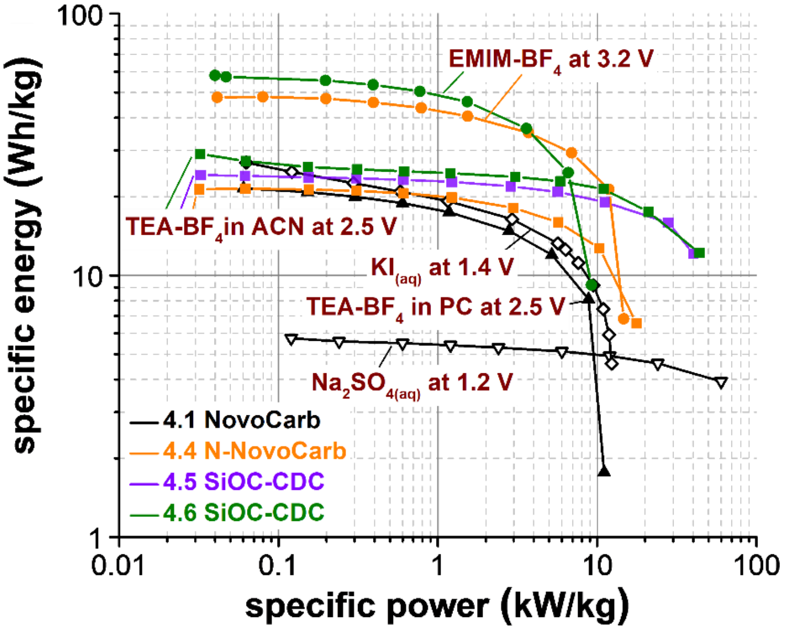

Figure 15: Ragone chart of symmetrical supercapacitors with various electrolytes and the different polymer-derived carbon materials produced in this work (normalized to the active mass of the electrode).[88, 169, 172, 175]

The CDI experiments with the CO_2 activated novolac-derived carbon beads showed that a low number of oxygen functional groups are crucial for a high salt sorption capacity and stable performance. These functional groups are less critical in aqueous supercapacitors but can also reduce the performance stability for other electrolytes (e.g., TEA-BF_4 in ACN).

State-of-the-art Li-ion batteries use graphitic carbon as anode material, which has a theoretical capacity of only 372 mAh/g.[154] The SiOC beads intermediate products, which were used to produce CDCs, are well suited as anode material for Li-ion batteries, due to its higher specific capacity than graphitic carbon. **Fig. 16A** compares the specific capacity of a commercial carbon black with the SiOC beads produced in this work, normalized to the mass of the electrodes. The specific capacity of the SiOC is at low specific currents more than three times higher than the specific capacity of the carbon material. It also remains higher at high specific currents of 1.4 Ah/g. A challenge for silicon-based electrode materials is the longtime performance. The carbon black shows no capacity decrease after 100 cycles, while the capacity of the SiOC beads is reduced by around 17 %. Nevertheless, the SiOC beads produced in this thesis are relatively stable compared to other SiOC materials in the literature.[86, 179-180]

The novolac-derived carbon beads and gyroidal porous carbon materials were also investigated as host for sulfur for LiS batteries. The best performance of both materials is plotted in **Fig. 16B**, where they were melt infiltrated with 66 mass% of sulfur. The number of micropores of the activated novolac-derived carbon beads was large enough to host all sulfur inside the micropores, while some sulfur was stored in the mesopores of the gyroidal carbon because the number of micropores was smaller. The electrode normalized specific capacity of the CO_2 activated novolac-derived carbon beads is at low specific currents with ~380 mAh/$g_{electrode}$ after 10 cycles lower than the gyroidal porous carbon with ~480 mAh/$g_{electrode}$ after 10 cycles. The hierarchical gyroidal pore structure seems to improve the stability of the LiS battery, but the high amount of sulfur within the mesopores reduces the specific capacity at high specific currents. The novolac-derived carbon bead hosted the sulfur entirely in the micropores, which enabled a high specific capacity at a fast charge and discharge rates. The gyroidal carbons were also treated with NH_3 during the pyrolysis, which led to a higher specific capacity but reduced the performance stability.

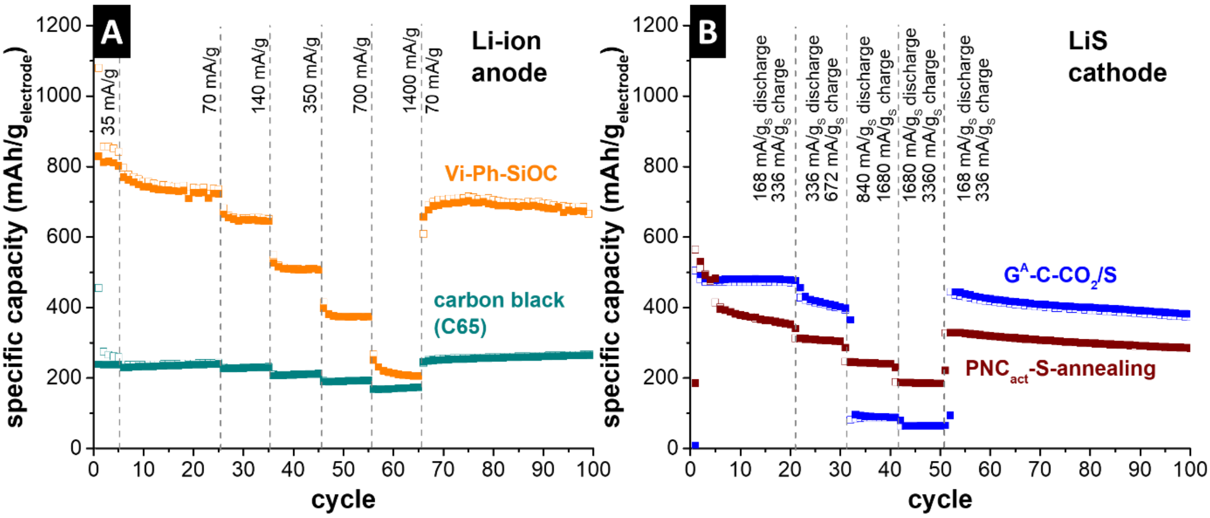

Figure 16: Rate capability test of the SiOC (A) and C/S electrodes (B) measured in a half-cell configuration vs. metallic lithium.[173-174, 176]

This work presented how spherical carbon precursors can be produced with scalable methods, via a self-emulsifying process or the continuous MicroJet reactor technique. It was shown how the porosity can be tuned for each carbon material and how the pore structure and heteroatoms influence the performance of supercapacitors, CDI, and LiS batteries. Further optimization regarding the chemical composition and pore structure is essential to improve the performance of future electrochemical energy device.

References

1. Mote Jr, C.; Dowling, D. A.; Zhou, J., The Power of an Idea: The International Impacts of the Grand Challenges for Engineering. *Engineering* **2016,** *2* (1), 4-7.
2. Gleick, P. H., *Water in Crisis: a Guide to the Worlds Fresh Water Resources*. Oxford University Press, New York: 1993.
3. Porada, S.; Zhao, R.; Van Der Wal, A.; Presser, V.; Biesheuvel, P., Review on the Science and Technology of Water Desalination by Capacitive Deionization. *Progress in Materials Science* **2013,** *58* (8), 1388-1442.
4. Presser, V.; Heon, M.; Gogotsi, Y., Carbide-Derived Carbons–From Porous Networks to Nanotubes and Graphene. *Advanced Functional Materials* **2011,** *21* (5), 810-833.
5. Borchardt, L.; Oschatz, M.; Kaskel, S., Carbon Materials for Lithium Sulfur Batteries—Ten Critical Questions. *Chemistry-A European Journal* **2016,** *22* (22), 7324-7351.
6. Reungoat, J.; Escher, B.; Macova, M.; Argaud, F.; Gernjak, W.; Keller, J., Ozonation and Biological Activated Carbon Filtration of Wastewater Treatment Plant Effluents. *Water research* **2012,** *46* (3), 863-872.
7. BMW, Der neue BMW i3 und der neue BMW i3s. In *Preisliste*, München, 2018; Vol. 1.
8. Mapelli, F.; Tarsitano, D.; Annese, D.; Sala, M.; Bosia, G. In *A Study of Urban Electric Bus with a Fast Charging Energy Storage System based on Lithium Battery and Supercapacitors*, Ecological Vehicles and Renewable Energies (EVER), 2013 8th International Conference and Exhibition on, IEEE: 2013; pp 1-9.
9. Iannuzzi, D.; Tricoli, P. In *Metro Trains Equipped Onboard with Supercapacitors: A Control Technique for Energy Saving*, Power Electronics Electrical Drives Automation and Motion (SPEEDAM), 2010 International Symposium on, IEEE: 2010; pp 750-756.
10. Schoeggl, P.; Haimann, A.; Ress, L., Electrification in Motorsports. *ATZautotechnology* **2012,** *12* (1), 32-39.
11. Conte, F., Battery and Battery Management for Hybrid Electric Vehicles: a Review. *E & I Elektrotechnik und Informationstechnik* **2006,** *123* (10), 424-431.
12. Zuo, W.; Li, R.; Zhou, C.; Li, Y.; Xia, J.; Liu, J., Battery-Supercapacitor Hybrid Devices: Recent Progress and Future Prospects. *Advanced Science* **2017**.
13. Hagen, M.; Hanselmann, D.; Ahlbrecht, K.; Maça, R.; Gerber, D.; Tübke, J., Lithium–Sulfur Cells: The Gap between the State-of-the-Art and the Requirements for High Energy Battery Cells. *Advanced Energy Materials* **2015,** *5* (16).
14. Jäckel, N.; Weingarth, D.; Zeiger, M.; Aslan, M.; Grobelsek, I.; Presser, V., Comparison of Carbon Onions and Carbon Blacks as Conductive Additives for Carbon Supercapacitors in Organic Electrolytes. *Journal of Power Sources* **2014,** *272*, 1122-1133.
15. Moseley, P.; Nelson, R.; Hollenkamp, A., The Role of Carbon in Valve-regulated Lead–acid Battery Technology. *Journal of Power Sources* **2006,** *157* (1), 3-10.
16. Besenhard, J.; Eichinger, G., High Energy Density Lithium Cells: Part I. Electrolytes and Anodes. *Journal of Electroanalytical Chemistry and Interfacial Electrochemistry* **1976,** *68* (1), 1-18.
17. Wang, H.; Yoshio, M., Carbon-coated Natural Graphite Prepared by Thermal Vapor Decomposition Process, a Candidate Anode Material for Lithium-ion Battery. *Journal of Power Sources* **2001,** *93* (1-2), 123-129.
18. Béguin, F.; Presser, V.; Balducci, A.; Frackowiak, E., Carbons and Electrolytes for Advanced Supercapacitors. *Advanced materials* **2014,** *26* (14), 2219-2251.
19. Imoto, K.; Takahashi, K.; Yamaguchi, T.; Komura, T.; Nakamura, J.-i.; Murata, K., High-performance Carbon Counter Electrode for Dye-sensitized Solar Cells. *Solar Energy Materials and Solar Cells* **2003,** *79* (4), 459-469.
20. Hokao, M.; Hironaka, S.; Suda, Y.; Yamamoto, Y., Friction and Wear Properties of Graphite/Glassy Carbon Composites. *Wear* **2000,** *237* (1), 54-62.
21. McColm, I. J., *Ceramic Hardness*. Plenum Press: New York, 1990; p 246-253.

22. Petzold, A., *Anorganisch-nichtmetallische Werkstoffe: Charakterisistik, Eigenschaften, Anwendungsverhalten*. Deutscher Verlag für Grundstoffindustrie GmbH: Leipzig, 1992; Vol. 3, p 123, 210.

23. Porada, S.; Weinstein, L.; Dash, R.; Van Der Wal, A.; Bryjak, M.; Gogotsi, Y.; Biesheuvel, P., Water Desalination using Capacitive Deionization with Microporous Carbon Electrodes. *ACS Applied Materials & Interfaces* **2012,** *4* (3), 1194-1199.

24. Thommes, M.; Kaneko, K.; Neimark, A. V.; Olivier, J. P.; Rodriguez-Reinoso, F.; Rouquerol, J.; Sing, K. S. W., Physisorption of Gases, with Special Reference to the Evaluation of Surface Area and Pore Size Distribution. *Pure and Applied Chemistry* **2015,** *87* (9-10), 1051-1069.

25. Hu, Z.; Srinivasan, M., Mesoporous High-surface-area Activated Carbon. *Microporous and Mesoporous Materials* **2001,** *43* (3), 267-275.

26. Carrott, P.; Carrott, M. R., Lignin–from Natural Adsorbent to Activated Carbon: a Review. *Bioresource Technology* **2007,** *98* (12), 2301-2312.

27. Fitzer, E.; Schaefer, W.; Yamada, S., The Formation of Glasslike Carbon by Pyrolysis of Polyfurfuryl Alcohol and Phenolic Resin. *Carbon* **1969,** *7* (6), 643-648.

28. Singh, A.; Lal, D., Microporous Activated Carbon Spheres Prepared from Resole-type Crosslinked Phenolic Beads by Physical Activation. *Journal of Applied Polymer Science* **2008,** *110* (5), 3283-3291.

29. Ra, E.; Raymundo-Piñero, E.; Lee, Y.; Béguin, F., High Power Supercapacitors using Polyacrylonitrile-based Carbon Nanofiber Paper. *Carbon* **2009,** *47* (13), 2984-2992.

30. Maciá-Agulló, J.; Moore, B.; Cazorla-Amorós, D.; Linares-Solano, A., Activation of Coal Tar Pitch Carbon Fibres: Physical Activation vs. Chemical Activation. *Carbon* **2004,** *42* (7), 1367-1370.

31. Nishihara, H.; Yang, Q.-H.; Hou, P.-X.; Unno, M.; Yamauchi, S.; Saito, R.; Paredes, J. I.; Martínez-Alonso, A.; Tascón, J. M.; Sato, Y., A Possible Buckybowl-like Structure of Zeolite Templated Carbon. *Carbon* **2009,** *47* (5), 1220-1230.

32. Werner, J. r. G.; Hoheisel, T. N.; Wiesner, U., Synthesis and Characterization of Gyroidal Mesoporous Carbons and Carbon Monoliths with Tunable Ultralarge Pore Size. *ACS Nano* **2013,** *8* (1), 731-743.

33. Tee, E.; Tallo, I.; Kurig, H.; Thomberg, T.; Jänes, A.; Lust, E., Huge Enhancement of Energy Storage Capacity and Power Density of Supercapacitors Based on the Carbon Dioxide Activated Microporous SiC-CDC. *Electrochimica Acta* **2015,** *161*, 364-370.

34. Gao, Y.; Presser, V.; Zhang, L.; Niu, J. J.; McDonough, J. K.; Pérez, C. R.; Lin, H.; Fong, H.; Gogotsi, Y., High Power Supercapacitor Electrodes Based on Flexible TiC-CDC Nano-felts. *Journal of Power Sources* **2012,** *201*, 368-375.

35. Borchardt, L.; Oschatz, M.; Lohe, M.; Presser, V.; Gogotsi, Y.; Kaskel, S., Ordered Mesoporous Carbide-derived Carbons Prepared by Soft Templating. *Carbon* **2012,** *50* (11), 3987-3994.

36. Suzuki, M., Activated Carbon Fiber: Fundamentals and Applications. *Carbon* **1994,** *32* (4), 577-586.

37. Chuenchom, L.; Kraehnert, R.; Smarsly, B. M., Recent Progress in Soft-templating of Porous Carbon Materials. *Soft Matter* **2012,** *8* (42), 10801-10812.

38. Oschatz, M.; Thieme, S.; Borchardt, L.; Lohe, M. R.; Biemelt, T.; Brückner, J.; Althues, H.; Kaskel, S., A New Route for the Preparation of Mesoporous Carbon Materials with High Performance in Lithium–sulphur Battery Cathodes. *Chemical Communications* **2013,** *49* (52), 5832-5834.

39. Fechler, N.; Fellinger, T. P.; Antonietti, M., “Salt templating”: a Simple and Sustainable Pathway Toward Highly Porous Functional Carbons from Ionic Liquids. *Advanced Materials* **2013,** *25* (1), 75-79.

40. Burket, C. L.; Rajagopalan, R.; Marencic, A. P.; Dronvajjala, K.; Foley, H. C., Genesis of Porosity in Polyfurfuryl Alcohol Derived Nanoporous Carbon. *Carbon* **2006,** *44* (14), 2957-2963.

41. Xue, T. J.; McKinney, M. A.; Wilkie, C. A., The Thermal Degradation of Polyacrylonitrile. *Polymer Degradation and Stability* **1997,** *58* (1-2), 193-202.

42. Alves, W. F.; Venancio, E. C.; Leite, F. L.; Kanda, D. H.; Malmonge, L. F.; Malmonge, J. A.; Mattoso, L. H., Thermo-analyses of Polyaniline and its Derivatives. *Thermochimica Acta* **2010,** *502* (1-2), 43-46.

43. Zornitta, R. L.; García-Mateos, F. J.; Lado, J. J.; Rodríguez-Mirasol, J.; Cordero, T.; Hammer, P.; Ruotolo, L. A., High-performance Activated Carbon from Polyaniline for Capacitive Deionization. *Carbon* **2017,** *123*, 318-333.

44. Lee, Y. K.; Kim, D. J.; Kim, H. J.; Hwang, T. S.; Rafailovich, M.; Sokolov, J., Activation Energy and Curing Behavior of Resol-and Novolac-type Phenolic Resins by Differential Scanning Calorimetry and Thermogravimetric Analysis. *Journal of Applied Polymer Science* **2003,** *89* (10), 2589-2596.

45. Tennison, S., Phenolic-resin-derived Activated Carbons. *Applied Catalysis A: General* **1998,** *173* (2), 289-311.

46. Suzuki, K.; Matsumoto, H.; Minagawa, M.; Kimura, M.; Tanioka, A., Preparation of Carbon Fiber Fabrics from Phenolic Resin by Electrospray Deposition. *Polymer Journal* **2007,** *39* (11), 1128.

47. Blanco, C.; Santamarıa, R.; Bermejo, J.; Menendez, R., Pitch-based Carbon Composites with Granular Reinforcements for Frictional Applications. *Carbon* **2000,** *38* (7), 1043-1051.

48. Kim, D.-Y.; Nishiyama, Y.; Wada, M.; Kuga, S., High-yield Carbonization of Cellulose by Sulfuric Acid Impregnation. *Cellulose* **2001,** *8* (1), 29-33.

49. Li, W.; Yang, K.; Peng, J.; Zhang, L.; Guo, S.; Xia, H., Effects of Carbonization Temperatures on Characteristics of Porosity in Coconut Shell Chars and Activated Carbons Derived from Carbonized Coconut Shell Chars. *Industrial Crops and Products* **2008,** *28* (2), 190-198.

50. Sharma, R. K.; Wooten, J. B.; Baliga, V. L.; Lin, X.; Chan, W. G.; Hajaligol, M. R., Characterization of Chars from Pyrolysis of Lignin. *Fuel* **2004,** *83* (11-12), 1469-1482.

51. Sharma, R. K.; Wooten, J. B.; Baliga, V. L.; Martoglio-Smith, P. A.; Hajaligol, M. R., Characterization of Char From the Pyrolysis of Tobacco. *Journal of Agricultural and Food Chemistry* **2002,** *50* (4), 771-783.

52. Tieke, B., *Makromolekulare Chemie: Eine Einführung*. John Wiley & Sons: Weinheim, 2005; Vol. 2, p 44-47.

53. Elias, H.-G., *Makromoleküle*. Basel, 1992; Vol. 5, p 149-150.

54. Ogale, A.; Lin, C.; Anderson, D.; Kearns, K., Orientation and Dimensional Changes in Mesophase Pitch-based Carbon Fibers. *Carbon* **2002,** *40* (8), 1309-1319.

55. Trick, K. A.; Saliba, T. E., Mechanisms of the Pyrolysis of Phenolic Resin in a Carbon/Phenolic Composite. *Carbon* **1995,** *33* (11), 1509-1515.

56. Tseng, R.-L.; Tseng, S.-K.; Wu, F.-C., Preparation of High Surface Area Carbons from Corncob with KOH Etching plus CO_2 Gasification for the Adsorption of Dyes and Phenols from Water. *Colloids and Surfaces A: Physicochemical and Engineering Aspects* **2006,** *279* (1-3), 69-78.

57. Schneidermann, C.; Jäckel, N.; Oswald, S.; Giebeler, L.; Presser, V.; Borchardt, L., Solvent-Free Mechanochemical Synthesis of Nitrogen-Doped Nanoporous Carbon for Electrochemical Energy Storage. *ChemSusChem* **2017,** *10* (11), 2416-2424.

58. Huidobro, A.; Pastor, A.; Rodrıguez-Reinoso, F., Preparation of Activated Carbon Cloth from Viscous Rayon: Part IV. Chemical Activation. *Carbon* **2001,** *39* (3), 389-398.

59. Dıaz-Terán, J.; Nevskaia, D.; Fierro, J.; López-Peinado, A.; Jerez, A., Study of Chemical Activation Process of a Lignocellulosic Material with KOH by XPS and XRD. *Microporous and Mesoporous Materials* **2003,** *60* (1-3), 173-181.

60. Kopyscinski, J.; Rahman, M.; Gupta, R.; Mims, C. A.; Hill, J. M., K_2CO_3 Catalyzed CO_2 Gasification of Ash-free Coal. Interactions of the Catalyst with Carbon in N_2 and CO_2 Atmosphere. *Fuel* **2014,** *117*, 1181-1189.

61. Rhead, T. F. E.; Wheeler, R. V., The Effect of Temperature on the Equilibrium $2\ CO \rightleftharpoons CO_2 + C$. *Journal of the Chemical Society, Transactions* **1910,** *97*, 2178-2189.

62. Lillo-Ródenas, M.; Cazorla-Amorós, D.; Linares-Solano, A., Understanding Chemical Reactions Between Carbons and NaOH and KOH: an Insight Into the Chemical Activation Mechanism. *Carbon* **2003,** *41* (2), 267-275.

63. Wigmans, T., Industrial Aspects of Production and Use of Activated Carbons. *Carbon* **1989,** *27* (1), 13-22.

64. Olivares-Marín, M.; Fernández-González, C.; Macías-García, A.; Gómez-Serrano, V., Preparation of Activated Carbon from Cherry Stones by Physical Activation in Air. Influence of the Chemical Carbonisation with H_2SO_4. *Journal of Analytical and Applied Pyrolysis* **2012,** *94*, 131-137.

65. Stöhr, B.; Boehm, H.; Schlögl, R., Enhancement of the Catalytic Activity of Activated Carbons in Oxidation Reactions by Thermal Treatment with Ammonia or Hydrogen Cyanide and Observation of a Ssuperoxide Species as a Possible Intermediate. *Carbon* **1991,** *29* (6), 707-720.

66. Mangun, C. L.; Benak, K. R.; Economy, J.; Foster, K. L., Surface Chemistry, Pore Sizes and Adsorption Properties of Activated Carbon Fibers and Precursors Treated with Ammonia. *Carbon* **2001,** *39* (12), 1809-1820.

67. Boehm, H. P.; Mair, G.; Stoehr, T.; De Rincón, A. R.; Tereczki, B., Carbon as a Catalyst in Oxidation Reactions and Hydrogen Halide Elimination Reactions. *Fuel* **1984,** *63* (8), 1061-1063.

68. Świetlik, U.; Grzyb, B.; Torchała, K.; Gryglewicz, G.; Machnikowski, J., High Temperature Ammonia Treatment of Pitch Particulates and Fibers for Nitrogen Enriched Microporous Carbons. *Fuel Processing Technology* **2014,** *119*, 211-217.

69. Presser, V.; McDonough, J.; Yeon, S.-H.; Gogotsi, Y., Effect of Pore Size on Carbon Dioxide Sorption by Carbide Derived Carbon. *Energy & Environmental Science* **2011,** *4* (8), 3059-3066.

70. Yeon, S.-H.; Reddington, P.; Gogotsi, Y.; Fischer, J. E.; Vakifahmetoglu, C.; Colombo, P., Carbide-Derived-Carbons with Hierarchical Porosity from a Preceramic Polymer. *Carbon* **2010,** *48* (1), 201-210.

71. Vakifahmetoglu, C.; Presser, V.; Yeon, S.-H.; Colombo, P.; Gogotsi, Y., Enhanced Hydrogen and Methane Gas Storage of Silicon Oxycarbide Derived Carbon. *Microporous and Mesoporous Materials* **2011,** *144* (1-3), 105-112.

72. Osswald, S.; Chmiola, J.; Gogotsi, Y., Structural Evolution of Carbide-derived Carbons upon Vacuum Annealing. *Carbon* **2012,** *50* (13), 4880-4886.

73. Mangarella, M. C.; Walton, K. S., Tailored Fe_3C-derived Carbons with Embedded Fe Nanoparticles for Ammonia Adsorption. *Carbon* **2015,** *95*, 208-219.

74. Chmiola, J.; Yushin, G.; Dash, R.; Gogotsi, Y., Effect of Pore Size and Surface Area of Carbide Derived Carbons on Specific Capacitance. *Journal of Power Sources* **2006,** *158* (1), 765-772.

75. Pérez, C. R.; Yeon, S. H.; Ségalini, J.; Presser, V.; Taberna, P. L.; Simon, P.; Gogotsi, Y., Structure and Electrochemical Performance of Carbide-Derived Carbon Nanopowders. *Advanced Functional Materials* **2013,** *23* (8), 1081-1089.

76. Xu, J.; Zhang, R.; Ge, S.; Wang, J.; Liu, Y.; Chen, P., Effect of Iron Catalyst on the Microstructure and Electrochemical Properties of Vanadium Carbide-derived Carbons. *Materials Chemistry and Physics* **2013,** *141* (1), 540-548.

77. Hoffman, E. N.; Yushin, G.; El-Raghy, T.; Gogotsi, Y.; Barsoum, M. W., Micro and Mesoporosity of Carbon Derived from Rernary and Binary Metal Carbides. *Microporous and Mesoporous Materials* **2008,** *112* (1-3), 526-532.

78. Colombo, P.; Mera, G.; Riedel, R.; Soraru, G. D., Polymer-derived Ceramics: 40 years of Research and Innovation in Advanced Ceramics. *Journal of the American Ceramic Society* **2010,** *93* (7), 1805-1837.

79. Oschatz, M.; Zeiger, M.; Jäckel, N.; Strubel, P.; Borchardt, L.; Reinhold, R.; Nickel, W.; Eckert, J.; Presser, V.; Kaskel, S., Emulsion Soft Templating of Carbide-Derived Carbon Nanospheres with Controllable Porosity for Capacitive Electrochemical Energy Storage. *Journal of Materials Chemistry A* **2015,** *3* (35), 17983-17990.

80. Zhang, C.; Babonneau, F.; Bonhomme, C.; Laine, R. M.; Soles, C. L.; Hristov, H. A.; Yee, A. F., Highly Porous Polyhedral Silsesquioxane Polymers. Synthesis and Characterization. *Journal of the American Chemical Society* **1998,** *120* (33), 8380-8391.

81. Stöber, W.; Fink, A.; Bohn, E., Controlled Growth of Monodisperse Silica Spheres in the Micron Size Range. *Journal of Colloid and Interface Science* **1968,** *26* (1), 62-69.

82. Guo, A.; Roso, M.; Modesti, M.; Liu, J.; Colombo, P., Preceramic Polymer-Derived SiOC Fibers by Electrospinning. *Journal of Applied Polymer Science* **2014,** *131* (3).

83. Tolosa, A.; Krüner, B.; Jäckel, N.; Aslan, M.; Vakifahmetoglu, C.; Presser, V., Electrospinning and Electrospraying of Silicon Oxycarbide-Derived Nanoporous Carbon for Supercapacitor Electrodes. *Journal of Power Sources* **2016,** *313*, 178-188.

84. Oschatz, M.; Boukhalfa, S.; Nickel, W.; Hofmann, J. P.; Fischer, C.; Yushin, G.; Kaskel, S., Carbide-derived Carbon Aerogels with Runable Pore Structure as Versatile Electrode Material in High Power Supercapacitors. *Carbon* **2017,** *113*, 283-291.

85. Kleebe, H.-J.; Blum, Y. D., SiOC Ceramic with High Excess Free Carbon. *Journal of the European Ceramic Society* **2008,** *28* (5), 1037-1042.

86. Kaspar, J.; Graczyk-Zajac, M.; Choudhury, S.; Riedel, R., Impact of the Electrical Conductivity on the Lithium Capacity of Polymer-derived Silicon Oxycarbide (SiOC) Ceramics. *Electrochimica Acta* **2016,** *216*, 196-202.

87. Ma, J.; Shi, L.; Shi, Y.; Luo, S.; Xu, J., Pyrolysis of Polymethylsilsesquioxane. *Journal of Applied Polymer Science* **2002,** *85* (5), 1077-1086.

88. Krüner, B.; Odenwald, C.; Tolosa, A.; Schreiber, A.; Aslan, M.; Kickelbick, G.; Presser, V., Carbide-derived Carbon Beads with Tunable Nanopores from Continuously Produced Polysilsesquioxanes for Supercapacitor Electrodes. *Sustainable Energy & Fuels* **2017,** *1* (7), 1588-1600.

89. Ionescu, E.; Papendorf, B.; Kleebe, H. J.; Riedel, R., Polymer-Derived Silicon Oxycarbide/Hafnia Ceramic Nanocomposites. Part II: Stability Toward Decomposition and Microstructure Evolution at T≫ 1000° C. *Journal of the American Ceramic Society* **2010,** *93* (6), 1783-1789.

90. Scarmi, A.; Sorarù, G. D.; Raj, R., The Role of Carbon in Unexpected Visco (An) Elastic Behavior of Amorphous Silicon Oxycarbide Above 1273 K. *Journal of Non-Crystalline Solids* **2005,** *351* (27-29), 2238-2243.

91. Kaspar, J.; Graczyk-Zajac, M.; Riedel, R., Lithium Insertion into Carbon-rich SiOC Ceramics: Influence of Pyrolysis Temperature on Electrochemical Properties. *Journal of Power Sources* **2013,** *244*, 450-455.

92. Pena-Alonso, R.; Mariotto, G.; Gervais, C.; Babonneau, F.; Soraru, G. D., New Insights on the High-Temperature Nanostructure Evolution of SiOC and B-doped SiBOC Polymer-derived Glasses. *Chemistry of Materials* **2007,** *19* (23), 5694-5702.

93. Hutchins, O. Method for the Production of Silicon Tetrachlorid. 1271713A, 1918.

94. Andersen, J. N. Silicon Tetrachloride Manufacture. 2739041A, 1956.

95. Welz, S.; McNallan, M. J.; Gogotsi, Y., Carbon Structures in Silicon Carbide Derived Carbon. *Journal of Materials Processing Technology* **2006,** *179* (1), 11-22.

96. Geng, D.; Chen, Y.; Chen, Y.; Li, Y.; Li, R.; Sun, X.; Ye, S.; Knights, S., High Oxygen-reduction Activity and Durability of Nitrogen-doped Graphene. *Energy & Environmental Science* **2011,** *4* (3), 760-764.

97. Jeong, H. M.; Lee, J. W.; Shin, W. H.; Choi, Y. J.; Shin, H. J.; Kang, J. K.; Choi, J. W., Nitrogen-doped graphene for high-performance ultracapacitors and the importance of nitrogen-doped sites at basal planes. *Nano letters* **2011,** *11* (6), 2472-2477.

98. Paek, E.; Pak, A. J.; Kweon, K. E.; Hwang, G. S., On the Origin of the Enhanced Supercapacitor Performance of Nitrogen-doped Graphene. *The Journal of Physical Chemistry C* **2013,** *117* (11), 5610-5616.

99. Sun, X. G.; Wang, X.; Mayes, R. T.; Dai, S., Lithium–Sulfur Batteries Based on Nitrogen-Doped Carbon and an Ionic-Liquid Electrolyte. *ChemSusChem* **2012,** *5* (10), 2079-2085.

100. Song, J.; Gordin, M. L.; Xu, T.; Chen, S.; Yu, Z.; Sohn, H.; Lu, J.; Ren, Y.; Duan, Y.; Wang, D., Strong Lithium Polysulfide Chemisorption on Electroactive Sites of Nitrogen-doped Carbon Composites for High-performance Lithium–sulfur Battery Cathodes. *Angewandte Chemie International Edition* **2015,** *54* (14), 4325-4329.

101. Shao, Y.; Zhang, S.; Engelhard, M. H.; Li, G.; Shao, G.; Wang, Y.; Liu, J.; Aksay, I. A.; Lin, Y., Nitrogen-doped Graphene and its Electrochemical Applications. *Journal of Materials Chemistry* **2010,** *20* (35), 7491-7496.

102. Arrigo, R.; Hävecker, M.; Schlögl, R.; Su, D. S., Dynamic Surface Rearrangement and Thermal Stability of Nitrogen Functional Groups on Carbon Nanotubes. *Chemical Communications* **2008,** (40), 4891-4893.

103. Zhao, Y.; Liu, X.; Han, Y., Microporous Carbonaceous Adsorbents for CO_2 Separation via Selective Adsorption. *RSC Advances* **2015,** *5* (38), 30310-30330.

104. Liu, Z.; Xiao, K.; Guo, H.; Ning, X.; Hu, A.; Tang, Q.; Fan, B.; Zhu, Y.; Chen, X., Nitrogen-doped Worm-like Graphitized Hierarchical Porous Carbon Designed for Enhancing Area-normalized Capacitance of Electrical Double Layer Supercapacitors. *Carbon* **2017,** *117*, 163-173.

105. Hulicova, D.; Yamashita, J.; Soneda, Y.; Hatori, H.; Kodama, M., Supercapacitors Prepared from Melamine-based Carbon. *Chemistry of Materials* **2005,** *17* (5), 1241-1247.

106. Xu, G.; Han, J.; Ding, B.; Nie, P.; Pan, J.; Dou, H.; Li, H.; Zhang, X., Biomass-derived porous carbon materials with sulfur and nitrogen dual-doping for energy storage. *Green Chemistry* **2015,** *17* (3), 1668-1674.

107. Bashkova, S.; Bandosz, T. J., The Effects of Urea Modification and Heat Treatment on the Process of NO_2 Removal by Wood-based Activated Carbon. *Journal of Colloid and Interface Science* **2009,** *333* (1), 97-103.

108. Noh, J. S.; Schwarz, J. A., Effect of HNO_3 Treatment on the Surface Acidity of Activated Carbons. *Carbon* **1990,** *28* (5), 675-682.

109. Wang, X.; Liu, C.-G.; Neff, D.; Fulvio, P. F.; Mayes, R. T.; Zhamu, A.; Fang, Q.; Chen, G.; Meyer, H. M.; Jang, B. Z., Nitrogen-enriched Ordered Mesoporous Carbons Through Direct Pyrolysis in Ammonia with Enhanced Capacitive Performance. *Journal of Materials Chemistry A* **2013,** *1* (27), 7920-7926.

110. Travlou, N. A.; Bandosz, T. J., N-doped Polymeric Resin-derived Porous Carbons as Efficient Ammonia Removal and Detection Media. *Carbon* **2017,** *117*, 228-239.

111. Chen, L.-F.; Zhang, X.-D.; Liang, H.-W.; Kong, M.; Guan, Q.-F.; Chen, P.; Wu, Z.-Y.; Yu, S.-H., Synthesis of Nitrogen-Doped Porous Carbon Nanofibers as an Efficient Electrode Material for Supercapacitors. *ACS Nano* **2012,** *6* (8), 7092-7102.

112. Porada, S.; Schipper, F.; Aslan, M.; Antonietti, M.; Presser, V.; Fellinger, T. P., Capacitive Deionization using Biomass-based Microporous Salt-Templated Heteroatom-Doped Carbons. *ChemSusChem* **2015,** *8* (11), 1867-1874.

113. Liu, X.; Zhou, Y.; Zhou, W.; Li, L.; Huang, S.; Chen, S., Biomass-derived Nitrogen Self-Doped Porous Carbon as Effective Metal-Free Catalysts for Oxygen Reduction Reaction. *Nanoscale* **2015,** *7* (14), 6136-6142.

114. Shen, W.; Fan, W., Nitrogen-Containing Porous Carbons: Synthesis and Application. *Journal of Materials Chemistry A* **2013,** *1* (4), 999-1013.

115. Beguin, F.; Frackowiak, E., *Supercapacitors: Materials, Systems and Applications*. Wiley-VCH Verlag: Weinheim, Germany, 2013; p 568.

116. Simon, P.; Gogotsi, Y., Materials for Electrochemical Capacitors. *Nature Materials* **2008,** *7* (11), 845-854.

117. Tipler, P. A.; Mosca, G., *Physik: für Wissenschaftler und Ingenieure*. Spektrum Akademischer Verlag Heidelberg: 2009; Vol. 6.

118. Jäckel, N.; Rodner, M.; Schreiber, A.; Jeongwook, J.; Zeiger, M.; Aslan, M.; Weingarth, D.; Presser, V., Anomalous or Regular Capacitance? The Influence of Pore Size Dispersity on Double-layer Formation. *Journal of Power Sources* **2016,** *326*, 660-671.

119. Jackel, N.; Simon, P.; Gogotsi, Y.; Presser, V., Increase in Capacitance by Subnanometer Pores in Carbon. *ACS Energy Letters* **2016,** *1* (6), 1262-1265.

120. Chmiola, J.; Largeot, C.; Taberna, P. L.; Simon, P.; Gogotsi, Y., Desolvation of Ions in Subnanometer Pores and Its Effect on Capacitance and Double-Layer Theory. *Angewandte Chemie* **2008,** *120* (18), 3440-3443.

121. Yang, C.-M.; Kim, Y.-J.; Endo, M.; Kanoh, H.; Yudasaka, M.; Iijima, S.; Kaneko, K., Nanowindow-regulated Specific Capacitance of Supercapacitor Electrodes of Single-wall Carbon Nanohorns. *Journal of the American Chemical Society* **2007,** *129* (1), 20-21.

122. Shannon, R. D., Revised Effective Ionic Radii and Systematic Studies of Interatomic Distances in Halides and Chalcogenides. *Acta Crystallographica Section A: Crystal Physics, Diffraction, Theoretical and General Crystallography* **1976,** *32* (5), 751-767.

123. Slesinski, A.; Matei-Ghimbeu, C.; Fic, K.; Béguin, F.; Frackowiak, E., Self-buffered pH at Carbon Surfaces in Aqueous Supercapacitors. *Carbon* **2018,** *129*, 758-765.
124. Khomenko, V.; Raymundo-Piñero, E.; Béguin, F., A New Type of High Energy Asymmetric Capacitor with Nanoporous Carbon Electrodes in Aqueous Electrolyte. *Journal of Power Sources* **2010,** *195* (13), 4234-4241.
125. Fic, K.; Meller, M.; Menzel, J.; Frackowiak, E., Around the Thermodynamic Limitations of Supercapacitors Operating in Aqueous Electrolytes. *Electrochimica Acta* **2016,** *206*, 496-503.
126. Weingarth, D.; Noh, H.; Foelske-Schmitz, A.; Wokaun, A.; Kötz, R., A Reliable Determination Method of Stability Limits for Electrochemical Double Layer Capacitors. *Electrochimica Acta* **2013,** *103*, 119-124.
127. Weingarth, D.; Drumm, R.; Foelske-Schmitz, A.; Kötz, R.; Presser, V., An Electrochemical In Situ Study of Freezing and Thawing of Ionic Liquids in Carbon Nanopores. *Physical Chemistry Chemical Physics* **2014,** *16* (39), 21219-21224.
128. Helmholtz, H., Studien über electrische Grenzschichten. *Annalen der Physik* **1879,** *243* (7), 337-382.
129. Gouy, M., Sur la constitution de la charge électrique à la surface d'un électrolyte. *Journal de Physique Théorique et Appliquée* **1910,** *9* (1), 457-468.
130. Chapman, D. L., LI. A Contribution to the Theory of Electrocapillarity. *The London, Edinburgh, and Dublin Philosophical Magazine and Journal of Science* **1913,** *25* (148), 475-481.
131. Stern, O., Zur Theorie der elektrolytischen Doppelschicht. *Berichte der Bunsengesellschaft für physikalische Chemie* **1924,** *30* (21-22), 508-516.
132. Grahame, D. C., The Electrical Double Layer and the Theory of Electrocapillarity. *Chemical Reviews* **1947,** *41* (3), 441-501.
133. Huang, J.; Sumpter, B. G.; Meunier, V., Theoretical Model for Nanoporous Carbon Supercapacitors. *Angewandte Chemie* **2008,** *120* (3), 530-534.
134. Shim, Y.; Kim, H. J., Nanoporous Carbon Supercapacitors in an Ionic Liquid: a Computer Simulation Study. *ACS nano* **2010,** *4* (4), 2345-2355.
135. Prehal, C.; Koczwara, C.; Jäckel, N.; Amenitsch, H.; Presser, V.; Paris, O., A Carbon Nanopore Model to Quantify Structure and Kinetics of Ion Electrosorption with In Situ Small-angle X-ray Scattering. *Physical Chemistry Chemical Physics* **2017,** *19* (23), 15549-15561.
136. Muralidharan, A.; Pratt, L. R.; Hoffman, G. G.; Chaudhari, M. I.; Rempe, S. B., Molecular Simulation Results on Charged Carbon Nanotube Forest-Based Supercapacitors. *ChemSusChem* **2018,** *11*, 1927-1932.
137. Suss, M. E.; Presser, V., Water Desalination with Energy Storage Electrode Materials. *Joule* **2018,** *2* (1), 10-15.
138. Porada, S.; Borchardt, L.; Oschatz, M.; Bryjak, M.; Atchison, J.; Keesman, K.; Kaskel, S.; Biesheuvel, P.; Presser, V., Direct Prediction of the Desalination Performance of Porous Carbon Electrodes for Capacitive Deionization. *Energy & Environmental Science* **2013,** *6* (12), 3700-3712.
139. Aslan, M.; Zeiger, M.; Jäckel, N.; Grobelsek, I.; Weingarth, D.; Presser, V., Improved Capacitive Deionization Performance of Mixed Hydrophobic/Hydrophilic Activated Carbon Electrodes. *Journal of Physics: Condensed Matter* **2016,** *28* (11), 114003.
140. Kim, T.; Dykstra, J.; Porada, S.; Van Der Wal, A.; Yoon, J.; Biesheuvel, P., Enhanced Charge Efficiency and Reduced Energy use in Capacitive Deionization by Increasing the Discharge Voltage. *Journal of Colloid and Interface Science* **2015,** *446*, 317-326.
141. Wu, P.; Huang, J.; Meunier, V.; Sumpter, B. G.; Qiao, R., Voltage Dependent Charge Storage Modes and Capacity in Subnanometer Pores. *The Journal of Physical Chemistry Letters* **2012,** *3* (13), 1732-1737.
142. Kim, C.; Srimuk, P.; Lee, J.; Fleischmann, S.; Aslan, M.; Presser, V., Influence of Pore Structure and Cell Voltage of Activated Carbon Cloth as a Versatile Electrode Material for Capacitive Deionization. *Carbon* **2017,** *122*, 329-335.
143. Zornitta, R. L.; Srimuk, P.; Lee, J.; Krüner, B.; Aslan, M.; Ruotolo, L. A. M.; Presser, V., Charge and Potential Balancing for Optimized Capacitive Deionization using Lignin-derived, Low-cost Activated Carbon Electrodes. *ChemSusChem* **2018**.

144. Bouhadana, Y.; Avraham, E.; Noked, M.; Ben-Tzion, M.; Soffer, A.; Aurbach, D., Capacitive Deionization of NaCl Solutions at Non-steady-state Conditions: Inversion Functionality of the Carbon Electrodes. *The Journal of Physical Chemistry C* **2011,** *115* (33), 16567-16573.

145. Gao, X.; Omosebi, A.; Landon, J.; Liu, K., Surface Charge Enhanced Carbon Electrodes for Stable and Efficient Capacitive Deionization using Inverted Adsorption–desorption Behavior. *Energy & Environmental Science* **2015,** *8* (3), 897-909.

146. Srimuk, P.; Kaasik, F.; Krüner, B.; Tolosa, A.; Fleischmann, S.; Jäckel, N.; Tekeli, M. C.; Aslan, M.; Suss, M. E.; Presser, V., MXene as a Novel Intercalation-type Pseudocapacitive Cathode and Anode for Capacitive Deionization. *Journal of Materials Chemistry A* **2016,** *4* (47), 18265-18271.

147. Scrosati, B.; Garche, J., Lithium Batteries: Status, Prospects and Future. *Journal of Power Sources* **2010,** *195* (9), 2419-2430.

148. Mizushima, K.; Jones, P.; Wiseman, P.; Goodenough, J. B., LixCoO2 (0< x<-1): A New Cathode Material for Batteries of High Energy Density. *Materials Research Bulletin* **1980,** *15* (6), 783-789.

149. Bang, H. J.; Donepudi, V.; Prakash, J., Preparation and Characterization of Partially Substituted $LiM_yMn_{2-y}O_4$ (M= Ni, Co, Fe) Spinel Cathodes for Li-ion Batteries. *Electrochimica Acta* **2002,** *48* (4), 443-451.

150. Chen, Z.; Dahn, J., Methods to Obtain Excellent Capacity Retention in $LiCoO_2$ Cycled to 4.5 V. *Electrochimica Acta* **2004,** *49* (7), 1079-1090.

151. Brandt, K., Historical Development of Secondary Lithium Batteries. *Solid State Ionics* **1994,** *69* (3-4), 173-183.

152. Ozawa, K., Lithium-ion Rechargeable Batteries with $LiCoO_2$ and Carbon Electrodes: the $LiCoO_2$/C System. *Solid State Ionics* **1994,** *69* (3-4), 212-221.

153. Zhang, W.-J., A Review of the Electrochemical Performance of Alloy Anodes for Lithium-ion Batteries. *Journal of Power Sources* **2011,** *196* (1), 13-24.

154. Li, H.; Wang, Z.; Chen, L.; Huang, X., Research on Advanced Materials for Li-ion Batteries. *Advanced Materials* **2009,** *21* (45), 4593-4607.

155. Pradeep, V. S.; Graczyk-Zajac, M.; Riedel, R.; Soraru, G. D., New Insights in to the Lithium Storage Mechanism in Polymer Derived SiOC Anode Materials. *Electrochimica Acta* **2014,** *119*, 78-85.

156. Kasavajjula, U.; Wang, C.; Appleby, A. J., Nano-and Bulk-Silicon-based Insertion Anodes for Lithium-ion Secondary Cells. *Journal of Power Sources* **2007,** *163* (2), 1003-1039.

157. Wadia, C.; Albertus, P.; Srinivasan, V., Resource Constraints on the Battery Energy Storage Potential for Grid and Transportation Applications. *Journal of Power Sources* **2011,** *196* (3), 1593-1598.

158. Jayaprakash, N.; Shen, J.; Moganty, S. S.; Corona, A.; Archer, L. A., Porous Hollow Carbon@Sulfur Composites for High-Power Lithium–Sulfur Batteries. *Angewandte Chemie International Edition* **2011,** *50* (26), 5904-5908.

159. Tao, X.; Chen, X.; Xia, Y.; Huang, H.; Gan, Y.; Wu, R.; Chen, F.; zhang, W., Highly mesoporous carbon foams synthesized by a facile, cost-effective and template-free Pechini method for advanced lithium-sulfur batteries. *Journal of Materials Chemistry A* **2013,** *1* (10), 3295-3301.

160. Wild, M.; O'Neill, L.; Zhang, T.; Purkayastha, R.; Minton, G.; Marinescu, M.; Offer, G. J., Lithium sulfur batteries, a mechanistic review. *Energ Environ Sci* **2015,** *8* (12), 3477-3494.

161. Manthiram, A.; Fu, Y.; Chung, S.-H.; Zu, C.; Su, Y.-S., Rechargeable Lithium–Sulfur Batteries. *Chemical Reviews* **2014,** *114* (23), 11751-11787.

162. Fu, C.; Wong, B. M.; Bozhilov, K. N.; Guo, J., Solid State Lithiation–delithiation of Sulphur in Sub-nano Confinement: a New Concept for Designing Lithium–sulphur Batteries. *Chemical Science* **2016,** *7* (2), 1224-1232.

163. Li, Z.; Li, X.; Liao, Y.; Li, X.; Li, W., Sulfur Loaded in Micropore-rich Carbon Aerogel as Cathode of Lithium-sulfur Battery with Improved Cyclic Stability. *Journal of Power Sources* **2016,** *334*, 23-30.

164. Xu, G.; Ding, B.; Nie, P.; Shen, L.; Dou, H.; Zhang, X., Hierarchically Porous Carbon Encapsulating Sulfur as a Superior Cathode Material for High Performance Lithium–sulfur Batteries. *ACS Applied Materials & Interfaces* **2013,** *6* (1), 194-199.

165. Kim, J.-J.; Kim, H. S.; Ahn, J.; Lee, K. J.; Yoo, W. C.; Sung, Y.-E., Activation of Micropore-confined Sulfur within Hierarchical Porous Carbon for Lithium-sulfur Batteries. *Journal of Power Sources* **2016,** *306*, 617-622.

166. Reitz, C.; Breitung, B.; Schneider, A.; Wang, D.; von der Lehr, M.; Leichtweiss, T.; Janek, J. r.; Hahn, H.; Brezesinski, T., Hierarchical Carbon with High Nitrogen Doping Level: A Versatile Anode and Cathode Host Material for Long-Life Lithium-Ion and Lithium–Sulfur Batteries. *ACS Applied Materials & Interfaces* **2016,** *8* (16), 10274-10282.

167. Choudhury, S.; Zeiger, M.; Massuti-Ballester, P.; Fleischmann, S.; Formanek, P.; Borchardt, L.; Presser, V., Carbon Onion–sulfur Hybrid Cathodes for Lithium–sulfur Batteries. *Sustainable Energy & Fuels* **2017,** *1* (1), 84-94.

168. Schneider, A.; Janek, J.; Brezesinski, T., Improving the Capacity of Lithium–Sulfur Batteries by Tailoring the Polysulfide Adsorption Efficiency of Hierarchical Oxygen/Nitrogen-Functionalized Carbon Host Materials. *Physical Chemistry Chemical Physics* **2017,** *19* (12), 8349-8355.

169. Krüner, B.; Lee, J.; Jäckel, N.; Tolosa, A.; Presser, V., Sub-Micrometer Novolac-Derived Carbon Beads for High Performance Supercapacitors and Redox Electrolyte Energy Storage. *ACS Applied Materials & Interfaces* **2016,** *8* (14), 9104-9115.

170. Krüner, B.; Srimuk, P.; Fleischmann, S.; Zeiger, M.; Schreiber, A.; Aslan, M.; Quade, A.; Presser, V., Hydrogen-treated, Sub-micrometer Carbon Beads for Fast Capacitive Deionization with High Performance Stability. *Carbon* **2017,** *117*, 46-54.

171. Jäckel, N.; Emge, S. P.; Krüner, B.; Roling, B.; Presser, V., Quantitative Information about Electrosorption of Ionic Liquids in Carbon Nanopores from Electrochemical Dilatometry and Quartz Crystal Microbalance Measurements. *The Journal of Physical Chemistry C* **2017,** *121* (35), 19120-19128.

172. Krüner, B.; Schreiber, A.; Tolosa, A.; Quade, A.; Badaczewski, F.; Pfaff, T.; Smarsly, B. M.; Presser, V., Nitrogen-containing novolac-derived carbon beads as electrode material for supercapacitors. *Carbon* **2018,** *132*, 220-231.

173. Choudhury, S.; Krüner, B.; Massuti-Ballester, P.; Tolosa, A.; Prehal, C.; Grobelsek, I.; Paris, O.; Borchardt, L.; Presser, V., Microporous Novolac-derived Carbon Beads/Sulfur Hybrid Cathode for Lithium-Sulfur Batteries. *Journal of Power Sources* **2017,** *357*, 198-208.

174. Krüner, B.; Dörr, T. S.; Shim, H.; Sann, J.; Janek, J.; Presser, V., Gyroidal porous carbon activated with NH_3 or CO_2 as lithium-sulfur battery cathodes. *Batteries & Supercaps* **2018,** *1* (2), 83-94.

175. Krüner, B.; Odenwald, C.; Quade, A.; Kickelbick, G.; Presser, V., Influence of Nitrogen-Doping for Carbide-Derived Carbons on the Supercapacitor Performance in an Organic Electrolyte and an Ionic Liquid. *Batteries & Supercaps* **2018**. [DOI: 10.1002/batt.201800051]

176. Krüner, B.; Odenwald, C.; Jäckel, N.; Tolosa, A.; Kickelbick, G.; Presser, V., Silicon Oxycarbide Beads from Continuously Produced Polysilsesquioxane as Stable Anode Material for Lithium-ion Batteries. *ACS Applied Energy Materials* **2018,** *1* (6), 2961-2970.

177. Werner, J. r. G.; Johnson, S. S.; Vijay, V.; Wiesner, U., Carbon–sulfur Composites from Cylindrical and Gyroidal Mesoporous Carbons with Tunable Properties in Lithium–sulfur Batteries. *Chemistry of Materials* **2015,** *27* (9), 3349-3357.

178. Choudhury, S.; Agrawal, M.; Formanek, P.; Jehnichen, D.; Fischer, D.; Krause, B.; Albrecht, V.; Stamm, M.; Ionov, L., Nanoporous Cathodes for High-energy Li–S batteries from Gyroid Block Copolymer Templates. *ACS Nano* **2015,** *9* (6), 6147-6157.

179. Wilamowska-Zawlocka, M.; Puczkarski, P.; Grabowska, Z.; Kaspar, J.; Graczyk-Zajac, M.; Riedel, R.; Sorarù, G. D., Silicon Oxycarbide Ceramics as Anodes for Lithium Ion Batteries: Influence of Carbon Content on Lithium Storage Capacity. *RSC Advances* **2016,** *6* (106), 104597-104607.

180. Pradeep, V. S.; Ayana, D. G.; Graczyk-Zajac, M.; Soraru, G. D.; Riedel, R., High Rate Capability of SiOC Ceramic Aerogels with Tailored Porosity as Anode Materials for Li-ion Batteries. *Electrochimica Acta* **2015,** *157*, 41-45.

Curriculum vitae

Benjamin Krüner

- **Born: 31.05.1988 in Herborn (Germany)**
- **Nationality: German**
- **Family status: married**

- **PhD Student**
- **Saarland University & INM-Leibniz Institute for New Materials**
- **Division Energy Materials**

Education

since 06/2015	**PhD student** Saarland University & INM-Leibniz Institute for New Materials, Saarbrücken, Germany Thesis: *„Polymer-derived carbides and carbons with and without nitrogen-doping for electrochemical energy applications“*
since 06/2015	**Member of Graduate School „Synthesis and characterization of materials“ (SYCMA)** Saarland University, Saarbrücken, Germany
04/2013 – 05/2015	**Master of Science in Material Chemistry** Saarland University, Saarbrücken, Germany Thesis: *„Synthesis and characterization of carbon-derived carbon beads“*
09/2009 – 09/2012	**Bachelor of Science in Advanced Materials** Justus-Liebig University, Giessen, Germany Thesis: *„Synthesis of organically functionalized oxoclusters”*
08/2004 – 01/2008	**Apprenticeship as Chemical Laboratory Technician** Wendel GmbH, Enamel and Glazes Factory, Dillenburg, Germany Werner von Siemens School, Wetzlar, Germany

Professional experience

since 06/2015	**PhD student** INM-Leibniz Institute for New Materials, Saarbrücken, Germany
06/2008 – 02/2009	**Community service as an alternative to military service** Stuttgarter Jugendhaus gGmbH, Stuttgart, Germany
04/2009 – 07/2009	**Chemical Laboratory Technician** Henkel Australia Pty Ltd, Sydney, Australia
02/2008 – 04/2008	**Chemical Laboratory Technician** Wendel GmbH, Enamel and Glazes Factory, Dillenburg, Germany

Scholarships & awards

- GDCh travel award to participate the first annual meeting of the section Chemistry and Energy 2016, 10/2016
- Central Study Funds of Nassau, 09/2013 – 03/2015
- GDCh travel award to participate the Wöhler-Conference 2014, 09/2014
- RISE Worldwide scholarship from German Academic Exchange Service (DAAD) for research internship in Padua, Italy, 06/2012 – 07/2012

Publications

Overview: 27 peer-review publications; 8x first author; h-index: 12; i10-index: 16; citations: 362

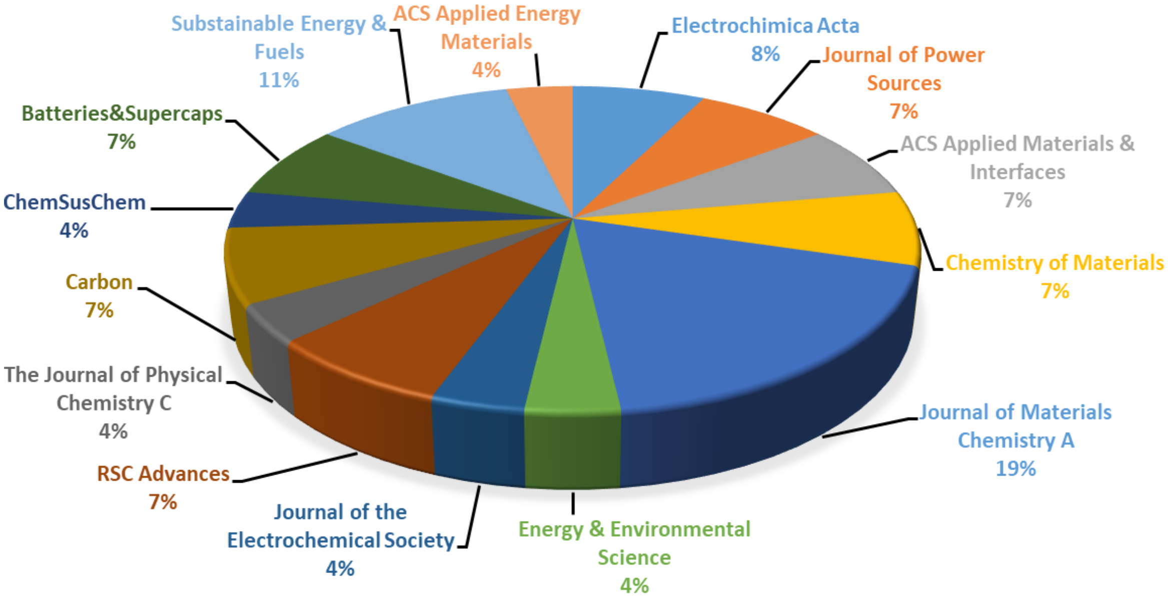

J-1 **Krüner, B.**, Odenwald, C., Quade, A., Kickelbick, G., Presser, V. (2018): Influence of Nitrogen-Doping for Carbide-Derived Carbons on the Supercapacitor Performance in an Organic Electrolyte and an Ionic Liquid. *Batteries & Supercaps*. DOI:10.1002/batt.201800051

J-2 **Krüner, B.**, Odenwald, C., Jäckel, N., Tolosa, A., Kickelbick, G., Presser, V. (2018): Silicon Oxycarbide Beads from Continuously Produced Polysilsesquioxane as Stable Anode Material for Lithium-Ion Batteries. *ACS Applied Energy Materials*, 1 (6), 2961-2970.

J-3 Zornitta, R. L., Srimuk, P., Lee, J., **Krüner, B.**, Aslan, M., Martins Ruotolo, L. A., Presser, V. (2018): Charge and Potential Balancing for Optimized Capacitive Deionization Using Lignin-Derived, Low-Cost Activated Carbon Electrodes. *ChemSusChem*, 11, 2101-2113.

J-4 **Krüner, B.**, Dörr, T. S., Shim, H., Sann, J., Janek, J., Presser, V. (2018): Gyroidal Porous Carbon Activated with NH_3 or CO_2 as Lithium-Sulfur Battery Cathodes. *Batteries & Supercaps*, 1 (2), 83-94.

J-5 **Krüner, B.**, Schreiber, A., Tolosa, A., Quade, A., Badaczewski, F., Pfaff, T., Smarsly, B. M., Presser, V. (2018): Nitrogen-containing novolac-derived carbon beads as electrode material for supercapacitors. *Carbon*, 132, 220-231.

J-6 Tolosa, A., Widmaier, M., **Krüner, B.**, Griffin, J. M., Presser, V. (2018): Continuous silicon oxycarbide fiber mats with tin nanoparticles as high capacity anode for lithium-ion batteries. *Sustainable Energy & Fuels*, 2, 215-228.

J-7 Feischmann, S., Leistenschneider, D., Lemkova, V., **Krüner, B.**, Zeiger, M., Borchardt, L., Presser, V. (2017): Tailored Mesoporous Carbon/Vanadium Pentoxide Hybrid Electrodes for High Power Pseudocapacitive Lithium and Sodium Intercalation. *Chemistry of Materials*, 29 (20), 8653-8662.

J-8 Jäckel, N., Emge, S. P., **Krüner, B.**, Roling, B., Presser, V. (2017): Quantitative Information about Electrosorption of Ionic Liquids in Carbon Nanopores from Electrochemical Dilatometry and Quartz Crystal Microbalance Measurements. *The Journal of Physical Chemistry C*, 121 (35), 19120-19128.

J-9 **Krüner, B.**, Odenwald, C., Tolosa, A., Schreiber, A., Aslan, M., Kickelbick, G., Presser, V. (2017): Carbide-Derived Carbon Beads with Tunable Nanopores from Continuously Produced Polysilsesquioxanes for Supercapacitor Electrodes. *Sustainable Energy & Fuels*, 1 (7), 1588-1600.

J-10 Fleischmann, S., Zeiger, M., Jäckel, N., **Krüner, B.**, Lemkova, V., Widmaier, M., Presser, V. (2017): Tuning Pseudocapacitive and Battery-like Lithium Intercalation in Vanadium Dioxide/Carbon Onion Hybrids for Asymmetric Supercapacitor Anodes. *Journal of Materials Chemistry A*, 5 (25), 13039-13051.

J-11 Choudhury, S., **Krüner, B.**, Massuti-Ballester, P., Tolosa, A., Prehal, C., Grobelsek, I., Paris, O., Borchardt, L., Presser, V. (2017): Microporous Novolac-Derived Carbon Beads / Sulfur Hybrid Cathode for Lithium-Sulfur Batteries. *Journal of Power Sources*, 357 (1), 198-208.

J-12 Lee, J., Tolosa, A., **Krüner, B.**, Kim, D., Fleischmann, S., Zeiger, M., Presser, V. (2017): Asymmetric Tin-Vanadium Redox Electrolyte for Carbon Electrodes with High Power Energy Storage. *Sustainable Energy & Fuels*, 1 (2), 299-207.

J-13 **Krüner, B.**, Srimuk, P., Fleischmann, S., Zeiger, M., Schreiber, A., Aslan, M., Quade, A., Presser, V. (2017): Hydrogen-Treated, Sub-Micrometer Carbon Beads for Fast Capacitive Deionization with High Performance Stability. *Carbon*, 117, 46-54.

J-14 Fleischmann, S., Tolosa, A., Zeiger, M., **Krüner, B.**, Peter, N., Grobelsek, I., Quade, A., Kruth, A., Presser, V. (2017): Vanadia-titania multilayer nanodecoration of carbon onions via atomic layer deposition for high performance electrochemical energy storage. *Journal of Materials Chemistry A*, 5, 2792-2801.

J-15 Srimuk, P., Zeiger, M., Jäckel, N., Tolosa, A., **Krüner, B.**, Fleischmann, S., Grobelsek, I., Aslan, M., Shvartsev, B., Suss, M. E., Presser, V. (2017): Enhanced performance stability of carbon/titania hybrid electrodes during capacitive deionization of oxygen saturated saline water. *Electrochimica Acta*, 224, 314-328.

J-16 Jäckel, N., **Krüner, B.**, van Aken, K., Alhabeb, M., Anasori, B., Kaasik, F., Gogotsi, Y., Presser, V. (2016): Electrochemical in situ tracking of volumetric changes in two-dimensional metal carbides (MXenes) in ionic liquids. *ACS Applied Materials & Interfaces*, 8 (47), 32089-32093.

J-17 Zeiger, M., Ariyanto, T., **Krüner, B.**, Peter, N. J., Fleischmann, S., Etzold, B. J. M., Presser, V. (2016): Vanadium Pentoxide / Carbide-Derived Carbon Core-Shell Hybrid Electrodes for high Performance Electrochemical Energy Storage. *Journal of Materials Chemistry A*, 4, 18899-18909.

J-18 Srimuk, P., Kaasik, F., **Krüner, B.**, Tolosa, A., Fleischmann, S., Jäckel, N., Tekeli, M. C., Suss, M., Aslan, M., Presser, V. (2016): MXene as a novel intercalation-type pseudocapacitive cathode and anode for capacitive deionization. *Journal of Materials Chemistry A*, 4, 18265-18271.

J-19 Zeiger, M., Fleischmann, S., **Krüner, B.**, Tolosa, A., Bechtel, S., Baltes, M., Schreiber, A., Presser, V. (2016): Influence of Carbon on the Electrochemical Performance of Carbon/Manganese Oxide Hybrids in Aqueous and Organic Electrolytes. *RSC Advances*, 107163-107179.

J-20 Srimuk, P., Ries, L., Zeiger, M., Fleischmann, S., Jäckel, N., Tolosa, A., **Krüner, B.**, Aslan, M., Presser, V. (2016): High performance stability of titania decorated carbon for desalination with capacitive deionization in oxygenated water. *RSC Advances*, 6 (108), 106081-106089.

J-21 Widmaier, M., **Krüner, B.**, Jäckel, N., Aslan, M., Fleischmann, S., Engel, C., Presser, V. (2016): Carbon as Quasi-Reference Electrode in Unconventional Lithium-Salt Containing electroly. *Journal of The Electrochemical Society*, 163 (14):A2956-A2964.

J-22 Lee, J., **Krüner, B.**, Tolosa, A., Daekyu, K., Choudhury, S., Seo, K. H., Presser, V. (2016): Tin/vanadium redox electrolyte combining battery-like energy storage capacity with supercapacitor-like power handling. *Energy & Environmental Science*, 9, 3392-3398.

J-23 Tolosa, A., **Krüner, B.**, Fleischmann, S., Jäckel, N., Zeiger, M., Aslan, M., Grobelsek, I., Presser, V. (2016): Make two out of one: niobium carbide nanofibers as a versatile precursor for supercapacitor and battery electrodes. *Journal of Materials Chemistry A*, 2016, 4, 16003-16016.

J-24 Fleischmann, S., Jäckel, N., Zeiger, M., **Krüner, B.**, Grobelsek, I., Formanek, P., Choudhury, S., Weingarth, D., Presser, V. (2016): Enhanced Electrochemical Energy Storage by Nanoscopic Decoration of Endohedral and Exohedral Carbon with Vanadium Oxide via Atomic Layer Deposition. *Chemistry of Materials*, 28 (8), 2802-2813.

J-25 **Krüner, B.**, Lee, J., Jäckel, N., Tolosa, A., Presser, V. (2016): Sub-micrometer novolac-derived carbon beads for high performance supercapacitors and redox electrolyte energy storage. *ACS Applied Materials & Interfaces*, 8, 9104-9115.

J-26 Tolosa, A., **Krüner, B.**, Jäckel, N., Aslan, M., Vakifahmetoglu, C., Presser, V. (2016): Electrospinning and Electrospraying of Silicon Oxycarbide-Derived Nanoporous Carbon for Supercapacitor Electrodes. *Journal of Power Sources*, 313 (1), 178-88.

J-27 Jäckel, N., Weingarth, D., Schreiber, A., **Krüner, B.**, Zeiger, M., Tolosa, A., Aslan, M., Presser, V. (2016): Performance Evaluation of Conductive Additives for Activated Carbon Supercapacitors in Organic Electrolyte. *Electrochimica Acta*, 191 (1), 284–98.

Talks

T-1 **Krüner, B.**, Odenwald, C., Kickelbick, G., Presser, V.: Carbide-derived Carbon Beads with Tunable Nanopores from Continuously Produced Polysilsesquioxanes for Energy Storage Devices. *Carbon2018 – The World Conference on Carbon*, Madrid (Spain), July 1st-6th, 2018. (**Keynote**)

T-2 **Krüner, B.**, Lee, J., Choudhury, S., Presser, V.: Sub-micrometer Novolac-Derived Carbon Beads as Electrodes for Supercapacitors, Redox Electrolyte Hybrids, and Li-S Batteries. *254th American Chemical Society National Meeting & Exposition*, Washington D.C. (USA), August 20th-24th, 2017.

T-3 Jäckel, N., **Krüner, B.**, van Aken, K. L., Alhabeb, M., Anasori, B., Kaasik, F., Gogotsi, Y., Presser, V.: Electrochemical In Situ Tracking of Volumetric Changes in Two-dimensional Metal Carbides (MXenes) in Ionic Liquids. *5th International Symposium on Enhanced Electrochemical Capacitors* (ISEE'Cap17), Jena (Germany), July 10th-14th, 2017.

T-4 Widmaier, M., **Krüner, B.**, Jäckel, N., Aslan, M., Fleischmann, S., Engel, C., Presser, V.: Activated Carbon Based Quasi-reference Electrodes for Unconventional Lithium-salt Containing Organic Electrolytes. *231st Meeting of the Electrochemical Society*, New Orleans (USA), May 28th-June 1st, 2017.

T-5 **Krüner, B.**, Lee, J., Tolosa, A., Presser, V.: Polymer-derived Carbon Spheres for Energy Storage Applications. *BMBF Junior Investigation Workshop Energy Research*, Dresden (Germany), November 23rd-24th, 2016.

T-6 Fleischmann, S., **Krüner, B.**, Zeiger, M., Jäckel, N., Presser, V.: Crystallization of Vanadium Oxide Coatings Fabricated by Atomic Layer Deposition on Carbon Substrates for Hybrid Energy Storage Devices. *XXV. International Materials Research Congress*, Cancun (Mexico), August 14th-19th, 2016.

T-7 Tolosa, A., **Krüner, B.**, Fleischmann, S., Jäckel, N., Aslan, M., Presser, V.: Electrospun Microporous Carbon Fibers and Niobia/Carbon Hybrid Fibers for Energy Storage. *Electrospinning for Energy Conference* (ELEN2016), Montpellier (France), June 22nd-24th, 2016

T-8 Jäckel, N., Schreiber, A., Röder, M., **Krüner, B.**, Zeiger, M., Tolosa, A., Aslan, M., Weingarth, D., Presser, V.: Influence of Surface Chemistry and Electrode Morphology on Supercapacitor Performance. *11th International Symposium on Electrochemical Micro & Nanosystem Technologies* (IEMNT2016), Brüssel (Belguim), August 17th-19th, 2016.

T-9 Lee, J., **Krüner, B.**, Tolosa, A., Sathyamoorthi, S., Kim, D., Choudhury, S., Seo, K., Presser, V.: Tin/Vanadium Redox Electrolyte Combining Battery-like Energy Storage Capacity with Supercapacitor like Power Handling. *11th International Symposium on Electrochemical Micro & Nanosystem Technologies* (IEMNT2016), Brüssel (Belguim), August 17th-19th, 2016.

T-10 Tolosa, A., Aslan, M., Jäckel, N., **Krüner, B.**, Presser, V.: Electrospun Nanofibers for Energy Storage Applications. *German-Estonian Symposium on Future Capacitive Technologies*, Tartu (Estonia), December 10st-12th, 2015.

T-11 **Krüner, B.**, Aslan, M., Zeiger, M., Presser, V.: Carbide-derived Carbon Beads. *ECUST – UdS Summer School on Materials Science and Chemistry*, Saarbrücken (Germany), October 6th-15th, 2015.

T-12 Tolosa, A., Aslan, M., Jäckel, N., **Krüner, B.**, Presser, V.: Electrospun Microporous Carbon Fibers and Carbon Hybrid Fibers for Electrochemical Applications. *8th EEIGM conference on Advanced Materials Research*, Valencia (Spain), June 11st-12th, 2015.

Posters

P-1 **Krüner, B.**, Presser, V.: Novolac-derived Carbon Beads for LiS-Batteries, Supercapacitors, and Capacitive Deionization, *8th Regionalforum Saar*, Saarbrücken (Germany), January 30th, 2018.

P-2 **Krüner, B.**, Presser, V.: Novolac-derived Carbon Beads for LiS-Batteries, Supercapacitors, and Capacitive Deionization, *5th PhD Student Day of Saarland University*, Saarbrücken (Germany), November 15th, 2017.

P-3 Tian, M., Düren, T., Lennox, M., **Krüner, B.**, Presser, V., Mays, T., Rudic, S., Ting, V. P.: Does Pore Geometry Influence Hydrogen Storage?, *COPS-XI Conference*, Avingnon (France), May 14th-17th, 2017.

P-4 Zeiger, M., Ariyanto, T., **Krüner, B.**, Peter, N. J., Fleischmann, S., Etzold, B. J., Presser, V.: V_2O_5/Carbide-derived Carbon Core-shell Particles for High Performance Electrochemical Energy Storage, *5th International Conference on Multifunctional, Hybrid and Nanomaterials*, Lisbon (Portugal), March 6th-10th, 2017.

P-5 Fleischmann, S., Tolosa, A., Zeiger, M., **Krüner, B.**, Presser, V.: Vanadia-titania Multilayer Nanodecoration of Carbon Onions via ALD for Electrochemical Energy Storage, *5th International Conference on Multifunctional, Hybrid and Nanomaterials*, Lisbon (Portugal), March 6th-10th, 2017.

P-6 Tian, M., Düren, T., Lennox, M., **Krüner, B.**, Presser, V., Mays, T., Rudic, S., Ting, V. P.: Does Pore Geometry Influence Hydrogen Storage?, *MRS Fall Meeting & Exhibit*, Boston (USA), November 27th-December 2nd, 2016.

P-7 **Krüner, B.**, Lee, J., Jäckel, N., Tolosa, A., Presser, V.: Sub-micrometer Novolac-Derived Carbon Beads for High Performance Supercapacitors and Redox Electrolyte Energy Storage, *4th PhD Student Day of Saarland University*, Saarbrücken (Germany), November 9th, 2016.

P-8 **Krüner, B.**, Lee, J., Jäckel, N., Tolosa, A., Presser, V.: Sub-micrometer Novolac-Derived Carbon Beads for High Performance Supercapacitors and Redox Electrolyte Energy Storage, *1st Conference of the GDCh section Chemistry & Energy*, Jena (Germany), October 6st-7st, 2016.

P-9 Tolosa, A., **Krüner, B.**, Fleischmann, S., Aslan, M., Presser, V.: Niobium carbide nanofibers as a precursor for supercapacitor and battery electrodes. *1st Conference of the GDCh section Chemistry & Energy*, Jena (Germany), October 6st-7st, 2016.

P-10 Tolosa, A., **Krüner, B.**, Fleischmann, S., Aslan, M., Presser, V.: Electrospun Microporous Carbon Fibers and Niobia/Carbon Hybrid Fibers for Electrochemical Applications. *Materials Science and Engineering*, Darmstadt (Germany), September 27th-29th, 2016.

P-11 Jäckel, N., Weingarth, D., Schreiber, A., **Krüner, B.**, Zeiger, M., Tolosa, A., Aslan, M., Presser, V.: Performance evaluation of conductive additives for supercapacitors. *67th Annual Meeting of the International Society of Electrochemistry*, The Hague (Netherlands), August 21st-26th, 2016.

P-12 **Krüner, B.**, Tolosa, A., Zeiger, M., Presser, V.: Carbide-Derived Carbon Beads for Supercapacitors, *3rd PhD Student Day of Saarland University*, Saarbrücken (Germany), November 11th, 2015.

P-13 **Krüner, B.**, Gross, S.: Synthesis and Characterization of Organic Functionalized Zirconium-Oxocluster, *18th Conference of the Wöhler Association for Inorganic Chemistry*, Saarbrücken (Germany), September 24st-26st, 2014.